The calibration process in uPVC profile extrusion.

Conrad, Ulrich

School of Engineering
University of Wales Swansea

THE CALIBRATION PROCESS IN uPVC PROFILE EXTRUSION

by

Ulrich Conrad

A Thesis Submitted for the Degree of

Doctor of Philosophy (Ph.D.)

DECLARATION AND STATEMENTS

DECLARATION

This work has not previously been accepted in substance for any degree and is not being concurrently submitted in candidature for any degree.

Signed.... .....(candidate)

Date 18.12.03

STATEMENT 1

This thesis is the result of my own investigations, except where otherwise stated.

Other sources are acknowledged by footnotes giving explicit references. A bibliography is appended.

Signed.....(candidate)

Date 18.12.03

STATEMENT 2

I hereby give consent for my thesis, if accepted, to be available for photocopying and for inter-library loan, and for the title and summary to be available to outside organisations.

Signed..... .....(candidate)

Date 18.12.03

ACKNOWLEDGEMENTS

First I would like to express my utmost gratitude to Dr. J. F. T. Pittman for his encouraging support, ideas and far-reaching discussions throughout this work.

Furthermore I would like to acknowledge Dr. Ralf Sander and Dr. Werner Schuler, formerly working for the supporting company K mmerling in P irmasens, Germany, now a member of the Profine group, at the beginning of this project, for the intention to set up this project.
I must also express my gratitude to Ivo Szarvasy formerly of the same company. Beside his work on development of software to simulate the calibration process, he has supported me in the experimental trials in the company, together with Dr. Sander and Dr. Schuler. And I must acknowledge also the team in the lab at K mmerling, who assisted in setting up and running the experimental trials.

This work was substantially supported by the European Union through the Training and Mobility of Researchers (TMR) scheme with contract number ERBFMBICT931419.

to Elfy

SUMMARY

A comprehensive experimental investigation of the calibration process in uPVC profile extrusion has been carried out. A highly instrumented calibration line was set up for a simple hollow rectangular profile (32 mm x 34 mm). Some 200 quantities monitored on line included profile surface temperatures, calibrator wall temperatures, vacuum at the profile surface, coolant temperatures and flow rate, frictional drag on each calibrator and total haul-off force. Examinations of the finished profile provided data on shrinkage, impact strength, residual stresses and profile geometry and dimensions. The following operating parameters were varied: wet versus dry calibration, applied vacuum (-0.2 bar to –0.8 bar), line speed (1 m/min to 8 m/min), mass flow rate (50 kg/h to 250 kg/h), melt extrusion temperature (180°C to 200°C), coolant temperature (16°C to 40°C), number of water injection points in Calibrator 1 die exit dimension (1.50 mm or 2.50 mm) and profile wall thickness (1.50 mm to 3.25 mm).

The extensive data collected provide detailed insights into the dependence of the temperature courses along the line, haul-off forces, and finished profile properties on operating parameters.

A finite difference calculation is set up to estimate heat transfer coefficients from the recorded temperatures.

The overall thermal resistance is broken down into profile-calibrator contact, metal and coolant film components, thus displaying the dependence of contact resistance on operating conditions. Results for final profile geometry and haul-off forces are compared with predictions from finite element simulations developed in a parallel project. Results of this preliminary comparison are encouraging.

The results of this work, because of its uniquely comprehensive approach, provide further insights into the process and support parallel projects developing simulations and optimization methods for profile calibration.

Table of contents

CHAPTER 1

Introduction

Profile extrusion delivers semifinished products as a basis for a wide range of applications. The materials used cover a wide range from metals to polymers. For all applications, the production must be made as economical as possible whilst maintaining a high level of product properties. Here, the whole process chain must be considered and investigated, with a view to optimization on the basics of present knowledge, and for the introduction of new technologies.

This work is a part of a cluster of projects with the vision to simulate and optimize the profile extrusion process for uPVC, from the entrance of the die to the final profile. The particular parts of the uPVC profile extrusion process are shown in outline in Figure 1.1.

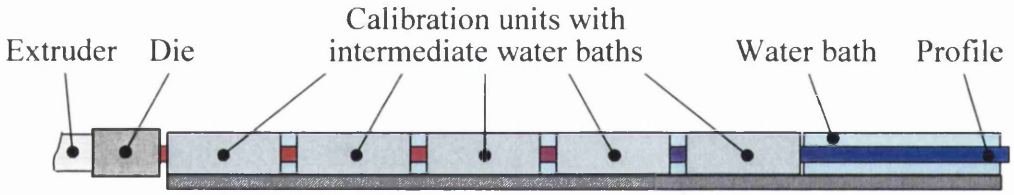

Figure 1.1: Section of profile extrusion process

The raw uPVC used here is processed with additives on an extruder, which melts and homogenises the components, and builds up a pressure to overcome the flow resistance of the die in downstream direction. In the die, the melt is distributed to a preliminary profile shape at the die exit. From the die exit, the melt goes into the calibration section, where the molten PVC is cooled down and its dimensions fixed for final profile. More details of the overall profile extrusion process will be given in Chapter 3 of this work.

Unplasticised PVC is commonly used in a wide range of applications and in large quantities e.g. in the building area, tailor made with additives to achieve the required material properties. In 2001, 2.862 million tonnes of PVC were consumed by the European construction industry, from which in the profiles section 1.32 million tonnes (46% of total) were used [1]. The uPVC is used due to its the well-known handling and robustness behaviour. During recent

years, the requirements on the material properties for window profiles have become more stringent, e.g. better insulation, higher stiffness. The demands from the market have to be fulfilled and due to the increased complexity of the window profiles, a better understanding of the process is required to indicate the key problems and cost origins. Furthermore, the output of the production has also to be increased by an increase of line speed, and also by using double line extrusion, together with improved design of the extruder giving higher throughputs at the same or better product quality.

A key problem in the profile calibration process is the time-consuming trial and error procedure used to adjust the manufactured tools, from the entrance of the die to the end of the calibration section, to get the required profile dimensions at given throughput or line speed.

Manual optimization of dies and calibration units is traditionally used in the so-called "run-in" procedure, where the die and calibration section is mounted on a calibration line and run under the specified processing conditions, and in the light of the outcome of the trail runs, the die and calibration units are modified to fulfil the product and production demands. Proper documentation of earlier designs can assist with the development of new tools for profiles with similar features.

However, given the demands for ever more complex profiles designs, and for increased productivity, this approach has serious limitations. Development costs and time to market can be reduced by improved understanding of the complexities of the process, and the incorporation of this into computer simulations, allowing virtual "run-in" trails, replacing or supplementing the expensive traditional development methods. Furthermore, computer methods can be used to automatically optimize tooling design and processing conditions. Objective functions are defined to measure the quality the outcomes, and these are evaluated from computer simulations of the process. Mathematical optimization methods are then used to adjust key tooling dimensions or processing conditions to maximise the quality, productivity etc..

This can reduce the number of loops of the run-in procedure, which for complex uPVC profiles can be as large as 20 cycles using traditional methods. If the cycles can be reduced by 50%, half of costs in developments could be saved. Typical costs are e.g. € 50,000 for the traditional run-in of one tool set and it is estimated that 1,000 tools sets are manufactured every year in Europe. The reduction of costs would then be € 25,000,000 per year.

In the present cluster of projects, this approach is being used for the design of profile extrusion dies. Simulations of the calibration process have also been developed and will be applied within an optimization scheme.

The present work is concerned with a detailed experimental investigation of the profile calibration process, to provide insights and to guide and validate computer simulations.

The investigations in the following Chapters are believed to be the most comprehensive ever undertaken, in terms of the number of process variables and outcomes simultaneously monitored, and in the range of processing conditions examined.

In the first sections of this work, an overview of the process chain will be presented. This includes the properties of the base materials, followed by a description of the profile calibration process. With the basic understanding of the profile extrusion process, an experimental set-up will be described to investigate the effects of the process parameters on the dependent parameters measured on-line in the of the calibration process, and on the properties of the final product.

Experimental results are then presented under the headings: temperatures and haul-off forces along the calibration line, final profile geometry, shrinkage and impact properties of the finished profile. A detailed study of heat transfer is carried out, using finite difference calculations, leading to evaluation of the heat transfer coefficients. Finally, the geometry and dimensions of the finished product are compared with results of the finite element simulations carried out in a parallel project, to indicate further developments needed for simulations of the profile extrusion process in the near future.

CHAPTER 2

PVC properties

This Chapter gives a brief overview of the raw PVC material production and the use of additives, modifiers, fillers, etc. More specific details can be found in a wide range of literature. Furthermore some material properties of uPVC will be presented as well.
The main material used nowadays in the building area, especially for window profiles, is uPVC in combination with weather stripping made of rubber mixtures. Plastizied PVC can also be produced from the raw basic material of PVC, but this Chapter is focussed on uPVC due to the topic of this work.

To obtain accepted and standardized material properties, the basic raw material of PVC is modified with additives, fillers, etc., because it does not fulfil the required standards after the polymerisation. Additionally, the material properties can be influenced by the process parameters in the production chain from the polymerisation to produce the raw material through to the final product. But if they are controlled appropriately, they can contribute to obtaining the required material properties.

In Figure 2.1, the production chain is shown from the monomer, the vinyl chloride, to the final fabricated part.

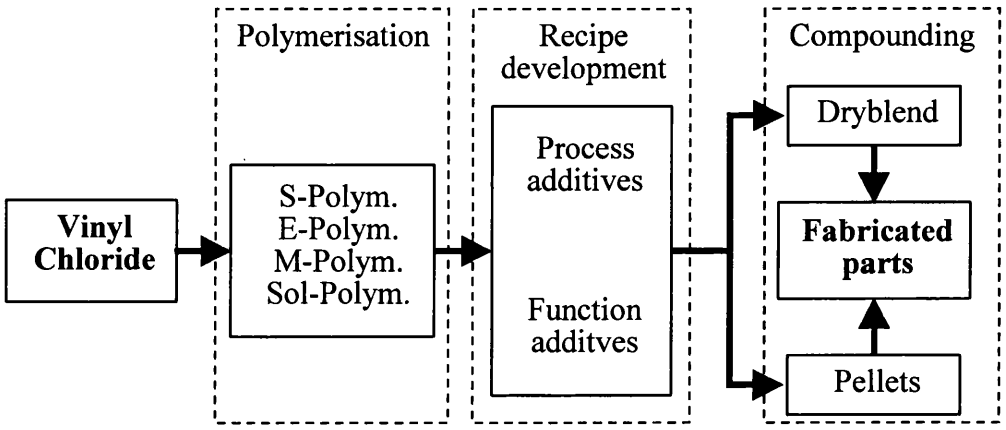

Figure 2.1: Production chain from the raw material to the final product

The starting point is the vinyl chloride, which is produced on a large commercial scale. In the next step follows the polymerisation and the final product is the raw PVC. With the use of additives, the raw PVC is mixed and can be compounded afterwards in two ways. First, the dry blend is used for the direct extrusion of the final product uPVC [2], e.g. in the profile extrusion. The second route is to compound and pelletize the PVC. Here, the pellets are used mainly in special applications, e.g. injection moulding, low throughput, etc..

In the next sections the steps of the production chain are presented in more detail.

2.1 Production of PVC compounds

2.1.1 Production of raw PVC

As mentioned before, the origin of the raw PVC is the vinyl chloride. More details of the mass production of vinyl chloride are presented e.g. in [3-6].

The vinyl chloride is then used in the polymerisation process to get to the raw PVC. There are different polymerisation processes available:

- Emulsion polymerization (E-PVC)
- Mass or bulk polymerisation (M-PVC)
- Suspension polymerisation (S-PVC)
- Solution polymerisation (Sol-PVC)

The most widely used commercial process for the production of the high molecular weight polymer [7] is the suspension polymerisation, followed by emulsion, mass and solution polymerisation [5]. This is mainly based on the use, the properties and the costs of production of the raw PVC.

The suspension-polymerised raw PVC is mainly used in the profile extrusion process, followed by the mass polymerised raw PVC [8,9].

An important factor for the raw PVC properties is the type of the polymerisation process [10]. The grain size and K-Values are polymerisation process dependent [11]. Here, the K-Value describes the viscous behaviour of the PVC, which is measured using a solvent. But the measured K-Value is also dependent on the type of solvent [5]. The ISO standard 1628-2 can

be used to describe the viscosity of the PVC, but the K-Value is used more commonly. Correlations of K-Value and viscosity according to ISO1628-2 are shown in the literature, e.g. in [5]. Furthermore, a correlation of the K-Value can be made with the molecular weight [5,12].

The K-Value is used to define the application of the PVC. Raw PVC with K-Values of 55-60 is used for blow and injection moulding; K-Values of 58-63 for extrusion and calandering of sheets [11] and for profile extrusion, raw PVC with higher K-Values is used [11,13]. An overview of the K-Value and the corresponding applications are presented in [6].

A correlation was shown for the influence of the K-Value on the plastification, where a lower plastification was observed with a higher content of additives at higher K-values [11]. But here, the additives might be the reason for the lower level of plastification.

Altogether, the properties are dependent on the history of the process [10], which includes the raw materials, mixing and compounding conditions. This leads to the conclusion that the PVC properties are strongly correlated with its structure, and this is confirmed in [7], where it was shown that the properties of PVC are bound up closely with the structure of the PVC grains for grain sizes bigger than 50-100 μm.

2.1.2 Structure of PVC

The structure of PVC is commonly described in terms of grains containing smaller globules, which are in turn made up from smaller particles named nodules [10], see Figure 2.2.

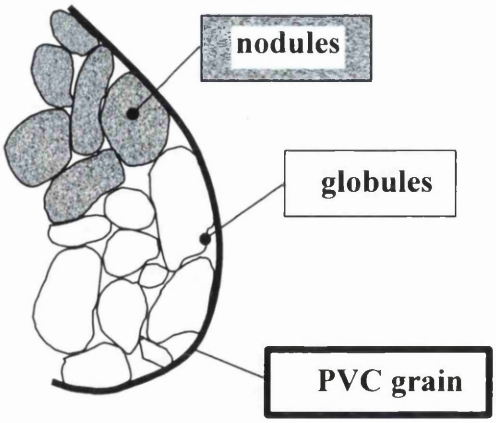

Figure 2.2: Structure of a PVC grain [10]

Menges *et al.* [14] have presented a more detailed description of the structure of PVC. The most commonly used S-PVC consists of 10-20 nm microstructures that form a 0.1-0.5 μm mid-structure, which are parts of a course structure of 1-10 μm in size. Several course structures build a primary grain, with dimensions of approximately 100 μm diameter. The structures are similar to those found by [15], where S-PVC droplets of polymerized PVC with 30-150 μm in diameter agglomerate to form grains of 100-200 μm.

Compared with the S-PVC, the E-PVC grains are built only out of particles with size of 0.1-1 μm. The M-PVC shows a two-phase microstructure. Microstructures of 30-60 nm size are formed into 5μm particles, and together with microstructures of 2 nm formed into 1-2 μm structures, the powder grain is formed. It was also mentioned that the globular structure is unchanged up to a temperature of 140°C. Then the grain boundaries are less sharp-edged and melt together with the surface. Furthermore, the globules are present up to temperatures of 170°C independent of size, type of polymerisation and conditions [14]. This is the same temperature range as presented in [15]. Here it was found that from 140-180°C, the grains first have their skins torn open, and then break down to primary particle flow units.

In [10], the structure of PVC is described similarly. With nodules up to 10 nm as sub-micro-particles, globules are created with a size of 0.2 to 2 μm as micro-particles, and grains of approx. 100 μm are formed.

Another reference [16] has described the structure hierarchy as macro-radicals, 100-200 (Angstr m) micro -domains, 0.1-0.2 μm domains, 0.6-0.8 μm primary particles, 1-10 μm agglomerates and finally PVC grains.

If the globules are not packed very close together, an incorporation of additives is possible [7]. This may contribute to varying mechanical behaviour of PVC. A honeycomb structure has given higher impact values than a homogenous structure of the material [17].

More details of the PVC structure are presented in [7] and [4].

2.1.3 Crystallinity

Although PVC is commonly regarded as an amorphous polymer, the material contains important crystalline parts. A primary crystallinity is present after polymerisation of the raw PVC. The secondary crystallinity occurs during melt processing and is formed during the

cooling which affects the mechanical properties of the final grade [18]. The crystallinity and melt behaviour are dependent on the number, size and order of the crystalline areas, and on the thermal history above the glass transition temperature [7]. Also important is the processing temperature and the cooling rate, and the higher these are, the lower is the crystallinity [7].

The crystallinity of a commercial PVC grade is given in literature as between 5% and 10%; in detail, 5% [17], 5-10% [18], 5-8% for polymerisation at normal temperatures [19], approx. 10% [7,20] and 10% for unorientated PVC [21]. So the uPVC can be more correctly classified as a semi-crystalline polymer [20].

The range of crystallinity can be varied with the conditions of the polymerisation and in further processing steps. The crystallinity can be restricted by the length of syndiotactic units, i.e. ordered regions along the polymer chain [18]. In [7], a crystalinity of 6% was shown for an S-PVC for a density of 1.53 g/cm^3 and molecular weight of 84000 g/mol), for M-PVC 12% at the same density and molecular weight, and 5% for E-PVC at a density of 1.53 g/cm^3 and molecular weight of 76500 g/mol.

Further data on densities of PVC and crystallinity are shown in the literature. A density of 1.45 g/cm^3 was given for the crystalline phase and 1.396 g/cm^3 for the amorphous phase. With a portion of 8% for the crystalline and 92% of the amorphous phase, a density of 1.40 g/cm^3 was calculated [19]. This corresponds to the densities in [7], where densities of 1.4038 g/cm^3 are given for S-PVC, for M-PVC a density of 1.3953 g/cm^3 and for E-PVC of 1.3944 g/cm^3 for an unknown degree of crystallinity.

The values for the amorphous phase are in the same range, as presented in the literature. Densities of 1.377 g/cm^3 for S-PVC, 1.373 g/cm^3 for M-PVC and 1.387 g/cm^3 for E-PVC are shown in [7].

Another reference has given a slightly higher density for the crystalline phase of approx. 1.53 g/cm^3 and for the amorphous phase of approx. 1.373 g/cm^3 [21].

Changes of crystallinity are noted with stretching or orientation of material [7]. Stretching with a maximum increase of density of 0.002 g/cm^3 leads to a change in crystallinity of approx. 1.3% [21]. The effect of stretching is present in the calibration process. Here, thin surface layers are stretched during the cooling due to applied forces in the calibration units after leaving die exit.

As mentioned before, the processing conditions have an influence on the crystallinity. The temperature range of crystalline melting goes from 160°C to approx. 230°C, due to the formation by syndiotactic sequences [22] and so the maximum melting point of crystallites is never reached in the PVC extrusion process [23]. An increase of melt temperatures leads to a melting of low-order crystallites, and up to 180°C to 190°C the primary crystallites seem to be dominant. Above this temperature, the secondary crystallinity is dominant [23].

2.1.4 Gelation

The gelation (fusion in the US) can be defined as the melting of PVC particles to a homogeneous mass under the influence of temperature and mechanical shear [11]. The level of gelation is given as a percentage of the fully homogenised mass and the level is dependent on the processing conditions and shows relations with the properties of the processed PVC. Wide ranges of investigations have been done and are presented in the literature to show the influences of the process parameters, e.g. in [24]. A short overview is now presented.

The gelation seems to be an attractive way to describe the properties of the processed PVC, but it is quite complex and so cannot be used for a simple description of the influence of processing conditions on the material properties [25].

The gelation level increases with increase of barrel temperatures and with the increase of screw speed in a twin-screw extruder [2,26,27]. An increase can also be achieved with a change of lubricants in the formulation at constant extruder settings, resulting in an increase of melt temperature [28]. Another phenomena was presented in [26], where the gelation stays at the same level up to a certain melt temperature, due to the presence of a particle structure. This author has also mentioned an increase of gelation level for an increase of processing time in a kneader.
Furthermore the rate of gelation seems to be dependent on lubricants in the compound as mentioned in [11], and it was found that an increase of lubricants delays the gelation [29].

In several publications an optimum gelation level was found for maximum properties of the PVC. A gelation level of 50%-70% leads to maximum notched impact strength for a PVC with ethylene vinyl acetat (EVA) as an impact modifier and, with higher gelation levels, the

impact strength decreases [26]. This is confirmed in [11], where a gelation level of 75% leads to a maximum of tensile strength, showing also a decrease at higher gelation levels as in the previous reference. Also the fracture stress and strain are dependent on the gelation, as shown in [2], where an increase of fracture stress and strain was obtained with an increase of the gelation level.
The gelation level seems to have an optimum, as shown in [30] in processing with a rolling mill and Brabender extruder. The gelation increases with the increase of melt temperature from 150°C to a maximum gelation level at 200°C.

Comparisons of the processing on a single screw extruder (SSE) and a twin-screw extruder (TSE) have been made. Here, higher gelation levels are necessary on a single screw extruder to obtain the same mechanical properties [31]. To interpret these findings, more details must be known, e.g. the energy input of the heaters, surface area for heat transfer from the barrels to the polymer, residence time, specific energy input of the screw and the melt temperature. All these listed process parameters have an influence on the gelation, and influence the results in literature presented above.

The K-Value of the PVC influences the gelation temperature. It is shown in [26] that the gelation temperature increases with the K-Value for a gelation level of approx. 50%. And in [29] it was stated that a higher melt temperature is needed to achieve the same gelation as the K-value increases.

Furthermore, the toughness of PVC is also sensitive to level of gelation as reported in [32], whereas the tensile properties are not sensitive to the gelation level.

Finally, the gelation level seems to have an influence on the die swell. An increase of die swell was observed with an increase of the gelation level [26].

2.1.5 Orientation

The mechanical properties of PVC can also be influenced by the orientation of the material.

It has been shown, that for uPVC, the tensile stress at break could be increased by 43% for a draw ratio of 1.5 with reduction of elongation at break at 90°C, and the tensile stress at break was also increased by a factor of 1.74 [33].
The increase of orientation can be produced by stretching above 80°C, as shown in [11]. More results for dependence of material properties on orientation are given in [34,35].

The material properties are dependent on stretching or drawing ratio. A uni-axial stretching of a specimen leads to a preferred orientation of chains, which is explained as a frozen-in non-equilibrium state [7]. In [21] it was stated that stretching of a specimen increases the density of PVC with an increase of orientation; a maximum increase of density is achieved for a uni-axial stretched specimen, and less for equi-biaxial stretching. This was confirmed in [18], where uni-axial stretching increases the tensile strength by 56% in the tensile direction, but transversely, the value dropped by 38% for a draw ratio of 2.0 without annealing. An annealing for 60 min at 110°C increased the strength by 11%, whereas in the transverse direction, the strength was reduced by only 0.3% for the same draw ratio.

2.2 Additives for PVC

The raw PVC cannot resist destruction of the structure in the compounding steps, and to fulfil the required standards for the applications of the final product, additives are necessary to improve the properties.
The additives, added to the PVC after the polymerisation, can be split into two groups, the processing and the functional additives, see Figure 2.3

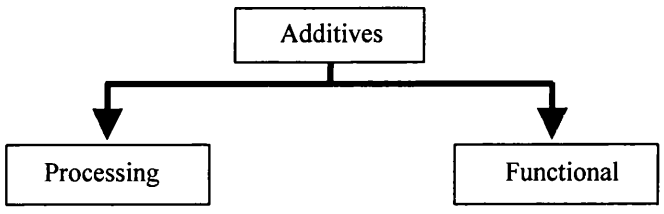

Figure 2.3: Additives of PVC

The processing additives can be separated into the stabilizers, e.g. thermal stabilizer and anti-oxidants, and the processing aids, e.g. lubricants.

The functional additives are used for flame protection, colouring, weather resistance and improvement of the impact.

Altogether, the additives and fillers work with complex interactions, but they can be optimised in combination with the compounding step to achieve the required material properties. To understand all the influences of the additives and fillers, a systematic approach is necessary to get as much information as possible under realistic processing conditions.
It is useful to establish trends using lab-scale equipment, but full-scale tests must be carried out to provide the information for the final process [36].

2.2.1 Process additives

2.2.1.1 Stabilizer

Stabilizers are used to protect the polymer against thermal degradation and oxidation during the processing.
They are necessary because the PVC has a low thermal stability and the destruction starts at 100°C, dependent on the time-temperature function [37-39], and to avoid the separation of hydrogen chloride (HCl) [38,40], which occurs at low temperatures for long residence times, and at high temperatures for short residence times [41].
Lead, calcium/zinc or organic stabilizers are used at the moment [40], where the complex calcium/zinc system consists of different calcium, zinc and organic combinations [39]. The trend is towards use of the calcium/zinc system and this will be reinforced in the continuous development of stabilizer systems [42], due to the demands by producers for higher output rates and increased acceptance from an ecological point of view (reduction of lead stabilized systems) [43]. And in the near future, organic calcium-based stabilizers will also be more frequently requested from the market [42].

A good overview of stabilizer systems and the demands of the recent market are presented in [43].

2.2.1.2 Lubricants

The lubricants are used to reduce the friction of polymer with the surface of the extruder (outer effect), and to reduce viscous heat generation due to mechanical energy dissipation (inner effect) [17]. This is required to reduce uncontrolled friction between particles to protect sensitive particles and also to protect the stabilizer in the system [40]. Furthermore, the choices of lubricant types are important for the toughness of the PVC, as found in [44], but they should be compatible with the type of PVC used [37].

The internal types of lubricants are soluble, having a high polarity in PVC [45] and reducing the melt viscosity; whereas external lubricants surround the PVC grains and decrease the internal and external friction coefficients [22]. At later stages in the processing, the external lubricants may exude from the material stream and create a low viscosity film separating the PVC from the channel surface [22].
A comparison of internal and external lubricants has shown higher values for the impact strength for the internal lubrication system [17].

The lubricants also have an effect on the final material strength. In [10], the tensile strength, tensile strain, elastic modulus and the impact are increased with the use of dry blend and lubricants, which cover the PVC particles, due to the inner reduction of frictional forces. An investigation has shown that the use of different types of lubricants can influence the gelation level and the level of melt temperature as well [28]. Furthermore, the amount of lubricants used can have an influence, as presented in [46].

The compatibility of the lubricants is also important for the whole system, including the compounding step and the final product quality [40], and they are used also for the adjustment of the rheological properties of the melt [39].

An overview of recent development of lubricants is given in [45].

2.2.1.3 Processing aids

Processing aids, e.g. based on PMMA, are used for the reduction of plastification time, an accelerate of the gelation, improvement of the rheological properties, increase of the line output for more complex profile geometries, improvement of the optical properties, and higher light and weather resistance [39]. They can thus also sometimes be seen as a functional additive.

2.2.2 Functional additives

2.2.2.1 Impact modifier

The reason for the use of impact modifiers is to reduce peak stresses, stop micro-cracks, allow plastic flow and obtain a heterogeneous structure with separated phase areas [12]. They are essential to improve the bad impact behaviour (brittleness and notch sensitiveness) of the raw PVC, for the improvement of the final material properties.

The impact values vary with the type and amount of impact modifiers and the processing conditions [12,47-49].
It was noted in [17], that the structure of the processed material also has an influence on the mechanical properties.

Types of impact modifiers are: Copolymers, CPE (chlorinated poly(ethylene)), EVA (ethylene/vinyl acetate), polyacrylate, EVA/VC (ethylene/vinyl acetate – vinyl chloride), and ABS can also be used [12,17,27,47]. Nowadays, the preferred modifiers, namely co-polymers, are based on cross-linked polybutylacrylates due to the wide processing window at highest gelation [6].

The impact modifier can be added in different ways, and in [12,17], the options for adding EVAC are presented. It can be added in the normal mixing process, using a graft polymerisation, or using a HI-(High Impact)-PVC concentrate mixed with normal PVC material.

The impact values of PVC compounded on a twin-screw-extruder (TSE) were found to be higher than for a single screw extruder [50]. On a TSE, the processing temperature dominates the impact properties [44].
In [11], a dependency of impact on rolling, pressing and injection temperature was found, as well as a dependence on the test temperatures, as is well known. This was confirmed in [50], where specimens of PVC were prepared using a pressing procedure after the processed material has left the die exit, which gave higher impact values than without pressing.

The impact behaviour of PVC can be influenced by the molecular weight. In the literature, higher impact values have been found at higher molecular weight [15] and Summers [51]. A small variation of impact values can also lead to a rapid increase of fracture stress values [2].

In conclusion, the optimisation of the content and types of impact modifiers is important together with the development of stabilizers and processing conditions in meeting the final product requirements.

2.2.2.2 Stabilizers

Stabilizers are used to protect the final PVC material against ultraviolet light and thermal degradation due to weathering, e.g. variation of temperatures due to the use in various climate zones [37,38,40]. The stabilizers needed here are similar to the stabilizers used to avoid thermal degradation in the processing of the PVC. So good combinations of both aspects have to be considered in the choice of the stabilizers.

Furthermore, discolouration must also be voided in the same way, as a loss of gloss is not acceptable for the final product, and this means that the material must be resistant to aging. The use of processing aids, shown in a Section above, also gives an improvement of weather and light resistance and so they are similar to stabilizers mentioned here.

A good overview of stabilizer systems is given in [40], and results of tests to evaluate weather protection are presented in [43].

2.2.2.3 Pigments

Inorganic and organic pigments are used in the uPVC formulation, depending on the purpose of the requirements. Some of the influences of the pigments on the material properties are presented in [41].

White pigments are defined as pigments with refractive index above 1.7, namely titanium dioxide (TiO_2) [41], which is mainly used for PVC [39]. The titanium dioxide pigment is surface treated to improve the reflective behaviour and resistance to ultraviolet light [39].

Higher titanium dioxide fractions increase the notched impact strength at higher melt extrusion temperatures, reaching a peak at 187°C [50].

A more detailed overview of recent development and aspects of use of pigments is presented in [52].

2.2.2.4 Fillers

The use of fillers can influence the material properties as well.

Calcium carbonate ($CaCO_3$) is widely used as a mineral filler, and this can increase the elastic modulus and reduce the plate-out, as was reported in [53]. The calcium carbonate can also have a big influence on the gloss of the profile [54]. It can also reduce the price, dependent on the price of the base polymer [39]. Two types of calcium carbonate are available, the natural mineral and that produced synthetically. The natural chalk needs more processing steps before final use, such as milling and surface treatment, compared to the synthetic chalk; but each type has its advantages and disadvantages in relation to e.g. agglomeration, conveying, etc. [39].

The size of the filler particles also has an influence on the impact properties. Small particles of calcium carbonate with diameter of 1 μm give higher impact values than for 2 μm particles at concentrations of 0%-50% [7]. This was also shown in [39].

2.3 Plate out

Plate out can be defined as an uncontrolled appearance of material deposits on tools in the extrusion process after longer running times. This may cause problems regarding process stability and quality requirements of the final product.

The causes of the plate-out are related to the formulation recipe, processing conditions and the design of the tools used in the calibration process. More information about plate out is shown in [55-59].

2.4 Physical properties

For design calculations and modelling of the extrusion and calibration processes, it is necessary to have the physical properly data of the material to be processed.

In this Section, a brief overview of the main properties relevant to the present work is given:

- Specific volume
- Thermal conductivity
- Heat capacity
- Thermal diffusivity
- Enthalpy
- Rheology

Sources for more detailed information are given in the next Sections.

2.4.1 Specific volume

The specific volume v of polymers is dependent on temperature and pressure. The influence of pressure is significant for the injection moulding process. To display the dependencies, p-v-T (pressure-specific volume-temperature) diagrams are used. More detailed information can be found e.g. in [7,60-62].

Furthermore, the cooling rate also has an important influence on the specific volume for largely amorphous material such as PVC. Different cooling rates are present in processing,

e.g. higher cooling rates on the outer layers of a sheet. Higher cooling rates lead to higher specific volume [7,60], see Figure 2.4.

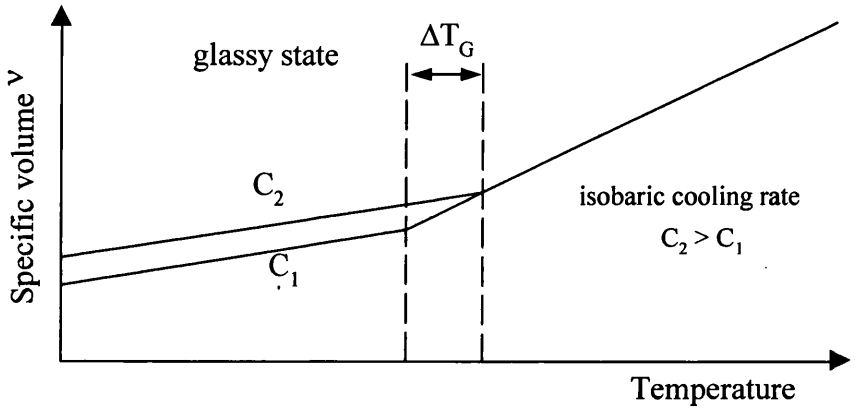

Figure 2.4: Specific volume at different cooling rates

The glass transition temperature T_G is shifted towards lower temperatures at lower cooling rates [60,63], the same effect being observed with increase of annealing temperatures and time [63,64].

Higher temperatures below T_G accelerate the process of aging [7] and this reduces the specific volume in the same way as a reduced cooling rates. So the history of the processed part is important, as reported in [64] and [7].

Figures for the specific volume of PVC as function of pressure at different cooling rates are available in [65].

The influence of the cooling rate seems to be limited at higher cooling rates, as presented in [66], where the specific volume did not change for cooling rates higher than 10 K/s, (however, this may be due to the measurement equipment not being capable of measuring the small differences).

The specific volume is also used for the calculation of the temperature dependence of the expansion coefficient. For isotropic behaviour, the change in length due to temperature can be calculated with

$$\frac{\Delta l}{l_0} = \frac{1}{3}\frac{\Delta v}{v} \qquad (2.1).$$

The stretching of the material also has an influence on the specific volume, or rather the density, as noted in [21]. Here, higher change in density was obtained for uni-axial stretching

than for bi-axial stretching as mentioned above. Finally, the crystallinity also has an influence on the specific volume, as presented in the previous Section on crystallinity.

Approximate equations of the specific volume v [m^3/kg] of PVC are given e.g. in [67] for

Temperature range 10°C<T<110°C

$v = 1/\rho = 7.154 * 10^{-1} + 1.020 * 10^{-4} * T + 7.814 * 10^{-7} * T^2 - 1.669 * 10^{-9} * T^3 + + 5.244 * 10^{-11} * T^4$

Temperature range 110°C<T<200°C

$v = 1/\rho = 0.679 + 5.67 * 10^{-4} * T$

and in [68] for

Temperature range 20°C<T<85°C

$v = 1/\rho = 0.702 + 1.575 * 10^{-4} * T$

Temperature range 85°C<T<250°C

$v = 1/\rho = 0.674 + 4.85 * 10^{-4} * T.$

2.4.2 Free volume and glass transition temperature

The specific volume of the melt can be expressed as the addition of the partial molecular volume v_M and the free volume v_F [69]

$$v = v_M + v_F \tag{2.2}$$

and this in shown in Figure 2.5.

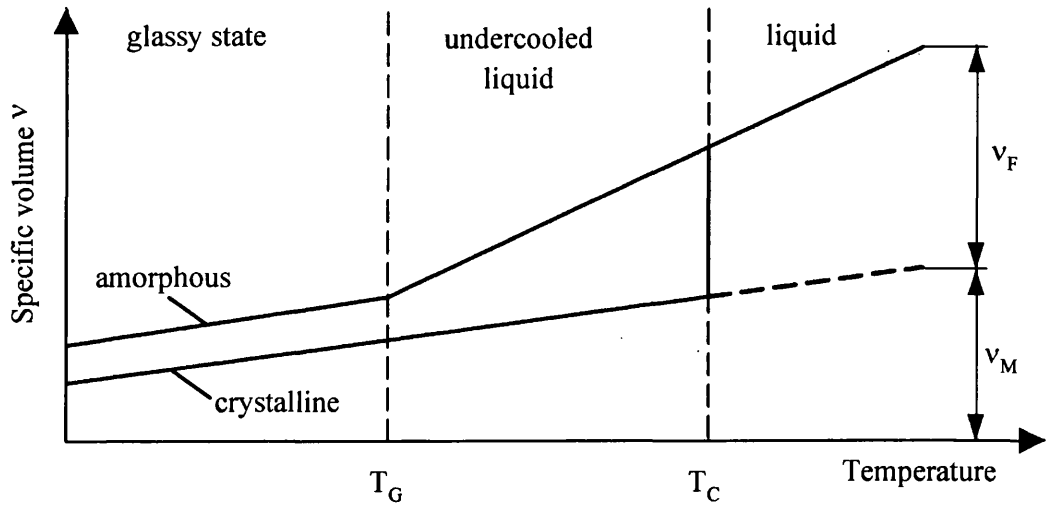

Figure 2.5: Free volume v_F and molecular volume of polymers v_M [69]

The molecular volume v_M describes the volume due to the oscillating expansion volume of the molecules [69]. In the Figure above, the amorphous volume is higher compared with the crystalline volume, as mentioned in Section 2.5, on orientation. The free volume can be influenced by the use of lubricants [28].

Below the glass transition temperature T_G the polymer is in a frozen or glassy condition. The free volume for amorphous polymers can be assumed as nearly constant below T_G [69] and can be expressed with

$$v_F \approx 0.025\, v \qquad (2.3).$$

2.4.3 Thermal conductivity

For the temperature dependence of the thermal conductivity λ of PVC several sources are available.

In [70] the thermal conductivity is given for uPVC in the range of $\lambda = 0.168$-0.174 W/m K, close to the constant value of $\lambda = 0.168$ W/m K used in [71].

A description in equation form was presented in [68] with the values of λ [W/m K] as given below:

Temperature range 20°C<T<50°C

$\lambda = 0.176 + 0.000105*T$

Temperature range 50°C<T<100°C

$\lambda = 0.18125$

Temperature range 100°C<T<150°C

$\lambda = 0.19175 - 0.000105*T$

Temperature range 150°C<T<250°C

$\lambda = 0.1865 - 7.0*T$.

Furthermore, additional figures for the thermal conductivity are shown in [65] for different plasticizer contents.

2.4.4 Heat capacity

The specific heat capacity c_P is relevant for non-stationary heat transfer processes with heating or cooling. Figures for the heat capacities are presented in [65,72]. In [71] equations are presented, as shown below:

Temperature range 10°C<T<67°C

$c_P = 0.75 + 4.657*10^{-3} *T$ [kJ/kg K]

Temperature range 67°C<T<96°C

$c_P = 136.111-6.643*T+1.211*10^{-1} *T^2 -9.715*10^{-4} *T^3$ [kJ/kg K].

Temperature range 96°C<T<200°C

$c_P = 1.208+2.962*10^{-3} *T$ [kJ/kg K].

2.4.5 Thermal diffusivity

The thermal diffusity can be calculated by

$$a = \frac{\lambda \rho}{c_P} \left[\frac{m^2}{s}\right] \qquad (2.4)$$

with the thermal conductivity λ, density ρ and the specific heat capacity c_P. All parameters on the right hand side are temperature dependent. Values of the thermal diffusivity can be found e.g. in [72].

2.4.6 Enthalpy

The specific enthalpy Δh can be calculated between two temperatures T_1 and T_2 using the specific heat capacity c_P

$$\Delta h = \int_{T_1}^{T_2} c_P(T)dT \qquad (2.5).$$

Values for the specific enthalpy can be found e.g. in [65,70,72].

2.5 Material characterisation

2.5.1 Characterisation of the solid properties

The solid properties of the raw material in powder or pellet for, e.g. bulk density, pourability, grain size analysis and distribution, are used to design the devices for the mixing, handling, storage and finally feeding of the extruder.

2.5.2 Mechanical properties of the solid

The mechanical properties of the dense solid uPVC are relevant to the deformation and residual stresses produced in during the calibration process. An extensive literature review is available, and as introduction to the topic, the references are cited: [73-76].

These were reviewed in [77] where extensive series of relaxations tests were carried out and the behaviour represented by a 4-element Maxwell model.

2.5.3 Characterisation of the polymer melt

The rheology is used to describe the material behaviour of the molten polymer. An overview of the basic rheological characterisation is given in [78] and [72].
The additives, raw materials and processing conditions have a big influence on the rheology and their effects are presented e.g. in [79-81]. More details of the rheology of PVC can be also found in [82-89].
The literature is extensive, and a full review is not appropriate here. The cited references will provide an entry into this subject area.

2.5.4 Wall stick and wall slip at the interface of polymer and die wall

Another, but important parameter in the die design is the flow behaviour of the polymer at the boundary of polymer and the die wall. Here a wall stick or wall slip condition is present. In

general, the worse case for a die design is the variation of boundary conditions (fluctuation) at the interface of the polymer and the die.

The wall slip is described e.g. in [72] as a non-constant wall shear stress and there, a base was shown to describe the wall slip, which are valid for some uPVC formulations. The author has also mentioned, that a calculation of the wall slip is not practicable, because the problem is the unknown friction coefficient between the polymer and the wall of the die. But in [90] is remarked, that the wall slip must be consider in the die layout. It was also mentioned that wall slip effect exits at a limiting shear stress about 105 Pa especially at low processing temperature under 190°C. More results on wall slip for uPVC are also shown in [91,92].

To have stable processing conditions in the die, the properties of the melt should be consistent as possible to provide constant process conditions in the die, as mentioned before. Here, the target is to get a uniform wall slip or wall stick effect at the interface of polymer melt and the walls of the die. In [91] it is proposed, in common with other in the literature that wall slip is due to the accumulation of low molecular weight components at the melt-metal interface. It is further asserted that the slip layer thickness along the flow path, leading to lower pressure gradients at the downstream end the die. Slip also was found to depend on surface roughness.

CHAPTER 3

Profile extrusion process

In this Chapter, an overview of the process chain from the profile extrusion to the finished product will be given.
Before the details are presented, a general introduction is given to the sequence from the initial concept to the final product.

3.1 Introduction: From the idea to the final product

Every production process must be made as economical as possible; costs must be reduced and higher output rates used. This is also appropriate for the profile extrusion process.

The complete process from the enquiry of the customer to the delivered product must be investigated and analysed with the use of a quality control system. This leads to reduction of production time from customer enquiry to delivered product.
To achieve this, the structure of the organisation must be optimised, e.g. by reducing the production costs whilst increasing the productivity and reducing the development times for profiles systems and the manufacturing of tools, using simultaneous engineering [93].
Altogether, the process must be optimized from the material supplier, the tool manufacturer and extrusion company to achieve the best outcome [94].

3.2 The process chain of the profile extrusion process

The process chain starts with the basic polymer and the additives, which are mixed to the so-called dry blend and stored temporarily, or are alternatively compounded and pelletized. The dry blend or pellets go next to the extruder. The extruder is used to melt the polymer and to build up the pressure for flow through the die. The die gives the polymer the preliminary shape of the profile at its exit, and in the following downstream calibration and cooling section, the profile is given the final shape and is cooled down. The profile is pulled through

the calibration section with the haul-off unit. After the haul-off, a unit is used to cut the profile into lengths, and a handling unit prepares it for transportation, e.g. by storing in special storage boxes.

All the foregoing stages are shown in Figure 3.1.

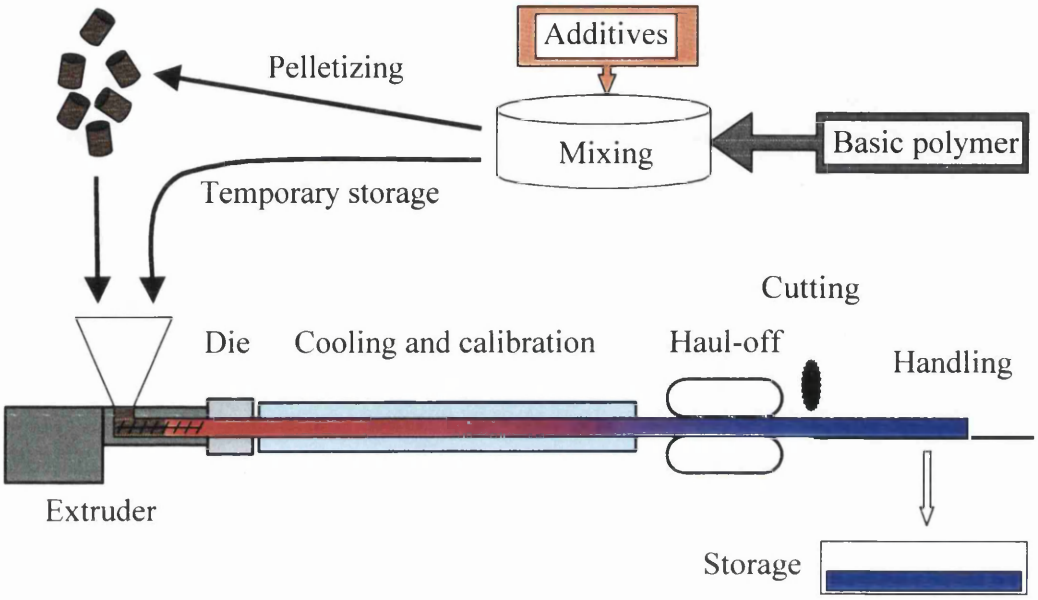

Figure 3.1: The process chain for the profile extrusion

In the next Sections more details are presented.

3.3 Mixing and material handling

As shown above, the process chain starts with the raw polymer and the additives. Details of the production of the raw material and the use of additives were presented briefly for uPVC in the foregoing Chapter 2. All components are mixed together and afterwards, two routes in the process chain can be used. The first option is to pelletize the mixture for special application, e.g. lower throughputs, injection moulding, blow moulding or easier handling due to the better pourability of the pellets. More details for the pelletization of uPVC, which is approximately 20% of the European production, are shown in [95]. The second possibility is to use the dry blend, a mixture of raw polymer powder and additives, which is predominately used for uPVC. Furthermore, recycled material is also used in the process and details of the recycling are shown in [96].

More details of the mixing, storage and transport processes are presented in [54,97-100]. Additionally, in the mixing process, the properties of the additives are important and must be

taken into consideration in the mixing process to avoid problems. Some of the aspects, e.g. properties and dispersivity of additives, are presented in [43].

Finally, contaminations or impurities of the material must be avoided to ensure the properties of the final product. Contamination may occur anywhere in the complete production process, from the manufacture of the raw material, the transport to the customer, the mixing, transport and storage at the manufacturer and in the extrusion of the final product [101].

3.4 Extruder

The extruder is used to melt and mix the polymer and finally to build up the necessary pressure behind the die. Many parameters in the extruder, e.g., screw design, screw cooling, degree of fill, screw speed and barrel temperatures have an influence on the melt temperature and properties of the extrudate (as mentioned in Chapter 2).
A good design of the extruder gives a homogenised melt with uniform temperature distribution at the exit of the extruder, before the melt flows in the die.

Schuler [102] has given an account of recent extruder technology and methods for optimizing the processing conditions in the extruder. He has also shown the adjustment of the extruder and the formulation of the uPVC to get an economical success. Furthermore, it was mentioned that the extruder has to be designed to run independently of the die used and this leads to flexible production. More influences of the extruder parameters are presented in e.g. [17,26,50].

The feeding with a full hopper can be used if the bulk density is nearly constant and uniform for all the formulations used in the process [36].

3.5 Die

The die is used to pre-form the molten polymer coming from the extruder to a preliminary shape of the profile.

3.5.1 Design

The die design plays an important role in the calibration process. It must ideally deliver a defined cross section of the profile with correct mass flow rate to each part of the cross section. A uniform melt flow velocity over the die exit cross section is also desirable, but difficult to combine with the required mass flow distribution, as a result of the construction constraints. A general overview of die designs is presented in [103] and [72]. Further information can be found in [90,94,104,105].

Die designs in the past have been based mainly on dies that were used before for similar profiles - a knowledge driven approach -, or based on simple analytical calculation methods. Now, the Finite Element Method (FEM) is used more frequently for the calculations of the complex flow in the die. This can include complex flow phenomena, such as wall slip together with no-isothermal effects. More information for FEM calculations of the flow in the die are given in [71,103,106-112]. Both research and commercial FEM packages are available for analysis of complex flow and heat transfer, e.g. FANTAZT [113], POLYFLOW, FIDAP [114], etc..

As mentioned in Chapter 2, the additives and the mixing have an important and not to be ignored influence on the flow behaviour, as do the processing conditions in the extruder. In [71] it was shown that the formulation of uPVC can have an influence on the velocities at the die exit due to the different rheological behaviour. Good rheology data for the melt is required for more accurate calculations of the flow in the die, including characterisation of wall slip of melt-metal interface, see Section 2.5.3 in Chapter 2 for more details.

The die must be also designed for an easy assembling and fixing of segments, and for cleaning and adaptation with the extruder [115].

Recent developments have brought some new ideas onto the market, e.g. the bolt-less die [116]. This die system uses clamping system of the separate die plates. With the lower volume of metal used, the heating time is claimed to be shorter and the assembling is easier and faster due to the lower weight.

In general, the die design should be based on a modular system to exploit also similarities between profiles. In [117], a tailor-made CAD system for the tool layout is presented. The idea of this is to reduce the development time and thus the costs for the design of a calibration line including the die. The system is based on the experience of the tool manufacturer, derived from tools manufactured in the past. In the design of a new profile, the required profile sections are compared with existing profile sections in the database and, if similar, they are used to create tools for the new profile. With a modular design of the die and calibration sections, a shorter development time and effective tool design is possible.
Due to the demands for higher throughputs, a double calibration line is used increasingly frequently, and so the die design must be adjusted to this. For this, the die flows must be balanced for both flows at the die exit. To achieve this, best possible constant flow velocities and uniform temperature distribution at the inlet of the die must be present, and this relies on correct conditions in the extruder. These are also necessary for single line calibrations, where deviation in temperature leads to different flow properties of the melt, which can change the flow behaviour in the die.
Die design becomes more complicated as an increased number of inner chambers are demanded by the market, to reduce the heat loss through window frames. Recently, computerized optimization methods have been applied to the design of complex profile dies. An optimization shell surrounds the flow simulation, from which an objective function measuring die performance is estimated. The optimizer automatically adjusts die dimensions to achieve the required die balancing [118-120]. The computed optimization reduces the number of practical extrusion trails required and so reduces the costs to run in the die.

3.5.2 Die swell of the material at the die exit

Due to the elasticity of the melt, the polymer recovers at the die exit. This can be explained in term of a relaxation or strain recovery of the polymer at the die exit. In [121] the die swell is described as a reduction of elastic stored deformation due to outer shape restraints (die walls)

and this deformation releases at the die exit. In addition to shear, elongational stresses at the die entrance are partially involved [122].

The die swell is influenced by several parameters in the process. An increase of die swell can occur due to

- increase of volumetric flow rate [123]
- decrease of residence time in the die [123]
- increase of shear rate [124] (based on the increase of flow rate)
- lower filler content [122]
- higher content of processing aids [122]
- decrease of the ratio length/diameter (L/D) in the die [123,124]
- increase of melt temperature [10,50,122,123].

A low die swell could be expected using an L/D ratio from 5 to 20 [125]. More information can be found in [72,80,122,123,125-133] including numerical approaches to describe the die swell behaviour.
The die swell is at the maximum if no restraints are present after the polymer leaves the die exit, see Figure 3.2.

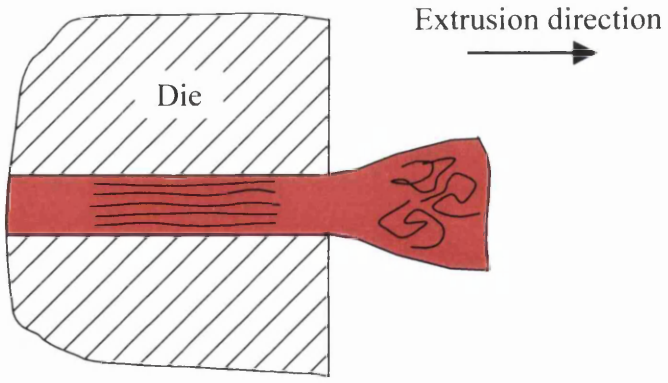

Figure 3.2: Swelling of the polymer at the die exit

In the calibration process, the melt cannot swell intensively due to the imposed velocity of the melt as it goes into the inlet of Calibrator 1. The distance between die exit and inlet of Calibrator 1 is very small, and, if the velocity of the melt at the inlet is approximately the same as at the die exit, the recovery is reduced to minimum. This situation changes if the velocity of the melt is reduced at the inlet of Calibrator 1. Then the recovery is more

pronounced and occurs together with the increase of the wall thickness at the inlet required to maintain mass flowrate.

3.6 Draw down

Draw down depends on the relationship between the cross-sectional size of the profile at the die outlet area and the inlet of Calibrator 1. Draw down refers to the overall dimensions, not to the profile wall thickness.

The draw down is mainly used to define the outer profile surface in the inlet of Calibrator 1. The outer profile surface is forced by the draw down to make contact with calibrator walls, and this forces it to take the shape of the outer surface of the profile at the inlet of Calibrator 1.

The draw down can be described as the reduction of the inlet dimensions of Calibrator 1 compared to the dimensions of the die exit, see Figure 3.3.

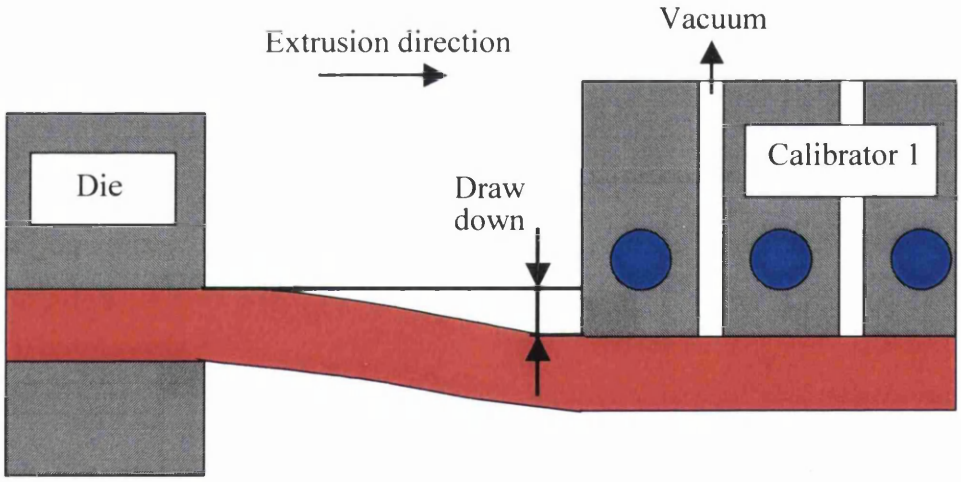

Figure 3.3: Draw down form the die to the inlet of Calibrator 1

The draw down ratio is quoted as the percentage decrease of the profile cross section at the entry of Calibrator 1 compared with the die exit.

For uPVC, draw down ratios of 3% were quoted for bigger profiles in [134] and 8% for smaller profiles. In [70], draw down rations of 2 to 3% are noted. The draw down can be

different for the horizontal and vertical dimensions. More information on draw down can be found e.g. in [123,130].

The draws down ratios nowadays are in a range of 0 to 2%, depending on the process conditions and profiles. This is mainly related to the development of new die and calibrator concepts, based on the continuously improving understanding of the melt behaviour in the processing stages.

3.7 Calibration and Cooling

In the calibration section, the preformed molten profile comes from the die and it is cooled down in the calibration section whilst the dimensions of the final profile are fixed. It looks simple, but the handling of the overall process can be critical, if the components and processing conditions are not chosen very carefully. In the choice of the components, the continuous development of profiles and increase of capacities must be regarded as well, e.g the increase of line speed. Due to more systematic investigations and introduction of new concepts in the profile calibration, the line speeds are increasing continuously, e.g. the line speed at the end of the 80's for main window profiles was in the range from 1.5 to 2 m/min, whereas the line speed has increased in the mid of the 90's up to 4 m/min for a double line calibration with throughputs of 550 kg/h [135]. This was also noted in [93], where the increase of top line speeds from 1993 to 1995 are presented, e.g. for main profiles of 125%. Another trend is shown in [116], where the portion of double line extrusion increases continuously, whilst the single line extrusion decreases. This effect is more pronounced for the side profiles than for the main profiles. Here the quantity of double line extrusion has increased from 20% in 1990 to 65% in 2002, whereas for the main profiles, an increase was shown from 5% in 1990 to over 20% in 2002.

For an increase of the output, the complete process has to be investigated. The key points are the compounding of the melt with the extruder and the design of the die and the calibrators. The recent developments of the extruder and dies were shown in Sections above. Here an overview of the calibration section will be given. For the calibration is necessary to investigate the process chain from the enquiry of the customer for a profile up to the final product, because many parameters have an influence on calibration process.

They cover the range of

- profile design
- polymer type
- line speed
- processing limits in the manufacturing of tools used in the calibration process, e.g. die and calibrators.
- life time cycle

First of all, the profile properties must be evaluated.

3.7.1 Profile properties and design

The extruded profiles must fulfil several demands, which are defined by the quality standard of the producer or by the market:

- weather resistance, e.g. ultra violet protection
- good surface quality, e.g. gloss
- realisation of the function, e.g. thermal insulation
- high thermal and mechanical resistance, e.g. no warping of profiles in extremes of temperatures and forces, high impact
- dimensional accuracy, e.g. tolerances

Some of the required properties are influenced by the additives, e.g. impact behaviour, as described in Chapter 2, or by processing conditions in the extruder as mentioned previously. But several properties are strongly dependent on the calibration process and on conditions in the die, e.g. warping, shrinkage.

The design of the profile also has an influence on the design of the calibration process. An increase the number of chambers in the profile, see Figure 3.4, increases the insulation of the profile, e.g. the effective thermal conductivity decreases for a profile with 3 chambers in comparison with a 6 chambers from 0.87 W/m^2K to 0.76 W/m^2K [116]. But the more chambers there are in the profile, the more complicated the design of the die becomes. And the cooling of the inner wall becomes more difficult due to the low thermal conductivity of PVC and the insulation effect of the air cavities and the profile needs a longer cooling time to

reach the same temperature level. It must also be taken in account that the properties of the polymer used here must fulfil the required specifications, e.g. good flow behaviour.

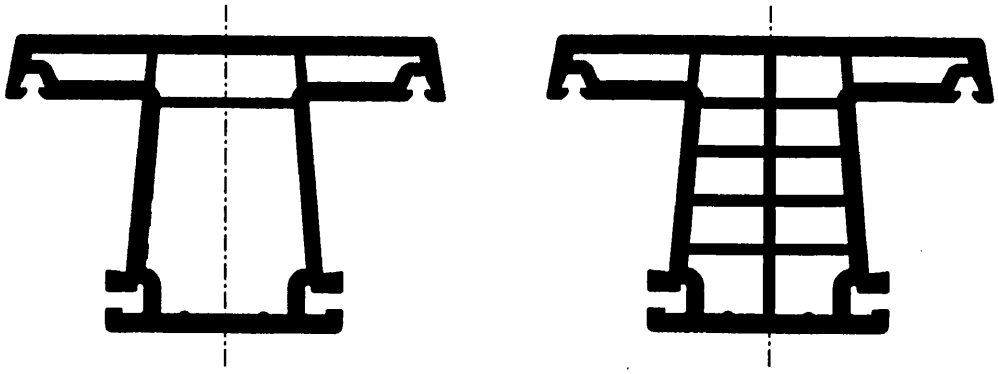

Figure 3.4: Increase of number of chambers in a profile, right side

In the design of profiles the following features are important:

- symmetric design
- uniform wall thickness
- thinner walls at the inside
- avoidance of material accumulation
- avoidance of undercuts

In Figure 3.5, a profile with a bad design is shown.

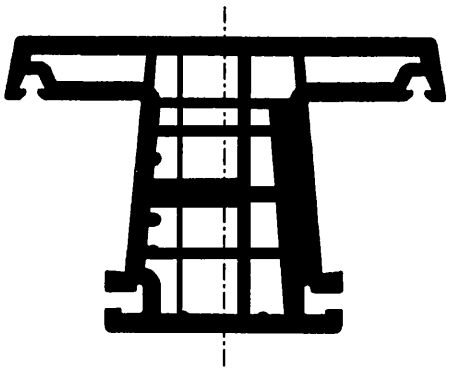

Figure 3.5: Example of an asymmetric profile with non-uniform wall thickness and accumulation of material at the inside.

All the foregoing aspects must be taken into account for the layout of the calibration line, and this is presented in the next Section.

3.7.2 Layout of calibration lines

The layout of the calibration line is based on the parameters mentioned before. In general, two types of calibration system are used, the dry and wet calibration. The dry calibration uses the coolant agent only in the coolant channels of calibrators, whereas in wet calibration the coolant is also used in the gaps between the calibrators units, the so-called intermediate water baths, and at the downstream end of the line in water baths and vacuum tanks. Water is normally used as the coolant and is treated with chemicals to avoid corrosion, etc..

An overview of alternative calibration layouts is given in Figure 3.6.

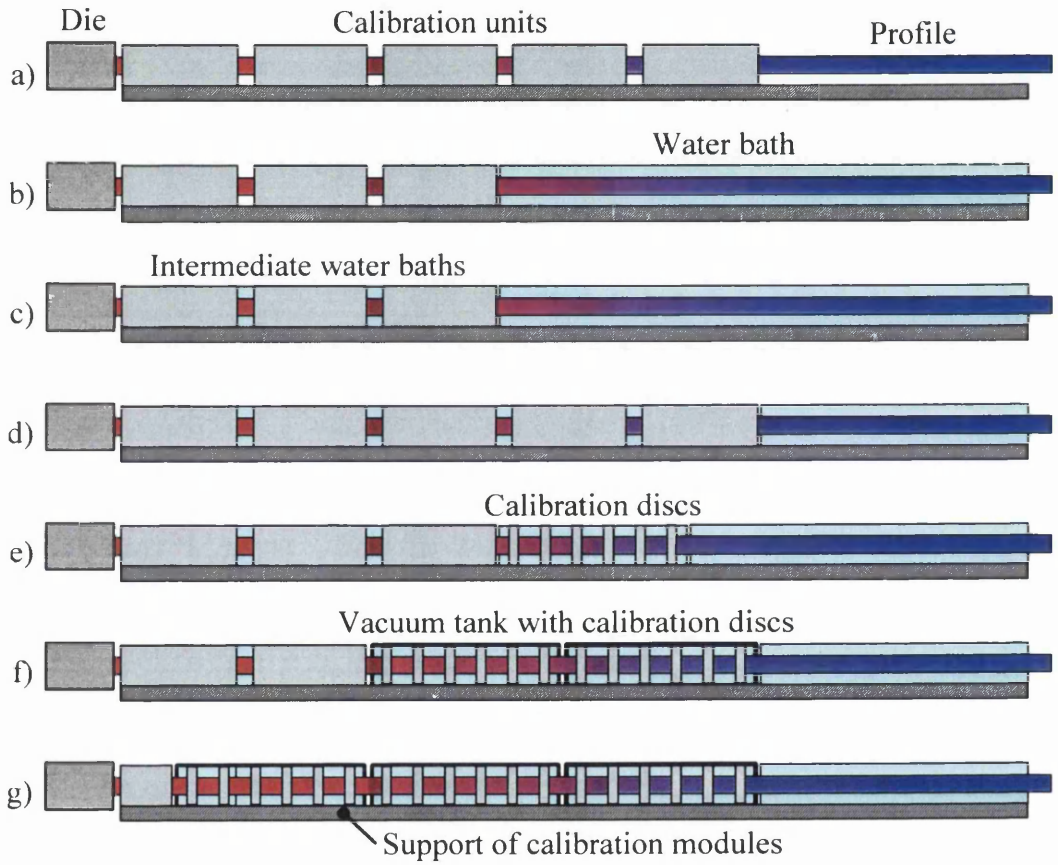

Figure 3.6: Alternative layouts of calibration lines.

As mentioned before, the dry calibration uses no water to cool down the profile directly on the profile surface and this is shown in Figure 3.6-a. The dry calibration line consists of the die and the calibrators in downstream direction. All parts of the cooling section are mounted on basic support, and if the design has a modular set up, the parts can be changed very quickly to alter the layout of the calibrators. In Figure 3.6-b, a water bath is used downstream of the calibrators. This improves the cooling of the profile due to the higher heat transfer from the profile to the coolant. For further improvements of the cooling, intermediate water baths are

used between the calibrators, see Figure 3.6-c. In Figure 3.6-d, more calibrators are used for the fixing of the profile geometries, e.g. due to higher lines speeds or more chambers in the profile, where longer cooling time is required.

Figure 3.6-e shows a replacement of the last two calibrators with calibration discs in a water bath. The discs are used to fulfil the same requirements as the calibrators and with the water in between the discs, the profile is cooled down whilst the discs are fixing the profile geometry. Additionally, the cooling on the outer surface of the profile is more uniform due to the water surrounding of the profile. The discs also have another effect on the heat transfer. They remove the boundary layer of water on the profile surface and this allows cooler water to can get into contact with profile surface, leading to a better cooling effect. The use of vacuum in combination with the discs is shown in Figure 3.6-f. The cooling effect is the same as before, but with the vacuum, the profile is pulled against the inner surface of the discs, similar to the action of the vacuum in the calibrators. This system has advantages compared with a conventional calibrator. The manufacturing is easier and the discs can be tailored to the profile in more detail than the calibrators. Furthermore, the cooling of the profile surface is more uniform, as mentioned before. Finally, the calibrators are replaced in Figure 3.6-f with calibration discs except for the first calibrator, named as Calibrator 1 in Figure 3.6-g. The functions are the same as discussed before, but here, the flexibility for changes, e.g. due to a slight change of tools dimensions to get the right profile dimensions, are easier as compared to a calibrator. And for a fast change of the calibration section to produce another type of profile, this can be carried out more easily by changing the Calibrator 1 and the numbered calibration discs.

Finally this concept is also used, with a reduced number of calibration discs, as a low cost tooling system, which does not provide a high life cycle, but fulfils the requirement for producing low quantities of profiles [116].

3.7.3 Design of the calibration system

For the design of the calibration system, the key parameters must be known, e.g. profile design and on-line processing parameters e.g. line speed, etc., as mentioned above.

The basic target is to design a system, which runs in a stable way without problems. Also required is a fast start-up time, including mounting of the calibration system.

3.7.3.1 Design of cooling

The design must provide the best possible uniform cooling of the profile surface to avoid problems, e.g. bending or warping of the profile due to asymmetric stresses in the profile arising from the cooling.

In Calibrator 1, the profile must cool down rapidly to get a solidified surface layer to take the haul-off force, and in the downstream direction, the cooling must be efficient in cooling down the profile to ambient temperatures, so that the profile cannot be deformed due to thermal shrinkage.

So the cooling system must have the right dimensions in relation to the profile surface, to provide the heat transport from the profile surface to the coolant. An example of the layout of cooling channels is given in Figure 3.7. Included also is the inlet section, which is shown magnified here.

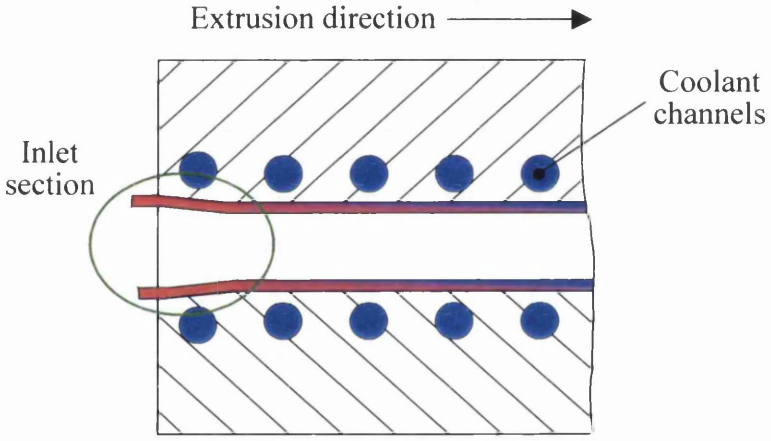

Figure 3.7: Example of cooling channels in Calibrator 1

For calibrators, the main factors in the layout are the coolant channel positions and dimensions. In water baths and vacuum tanks, devices are used to provide turbulent flow of the coolant to increase the heat transfer from the profile surface to the coolant. And in all systems the reverse direction flow is preferred due to better cooling. Spray cooling could be also used, but this system sometimes shows problems with blocked spray nozzles, and this would lead to non-uniform cooling.

In wet calibration, the coolant is present between the calibrators to cool down the profile surface and avoid the reheating of the profile surface by conduction from the hotter material below, which could give a thinner solidified layer to carry the forces. The water from the intermediate water baths can flow into a gap between the profile and calibrator under the

action of the applied vacuum, if such a gap is formed due to thermal shrinkage or draw down of the profile.
Optimization methods have been used in combination with the FEM to optimize the positions of the coolant channels to provide uniform calibrator wall temperature with uniform cooling. Some examples are presented in [70,136,137].

Altogether, the heat transfer is a key factor in the calibration process. More details regarding the heat transfer are presented in Chapter 7.

3.7.3.2 Design of calibrator dimensions

The die exit is designed to be larger than the final profile due to the thermal shrinkage of the polymer. This effect must be considered throughout in the design of the calibration section. Here, the ideal cross-sections of the calibrators would follow the reduction of dimensions during cooling.

The length of the calibrators is mainly dependent on the tooling capacities and, if used, on the modular calibration system. The overall length of the calibration section is based on the process parameters, line speed, design of the profile, etc., as mentioned before.

The Calibrator 1 plays the most important role in the calibration process. Here, the dimensions and details, e.g. noses and slots, get their shape, and in the downstream calibrators, the dimensions are chosen mainly to avoid jamming of the profile. The small details, e.g. undercuts, are only formed in some cases in the downstream calibrators.
Furthermore, the quality of the profile surface is determined during calibration. This is sometimes supported with the use of die heating, which is close to the surface of the outer profile surface at the die exit.
For rapid cooling of the inner sides of the profile wall, special cooling sections have been developed to cool the melt from the inner chambers of the profile. This becomes excessively complicated with more complex profiles.

Furthermore, the calibrations section must be aligned exactly in line direction to avoid that the profile setting stuck or cooling down in a "zigzag" configuration.

3.7.3.3 Design of vacuum system

Vacuum is used to pull the outer profile against the calibration section to fix the dimensions in the cooling process.

The first vacuum positions have to be at the right place to pull the melt immediately against the cool calibrator wall to form a solid surface layer to carry the haul-off forces. The next vacuum positions should pull the profile against the calibrator to get a good heat flux and to cool down the profile in an optimal way. The shapes of the vacuum devices are slots or holes, where holes are better for sensitive pulling of the profile against the calibrator wall. Figure 3.7 is extended in Figure 3.8 to show how the vacuum is applied to the system.

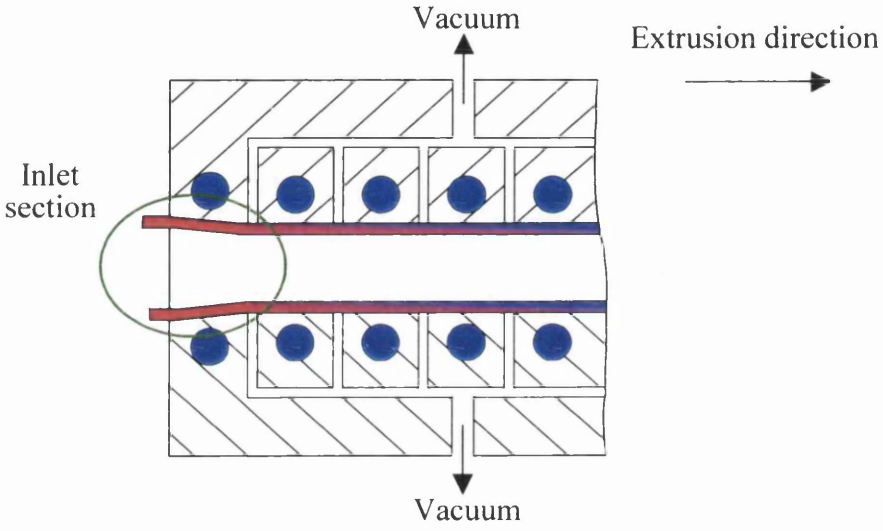

Figure 3.8: Example of vacuum and cooling channels in Calibrator 1

The vacuum used here is provided by vacuum pumps, usually placed underneath the calibration sections to avoid long paths for the vacuum and loss of vacuum. A stable vacuum is necessary to provide constant processing conditions, especially for more complex profiles and/or for higher lines speeds. A possibility for controlling the vacuum more accurately is to use pressure transducers close to the connection point of vacuum to the calibrator.

The positions and dimensions of the vacuum holes or slots are based on the experience of the tool manufacturer and the processing conditions, e.g. line speed.

3.7.4 Design of the water bath and vacuum tanks

Water baths and vacuums tanks are used to cool down and fix the profile dimensions, similar to the function of the calibrators. But unlike the situation in the calibrators, the outer profile surface has direct contact with the coolant. This gives a more uniform profile surface temperature. The water bath can be used with or without calibration discs. Here the calibration discs provide a support for the profile so as not to lose the outer dimensions during cooling. The permanent vacuum pulls the profile against the calibration discs to fix the dimensions during cooling. All three types are shown in Figure 3.9.

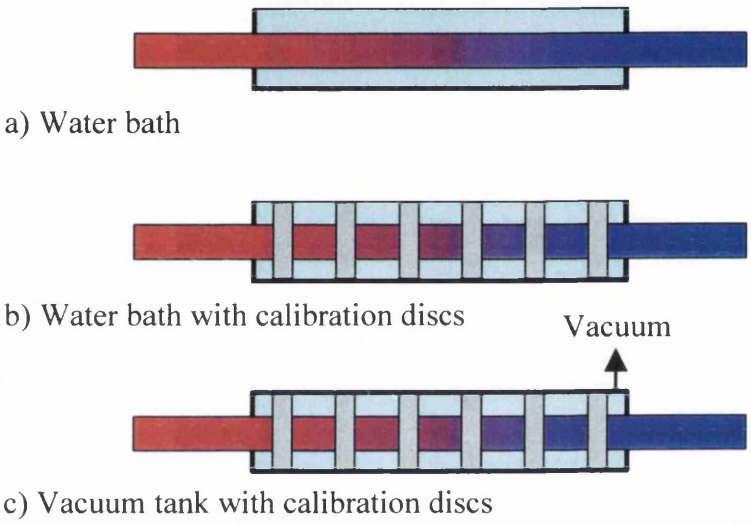

a) Water bath

b) Water bath with calibration discs

c) Vacuum tank with calibration discs

Figure 3.9: Water bath and vacuum tank.

3.7.5 Material of the calibrators

The calibrators are manufactured out of steel, brass or sometimes aluminium, and which materials differ in their thermal conductivity and the wear behaviour.

The thermal conductivity of steel type 1.4301 (X 5 Cr Ni 18 10) has a thermal conductivity of 25 W/m K, brass 113 W/m K and aluminium of 125 W/m K, which is high in comparison with the value 0.17 W/m K for PVC [138,139]. But the difference between steel and brass is remarkable.

The influences of steel or brass on the calibrator surface temperature are shown in FEM simulations in [140].

The selection of the material of construction cannot be based solely on the thermal conductivity and with regard to the surface temperature of the calibrators.
Also the life time cycle must be regarded, e.g. if a calibration line designed for a high life time it cannot be manufactured only of brass due to the abrasion behaviour. Here the surface must be protected, and some details are given in the next section.

3.7.6 Wear protection

Wear protection has an influence on the profile properties e.g. quality and output, but it also provides a stable process. The reasons for wear can vary. It may result from the PVC formulation, where abrasive materials are used, e.g. TiO_2. Also the design of the calibrators can increase the wear. If a gap is to small for a section of a profile, the PVC gets pulled in and due to the friction, abrasion occurs on the profile, and also on the calibrator. In the operation of the calibration process, the on-line parameters can influence the wear. This is possible when a higher throughput than the line was designed for. The use of higher vacuum level can increase the abrasion as well, due to the higher friction forces.

To minimize wear problems, the calibrators are coated with surface protection systems.
Different types of coatings are available on the market. The most widely used is the hard-chrome plating for brass calibrators. Other methods are nitride hardening, anodic oxidation, nickel-plating, chemical vapour deposition (CVD) and physical vapour deposition (PVC) [141].

More information is available e.g. in [141,142].

3.7.7 Forces and friction coefficients in the calibration process

To move the profile down in the line to the cutting section, haul-off forces are used. They are the counter part of the frictional forces appearing in the calibration sections. Here, the vacuum pulls the profile against the calibrator, or the inner surface of the discs in vacuum water baths. Furthermore, the reduction of profile dimensions in the cooling stage can also cause forces if restraints are present, e.g. due to undercuts. This gets more complicated the more complex the

profile. Gravitation forces and buoyancy forces in a water bath are also present, but these are not as significant as forces due to vacuum and restraints.

The friction force $F_{FRICTION}$ can be calculated by

$$F_{FRICTION} = F_{NORMAL}\,\mu \qquad (3.1).$$

with the normal force F_{NORMAL}, which is perpendicular to the sliding surface, and the friction coefficient μ of course, normal forces and friction coefficients will vary locally around the profile, and along the line.

To get an idea of the magnitude of haul-off forces in the window profile extrusion process, values of 8 to 12 kN are mentioned in [134].

The friction coefficient can change due to several effects in the process. It increases with temperature, as shown in [143] for medium hard PVC from 0.25 at 60°C to 0.6 at 160°C. This means that the friction forces are highest at the inlet of Calibrator 1. Here the profile surface temperature is close to the melt temperature at the die exit, and effective cooling of the outer surface before entry to Calibrator 1 is not possible due to the low heat transfer from the profile to the air and the very short cooling time.

Friction coefficients are also given in [144]. For PVC, a friction coefficient of 0.22 is presented for polished brass and steel as calibrator material for a surface temperature of 40°C, sliding velocity of 20 mm/s and load of 500 N/mm^2. For a surface temperature of 80°C, the coefficient has decreased slightly to 0.17, whereas the coefficient for the steel increased to 0.25. The surface property has also a big influence. In [69], friction coefficients for LDPE are presented. The coefficients differ from 0.4 for a rough sandblasted surface, 0.9 for a micro-polished surface and 1.3 for highly-polished surfaces. Similar coefficients for PVC are presented in [145], where the friction coefficient in combination with a steel surface was 0.35-0.4.

Plate-out can also affect the friction by increasing the surface roughness. The water used in wet calibration is a good lubricant to reduce the friction between profile surface and calibrator surface. Furthermore, insufficient mixing of the additives, e.g. lubricant, into the base polymer can give unstable friction behaviour.

An overview of influences on the friction coefficient is given in Figure 3.10.

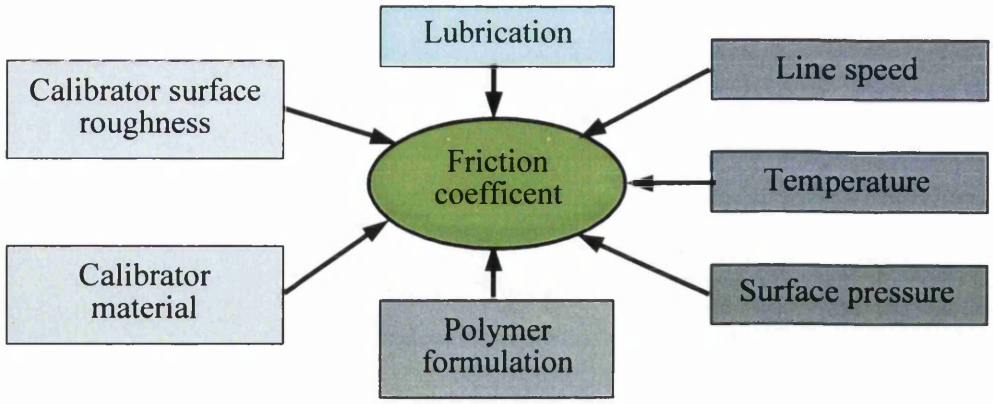

Figure 3.10: Influences on friction coefficients in the calibration process

Altogether, the forces in the calibration are dependent on the calibrator surface roughness and material properties, the sliding behaviour of the polymer formulation, lubrication effects, range and number of the vacuum holes, level of vacuum, temperature of the profile surface and finally the restraints of the design including the inlet of calibrator 1. Results of measured forces will be presented in the next Chapters.

3.8 Haul-off, cutting and handling units

The haul-off is placed at the end of the calibration line to pull the profile through the calibrators, water baths and vacuum tanks. Different types are used, e.g. roller-, belt- or pad-chain (caterpillar)-systems for pulling the profile.

For cutting of the profiles into lengths after the haul-off, cutting tools such as rotating saws or knife blade devices are used. The advantage of the knife devices is the cutting without shavings, but the system must be appropriate due the properties of the cut needed. The rotating saw gives a smother cut with higher precision and is used for larger profiles, but the shaving must be removed out of the processing area of the saw.

Finally, the handling follows at the last step in the process. Handling units transfer the profile lengths from the saw to a place beside it, where they are stored in special boxes for transportation.

3.9 Run-in of the calibration line

The run-in of the calibration line is a key aspect of the calibration process. Here, a trial and error method is used to obtain the required profile geometries. And, if the initial design is not good, the costs here can increase rapidly. In [146] the costs for the tooling and the run-in are estimated to be approximately equal.
After the tooling of each part of the calibration line, the line is assembled, the die is attached at the extruder, and the calibrators and water baths are aligned and fixed on the calibration table. Now the profile calibration process is tested with regard to stability, throughput and the required properties of the final product. Using technologies such as scanners, the profile dimensions are checked, and if the dimensions and the other properties are proved to be within the quality standard, the calibration line can be handed over to production. If not, the tools must be reworked, and the same procedure repeated, until the target quality is achieved.

Altogether, this Chapter has shown the wide range and complexity of parameters in the profile calibration process.
Nevertheless, the technology and economics of the process can be further developed in some areas, e.g. in die and calibration design by using modern technology and tools, like the FEM and optimization schemes. Systematic experimental investigations of the calibration process provide insights leading to improved design and operation.

The influences of process parameters are presented in detail in the Chapters 6 and 7 based on the extensive trials carried out in the present work.

CHAPTER 4

Definition of the controlled and resultant process parameters and design experimental set-up

The first step in investigating the calibration process is to identify the relevant parameters, the second is the selection of a trial profile, and the third is to set up a system to measure the parameters.

In the calibration process, the parameters can be separated into main groups with several subdivisions, and can be listed as follows:

- Temperatures
- Melt temperatures and distribution on the cross-section, ideally from a position at the entrance of the die and downstream direction
- Calibrator wall temperatures
- Profile surface temperatures
- Coolant water temperatures in the cooling channels of the calibration units and in water baths

- Forces
- Line direction forces on each calibrator unit
- Haul-off forces

- Water flow rates
- Cooling channels of the calibration units
- Coolant water, drawn by the applied vacuum from the water baths between the calibration units into the vacuum system of each calibrator

- Vacuum
- At various points around the profile within the calibrators
- Vacuum in the distribution units

- Extruder
- Screw revolution speed
- Barrel and die temperatures
- Material pressure at exit of extruder

Descriptions of the methods for each measurement, and the design of the measurement system follow.

4.1 Selection of the profile geometry

The profile geometry is selected with a view to the parameters to be measured. The measurements should not be complicated by the profile geometry and its specific behaviour in the calibration process, e.g. by increasing frictional forces due to shrinking on to the calibrator during cooling. In consideration of all the influences, the best choice was a simple profile with a rectangular cross section, the so-called EU-profile, previously used in an EU project on profile die design. The outside dimensions for this profile are fixed and, additionally, with an interchangeable torpedo in the die, a die exit width of 1.50 mm or 2.50 mm can be realised, see Figure 4.1.

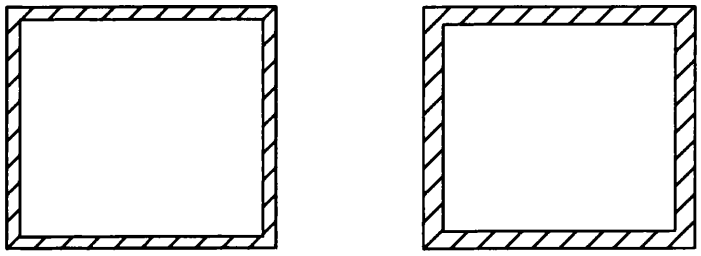

Figure 4.1: Rectangular EU profiles with 1.50 mm (a) and 2.50 mm (b) wall thickness

The vertical drawdown form the die to the entrance of the first calibrator is 2.6% and the horizontal is 2.2%.

Four calibrators were used to build up this line, the first two with a length of 450 mm and the following with 400 mm, Figure 4.2. For wet calibration, water baths of 50 mm length, made of PMMA, were provided. Furthermore, a 100 mm water bath was attached after the fourth

calibrator. For further cooling, a 4 m water bath followed the short water bath after fourth calibrator, and this was necessary in order to run higher liner speeds.

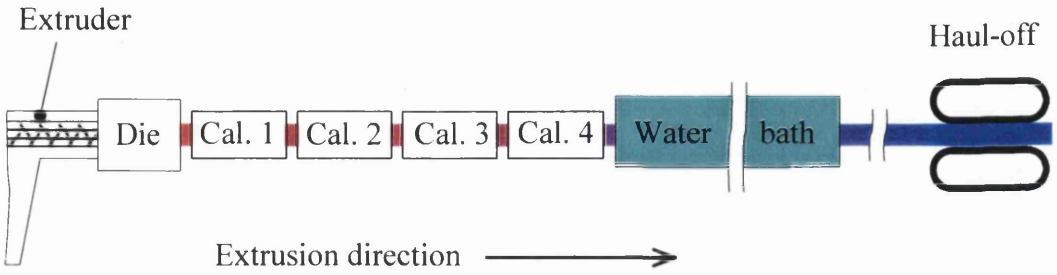

Figure 4.2: Set-up of calibration line

4.2 In-line measurements

4.2.1 Temperatures

For temperature measurements, thermocouples are chosen, because of their compactness and ruggedness. There are several types available with different temperature and application ranges. They can be designed for different conditions. One important point of design is the response characteristic. In general, the thermocouples consist of two wires of different materials, which are welded together at one end. The two materials have different thermoelectric characteristics, and as a result, it is possible to measure a temperature as a voltage difference at the non-welded end. To avoid contact of the thermoelectric wires before the junction, which would result in false measurements, they are separated by insulation, and a stainless steel sheath protects all components.

Now there are two possibilities for the structure of such thermocouple. In the grounded type, the junction of the two wires is welded together to the tip of the outer steel sheath. In the ungrounded type, insulation is present between the junction and the sheath, Figure 4.3.

Figure 4.3:
Type of Thermocouples

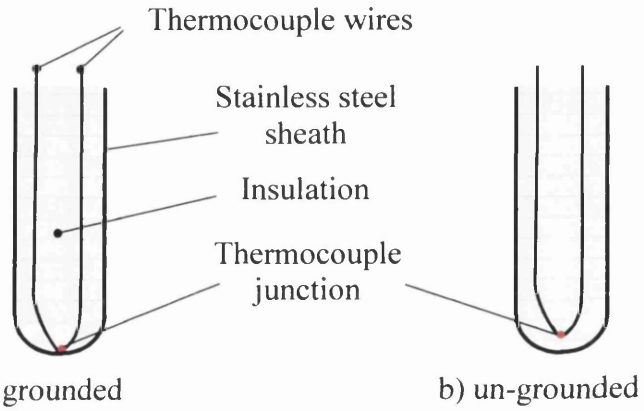

The grounded type of thermocouple will generally provide better readings and a more rapid response, and is the type chosen here. It is clear that the measured temperatures for the grounded thermocouple are more precise, e.g. for measuring of profile surface temperatures, due to smaller thermal resistance between the junction and the measurement point. However, it is then essential to choose a measuring system such that no other earth points occur in the thermocouple circuit, otherwise earth loops will give rise to false readings.

4.2.1.1 Melt temperature and distribution

The collaborating company K mmerling has developed a measurement system for the melt temperatures. The so-called "Measurement cross" measures the melt temperatures along horizontal and vertical diameters in a universal adapter using an array of 13 upstream pointing thermocouples, and this was built-in between extruder exit and die entrance, see Figure 4.4.

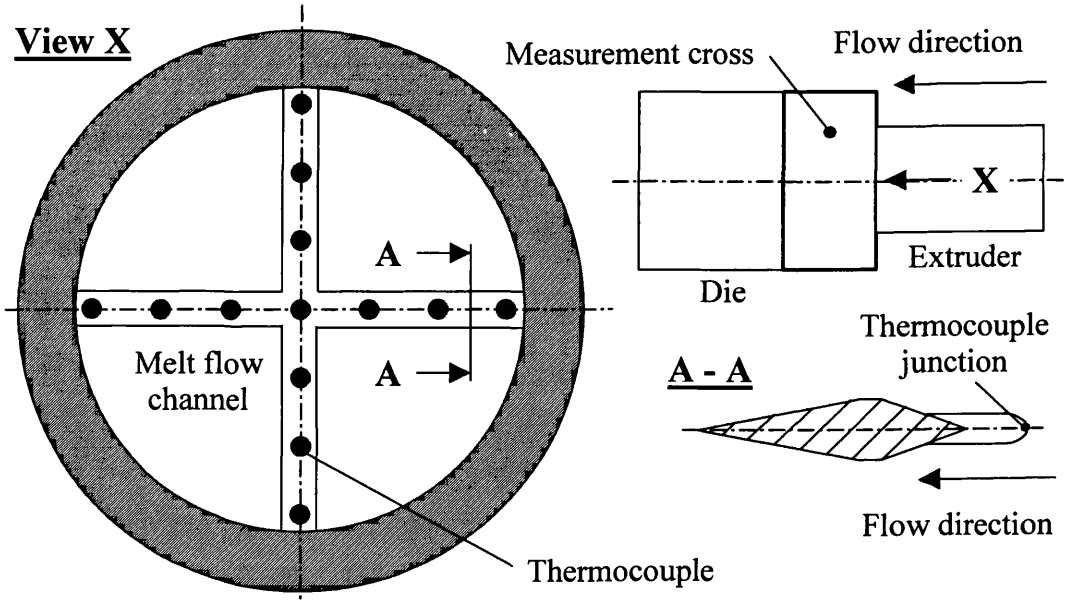

Figure 4.4: Measurement cross to measure the melt temperature and built-in position

The measurement cross was calibrated in an oil bath at 195°C, which is similar to the extrusion melt temperature.

4.2.1.2 Internal calibrator wall temperature

There are two problems to solve for this measurement: first, to reduce the effect of thermal conduction between the calibrator block and the thermocouple; and second to get good thermal contact between the thermocouple and the internal surface of the calibrator wall.
The insulation of the thermocouple from the calibrator block was achieved by enclosing it within a ceramic pipe, Figure 4.5.

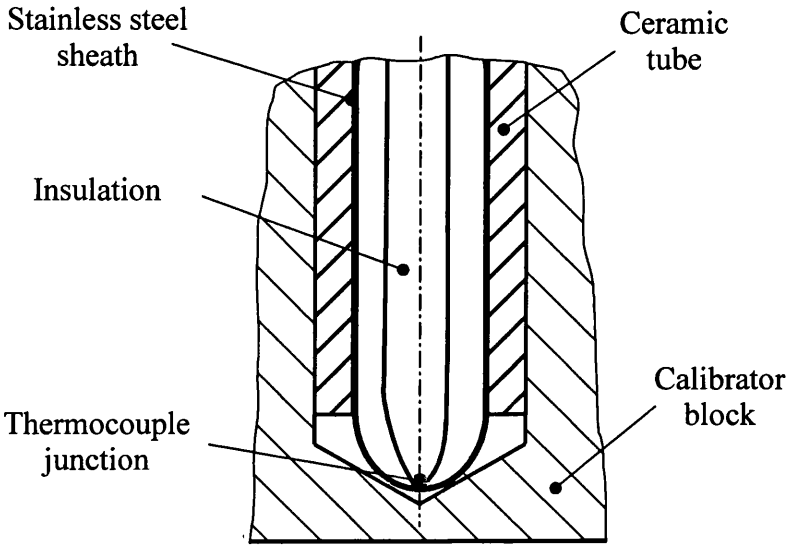

Figure 4.5: Thermocouple positioned in a drilled hole in the calibrator block

The next problem was to get the thermocouple as close as possible to the internal calibrator wall surface. It is necessary to machine this hole as deep a possible, but without damaging the internal calibrator surface.

A further problem is the thermal contact between the thermocouple tip and the metal. A drilled hole has a cone shaped end, corresponding to the shape of the twist drill. This geometry differs from that of the thermocouple, this is visible in Figure 4.5. Another mechanical machining system is milling, but here the diameter of the hole sets the limit of the manufacturing.

The alternative is spark erosion, in which the electrode can define the end shape, and so manufacture of a flat base to the hole is possible, see Figure 4.6.

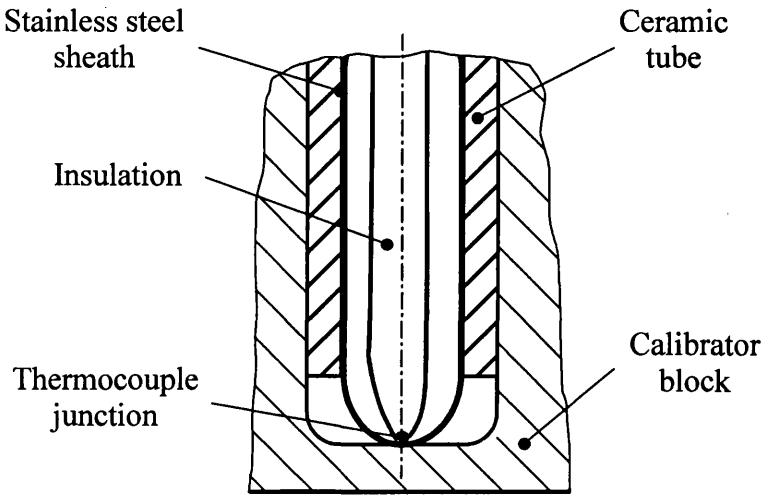

Figure 4.6: Eroded hole for the positioning of thermocouple to provide a good contact between the tip of thermocouple and the calibrator block

We can see that this is the best option for the calibrator wall temperature measurement. There is also another advantage with spark erosion, because this is more suitable for manufacturing deep, narrow holes where the highest surface quality is not required. The remaining metal thickness between the internal calibrator wall and the tip of the thermocouple can be controlled more accurately than with a twist drill. The minimum wall thickness achievable was 0.5 mm, as identified in some tests in the tool department.

To get as much information as possible, the thermocouples are positioned in rows of three at the left and right side and at the centre on the upper profile surface, and they are close to the positions of the calibrator wall temperature measurements. This will be shown in Figures 4.15 and 4.16 together with the position of the profile surface temperature measurements

4.2.1.3 Profile surface temperature

Determination of the profile temperatures is the most complicated of the temperature measurements, because of the motion of the profile. To measure these within the calibrators, the calibrators must be prepared in a special way. The easiest way is to drill a hole through the calibrator and put the thermocouple through it to make contact with the profile surface. It is explained in the following section how the necessary system was designed.

This system consists of:

- Guiding device to guarantee free sliding in the hole through the calibrator block, precisely defining the measurement position and ensuring avoidance of bending and breaking during measurement
- An appropriate thermocouple design for the temperature measurement on the moving surface, including wear resistant tip
- Insulation of the thermocouple from the calibrator block metal
- A means to provide a defined contact force between the thermocouple tip and profile surface.

The profile surface measurements were made on the upper surface of the rectangular profile, because of the considerably greater difficulty of measurements on the sides and lower surface. For the guiding device, a drilled and reamed hole was the best choice, which avoids sticking by ensuring a smooth surface. The counterpart of the sliding system is a thin-walled stainless steel tube, with a high precision ceramic tube glued within this for the insulation. Additionally, the steel tube also avoids breaking of the ceramic tube. The thermocouple can be glued into the ceramic tube, after the tip of the thermocouple has been suitably designed.
For this, the company Conatex [147], supplier of the collaborating company, was contacted and their suggestions for the design were very useful in matching the requirements.
To avoid wear of the thermocouple, a thin stainless steel plate was welded at the tip. The grounded type was chosen for these measurements, as mentioned previously, and the junction was welded to the thin plate.
The end of the thermocouple, to which the plate is welded, can be of various shapes, for example a cylindrical or conical shape. It was necessary to investigate their influence on the measured temperature, together with the influence of the size of plate and the contact force.

Three types of thermocouples (TC) with the sheath diameter D were chosen to investigate these differences:

- TC 1: D = 2.6 mm, cylindrical, without insulation
- TC 2: D = 1.6 mm, cylindrical, thin stainless steel plate at the tip, ceramic insulation
- TC 3: D = 1.6 mm, conical to 1.3 mm, thin stainless steel plate at the tip, ceramic insulation.

These were fitted into a stainless steel tube with 2.6 mm inner and 3.0 mm outer diameter and the details are shown in the next figure, Figure 4.7.

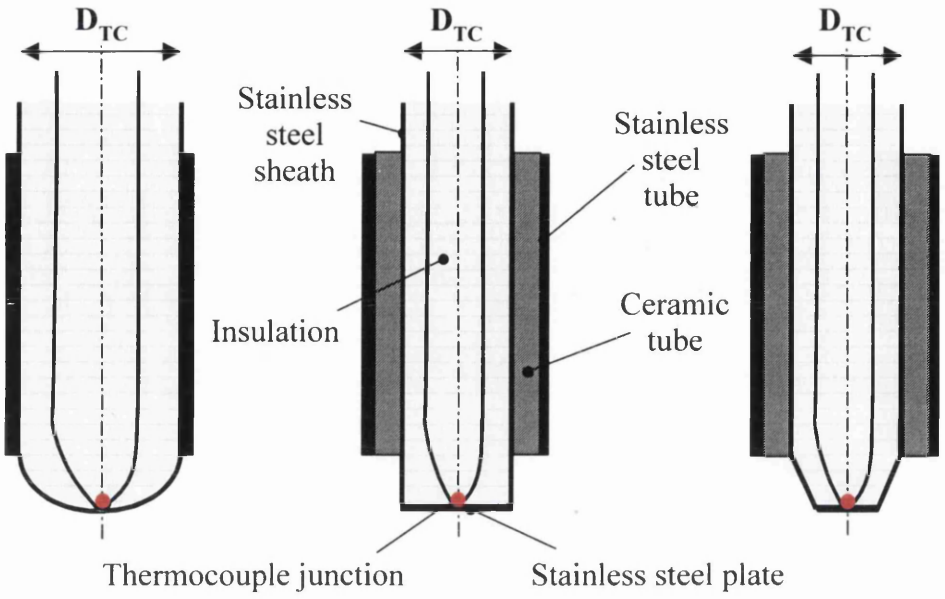

TC 1	TC 2	TC 3
D = 2.6 mm, cylindrical, no insulation	D = 1.6 mm, cylindrical, ceramic insulation	D = 1.6 mm, conical to 1.3 mm, ceramic insulation

Figure 4.7: Different thermocouple designs with stainless steel plate at the tip

For this investigation, a special test rig was used to simulate the parameters of the process in which the thermocouples would be used. Important parameters are the line speed and the presence or absence of water on the profile surface.

The test equipment is composed of a vessel with a massive rotating aluminium cylinder inside, to provide a large thermal mass. On this, a removable PVC disk is fixed to simulate the profile surface, and a square section bar is mounted on the vessel as a support for the thermocouples. The holes in this support were manufactured in the same way as the holes in the calibrator blocks. These were drilled in several positions from the middle to the outside of the bar to simulate a range of linear velocities at a constant revolution rate of the cylinder. Heating elements were additionally fitted on the inside of the vessel to maintain a constant temperature of the water surrounding the aluminium block, and this was achieved by a controller system.

The set-up used to simulate the conditions on the line is shown in Figure 4.8.

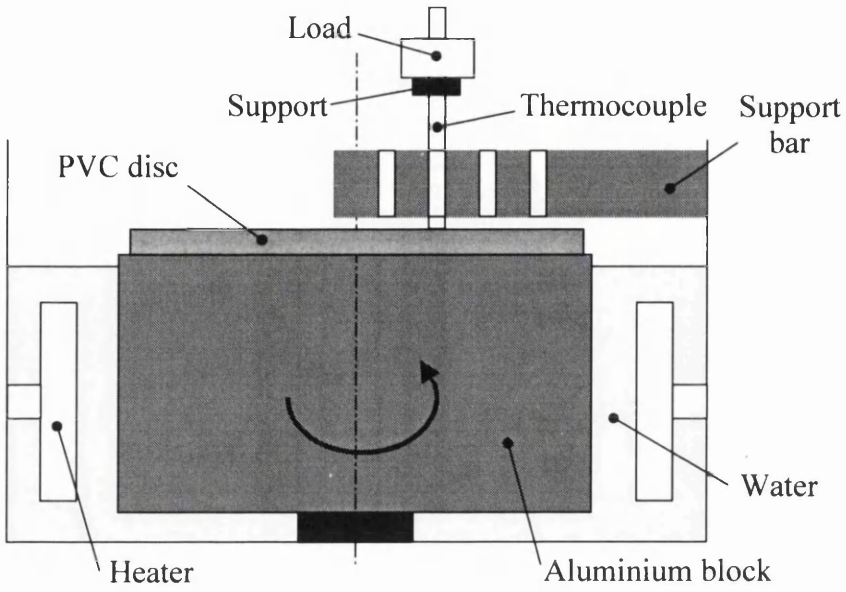

Figure 4.8: Set-up to simulate the conditions on the line

A load applied on the thermocouples generates a frictional force between the PVC disc and the thermocouple tip, and this can increase the measured temperature due to local heat generation, whilst the PVC temperature is constant. With this equipment, several tests were done under different conditions to get information about the influence of the tip design of the thermocouples, the limit of the loads to avoid scratches on the PVC surface, and the influence of the applied load on the measured temperatures.

After connecting the thermocouples to an available data logging system, they were calibrated at 25°C in an oil bath.

The calibrated thermocouples were used in the first set of experiments, where the load was varied at a fixed velocity. This set shows the influence of the load on the temperature measurements due to the higher friction force. In these measurements, the PVC stationary surface temperature was measured before and after the experiments to get the datum value for effects with different loads. In the Figures 4.9 to 4.11 will be shown the dynamic measurement results with variation of line speed and load for a dry PVC surface.

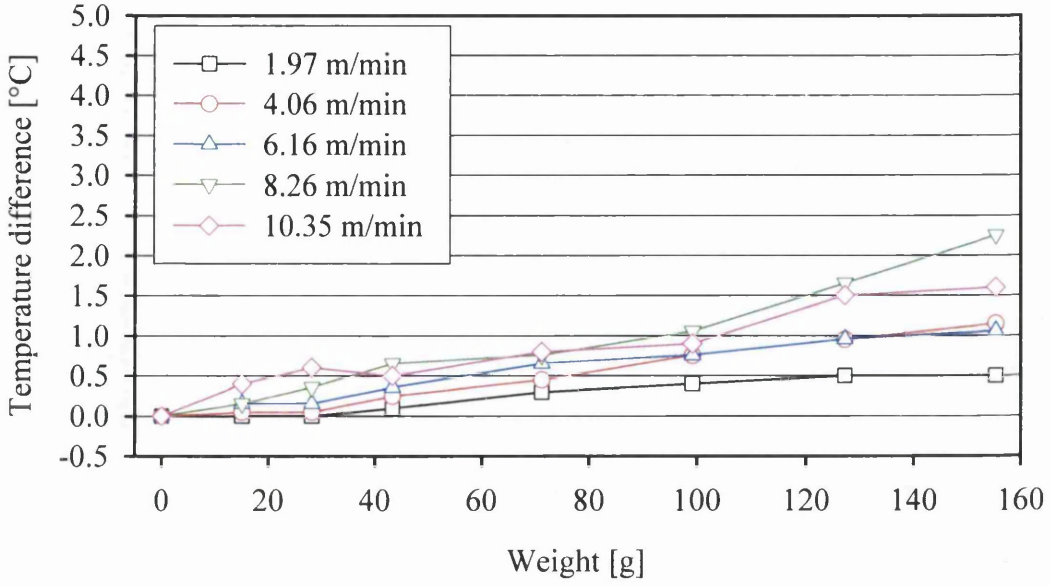

Figure 4.9: TC 1; 2.6 mm, cylindrical, no insulation, no water, 25°C; as a function of applied load and PVC surface velocity

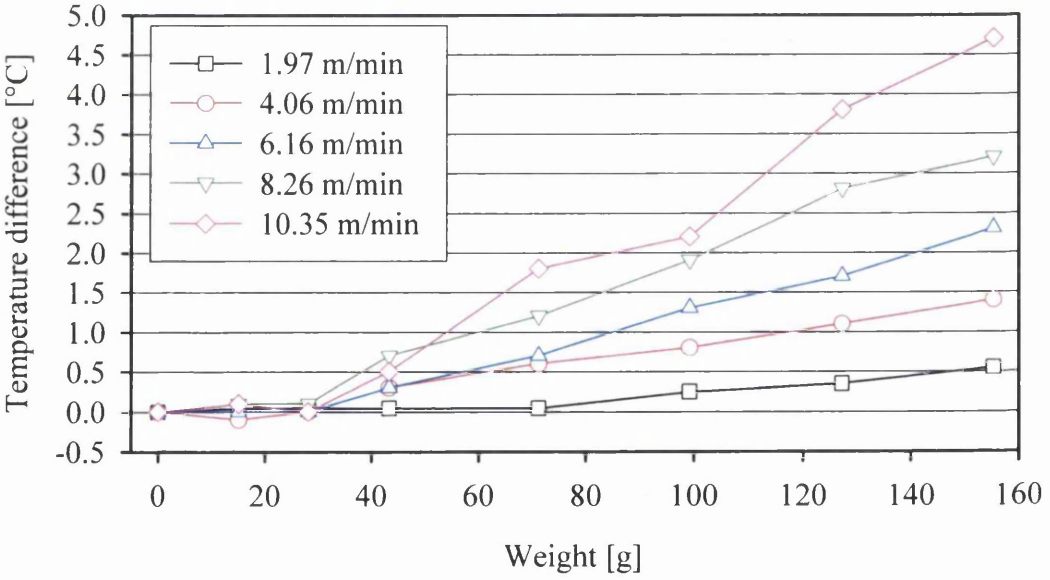

Figure 4.10: TC 2; 1.6 mm, cylindrical, ceramic insulation, no water, 25°C; as a function of applied load and PVC surface velocity

In direct comparison of the cylindrical thermocouples, the temperature of TC 2 (1.6 mm diameter, ceramic insulation) has increased more than TC 1, (2.6 mm diameter, no insulation) at the same weight and velocity. It seems that the conductivity of the steel sheath of the thermocouple has an influence on the measured profile surface temperature.

Thermocouple TC 3 has the same diameter as TC2, but the diameter of the tip is reduced to 1.3 mm and the results of the measurements for a dry PVC surface are presented in Figure 4.11.

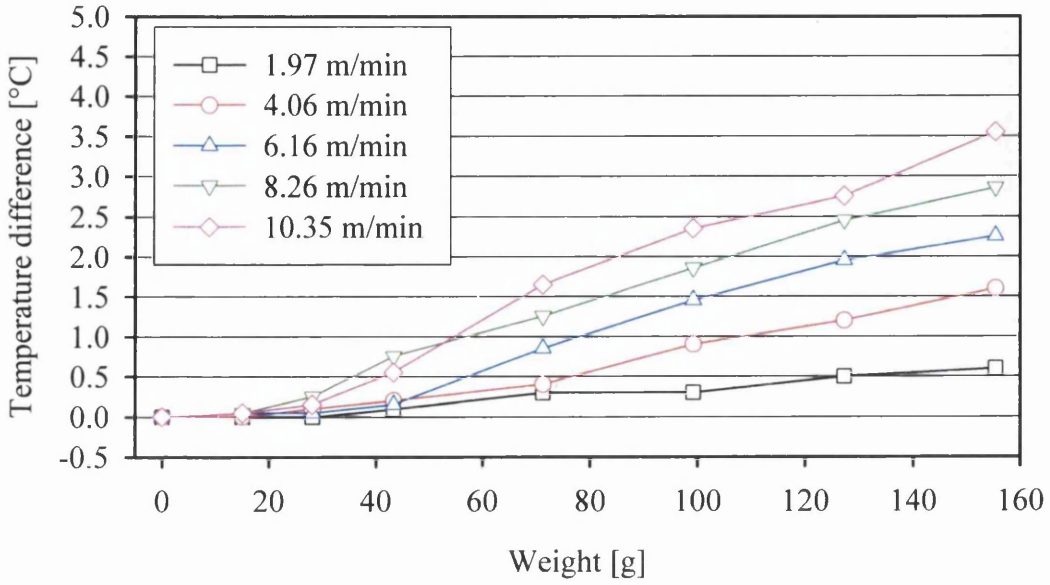

Figure 4.11: TC 3; 1.6 mm, conical to 1.3 mm, ceramic insulation, no water, 25°C; as a function of applied load and PVC surface velocity

The thermocouple type TC 3 (1.6 mm, conical to 1.3 mm, ceramic insulation) shows the same behaviour as the cylindrical thermocouple TC 2.
It was also noted, that the first scratches on the PVC surface have appeared at a load of 128 g.

The last figures have shown the results for a dry surface. To see the influence of the temperature measurements on presence or absence of water on the PVC surface, the water level in the vessel was raised, so that the PVC disc was covered with water and the results of the three different types of thermocouples are shown in the Figures 4.12 to 4.14.

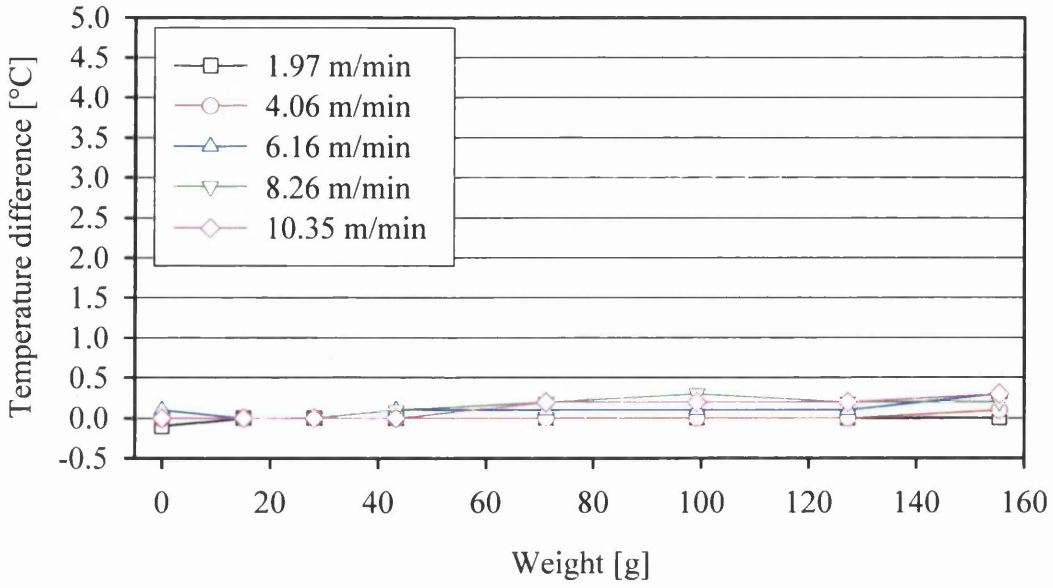

Figure 4.12: TC 1; 2.6 mm, cylindrical, no insulation, water, 25°C; as a function of appliedload and PVC surface velocity

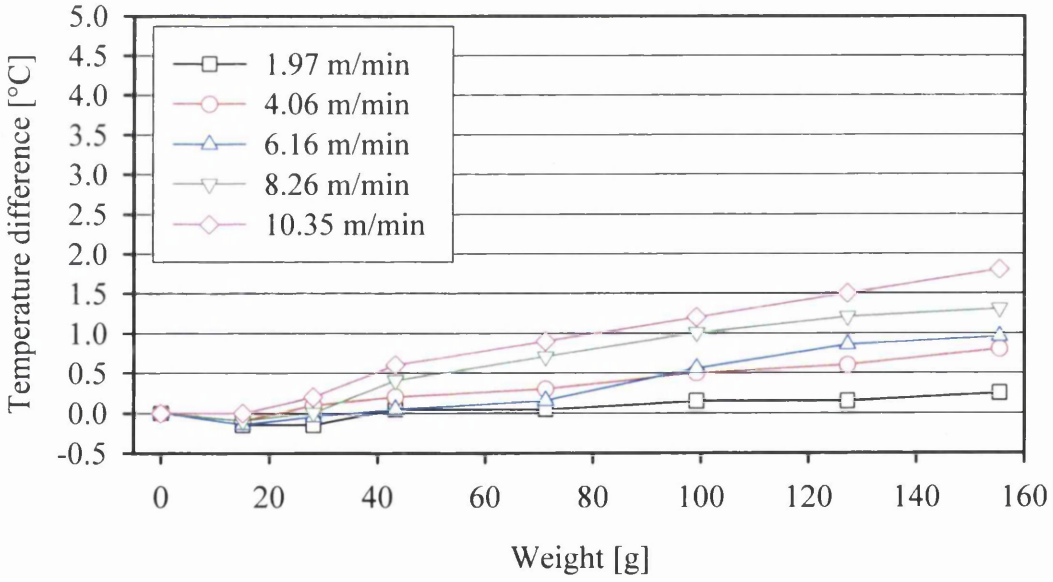

Figure 4.13: TC 2; 1.6 mm, cylindrical, ceramic insulation, water, 25°C; as a function of applied load and PVC surface velocity

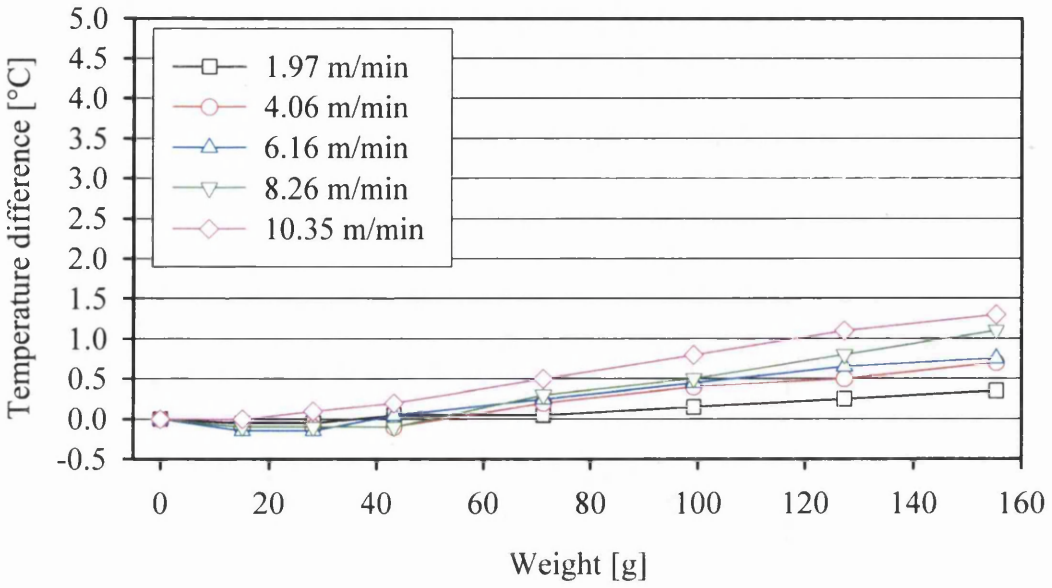

Figure 4.14: TC 3; 1.6 mm, conical to 1.3 mm, ceramic insulation, water, 25°C; as a function of applied load and PVC surface velocity

The thermocouple with 2.6 mm diameter, without insulation, has shown no significant influence on weight and velocity. The problem in wet calibration is to determine the absence or presence of water on the profile surface. So the appropriate thermocouple is the thermocouple TC 3 with conical end, because this has a low scatter in wet conditions at a weight of 43 g. The weight was also chosen in view of the need for profile surface measurements a short distance after the entry of the first calibrator, where the weight cannot be high due to weakness of the profile surface after only a few millimetres of cooling.
These results were subsequently used to correct the profile surface temperatures measured on the calibration line. In dry calibration, the correction was used, as shown in Figure 4.11. The problem for the correction in wet calibration is the condition of the profile surface. In the results for the wet calibration, a minor correction was made, not as large as for dry calibration.

The type of thermocouples to be used, e.g. Fe-CuNi (Typ J), is dependent on the data logging system, because some cannot handle certain types of thermocouples. This decision was therefore made after the selection of the data logging system, which will be described later.
After manufacturing the thermocouples according to the chosen design, as described above, they were glued into the ceramic pipe, providing a free sliding, wear resistant and insulated system. A weight was used to apply the load on the thermocouple, supported on a ring, glued 10 mm below the top of the stainless steel tube.

As mentioned before, the profile surface temperatures are measured across the profile surface with three thermocouples in a row as for the calibrator wall temperatures, see Figure 4.15.

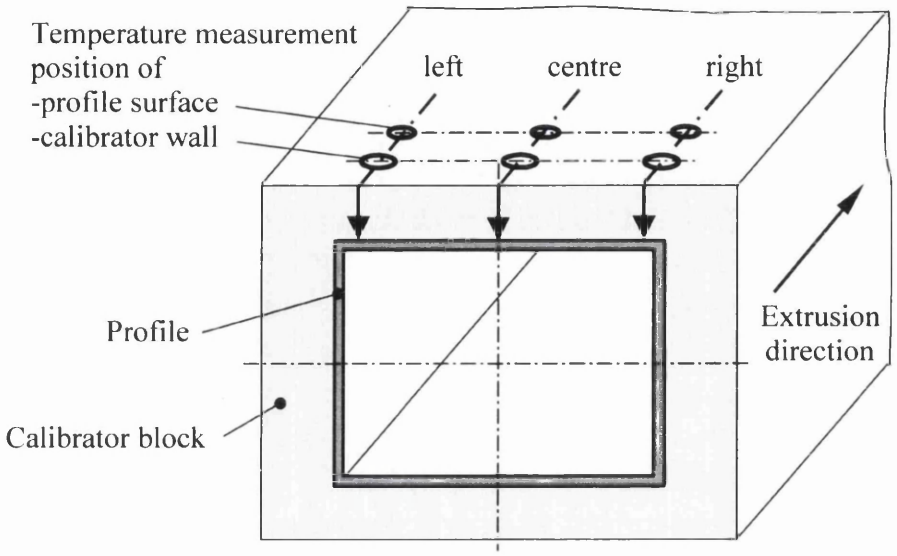

Figure 4.15: Position of thermocouples for the measurements of profile surface and calibrator wall temperatures across the profile

Each of these combined rows is positioned at the entrance and exit of each calibrator, and a further two are distributed along the length direction of the calibrator. This is shown for Calibrator 1 in Figure 4.16. Further details are shown in Appendix A.

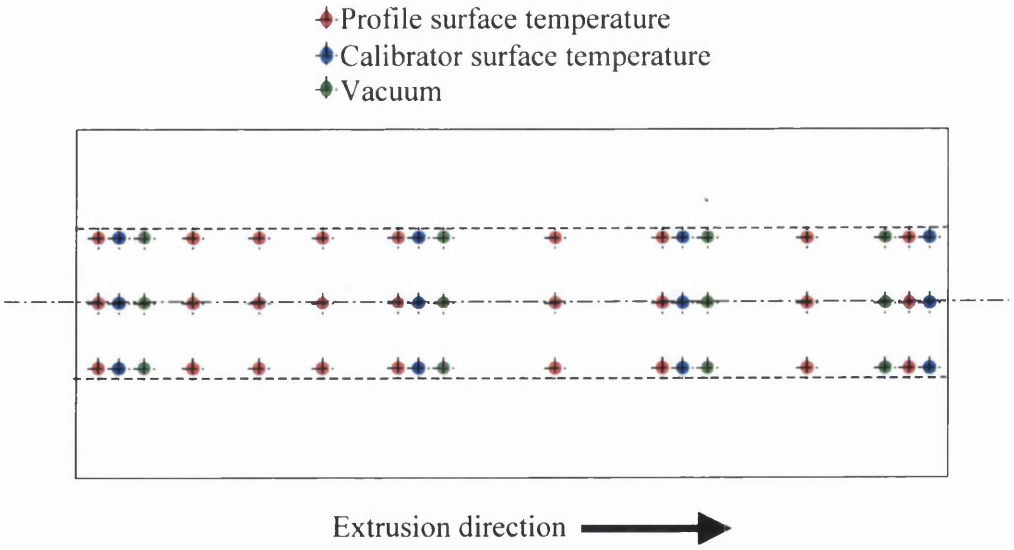

Figure 4.16: Positions of calibrator wall, profile wall temperatures and vacuum measurements

4.2.1.4 Coolant water temperatures in the cooling channels of the calibration units

To measure these, adapters were used, connected to the hoses of the cooling system. These adapters, made out of brass, had a location hole for thermocouples and included polymer insulation to avoid heat conduction from the metal to the thermocouple. The inlet cooling water temperatures were measured once for each calibrator, but the outlet temperatures were measured at each outlet.

4.2.2 Forces

The forces in the normal production process are measured only at the haul-off. By force balance, the haul-off force should equal the summed calibrator forces. To get information about the distribution of the forces in the process, these were additionally measured for each calibration unit.

4.2.2.1 Forces on each calibrator unit

For the calibrator forces a new system had to be designed, which had to fulfil several specifications. The most important of these is the reduction of sliding friction of calibrators during the small movement necessary for the force measurements. To get an overview of the possibilities, an established design method was used, the so-called morphologic box, see next Figure 4.17.

Position of calibration units					
	Fixed	Adjustable in steps	Free adjustable		
Guideway	Rail system	Frame system	Solid system		
Bearing type	Sliding friction bearing	Roller bearing	Recirculating linear ball bearings	Air	Steel prism
Force sensing device	Mechanical	Load cell			

Figure 4.17: Morphologic box for the design for support of calibration units

The load cells with an output of 0-10 Volts were chosen to provide a suitable system for data logging.

The selected aspects are highlighted and with these, a system was designed following specifications that would allow for general use in the collaborating company. To fix the calibrators on this system, special adapters were designed.

In the Figure 4.18 are shown the calibrators mounted on the rail system.

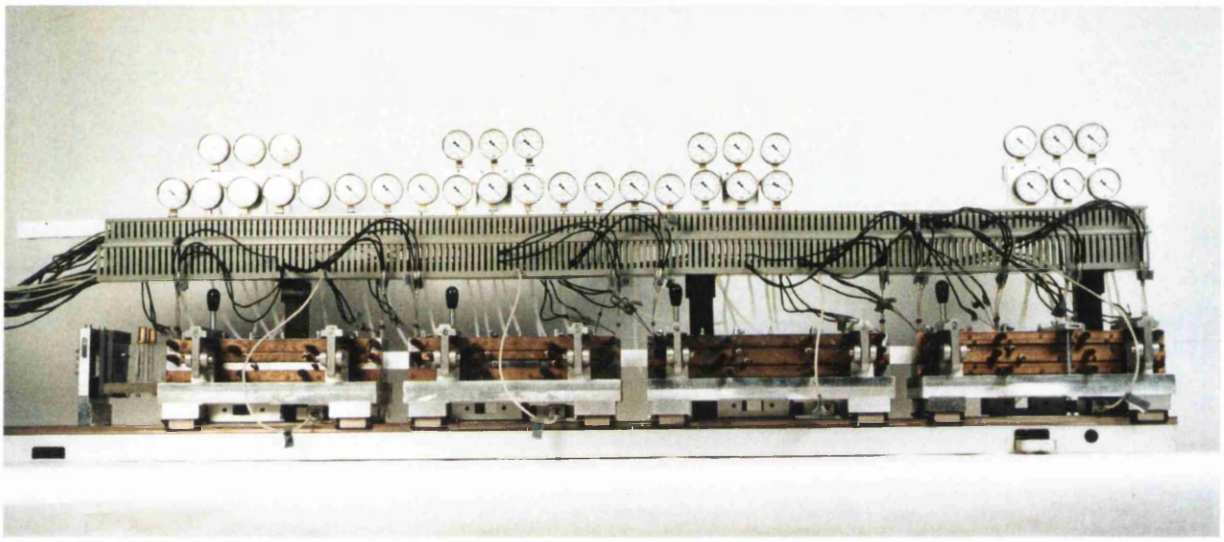

Figure 4.18: Calibrators mounted on rail system

The pressure gauges for the vacuum measurements are visible in the background. Furthermore, the plug-in thermocouples and cables with support can be seen in this Figure. More details are shown in the next Figure 4.19.

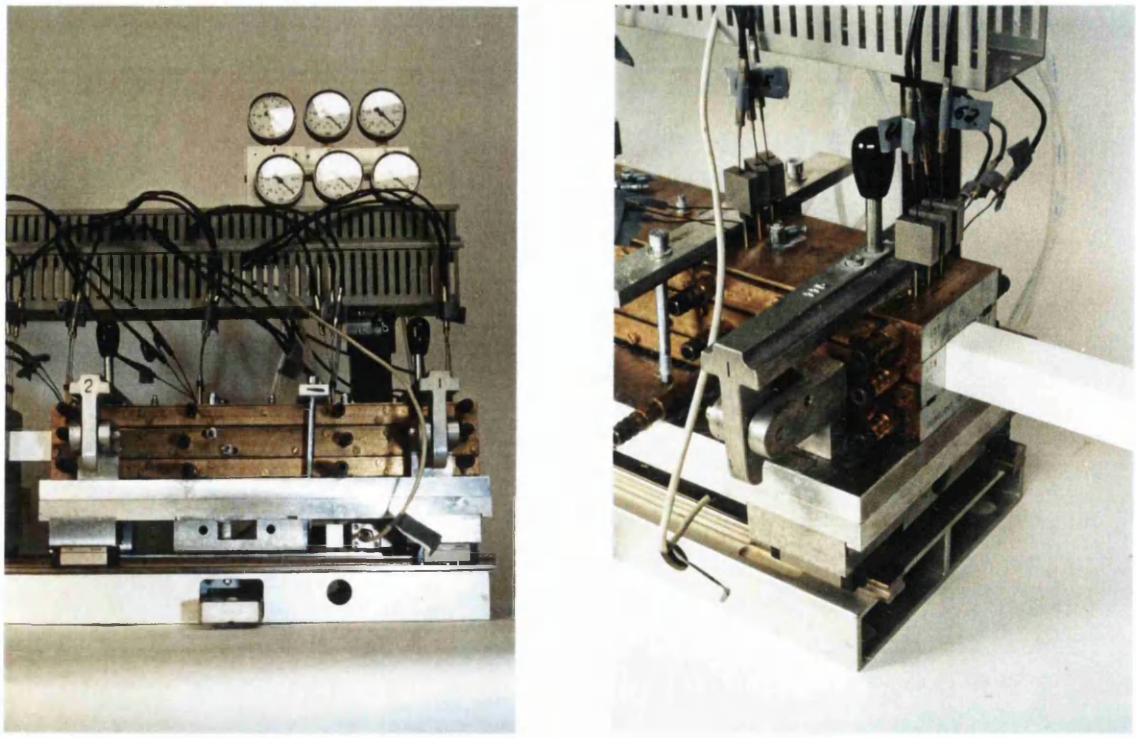

Figure 4.19: Position of force transducer and inlet of calibrator 1 with fitted thermocouples

The total set-up of the calibrator table is shown in the next figure.

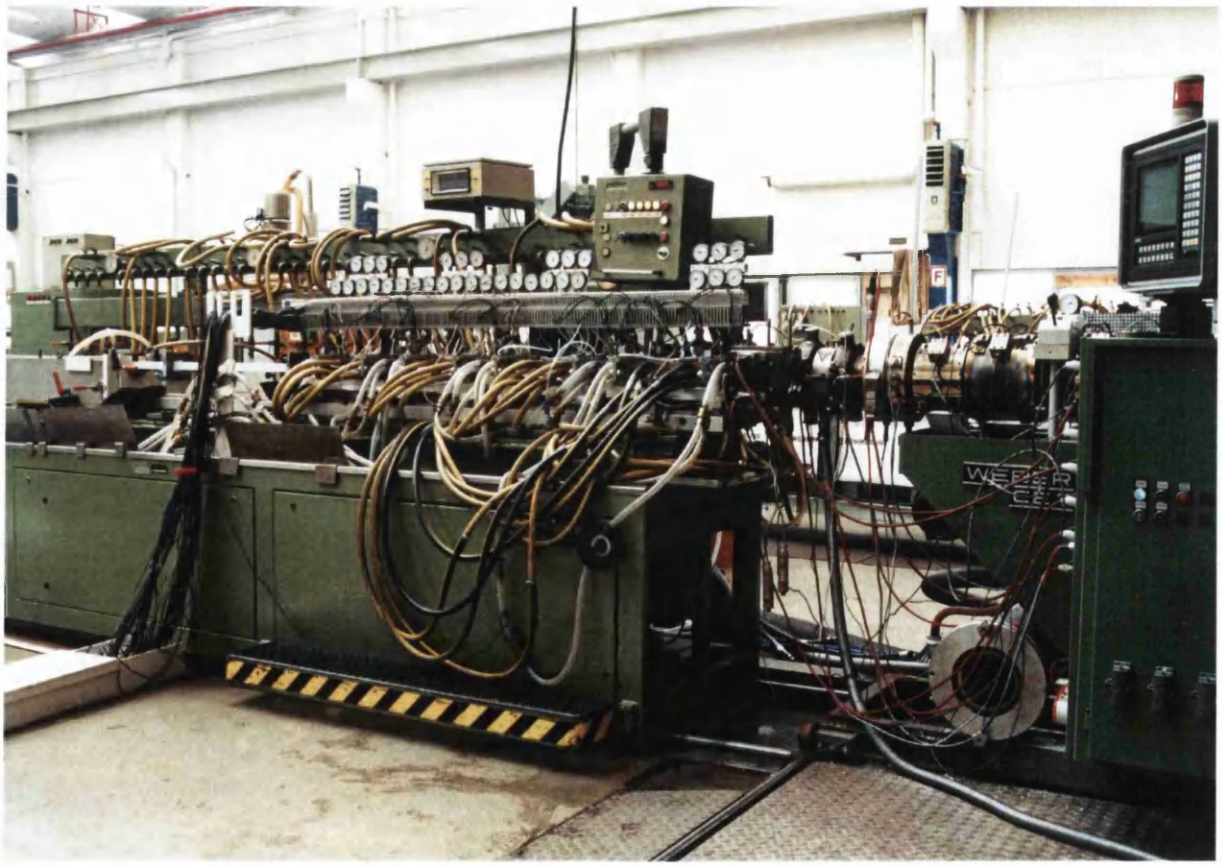

Figure 4.20: Total set-up of calibrator table and extruder

4.2.2.2 Haul-off force

In normal lines, haul-off units are mounted on a rails system and the haul-forces are measured with simple force transducers, mostly hydraulic based, against a support fixed to the ground. For our experiments, it was necessary to reduce the friction of the wheels of the haul-off unit, and set-up a data logging system. The forces were measured with load cells, and a reduction of the friction of the wheels was obtained with roller bearings. To reduce the friction on the rails, strips of metal with a polished surface were fitted on the old rails. For these measurements, load cells were also used, as for the calibrator forces with the same output voltage. All details are shown in figures in Appendix A.

4.2.3 Water flow rates

In general, the cooling of the profile can be separated into two parts. The first is the cooling in the calibration units themselves, and, relevant to this water flow rates were measured at the exit of each part of the calibrators. For these, a small tank was used and after a defined time, e.g. two or three minutes, the collected water volume gives the flow rate.

The second part of the cooling system is the intermediate water baths between the calibration units (wet calibration) and a water bath with or without vacuum after the last calibration unit. The vacuum draws water from the intermediate water baths into the ends of each calibrator and thence into the vacuum system. If the calibrator is designed to fit the profile very well, the flow rate of this water should be very small, however, for this case, the calibration units would have to be manufactured with internal taper, which is not usual. To investigate this water flow rate, a separation of the water-air mixture is necessary. For this, to get a first indication, it is practical to start with a simple separation system. The system that was designed is shown in the next Figure 4.21.

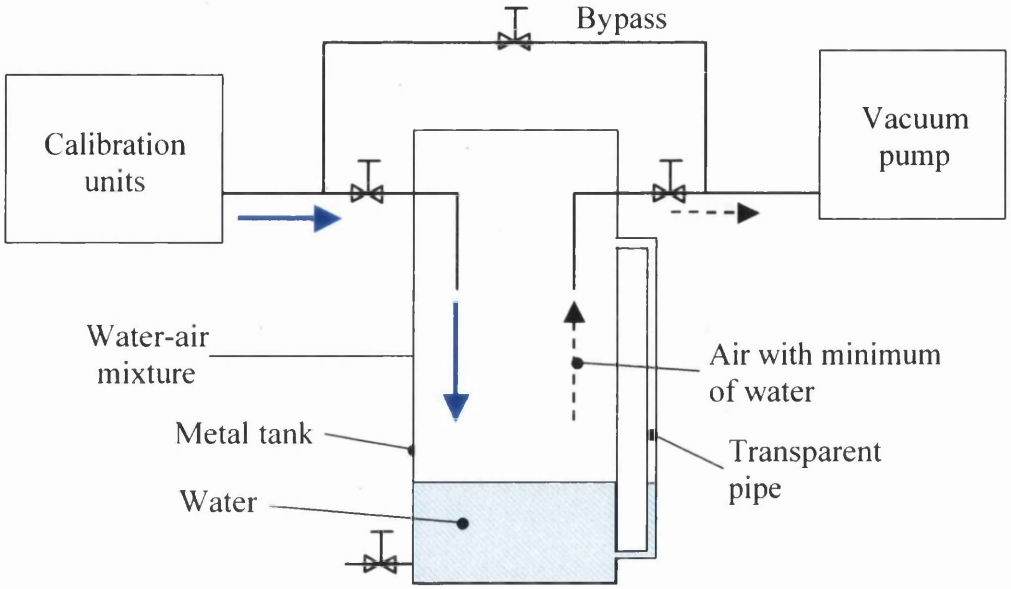

Figure 4.21: Mechanical separation device for water from air-water mixture

This separation unit was fitted between the calibration units and the main vacuum distribution bar. The measurement of the flow rate was more complicated, because the vacuum must be maintained during on-line measurements and an interruption can disturb the calibration process. To avoid this, a transparent pipe was fitted at the outside of the main steel tank to see the level of the water inside. Additionally, marks were made on the transparent pipe to determine the level of water. For these measurements, the bypass was closed and all the drawn in water had to go through the steel tank and was so separated from air by gravity. The time for the water level to rise between the marks was measured with a stopwatch and the flow rate was calculated afterwards.

4.2.4 Vacuum

First of all, the measured vacuum must be defined. The measured values relate to the environmental pressure, which is an absolute pressure of approximately 1 bar. A measured vacuum of –0.2 bar gauge is equal 0.8 bar absolute.

In a normal production line, the vacuum is measured only in the distribution main line by dial gauges. To get more information about the vacuum within each calibrator, holes were drilled through the calibration units to measure the vacuum at the profile surface in the calibration units. For these measurements, small dial gauges were used, which were connected with small pipes to the holes in the calibration units. The holes are mainly drilled in the upper surface, to

provide information together with the temperature measurements. Additionally, several holes were drilled at the sides and bottom of the calibrators. The positions of the holes for vacuum measurements were in rows of three close to the positions for temperature measurements, and the positions were shown in Figure 4.16.

4.2.5 Operating parameters of the extruder and the die

The extruder used was a Weber CE7 and the relevant process parameters are displayed on a screen based on the control system; the following values can be noted:

- Screw revolution speed
- Barrel temperatures
- Die temperatures
- Material pressure in die
- Material temperature at extruder exit, single measurement point.

4.3 Data logging system

Following establishment of the measurement methods, a data logging system was built to record the data. The favoured system was a PC based data logging solution to allow flexible handling for further applications. The two major components are the hardware and software, and their details are explained now.

4.3.1 Hardware

Conditional on the grounded thermocouples, the A/D input cards must provide a differential input to avoid wrong temperature measurements and also cold junction compensations must exist. Furthermore, the measurement cards must be able to handle the output voltage from the load cells of 0-10 Volt. The A/D converter card PCL-818HG from Advantech [148] was chosen in combination with the Amplifier and Multiplexer board PCLD 789D for the channel expansion. In addition to these cards, an available data logging system LSB36II from Linseis

[149] was added to provide the necessary data channels, The complete system is shown in the Appendix A.

4.3.2 Software

A data logging software package was used to record all the data. Several are available on the market. To find the most suitable package, the following specifications were identified:

- Handling of at least 120 data channels
- Handling of temperature measurements for different types of thermocouples
- Reading of parallel port
- Reading of I/O card
- Programmable input and output blocks
- Clear and easy arrangement of modules

Intensive tests and applications were carried out to find which software could fulfil these specifications. Finally the software DASYLAB® [150] was chosen for the data logging.

4.4 Post production measurements

4.4.1 Profile dimensions

The dimensions of the profile are measured after the production to investigate the influence of the process parameter. The total dimensions are the diameter width W and height H, and the average wall thickness t will be calculated with the wall thicknesses s_L, s_B s_R and s_T of each side. Further, the corner dimensions L*, B*, R* and T* were also measured, to see if there is a draw down effect due to processing conditions. All the measured dimensions are shown in Figure 4.22.

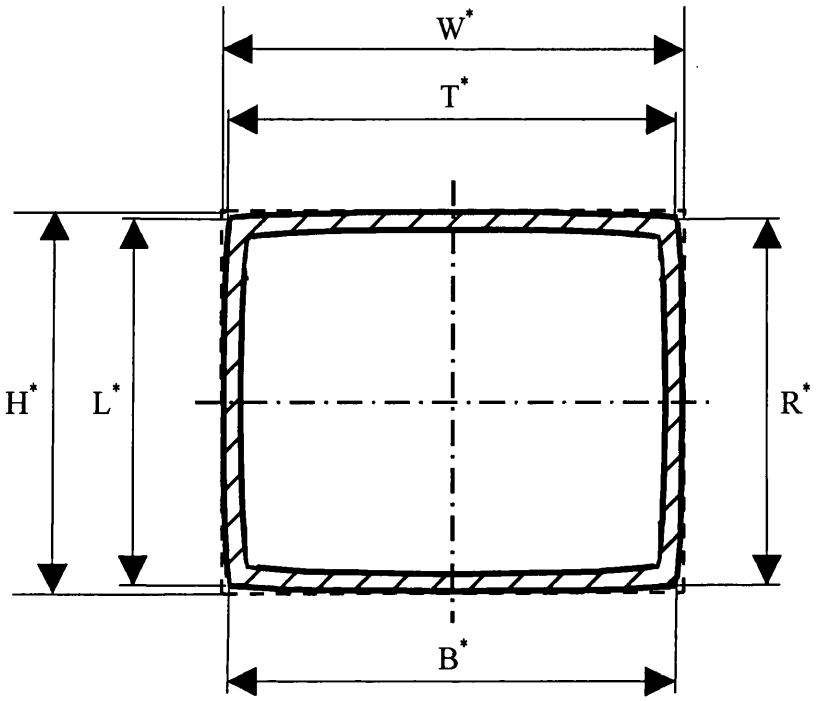

Figure 4.22: Measured profile dimensions

4.4.2 Shrinkage

The shrinkage is an important profile property parameter. The standard test according to DIN EN 479 is used to obtain a measured value. In this test, two holes are drilled a distance of 200 mm apart in the profile sample of a minimum length in line direction of 250 mm length. Then the prepared profile is reheated up to 100° for 1 hour, and after cooling at room temperature on a talcum covered steel or glass sheet, the distance between the drilled holes is measured and compared with the distances before heating. The difference is the shrinkage, declared as a percentage for simple comparison.

4.4.3 Impact

Another important profile property is the impact behaviour. Unmodified PVC is brittle and to avoid breaking of the profile, additives are used to improve it. Tests for the impact behaviour were carried out according to DIN 53 753 to see if there is a dependence on processing conditions. Sample strips were cut out of the top of the profile, along the line direction.

4.4.4 Bending of strips

Further measurements were done to investigate the dependence of the frozen-in stresses in line direction in the profile walls on the calibrator and haul-off forces. Strips were cut out of each side of the profile, Figure 4.23, and were put on a scanner immediately after cutting to record the bending. In addition, the dimensions of the strips were measured to estimate the residual stresses in the strips.

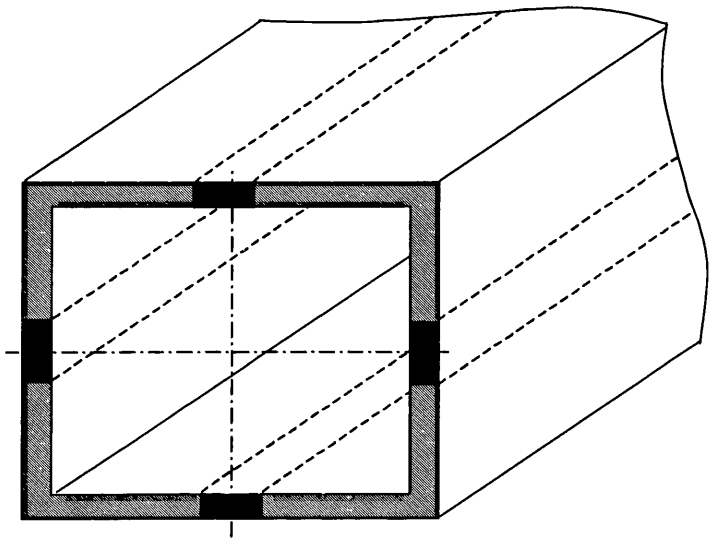

Figure 4.23: Positions of strips to be cut out of profile

CHAPTER 5

Overview of experimental results

This Chapter gives a general perspective of the direct influence of the controlled parameters on the dependent parameters of the calibration process that are measured on-line. Only a selection from the extensive results is shown, with brief comment. In the following Chapter 6, a more detailed analysis and discussion follows, including results of tests and measurements on the finished profiles, to provide information on the profile properties and how they are related to the processing conditions.

5.1 Selection of the ranges of the controlled parameters

To provide as much information as possible, process parameters were varied as widely as operating limitations and available time allowed. The limits of some process parameter became apparent only during the experiments, e.g. the line speed could not be increased to 10 m/min, because the process became unstable and the profile collapsed. There were also other limits, but when experiments were run near to a limit, much useful information could be obtained about the process.

Though a wide range of operating parameters was used, the die existed in only two forms. It was manufactured for the production of the rectangular EU-profile, and the torpedo was interchangeable to give a gap width at the die exit of 1.50 or 2.50 mm, see Figure 4.1 in Chapter 4.

The space between the calibrators could be filled with water for wet calibration, or not, for dry calibration. After the forth calibrator was another section, which could be run wet or dry, and this was followed by a final four meter water bath. The total layout was shown in Chapter 4 describing the experimental set-up.
The vacuum system allowed a variation from –0.2 to –0.8 bar gauge pressure in the vacuum main to the first Calibrator, and –0.4 to –0.8 bar to the others. The reason for this is that the

water ring vacuum pumps can handle only a limited inflow rate of water drawn in by the vacuum from the intermediate water baths.

An increase in the extruder throughput was used to vary the wall thickness of the profile at a constant line speed. In the first set of experiments the melt temperature varied from 176°C up to 191°C as the screw speed increased to get a profile wall thickness of 2.50 mm. In the second set of experiments the melt temperature was adjusted at 195°C by increasing or decreasing the barrel temperatures of the extruder. This was necessary, because a higher throughput requires higher speed, resulting in a higher dissipation of mechanical energy into the material, which increases the melt temperature.

An overview of the ranges of the set process parameters is shown in Table 5.1

Gap width at die exit [mm]	1.50				2.50			
Profile wall thickness [mm]	1.50	1.75	2.00		2.50	2.75	3.00	3.25
Calibration conditions	Wet	Dry						
Vacuum in cal. 1 [bar]	-0.2	-0.4	-0.6	-0.8				
Vacuum in cal. 2,3 and 4 [bar]	-0.4	-0.6	-0.8					
Line speed [m/min]	1	2	3	4	5	6	7	8
Melt temperature [°C]	180	185	190	195	200			
Coolant water temperatures in calibrator 1 [°C]	16	30	40					
Water injection points in cal. 1	1	2	3	4				

Table 5.1: Ranges of set process parameters

Tables showing the complete programme of experimental trials carried out are given in Appendix B.

5.1.1 Overview of selected results measured on-line

In the following figures are shown the relationship of the dependent process parameter measured on-line, to the set parameters of the calibration process.

5.1.2 Haul-off forces

In general, the haul-off force is found to be within a few percent of sum of the calibrator forces, as is required by the force balance. The next figure, Figure 5.1, shows the difference between the haul-off force and summed calibrator forces in percent.

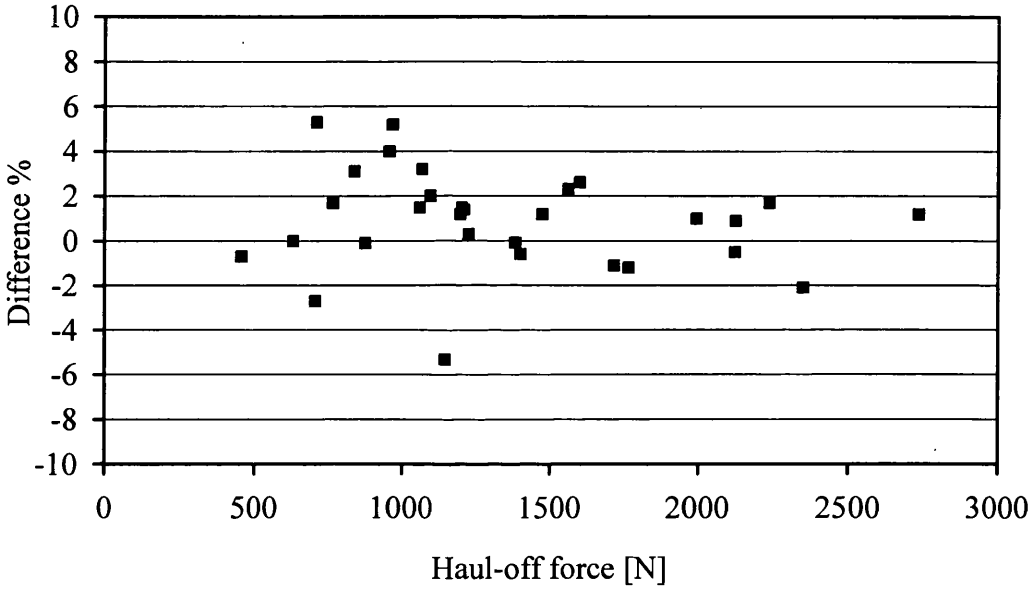

Figure 5.1: Differences between haul-off forces and summed calibrator forces

Bearing in mind the possibilities of friction in the rail system, and drag from the connection of cooling and vacuum tubes to the calibrators, the agreement found is very satisfactory.

It is well known that increasing vacuum in the calibration units causes higher frictional drag forces, and so higher haul-off forces. In the next figure, Figure 5.2, this is visible, together with the influence of the line speed and the absence or presence of water between the calibration units. The line was not stable above 5 m/min with vacuum greater than –0.4 bar gauge.

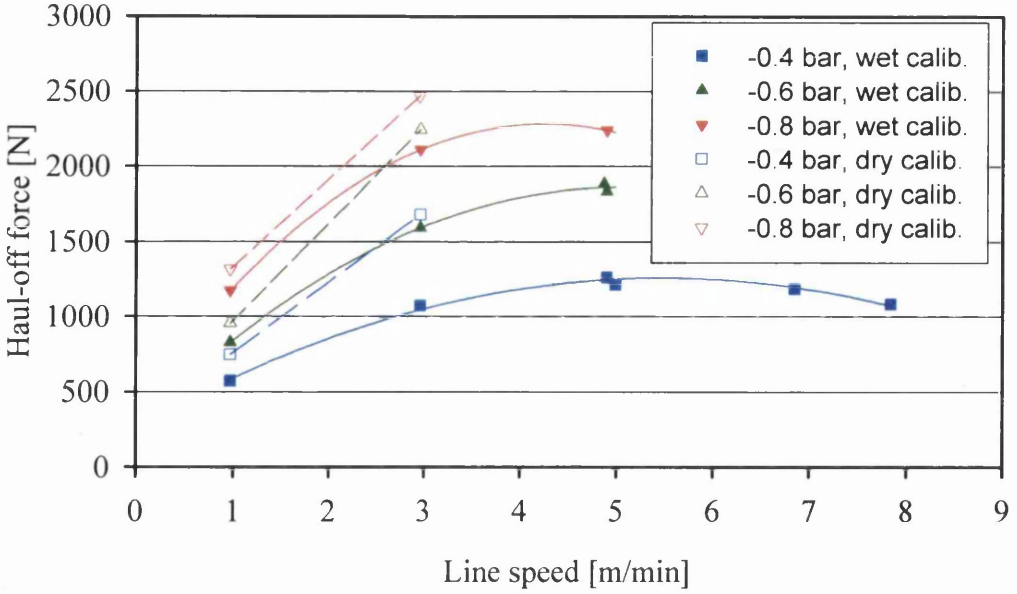

Figure 5.2: Haul-off force at different line speeds and applied vacuum, wet and dry calibration; 2.50 mm die exit; 2.50 mm profile wall thickness; vacuum constant in all calibration units. The same wall thickness at different line speeds was achieved using a higher throughput of the extruder.

As expected, we see that the higher the vacuum, the higher is the haul-off force. The haul-off force is also higher without water between the calibration units (dry calibration).
It is also to be observed that the haul-off force decreases above 6 m/min at –0.4 bar. This result, which is perhaps initially surprising, is explained later.

In another experiment, vacuum in Calibrator 1 was varied whilst a constant vacuum of –0.4 bar was applied in the other calibration units at a line speed of 4 m/min in wet calibration. Results are shown in the Figure 5.3.

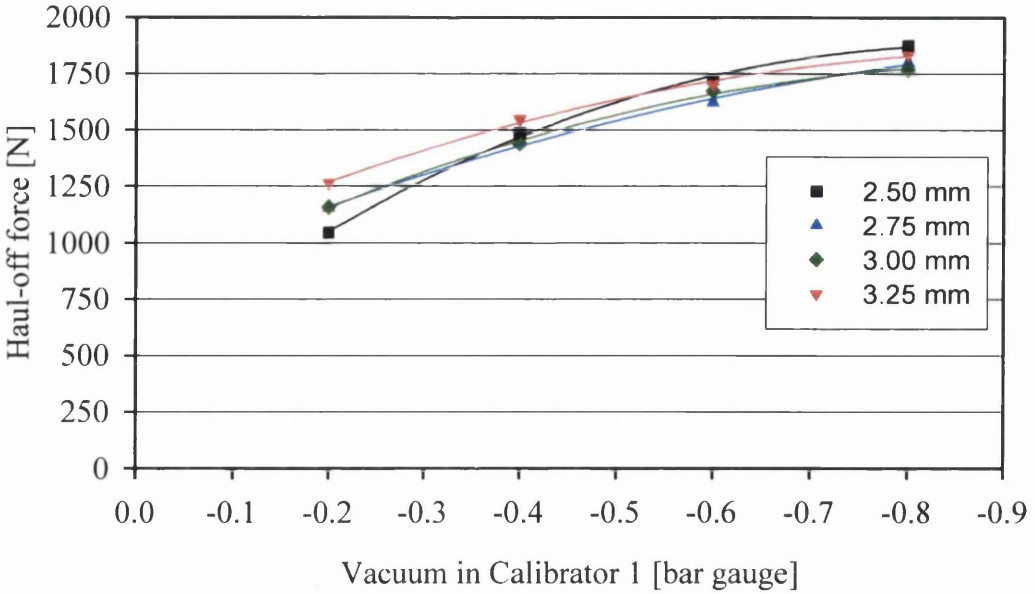

Figure 5.3: Haul-off forces as a function of applied vacuum in Calibrator 1 at a line speed of 4 m/min in wet calibration; constant vacuum of –0.4 bar in Calibration units 2, 3 and 4 for different profile wall thicknesses of 2.50 mm – 3.25 mm; 2.50 mm die exit

It is shown that a lower vacuum in Calibrator 1 gives the expected significantly lower haul-off force.

A significant parameter is the melt temperature. To get an idea of its influence, the melt temperatures were varied at a line speed of 4 m/min in wet calibration for a vacuum of –0.4 bar by changing the barrel temperatures of the extruder, Figure 5.4.

The shown melt temperatures are an average of 13 temperatures on the cross section between the extruder and die, measured on-line with the measurement cross.

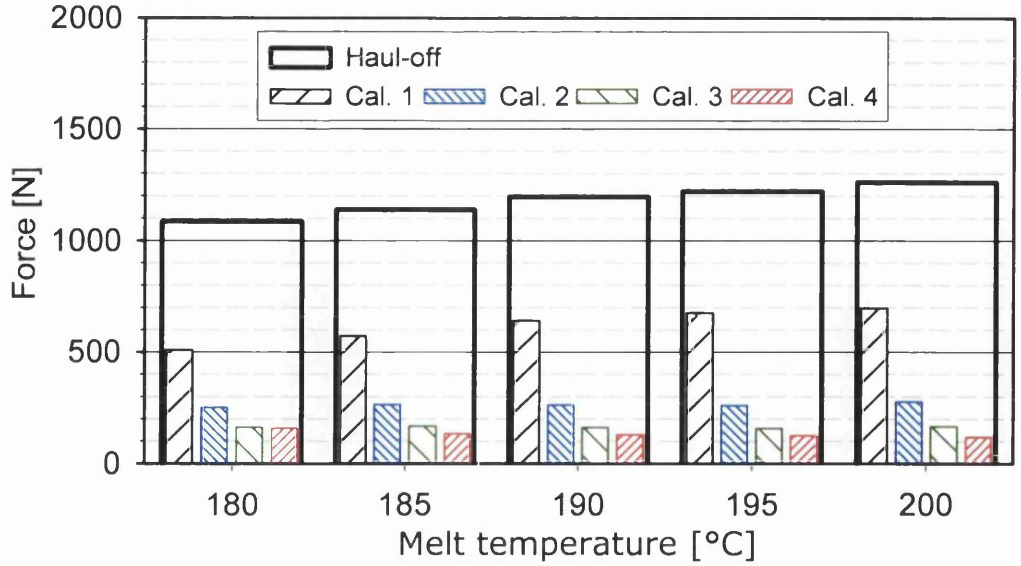

Figure 5.4: Haul-off and calibrator forces for different melt temperatures; 4 m/min line speed; 2.50 mm die exit; 2.75 mm profile wall thickness; wet calibration; constant vacuum of –0.4 bar

The forces at the haul-off and in Calibrator 1 have increased with an increasing melt temperature. The forces in the downstream calibrators are independent of the temperature change.

Following the variation of the melt temperature, the coolant temperatures in Calibrator 1 were varied, and the result was the opposite of that just obtained: the force decreases with higher coolant temperatures, Figure 5.5.

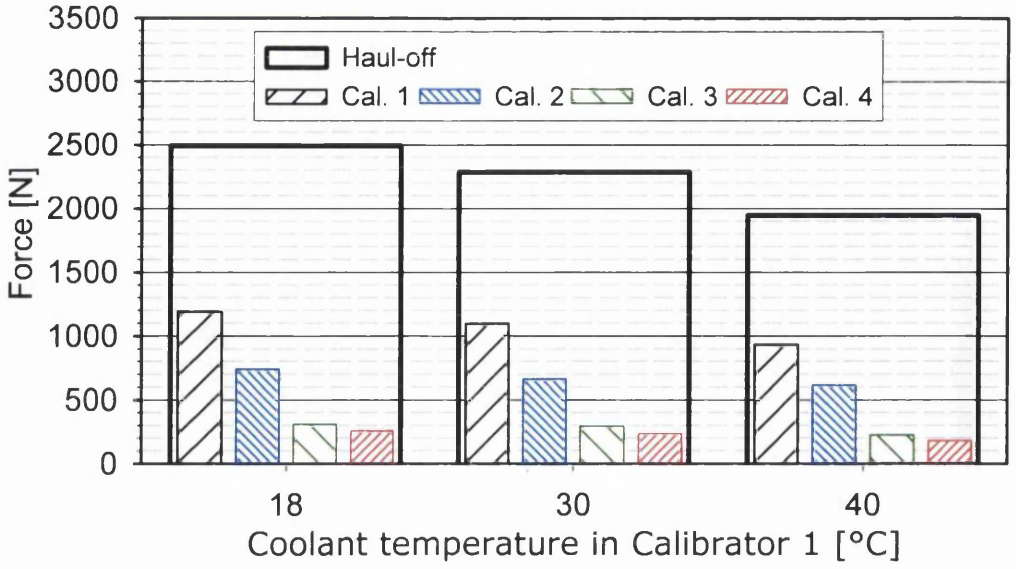

Figure 5.5: Haul-off and calibrator 1 forces for different coolant temperatures; 4 m/min line speed; 2.50 mm die exit; 2.75 mm profile wall thickness; wet calibration; vacuum constant of –0.8 bar

In a further, test water was injected into the first calibrator in an attempt to increase the cooling and reduce the friction coefficient and thus the force in Calibrator 1. For this experiment, grooves were milled on the inside of the calibrator block at four different positions along the calibrator. To the grooves on each side, a hole was drilled from the outside to provide a connection for a water supply. These holes were connected to a water tank and so the water was sucked into the calibrator by vacuum. The positions of the injection points are shown in the next Figure 5.6.

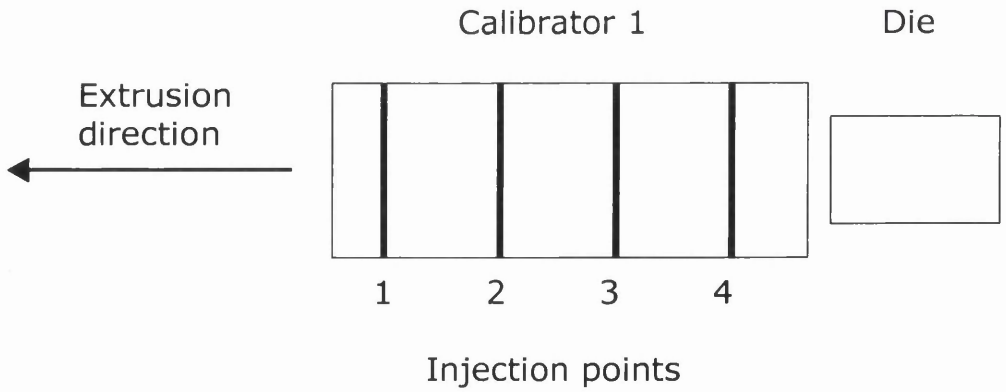

Figure 5.6: Positions of injection points

The injection procedure started with a reference measurement without injection to see the reduction due to injection. The experimental procedure was as follows. Firstly, the injection point 1 was switched on and the results were logged. Subsequently, the upstream injection

point 2 was switched on together with point 1. This was continued until all injection points were switched on together. The results are shown in Figure 5.7.

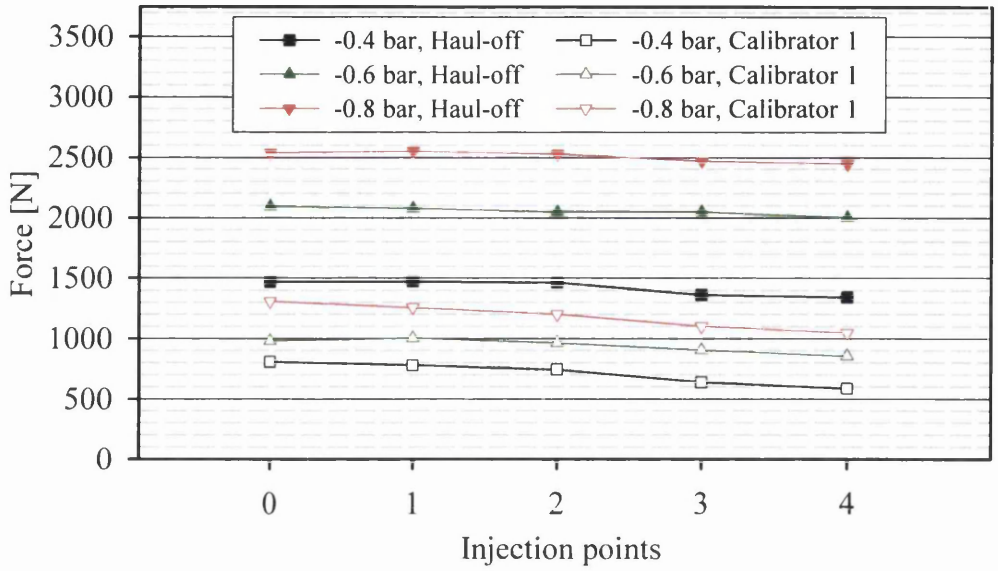

Figure 5.7: Haul-off forces with water injection into Calibrator 1; 4 m/min line speed; 2.50 mm die exit; 2.75 mm profile wall thickness; wet calibration

The benchmark was the force in Calibrator 1 without injection, marked in the figure as injection point zero. The results disappointingly show little effect; we had expected a bigger difference in the forces.

A further procedure was the pressure injection of water, which reduced the force in Calibrator 1 to 30% of the value without injection. However, this condition was not stable; this set of experiments had to be stopped, and no data are reported.

5.1.3 Temperatures

The dominant feature of the calibration process is the cooling. To get more information about the temperatures, the calibrator wall and the profile surface temperatures were measured on-line as described in Chapter 4. In the next figures are shown the temperatures of the profile surface at the centre of the upper surface of the profile at different line speeds, vacuum, wall thickness and melt temperature.

In Figure 5.8 is shown the influence of the line speed and vacuum on the temperatures in dry calibration.

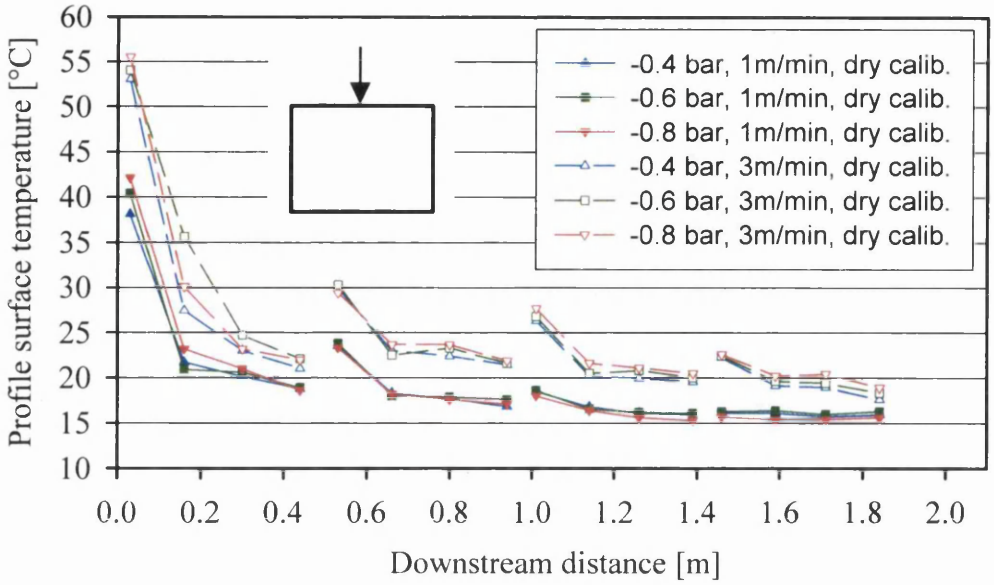

Figure 5.8: Temperatures for profile surface at different line speeds and vacuum; centre of profile; 2.50 mm die exit ; 2.50 mm profile wall thickness; dry calibration

It is obvious that the profile surfaces re-heat between the calibration units, and the re-heating increases at higher line speeds. This re-heating is well known in practice during dry calibration, and is due to the low heat transfer coefficient to air. The effect is not usually present during wet calibration. This is shown in Figure 5.9 in a direct comparison of the wet and dry system.

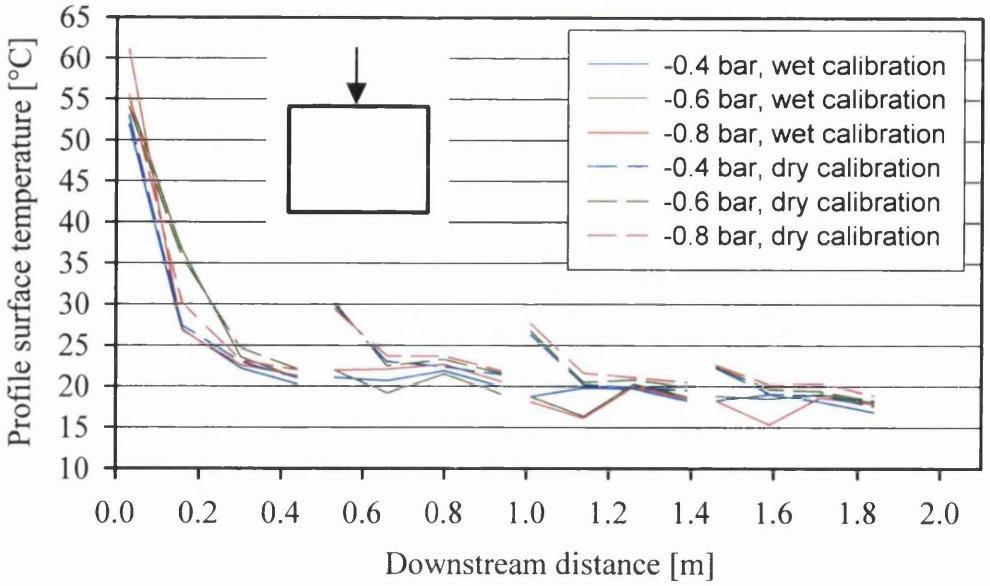

Figure 5.9: Temperatures for profile surface at different vacuum; centre; wet and dry calibration; 3 m/min line speed; 2.50 mm die exit; 2.50 mm profile wall thickness

The variation of vacuum has shown little influence on profile surface temperatures at the centre, especially in the downstream calibrators. In Calibrator 1, the profile surface temperature increase slightly with higher vacuum applied.

An increase in line speed should increase the profile temperature, because the time to cool is reduced, and this is confirmed by measurements, shown in Figure 5.10.

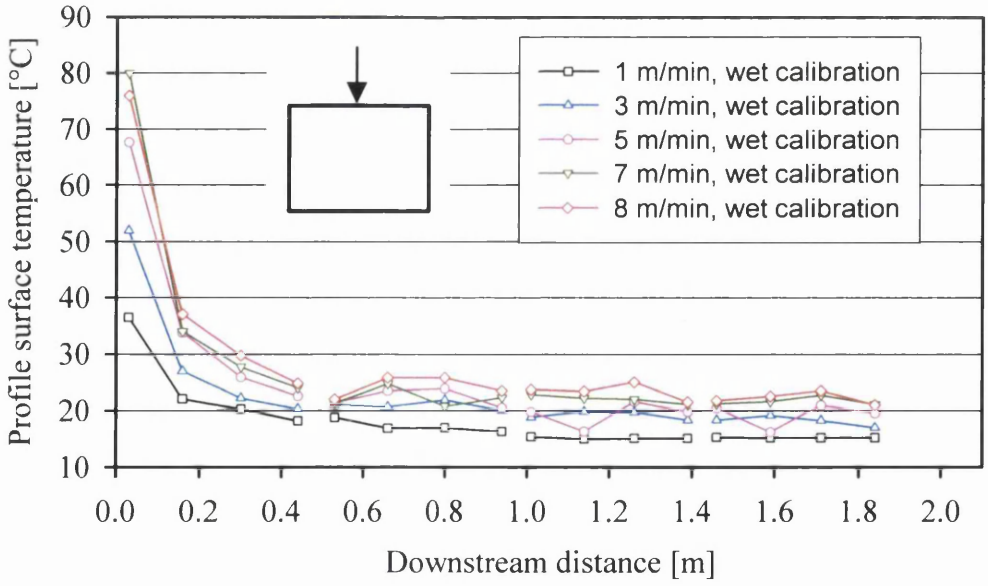

Figure 5.10: Temperatures for profile surface at different line speeds; centre; wet calibration; -0.4 bar vacuum; 2.50 mm die; 2.50 mm profile wall thickness

In the figures so far presented the temperatures were shown at the centre of the profile upper surface. Towards the right and left edges of the surface we have noticed re-heating within the calibration units during wet calibration, see Figure 5.11.

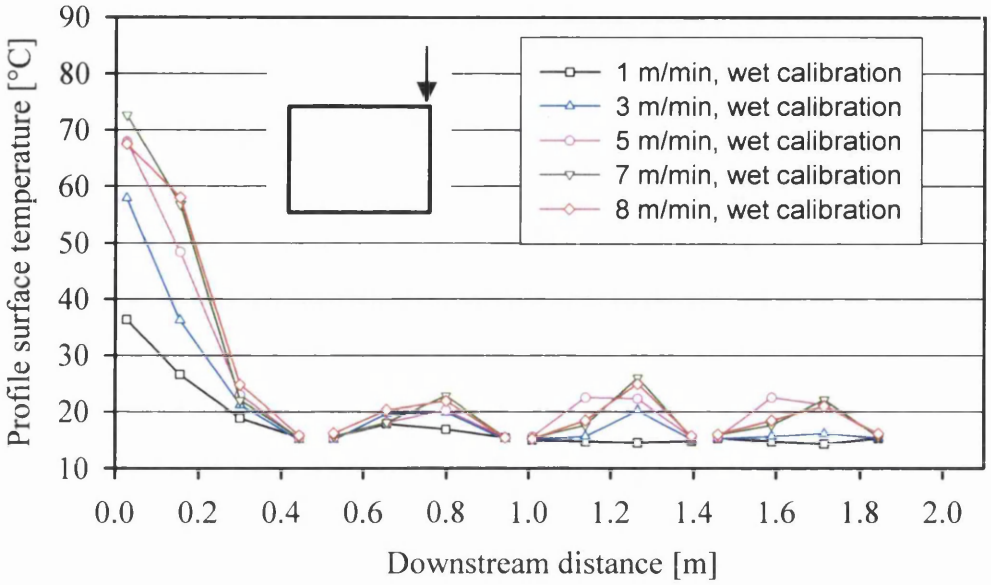

Figure 5.11: Temperatures for profile surface near to the right edge at different line speeds; -0.4 bar vacuum; 2.50 mm die exit; 2.50 mm profile wall thickness; wet calibration

This is believed due to reduced heat transfer coefficients resulting from loss of contact between profile surface and calibrator wall, and this can possibly be confirmed after investigating the profile dimensions.

The variation of the vacuum also has an influence on profile surface temperatures near the edges and this is shown together with the temperature of the centre in Figure 5.12.

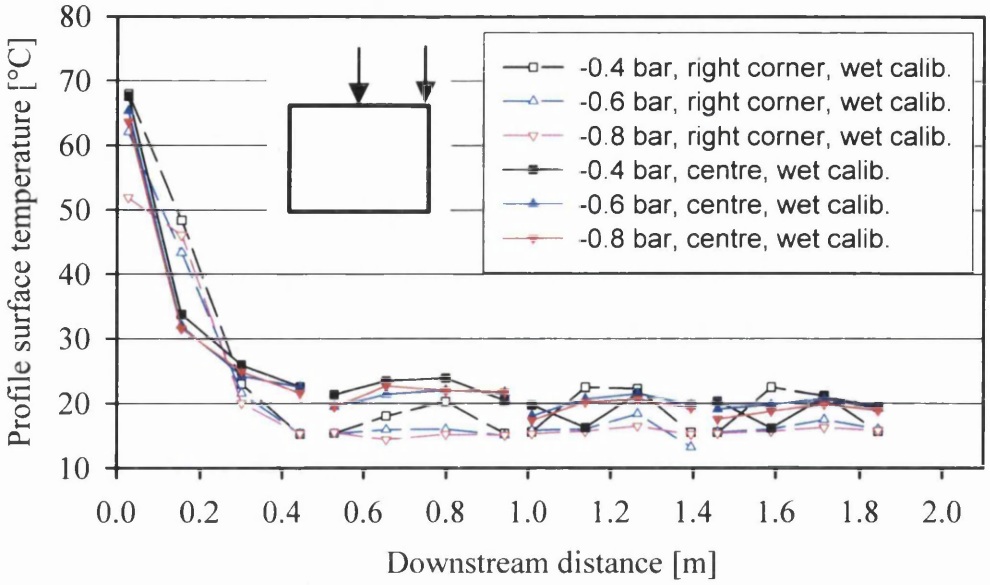

Figure 5.12: Temperatures of the profile upper surface at different vacuum at the centre and near to the right edge; 5 m/min line speed, 2.50 mm die exit; 2.50 mm profile wall thickness; wet calibration

It is noticeable that the most of the corner temperatures are below the centre temperatures of the profile. A reason for this could be a higher heat transfer coefficient at the corner. This might be explained due water penetration, drawn by vacuum into the gap between profile and calibrator.

In the foregoing figures, only the profile surface temperatures were shown. The calibrator wall temperatures were also measured to get further information about the cooling of the profiles. To get an overview of these, in the next figures the profile surface and calibrator wall temperatures are shown together for wet and dry calibration, at 3 m/min.

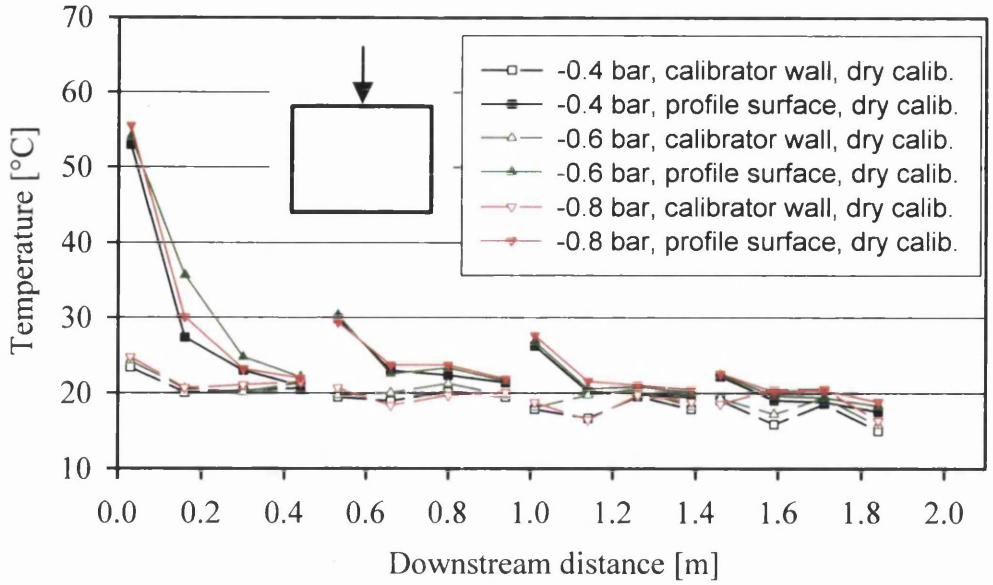

Figure 5.13: Profile surface and calibrator wall temperatures at the centre for different vacuum; 3 m/min line speed; 2.50 mm die exit; 2.50 mm profile wall thickness; dry calibration

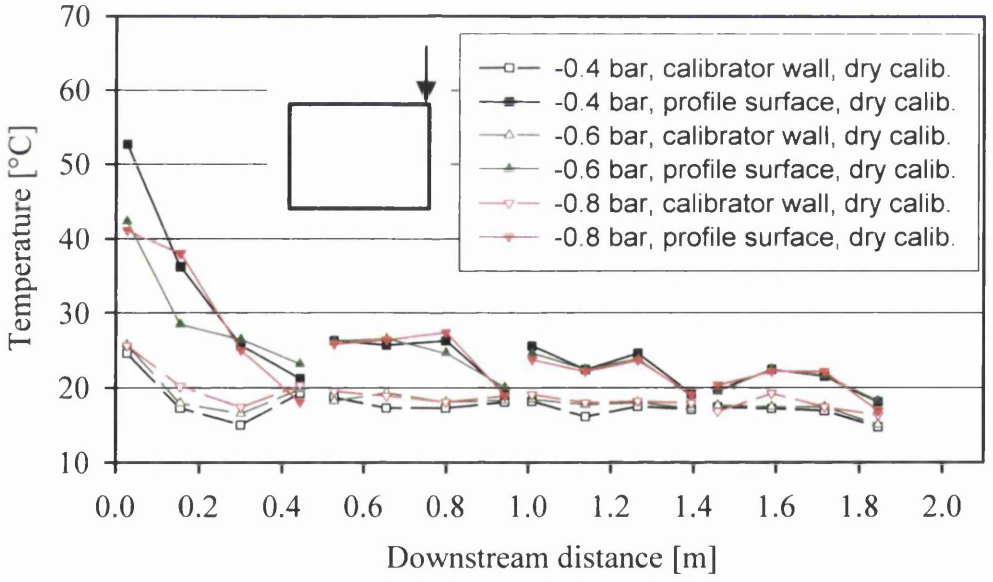

Figure 5.14: Profile surface and calibrator wall temperatures near the right edge for different vacuum; 3 m/min line speed; 2.50 mm die exit; 2.50 mm profile wall thickness; dry calibration

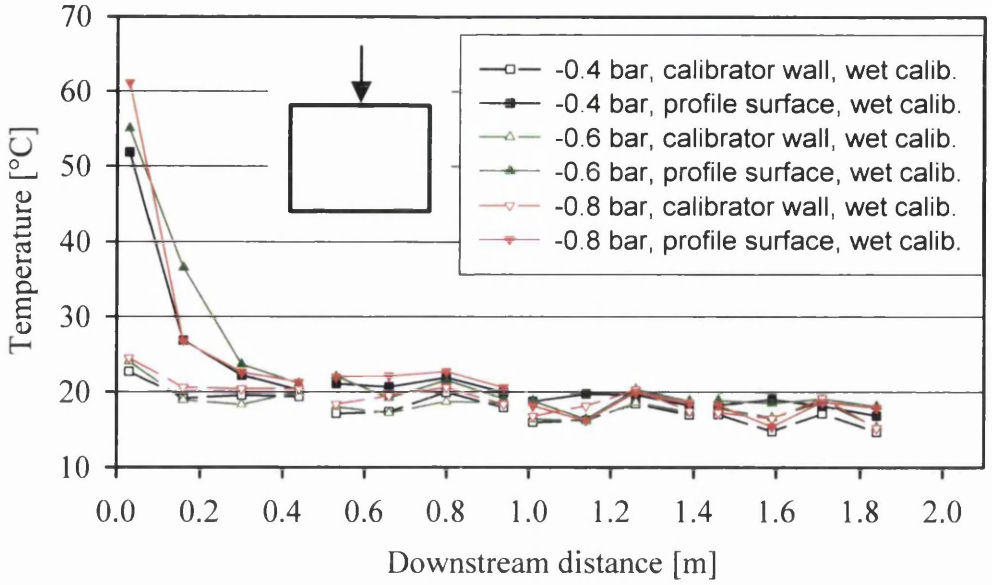

Figure 5.15: Profile surface and calibrator wall temperatures at the centre for different vacuum; 3 m/min line speed; 2.50 mm die exit; 2.50 mm profile wall thickness; wet calibration

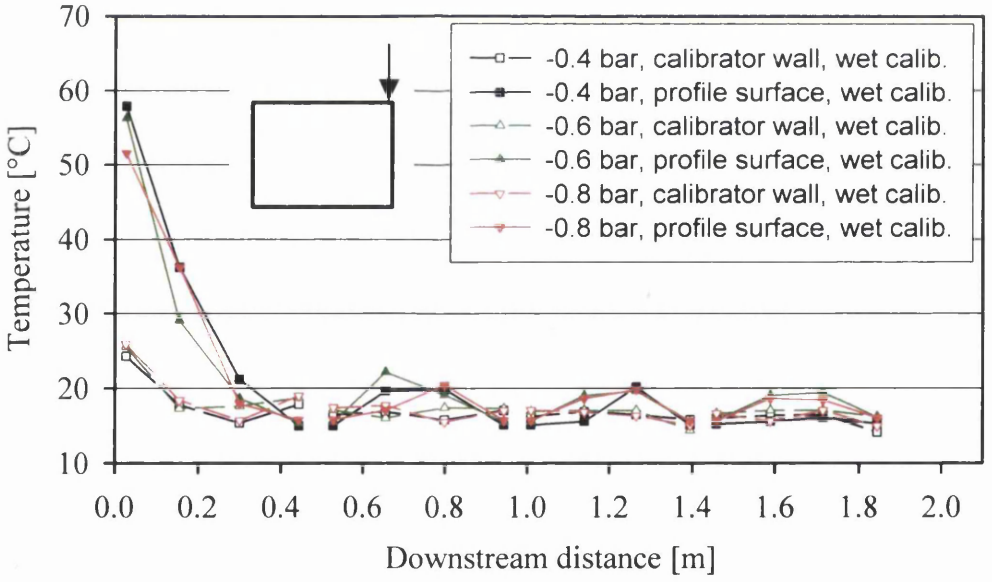

Figure 5.16: Profile surface and calibrator wall temperatures near the right edge for different vacuum; 3 m/min line speed; 2.50 mm die exit; 2.50 mm profile wall thickness; wet calibration

We next look at the influence of higher melt extrusion temperature on temperatures along the calibration line, see Figure 5.17.

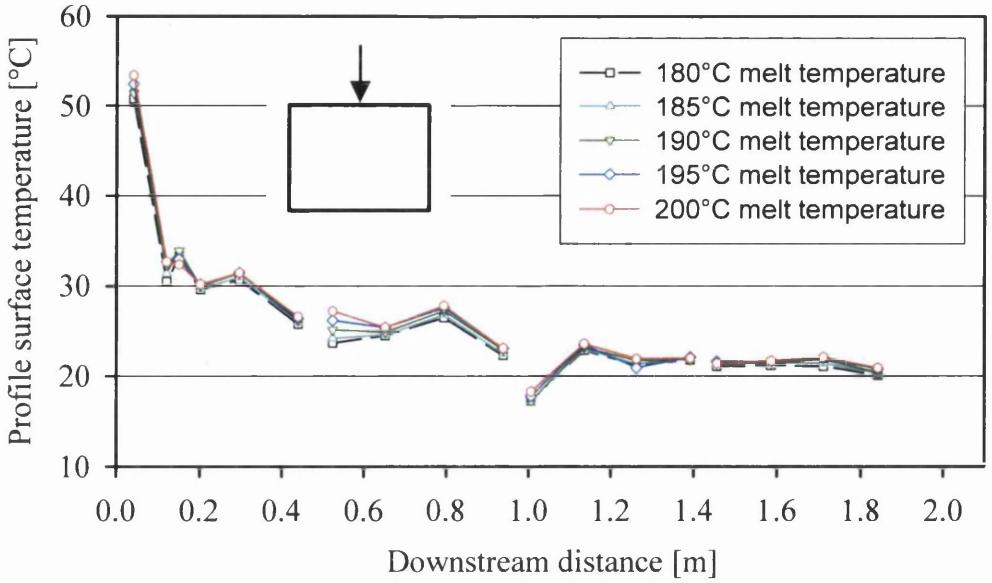

Figure 5.17: Profile surface temperatures for different melt extrusion temperatures; centre; 4 m/min line speed; 2.50 mm die exit; 2.75 mm profile wall thickness; wet calibration

The effect of melt temperature is seen only in increased reheating before Calibrator 2.

5.1.4 Vacuum

Finally, we show an example of the measured vacuum at the profile surface. At the centre zero bar is registered, but near the right and left edges a vacuum is shown, see Figure 5.18.

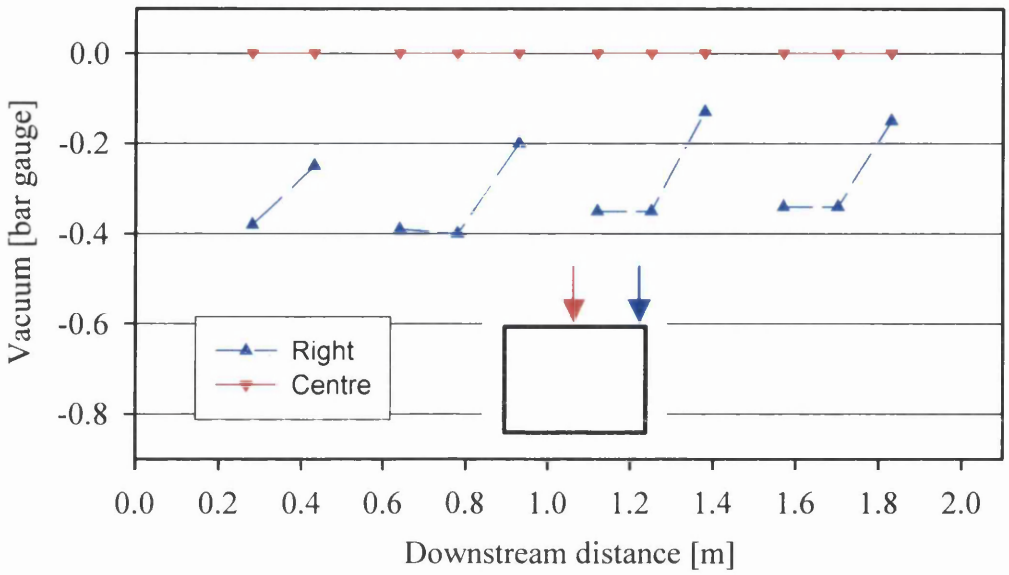

Figure 5.18: Measured vacuum at the centre and right side of the profile; 4 m/ min line speed; 2.50 mm die exit; 2.50 mm profile wall thickness; -0.8 bar vacuum in the distribution, wet calibration

This can be explained by the deformation behaviour of the profile inside the calibrators. At the centre, the vacuum pulls the profile against the calibrator and seals the vacuum connection, giving a (false) zero reading.

In comparison, the edges cannot be deformed so easily and this causes a gap between profile and calibrator wall.

With the applied vacuum in the calibrator, a vacuum can be measured at the edges, see Figure 5.19.

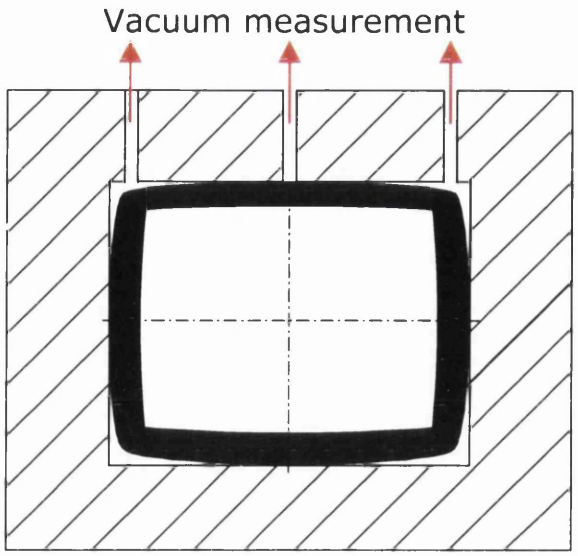

Figure 5.19: Cross section of calibrator and profile with measurement points for vacuum at the centre and edges. Distortion of the profile cross section is exaggerated.

5.2 Conclusion

This Chapter has provided an overview of the type of on-line measurements results obtained. A more comprehensive presentation and discussion of results follow in Chapter 6, whereas the heat transfer will be presented more detailed in Chapter 7.

CHAPTER 6

Experimental results

In this Chapter a more detailed analysis and discussion of on-line and post-production measurement results will be shown.

The data obtained must be reproducible for each kind of experiment in order to see the influence of the varied parameters. To prove the reliability of the data, several experiments were repeated under the same conditions. The deviations obtained were in a range of a few percent, so that the reproducibility was confirmed. This is recognizable in the figures, where the available data are plotted.

6.1 Haul-off and Calibrator Forces

6.1.1 Introduction

The forces in the calibration process have not previously been measured as comprehensively as in the present work. Barth [134] has shown examples of the courses of temperatures and forces in the profile calibration process. Kleindienst [67] has shown experimentally based force data for the pipe calibration process, in which the haul-off forces have increased with increase of vacuum from –0.1 to -0.8 bar gauge for a 25x3mm pipe at 0.82 m/min line speed. Breil [151] has confirmed an increase in force in the calibration of a shutter profile and a picture frame profile at 1.4 m/min line speed for a variation from -0.25 to -0.45 bar gauge. He has also mentioned a big fluctuation, up more than over 200%, in his measurements. Weiler [152] has also found a small scatter in his measurements for the haul-off forces and he has shown a deviation of long wavelength character. Semmler [153] has measured the haul-off forces for variation of line speed form 2.0, 2.5 and 3.0 m/min for a window profile. The forces have increased with an increase of line speed. Menges et al. [154] have measured the forces in Calibrator 1 for a curtain rail profile, but they have presented only one experimental condition, which was not given in detail.

In summary, most of the mentioned references have shown an increasing force with increasing vacuum, and this has been confirmed in the overview of the present experiments, Chapter 5. As mentioned, Breil and Weiler noted a scatter in their haul-off force measurements. A first step in the present experiments was to investigate this finding. The Figure 6.1 shows the forces for a measurement at a line speed of 4 m/min and vacuum of –0.8 bar gauge in wet calibration. A small scatter is visible together with a scatter with long time periodicity, behaviour confirming the findings of Weiler for the haul-off force. Overall, the scatter can be due to a small pulsation of the melt at die exit, slip-stick behaviour in profile / calibrator system and the continuity of the line speed, which is determined by the haul-off unit. This haul-off unit works with a caterpillar system, driven by electric drives via chain wheels. In the mechanical system of tooth wheels and chain, which connects drive and caterpillar, an irregularity of the chain velocity is well known, resulting from the polygon effect of the chain wheel [155].

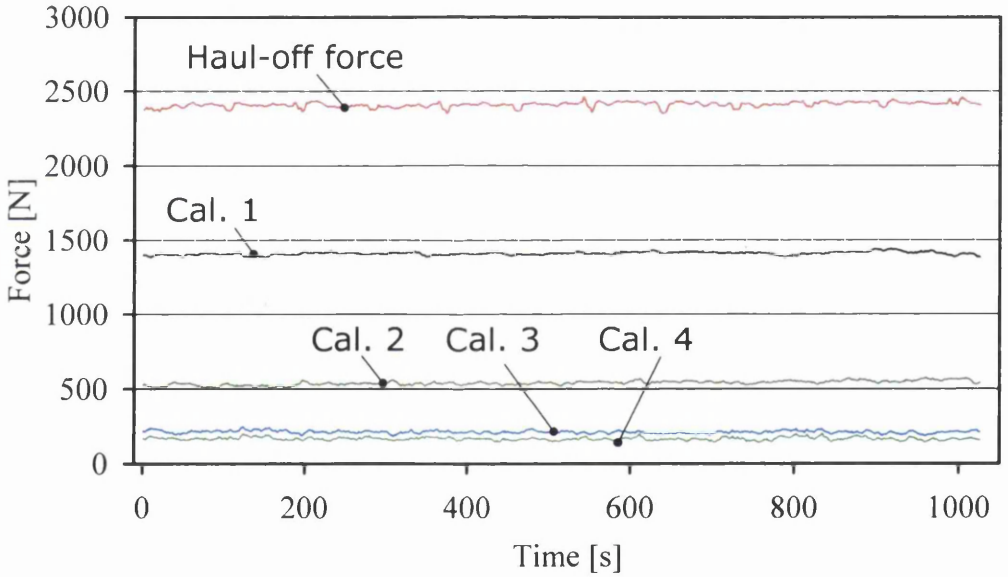

Figure 6.1: Haul-off and Calibrator forces for a profile wall thickness of 2.50 mm at 4 m/min and –0.8 bar gauges in wet calibration; 2.50 mm die exit

These three effects together could be the reason for the visible scatter in the forces. This could be neglected, because the scatter is small, e.g. within a range of +/- 2% for the haul-off force and much less when the average values over a time period of approximately 10-15 min are used. The data collecting has not been started before the system was running in a stable condition after changing a parameter in the experiments, and this time was dependent on the parameter changed, e.g. a change in the melt temperature takes longer to settle than a change of vacuum in the distribution main.

6.1.2 Effects of vacuum in wet and dry calibration at different line speeds

In the first set of experiments the uniform profile wall thickness was obtained for the various line speeds by varying the screw speed. Due to the increase of screw speed the melt temperature was increased from 176°C to 191°C. It was shown in Figure 5.2, how forces depend on the vacuum and line speed, and it was also seen how the haul-off forces in wet calibration at –0.4 bar increased with line speed up to 5m/min and then decreased at higher speeds up to 8 m/min. Reduced contact area of the profile and calibrators is believed to be the reason for this behaviour, resulting in reduced friction forces. Haul-off force tends to act against the vacuum in maintaining contact in the calibrator. The haul-off and friction forces are self-adjusting; if the haul-off force is higher, the profile is stretched in the line direction, reducing its cross-section, and so the contact area of the profile and calibrator is reduced.
To substantiate this explanation, it is necessary to get an idea of the relationship between forces in each calibrator as a percentage of the haul-off force, and this is shown in the next figure, Figure 6.2.

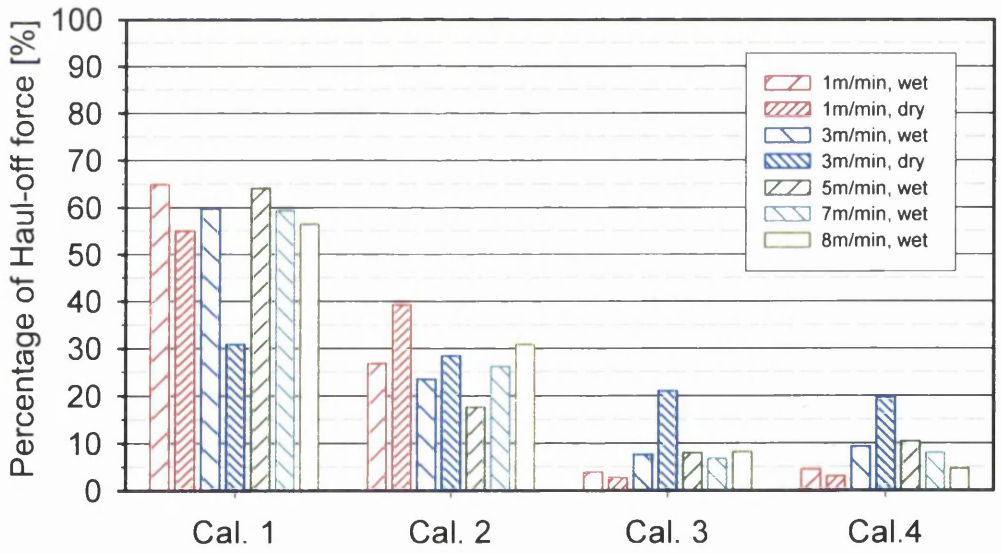

Figure 6.2: Percentage of total haul-off force in each calibrator at various line speeds; –0.4 bar vacuum; 2.50 mm die exit; 2.50 mm profile wall thickness; wet and dry calibration

In wet calibration, nearly 60 % of the haul-off force is built up in Calibrator 1, followed by Calibrator 2 with 25 % and the last two with approximately 7% each. It is clear to see that most of the haul-off forces are generated in Calibrator 1 for wet calibration. The distribution of the forces between the calibrators is rather different in dry calibration. In general, the forces

in the downstream calibrators are more significant. At a line speed of 1 m/min, 55% of the haul-off force was measured in Calibrator 1, 40% in Calibrator 2 and 3% in Calibrators 3 and 4. This distribution changes at a line speed of 3 m/min, with a decrease in the force in Calibrator 1 to 30%, and the forces in the other calibrators increased to 28%, 22% and 20% respectively. At 5 m/min, it would appear that the forces would be approximately the same in all calibrators, but this could not be proved, because the profile collapsed at this line speed.

The next step is to look at the absolute values of the forces, Figure 6.3.

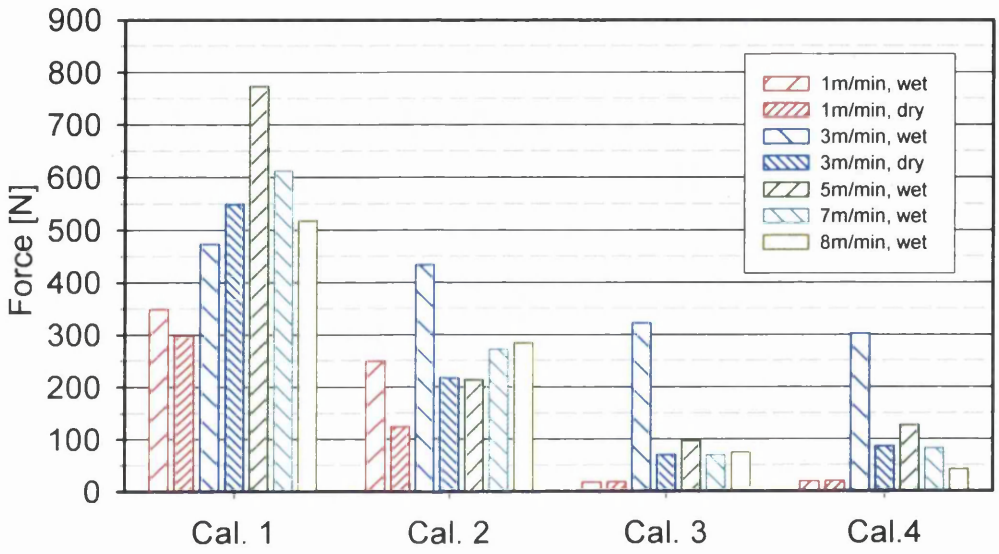

Figure 6.3: Absolute values of forces in each calibrator at various line speeds; –0.4 bar vacuum; 2.50 mm die exit; 2.50 mm profile wall thickness; wet and dry calibration

The force in Calibrator 1 increases up to 5 m/min and then decreases, as we have also seen for the total haul-off force. The background of this physical behaviour can be explained in terms of the opposing effects of haul-off and vacuum as already noted, and this is shown diagrammatically in Figure 6.4.

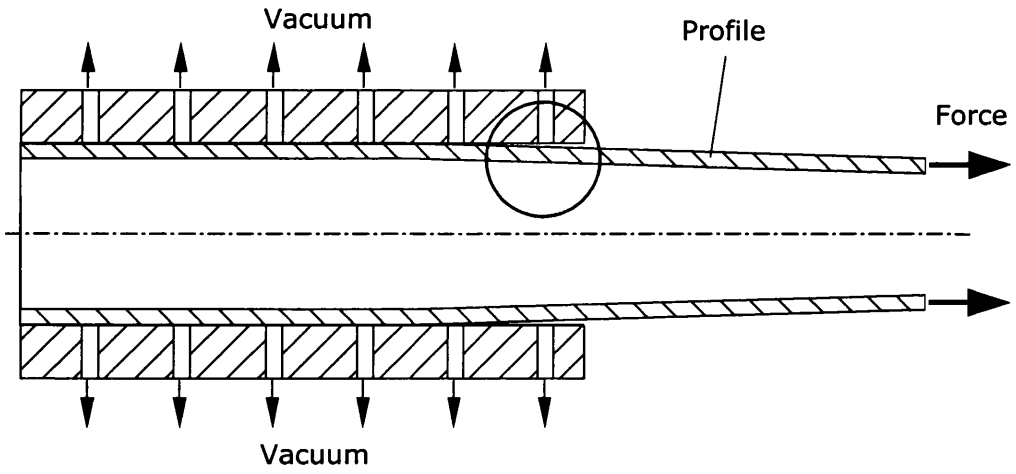

Figure 6.4: Opposing effects of haul-off and vacuum on contact between profile and calibrator

Towards the end of Calibrator 1, the profile loses contact with the calibrator wall (see circle in Figure 6.4) due to draw down resulting from the high axial force necessary to balance frictional forces in the upstream part of the calibrator.

An indication for this behaviour could be visible via the vacuum measurements in the calibrators and this was shown in Figure 5.18 before for a line speed of 5 m/min and 2.50 mm wall thickness. A zero vacuum was measured at the centre of the calibrator and at the edges a vacuum was measured. This measured zero vacuum is based on the sealing effect, in which the profile is pulled at the centre against the calibrator wall due to applied vacuum and flexibility of the profile at the centre. The edges could not be pulled, because the stiffness of the corners is higher than the force of the vacuum. For all experiments, the vacuum was zero at the centre in all calibrators. The mentioned draw down, Figure 6.4, could exits only at the edges. This is supported by the vacuum measurements at the edges, where the values are non-zero. In total, the draw down occurs at the edge, that is at the corners of the profile, whilst at the centre, the profile is pulled under applied vacuum against the calibrator wall. More insights could be found with the profile dimensions, which follow.

A correlation of forces and vacuum was shown in the overview in Chapter 5. In the next Figure, the vacuum measurements are presented for wet calibration and –0.4 bar applied vacuum in main distribution, and related to the effect of draw down.

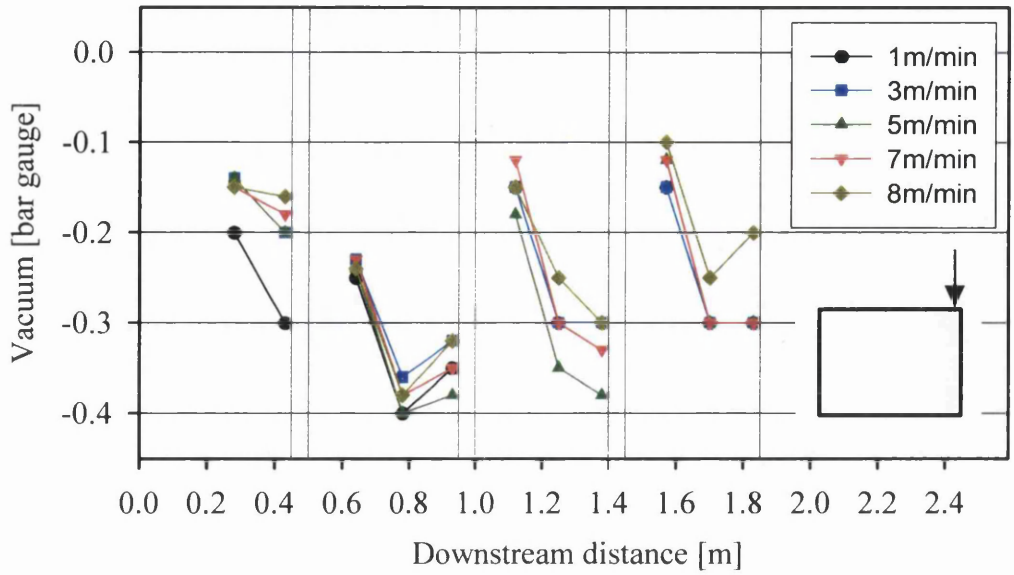

Figure 6.5: Vacuum measurements near to the edge of the profile for different line speeds; -0.4 bar; 2.50 mm profile wall thickness; 2.50 mm die exit; wet calibration

The vacuum was measured in two positions in Calibrator 1 and in three positions in downstream calibrators. From the measurements it appears that the vacuum is increased in the downstream direction in each calibrator. This may be based on two effects. First, a loss of contact between profile and calibrator, in which the contact condition (zero vacuum) has changed into a non-contact and the effect of the applied vacuum in main distribution is measured; and second, a loss of contact make it possible to reduce the vacuum level due to inflow of air or water at ambient pressure, sucked in between the profile and the calibrator. The measured values in Figure 6.5 are the combination of these effects. At highest line speed, the vacuum is lowest and the reason for this could be a thinner solidified layer, which allows an easier deformation of the profile. It seems that the profile has contact at the entrance of each calibrator, since if a trend line is extrapolated towards the entrance of each calibrator a zero measured vacuum value is approached. This indicates good contact at the calibrator inlets.

In wet calibration, the water should seal the ends of the calibrator, so that the applied vacuum on the profile should be higher than in dry calibration. The direct comparison of wet and dry calibration is shown in Figure 6.6 for a line speed of 3 m/min, and 2.50 mm wall thickness at lowest and highest vacuum.

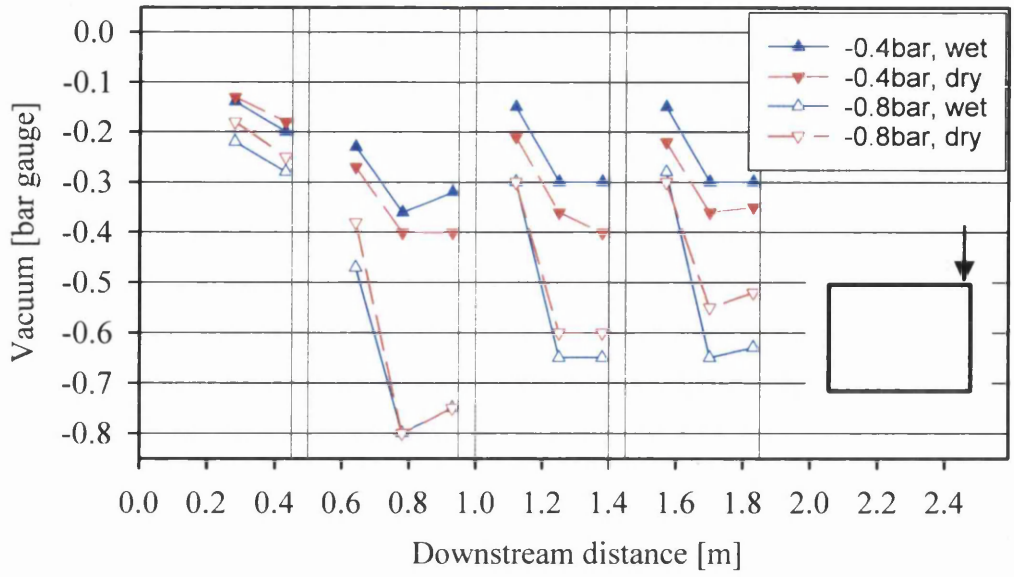

Figure 6.6: Vacuum measurements at the side of the profile in wet and dry calibration at different vacuum levels, 3 m/min; 2.50 mm profile wall thickness; 2.50 mm die exit

As in the foregoing Figure 6.5, a zero vacuum would be obtained on extrapolation to the entrance of the calibrators.

The measured values for wet and dry calibration show opposite trends at high and low applied vacuum.

At high vacuum, the lower values in dry calibration may be based on a reduced cooling and higher draw down due to a thinner solidified layer.

Additionally, a sealing effect at the ends of the calibrators in wet calibration increases the vacuum. An idea of the dependence on a reduced solidified layer is given by results at higher line speed, Figure 6.7.

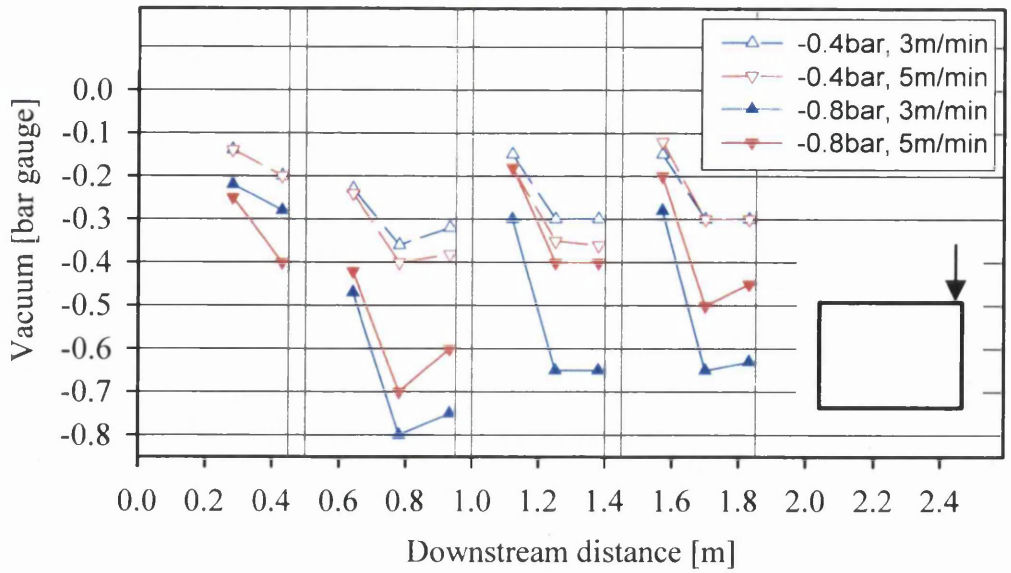

Figure 6.7: Vacuum measurements at the side of the profile at different vacuum levels and line speeds, 2.50 mm profile wall thickness; 2.50 mm die exit; wet calibration

At –0.8 bar, measured vacuum is lower at higher line speed, probably due to the easier deformation of the profile with a thinner solidified layer. At low vacuum of –0.4 bar, the values in Figures 6.6 and 6.7 show the opposite behaviour, and the effect of line speed is smaller in both wet and dry calibration. An explanation could be a better contact of profile and calibrator in wet calibration due to lower draw down at low vacuum.

Overall, the measured haul-off forces are higher for dry calibration. This effect results from a combination of reduced cooling and a higher friction coefficient between the PVC profile and the dry calibrator surface. With lower cooling rate, shrinkage (thermal contraction) is less rapid and the profile dimensions remain larger, resulting in more contact and more friction. Additionally, the lubricating effect of water is not present.

6.1.3 Effects of wall thicknesses and vacuum in wet calibration at different line speeds

In the foregoing figures, results were shown for a 2.50 mm profile wall thickness based on 2.50 mm die exit. In practice, the thickness of the profile wall can vary due to process conditions, e.g. a temperature shift, which can cause different flow behaviour in the die. In the following experiments, the different wall thickness was produced at given line speed, by varying the mass flow rate, whilst maintaining a constant melt extrusion temperature of

195°C. The next figures present more detailed information for various wall thicknesses with 2.50 mm die exit.

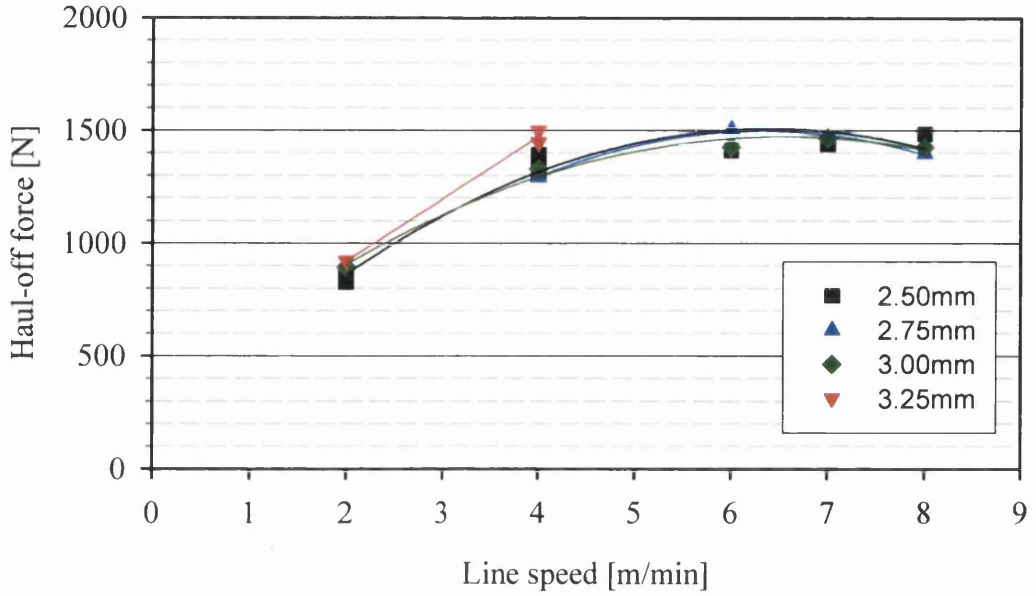

Figure 6.8: Haul-off forces as function of line speed at different profile wall thickness; 2.50 mm die exit; -0.4 bar vacuum; wet calibration

The haul-off forces show little effect of wall thickness, though there is a suggestion that lower forces are obtained with thinner walls. Between line speeds of 2 and 4 m/min the forces increase rapidly and then remained approximately at the same level, apart from slightly decreasing at higher line speed for a vacuum of –0.4 bar. This behaviour has already been seen in Figure 5.2.

The same trend is also recognizable at –0.6 bar, but here, the maximum level is shifted to a lower line speed, Figure 6.9.

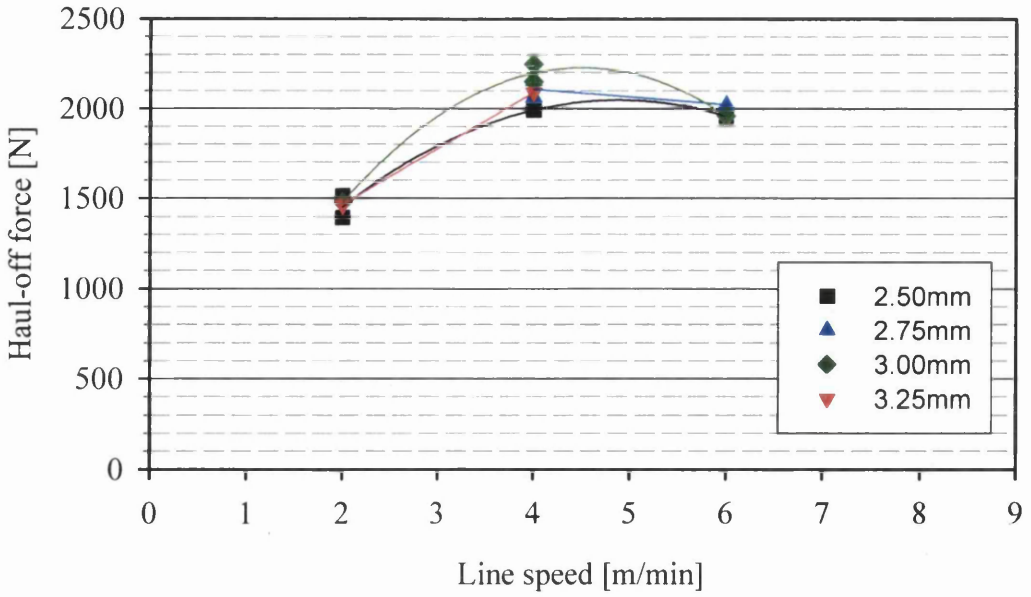

Figure 6.9: Haul-off forces as function of line speed at different profile wall thickness; 2.50 mm die exit; -0.6 bar vacuum; wet calibration

At highest vacuum of –0.8 bar, the haul-off forces are the highest, as expected, Figure 6.10.

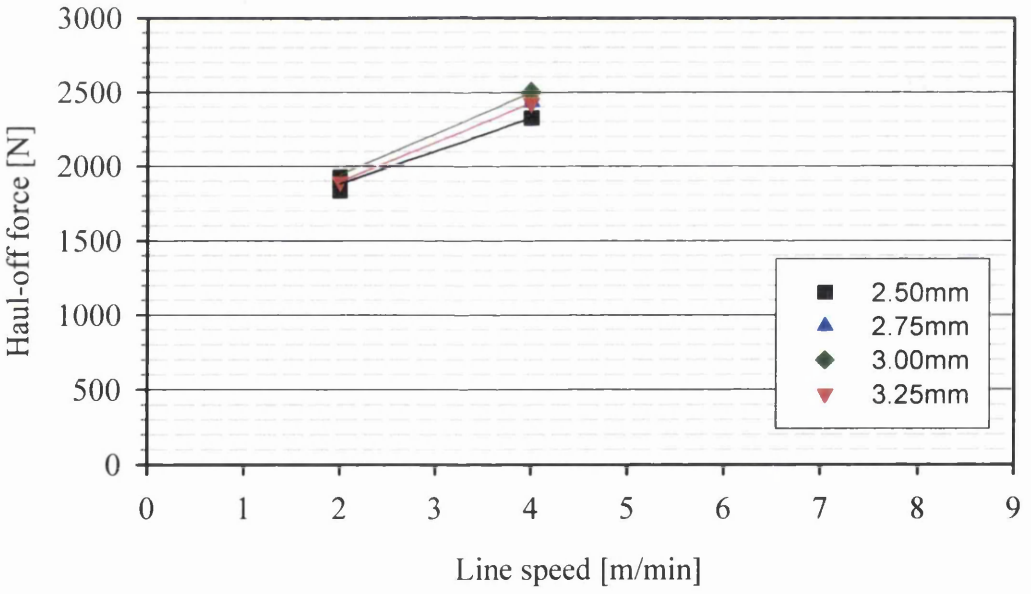

Figure 6.10: Haul-off forces as function of line speed at different profile wall thickness; 2.50 mm die exit; -0.8 bar vacuum; wet calibration

Completion of the figures for the whole range of variation was not possible, because the processing conditions became unstable at higher speeds and higher vacuum, and the profile collapsed almost certainly in the first calibrator.

In contrast to the haul-off forces, forces in Calibrator 1 are more dependent on wall thickness.

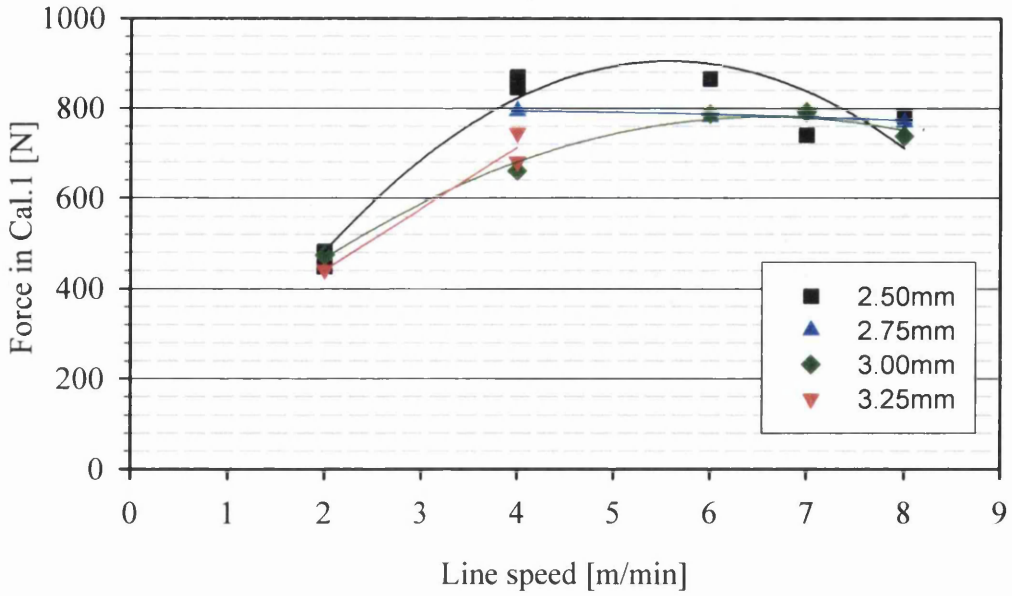

Figure 6.11: Force in Calibrator 1 as function of line speed at different profile wall thickness; 2.50 mm die exit; -0.4 bar vacuum; wet calibration

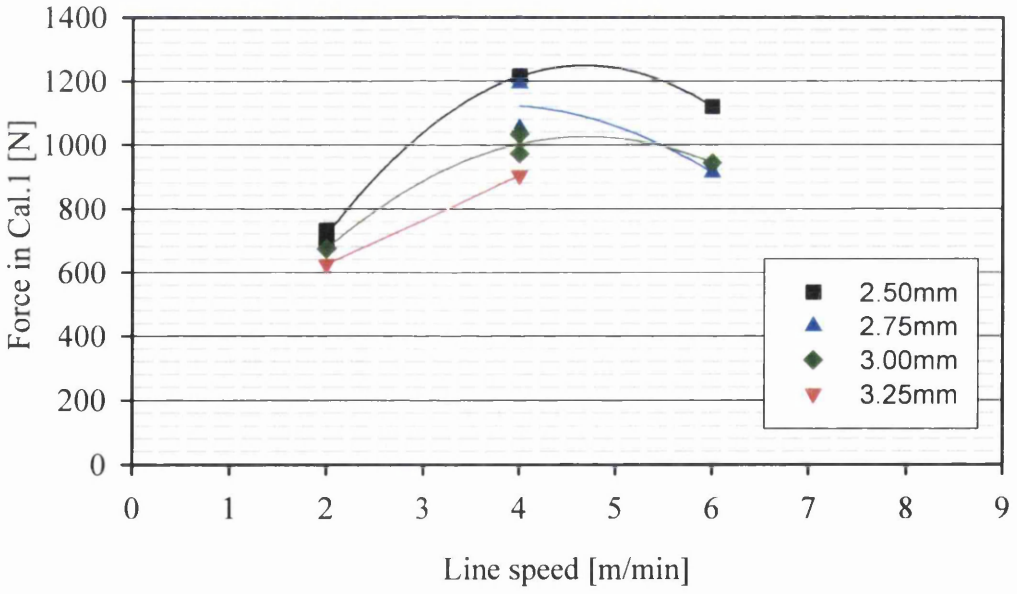

Figure 6.12: Force in Calibrator 1 as function of line speed at different profile wall thickness; 2.50 mm die exit; -0.6 bar vacuum; wet calibration

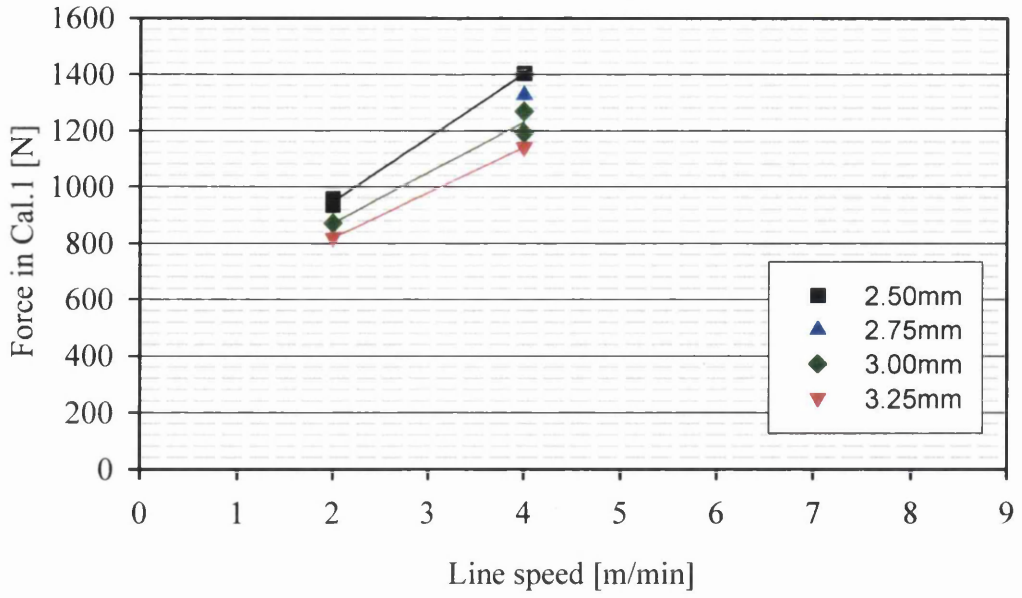

Figure 6.13: Force in Calibrator 1 as function of line speed at different profile wall thickness; 2.50 mm die exit; -0.8 bar vacuum; wet calibration

The effect of wall thickness increases with increasing vacuum. In contrast to the effect on total haul-off, higher Calibrator 1 forces are obtained with thinner walls. The differences are small at 2 m/min line speed, but increase at 4 m/min, then appear to decrease again at higher line speeds.

These effects can be explained as follows. We have already seen how forces increase with line speed, for constant wall thickness, and then level off at higher line speeds. This latter effect is believed to be due to reduced contact in the downstream part of the calibrator, due to draw down of the profile under the influence of higher forces in line direction. The effects of wall thickness variation shown here (Figures 6.11 to 6.13) are believed to be due to changes in contact at the upstream part of Calibrator 1.

To understand the progress of the material flow in the transition region from die to first calibrator, Figure 6.14 gives an overview of the equipment design.

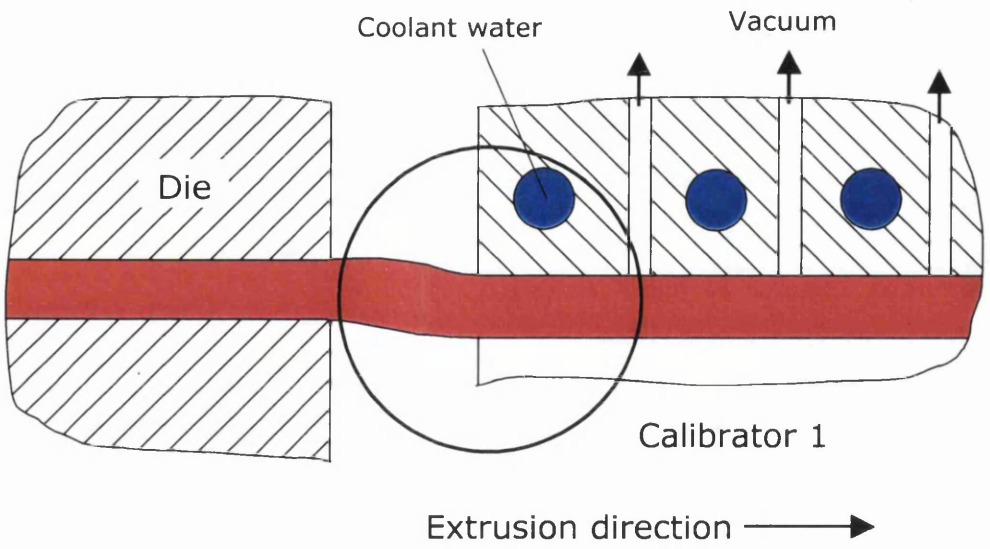

Figure 6.14: Transition region from die to Calibrator 1

As reported in Chapter 3 about the calibration process, the relationship of the dimensions of die exit to the inlet of the first calibrator can be varied. In our set-up, the die exit dimensions are 2.2% larger in the horizontal and 2.6% larger in the vertical direction than the calibrator inlet. These ratios and the inlet area of Calibrator 1 are based on practical experience and are designed to ensure good contact of the profile at entry to the calibrator. To understand the resulting melt flow, the marked circle in the last figure is enlarged, Figure 6.15.

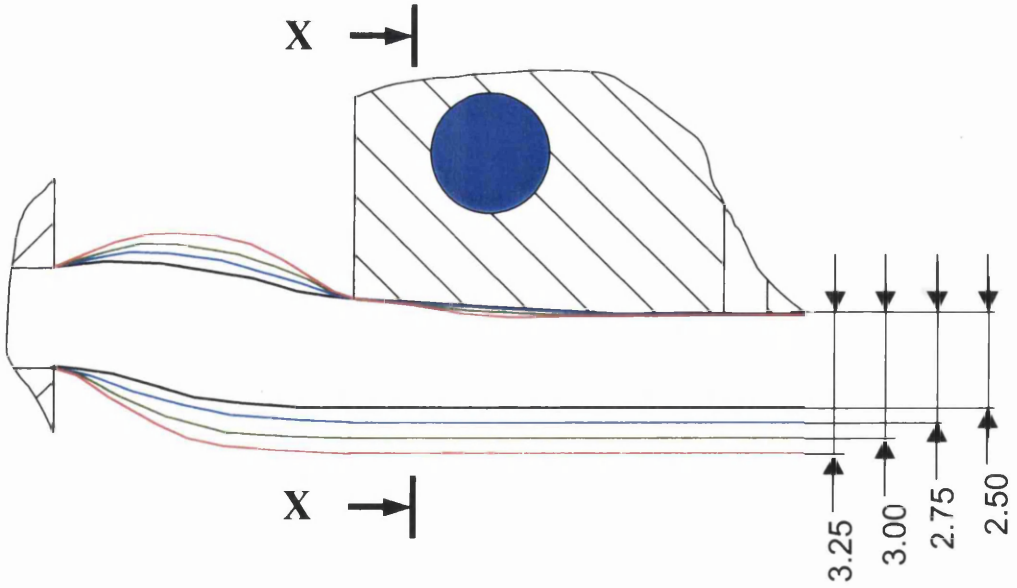

Figure 6.15: Enlarged view of the transition region from die to Calibrator 1

The figure shows in more detail the swelling after the die exit. This is based in general on two effects. Firstly the swelling due to elastic recovery at die exit and, secondly, the swelling due to reduction of melt velocity to match the haul-off speed. This swelling builds up melt around the entrance of the calibrator and requires a higher force in the line direction. This could be one reason for the practical limit to line speed. A build up of melt at the leading face of Calibrator 1 cause flow resistance, resulting in larger forces, draw down and, ultimately, in breakage of the profile. Immediately downstream of the calibrator inlet draw down occurs due to the force necessary to overcome resistance at the inlet, resulting in loss of contact. For low wall thickness, the vacuum more rapidly pulls the profile back into contact with the calibrator wall, giving increased frictional force. The difference between the effects of different vacuum levels is increased at higher line speeds. The finite time required for the vacuum to pull the profile into contact with the calibrator corresponds to a longer downstream distance at higher line speeds, resulting in an increased area of poor contact and reduced friction forces. The effect of swelling, as mentioned before, is further enhanced by the design of the die exit to inlet of Calibrator 1 dimensions. As explained in the measurement set-up, Chapter 5, the outer dimension of the die exit is designed larger than the entrance of Calibrator 1.

In Figure 6.6 were shown the effects of different vacuum levels in the main distribution and a reduction of measure vacuum in the calibrator noted. To confirm former findings, the vacuum was varied in the main distribution from –0.4 bar to –0.8 bar and the applied vacuum in the Calibrator was measured for a wall thickness of 2.50 mm at 4 m/min line speed, Figure 6.16.

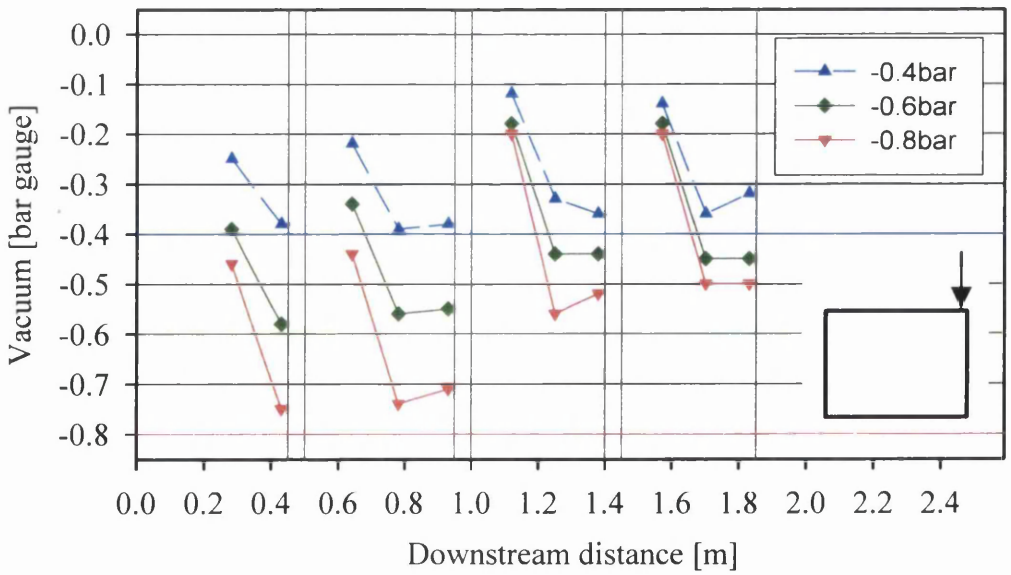

Figure 6.16: Vacuum measurements at the side of the profile at different vacuum levels; 4 m/min; 2.50 mm profile wall thickness; 2.50 mm die exit; wet calibration

At highest applied vacuum, the measured vacuum in the calibrators dropped down to 67%, where the intermediate vacuum is reduced to 78% and for lowest applied vacuum, the measured values decreased to 85%. This leads to the conclusion that a higher draw down is expected at the corners and this will be investigated in the section about the profile dimensions.

All these effects, of course, occur simultaneously with the draw down noted above, which reduces contact in the downstream region of the calibrator. It can be anticipated that this is more pronounced for low wall thickness, due to a weaker profile, and the effect will thus act in the opposite sense (by reducing forces) to the upstream effects just described. This may explain why the influence of wall thickness on forces in Calibrator 1 (Figures 6.11 to 6.13) increases with line speed up to 4m/min, and then become less apparent at higher speeds. At higher speeds, with higher forces, the draw down effect for thinner walls becomes more significant. Draw down also influences contact in the downstream calibrators, and its effects on the total haul-off force are apparently more significant than the variations in contact at the entrance to Calibrator 1. The reduced haul-off forces at low wall thickness, shown in Figures 6.8 to 6.10, indicate this. The profile still has contact with the calibrator walls in the downstream calibrators, but only at the centre, where a zero vacuum is measured in all experiments. This value of zero indicates contact, whereas a non-zero value is an indication of non-contact, see also Figure 5.18.

Further measurements were done with the 1.50 mm die, but will be presented in the paragraph about shrinkage, because the variation was not so wide-ranging.

6.1.4 Effects of vacuum in Calibrator 1 and wall thicknesses in wet calibration

As seen before, the vacuum in Calibrator 1 has a significant influence on the haul-off forces. In the next experiments the vacuum was varied in Calibrator 1 from –0.2 to –0.8 bar, with a constant vacuum of –0.4 bar in the other calibrators. In the next figures are shown the forces for different wall thicknesses at a line speed of 4 m/min for the 2.50 mm die exit.

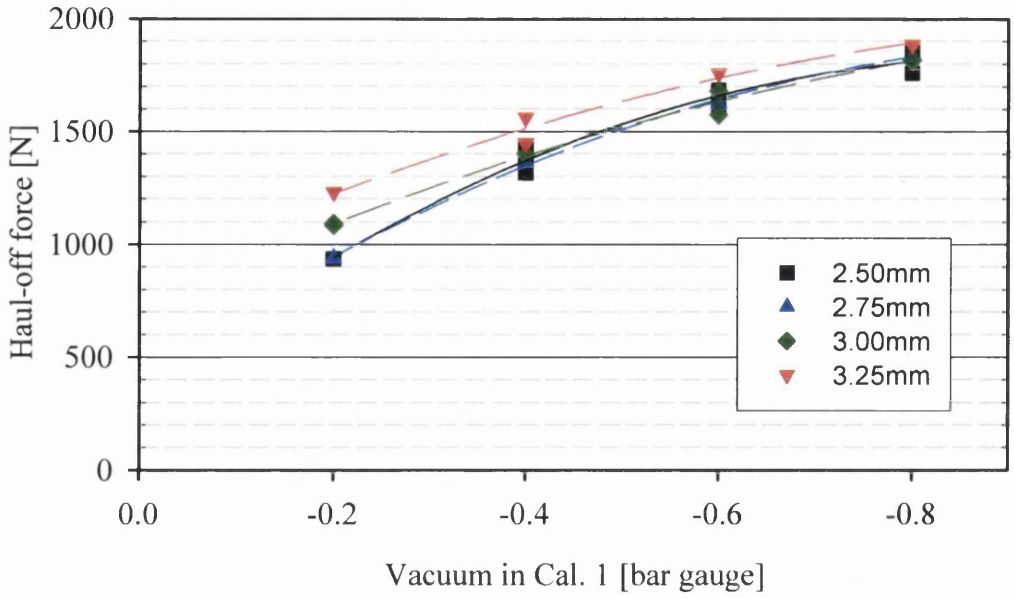

Figure 6.17: Haul-off forces for different vacuum levels in Calibrator 1; different profile wall thickness 2.50 –3.25 mm; vacuum in Calibrator 2,3 and 4 constant at –0.4 bar; 4 m/min line speed; 2.50 mm die exit; wet calibration

The higher vacuum increases the haul-off forces as expected from previous results. Since they are nominally the same operating conditions, we can compare the results at –0.4 bar in Figure 6.17 with the 4 m/min results in Figure 6.8; they are quite similar and the reproducibility is close. Consistent with our previous explanations, we see the effect of wall thickness on haul-off force to be pronounced at low vacuum (in Fig 6.17), where the different stiffness of the different thickness walls has most influence. Higher vacuum is more effective in resisting profile draw down, giving similar calibrator contact and similar forces for the different wall thicknesses.

Maybe the forces in Calibrator 1 have a significant influence on the process. In Figure 6.18, the forces on Calibrator 1 are presented.

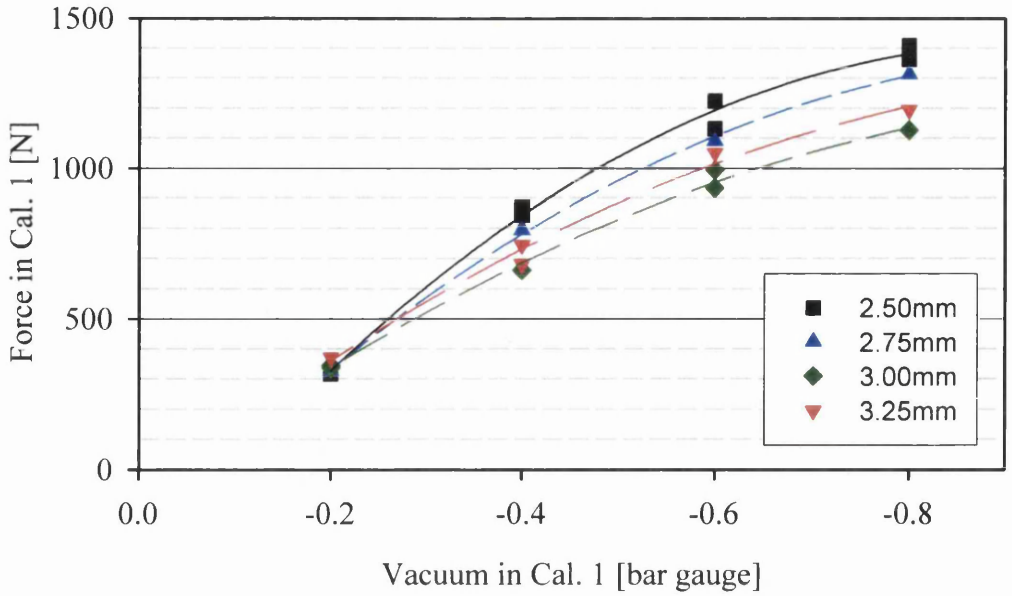

Figure 6.18: Forces in Calibrator 1 for different vacuum levels in Calibrator 1 at different profile wall thicknesses of 2.50 – 3.25 mm; vacuum in Calibrator 2, 3 and 4 constant at –0.4 bar; 4 m/min line speed; 2.50 mm die exit; wet calibration

Results at –0.4 bar in Figure 6.18 can be compared with those at 4 m/min in Figure 6.11. The values are quite close, indicating satisfactory reproducibility. As expected, in Figure 6.18 we see higher forces in Calibrator 1 for thinner wall thickness - the effect being more pronounced at higher vacuum. It is also to be remarked that forces extrapolate approximately to zero at zero vacuum, showing the dominant effect that vacuum has on frictional forces in the calibrator. This is only possible with the presently used profile, because there are no noses, undercuts or other complex profile geometry features, which can cause sticking or constrained shrinkage onto the calibrator during cooling, Figure 6.19.

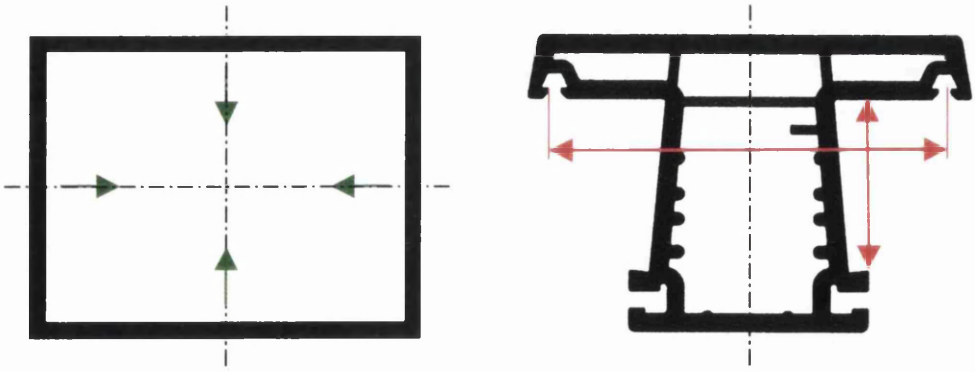

Free shrinkage
experimental EU profile

Constrained shrinkage
window profile

Figure 6.19: Comparison of free and constrained shrinkage for different profile geometries

The individual forces in all four calibrators in these experiments are shown in the following figures.

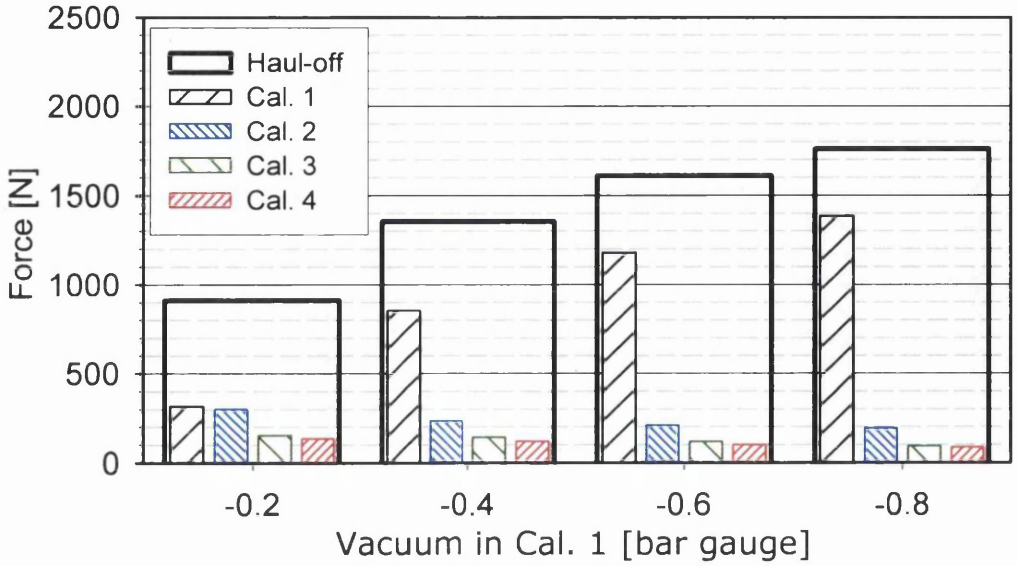

Figure 6.20: Forces in Calibrator 1 for different vacuum levels in Calibrator 1 at 2.50 mm profile wall thickness; vacuum in Calibrator 2, 3 and 4 constant at –0.4 bar; 4 m/min line speed; 2.50 mm die exit; wet calibration

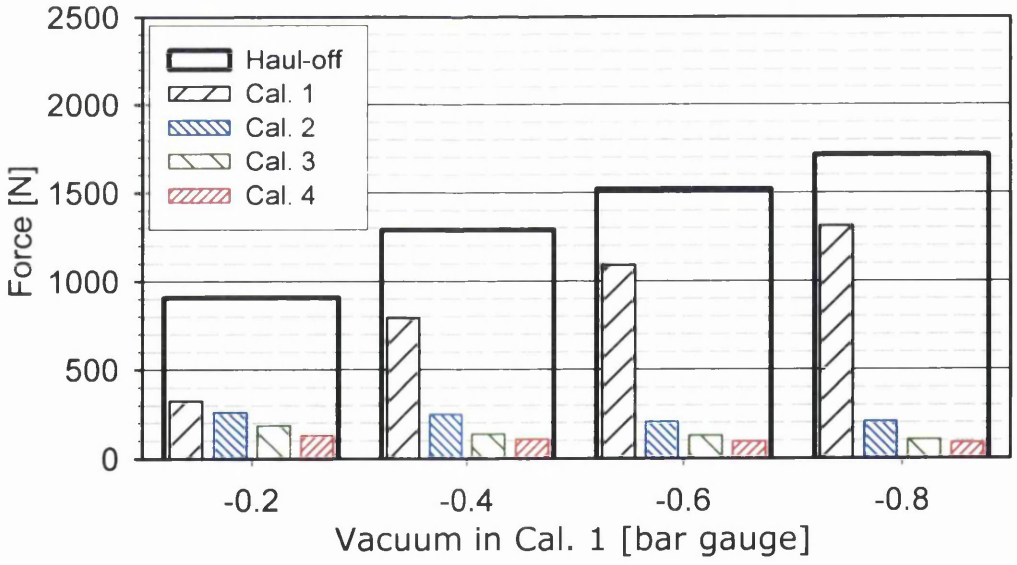

Figure 6.21: Forces in Calibrator 1 for different vacuum levels in Calibrator 1 at 2.75 mm profile wall thickness; vacuum in Calibrator 2, 3 and 4 constant at –0.4 bar; 4 m/min line speed; 2.50 mm die exit; wet calibration

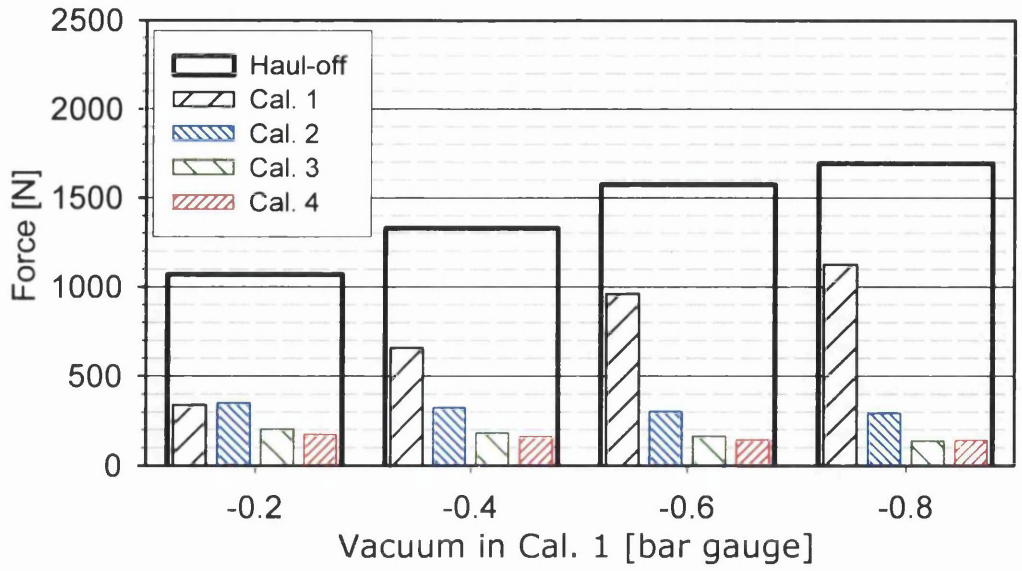

Figure 6.22: Forces in Calibrator 1 for different vacuum levels in Calibrator 1 at 3.00 mm profile wall thickness; vacuum in Calibrator 2, 3 and 4 constant at –0.4 bar; 4 m/min line speed; 2.50 mm die exit; wet calibration

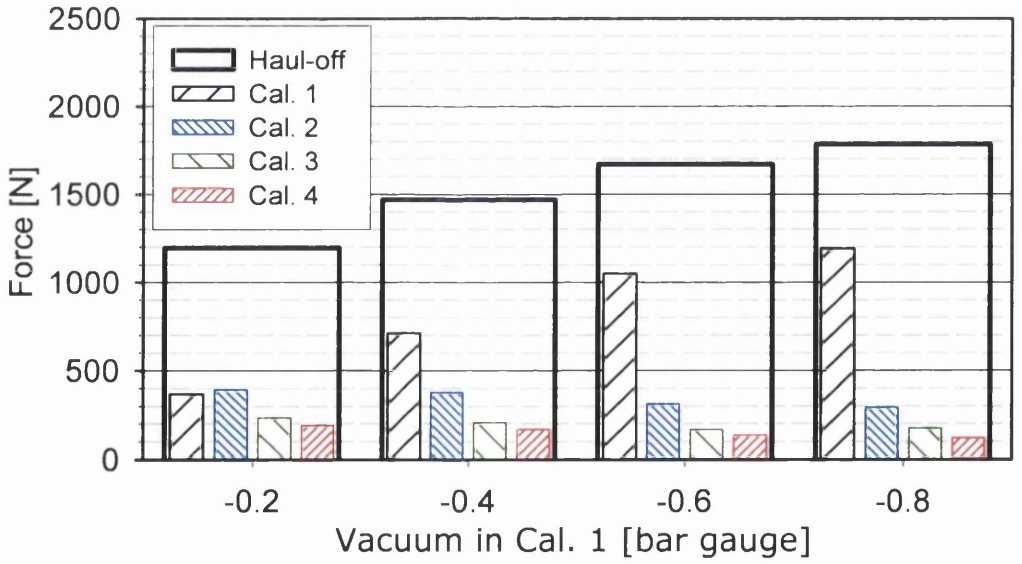

Figure 6.23: Forces in Calibrator 1 for different vacuum levels in Calibrator 1 at 3.25 mm profile wall thickness; vacuum in Calibrator 2, 3 and 4 constant at –0.4 bar; 4 m/min line speed; 2.50 mm die exit; wet calibration

It is apparent that the forces in the downstream calibrators decrease with an increasing force in Calibrator 1. As a result of this increased force, the profile is stretched in and after

Calibrator 1, reducing the contact area in the downstream calibrators, and thus also reducing the friction forces in the other calibrators, as mentioned before.

The four last figures will be useful in understanding the influence of the forces on the profile properties, e.g. the shrinkage and dimensions, which will be discussed in the following sections.

6.1.5 Effects of vacuum in Calibrators 2, 3 and 4 in wet calibration

The following experiments are used to back up the explanations of the foregoing figures. Now, the vacuum in Calibrator 1 was set as constant, but varied in the downstream calibrators; the results are shown in Figures 6.24 to 6.26 for a wall thickness of 3.00 mm.
As already known, an increase of vacuum increases the forces in the downstream calibrators. At a vacuum of –0.4 bar in Calibrator 1, the vacuum variations in the downstream calibrators had no influence on the force in Calibrator 1, Figure 6.24.

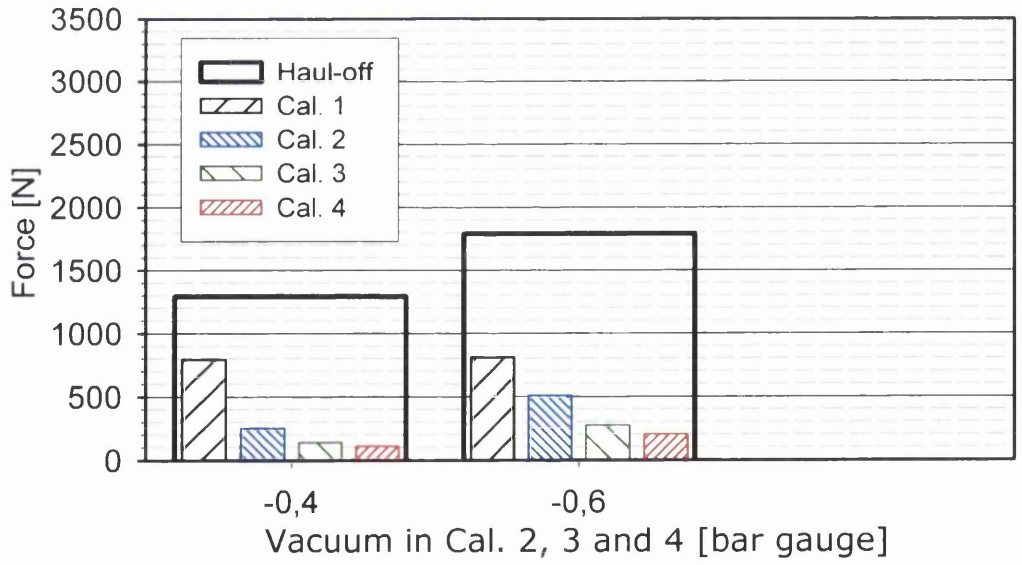

Figure 6.24: Forces in each calibrator for different vacuum levels in Calibrator 2, 3 and 4; –0.4 bar vacuum in Calibrator 1; 3.00 mm profile wall thickness; 4 m/min line speed; 2.50 mm die exit; wet calibration

A change of the forces in Calibrator 1 is recognizable at higher vacuum in following figures.

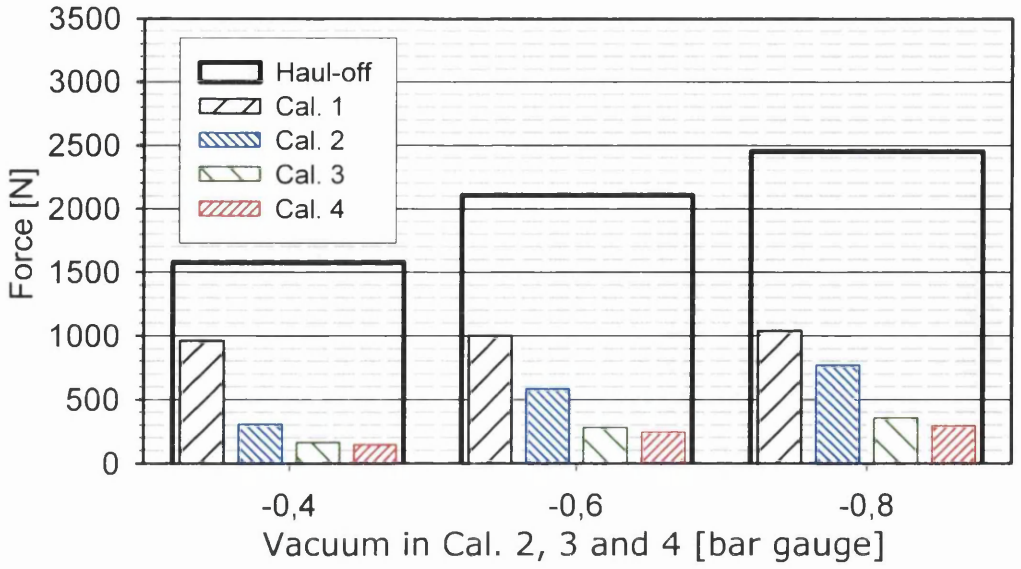

Figure 6.25: Forces in each calibrator for different vacuum levels in Calibrator 2, 3 and 4; –0.6 bar vacuum in Calibrator 1; 3.00 mm profile wall thickness; 4 m/min line speed; 2.50 mm die exit; wet calibration

The force in Calibrator 1 has increased slightly with increasing vacuum in the downstream calibrators. The higher downstream vacuum resists draw down in Calibrator 2 and this feeds back upstream to Calibrator 1, where better contact is then obtained at the end of Calibrator 1. This behaviour occurs also for highest vacuum of –0.8 bar in Calibrator 1.

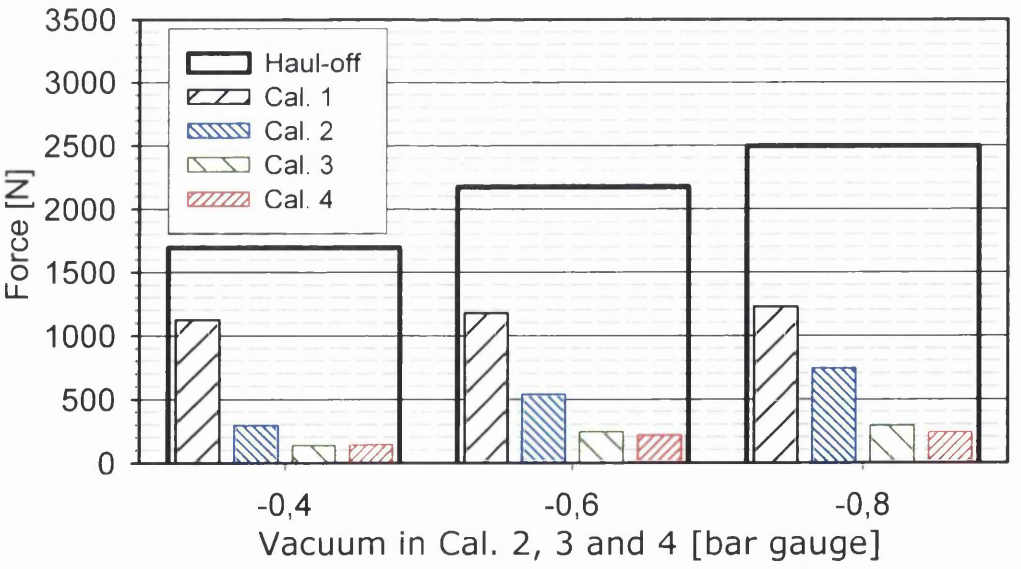

Figure 6.26: Forces in each calibrator for different vacuum levels in Calibrator 2, 3 and 4; –0.8 bar vacuum in Calibrator 1; 3.00 mm profile wall thickness; 4 m/min line speed; 2.50 mm die exit; wet calibration

These last figures have confirmed the existence of the draw down effect.

6.1.6 Effects of melt extrusion and coolant temperatures in wet calibration

As indicated in the overview of results, the temperatures of coolant water in Calibrator 1 and melt temperature were varied, and the resulting haul-off forces were shown. Now further detail and discussion is presented and, first, the dependence of the forces on the melt extrusion temperature is shown for each calibrator, Figure 6.27.

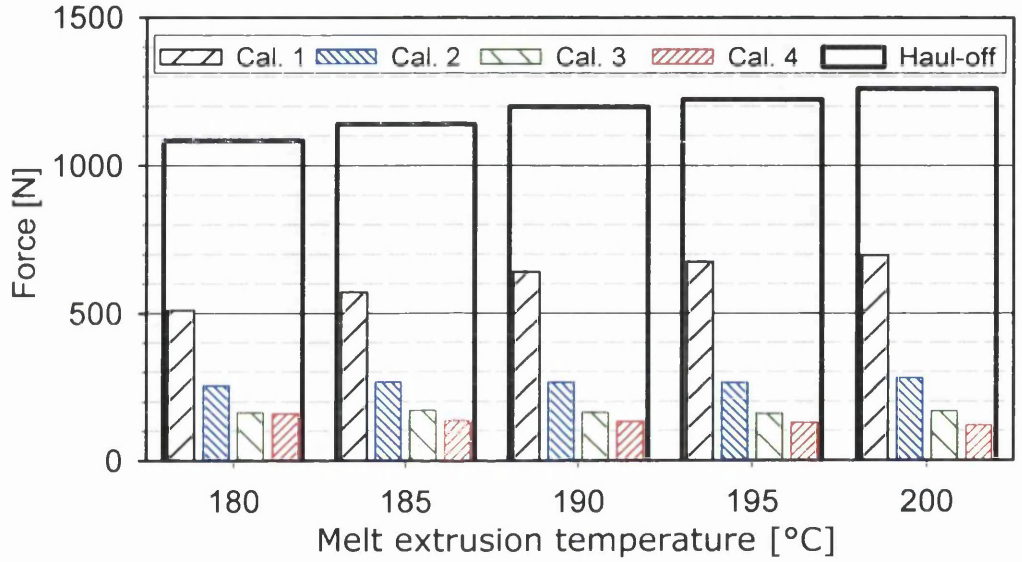

Figure 6.27: Forces in each calibrator for different melt extrusion temperatures; constant vacuum at –0.4 bar; 2.75 mm profile wall thickness; 4 m/min line speed; 2.50 mm die exit; wet calibration

An increase in the forces is perceptible with increasing melt temperature. The haul-off force has increased 16% with melt temperature change from 180°C to 200°C, and the force in Calibrator 1 has increased by 37%. In all cases the force in Calibrator 1 is about half the total haul-off force; however Calibrator 1 forces are influenced more strongly by increasing melt temperature than the downstream forces. The reason for this is the temperature dependent friction behaviour of the polymer. As mentioned in the basics of the calibration process, a higher melt temperature increases the friction coefficient rapidly, and increased extrusion temperature has most influence on the profile surface temperature in Calibrator 1. Experiments using variation of the coolant temperature in Calibrator 1 completes this investigation of temperature effects.

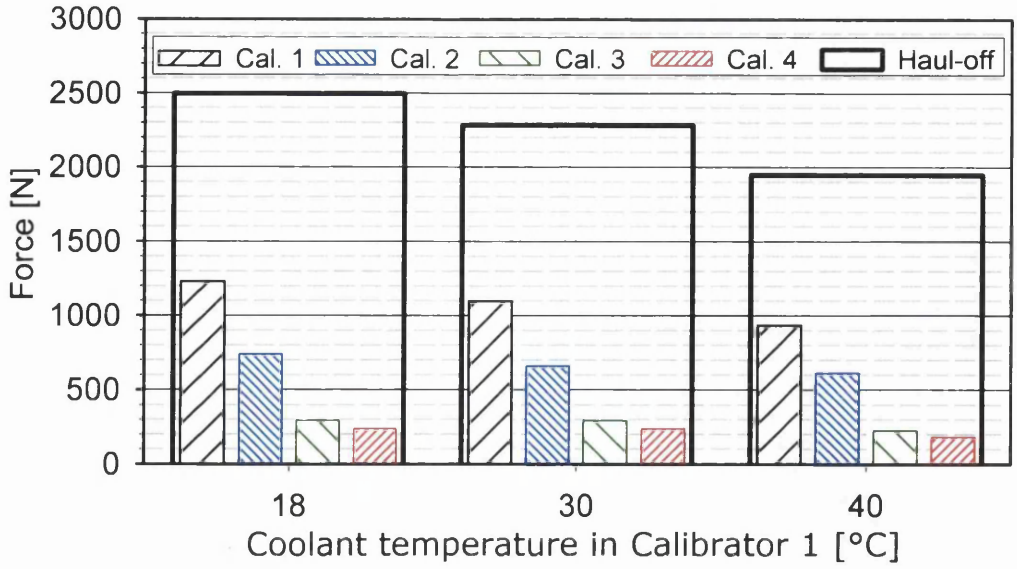

Figure 6.28: Forces in each calibrator for different coolant temperatures in Calibrator 1; constant vacuum at –0.8 bar; 3.00 mm profile wall thickness; 4 m/min line speed; 2.50 mm die exit; wet calibration

In contrast to the effect of extrusion temperature, the forces decrease with higher coolant temperature. It is remarkable that the haul-off and Calibrator 1 forces decrease by the same percentage. The reason for this can be explained by noting that a thinner solidified layer is produced by the slower cooling resulting from the higher coolant temperature, and the result is increased stretching of the profile, which causes a loss of contact between profile and calibrator. This is clearly noticeable for the Calibrator 1 forces. Also the decreasing forces in the downstream calibrators confirm this explanation.

Summary

In general, the haul-off forces are lower in wet calibration than in dry calibration. The forces on Calibrator 1 are nearly the same for both systems, but the difference occurs in the downstream calibrators. For wet calibration, the forces are smaller due to a lower friction coefficient between calibrator and profile surface. Additionally the cooling is better, and this leads to smaller profile dimension, resulting in lower contact forces between calibrator and profile surface.

Increasing vacuum or melt temperature increases the haul-off and Calibrator 1 forces in general. The vacuum increases the normal forces between the profile and the calibrator resulting in increased friction forces. The effect of the increase of the melt extrusion temperature is based on the rapid increase of the friction coefficient especially at higher temperatures.

In contrast to this, the forces at the haul-off and Calibrator 1 decrease with increasing coolant temperature. This results from increased stretching due to the reduced cooling in Calibrator 1.

Theses effects are shown qualitatively in the Figure 6.29.

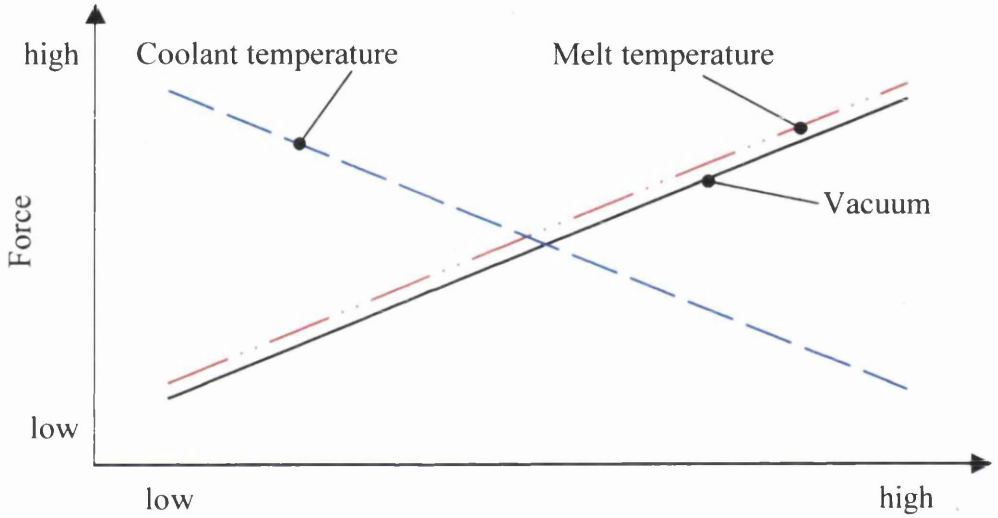

Figure 6.29: General dependencies of haul-off and Calibrator 1 forces on the vacuum, melt extrusion and coolant temperatures

Furthermore, the haul-off forces increased up to a line speed of 5 m/min and then decreased at higher line speed. This decrease is due to the reduced contact of the profile at the end of Calibrator 1, and also in the downstream calibrators due to draw down, and this altogether reduces the forces.

An increased profile wall thickness decreased the forces in Calibrator 1. This is believed to be due to reduced contact at the upstream end of Calibrator 1, due to a stiffer profile wall thickness resisting the effect of vacuum. However, the resulting reduction in draw down in Calibrator 1 results in increased forces in the downstream calibrators, leaving the total haul-off force rather insensitive to profile wall thickness.

6.2 Profile geometry

6.2.1 Key parameters

The geometry of the profile is an important outcome of the calibration process, as mentioned in Chapter 3. To investigate the dependence on the process parameters, the geometry was measured after the calibration process. Breil [156] investigated the possibilities of a general measurement of the profile dimensions on-line, but has not presented the dependence of the profile dimensions on the process parameters. He has mentioned a stretching of the profile in the gap between the die and inlet of Calibrator 1, and in the first 40-80 mm in Calibrator 1. Berger [157] has investigated the change in diameter for PVC pipes with 32 mm diameter and 2 mm wall thickness. He has found a reduction of 0.9% for the diameter with an increase of line speed from 2 up to 14 m/min. Additionally he has shown a further reduction in a calibration set-up with a long calibrator followed by a water bath, in comparison to systems where the calibrator was replaced by calibration discs to fix the geometry and water was used for the cooling between the discs.

In this work, the dependence on the process parameters will be shown in detail. For a simplification and systematisation of the data obtained, the summed diameter D and corner circumference C are introduced. The diameter D is obtained from the width W and height H, and the circumference C is the sum of the corner measures T*, L*, B* and R* of the profile. The measured profile dimensions are shown in Figure 6.30.

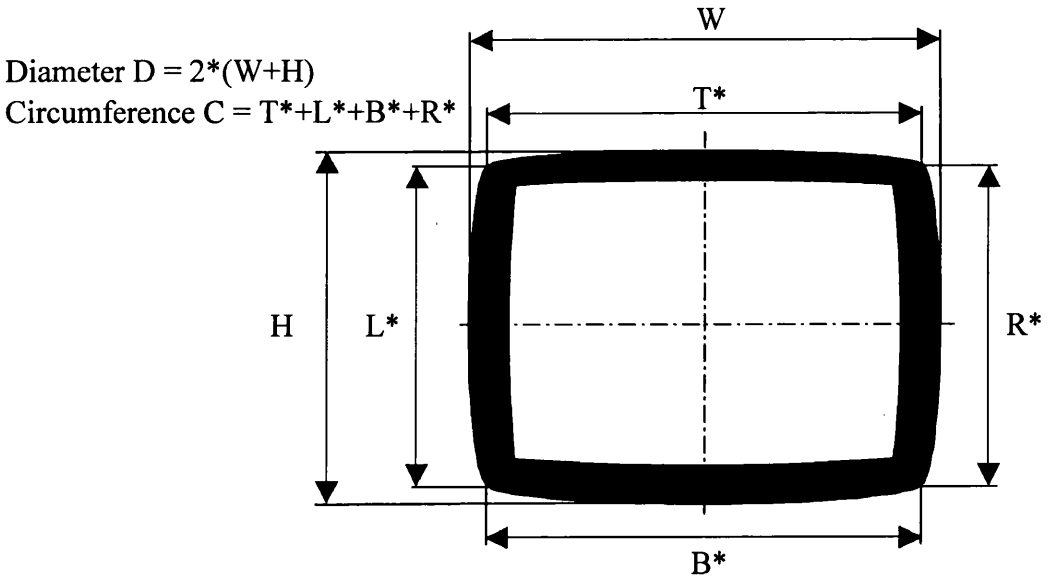

Figure 6.30: Dimensions of the manufactured EU-Profile

6.2.2 Effects of vacuum in wet and dry calibration at different line speeds

The first set of experiments was carried out with a constant profile wall thickness of 2.50 mm, with a range of line speeds and screw speeds, and a variation of melt temperatures due to increased screw speed from 178°C to 190°C, as mentioned before.

An independent value is introduced for comparison with the diameter D and circumference C. This value of 132.86 mm is the inlet dimension of Calibrator 1 and is visible as a line in the next two Figures, in which are shown the dependencies of the diameter D and circumference C on line speed. Additionally the reduced dimension of the Calibrator 1 inlet due to cooling from melt extrusion to ambient temperature is shown, based on the density increase of PVC and assuming isotropic shrinkage.

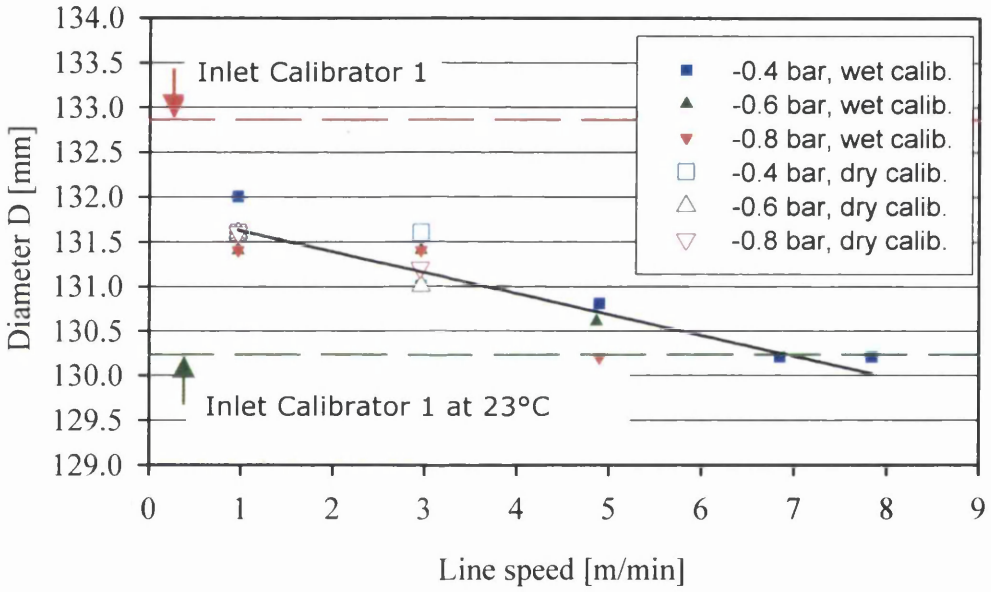

Figure 6.31: Profile diameter D at different line speeds and applied vacuum; wet and dry calibration; 2.50 mm die exit; 2.50 mm profile wall thickness

In general, profile dimensions are reduced at higher line speed, and this is well known is practice. To compensate, at higher line speeds, the initial dimensions of the calibrators are enlarged in practice to obtain the required final profile dimensions. The reductions in D shown in Figure 6.31 are small, but D is reduced by 1.4 mm, and this leads to a reduction of height or width by 0.35 mm. In the RAL-Standard for window profiles [158], a tolerance of ±0.3 mm is allowed for the height and for the width, a tolerance of ±0.5 mm is accepted for general dimensions and ±0.3 mm for fitting dimensions. Thus changes in D are not negligible. It is also visible that the dimension D is larger than the "cooled down" inlet dimension. The explanation for the reduction in diameter D at higher line speed is believed to be due to the

reduced solidified layer thickness. This leads to a weaker profile, which is stretched more and this reduces the profile dimensions. That the diameter of the finished profile is larger than the 'cooled down' inlet dimension is believed to be the result of two effects during calibration. The haul-off forces stretch the profile, and after the haul-off, the tensile force is released, elastic recovery occurs, and the profile shortens and increases in diameter. Additionally, when the constraints of the calibrator are removed, the profile cross section will change rapidly due to equilibrium of elastic components of the frozen-in stresses. Longer term changes may result from viscoelastic effects. The form of the stress field and the resulting 'spring-back' will depend in a complex way on the cooling process, which gives rise to thermal stresses, and the imposed stresses due to vacuum and haul-off. Cooling from the outside of the profile will, however, usually result in thermal stresses on the profile cross-section that are compressive at the outside and tensile at the inside. Release of the constraints by the calibrator will allow the profile wall to bow outwards, increasing D. It is significant, though, that the vacuum measurement on the profile centre line registers zero for all operating conditions and profile wall thicknesses, indicating close contact between the central part of the profile surface and the calibrator wall. Within the calibrators, the vacuum is able to resist the effects of draw down on D. On release from calibrators, however, draw down appears to exert a weak influence on D. The dependence of D on applied vacuum, which we have seen has a major influence on forces, is rather weak.

The corresponding results for the circumference C are shown Figure 6.32.

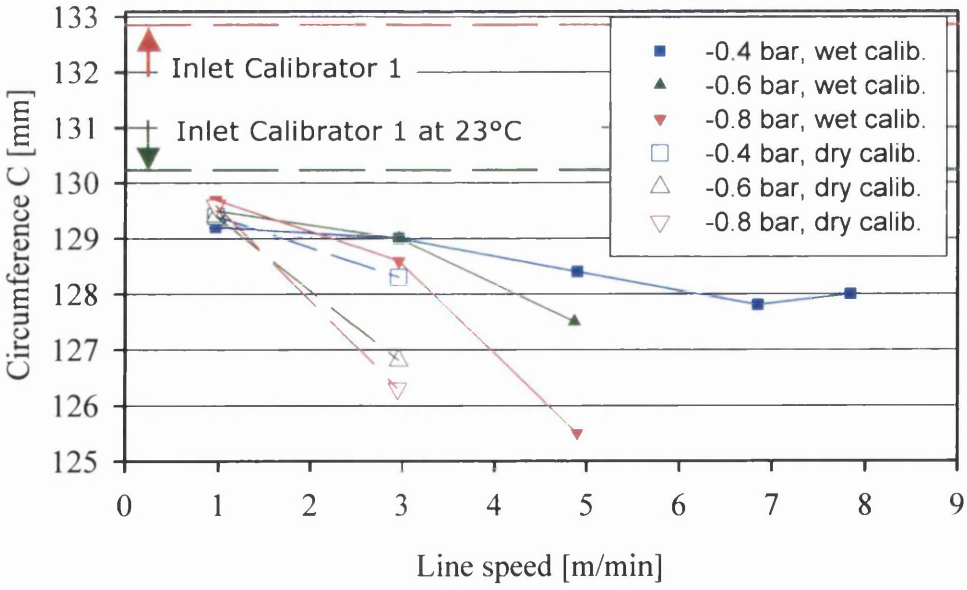

Figure 6.32: Circumference C at different line speeds and applied vacuum;
wet and dry calibration; 2.50 mm die exit; 2.50 mm profile wall thickness

Circumference C also shows a reduction at higher line speed. But in this case, the values are not close to a single trend line as for the diameter D. A clear distinction can be made between wet and dry calibration, and also for each vacuum. Increasing vacuum decreases the circumference, and in dry calibration, the reduction is higher than in wet calibration. It is remarkable, that with a line speed of 3 m/min, the circumference at –0.8 bar in wet calibration is close to the circumference at –0.4 bar in dry calibration. It is also to be noted that the reductions in C are substantially larger than seen for the diameter D. Altogether, it looks as if the circumference C is more strongly dependent on the forces in the calibration process, because the forces were higher in dry calibration than wet calibration, and higher at higher applied vacuum, as shown before. It is also clear that vacuum is not able to resists reductions in the corner-to-corner dimensions, C, due to draw down as effectively as it resist reductions in the diameter D. This is because maintenance of D can be achieved largely by bending the profile wall, whilst maintenance of C requires more stretching. Loss of contact near the corners of the profile accompanying draw down is evident from the non-zero values of vacuum registered for all operating conditions (see e.g. Figure 5.18).

Before looking further at this data, the reference calibrator inlet at 23°C value is used to provide comparisons in terms of percentages. The percentage changes of the profile dimension D and circumference C relative to the reference value are shown in Figures 6.33 and 6.34.

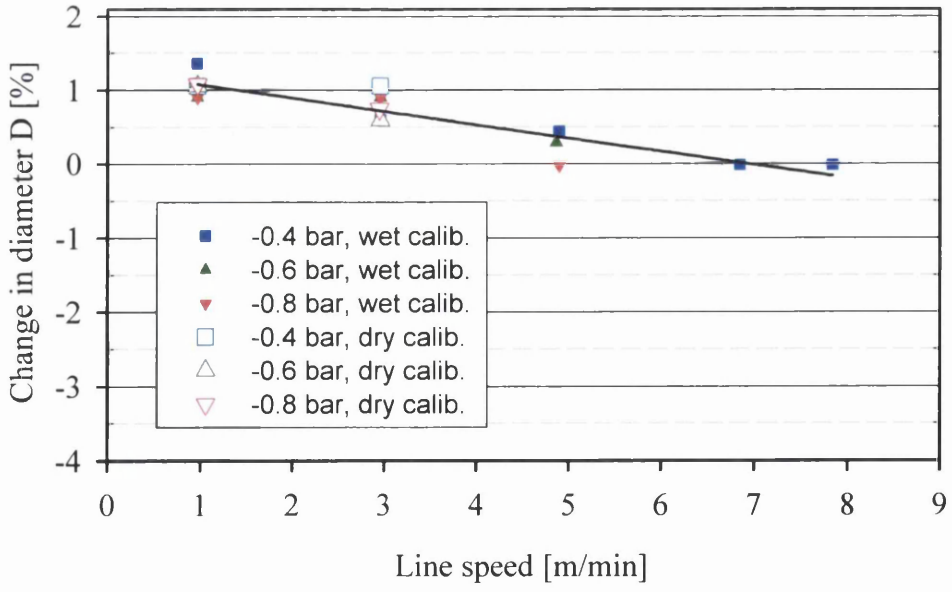

Figure 6.33: Change in profile diameter D for different line speeds and applied vacuum; wet and dry calibration; 2.50 mm die exit; 2.50 mm profile wall thickness

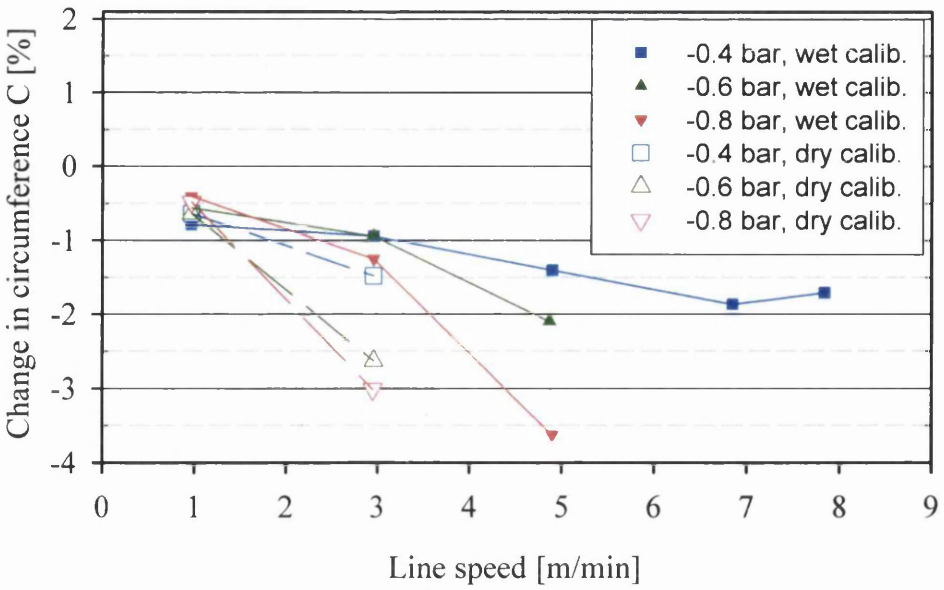

Figure 6.34: Change in circumference C for different line speeds and applied vacuum; wet and dry calibration; 2.50 mm die exit; 2.50 mm profile wall thickness

The direct comparison in the last two Figures makes clear the higher reduction of the circumference C compared to the diameter D, as mentioned before.

It was shown in the overview, in Figure 5.2, that the forces in dry calibration are higher than in wet calibration, and also higher at higher vacuum, and together with the findings in Figures 6.31 to 6.34, a correlation of profile dimensions and forces is suggested.

To examine this, the diameter D is shown as a function of haul-off force in Figure 6.35.

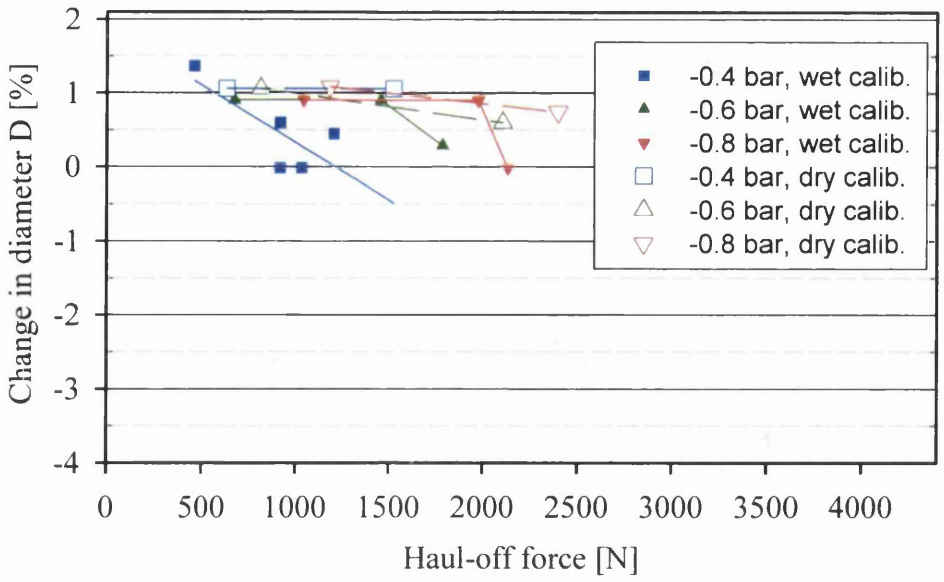

Figure 6.35: Dependence of change in profile diameter D on haul-off forces and applied vacuum; wet and dry calibration; 2.50 mm die exit; 2.50 mm profile wall thickness

In general, the diameter is reduced more in wet calibration than in dry calibration at the same applied vacuum and for a given haul-off force. In wet calibration at –0.4 bar vacuum, the diameter varies over a small range of the haul-off force, and this can be explained on the basis of a weaker profile at higher line speeds, which effect was also visible in Figure 6.33. At higher vacuum in wet calibration, it seems that the diameter is unchanged until a certain line speed is reached and then the diameter drops. Until this line speed, the solidified layer is thick enough to resist draw down due to forces in line direction. Additionally, it appears that vacuum is able to resist the effect of draw down on the diameter until a certain haul-off force is exceeded. This force is higher the higher the vacuum.

In dry calibration, the draw down of the profile seems less effected by the haul-off force than in wet calibration. The reason for this is probably that the greater part of the draw down occurs in Calibrator 1, where the profile is weakest. In wet calibration Calibrator 1 forces form a major part of the total haul-off force (60%) and result in large draw down. In dry calibration, the forces in each calibrator are more nearly equal, so for a given total haul-off, the force in Calibrator 1 is lower than in wet calibration. This results in lower draw down. This leads to the conclusion that the forces in Calibrator 1 are dominant for the diameter D. To investigate this, the diameter is plotted as a function of the Calibrator 1 forces in Figure 6.36.

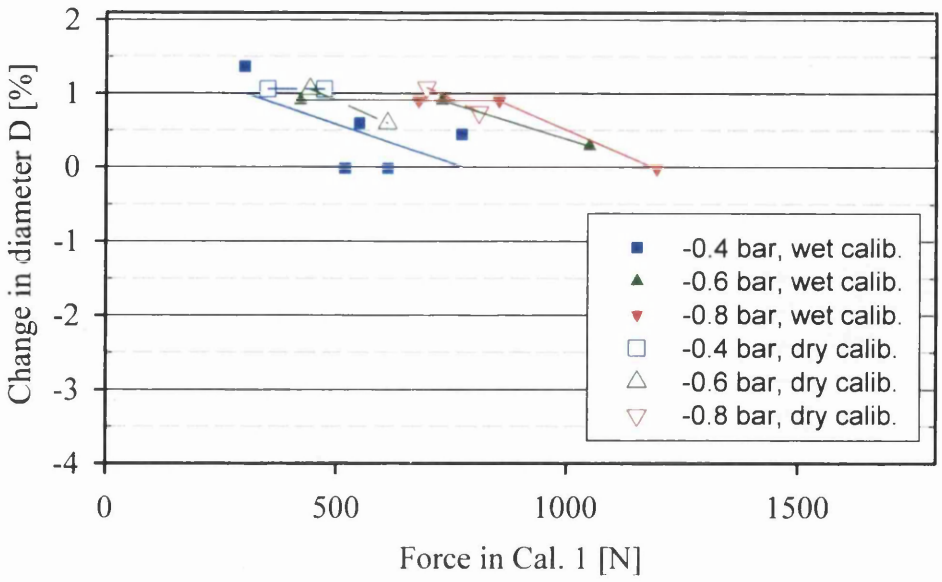

Figure 6.36: Change relative to maximum profile diameter D as a function of Calibrator 1 forces and applied vacuum; wet and dry calibration; 2.50 mm die exit; 2.50 mm profile wall thickness

For wet calibration the plot against Calibrator 1 forces shows a pattern very similar to the plot against haul-off forces, consistent with the dominance of Calibrator 1 forces in wet calibration. The correlation for dry calibration is now closer to the data for wet, confirming that Calibrator 1 forces are more relevant than haul-off force for reductions in D. The slopes of the dry calibration line are now similar to those for wet calibration, but at lower forces (for –0.6 bar and –0.8 bar vacuum). This may be due to slower cooling in dry calibration. The reduction of D in wet calibration looks like a stable process at higher vacuum up to a line speed of 3m/min. At higher line speed, the reduction is mainly effected by the weakness of the profile due to the thinner solidified layer. A trend line can be drawn in Figure 6.36 for a vacuum of –0.6 bar and –0.8 bar in wet calibration, showing how D is reduced at higher forces in Calibrator 1.

Considering now the circumference C, a better correlation with forces, in both wet and dry calibration may be obtained, because a clear distinction between these was visible in Figure 6.34 when plotted against line speed. The dependence on haul-off and Calibrator 1 forces is shown in Figures 6.37 and 6.38.

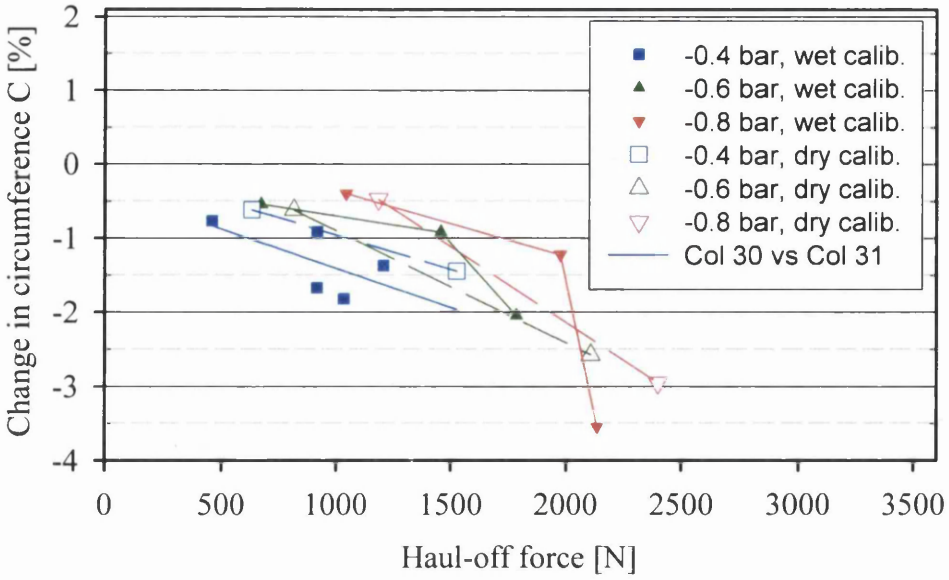

Figure 6.37: Change in circumference C as function of haul-off forces and applied vacuum; wet and dry calibration; 2.50 mm die exit; 2.50 mm profile wall thickness

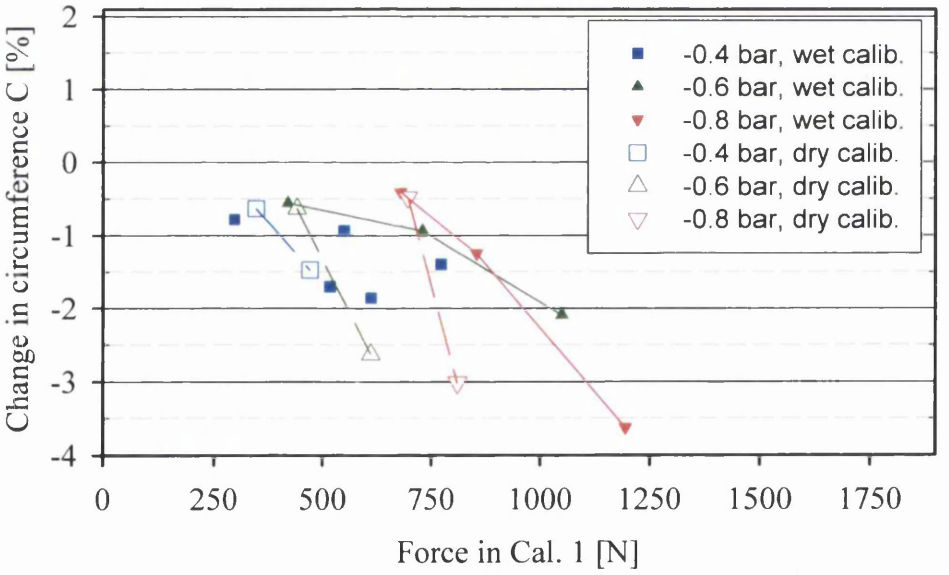

Figure 6.38: Change in circumference C on Calibrator 1 forces and applied vacuum; wet and dry calibration; 2.50 mm die exit; 2.50 mm profile wall thickness

In contrast to what was seen for the diameter D, it appears, from a comparison of Figures 6.37 and 6.38, that reductions in C correlate better with the haul-off than with Calibrator 1 forces. This suggests that reductions in C occur also in downstream calibrators, where effects on D are less significant. This may be because, as noted above, vacuum is able to maintain the

diameter close to the calibrator dimensions, whereas it is less able to resist reductions in the corner dimensions.

6.2.3 Effects of wall thicknesses and vacuum in wet calibration at different line speeds

The profile wall thickness is varied in the next set of experiments from 2.50 mm up to 3.25 mm in steps of 0.25 mm for a fixed die exit of 2.50 mm height. The wall thickness was varied by increasing the throughput of the extruder at constant line speed and constant melt temperature of 195°C. The constant melt temperature was achieved by adjusting the extruder temperature settings.

The following Figures 6.39 to 6.42 show the change in diameter D for vacua of –0.4, -0.6 and –0.8 bar.

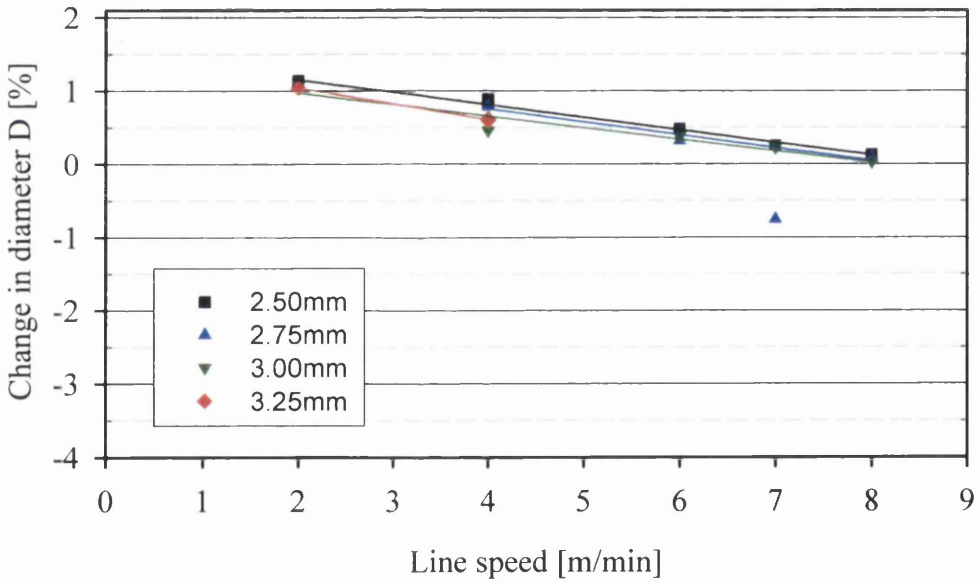

Figure 6.39: Change in diameter D as function of line speed for different profile wall thicknesses; 2.50 mm die exit; -0.4 bar vacuum; wet calibration

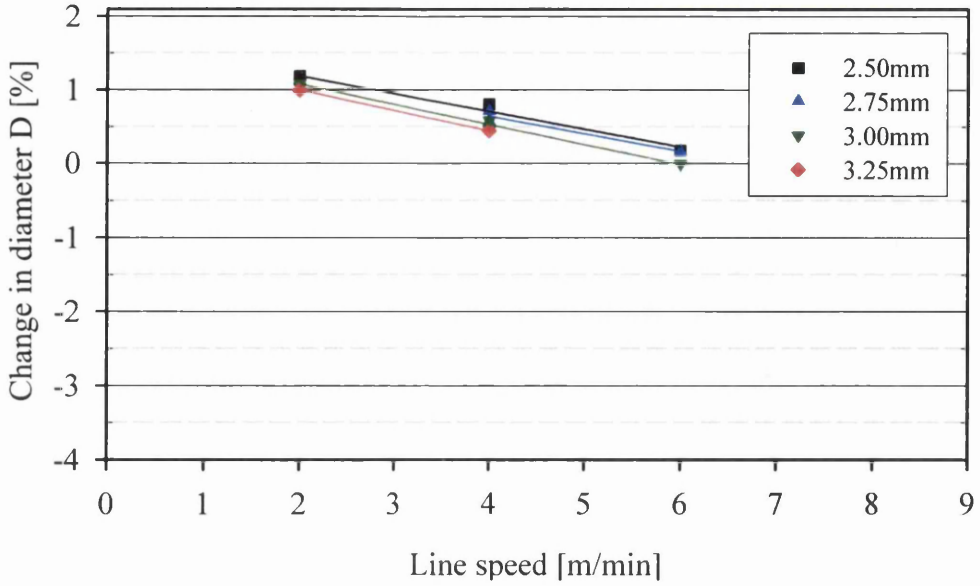

Figure 6.40: Change in diameter D as function of line speed for different profile wall thicknesses; 2.50 mm die exit; -0.6 bar vacuum; wet calibration

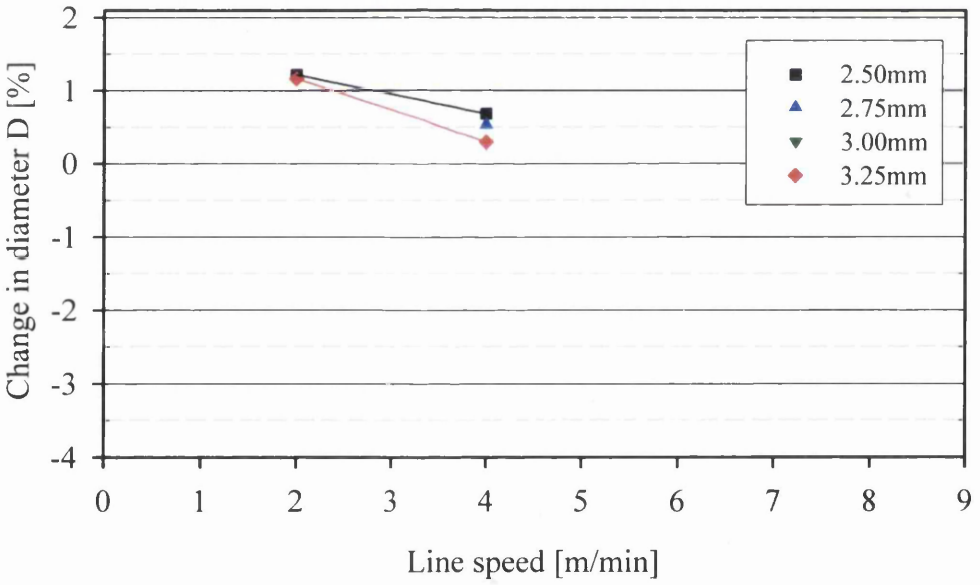

Figure 6.41: Change in diameter D as function of line speed for different profile wall thicknesses; 2.50 mm die exit; -0.8 bar vacuum; wet calibration

The results for 2.50 mm wall thickness in Figures 6.39 to 6.41 may be compared with those for wet calibration in Figure 6.33. Agreement is close, confirming the reproducibility of the experiments. As seen before, for the uniform wall thickness of 2.50 mm, the diameter D decreases, as expected, with higher line speed. An increasing vacuum decreases the diameter

faster and, additionally, the diameter is also lower for higher profile wall thickness, the effect of wall thickness becoming more pronounced at higher line speed.

An explanation for the opposing behaviour of the change in diameter and circumference with increasing profile wall thickness could be a cramming effect at the inlet of Calibrator 1. In the present set-up of the calibration line, the die exit is larger than the inlet of Calibrator 1. This system is commonly used to achieve good contact at the corners at the inlet of Calibrator 1. Here the material is crammed into the entrance of Calibrator 1. Between the corners, the melt is also pulled inside and due to the smaller dimensions of width and height at the Calibrator 1 inlet, the profile wall must be bend in the centre to get into the Calibrator 1 and the result is a less good contact. The vacuum tends to pull the profile wall back into contact with the calibrator wall, which is easier for thinner wall, to obtain the target dimension.

The Figure 6.42 shows this cramming effect in a view in the downstream line direction for the different wall thicknesses at the inlet area of Calibrator 1.

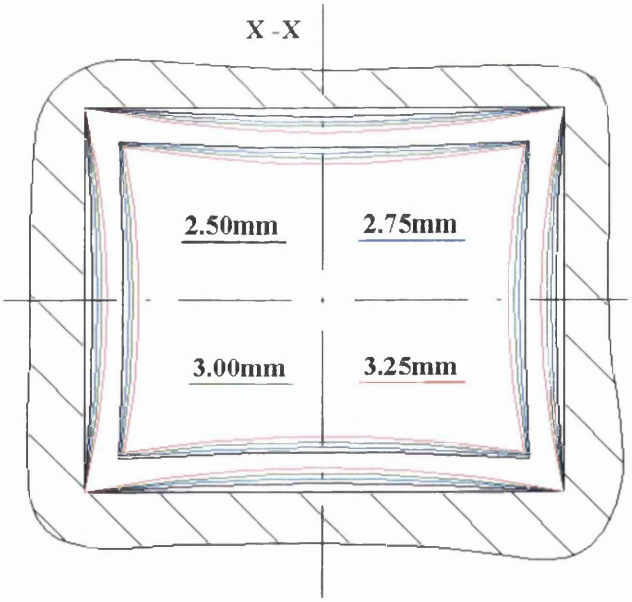

Figure 6.42: View X-X in Figure 6.15

The measurements of vacuum could not prove this behaviour, because the measurements of vacuum were not done directly at the inlet of Calibrator 1 due to the risk of damaging the extruded profile.

We next look at the circumference C to get a better overview of the influence of the wall thickness. The results for the circumference are shown in the Figures 6.43 to 6.45.

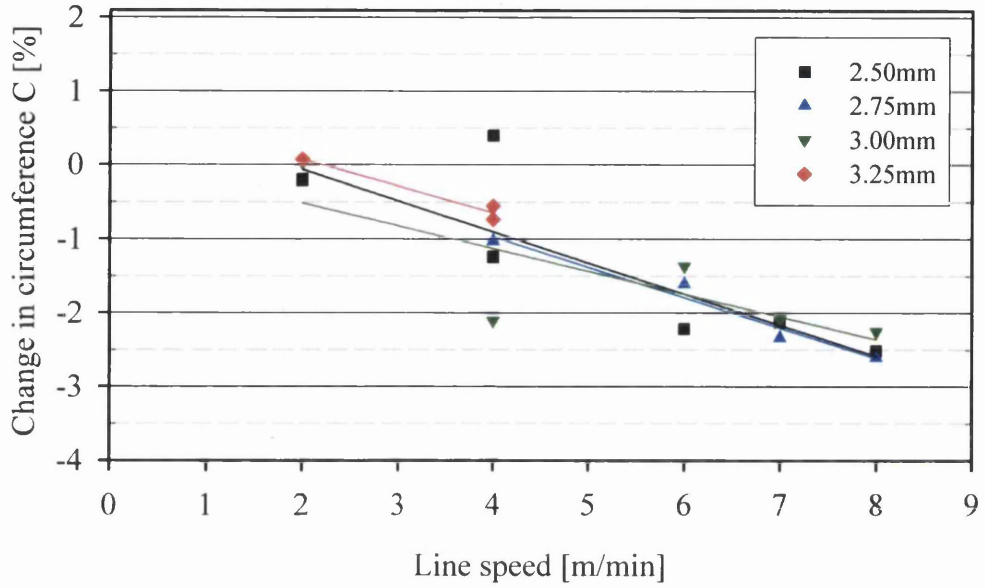

Figure 6.43: Change in circumference C as function of line speed for different profile wall thicknesses; 2.50 mm die exit; -0.4 bar vacuum; wet calibration

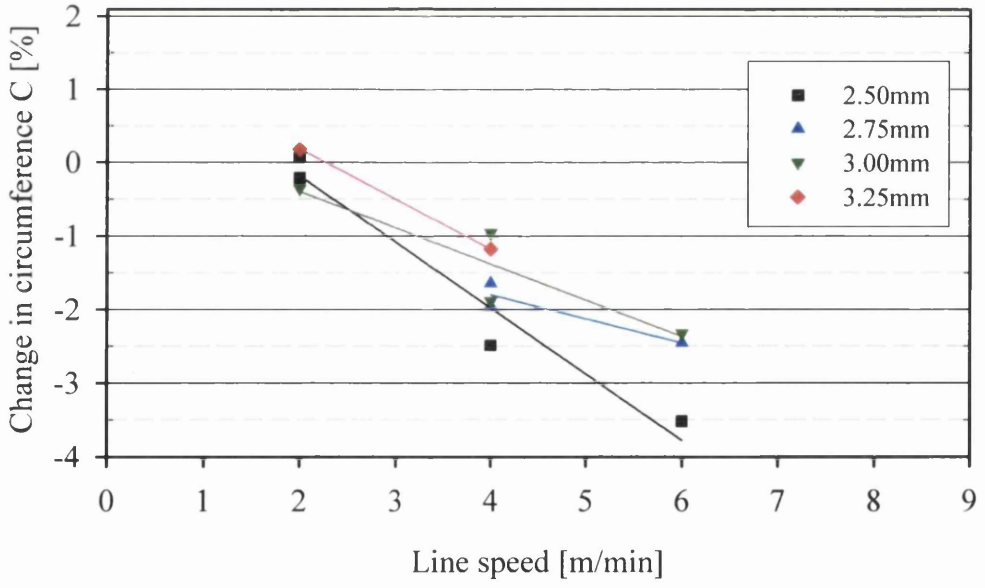

Figure 6.44: Change in circumference C as function of line speed for different profile wall thicknesses; 2.50 mm die exit; -0.6 bar vacuum; wet calibration

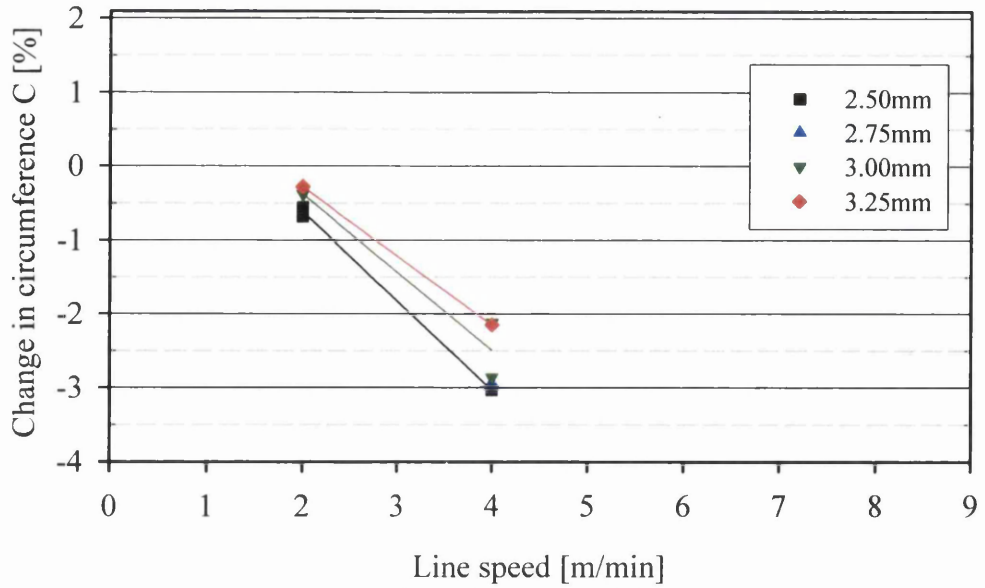

Figure 6.45: Change in circumference C as function of line speed at different profile wall thicknesses; 2.50 mm die exit; -0.8 bar vacuum; wet calibration

The circumference shows a reduction at higher line speeds, as did the diameter D, but the decrease is less for higher wall thickness, which is the opposite of the results for D. As for D, the decrease in C with line speed is more rapid for higher vacuum, and the wall thickness effect is more pronounced at higher line speed.

To understand the results we need to refer back to previous discussion. There it was suggested that effects in Calibrator 1 are most relevant for D. In Figures 6.11 to 6.13 we saw that Calibrator 1 forces were lower for higher wall thicknesses, which was explained in terms of the slower re-establishment of contact between the centre line of the profile and the calibrator downstream of the Calibrator 1 entrance, following the cramming effect at the entrance. The delayed expansion of the diameter, whilst cooling and solidification of the outer layers proceeds, may correlate with the final lower values of D for the thick wall profiles. Qualitative explanation of the effects on C is easier. It was argued previously that the haul-off force and draw down in all calibrators was more relevant for C. Figures 6.8 to 6.9 show little influence of wall thickness on haul-off force. For thinner walls and weaker profiles we would therefore expect larger draw down, reducing the corner dimension, C.

6.2.4 Effects of vacuum in Calibrator 1 and wall thickness in wet calibration

To substantiate the previous findings, the applied vacuum was varied only in Calibrator 1 whilst the applied vacuum in the downstream calibrators was maintained constant at –0.4 bar. Runs were carried out for a range of wall thicknesses, as before, and the results are shown in Figure 6.46.

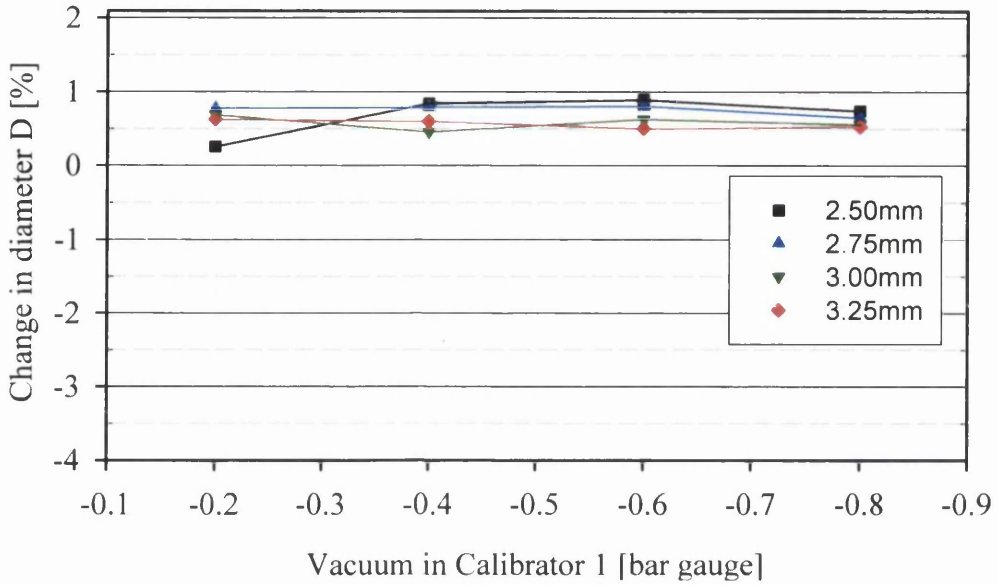

Figure 6.46: Change in diameter D for different vacuum in Calibrator 1 for different profile wall thickness; vacuum in Calibrator 2, 3 and 4 constant at –0.4 bar; 4 m/min line speed; 2.50 mm die exit; wet calibration

Results show that D is lower for higher wall thicknesses, as noted previously. Results at –0.4 bar may be compared with those at 4m/min in Figure 6.40. Agreement is close, confirming the reproducibility of the experiments. Significantly, Figure 6.46 shows that the reduction in D, for each wall thickness, is largely insensitive to vacuum in Calibrator 1, where the 2.50 mm point at –0.2 bar is probably due to experimental error. In previous discussion of calibrator forces, in Section 6.1, it was proposed that these are influenced by delayed profile-calibrator contact on the centre line at the upstream end, and by reduced contact area at the down stream end due to reduction of corner dimensions by draw down. These effects work in opposition as the vacuum and contact frictional forces increase. Higher vacuum tends to establish up-stream contact faster, but because it results in larger tensile forces, more draw down occurs in the downstream region. It was suggested above that delayed establishment of contact upstream in Calibrator 1 correlates with a final smaller diameter; and, conversely, more rapid contact with a larger final diameter. And, although diameter is maintained by

vacuum within the calibrators, draw down (reflected primarily in C values) does tend to reduce the final D value. The opposing upstream and downstream effects in Calibrator 1 may explain the insensitivity of D to applied vacuum up to -0.6 bar in Calibrator 1. At –0.8 bar a small reduction is present, except at 3.25 mm wall thickness.

Figure 6.47 shows results for the corner dimensions C.

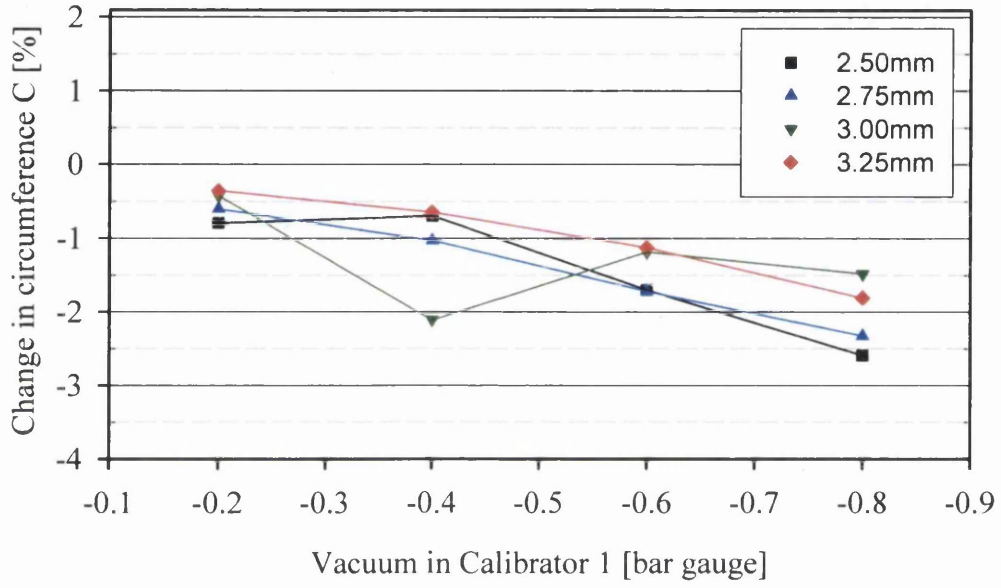

Figure 6.47: Change in circumference C for different vacua in Calibrator 1 for different profile wall thicknesses; vacuum in Calibrators 2, 3 and 4 constant at –0.4 bar; 4 m/min line speed; 2.50 mm die exit; wet calibration

As previously, we see that C is lower for small wall thickness. Results at –0.4 bar may be compared with those for 4 m/min in Figure 6.43. Despite some scatter in the values due to experimental error, agreement is quite good. For higher vacuum, tensile forces increase, see Figures 6.8 to 6.10 and more draw down and lower C values are to be expected. Apart from 2 points at –0.4 bar, which may be in error, the draw down is generally larger for thinner walls. Corner circumference C as a function of haul-off force, and Calibrator 1 force for different wall thicknesses are shown in Figures 6.48 and 6.49.

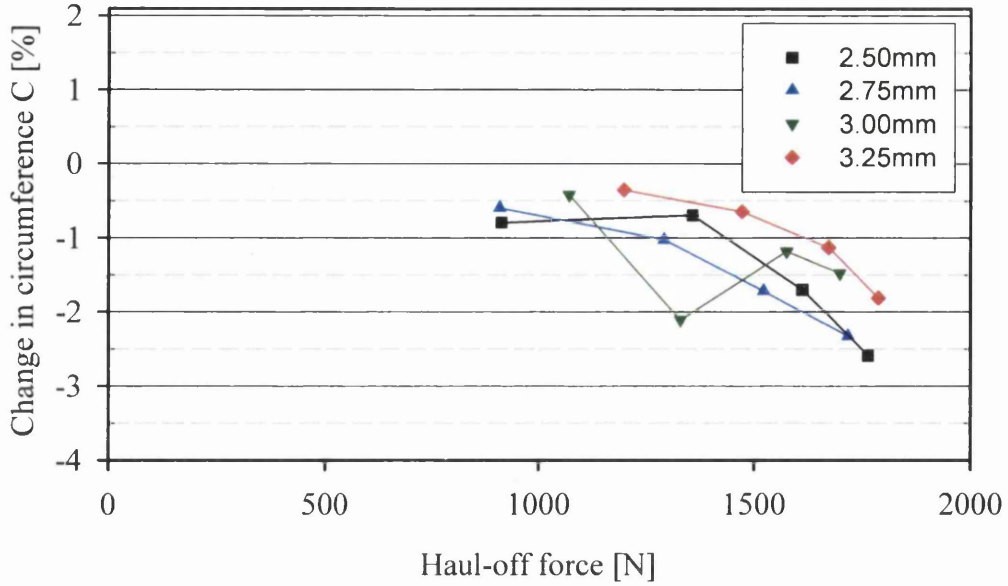

Figure 6.48: Change in circumference C as function of haul-off forces for different profile wall thicknesses; variation of vacua in Calibrator 1, vacuum in Calibrators 2, 3 and 4 constant at –0.4 bar; 4 m/min line speed; 2.50 mm die exit; wet calibration

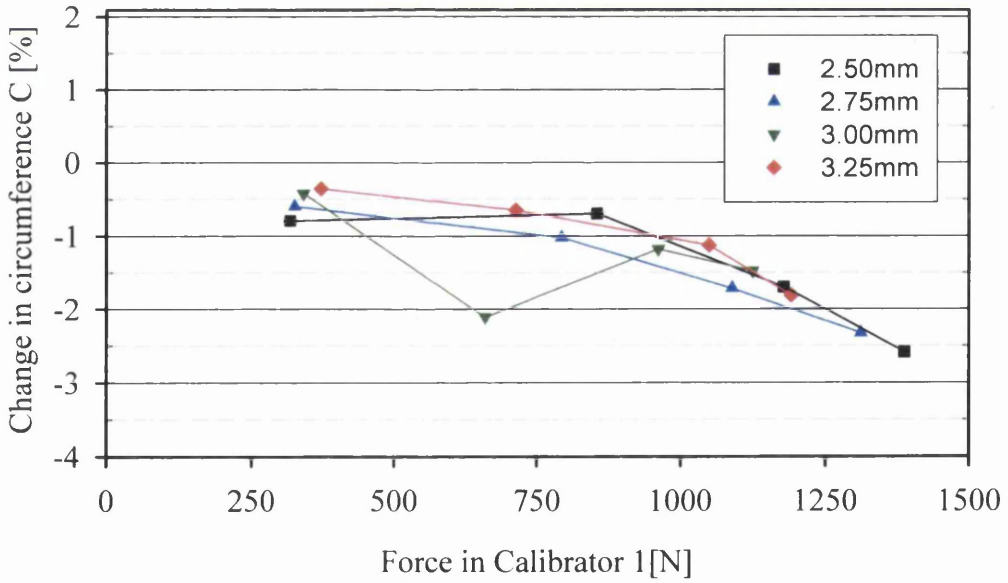

Figure 6.49: Change in circumference C as function of forces in Calibrator 1 for different wall thicknesses; variation of vacuum in Calibrator 1; vacuum in Calibrators 2,3 and 4 constant at –0.4 bar; 4 m/min line speed; 2.50 mm die exit; wet calibration

The pattern in both plots is similar, as expected from the dominance of Calibrator 1 forces in wet calibration. However, the effect of wall thickness is more pronounced in the plot versus Calibrator 1 forces. This may be because here the frozen layer thickness is smallest, and the

influence of different melt layer thicknesses is more significant. The rate of decrease in C with force is similar for all wall thicknesses, the curves being offset to higher forces at higher wall thicknesses.

6.2.5 Effects of vacuum in Calibrators 2,3 and 4 in wet calibration

In the following set of experiments, the vacuum in the downstream calibrators was varied whilst holding a constant vacuum in Calibrator 1, to confirm the last findings. Wall thickness was 3.00 mm in these runs.

The increase of vacuum in the downstream calibrators decreases the diameter as well as the circumference C, as shown in Figures 6.50 and 6.51. Results for D in Figure 6.50 agree well with the corresponding results in Figures 6.40 to 6.42. Those in Figure 6.51 generally agree well with data for C in Figures 6.43 to 6.40. The reduction in C is higher than the reduction in D as expected from previous results. With the variation of vacuum in the downstream calibrators, the haul-off forces have increased by 50%. As a consequence the reduction in diameter is increased by 20% and the reduction in circumference by 30%.

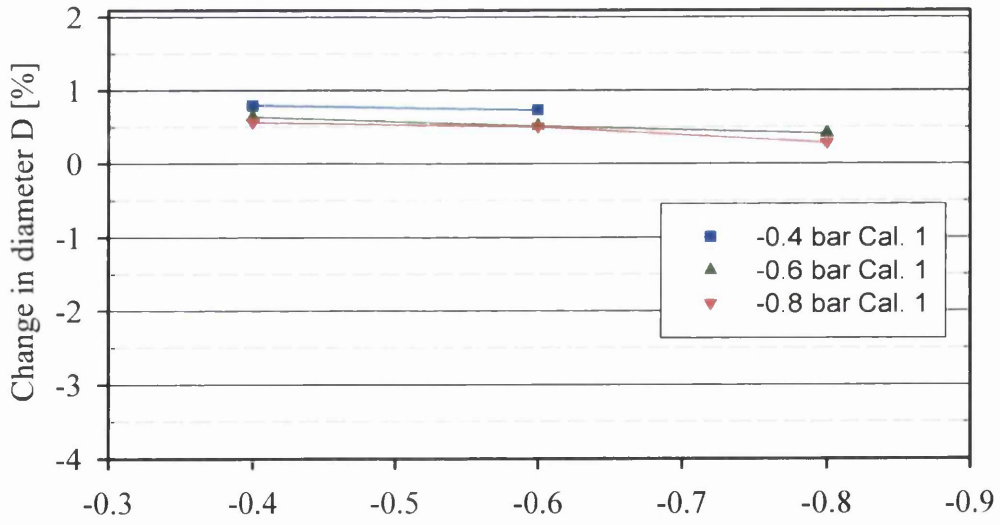

Figure 6.50: Change in diameter D as function of vacuum in Calibrator 2, 3 and 4 for different constant vacuum in Calibrator 1; 4 m/min line speed; 3.00 mm profile wall thickness; 2.50 mm die exit; wet calibration

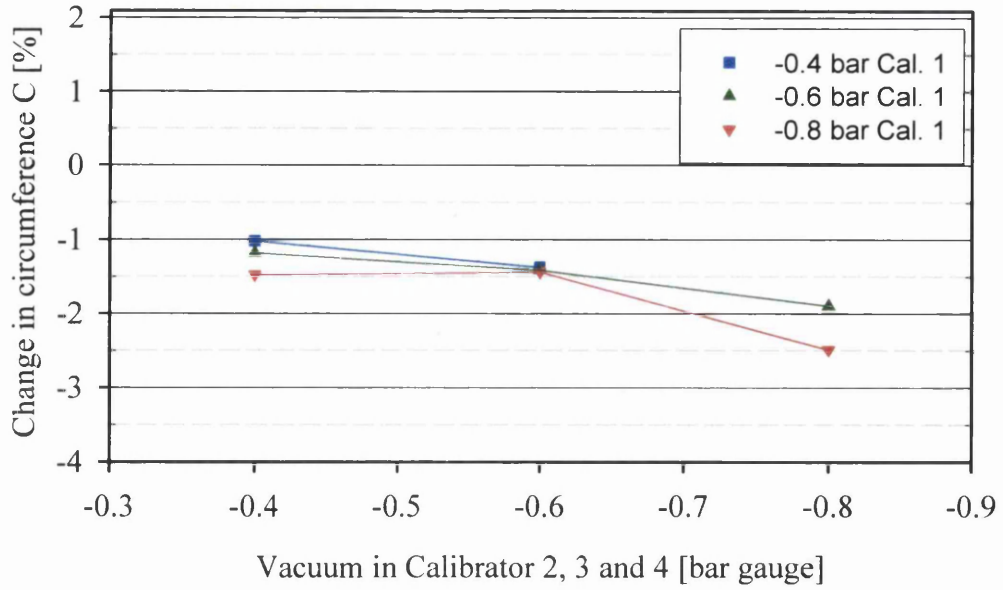

Figure 6.51: Change in circumference C as function of vacuum in Calibrator 2, 3 and 4 for different constant vacuum in Calibrator 1; 4 m/min line speed; 3.00 mm profile wall thickness; 2.50 mm die exit; wet calibration

Both these reductions are due to the increased draw down in the presence of higher forces.

6.2.6 Effects of melt extrusion and coolant temperatures in wet calibration

We have seen in Section 6.2.2 how the profile dimensions depend on the line speed. An important factor here is the reduced cooling time for the profile at higher speeds. An increase in extrusion temperature, or coolant temperature should give similar results, because a higher initial melt temperature or less strong cooling will reduce the thickness of the solidified layer in the calibration process, and we expect this to lead to a reduction of the final profile dimensions. In the following set of experiments melt extrusion temperature (as measured by the measurement cross, see Section 4.2.1.1) was varied from 180°C to 200°C by adjusting the extruder barrel temperatures and die temperatures. All other process parameters were held constant (including coolant temperature 16°C).

As shown in the Section 6.1, the forces increased with higher melt temperatures. This can be confirmed in Figure 6.52.

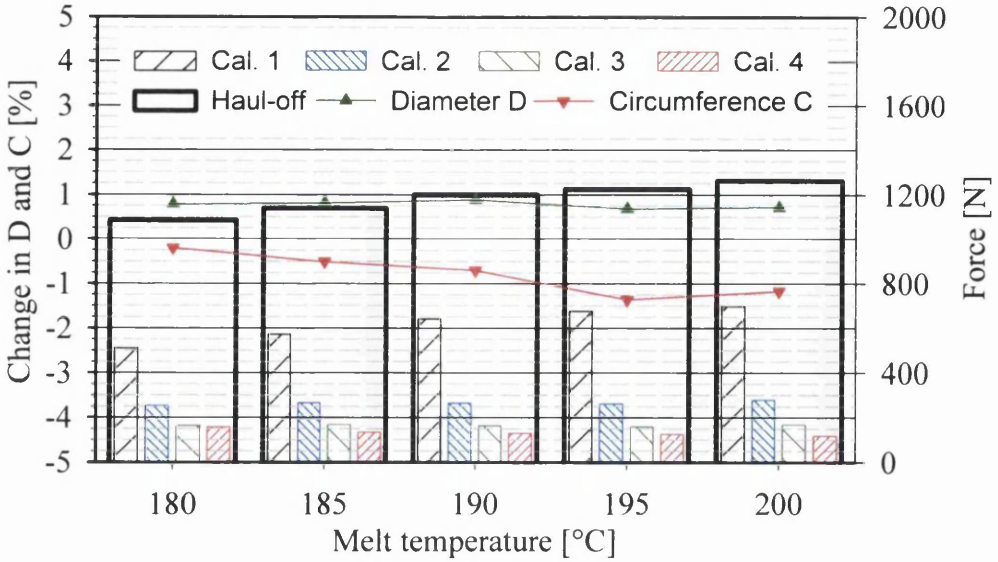

Figure 6.52: Change in diameter D and circumference C for different melt extrusion temperatures; constant vacuum at –0.4 bar; 2.75 mm profile wall thickness; 4 m/min line speed; 2.50 mm die exit; wet calibration

The Figure additionally shows the dependence of profile dimensions C and D on extrusion temperature. As expected, reductions in D are smaller than reductions in C. The diameter is nearly constant and the reduction in circumference is increased by 43% at the highest melt temperature. The larger decrease in C can be explained by a weaker profile due to a thinner solidified layer in combination with higher forces. The presence of a thinner solidified layer, such as also occurs at higher line speeds, is not reflected in the diameter values. So the reduced solidified layer cannot be the main explanation of the reduction of the diameter observed at higher line speed.

A final set of experiments examined the variation of the coolant temperature in Calibrator 1. The results are consistent with the effects of varying melt temperatures. The diameter is almost constant and the reduction in circumference is increased in the same range, approximately 45% from lowest to highest coolant temperature, see Figure 6.53. As noted previously, in Section 6.1, the forces are decreasing at higher coolant temperatures, the opposite trend to the effect of increasing melt extrusion temperature.

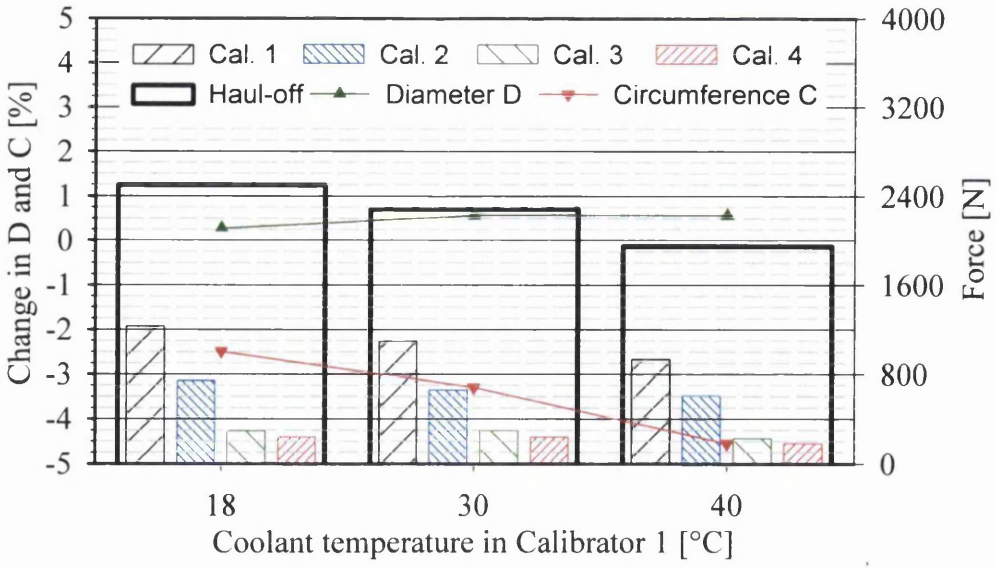

Figure 6.53: Change in diameter D and circumference C for coolant temperatures in Calibrator 1; constant vacuum at –0.4 bar; 2.75 mm profile wall thickness; 4 m/min line speed; 2.50 mm die exit; wet calibration

Some of the foregoing figures have shown a strong correlation of draw down and forces, especially for the corner dimension C. This leads to the conclusion that the profile is stretched in line direction. To investigate this, the weight per meter of the profile was measured for the runs where Calibrator 1 vacuum was varied and vacuum in downstream calibrators held constant. Mass flow rate of the extruder and haul-off speed were held constant.

In the next Figure 6.54 are shown the results, where the difference from the average value is plotted as function of vacuum in Calibrator 1.

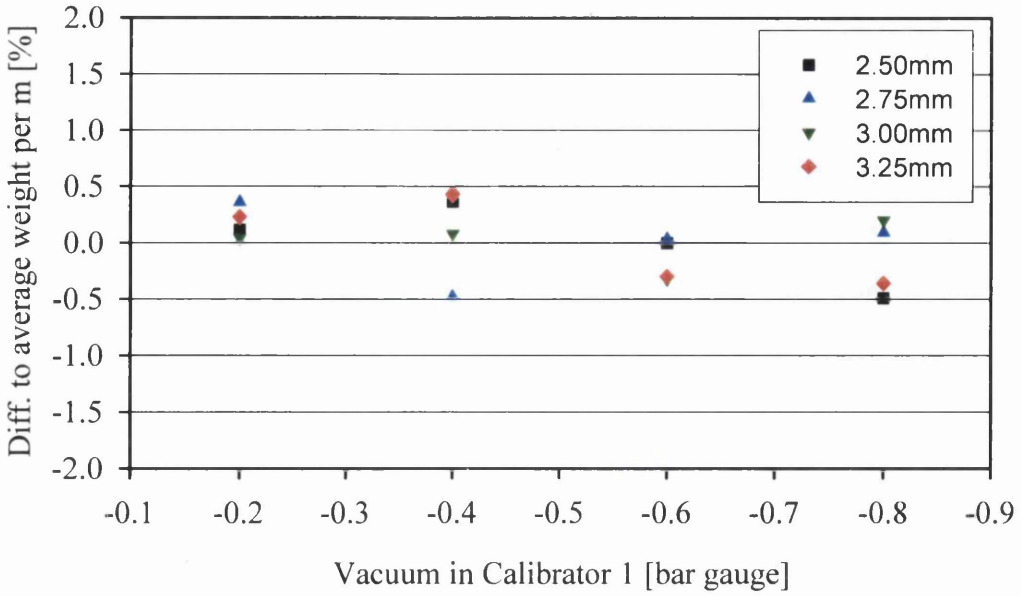

Figure 6.54: Difference from average weight per meter for different vacua in Calibrator 1 for different profile wall thicknesses; vacuum in Calibrators 2, 3 and 4 constant at –0.4 bar; 4 m/min line speed; 2.50 mm die exit; wet calibration

The differences are small, under 0.5%, and further scans of the profile cross section have given similar results. So a reduction of weight per meter due to stretching is not present, which is consistent with the fixed mass flow rate and haul-off speed. An effect compensating for the effect of draw down exits, Figure 6.55 explains this diagrammatically.

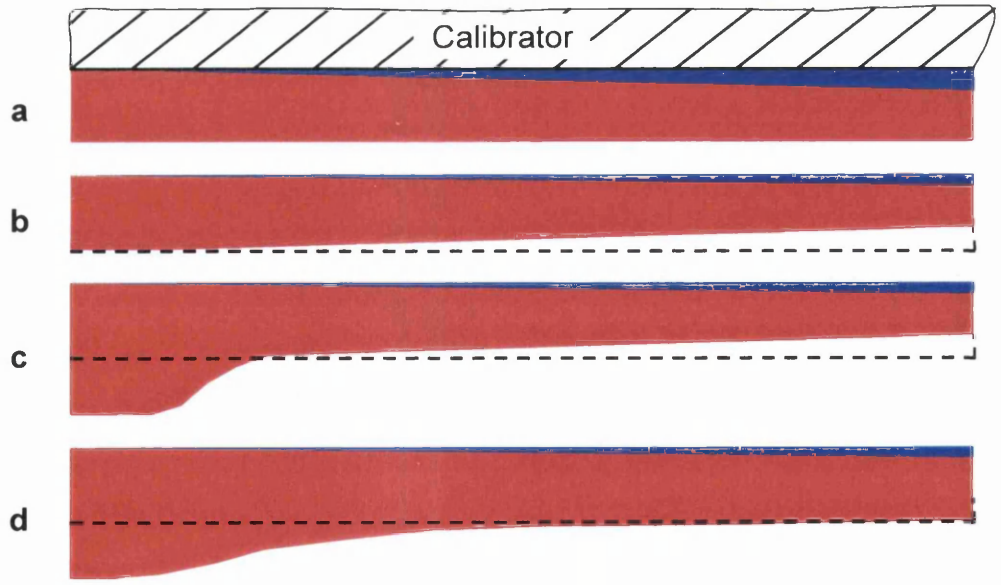

Figure 6.55: Compensation of wall thickness during stretching due to higher forces in line direction

In Figure 6.55a is shown the profile wall thickness at low force in line direction, such as exists with low level of applied vacuum. An increase of vacuum increases the forces, resulting in drawdown and a reduction in wall thickness, Figure 6.55b. Since the downstream haul-off speed is fixed, this results in a reduction of the profile line speed at the upstream end. Since mass flow rate from the extruder is fixed, this in turn results in an increase in initial wall thickness, Figure 6.55c, thus compensating for draw down and maintaining constant mass per unit length, see Figure 6.55d.

Summary

The final geometry of the hollow rectangular profile has been characterized by two external measurements: D, the summed diameter measuring the distance between the centres of opposite faces and multiplied by two, to get a value comparable with C, the sum of corner to corner dimensions. Additionally a reference value is introduced, based on the dimensions of Calibrator 1 inlet, adjusted for isotropic thermal shrinkage of the uPVC.

The dependence of D and C on process parameters is quite distinct. D is always greater than or equal to the reference value, whereas C is always less. Both C and D reduce with increased line speed, as is widely known. However, the reduction in D is quite small: up to 2% (% based on the reference value) as line speed increases from 1 m/min to 8 m/min, which is equivalent to an absolute reduction of 0.35 mm for the height. According to RAL [158], a difference of ±0.3 mm is tolerated for the height of a profile and the decrease due to higher line speed must therefore be considered in the design of the calibration line. The reduction in C is larger, up to 3.5% over the same range of line speed, and for applied vacuum of –0.4 bar to –0.8 bar. D shows little influence of vacuum, or of wet and dry calibration, whereas C shows higher reductions for higher vacua, and for dry calibration.
Plots of these reductions against haul–off and Calibrator 1 forces show that the results for D, for all vacua and for wet and dry calibration, correlate quite well with Calibrator 1 forces, suggesting that phenomena there are most significant. Reductions in C correlate better with haul-off force, suggesting that phenomena along the whole line are significant.

In experiments where profile wall thickness was varied (2.50 mm to 3.25 mm) by changing the mass flow rate at a given line speed, D was found to be a fraction of a percent lower for the thick wall profile, whereas C was 1% lower for the 2.50 mm wall than for the 3.25 mm.

In further experiments, vacuum in Calibrator 1 was varied whilst holding downstream calibrator vacuum constant. D was found to be insensitive to Calibrator 1 vacuum, whereas C decreased from around -0.5% to –1.5% or –2.5% as vacuum increased from –0.2 bar to –0.8 bar, the largest decrease corresponding to the thinnest wall.
A plot of C against Calibrator 1 forces for these experiments clearly shows a larger reduction in C for thinner walls at a given force.
In a complementary set of experiments, vacuum in downstream calibrators was varied whilst holding Calibrator 1 vacuum constant. Here, both D and C were found to decrease more at higher downstream vacuum, D by a fraction of 0.5% as vacuum increased from –0.4 bar to –0.8 bar, and C by 1%.

In experiments where melt extrusion temperature was varied from 180°C to 200°C (195° was the standard value in second set of experiments, where the wall thickness was varied) D was found to be insensitive, and C decreased by 1% as the temperature rose. Variation of the coolant temperature from 18°C to 40°C again caused little change in D, but a reduction of up to 2% in C at the highest temperature.

Detailed and conclusive explanations of these complex phenomena require a mathematical model that takes into account the cooling process and its interaction with the viscoelastic mechanics of the uPVC. Such a model is under development. Here, some qualitative explanations can be proposed.

Draw down of the profile occurs during calibration, as is widely known, due to the line direction tensile forces imposed by the haul-off to overcome friction forces in the calibrators. Draw down is clearly visible in the reduced corner dimension C, and this is larger for higher forces (high vacuum) and weaker profiles (higher line speeds, thinner walls, higher melt temperatures). The applied vacuum is unable to resist the reduction in corner dimensions by draw down. Evidence for loss of contact with the calibrator at the profile corners is provided by vacuum measurements. At exit from the haul-off, where tensile force is released, elastic

recovery causes the profile shorten and expand. This effect is not large enough to compensate for draw down, so the final corner dimensions are lower than the reference value.

General influences on C of the main parameters are shown for wet calibration in Figure 6.56.

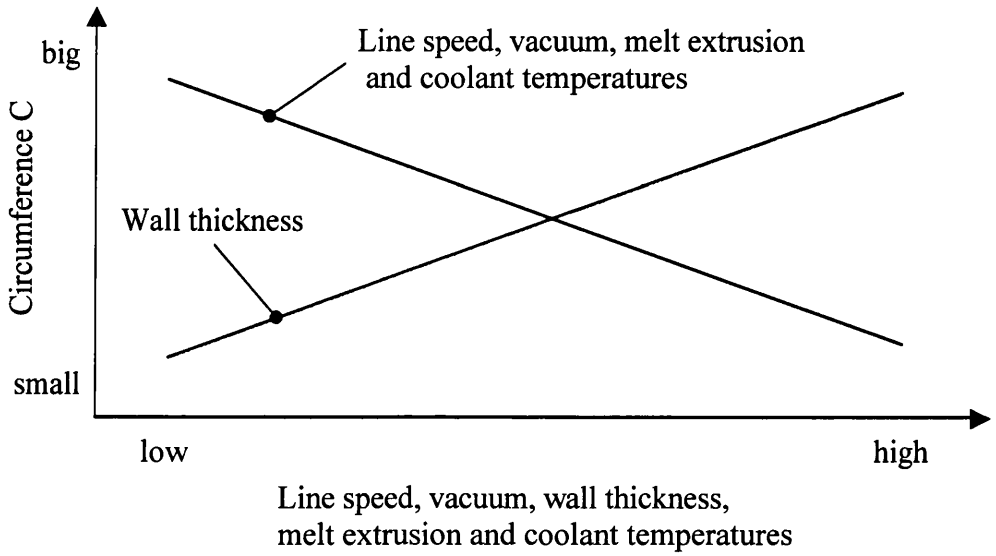

Figure 6.56: General dependencies of circumference C in wet calibration on line speed, vacuum, wall thickness and melt extrusion and coolant temperatures

Effects on D, which measure the profile size at the mid-sides, are more complex.
It is clear from the vacuum measurements of the mid-sides that the profile-calibrator contact is present over the whole line, except possibly near the Calibrator 1 inlet where no measurement was possible. Thus vacuum is able to maintain the value of D against the draw down within the calibrators, by pulling the mid-sides outwards. Then, elastic recovery from the tensile forces after the haul-off, as well as equilibration of forces on the profile cross-section after removal of the calibrator constraint, causes D to increase above the reference value. Although D is maintained by vacuum within the calibrator, its final value does fall as C is reduced by draw down, though the effects are small.

That D decreases with increased wall thickness, seems counter intuitive, in terms of draw down effects. The explanation is believed to be related to the cramming phenomena at the entrance to Calibrator 1. Die and Calibrator 1 dimensions are set such that draw down of 2% occurs into the calibrator. Together with the effect of die swell between the die and calibrator, this means that melt is crammed into the calibrator inlet. The resulting resistance probably

leads to draw down of the hot, soft profile immediately after the inlet. Vacuum restores contact with the calibrator wall, by a point some way down Calibrator 1 on the centre line. Restoration of contact is probably slower for the thicker wall profiles. The occurrence of some cooling and solidification of the outer layers whilst D is reduced, may result is lower final values of D. The general dependencies of D are shown in Figure 6.57.

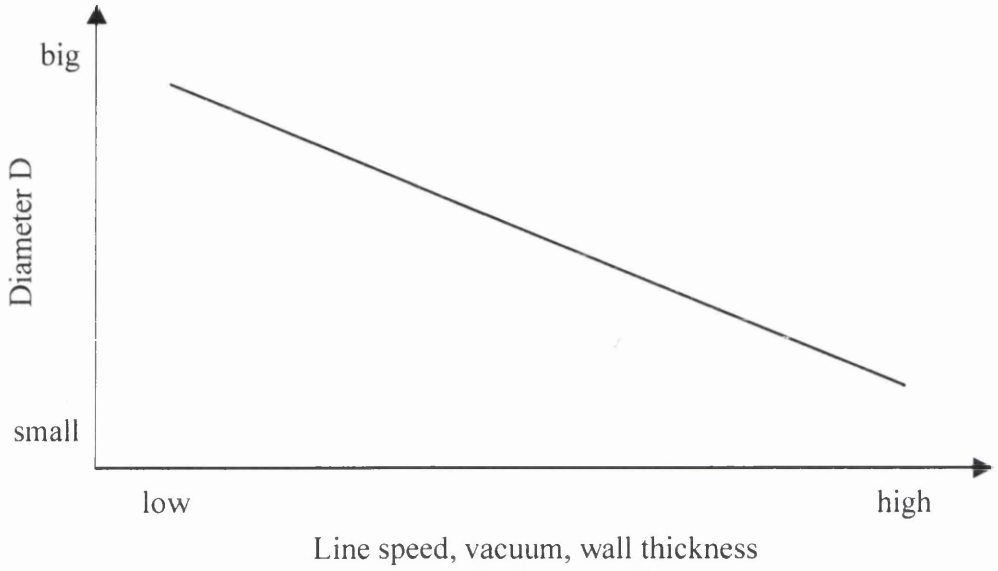

Figure 6.57: General dependencies of diameter D on line speed in wet and dry calibration on vacuum and wall thickness in wet calibration

The general combined effects of small draw down effect for D and larger effect for C are shown for the upper profile surface in Figure 6.58.

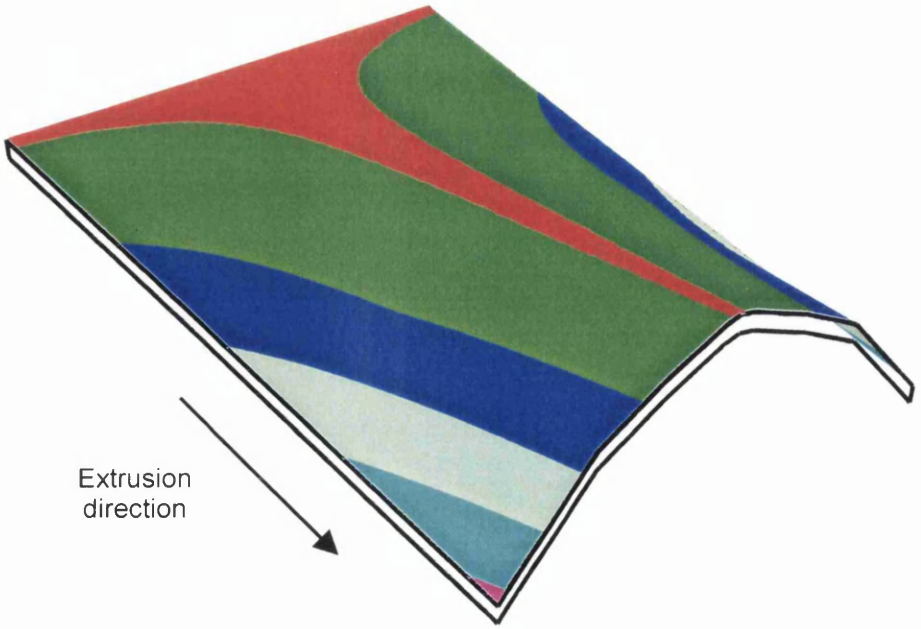

Figure 6.58: Draw down effect on the upper profile wall

An effect of the draw down on the profile mass per unit length was not found. This may be explained with a self-adjusting process. The stretching due to higher forces decreases the profile velocity upstream, since the downstream haul-off speed is fixed. Since mass flow rate from the extruder is also fixed, this reduction in upstream velocity increases the initial wall thickness, thus compensating for the effects of draw down on mass per unit length. Draw down may be correlated with shrinkage, and this will be investigated in the following section.

6.3 Shrinkage

6.3.1 Introduction

As mentioned in the description of the calibration process, the shrinkage is one important profile property. Production samples are routinely tested according to DIN EN 479, and the maximum permissible shrinkage in line direction is 2%.

In the literature there are several investigations of shrinkage for PVC extrusion. Berger [157] has investigated the dependence of shrinkage on line speed for PVC pipes with 32 mm diameter and a wall thickness of 2 mm. Shrinkage decreased from around 5% at 2 m/min line speed, to 3.5% at 14 m/min.

In another set of experiments he has shown the dependence of shrinkage for a square profile with 40 mm side length and 2 mm wall thickness [159]. In this investigation he varied the coolant temperatures from 10°C to 70°C and the melt extrusion temperature from 185°C to 205°C. Up to a coolant temperature of 30°C, the shrinkage stays at the same level of 3.0% for the different melt temperatures. With further increase of the coolant temperature the shrinkage increased for all the melt temperatures. At a coolant temperature of 70°C the shrinkage reached a value of 5.3% at a melt temperature of 185°C. Increase of the melt temperature to 195°C then decreased the shrinkage to 4.5%, and at the highest melt temperature the shrinkage dropped to 3.8%.

Rabinovitch [160] has carried out experiments for PVC profiles, where the profile went into an air or water bath (used for variation of coolant temperatures) after the die exit, without using calibration units. He has also investigated the influence of the annealing time and temperature on the shrinkage measurement and has shown that an annealing time of 60 min at 100°C is sufficient, because the shrinkage reaches a limiting value at times longer than 30 min. He also confirmed the findings of Berger, namely that higher coolant temperatures give higher shrinkage values. In his experiments the shrinkage increased from 3% at a coolant temperature of 2°C to 5.3% for 90°C coolant temperature. Breil [156] measured an increase of shrinkage of 0.02% for an increase in coolant temperature of 1°C. Furthermore, Rabinovitch has shown an increase of shrinkage from 2.2% to 3.5% for an increase of melt temperature from 160°C to 180°C, and then a decrease to 2.4% with further increase to 200°C melt temperature, which Berger has also noted. An increase of shrinkage from 2.4% up to 4.3% was found in his experiments with an increase of screw speed from 10 rpm to 30 rpm, corresponding respectively to shear rates, 275 s^{-1} to 825 s^{-1} at the die exit. The same effect

was found for increased shear rate brought about by reduction of die lip opening. The shrinkage increased from 2.4% to 5.9% with increase of shear rate from 53 s^{-1} to 960 s^{-1}. An extrapolation to a shear rate of zero lead to values of around 2%, which was considered to result from the freezing in of strains originating in the die. Breil obtained a lower value of 0.3% for the frozen-in strains. Draw down of the profile of up to 20% increased the shrinkage from the previously mentioned 2% (here at zero draw down), to 10%. Semmler [153] measured the shrinkage in several layers of a window profile. He found that the shrinkage is highest in the outside layer and decreases towards to the inside of the profile. Higher shrinkage was obtained in the outer layer with higher line speed (higher haul-off forces were measured at higher line speeds) and also for higher coolant temperatures, whereas the dependence of shrinkage on both parameters was only weak at the inner side of the profile wall. He also varied the melt temperature, and found that the shrinkage increased from 4.5% to 6.5% with an increase of melt temperature from 189°C to 197°C, which is opposite to the findings of Berger and Rabinovitch. Increase of the applied vacuum gave higher values for shrinkage, due to higher forces. Furthermore he has shown a reduction of shrinkage from 1.6% to 1.1% after storage for 30 days.

Harrell [161] developed a model to simulate and predict the shrinkage in extruded profiles. His calculated shrinkage values are based on the knowledge of the imposed strain in the profile during the creep process. In his investigation, he has used an annealing temperature of 82° for a time of 30 min according to ASTM standard. Using this shrinkage measurement procedure a final shrinkage value cannot be obtained, such as has been found by Rabinovitch. Harrell has also presented shrinkage measurements of an extruded profile. On changing the melt extrusion temperature from 179°C to 188°C to 195°C the shrinkage decreased from 1.1% to 0.65% down to 0.4% for an annealing time of 30 min at 100°C.

6.3.2 Effects of vacuum in wet and dry calibration at different line speeds

The forces and profile dimensions were presented as a function of line speed and vacuum in wet and dry calibration in earlier sections, and the dependence of shrinkage on the same parameters is now shown in Figure 6.59.

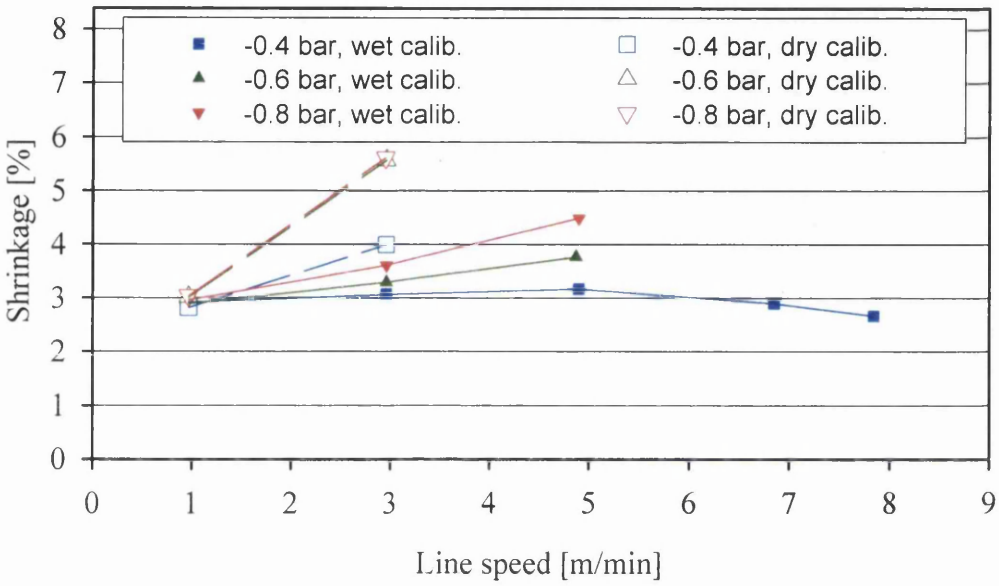

Figure 6.59: Shrinkage for different line speeds and various applied vacuum in wet and dry calibration; 2.50 mm die exit; 2.50 mm profile wall thickness

Here, melt extrusion temperature varies from 180°C at a line speed of 1 m/min to 192°C at 8 m/min due to higher extruder screw speed. First of all it is to be remarked that the values are higher than in normal production, where a maximum of 2% is tolerated. This may be due to the profile wall thickness being the same as the width of the die exit (This is confirmed below). At 1 m/min, Figure 6.59 shows that the shrinkage is not dependent on the vacuum or on wet or dry calibration. At higher line speed, the values in dry calibration are higher than for wet calibration. Additionally, the vacuum has a more significant influence in dry calibration. We have seen congruent trends for the haul-off forces in Figure 5.2, where they were shown for the same parameters. Also the data for the circumference C is similar, though reflected about the abscissa, see Figure 6.30. Altogether, this leads to the conclusion that the shrinkage is mainly dependent on forces and draw down in the calibration process.

To investigate this the shrinkage is first plotted as a function of haul-off force in Figure 6.60.

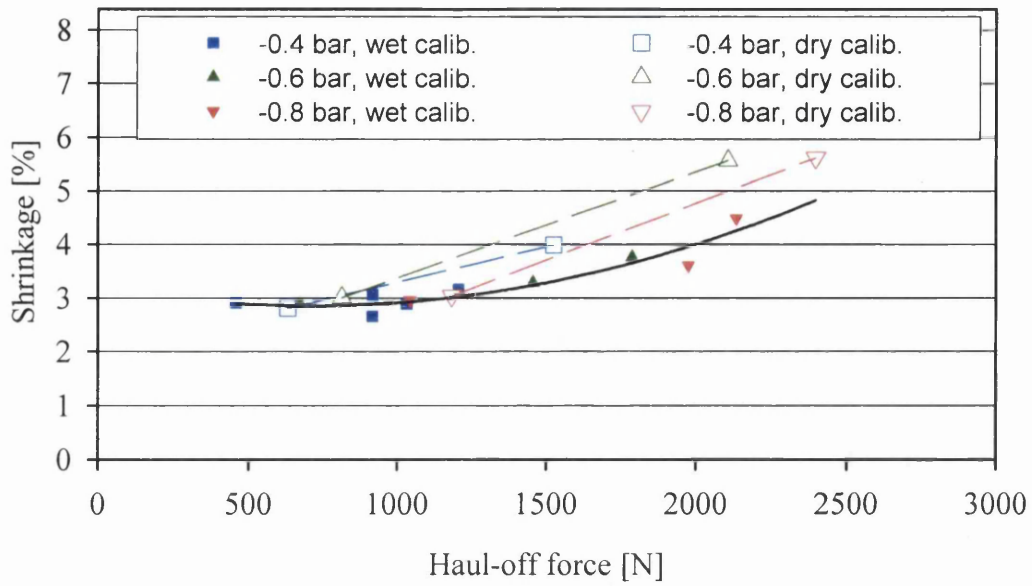

Figure 6.60: Shrinkage as function of haul-off force for various applied vacuum in wet and dry calibration; 2.50 mm die exit; 2.50 mm profile wall thickness

The trend lines show a general dependence on the haul-off forces. In wet calibration, a good correlation is visible, independent of vacuum, and this marked with the main trend line, whereas the values in dry calibration are more dependent on vacuum. The dependence on Calibrator 1 forces may give a better understanding, and this is shown in Figure 6.61.

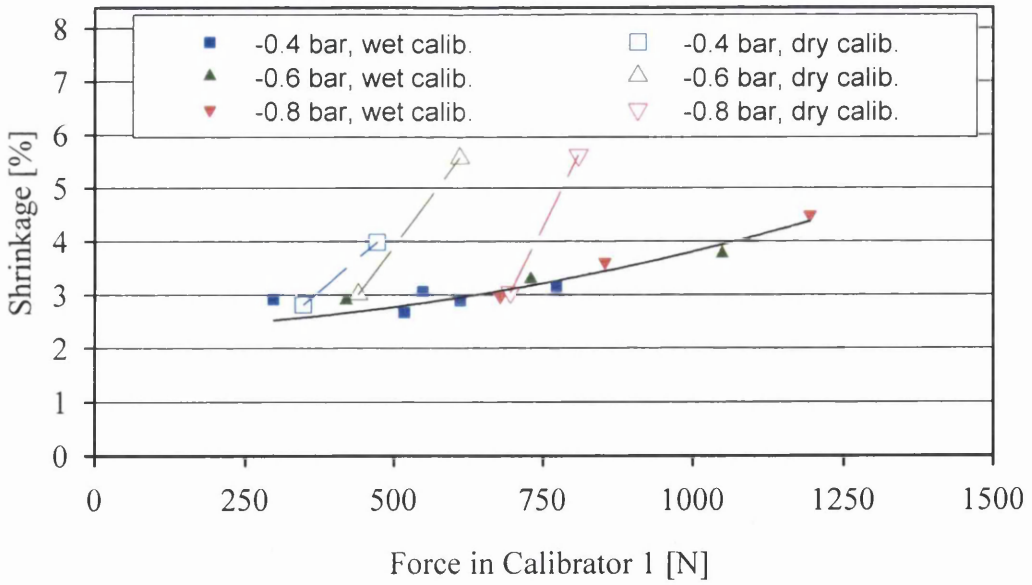

Figure 6.61: Shrinkage as function of forces in Calibrator 1 for various applied vacuum in wet and dry calibration; 2.50 mm die exit; 2.50 mm profile wall thickness

For wet calibration, shrinkage correlates very well with Calibrator 1 forces. However, for dry calibration a better correlation is obtained with the haul-off force. This can be explained with the more uniform distribution of calibrator forces and higher haul-off force in dry calibration. A reduction of line speed and so also of the forces, would lead to an extrapolated shrinkage value of around 2.5% at zero force. As mentioned before, this value is too high for normal production. Shrinkage may be reduced by allowing strain recovery after the die exit, as demonstrated in the next set of experiments.

6.3.3 Effects of wall thicknesses and vacuum in wet calibration at different line speeds

In a further set of experiments the profile wall thickness wall was increased, as explained previously, by increasing mass throughput of the extruder at constant line speed and at a constant melt temperature of 195°C. The experiments were carried out under applied vacua of –0.4, -0.6 and –0.8 bar gauge. The results are shown in the next Figures 6.62 to 6.64. Note that the values for the 2.50 mm wall thickness cannot be compared directly with Figure 6.59, because of the variation of melt temperature in the previous set of experiments. The low line speed results in Figure 6.62 are for higher melt temperature (195°C) than those in Figure 6.59 (182°C). We see that the increased temperature has resulted in lower shrinkage (3% down to 2%).

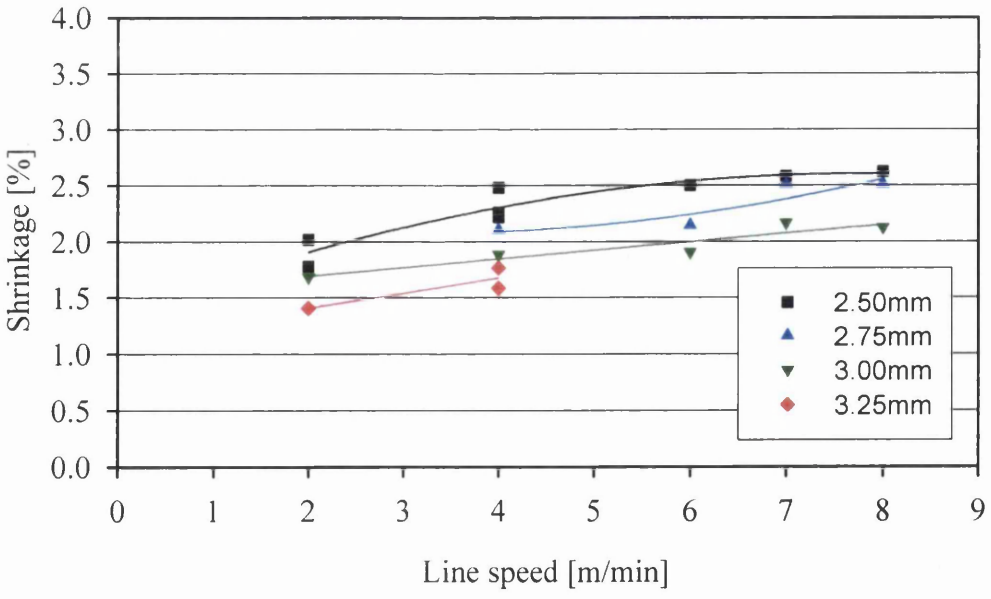

Figure 6.62: Shrinkage for different line speeds at different profile wall thickness; 2.50 mm die exit; -0.4 bar vacuum; wet calibration

Figures 6.62 to 6.64 show that shrinkage is reduced at higher profile wall thickness. The increase at higher line speeds, seen before, is again present. However, the shrinkage does not fall at higher line speeds at –0.4 bar vacuum as seen previously in Figure 6.59. A reduction of Calibrator 1 and haul-off force was also visible at higher line speeds in Figure 6.8 and 6.11 and a lower force should lead to less shrinkage. But here, the shrinkage increases with higher line speeds though values at low line speed are lower than in Figure 6.59. The reason for this is the higher melt temperatures at lower line speeds in Figure 6.62. At the high line speed of 8 m/min, the melt temperature in both sets of experiments is approximately equal (192°C and 195°C). The measured shrinkages agree closely. The extrapolation to a line speed of zero leads to a remaining average value of 1.4% at applied vacuum of –0.4 bar (Figure 6.62). At higher vacuum, the shrinkage increases more rapidly with line speed. This is visible on the following Figures 6.63 and 6.64, and would lead to lower extrapolated values of around 1%.

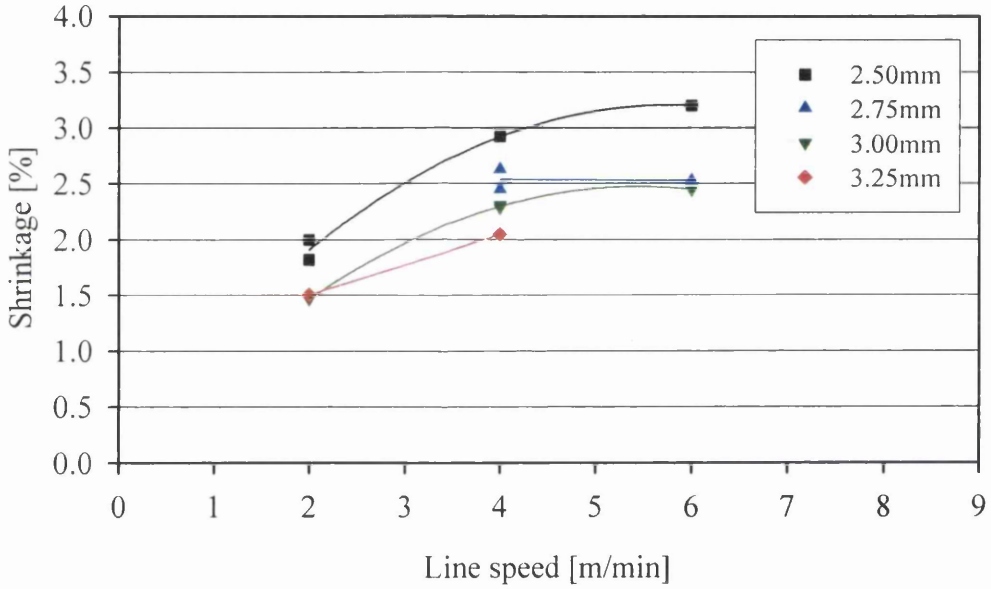

Figure 6.63: Shrinkage for different line speeds at different profile wall thickness; 2.50 mm die exit; -0.6 bar vacuum; wet calibration

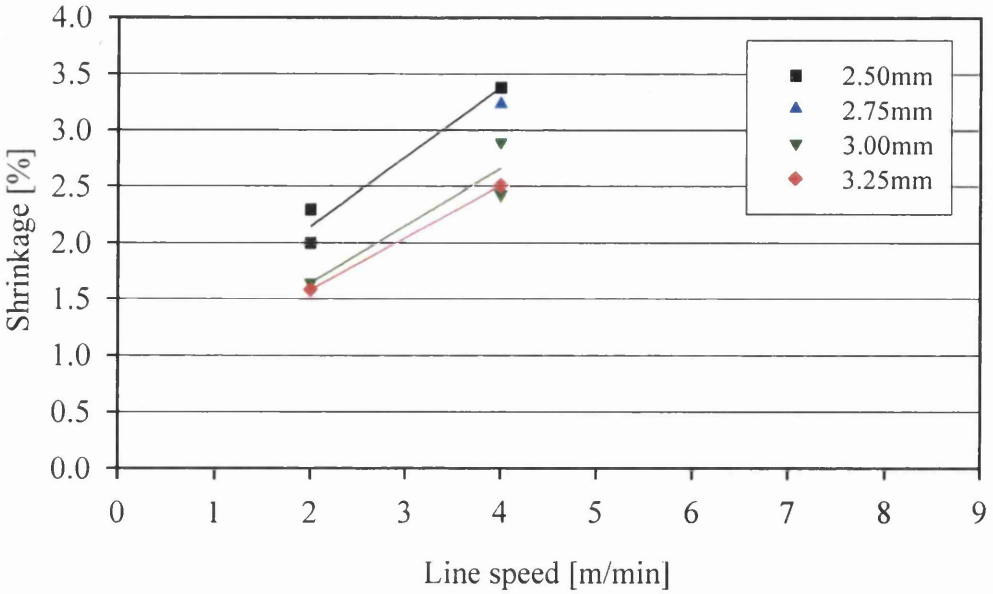

Figure 6.64: Shrinkage for different line speeds at different profile wall thickness; 2.50 mm die exit; -0.8 bar vacuum; wet calibration

As seen previously in Figures 6.60 and 6.61 at wall thickness of 2.50 mm in wet calibration, the shrinkage has shown a quite good correlation with the haul-off and Calibrator 1 forces. In the next Figures are shown the correlations of shrinkage with Calibrator 1 and haul-off forces for the various wall thicknesses.

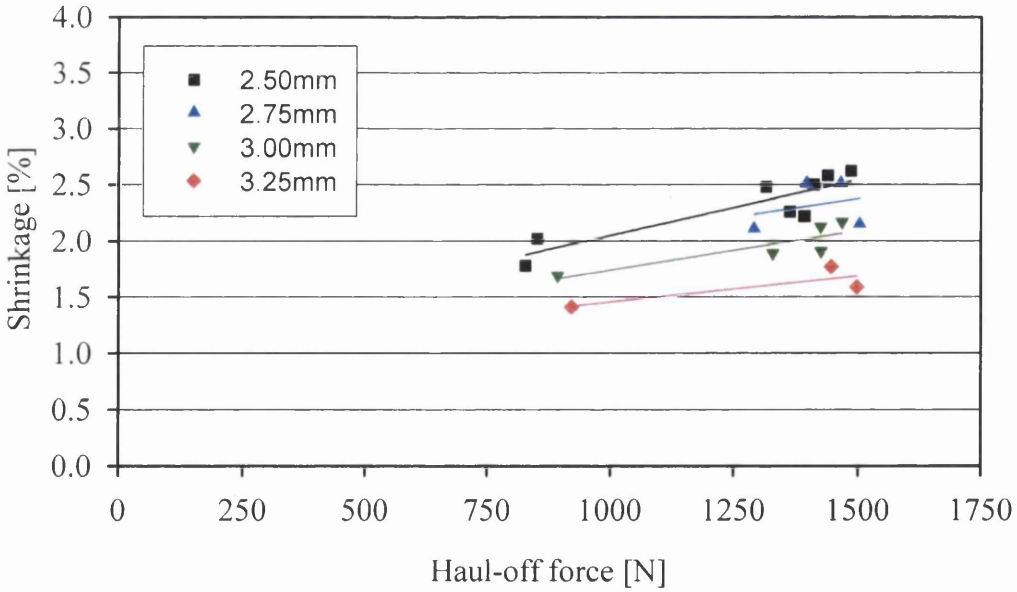

Figure 6.65: Shrinkage as function of haul-off force for different profile wall thicknesses; 2.50 mm die exit; -0.4 bar vacuum; wet calibration

The shrinkage is not only dependent on the haul-off force but also on wall thickness. This can be seen in Figure 6.65 where the shrinkage is less for thicker wall at a given haul-off force, and a clear dependence on wall thickness is perceptible. The same behaviour is also recognizable in a correlation with Calibrator 1 forces at –0.4 bar, Figure 6.66.

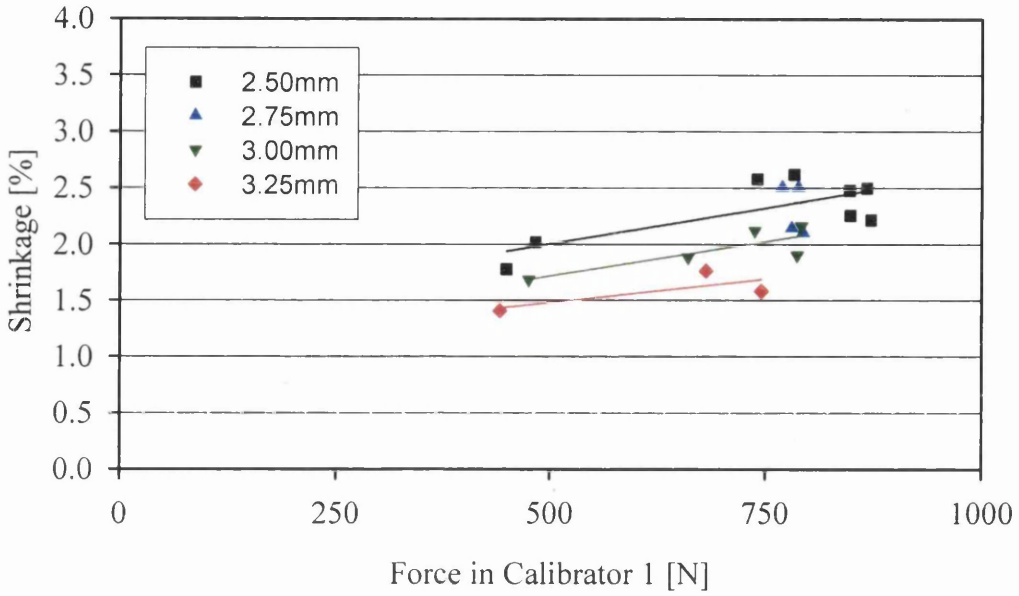

Figure 6.66: Shrinkage as function of force in Calibrator 1 for different profile wall thicknesses; 2.50 mm die exit; -0.4 bar vacuum; wet calibration

At higher vacuum, the shrinkage and forces increase, and this is shown for –0.6 and 0.8 bar in the Figures 6.67 to 6.70.

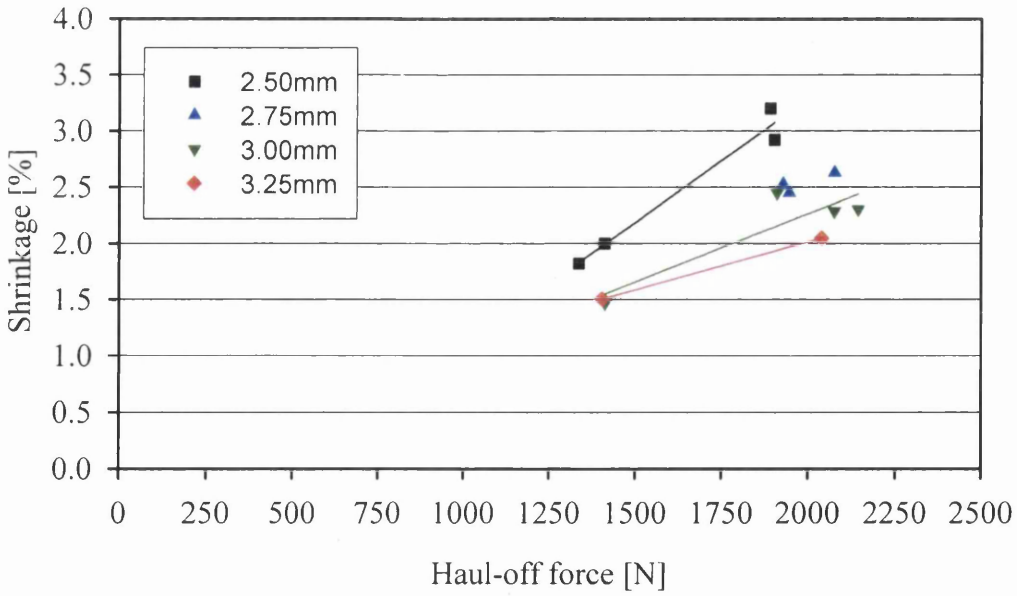

Figure 6.67: Shrinkage as function of haul-off force for different profile wall thicknesses; 2.50 mm die exit; -0.6 bar vacuum; wet calibration

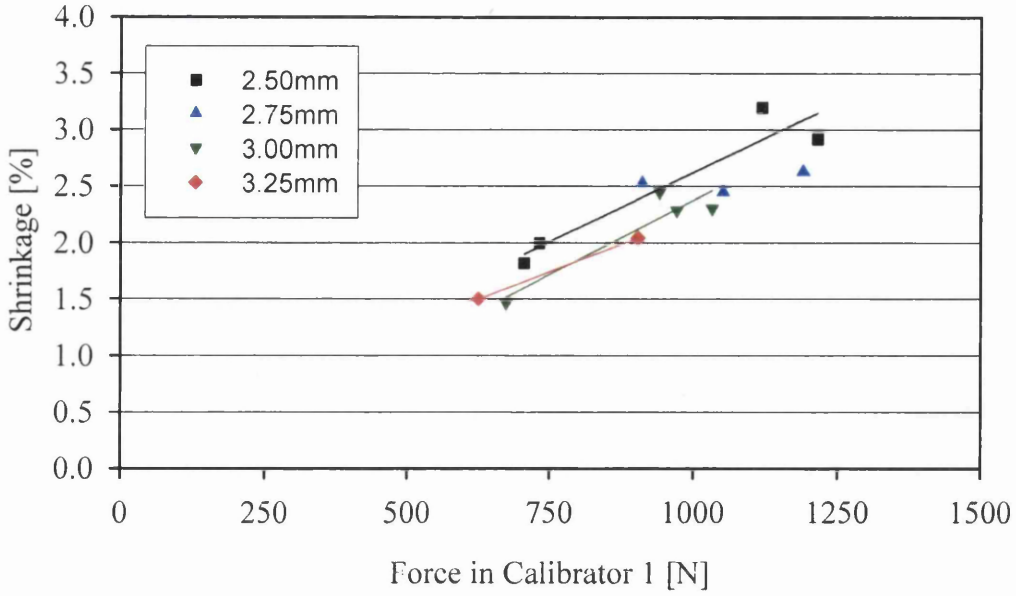

Figure 6.68: Shrinkage as function of force in Calibrator 1 for different profile wall thicknesses; 2.50 mm die exit; -0.6 bar vacuum; wet calibration

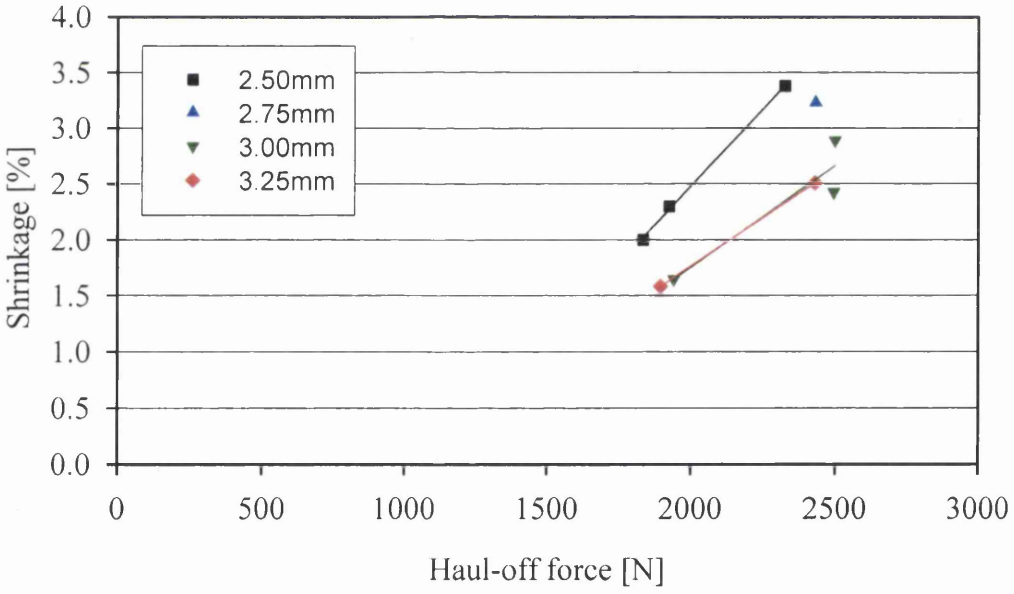

Figure 6.69: Shrinkage as function of haul-off force for different profile wall thicknesses; 2.50 mm die exit; -0.8 bar vacuum; wet calibration

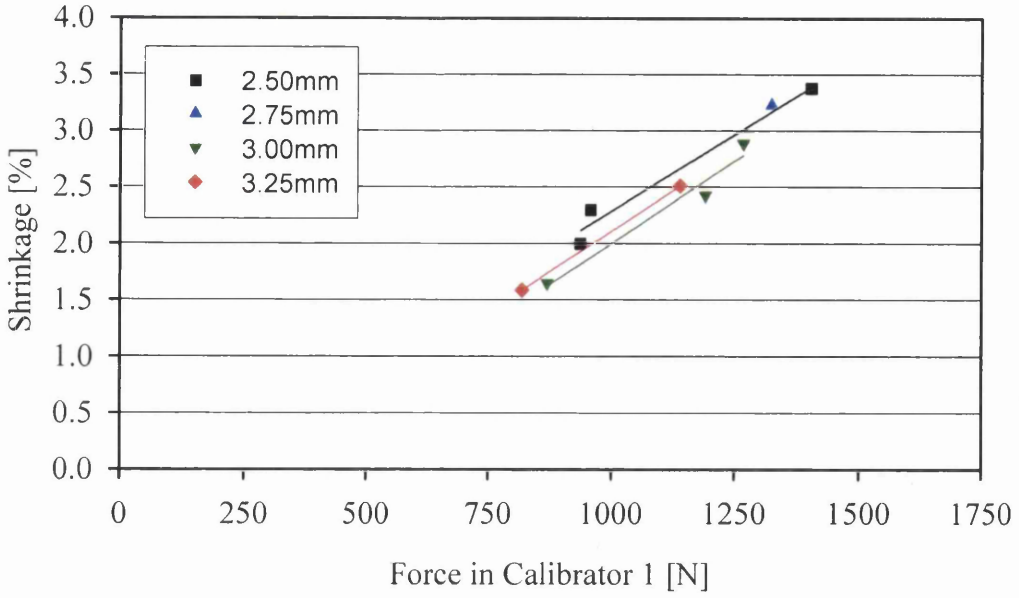

Figure 6.70: Shrinkage as function of force in Calibrator 1 for different profile wall thicknesses; 2.50 mm die exit; -0.8 bar vacuum; wet calibration

For all vacua, the shrinkage has varied, at lowest forces, from 1.5% at 3.25 mm wall thickness up to 2% at 2.50 mm wall thickness. These lowest forces were obtained at lowest line speed, here 2 m/min, which is not directly visible in the foregoing plots. At higher vacua, the shrinkage increases faster with higher forces from 2.5% at –0.4 bar up to 3.5% at –0.8 bar. This is related partially to forces, but also to the reduced solidified layer of the profile at higher line speeds, which influences the amount of draw down that occurs.

However, a direct comparison is not possible, because the influences of line speed on forces and solidified layer cannot be separated. To simplify the picture, and eliminate effects of line speed on solidified layer thickness, results for a fixed line speed of 4 m/min are presented in the following two Figures.

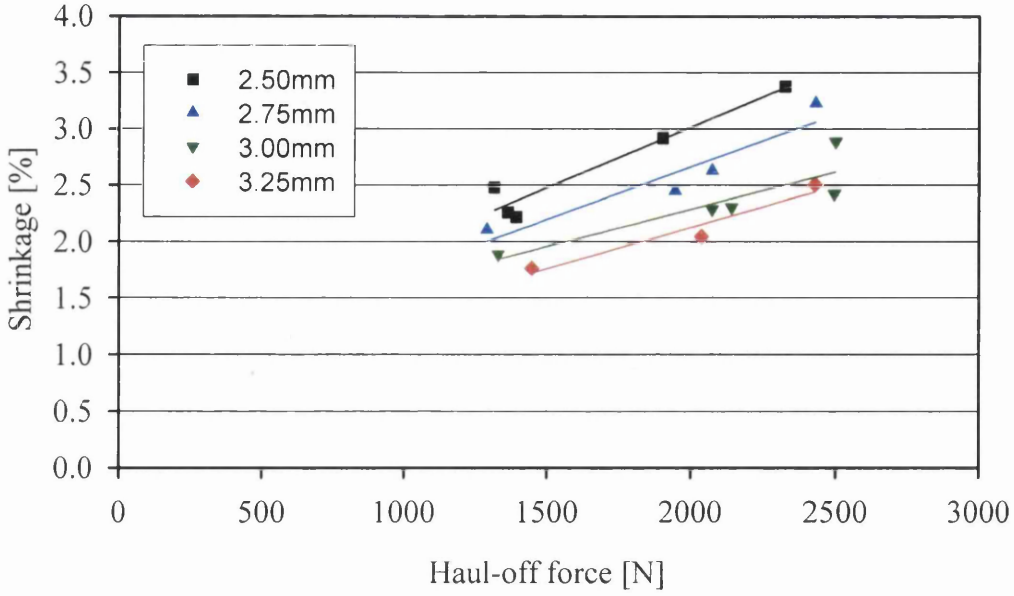

Figure 6.71: Shrinkage as function of haul-off force for different profile wall thicknesses; 4 m/min line speed; 2.50 mm die exit; wet calibration

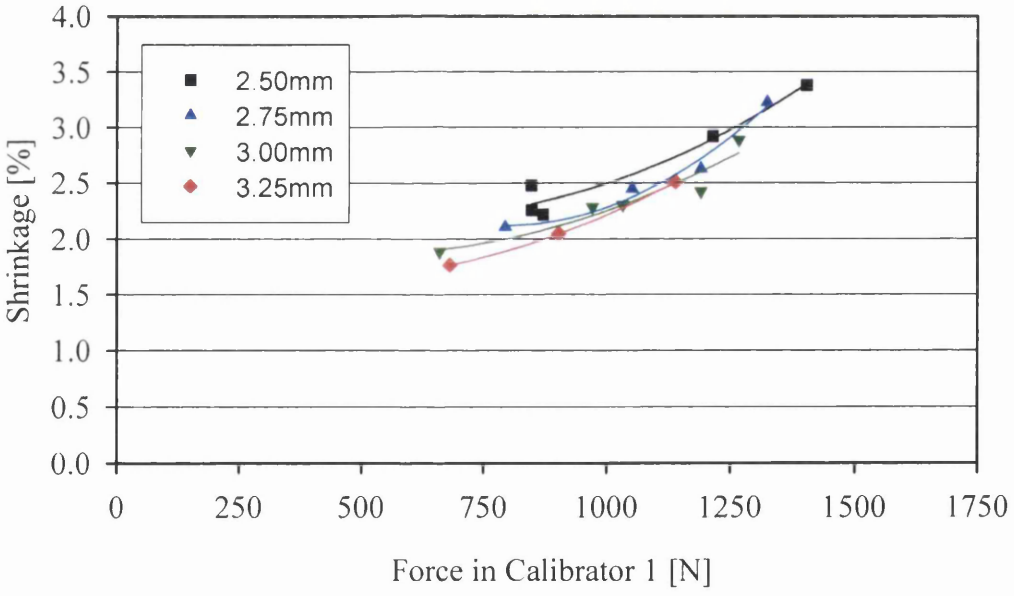

Figure 6.72: Shrinkage as function of force in Calibrator 1 for different profile wall thicknesses; 4 m/min line speed; 2.50 mm die exit; wet calibration

As expected, the higher wall thickness leads to a lower shrinkage, and in the plot against haul-off forces, a clear distinction can be made between the wall thicknesses, whereas the values are closer together for the Calibrator 1 forces. An extrapolation would give values of around 1.2% at a zero force. In the two forgoing Figures the vacuum was a hidden parameter. Now,

the shrinkage is plotted in Figure 6.73 against the vacuum to see the influence of vacuum at constant line speed of 4 m/min.

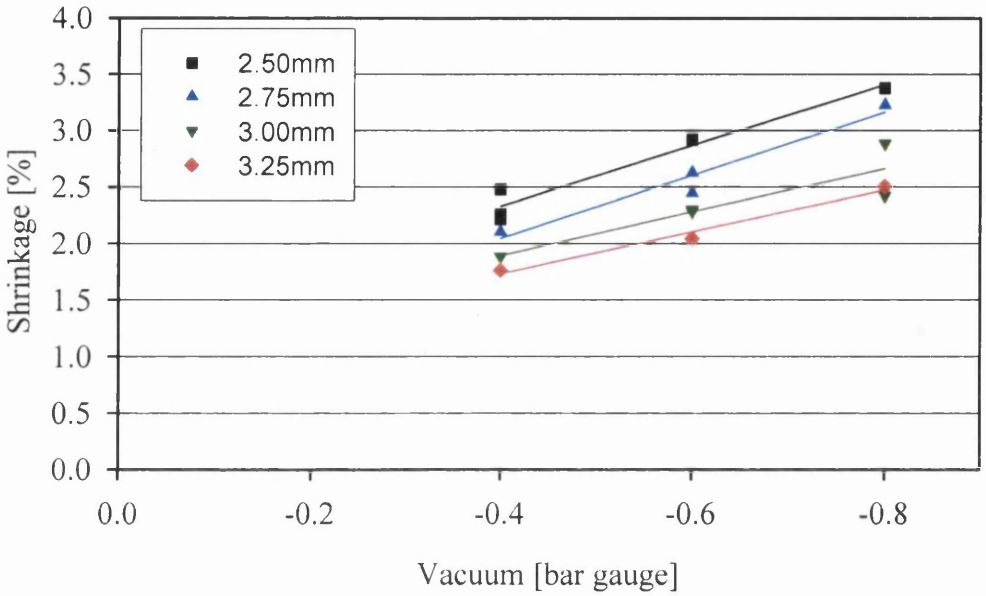

Figure 6.73: Shrinkage for different vacua for different profile wall thicknesses; 4 m/min line speed; 2.50 mm die exit; wet calibration

The residual shrinkage at zero vacuum (and zero forces), must be a result of the freezing-in of strains that were built up in the die. Further experiments were done, in which the shrinkage was measured without calibration to get the die related shrinkage. In these, a length of the molten profile was cut off directly after the die exit and cooled in a water bath. This section was used to determine the shrinkage, using the standard procedure. Experiments were carried out from 8 rpm up to 20 rpm, which covers the screw speed range. The obtained shrinkage was approximately 0.7 %, independent of screw speed, opposite to the findings of Rabinovitch [160], and higher than the value of 0.3%, measured by Breil [156].

The results shown above were for a die exit of 2.50 mm. Next the die exit was reduced to 1.50 mm and the effects of variation of wall thickness for the 1.50 mm die show the same trends as before.

A reduction of shrinkage was achieved with an increase of profile wall thickness and with reduction of vacuum, see Figure 6.74.

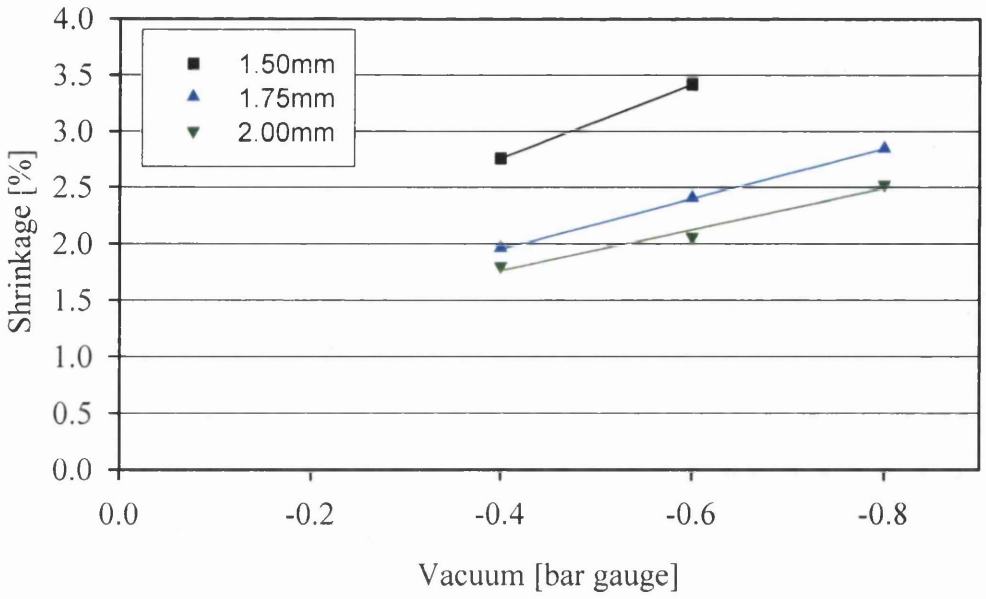

Figure 6.74: Shrinkage for different vacua at different profile wall thicknesses; 4 m/min line speed; 1.50 mm die exit; wet calibration

For a direct comparison of both dies, the wall thickness is replaced by the ratio R_{PD} of profile wall thickness s_P to die exit s_D

$$R_{PD} = \frac{s_P}{s_D} \tag{6.1}$$

and the results are presented in Figure 6.75.

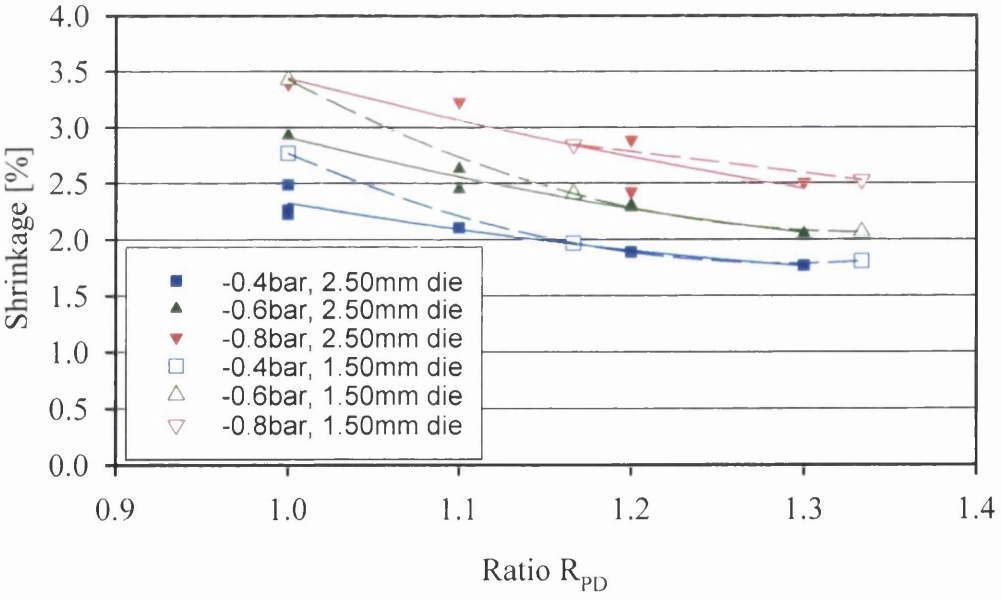

Figure 6.75: Shrinkage as function of ratio R_{PD} for different vacua; 4 m/min line speed; 1.50 mm and 2.50 mm die exit; wet calibration

The shrinkage shows a decrease with increasing thickness ration for each vacuum. Above a ratio of 1.15 the lines are identical for both dies, and below this value, the shrinkage is higher for the 1.50 mm die. This may be based on the higher shear rate of the 1.50 mm die, as mentioned also by Rabinovitch, who measured higher values at a higher shear rates. For both dies the strain recovery seems to be more important than the influence of the increasing shear rate with increasing wall thickness (increased mass flow rate of the extruder).

6.3.4 Effects of vacuum in Calibrator 1 and wall thickness in wet calibration

We have seen that the vacuum has a big influence on the shrinkage, and we have also seen a good correlation with forces in Calibrator 1 for wet calibration. In the next set of experiments, the vacuum was varied only in Calibrator 1 in wet calibration from –0.2 bar up to –0.8 bar with constant vacuum of –0.4 bar in downstream calibrators and 4 m/min line speed. The wall thickness was varied as before and the results are shown in Figure 6.76.

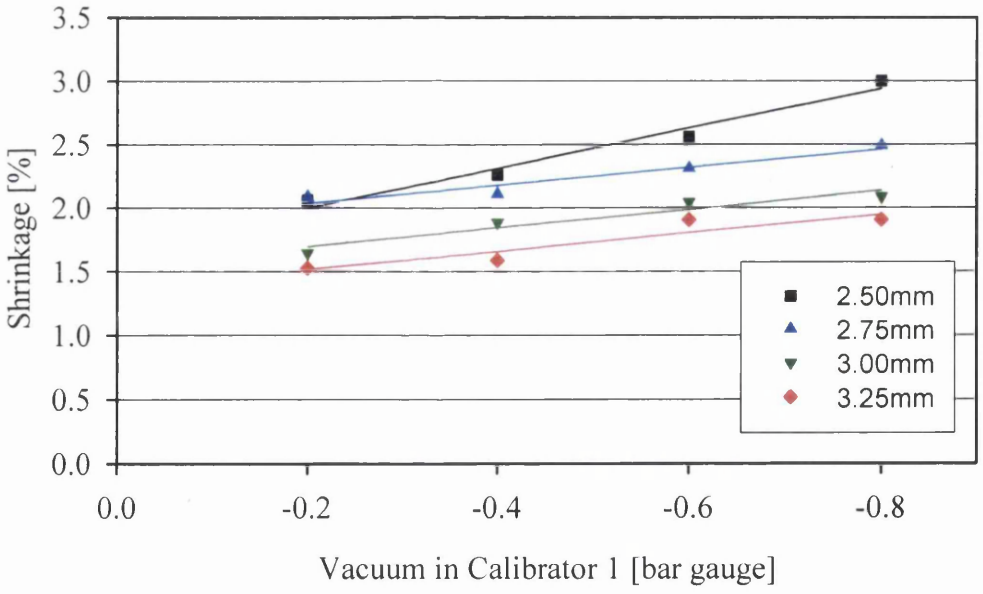

Figure 6.76: Shrinkage for different vacua in Calibrator 1 at different profile wall thicknesses; 4 m/min line speed; 2.50 mm die exit; -0.4 bar vacuum in calibrators 2, 3 and 4; wet calibration

As expected, a reduction of vacuum and increase of wall thickness reduces the shrinkage. The reduction of vacuum in Calibrator 1 decreases the shrinkage from 3.0% to 2.1% for a 2.50 mm wall thickness. At the highest wall thickness of 3.25 mm, a reduction of 0.5% was obtained, significantly less than for the thinnest wall where the reduction is ~1%. The

intercept at zero vacuum would give a shrinkage of approximately 1.7% on average. The same result is present when the shrinkage is plotted vs. force in Calibrator 1, Figure 6.77.

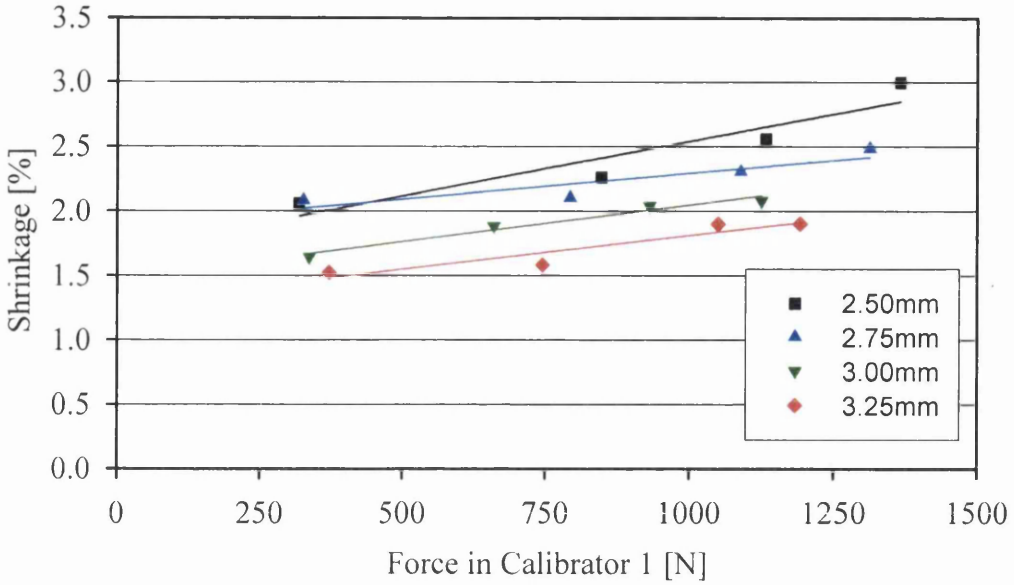

Figure 6.77: Shrinkage as function of force in Calibrator 1 at different profile wall thicknesses; 4 m/min line speed; 2.50 mm die exit; -0.4 bar vacuum in calibrators 2, 3 and 4; wet calibration

It is clear that the shrinkage can be reduced by increasing wall thickness (allowing strain recovery) at any given force in Calibrator 1.

6.3.5 Effects of vacuum in Calibrators 2, 3 and 4 in wet calibration

The last figures have shown the strong correlation of shrinkage with vacuum in Calibrator 1 for wet calibration. In the following set of experiments the vacuum was varied from –0.4 bar to –0.8 bar in the downstream calibrators at constant vacuum in Calibrator 1 for a profile wall thickness of 3.00 mm and a line speed of 4 m/min.

The variation of vacuum in the downstream calibrators shows an influence on the shrinkage. At vacuum of –0.4 bar in Calibrator 1, the effect of downstream vacuum variation is weak, but at higher vacuum in Calibrator 1, the shrinkage shows higher increases for higher downstream vacuum, see Figure 6.78.

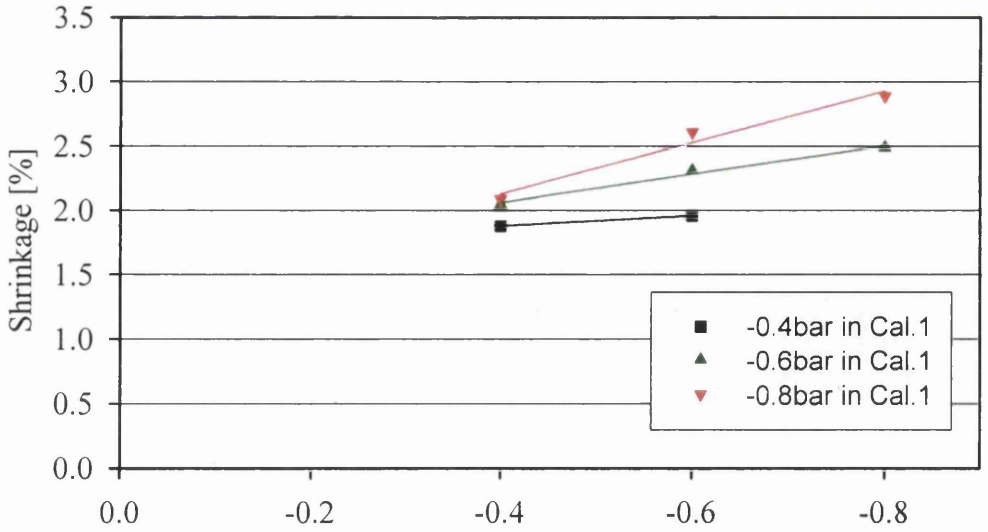

Figure 6.78: Shrinkage for different vacuum in calibrator 2,3 and 4 at different vacuum in Calibrator 1; 4 m/min line speed; 3.00 mm profile wall thickness; 2.50 mm die exit; wet calibration

According to the force measurements shown in a previous section, the forces in Calibrator 1 have increased slightly with increased downstream vacuum for this set of experiments. The shrinkage has increased by 1% at –0.8 bar (100% in total), but the force in Calibrator 1 has increased only by 10%, Figure 6.79.

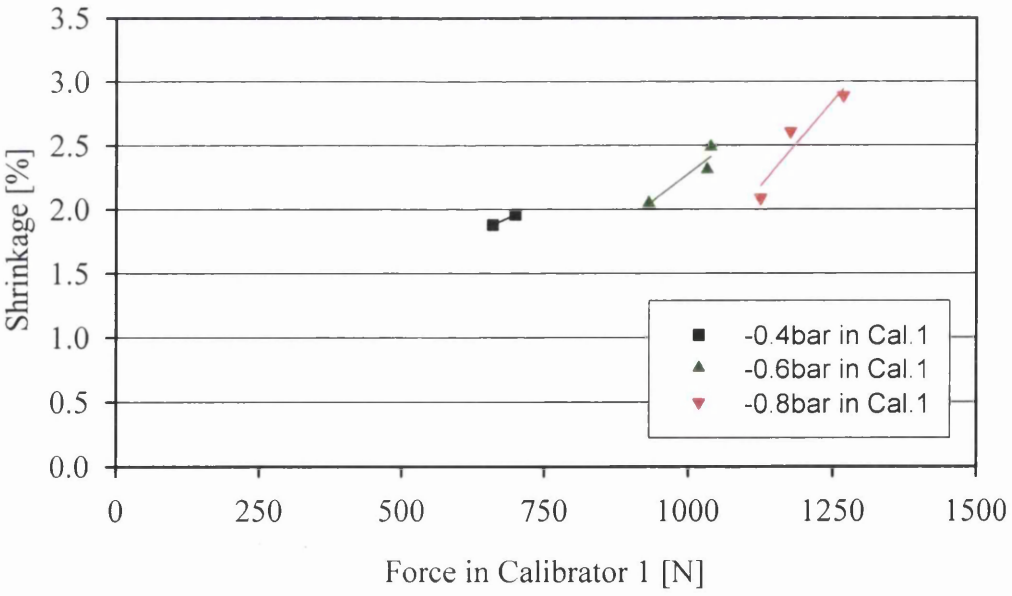

Figure 6.79: Shrinkage as function of force in Calibrator 1 for different vacua in Calibrator 1; various vacua in downstream calibrators; 4 m/min line speed; 3.00 mm profile wall thickness; 2.50 mm die exit; wet calibration

The influence of variation of vacuum in the downstream calibrators is more noticeable at higher Calibrator 1 vacuum. This was also shown in the foregoing Figure 6.78, and can again be seen in a plot versus haul-off force in Figure 6.80.

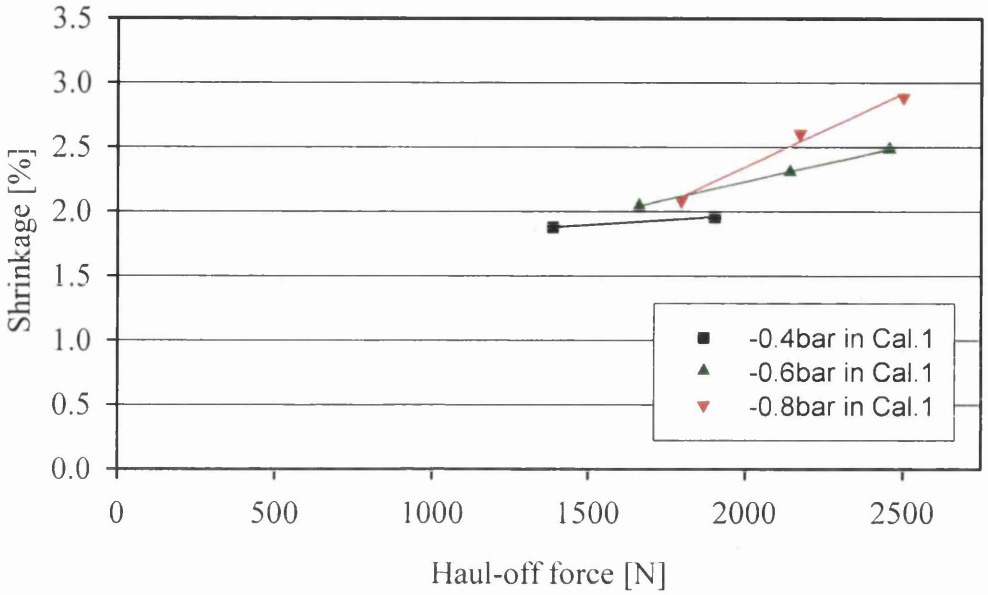

Figure 6.80: Shrinkage as function of Haul-off force for different vacua in Calibrator 1; various vacua in downstream calibrators; 4 m/min line speed; 3.00 mm profile wall thickness; 2.50 mm die exit; wet calibration

The effect of vacuum in the downstream calibrators is also important, especially at higher line speeds, where a thinner solidified layer has to carry the forces.

6.3.6 Effects of melt extrusion and coolant temperatures in wet calibration

As indicated in the foregoing sections, the melt temperature and the coolant temperature in Calibrator 1 were varied, and now the effect on shrinkage is shown.

An increase of melt temperature decreases the shrinkage and this is shown in Figure 6.81. Berger and Rabinovitch confirmed this, and Rabinovitch has explained this behaviour in terms of a lower elasticity at higher temperatures. In addition to this suggestion, the decrease may be accelerated by a more rapid recovery of molecular chain extension at higher temperatures.

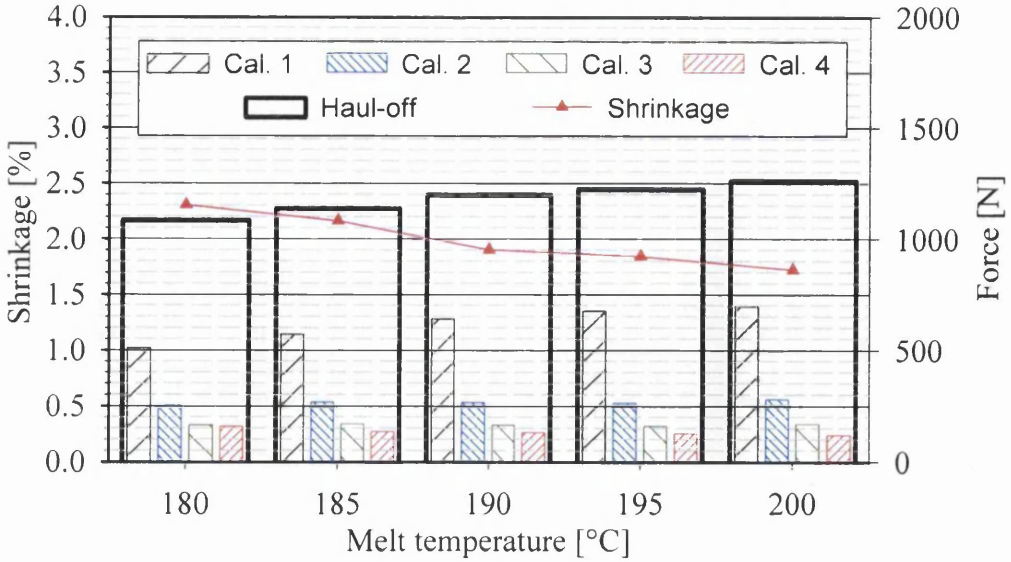

Figure 6.81: Shrinkage for different extrusion melt temperatures; constant vacuum of –0.4 bar; 2.75 mm profile wall thickness; 4 m/min line speed; 2.50 mm die exit, wet calibration

The increase of coolant temperature also has an effect on the shrinkage, Figure 6.82.

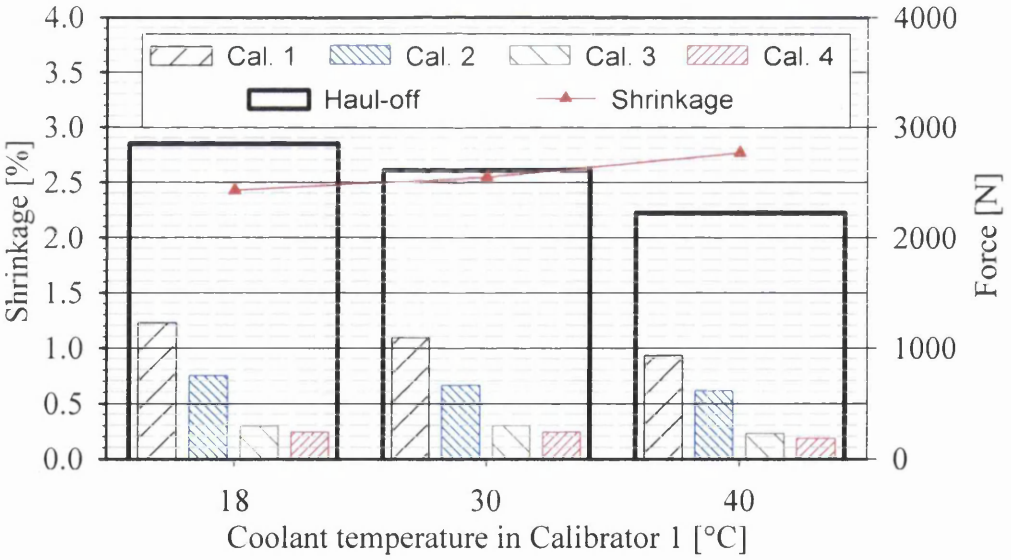

Figure 6.82: Shrinkage for different coolant temperatures in Calibrator 1; constant vacuum of –0.4 bar; 3.00 mm profile wall thickness; 4 m/min line speed; 2.50 mm die exit, wet calibration

At higher coolant temperatures, the solidified layer of the profile is thinner due to reduced cooling rate, and so the profile, in particular the solidified layer, can be stretched more easily in the line direction producing higher shrinkage. This may also lead to a loss of contact of the

profile with calibrator walls due to a reduction of the cross section, and in turn lead to reduced forces, as shown in Figure 6.82. However, the reduction in the solidified layer thickness seems to be more significant than reduction in the forces, because the overall effect is an increase in shrinkage with increased coolant temperatures.

6.3.7 Time dependence of shrinkage

An additional set of experiments was carried out to investigate the time dependent behaviour of shrinkage. For comparison, a second set of samples was stored for 10 months (300 days) and the shrinkage was measured with the standard procedure. The results are shown in Figure 6.83.

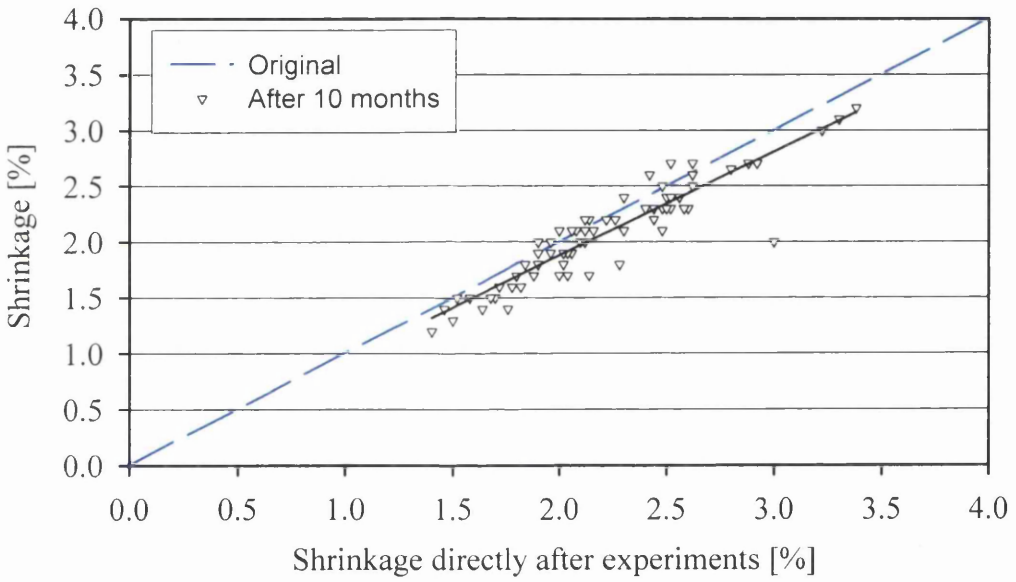

Figure 6.83: Reduction of shrinkage with time

The reduction found in the recent experiments is on average 10%, far less than the reduction of 31% found by Semmler, though the storage time was 10 times higher than for his measurements. The higher reduction found by Semmler could be due to higher temperatures. Semmler has given an environmental temperature of 30°C on average, whereas the recent samples were stored at 20°C.

6.3.8 Correlation of profile dimensions and shrinkage

The correlations of the profile dimensions and shrinkage with the process parameter were shown separately in foregoing sections.

Since the parameters in the calibration process that are reflected in changes in profile geometry appear to be key factors influencing shrinkage, the shrinkage is now examined as a function of profile dimensions, D and C.

In Figure 6.84 the relationship between shrinkage and the diameter D is shown for different line speeds, vacua and wall thicknesses in wet calibration with trend lines for each vacuum at each line speed.

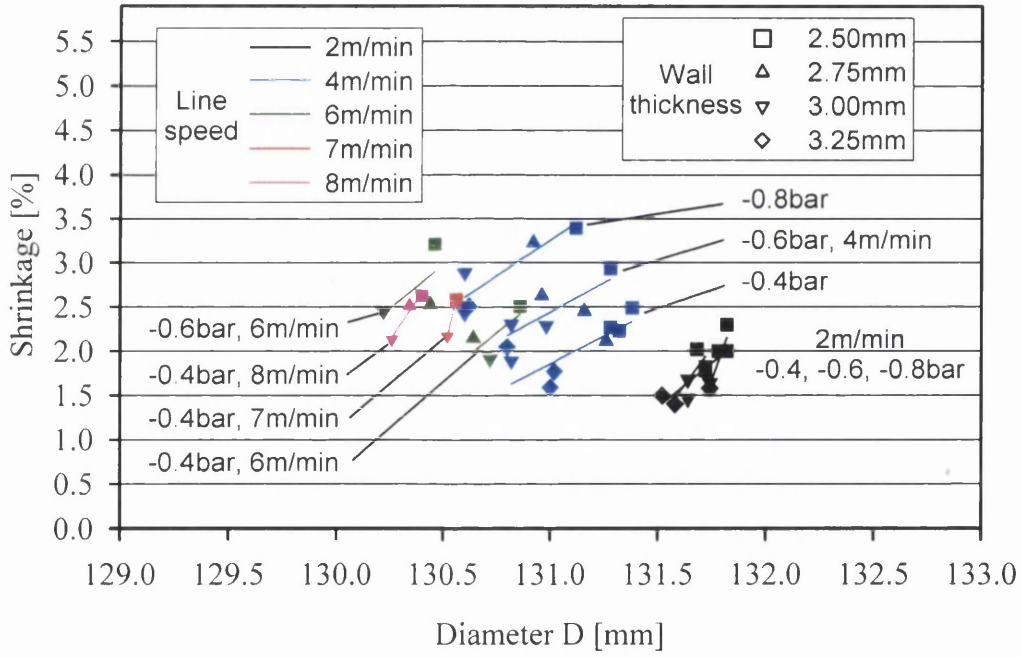

Figure 6.84: Diameter D as function of shrinkage at different line speeds, profile wall thicknesses and vacua in wet calibration; 2.50 mm die exit

As shown before, the thicker walls decrease the shrinkage due to strain recovery after leaving the die exit. The diameter D is reduced for thicker walls due to the cramming effect at the inlet of Calibrator 1, as previously shown in Figures 6.40 to 6.43. A clear distinction between the effects of vacuum cannot be made for the line sped of 2 m/min, whereas at higher line speeds, separate trend lines are visible for the different vacuum levels. This is because at higher line speeds, the solidified layer is thinner and so the profile is more sensitive to applied vacuum (and haul-off forces), and this leads to a slight reduction of D. The stretching of the

thinner solidified layer gives higher shrinkage, especially at the outer layer of the profile wall, as was measured by Semmler, and as mentioned in the introduction to this section. However, as noted previously, D is not a sensitive measure of draw down, a principal determinant of shrinkage, and a clearer correlation is to be expected with C and this will be shown in Figure 6.85, for the same process parameters.

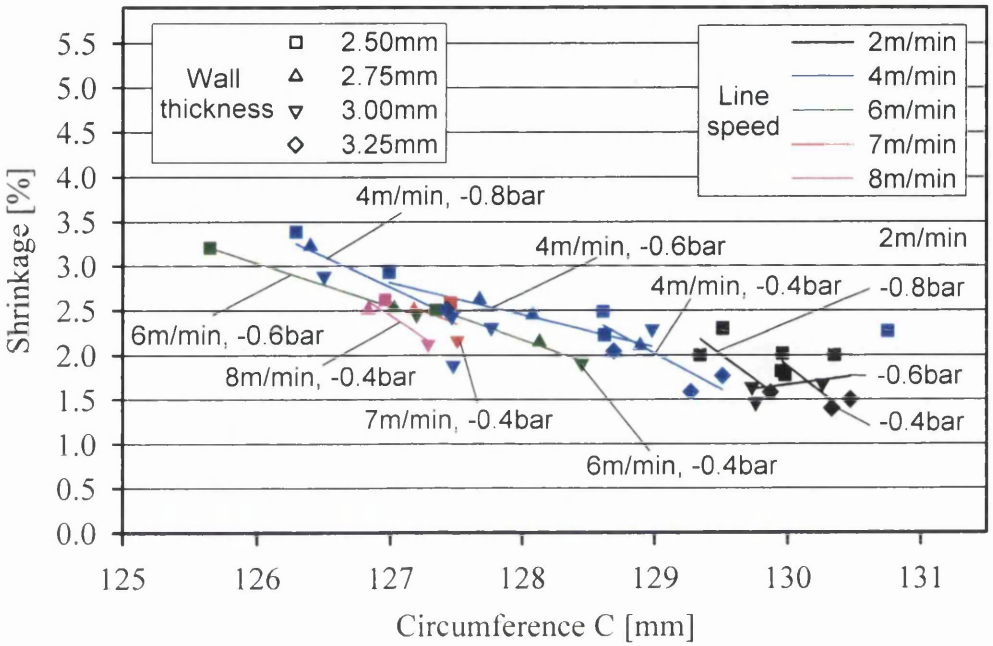

Figure 6.85: Shrinkage as function of C for different line speeds, profile wall thicknesses and vacua in wet calibration; 2.50 mm die exit

Shrinkage values increase as C reduces. At 2 m/min the change with vacua is small, but visible, whereas the differences at higher line speeds are more developed. A clear correlation is visible between shrinkage and C, and this confirms the importance of draw down – reflected in C values – on shrinkage for this profile.

The influence of wall thickness is present in Figure 6.85, but to clarify this, the same data are now shown in Figure 6.86, but with the wall thicknesses as the primary parameter, and with trend lines for each wall thickness.

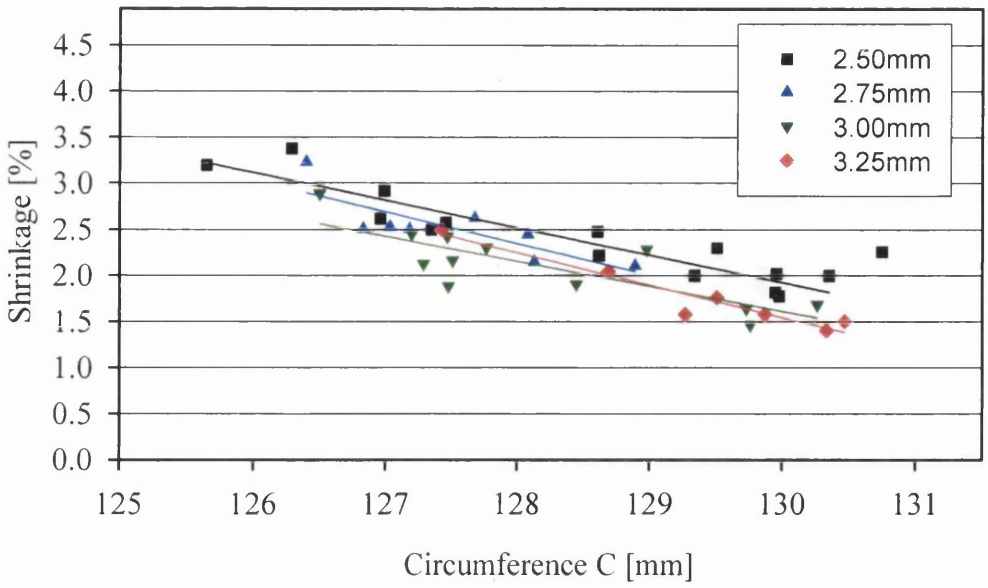

Figure 6.86: Shrinkage as function of C for different profile wall thicknesses in wet calibration; 2.50 mm die exit

Increased wall thickness generally reduces the shrinkage at a given value of C, though there is a certain amount of overlap between the data.

In the final set of experiments, the melt extrusion and coolant temperatures were varied and the correlations of the dimensions and shrinkage are shown in the next Figures.

The variation of melt temperature has little significant influence on D, but the shrinkage decreases with higher melt temperatures, see Figure 6.87. The higher melt temperature accelerates the molecular recovery process and this leads to a lower shrinkage.

In contrast to D, the circumference C decreases at higher melt temperatures due to a thinner solidified layer resulting from higher profile wall temperatures and a correlation between decreased shrinkage and decreasing C due to higher melt temperatures is clearly visible in Figure 6.87.

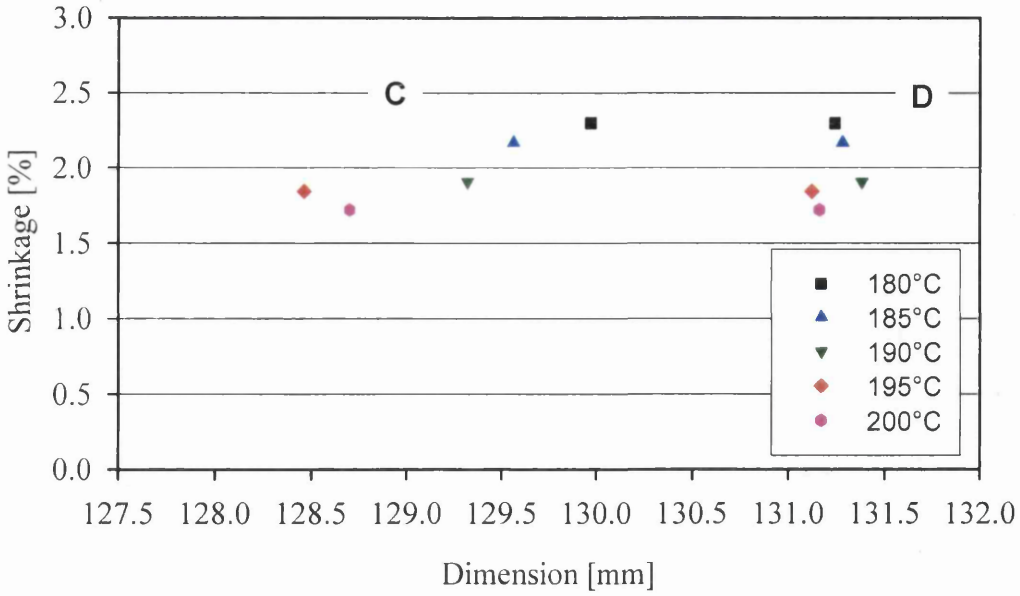

Figure 6.87: Shrinkage as a function of dimensions D and C for different melt extrusion temperatures; -0.4 bar vacuum; 2.75 mm profile wall thickness; 4 m/min line speed; 2.50 mm die exit; wet calibration

Finally, increase of the coolant temperature in Calibrator 1 produces a very slight increase of D as noted previously (Figure 5.63), whereas the effect on C (a decrease) is more pronounced.

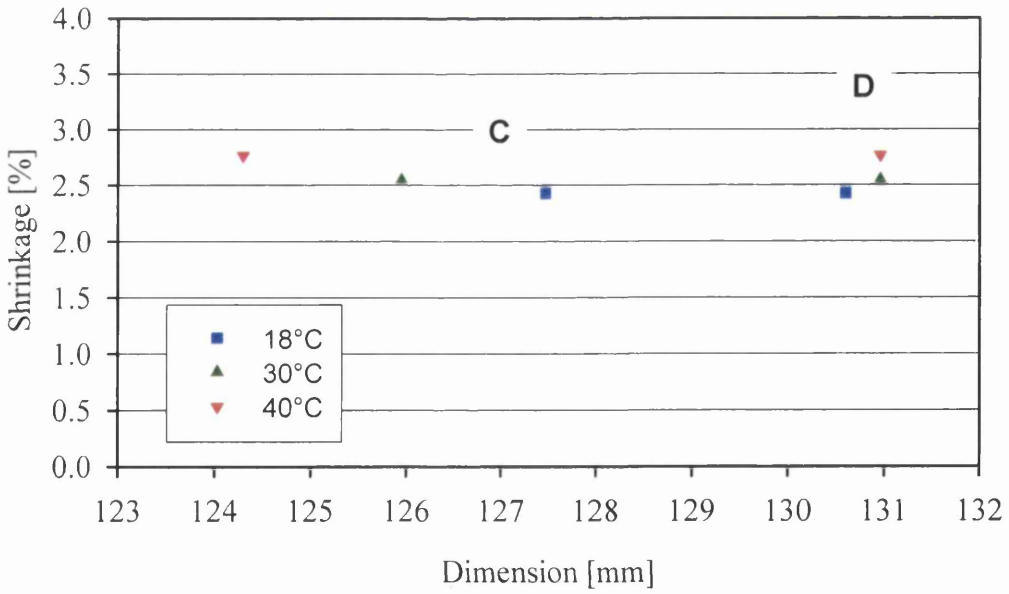

Figure 6.88: Shrinkage as a function of dimensions D and C for different coolant temperatures in Calibrator 1, -0.4 bar vacuum; 3.00 mm profile wall thickness; 4 m/min line speed; 2.50 mm die exit; wet calibration

The measured stretching associated with the reduction in C correlates well with measured shrinkage, see Figure 6.88. The most relevant factor here is reduction of the solidified layer thickness, since forces are reduced at higher coolant temperatures (Figure 6.29).

Summary

The results for shrinkage of the rectangular profile were obtained with the standard measurement according to DIN EN 479, where the profile is annealed for 1 hour at 100°C.

The measured values of shrinkage for a profile after manufacturing result in a complex way from superimposed effects during the calibration process. We can hypothesize two physical mechanisms that may be involved in causing shrinkage: reduction of free volume and reduction of polymer chain extension occurring slowly with aging, or more rapidly during the standard shrinkage test.

It is well known that the cooling rate has an influence on the specific volume of the PVC raw material and a higher cooling rate leads to a higher specific volume in the material below glass transition temperature, T_g. This cooling rate effect is most significant close to the outer surface of the profile wall, whereas the influence gets smaller toward the inner surface. To get an idea of the cooling rates at the outer profile surface, the cooling rate was calculated for a profile wall thickness of 3.25 mm with a constant heat transfer coefficient of 1000 $W/m^2 K$ on the outer profile surface, and the adiabatic condition at the inner side, with coolant temperature 18°C and melt temperature of 195°C.
For this, the finite difference simulation of cooling described in Chapter 7 was used. The results are presented in a 2D contour plots. In Figure 6.89a is shown the cooling rate as a function of time and position in the cooled profile for all temperatures and in Figure 6.89b, the cooling rates only for temperatures below the T_g of 80°C.

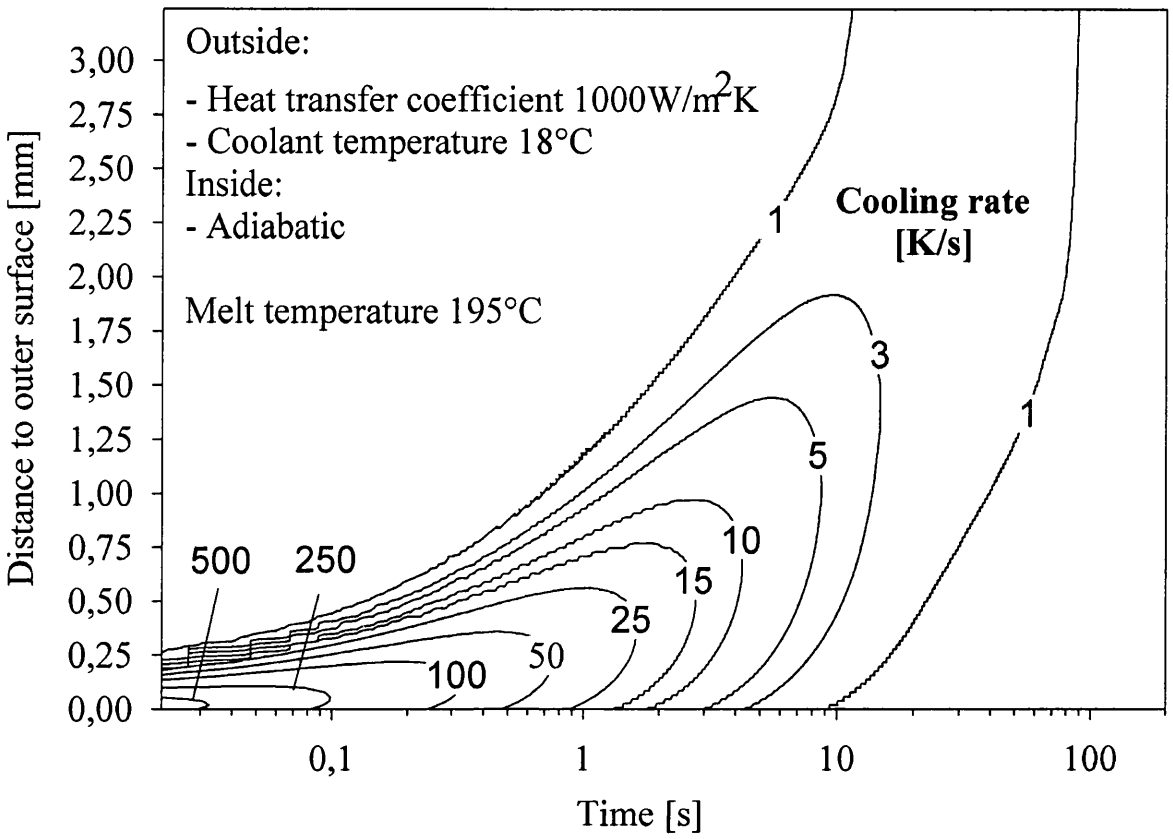

Figure 6.89a: Cooling rates in [K/s] for a 3.25 mm wall thickness profile with constant heat transfer coefficient of 1000 W/m^2 K for all temperatures; coolant temperature 18°C; melt temperature 195°C

The cooling rate is, of course, highest in initial moments immediately downstream of the beginning of cooling, at the inlet of Calibrator 1. The highest calculated cooling rate of 1835 K/s is not shown in Figure 6.89a.

The influence of cooling rate on specific volume becomes important at temperatures below T_g and these data are plotted for temperatures below 80°C in Figure 6.89b.

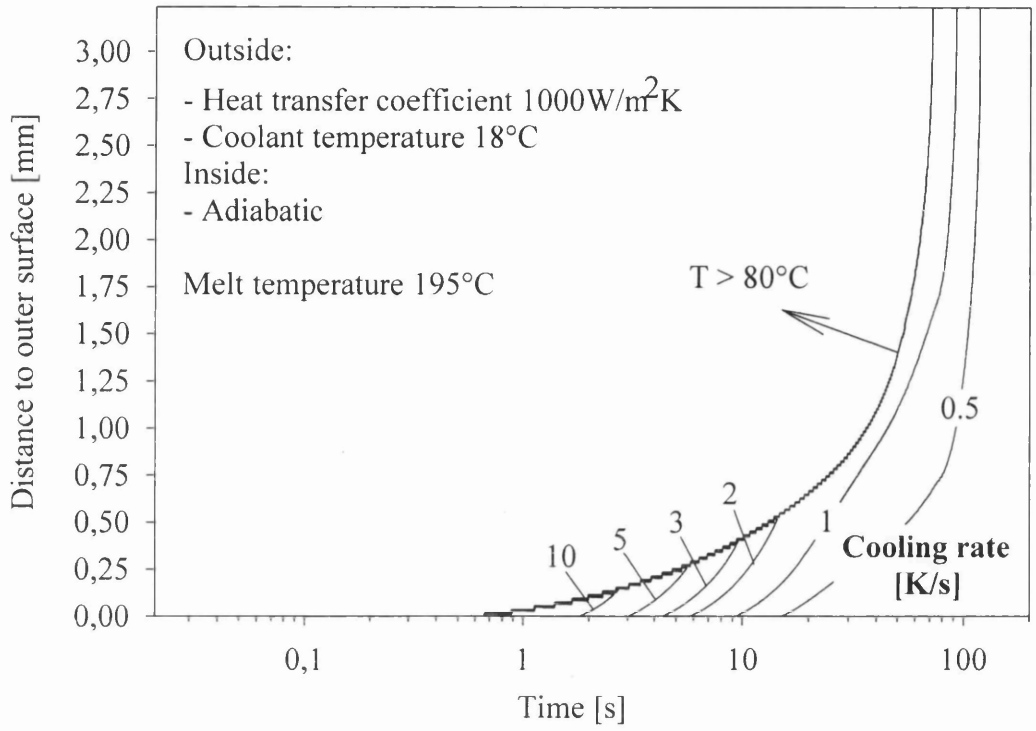

Figure 6.89b: Cooling rates in [K/s] for a 3.25 mm profile wall thickness with constant heat transfer coefficient of 1000 W/m^2 K for temperatures below T_g of 80°C; coolant temperature 18°C; melt temperature 195°C

The key problem, in general, is to measure the specific volume at higher cooling rates. Data are presented in [65] and they show an increase in specific volume with increase of cooling rates from 0.05 K/s to 4.0 K/s, Figure 6.90.

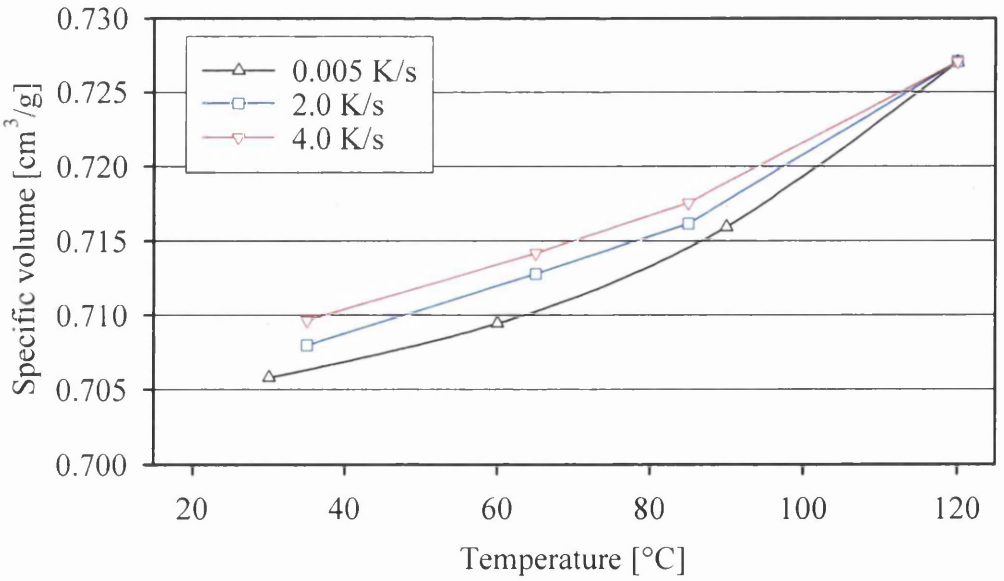

Figure 6.90: Specific volume of PVC (PIR930, Solvay) at different cooling rates [65]

The higher specific volume resulting from rapid cooling relaxes slowly with time, and so a higher shrinkage will be expected towards the outer surface in the profile calibration process. During the cooling stage in the shrinkage test, the material will cool down much more slowly and so the specific volume will fall to a lower value, resulting in apparent shrinkage.
Altogether, with higher cooling rates at the outer profile surface, higher shrinkage values will be present towards the outer profile surface. Semmler [153] confirmed this and measured a higher shrinkage at the outer side of the profile, whilst at the inner side, the shrinkage is lower, Figure 6.91.

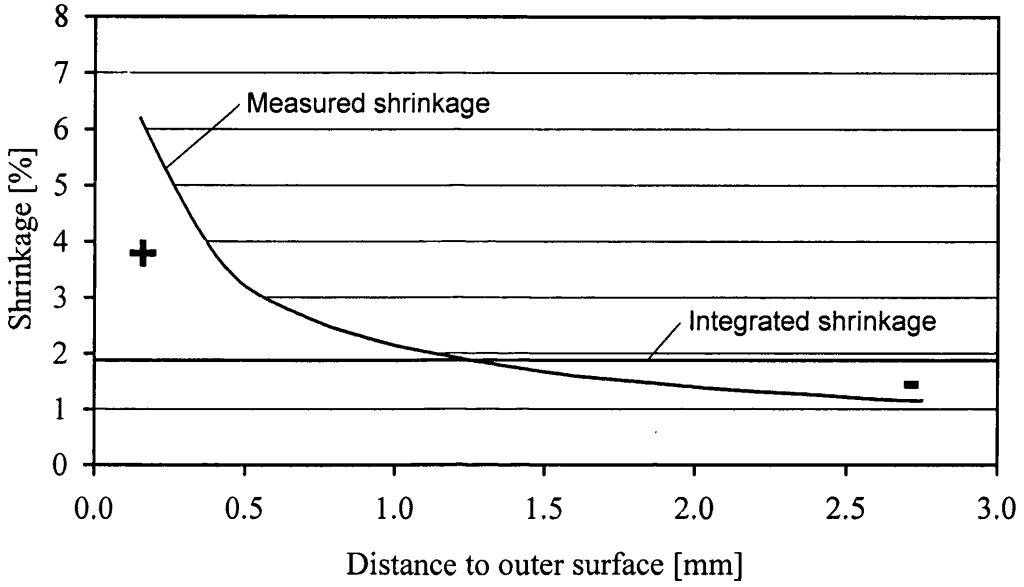

Figure 6.91: Shrinkage as function of distance to outer profile surface; melt temperature 192°C, line speed 2.5 m/min, haul-off force 7kN [153]

But, as mentioned before, the specific volume is not only the reason for the shrinkage; otherwise the shrinkage would be e.g. the same for wet or dry calibration under same cooling conditions at different vacua, which was disproved before.

In these experiments, the calibration process was investigated for dry and wet calibration and in dry calibration the shrinkage had higher values at higher applied vacuum level. This is mainly based on the forces, because the forces are higher in dry calibration, as shown in the section about forces. The forces in Calibrator 1 are nearly same for dry and wet calibration, but in the downstream calibrators, the forces are higher in dry calibration. This is a consequence of higher friction coefficient between profile and calibrator surface and slower cooling in dry calibration. The recent experiments have shown a decrease from 3.6% to 3.0% for a reduction of applied vacuum from –0.8 bar to –0.4 bar in wet calibration for a 2.50 mm

profile wall thickness at 3m/min line speed. Under the same conditions, the shrinkage was reduced in dry calibration from 5.5% to 4%. In total, the values are higher in dry than in wet calibration and the higher shrinkage must be based on the higher downstream forces, and thinner solidified layer.

In another set of experiments, the applied vacuum was varied only in Calibrator 1, to examine the importance of the vacuum in the first stage of the calibration process. A significant reduction of 2% was achieved with reduction of vacuum from –0.8 bar to –0.2 bar in Calibrator 1 at constant vacuum of –0.4 bar in downstream calibrators.

Furthermore, an increase of profile wall thickness at the same height of die exit allows a strain recovery after the die exit and this reduces the shrinkage. The experiments have shown a reduction in shrinkage of up to 0.8% with increase of wall thickness from 2.50 to 3.25 mm at 2.50 mm die exit at applied vacuum of –0.8 bar.

An increase of coolant temperature in Calibrator 1 increases the shrinkage, opposite to the effect of melt temperature, where an increase leads to a reduction of shrinkage.

Extrapolation to zero vacuum, or zero forces, has shown a residual value of shrinkage. This is based on the frozen-in strains due to shear of the melt in the die. Experiments without calibration units have shown a value of 0.7%, which is half of the extrapolated values of the experiments. This difference may be based on the experimental method. The section of a profile was cut off at the die exit, and kept in a reasonable shape for the shrinkage measurements during cooling in a water bath. The time between cut off and beginning of cooling could have allowed more strain recovery as compared to the calibration process, where the profile comes into contact with the calibrator after a distance of only 5 mm, e.g. in 0.3 s for a line speed of 1 m/min.

Altogether the shrinkage is a complex process, an idea of several basic mechanisms and their effects can be given as follows.

As seen before, a residual shrinkage was obtained for e.g. zero line speed or forces. This leads to the conclusion that this remaining value must due to the shear, resulting in molecular orientation, in the die. The molten PVC comes from the extruder and is distributed in the die to get the required profile shape. Due to the acceleration of the melt, coming from the main distribution channel, towards the end of the die, as well as shear in the land regions, the molecular chains are stretched, as shown in Figures 6.92a and b. In practice, the die land will

be made as long as possible to allow a recovery of stretching occurring in the accelerating flow upstream. However, stretching due to the shear flow continues.

Another factor for the reduction of shrinkage after the die is the swelling of the profile after the die exit. This swelling is visible in the absence of a calibrator, when the profile has time to recover. In the calibration process, this swelling behaviour is not visible, and is not present as a major influence on the measured shrinkage, because the molten profile goes directly into the inlet of Calibrator 1.

A strain recovery between die exit and entrance of Calibrator 1 can be achieved with an increase of the profile wall thickness at constant line speed, by increasing the mass flow rate of the extruder. The strain recovery leads to a recovery of the stretched molecular chains, see Figure 6.92b and c, and although increased mass flow rate through the die will produce more chain extension, this is apparently more than compensated by the strain recovery that then occurs.

In downstream direction after the inlet of Calibrator 1, the chain extension and orientation can be influenced by the process parameter in the line. In Figure 6.92d is shown a view with a cooled layer below T_g and a molten layer.

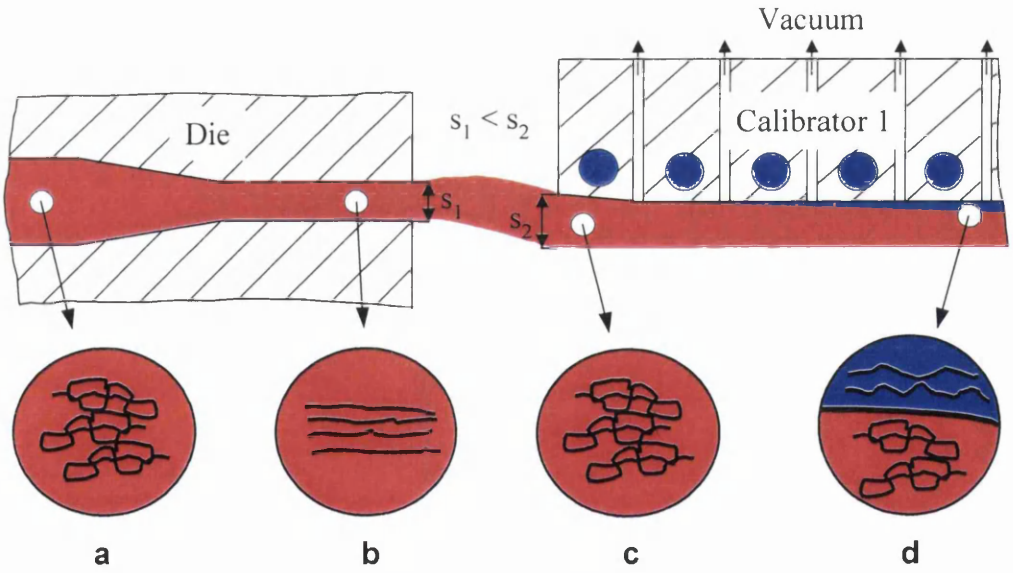

Figure 6.92: Molecular orientation in the die and Calibrator 1

Both layers are stretched due to forces. In the layer below T_g the induced molecular orientation cannot relax, in contrast to the molten layer. The ratio of the layer thicknesses can influence this behaviour, as also to the temperatures.

In the recent experiments, several parameters were varied and have shown their influence on shrinkage, that is on molecular orientation, or chain extension.

Higher vacuum increases the forces and so the solidified layer is stretched more than at lower vacuum. The same effect can be achieved with a higher line speed or higher coolant temperatures, resulting in a thinner solidified layer that will be stretched more.

Strain recovery, reducing orientation of the molecular chains, is present with an increase of wall thickness, between die and inlet of Calibrator 1, and on the line, with higher temperatures of the melt. But the higher melt temperature can also reduce the solidified layer. It is clear that the factors governing the shrinkage are quite complex, and all the foregoing effects, based on the results obtained in the experiments, are now summarised in Figure 6.93 in terms of their influences on shrinkage.

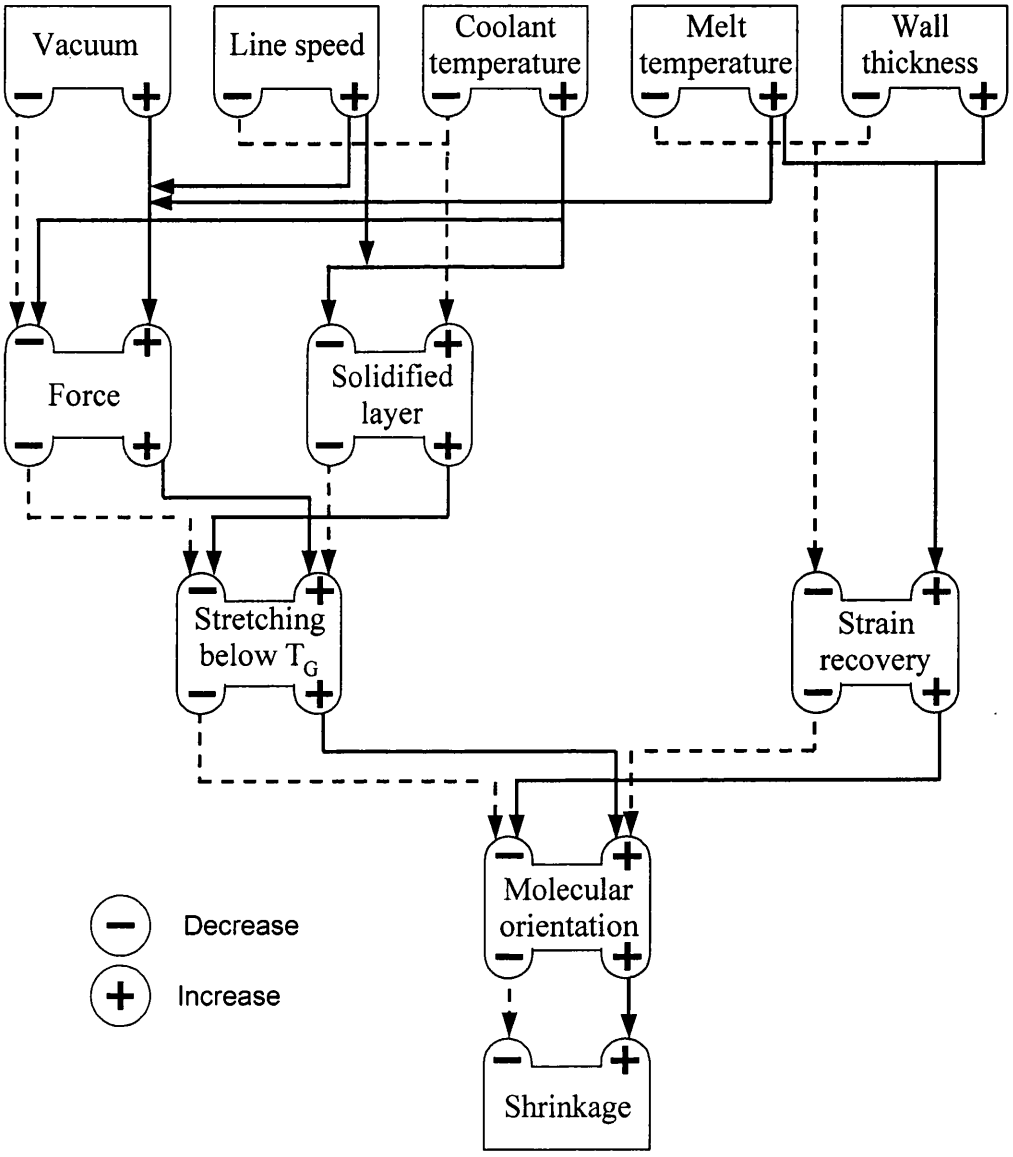

Figure 6.93: Effect of line parameters on shrinkage

In the last Figure 6.93 the influence of the cooling rate on shrinkage was not included, because, as discussed earlier, free volume effects are thought not to play a major part in shrinkage. Also the effects of shear and extension within the die are not included, to avoid excessive complexity in the diagram.

However, the last Figure has given an overview of the complexity of the origins of shrinkage.

6.4 Impact strength

6.4.1 Introduction

The impact strength is an important property of the produced profiles. As presented in the Chapter about the PVC properties, the value can be modified with additives, the so-called impact modifiers. In this section, the impact strength is now investigated as a function of the same processing parameters as used in foregoing sections.

Many investigations have shown in the past the dependence of impact strength on melt extrusion temperature. As a general trend, the impact strength values increase slightly from a low level at melt temperatures of around 150°C to 180°C or 185°C, increase suddenly towards a maximum value at 190°C, and then decrease towards higher temperatures. Several investigators found this behaviour for material from single screw extruders [14,50] and twin-screw extruders [28,30,46,51]. The maximum is not fixed at a certain temperature, and differences may be based on different residence times, which are also relevant for the morphology of PVC. The impact value can be varied with variations of temperature and time, as was found in experiments with a roll mill [17]. The different characteristics of extruders thus can lead to different value of impact strength, e.g. a twin-screw extruder gives higher impact strength values for the same material than a single screw extruder at the same melt extrusion temperature [50]. Another effect on impact could be the surface conditions of the profile, especially at higher throughputs of the extruder. A higher throughput causes melt fracture, as well known. Low, and more scattered, impact strength values were measured for higher throughput in the temperature region 180°C to 210°C [44]. The explanation for this might be the roughness of the profile surface, which had shown melt fracture. With a smoothed surface (press polishing at melt temperature) the impact strength values for any throughputs were close together.

Altogether, a correlation of impact strength and processing conditions is difficult to achieve due to the superimposed effects of morphology.

In the first set of experiments, the temperature varied at constant profile wall thickness as a result of screw speed changes, and, due to awareness of the dependence of impact strength on melt extrusion temperature, no impact strength measurements were done. The second set where melt temperatures were held constant was used for more detailed investigations of impact strength dependence on process parameters, which were varied as presented before. In

this section, the results for the 2.50 mm die, with die exit height of 2.50 mm, are presented first, followed by the results for the 1.50 mm die.

6.4.2 Effects of wall thicknesses and vacuum in wet calibration at different line speeds

The impact strength results are presented now in Figure 6.94 for different wall thicknesses as a function of line speed for an applied vacuum of –0.4 bar.

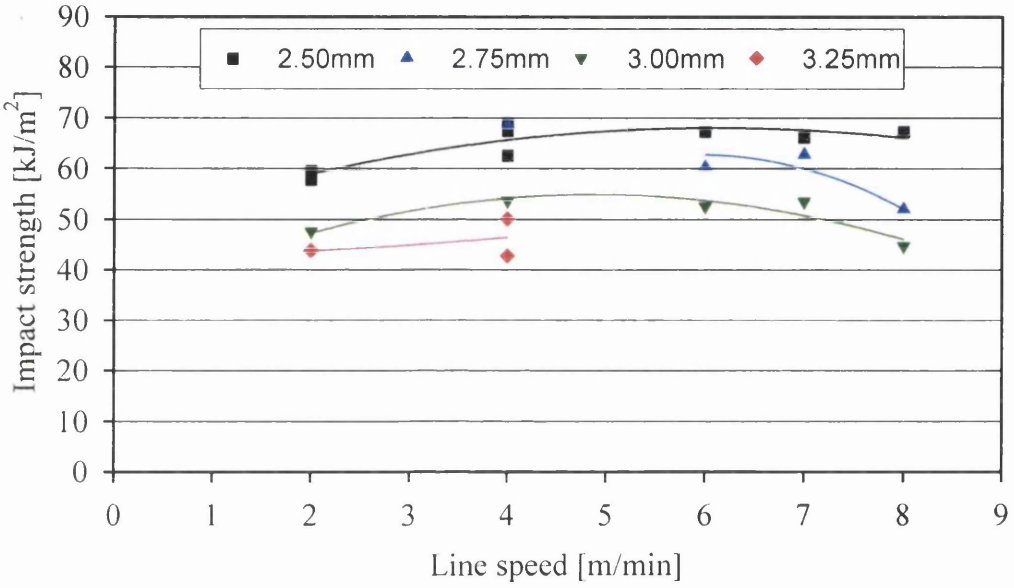

Figure 6.94: Impact strength as a function of line speed for different profile wall thicknesses at -0.4 bar vacuum; 2.50 mm die exit; wet calibration

The impact strength increase slightly up to a line speed of 5 to 6 m/min and then, the values decrease. The same pattern is present at –0.6 bar vacuum, except for one value at 6 m/min for a wall thickness of 2.75 mm, see Figure 6.95.

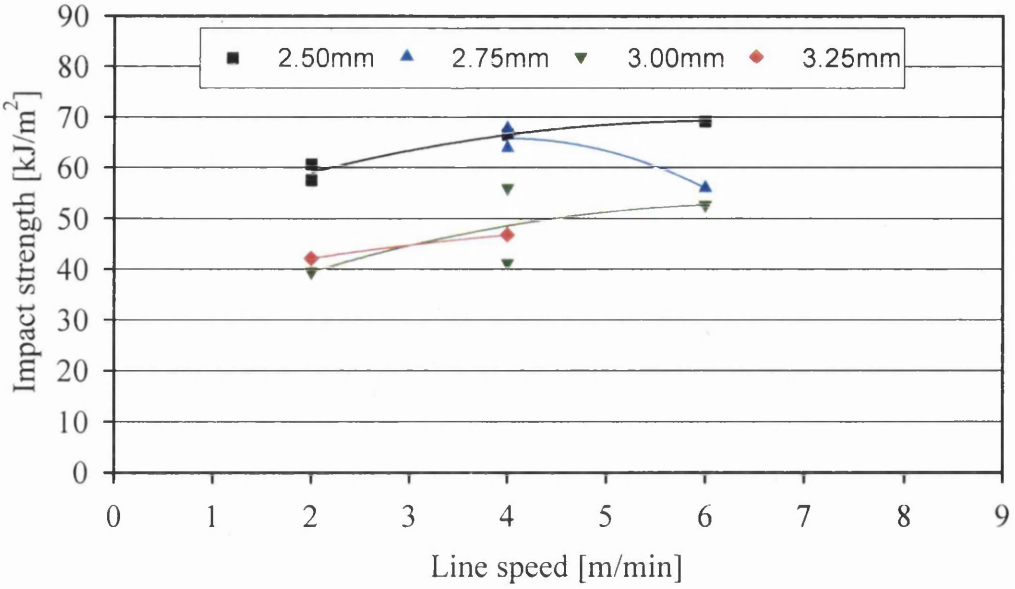

Figure 6.95: Impact strength as function of line speed for different profile wall thicknesses at -0.6 bar vacuum; 2.50 mm die exit; wet calibration

The trend is confirmed in Figure 6.96 for a vacuum of –0.8 bar.

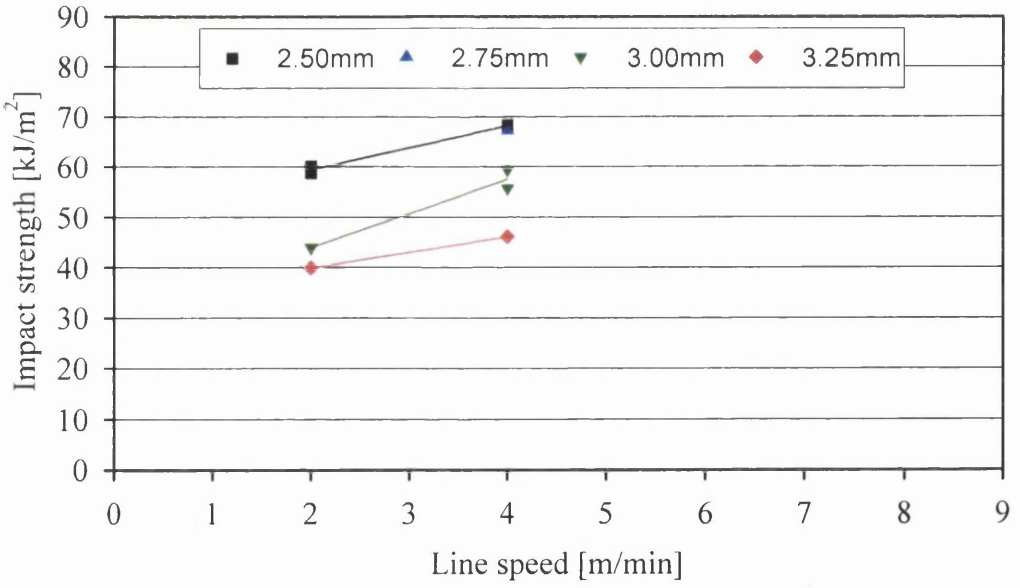

Figure 6.96: Impact strength as function of line speed for different profile wall thicknesses at -0.8 bar vacuum; 2.50 mm die exit; wet calibration

The values for each wall thickness and applied vacuum are in the same range of about 40 to 70 kJ/m^2. It is clear to see, that a higher profile wall thickness gives lower measured impact strength values. In the foregoing Figures 6.94 to 6.96, the impact strength values show a similar pattern to the dependence of shrinkage on line speed for the same parameters in

Figures 6.8 to 6.13. The shrinkage has been shown to correlate with forces. The impact strength may be also related to the forces in the calibration process, which could align the molecular chains in the profile.

An increase of impact strength with increased haul-off forces is visible in Figure 6.97 for each wall thickness and vacuum. In each data set the line speed is an implicit variable.

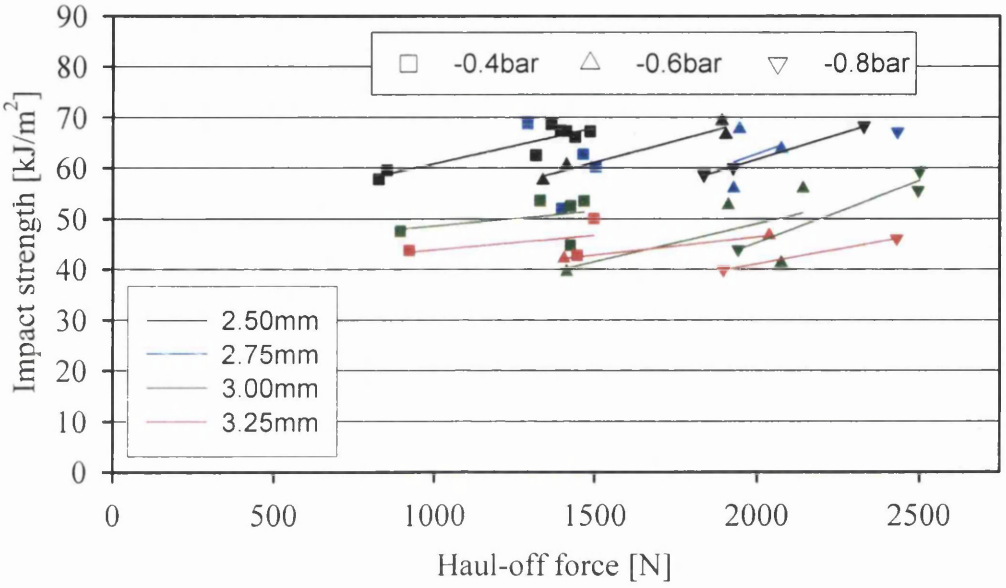

Figure 6.97: Impact strength as function of haul-off forces at different profile wall thicknesses and vacua; all line speeds; 2.50 mm die exit; wet calibration

In wet calibration, the Calibrator 1 forces are a major part of the haul-off force and so an increase of impact strength with Calibrator 1 forces should also be visible, and this is confirmed in Figure 6.98.

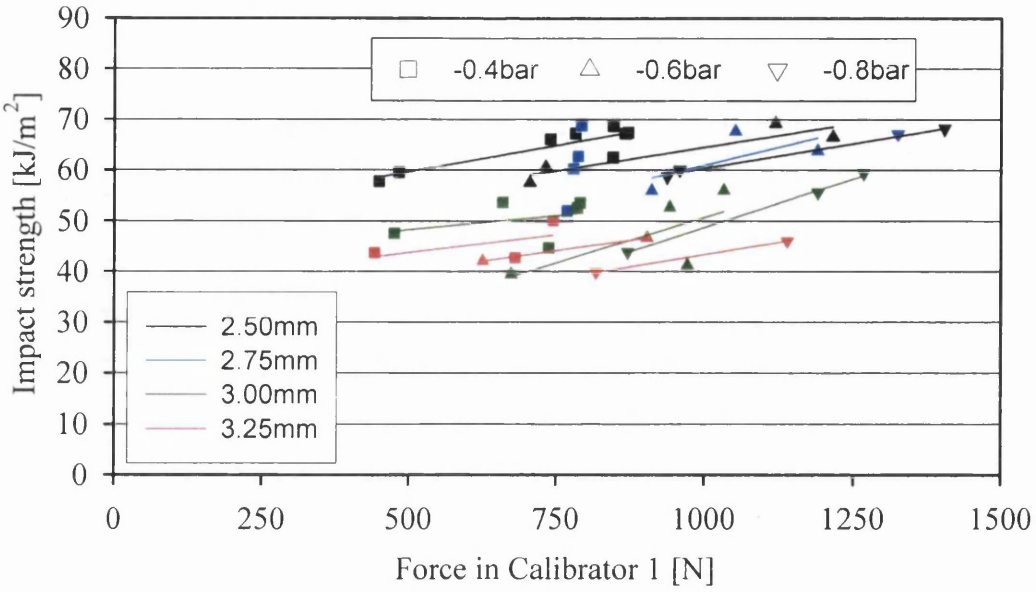

Figure 6.98: Impact strength as function of Calibrator 1 forces at different profile wall thicknesses and vacua; all line speeds; 2.50 mm die exit; wet calibration

The foregoing figures have shown an increase of impact strength with increasing forces for each wall thickness and vacuum, also lower values are obtained for thinner profile walls. In Figure 6.99 is shown a clear dependence (though some scatter is present) of impact strength on the profile wall thickness for all line speeds.

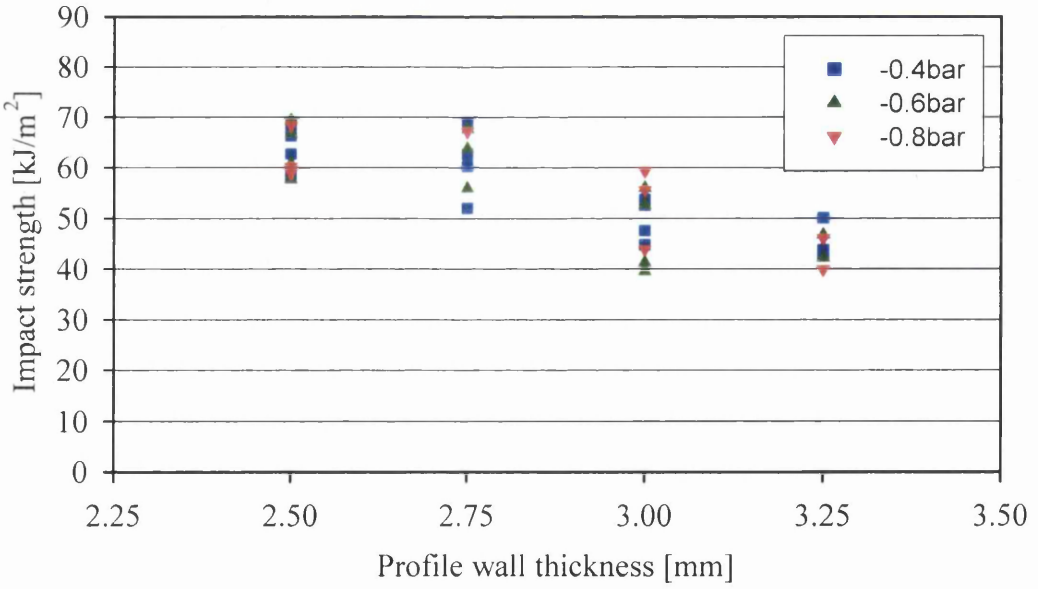

Figure 6.99: Impact strength as function of profile wall thickness at different vacua; all line speeds; 2.50 mm die exit; wet calibration

The line speed in these plots is not directly visible, as mentioned above. To exclude the influence of line speed, the impact strength is now plotted for a constant line speed of 4 m/min, Figure 6.100.

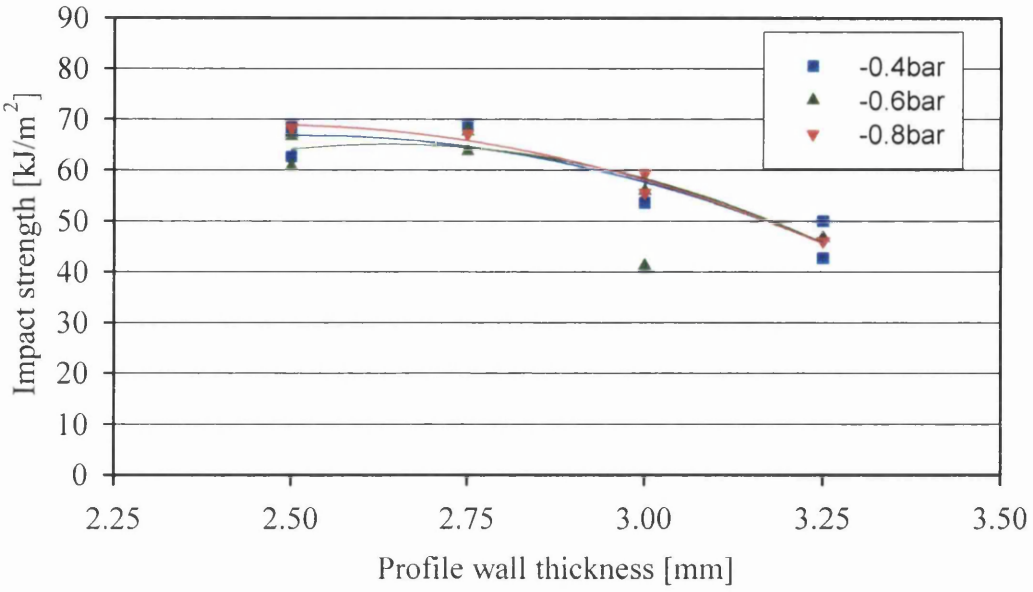

Figure 6.100: Impact strength as function of profile wall thickness at constant line speed of 4 m/min for different vacua; 2.50 mm die exit; wet calibration

At constant line speed, the impact strength increases from 45 kJ/m^2 at 3.25 mm profile wall thickness to 70 kJ/m^2 at 2.50 mm wall thickness for the 2.50 mm die. The increase of 55% is obtained with a reduction of the profile wall thickness of 24%. This increase may be based on a chain alignment in the polymer. Thicker walls with the same die exit have decreased the shrinkage, as shown before, and this was believed to be based on strain recovery between the die exit and entrance to Calibrator 1. This strain recovery may allow a recoiling of the chains, based on the entropy effect. The molecular chain configuration tends to highest state of entropy; stretching reduces the entropy and a recoil increases the entropy.

If this effect is present, results for the 1.50 mm die should show the same trend in Figure 6.101 as already observed for the 2.50 mm die.

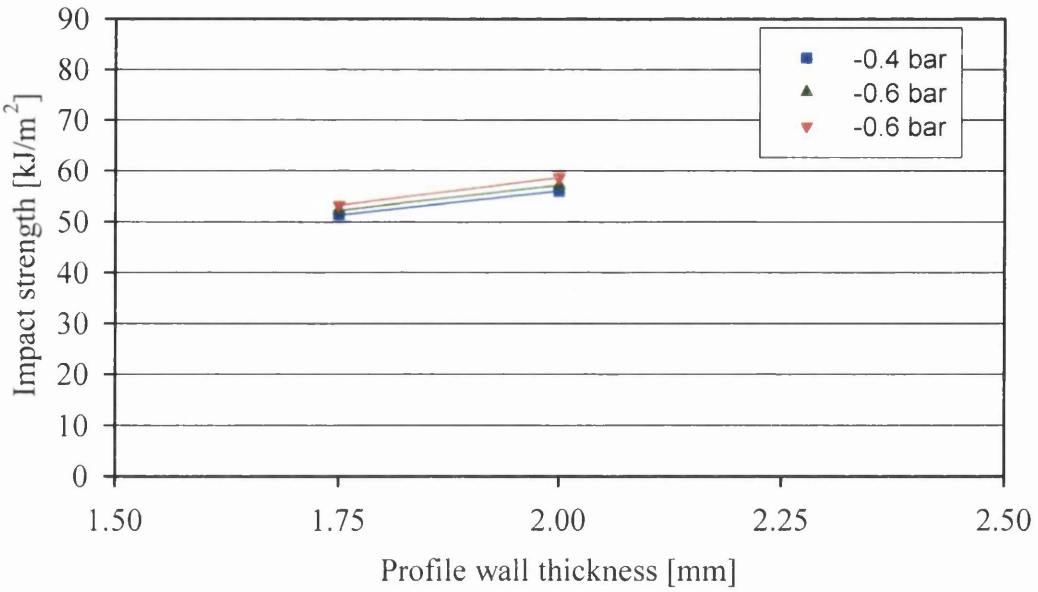

Figure 6.101: Impact strength as function of profile wall thickness at constant line speed of 4 m/min for different vacua; 1.50 mm die exit; wet calibration

However, the impact strength values for the 1.50 mm die at 4 m/min line speed show, that an increase of wall thickness increases the impact strength values, opposite to the trend for the 2.50 mm die. So another effect must be present. A combined plot of impact strength as a function of profile wall thickness for both dies is shown in Figure 6.102.

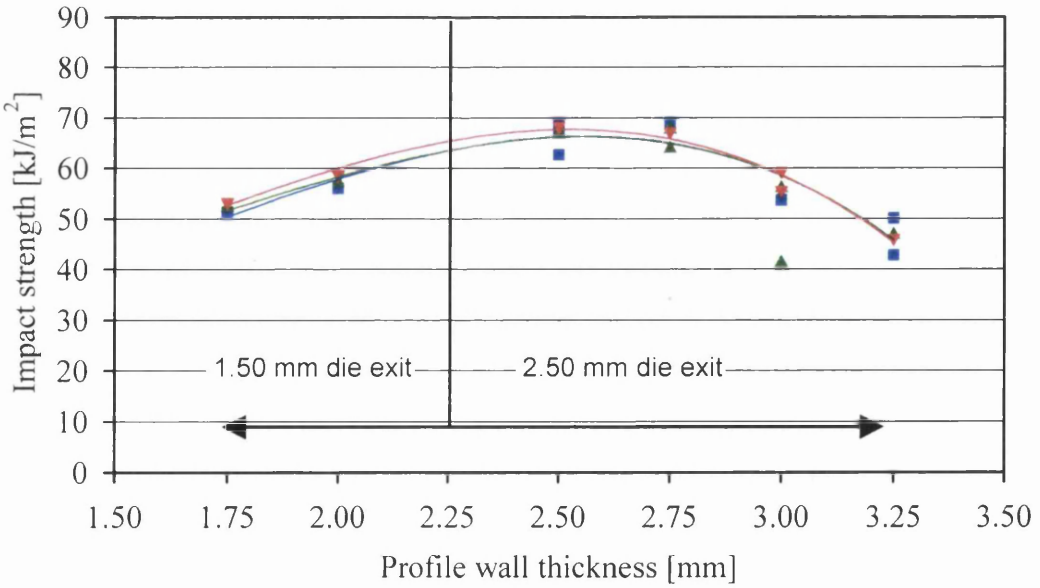

Figure 6.102: Impact strength as function of profile wall thickness for various vacua at constant line speed of 4 m/min; 1.50 mm and 2.50 mm die exit; wet calibration

The impact strength values increase from a wall thickness of 1.75 mm to reach a maximum value at a wall thickness of 2.50 mm and then decrease.

Calvert [27] also found decreasing impact strength values for thicker walls obtained by decreasing the line speed at constant extruder conditions. He reported a decrease of impact value from 13.32 kJ/m^2 at 2.39 mm wall thickness to 9.0 kJ/ m^2 for a wall thickness of 3.13 mm. Tempels [162] confirmed his findings, and measured an increase of impact strength from 16.8 kJ/m2 for a 4.0 mm wall thickness to 47.5 kJ/m2 for a 2.0 mm wall thickness. The explanation for this behaviour could be based on the mechanisms of the fracture mechanics, which are present in the impact strength testing. A good background to fracture mechanics is presented by Williams [163]. He describes the influence of profile wall thickness in terms of the stress intensity factor K_C. In Figure 6.103a is shown the plastic zone across the plate thickness, followed by a detailed view of K_C. K_C depends on the thickness of the specimen, B, and can vary between the values for plane strain K_{C1} and plane stress K_{C2}.

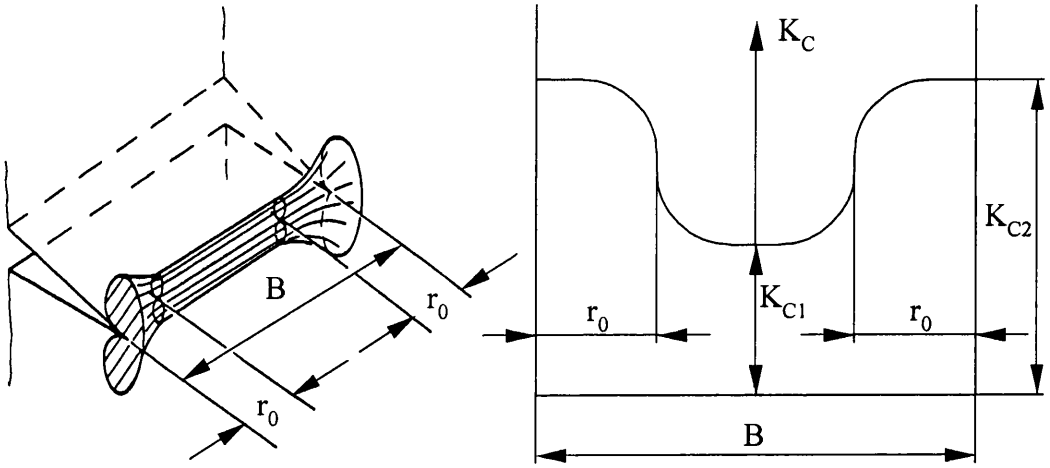

Figure 6.103: a) Plastic zone across plate thickness and b) K_C distribution across a crack front [163]

In Figure 6.103b are marked the thickness B of specimen and the surface zone thickness r_0. A plain strain condition requires a sufficient presence of elastic material surrounding the plastic zone to prevent contraction [164]. This leads to the conclusion that the thickness must be greater than this zone, and a minimum thickness B_{min} is required to fulfil this condition

$$B_{\min} = 2.5\left(\frac{K_{C1}}{\sigma_{yield}}\right)^2 \qquad (6.2)$$

with yield stress σ_{yield}.

If the specimen thickness B is less than the B_{min}, the measured impact values will be greater than the true strain values. The RAL [158] standard for testing of window profiles refers to DIN EN ISO 179, the test standard for impact strength tests. Here, the thickness of specimen, i.e. the profile wall thickness, is prescribed as a value of (4 ± 0.2) mm. According to RAL, the outer wall of the profile has a tolerance of (3 ± 0.2) mm, rather the required value for the DIN standard. The measured impact strength values must be reported, according RAL, with thickness of specimen to allow a comparison of different profiles, material formulation and processing conditions. Calvert stipulates a minimum specimen thickness of 2.50mm for impact strength tests [27].

The dependence of K_C on thickness B can be calculated [163]. The curve I in Figure 6.104 is calculated with

$$K_C = \sigma_{yield}\sqrt{\pi B} \tag{6.3}$$

and curve II is calculated with

$$K_C = K_{C1} + \frac{K_{C2}^{\ 2}}{\pi \sigma_{yield}^2 B}(K_{C2} - K_{C1}) \tag{6.4}$$

For the calculations, a yield stress of 42.3 N/mm^2 was used, obtained in a tensile test at 23°C with an annealed sample (60min, 100°C). Williams [163] presented values for K_{C1} of 3.99 $MPa\,m^{1/2}$ and 5.1 $MPa\,m^{1/2}$ for K_{C2}, and he mentioned that K_{C1} is in general smaller than K_{C2} for compounded PVC. This was confirmed in the literature and the values can vary from 2.4 $MPa\,m^{1/2}$ [165] [166] to 3.12 $MPa\,m^{1/2}$ [167].

In the calculations with equations (6.3) and (6.4), an average value of 2.76 $MPa\,m^{1/2}$ for K_{C1} and 5.1 $MPa\,m^{1/2}$ for K_{C2} were used to get an idea of the plane stress / plane strain limit B_{min}. The calculated values are plotted now in Figure 6.104 as function of the reciprocal value of specimen thickness B.

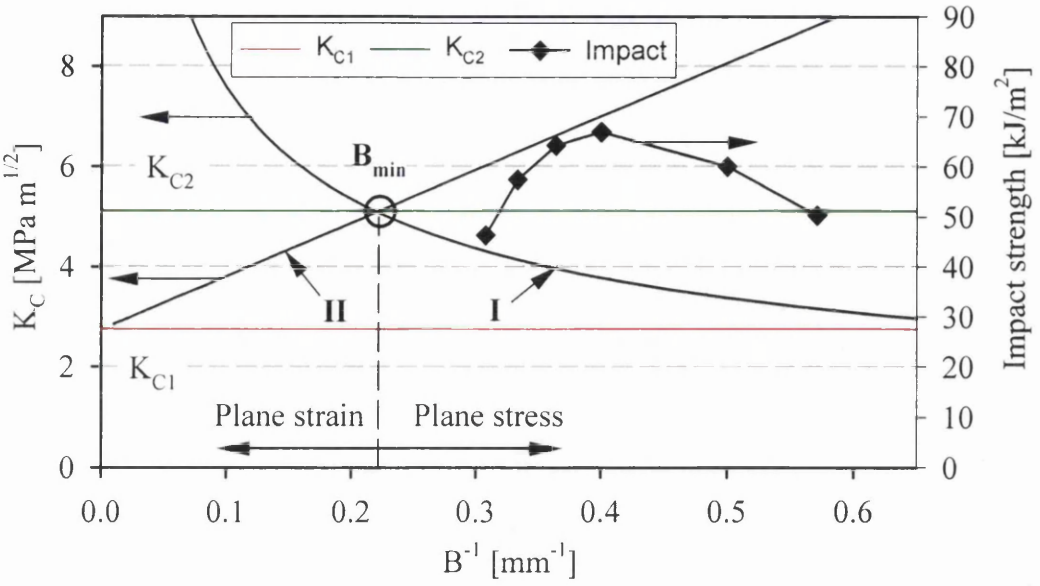

Figure 6.104: K_C values effected by plate thickness with plain stress and strain effects;
σ_{yield} = 42.3 N/mm^2, K_{C1} = 2.76 *MPa* $m^{1/2}$ and K_{C2} =5.1 *MPa* $m^{1/2}$

The intersection of the curves I and II gives the separation line between plane stress and plane strain conditions. Here a value of 4.50 mm is obtained, less than the value of 10.64 mm for B_{min} calculated with equation (6.2), and this equation is useful only for a rough estimate of B_{min}. But it is clear to see in the equations (6.2) to (6.4) that the yield stress σ_{yield} has an influence on the stress intensity factor K_C, and this is shown in Figure 6.105.

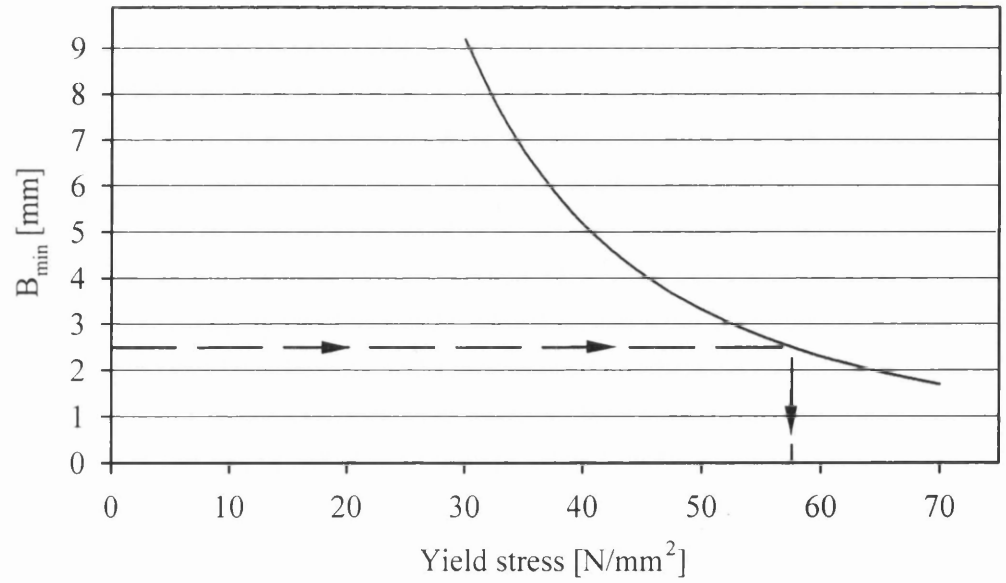

Figure 6.105: Effect of yield stress on thickness B_{min}

The maximum value of impact strength was measured for a profile wall thickness of 2.50 mm and estimation from Figure 6.105 leads to a yield stress of 57.6 N/mm^2 in order to get the maximum for impact strength at specimen thickness of 2.50 mm.

This higher yield stress may be obtained at higher strain rates. The yield of 42.3 N/mm^2 mentioned above was obtained with a strain rate of $5*10^{-5}$ s^{-1}. Kinloch [168] noted a strain rate for Charpy (3m/s) impact strength tests of 10 s^{-1} and mentioned the presence of strain rates up to $5*10^3$ s^{-1} in the notch.

Further tests were carried out to get the yield stress at higher strain rates and the results are shown in Figure 6.106.

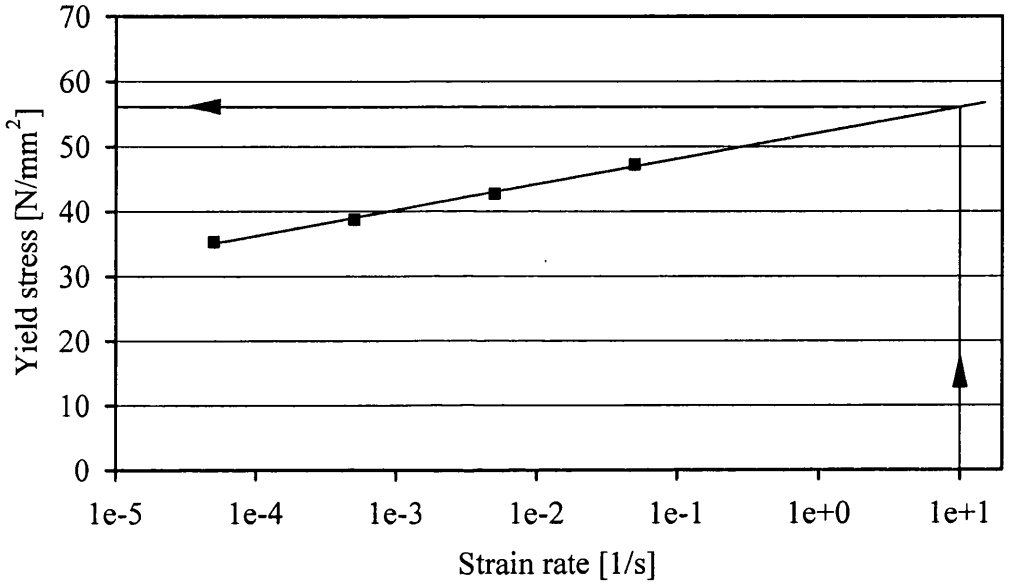

Figure 6.106: Correlation of yield stress and strain rate

For a strain rate of 10 s^{-1}, a yield stress of 56.1 N/mm^2 was calculated by extrapolation. This value was used to recalculate the stress intensity in Figure 6.104, and now the specimen thickness for maximum of the measured values of impact strength is close to thickness at the change from plane stress to plane strain conditions, Figure 6.107.

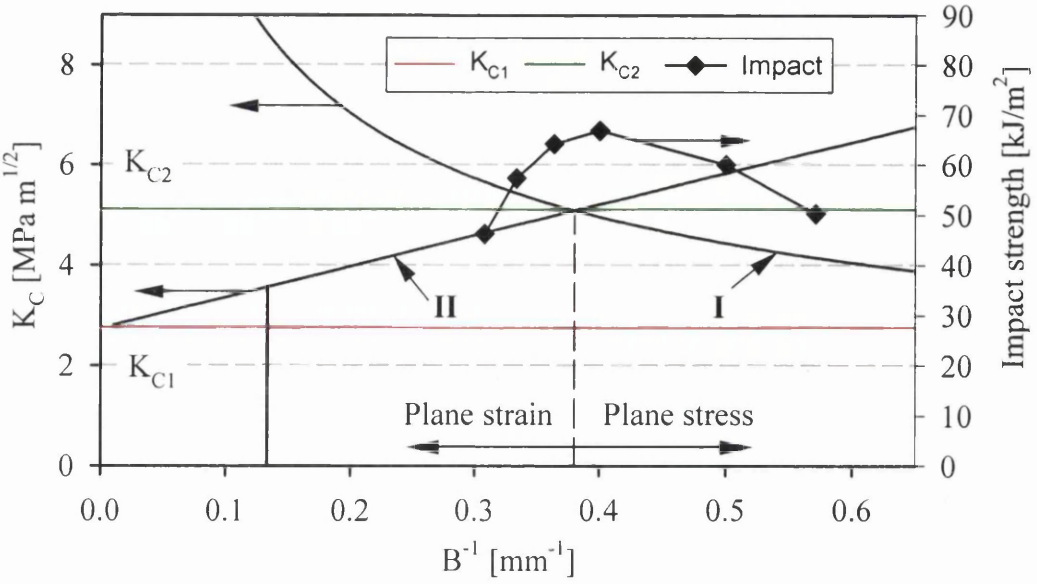

Figure 6.107: K_C values effected by plate thickness with plane stress and plane strain effects; σ_{yield} = 56.1 N/mm^2, K_{C1} = 2.76 *MPa* $m^{1/2}$ and K_{C2} =5.1 *MPa* $m^{1/2}$

The trend is clear to see, but there are some uncertainties present. The main problem, and the key parameter, is the correct yield stress in the impact strength tests. Further K_C, can vary slightly with screw speed and melt extrusion temperature [27], however the melt temperature was constant in the impact strength measurements shown above. K_C measurements are based on linear elastic fracture mechanics (LEFM) with small areas of yield [169]. It may be that plasticity terms are present in the impact strength testing, which could give different results in relation to plane stress / plane strain conditions.

The details of fracture mechanics show a wide range of possibilities, that can have an influence on measured impact strength, e.g., a bigger notch tips leads to higher impact strength values [168,170], The width has also an influence and a test conditions window for sample width and thickness to obtain satisfactory measurements is given by [171].

In the quality test according to RAL [158], further shock resistance tests, with a falling weight test according to DIN EN 477 are prescribed. As for the impact strength test, the falling weight test is also sensitive to specimen thickness [172]. But the impact strength values cannot be compared with falling weight values [162]. In reporting impact strength test results according to RAL, the wall thickness must be noted for a direct comparison with other tests, so that different batches of material (due to change in additives) can be compared, if the profile wall thickness is the same.

Another method, the J-method, was introduced for testing of small specimen [173]. But this method is not used in practice at the moment for the required quality tests in profile production.

Altogether, it seems that the measured impact strength varies with profile wall thickness. Thus seems to be based on the sensitivity of the test method to specimen thickness, rather than on the variation of material properties. In the development of new materials or compounds, a standardized size of specimens, injection moulded under the same processing conditions, is used to compare the material properties directly with each other. Otherwise, the results of the measured material properties will not be comparable.

6.4.3 Effects of vacuum in Calibrator 1 and wall thicknesses in wet calibration

A slight increase of impact strength values with increase of force for the same wall thickness and vacuum was noted before. The forces increase with increase of applied vacuum in Calibrator 1 and a slight increase in impact values is also visible in Figure 6.108.

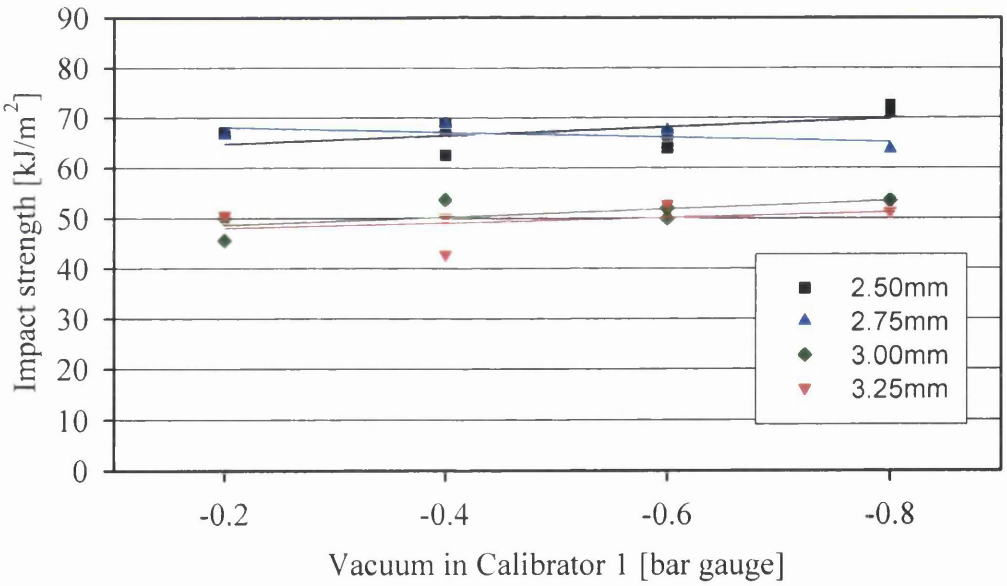

Figure 6.108: Impact strength as function of vacuum in Calibrator 1 at constant line speed of 4 m/min for different profile wall thicknesses; 2.50 mm die; wet calibration

A scatter is also visible. So the slight increase of the impact strength must be reviewed cautiously in the last Figure.

The details for the variation of vacuum in the downstream calibrators are not shown here, because there is no influence visible.

6.4.4 Effects of melt extrusion and coolant temperatures in wet calibration

As mentioned before, impact strength is known to show a strong dependence on melt extrusion temperature and the results from present work are shown in Figure 6.109.

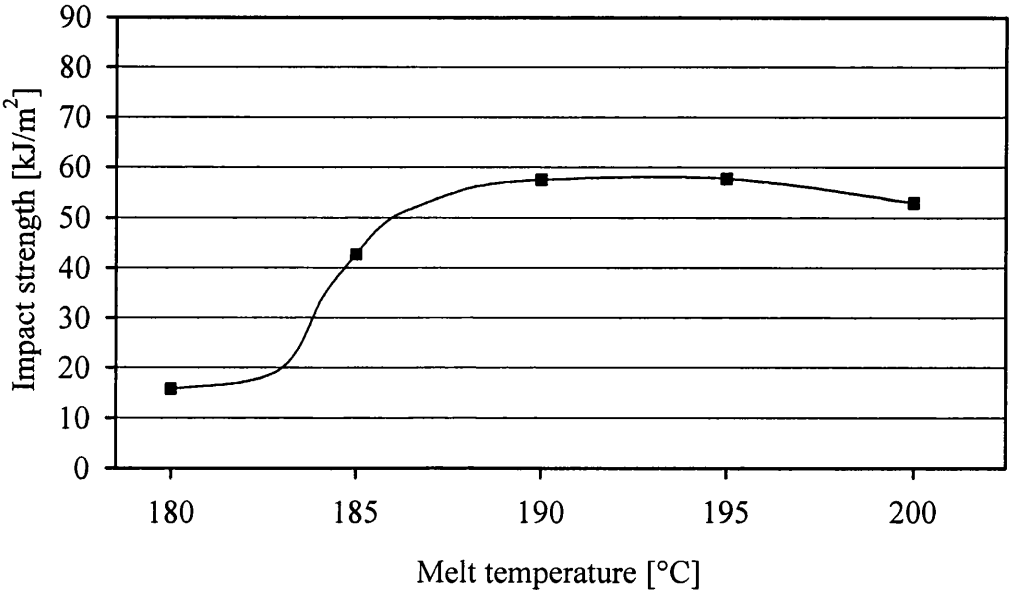

Figure 6.109: Impact strength for different extrusion melt temperatures; constant vacuum of –0.4 bar; 2.75 mm profile wall thickness; 4 m/min line speed; 2.50 mm die exit; wet calibration

The fitted line confirms the finding of the publications previously mentioned. Further measurement points would be needed to improve the fitting for the increase of impact strength between 180°C and 190°C. But a clear trend is visible and confirms the previous findings of a maximum around 190°C to 195°C melt extrusion temperature.

In the final set of experiments the coolant temperature was varied in Calibrator 1. An increase of coolant temperature slightly decreases the impact strength, Figure 6.110.

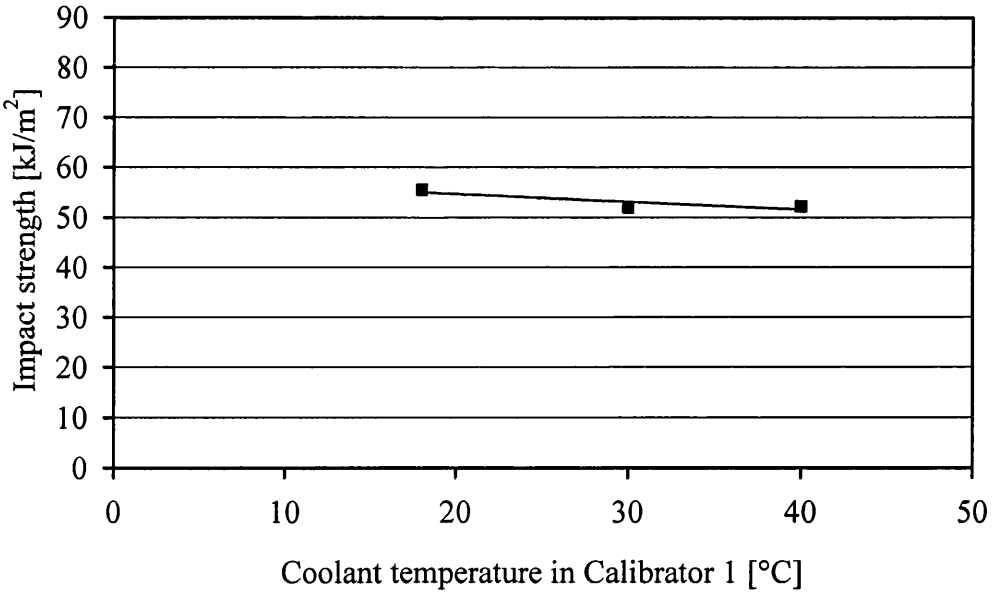

Figure 6.110: Impact strength for different coolant temperatures in Calibrator 1; constant vacuum of –0.4 bar; 3.00 mm profile wall thickness; 4 m/min line speed; 2.50 mm die exit; wet calibration

This may be based on higher temperatures in the profile due to less rapid cooling in Calibrator 1. To find out more about the effect of temperatures on impact strength values, the impact strength was measured after annealing for 1 hour at different temperatures up to 140°C. Measurements were made both along and across the line direction, Figure 6.111.

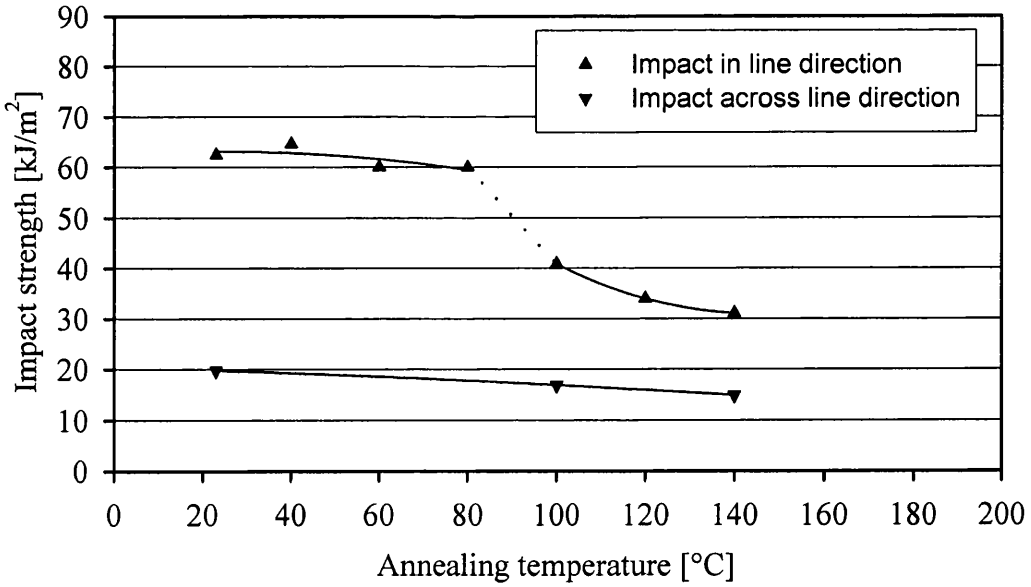

Figure 6.111: Impact strength along and across the extrusion direction after annealing for 1 h at various temperatures

In the line direction, the impact strength decreases slightly with annealing temperatures below T_g and a sharper drop is obtained for temperatures above T_g. In contrast, the values across line direction decrease only slightly over the whole range of annealing temperatures. This may indicate a strong correlation with molecular alignment in line direction, which can recover above glass transition T_g, whilst across the profile the molecular alignment is not so developed. Relaxation of extended polymer chains may be involved in the lower impact values found for higher coolant temperatures, Figure 6.110. With a higher coolant temperature, the molecular chains may recover faster due to higher temperatures in the profile.

6.4.5 Correlation of impact strength and shrinkage

The results just presented here suggested that polymer chain extension in the line direction is a factor in measuring impact strength. It was also concluded in Section 6.3 that chain extension was an important determinant of shrinkage. Some correlation of shrinkage and impact strength values might then be expected. Unfortunately, it is not possible to establish this from the present results, because for the tests on samples of different thickness, where shrinkage varied significantly, the results for impact strength are, at least to some extent, influenced by the sensitivity of the test method to sample thickness.

Summary

In this section was shown the dependence of measured impact strength on process parameters. The measured impact strength values increased slightly with higher forces. An increase was also obtained with reduction of profile wall thickness for a constant die exit for a 2.50 mm. In contrast to this, a reduction of wall thickness for a constant 1.50 mm die exit has shown an increase of impact strength. An initial interpretation assumed a degree of molecular orientation in the line direction, which increases the shrinkage and the impact strength for smaller wall thicknesses due to less opportunity for strain recovery. But this was inconsistent with the impact strength values obtained using the 1.50 mm die. So a conclusive correlation of impact strength and shrinkage is not possible from present measurements. The reason for this is related to the existence of plane stress / plane stress conditions in the impact strength tests.

At a certain specimen thickness, the plane strain goes into plane stress. It was shown in a foregoing Section, that this change occurred at around 2.60 mm specimen thickness, close to the sample thickness of 2.50 mm where the maximum measured impact strength value was found. This limit is mainly determined by yield stress of the specimen, which is, in turn, dependent on the strain rate. During impact strength tests, high strain rates are present in the specimen. Tensile test were carried out to estimate the yield stress at higher strain rates and an extrapolation (above the maximum strain rate of the tensile testing machine) to higher strain rates gave a value that led to good agreement between the sample thickness for impact strength maximum and the change of plane strain / plane stress conditions. It therefore appears that the variation of impact strength with sample thickness may be an artefact of the test method.

The dependence of impact strength on melt extrusion temperature has confirmed the findings in the literature. Values increased to a maximum at melt temperatures around 190°C, with a small plateau up to 194°C. Higher melt temperatures lead to a decrease of impact strength values.

The maximum impact strength is also dependent on the gelation level, which was not investigated in the recent experiments. At the maximum of gelation level, the impact strength reaches also a maximum according to Covas [23].

The dependence of impact strength and shrinkage on molecular alignment may be present, but this could not be investigated with the present measurements and methods. Further investigations and experiments in the future should give more insights into the influence of molecular alignment.

6.5 Stress in the profile

In profile calibration, the profile cools down from the extrusion temperature to ambient in presence of some imposed stresses, and others develop due to differential cooling rates. The following section shows the influence of the process parameters on the stress development in the profile.

6.5.1 Introduction

In the usual situation, where the profile wall cools from the outside, with an assumed adiabatic or lower cooling rate inside, the layers of material start to cool down from the outer towards the inner side. In the first stage, the length of layer is the same as at melt extrusion temperature, Figure 6.112a.

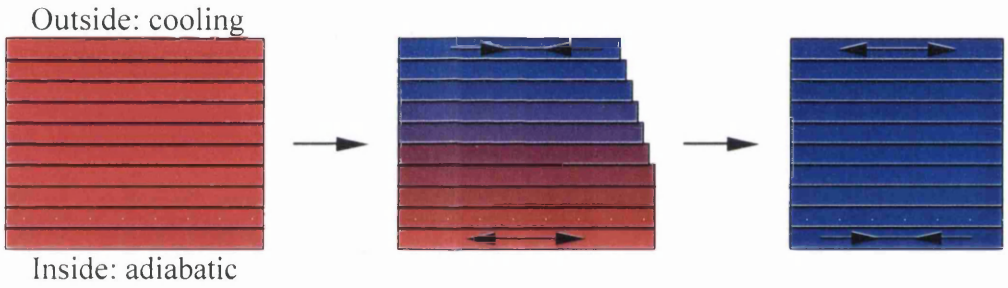

Figure 6.112: Development of stress in the profile wall due to cooling at the outside and adiabatic condition at the inside: a) initial, b) free shrinkage resulting from cooling, c) constrained condition

With cooling, the outer layers attempt to shorten due to thermal shrinkage, Figure 6.112 b. Due to constraints of the inner layers, tensile stresses are initially built up in the outer layer, whereas compressive stresses are arising in the layers near the inner side. Completion of cooling in the absence of any imposed stress leads to a build up of tensile stresses at the inside and compressive stress at the outside of the profile. This is well known and shown in the literature for the extrusion of pipes, sheets and profiles and widely in injection moulding.
The stress in the layers in the profile can be determined with several techniques. The most common is the layer removal technique. A defined layer is removed from the specimen, usually by milling, and the specimen bends due to the initial imbalance and re-equilibration of

forces. From this bending, the stress in the removed layer can be calculated, based on simplifying assumptions. Several investigations were done in the past, most of them for injection moulding. However, Menges *et. al.* [174] measured the stress in picture frame, hollow chamber and curtain rail profiles. Relatively small compressive stresses of 0.5 N/mm^2 were measured at the outside, and tensile stresses around 1.5 N/mm^2 at the inside of the profile wall. The forces at haul-off were found to have little influence on the stress.
The critical point in the process is not the haul-off force, i.e. the tensile stress due to haul-off force, but the forces in the individual calibration units and their influence on the profile properties.

To investigate this, strips were cut out from each side of the profile in the line direction. The strips rapidly bent, and were scanned to record the bending, as described in Chapter 4, the experimental set-up. The bending is defined as follows, Figure 6.113.

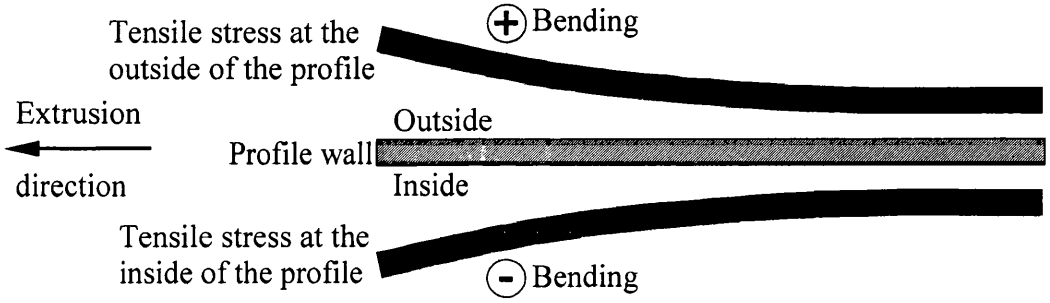

Figure 6.113: Definition of strip bending

A positive bending is obtained with tensile stresses at the outer side of the profile and negative for tensile stresses at the inner side.
Instead of using the layer removal, the residual stress of the strip is calculated in an appropriate way by using the bending dimension f and length l, as shown in Figure 6.114.

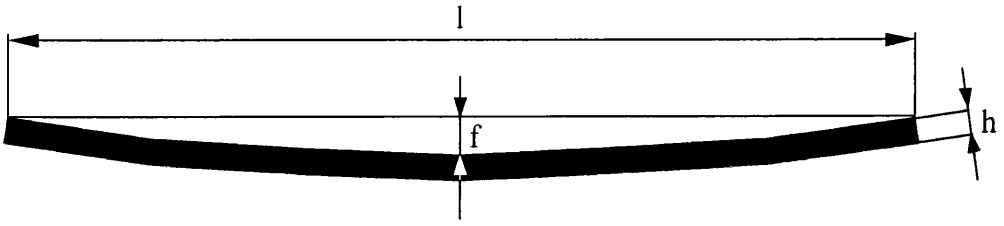

Figure 6.114: Dimensions for the calculation of maximal stress σ_{MAX} in strips

The width w and height h of the sample were also measured and the maximum stress σ_{MAX} in the strip can be calculated as

$$\sigma_{MAX} = \frac{M_b}{W_b} \tag{6.5}$$

with the bending moment M_b and section modulus W_b [175]. Transformation lead to the maximum stress

$$\sigma_{MAX} = \frac{6 E f h}{l^2} \tag{6.6}$$

with the height h of the strip. A constant elastic modulus E of 3000 N/mm^2 [175] is used for the calculations directly after the experiments.

6.5.2 Effects of wall thicknesses and vacuum in wet calibration at different line speeds

In the next Figures 6.115 to 6.117 are shown the stresses calculated as above, as function of line speed for different profile wall thicknesses (2.50 mm die exit) at vacua of –0.4 up to –0.8 bar.

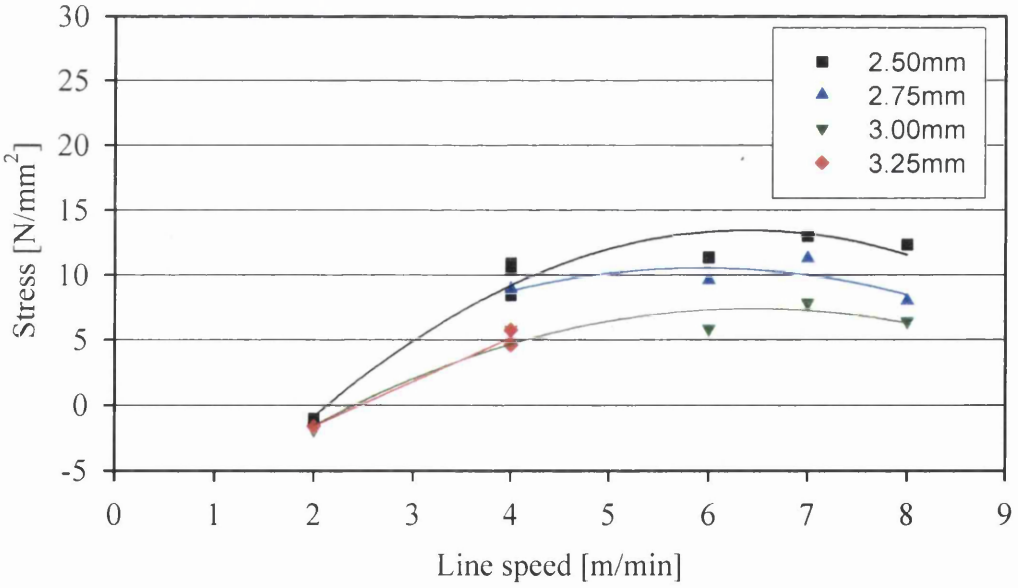

Figure 6.115: Stress in profile as function of line speed for different profile wall thicknesses at -0.4 bar vacuum; 2.50 mm die exit; wet calibration

The negative stress here means a bending towards the inside of the profile due to tensile forces at the inside, which is the case for cooling without constraints. This is obtained only for a line speed of 2 m/min and applied vacuum of –0.4 bar. At higher line speeds, the solidified

layer is thinner than for low line speeds at same downstream distance, furthermore the haul-off force is higher. Higher imposed tensile stresses are therefore carried by the solidified layers. The result is a final stress distribution that is tensile on the outer surface, leading to plus bending. At higher vacuum, tensile stresses at the inside are not present even at lower line speed, due to higher haul-off forces, and this is shown in the following Figures.

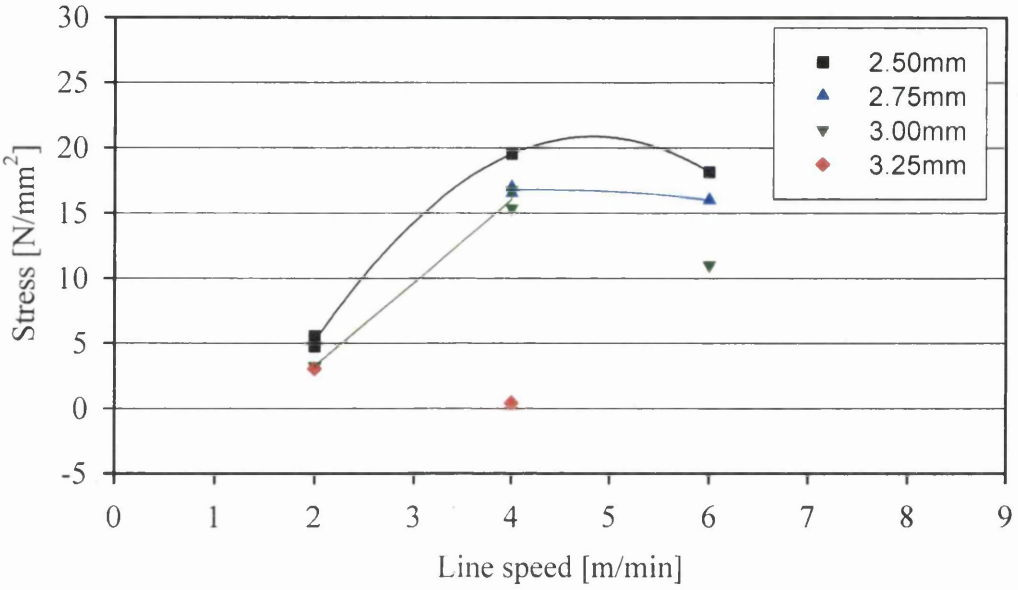

Figure 6.116: Stress in profile as function of line speed for different profile wall thicknesses at -0.6 bar vacuum; 2.50 mm die exit; wet calibration

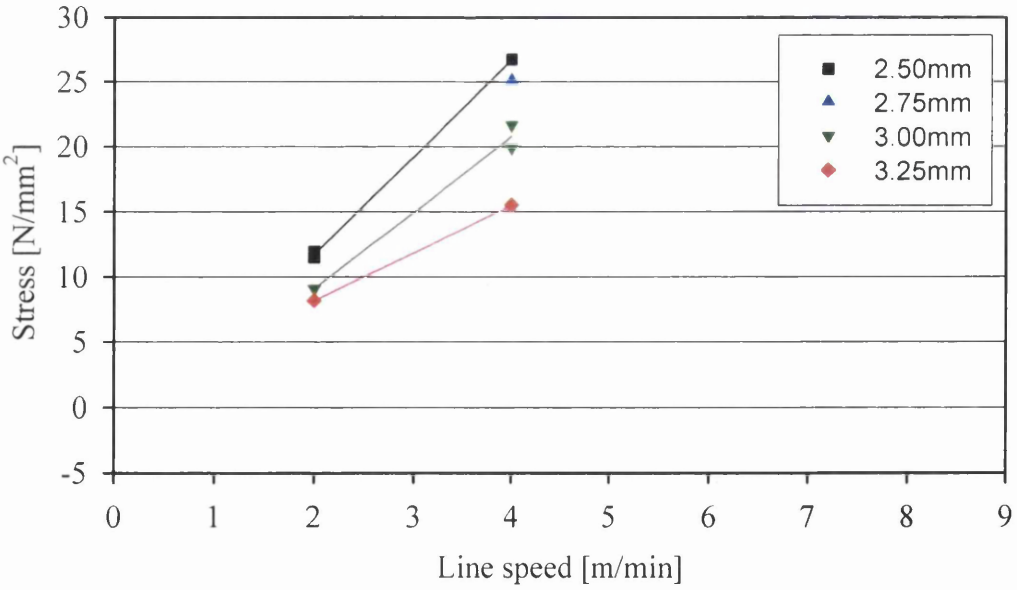

Figure 6.117: Stress in profile as function of line speed for different profile wall thicknesses at -0.8 bar vacuum; 2.50 mm die exit; wet calibration

The three foregoing Figures have shown a pattern similar to the Figures 6.8 to 6.13, which show the dependence of shrinkage on line speed. This is to be expected, as higher stresses correspond to higher strain, which lead to higher shrinkage. In Figure 6.118 are plotted the stresses as function of haul-off force for all line speeds, wall thicknesses and vacua.

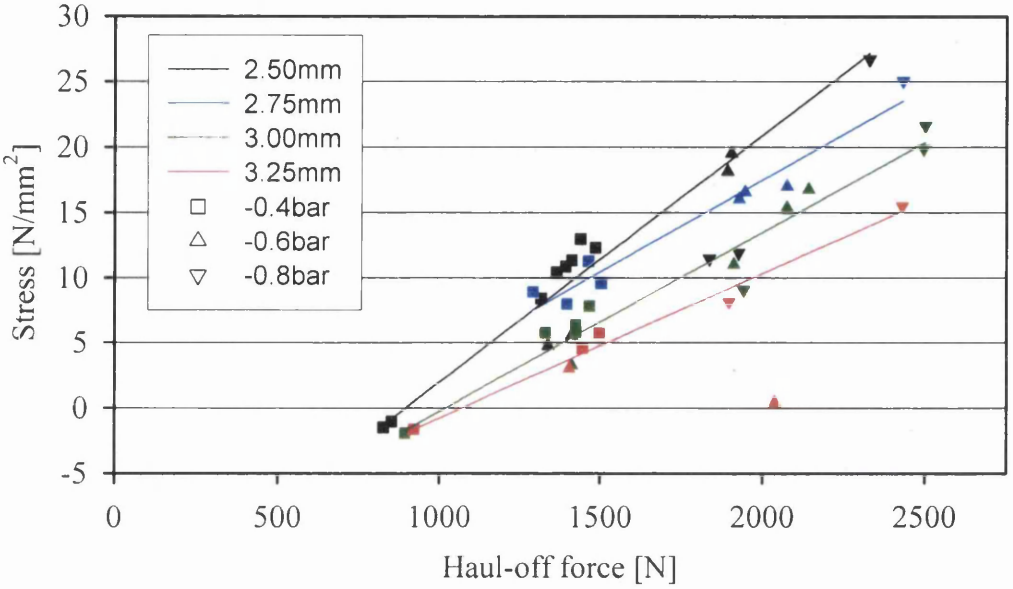

Figure 6.118: Stress in profile as function of haul-off forces for different profile wall thicknesses and vacua; 2.50 mm die exit; wet calibration

A decrease of stress is obtained with increase of profile wall thickness at constant haul-off force. This may be due to higher average temperatures in the profile, which accelerates the relaxation of stresses / strains in the calibration process.

The dependence of stresses on Calibrator 1 forces, presented in Figure 6.119, might give a further insight to the results shown in Figure 6.118.

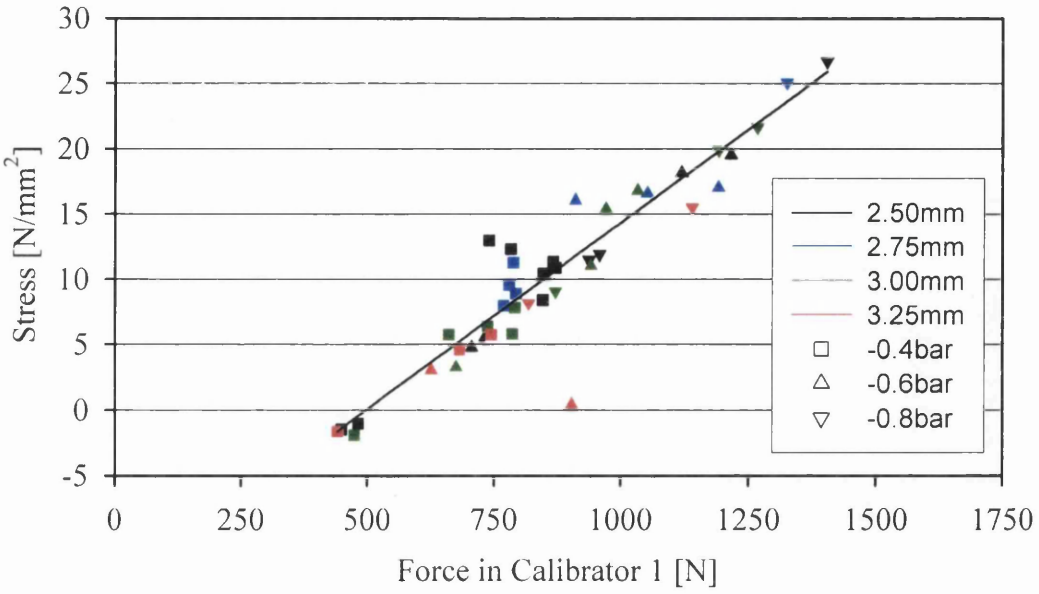

Figure 6.119: Stress in profile as function of forces in Calibrator 1 for different profile wall thicknesses and vacua; 2.50 mm die exit; wet calibration

The dependence has not shown a significant variation with wall thickness.

It might be anticipated, that a reduction of wall thickness would lead to higher stresses in the profile. The 1.50 mm die exit was used to produce thinner wall profiles and, as expected, the stresses show higher values at the same forces, compare Figures 6.18 and 6.19 Figure 6.120.

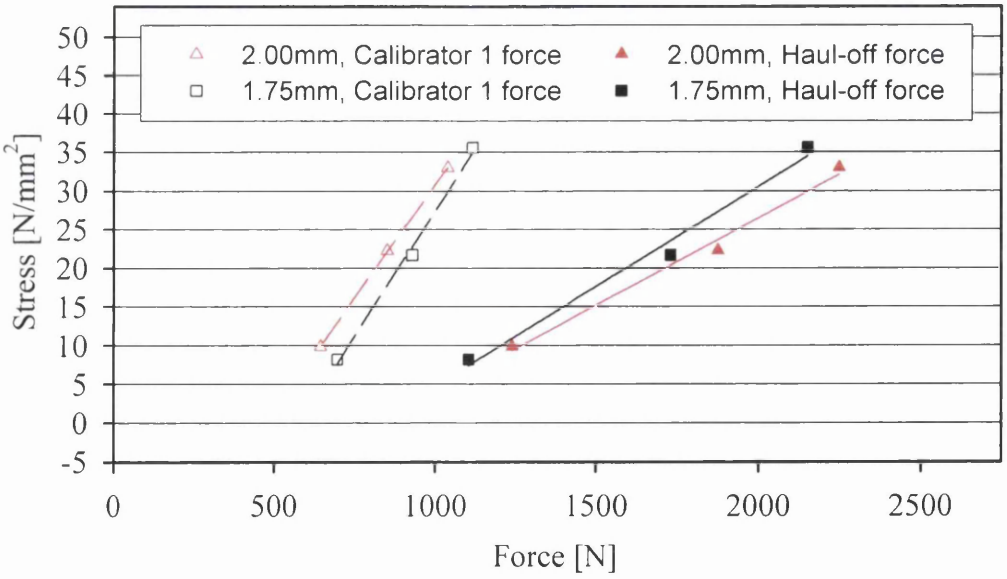

Figure 6.120: Stress in profile as function of forces for different profile wall thicknesses and vacua; 1.50 mm die exit; wet calibration

The maximum stresses were up to 35 N/mm^2 for thinner profile walls. The haul-off and calibrator forces can be clearly be used to control the stress in the profile.

6.5.3 Effects of vacuum in Calibrator 1 and wall thicknesses in wet calibration

A clear correlation between of stresses and haul-off forces was presented above, together with the dependence on profile wall thickness, with variation of wall thickness at constant height of the die exit. In a plot against haul-off forces, Figure 6.118, a clear influence of wall thicknesses was evident; however, when plotted against Calibrator 1 force, Figure 6.119, no systematic dependence on wall thickness was seen. This might be based on a stress / strain recovery in the thicker profile walls. To get more insight, further trials were carried out with the variation of vacuum in Calibrator 1 and the results are shown now, Figure 6.121.

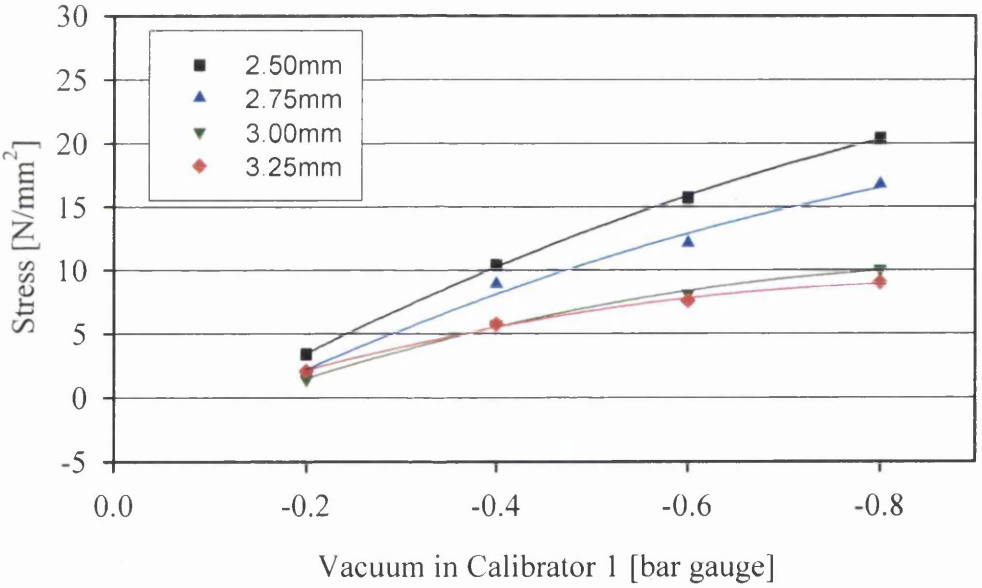

Figure 6.121: Stress for different vacua in Calibrator 1 at different profile wall thicknesses; 4 m/min line speed; 2.50 mm die exit; -0.4 bar vacuum in calibrators 2, 3 and 4; wet calibration

The trend lines confirm the findings of increase of stress with higher applied vacuum, which lead to higher forces and the reduction of stress for higher wall thicknesses. Notably a reduction of vacuum from –0.8 bar to –0.2 bar only in Calibrator 1 leads for a 2.75 mm profile wall to a significant reduction of stress from 17 N/mm^2 to 3 N/mm^2.

For completion of plots, the dependence of stress at haul-off and Calibrator 1 forces is shown in Figure 6.122 and 6.123.

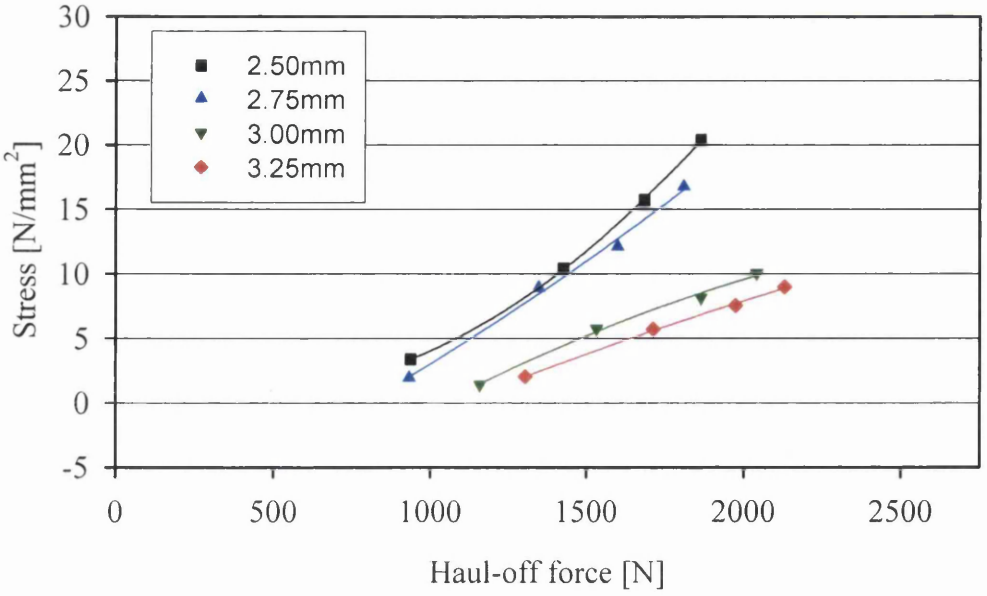

Figure 6.122: Stress as function of haul-off force at different profile wall thicknesses; various vacua in Calibrator1; 4 m/min line speed; 2.50 mm die exit; -0.4 bar vacuum in Calibrators 2, 3 and 4; wet calibration

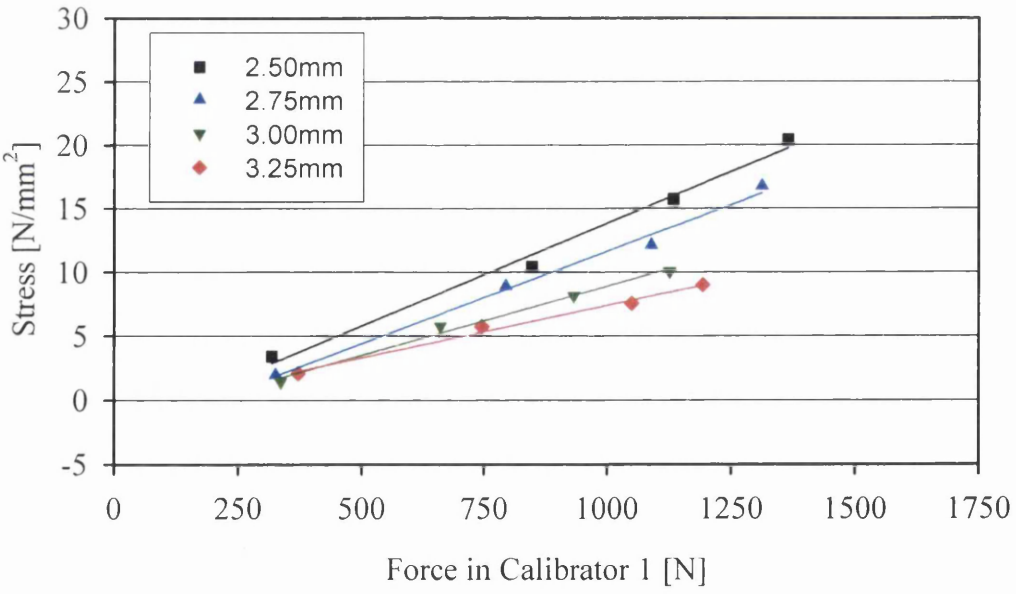

Figure 6.123: Stress as function of force in Calibrator 1 at different profile wall thicknesses; various vacua in Calibrator1; 4 m/min line speed; 2.50 mm die exit; -0.4 bar vacuum in Calibrators 2, 3 and 4; wet calibration

In the plots against haul-off and Calibrator 1 forces, distinguishable trend lines for different wall thicknesses are visible.

6.5.4 Effects of vacuum in Calibrators 2, 3 and 4 in wet calibration

In the next set of experiments, the applied vacuum is varied in downstream calibrators, with constant vacuum in Calibrator 1, to see the influence on stress in the profile. As expected, higher vacuum increase the stress, Figure 6.124.

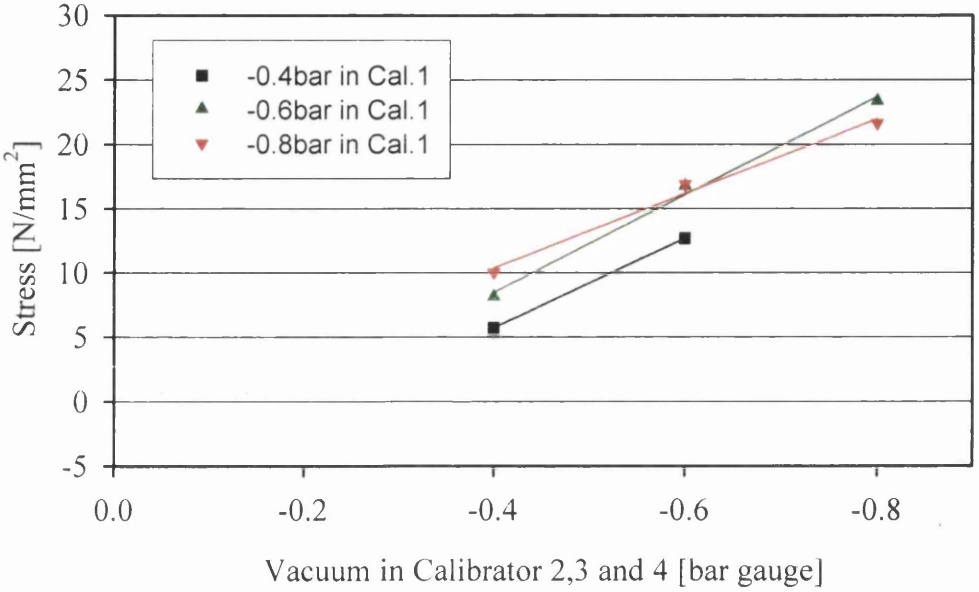

Figure 6.124: Stress for different vacua in Calibrator 2, 3 and 4 for different vacua in Calibrator 1; 4 m/min line speed; 3.00 mm profile wall thickness; 2.50 mm die exit; wet calibration

The increase of stress with haul-off force is plotted in Figure 6.125.

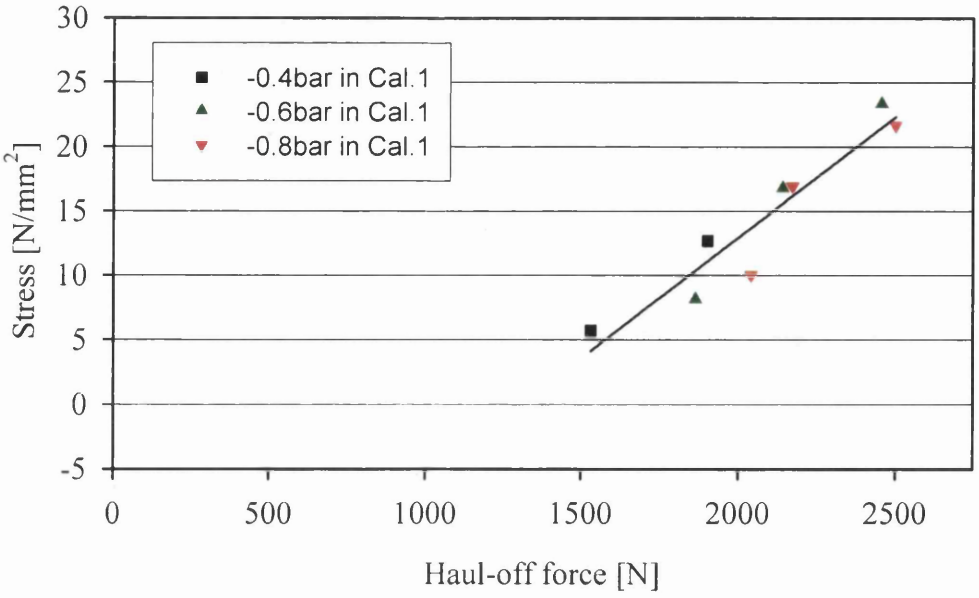

Figure 6.125: Stress as a function of haul-off force for different vacua in Calibrator 1; various vacua in downstream calibrators; 4 m/min line speed; 3.00 mm profile wall thickness; 2.50 mm die exit; wet calibration

Overall, the stress level can be adjusted with level of applied vacuum in Calibrator 1 and also with the vacuum in downstream calibrators.

6.5.5 Effects of melt extrusion and coolant temperatures in wet calibration

In the final set of experiments, the melt extrusion and coolant temperature in Calibrator 1 were varied.

The stress is nearly independent of extrusion temperature, except for the low melt temperature of 180°C, Figure 6.126.

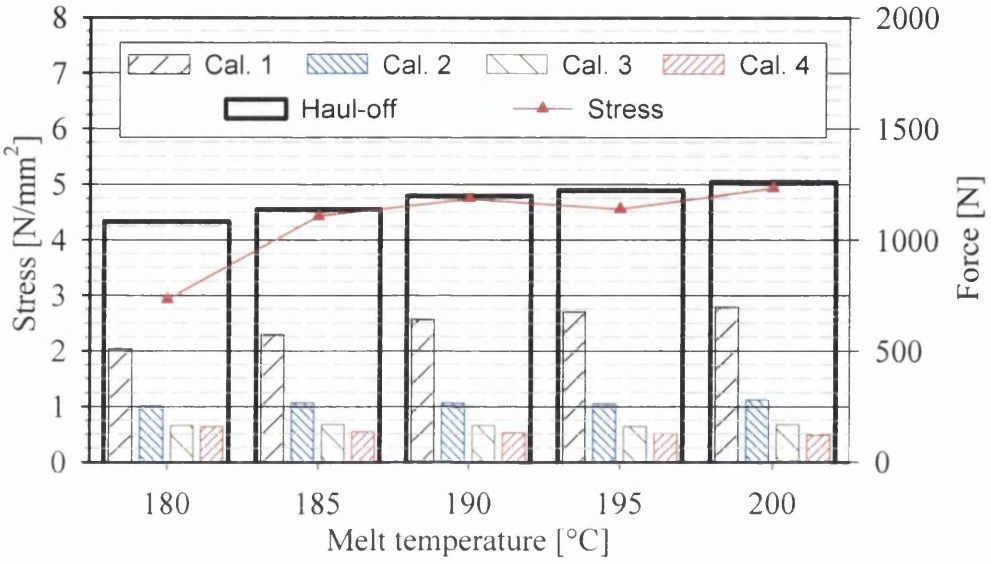

Figure 6.126: Stress for different extrusion melt temperatures; constant vacuum of –0.4 bar; 2.75 mm profile wall thickness; 4 m/min line speed; 2.50 mm die exit; wet calibration

This may be based on the different structure of PVC at lower extrusion temperatures.

Opposite to this, the stress decreases with higher coolant temperatures. Several effects could be the reason for this. On one hand, the increase of coolant temperature accelerates the relaxation of stresses, but on the other, it also reduces the thickness of the solidified layer below the glass transition temperature T_g, which could lead to higher stresses at the same haul-off forces. But as shown in Figure 6.127, the forces are reduced at higher coolant temperatures and overall this leads to reduced stresses in the profile.

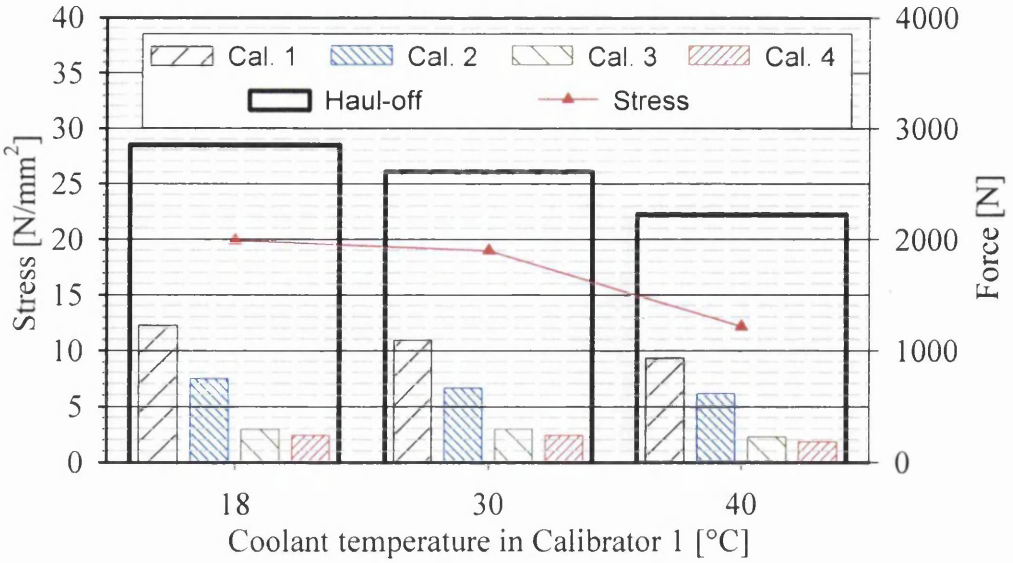

Figure 6.127: Stress for different coolant temperatures in Calibrator 1; constant vacuum of –0.4 bar; 3.00 mm profile wall thickness; 4 m/min line speed; 2.50 mm die exit; wet calibration

All the foregoing Figures have shown the stress dependence on process parameters. The stress was calculated using the bending of strips, which where cut out of the profile in line direction directly after the calibration process.

6.5.6 Time dependence of stress

As is well known, the stresses relax in polymers. To investigate this behaviour, a second set of samples, of the same batch of processed profiles, were stored for 10 months. From the degree of bending after storage, the stress was calculated with same procedure as used before for the first set. The reduction of stresses is visible in Figure 6.128.

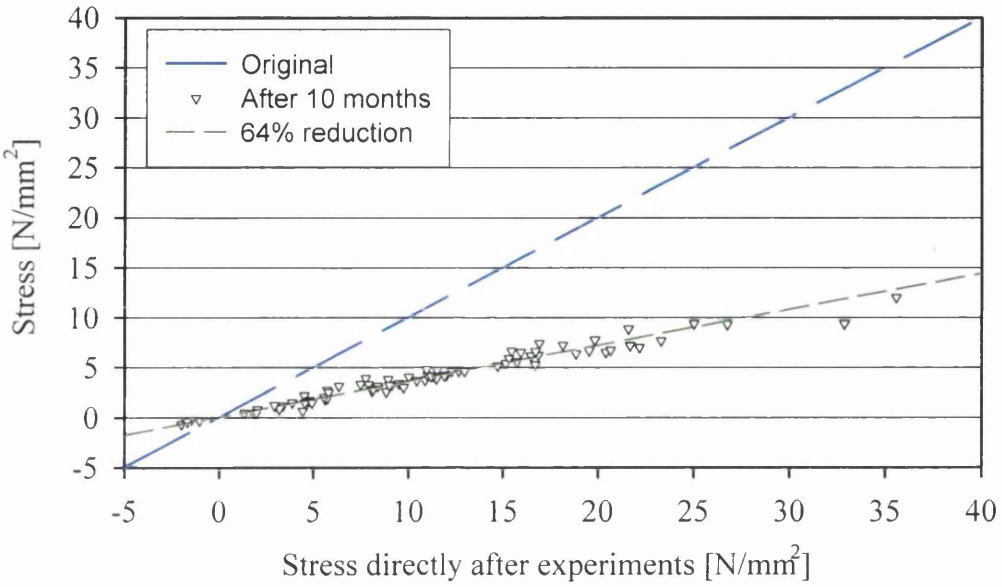

Figure 6.128: Time dependence of stress in strips

The stress relaxed, and an average reduction of 64% was obtained, as marked in Figure 6.128. The reduction of stress is larger than the reduction of shrinkage with time. In Figure 6.83 was shown a reduction of 10 % for shrinkage after 5 months.

6.5.7 Correlation of stress and shrinkage

In the foregoing Sections 6.3 and 6.5, correlations of both shrinkage and stress in the profile on forces in the calibration process were presented. This leads to the conclusion that stress and shrinkage may also be correlated.

A correlation of stress and shrinkage is shown in Figure 6.129 for different line speeds, wall thickness and vacua in wet calibration.

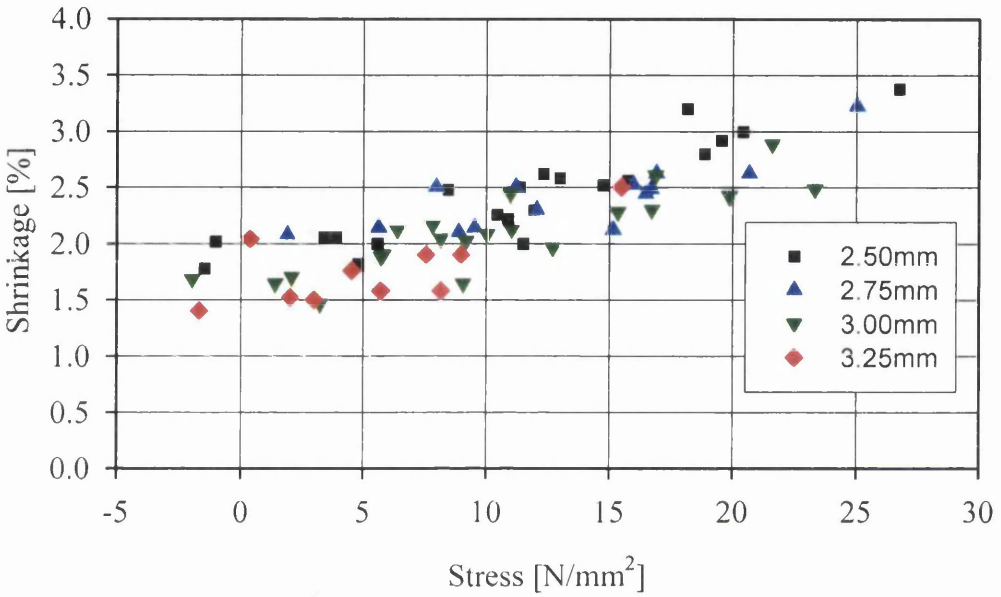

Figure 6.129: Shrinkage as function of stress for different line speeds, profile wall thicknesses and vacua in wet calibration; 2.50 mm die exit

A trend is visible, but a wide scatter is present due to the variation of other parameters present (e.g. line speed, vacua). The trend gets clearer for results with line speed of 4 m/min at different vacua and wall thicknesses, Figure 6.130.

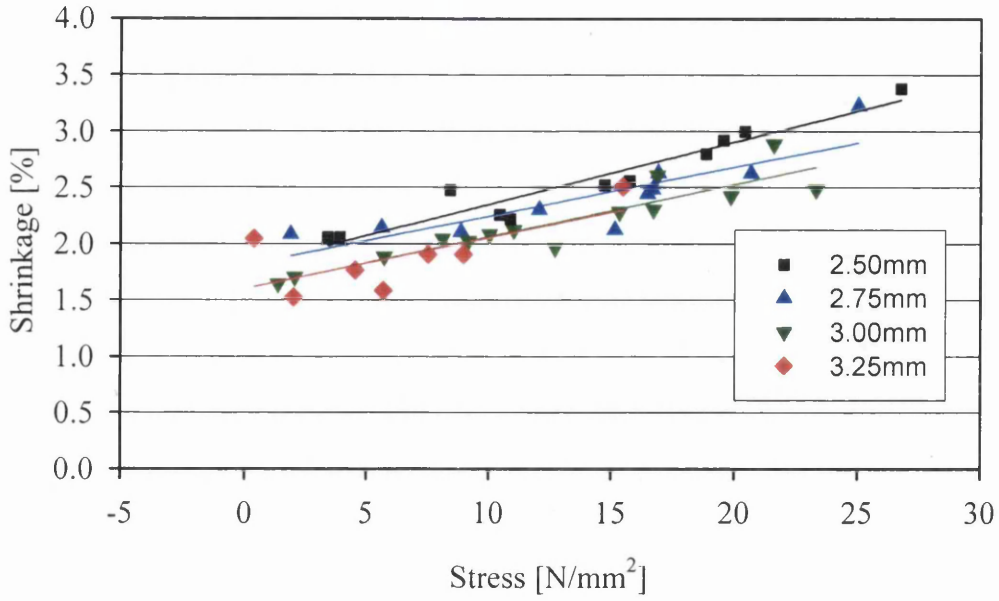

Figure 6.130: Shrinkage as function of stress for different profile wall thicknesses and vacua in wet calibration at 4 m/min line speed, 2.50 mm die exit

The shrinkage increases with an increase of wall thickness at the same stress level in the profile due to strain recovery, as noted previously. For each wall thickness a quite high correlation with stresses is visible. A correlation with dimensions should be present as well, and this is shown in Figure 6.131 for the circumference C, corner dimensions of the profile, for a constant line speed of 4 m/min.

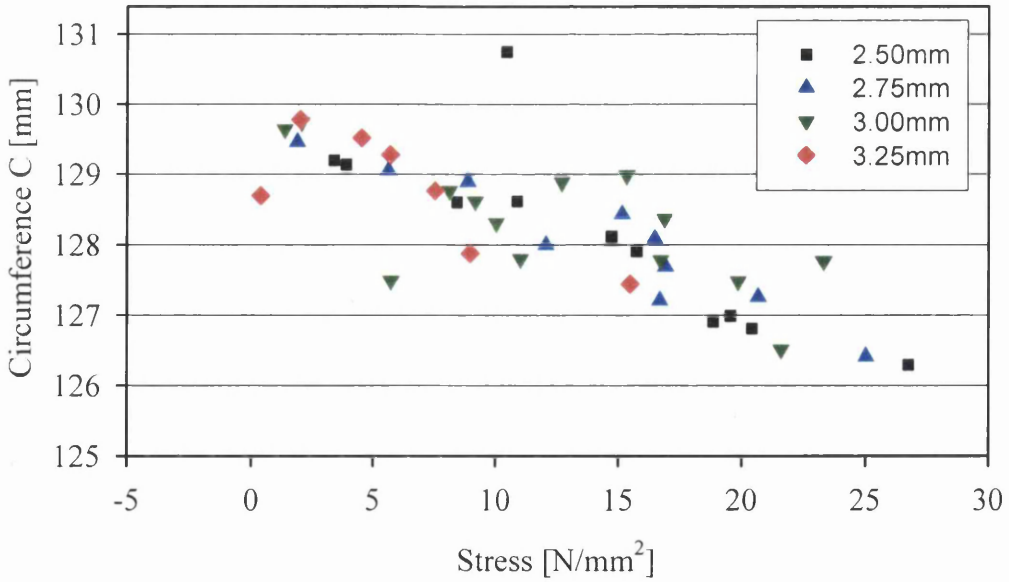

Figure 6.131: Circumference C as function of stress for different profile wall thicknesses and vacua in wet calibration at 4 m/min line speed, 2.50 mm die exit

An increase of stress in the profile leads to a reduction of circumference C, due to measured draw down strain.

Summary

In general, the stress shows a good correlation with forces (or vacuum) in the extrusion process. The higher the forces, the higher are the stresses in the profile. The wall thickness also has an influence on the stress. At the same level of force, the stress is higher for thinner profiles.

A reduction of vacuum in Calibrator 1 from –0.8 bar to –0.2 bar reduces the stress from 17 N/mm^2 to 3 N/mm^2 for a 2.75 mm profile wall and line speed of 4 m/min. Like the vacuum in Calibrator 1, the vacuum in downstream calibrators is also relevant in the process, especially at higher line speeds.

The stress stays at the same level with increase of melt extrusion temperature. Different behaviour is shown with variation of coolant temperature in Calibrator 1. Here, an increase leads to a reduction of stress, mainly resulting from decrease of forces at higher coolant temperatures.

All these effects are shown qualitatively in the Figure 6.132.

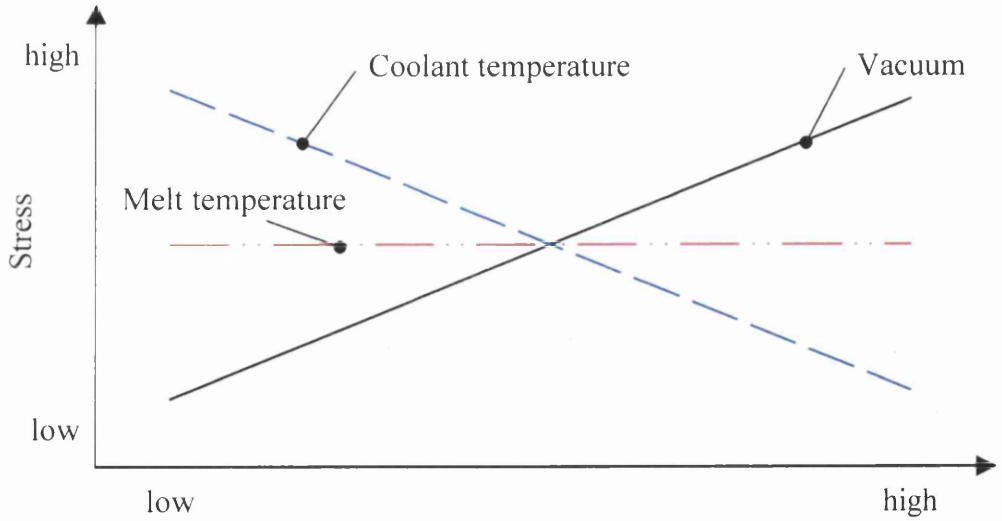

Figure 6.132: General dependencies of stress in the profile on the vacuum, melt extrusion and coolant temperatures

The stress relaxes with time and a reduction of 64% was measured over a period of 10 months. Shrinkage has also decreased with time, but a reduction of only 10% was obtained in the measurements, on the stored samples. It is clear, therefore, that different effects are responsible for the dependence of stress and shrinkage on time.

It seems that shrinkage is mainly based on longer-range chain extension, which cannot recover below glass transition temperature T_g. The stress is more dependent on the short-range deformation due to bending and stretching. Unlike the shrinkage, the stress can relax due to thermal motions below T_g.

CHAPTER 7

Heat transfer

7.1 Introduction

During calibration of profile and pipe in general, the heat transfer is an important parameter in the process. The profitability of the profile production depends mainly on higher throughput whilst maintaining constant quality of the profile. An increase of throughput, i.e. of the line speed, means that a sufficient cooling is essential to cool the profile down to the same temperature after the same length of the calibration line. Another, not to be underestimated, factor is the temperature dependence of the material data, e.g. the specific volume, which was presented in Chapter 1 about the PVC properties. Additionally, the cooling process influences the frozen-in strains, which in turn influence shrinkage, and the residual stresses and deformation of the profile. In this Chapter, the heat transfer is investigated to get more information about it. The fundamentals of heat transfer are discussed first, followed by presentation of the temperature profiles along the calibration line for different extrusion parameters and, finally, the heat transfer is estimated using temperatures obtained in the calibration line. For the simulation of cooling, the Finite-Difference-Method (FDM) is used to calculate the heat transfer coefficients.

7.2 Fundamentals of heat transfer

Heat transfer is fundamental to a wide range of polymer processing operations, e.g. in film, sheet, pipe and profile extrusion. Heat transfer can occur by three mechanisms: conduction, radiation and convection.

The present heat transfer process (in calibration) can be characterised with a dimensionless number, the Biot number Bi. This represents the ratio of the thermal resistance to heat transfer from the surface by convection 1/h to the resistance to conduction within the material X/λ

$$Bi = \frac{hX}{\lambda} \qquad (7.1).$$

with heat transfer coefficient h, thermal conductivity λ of the material and characteristic length X (which is half the thickness of the body for cooling from both sides, and equal to the total thickness for cooling from one side).

For Bi < 0.1, e.g. in film extrusion, medium air, with h = 10 W/m^{2}K and thickness of 100 μm the temperature difference in the body is very small. For Bi > 100, a high temperature gradient is present in the body, e.g. in sheet extrusion, with good contact with the roll, h = 2,000 W/m^{2}K, and thickness of 10 mm [176].

Another useful number is the Fourier number, Fo, and it is used to introduce the dimensionless time for transient cooling. This can be calculated by

$$Fo = \frac{at}{l^2} \tag{7.2}$$

with the thermal diffusivity α, time t and characteristic length l. The thickness of a sheet or profile wall is commonly used for l in estimates of the required calibration length. For a simple comparison for the cooling of two profiles with e.g. different thickness, the Fo number is set to be equal for both cases. Solving the equation leads to an estimation of time needed to reach same cooling condition of both specimens under the same conditions.

But profile extrusion is more complex due to the influence of the geometry, and this is shown schematically in Figure 7.1.

Conduction is present in the calibrator block and the profile walls. The heat stored in the profile is transported by thermal diffusion through the PVC to the outer surface of the profile. If the profile is in contact with the calibrator, the conduction is continued and the heat is transported from the contact area of profile and calibrator towards the cooling channels in the calibrator.

The convective process in the cooling plays a role in the heat transfer from the surface of the coolant channels to the coolant liquid. Here, the convection is called forced convection, because the coolant flow over the surface of the coolant channel is due to a driving force, the pressure difference between inlet and outlet supply of the coolant channel. The second type of convection, free or natural convection, results from the change in density due to temperature change. This is present in a simple water bath adjacent to outer profile surface, as shown at the right sight in Figure 7.1. It is also significant in the air chambers within the profile. Here, the process is driven by the temperature difference between the outer and inner walls of the

profile, as shown schematically in the right chamber of the profile in Figure 7.1. In the left chamber, the radiation heat transfer is shown schematically.

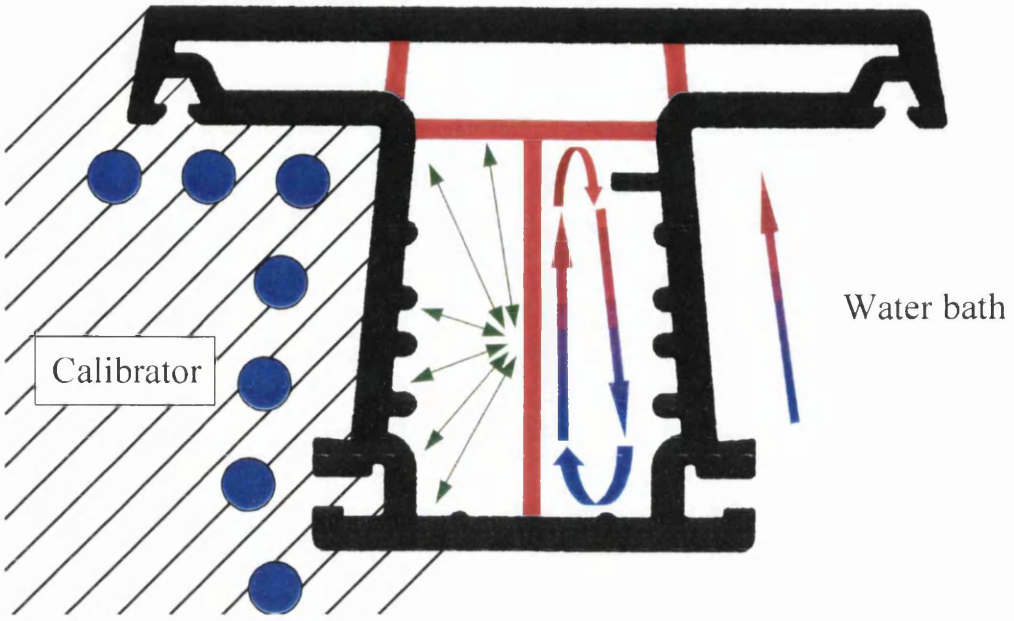

Figure 7.1: Conduction, radiation and convection in the profile cooling process

The three mechanisms of heat transfer and the relevant parameters for each case are explained in more detail in the following sections.

7.2.1 Conduction

The conduction term is valid for the transport of heat in a solid body, and for isotropic materials, energy conservation leads, in Cartesian form, to

$$\left(\frac{\partial \dot{q}_X}{\partial x}+\frac{\partial \dot{q}_Y}{\partial y}+\frac{\partial \dot{q}_Z}{\partial z}\right)+\rho c_p \frac{\partial T}{\partial t}=S \qquad (7.3)$$

where $\dot{q}=(\dot{q}_X,\dot{q}_Y,\dot{q}_Z)$ is the heat flux vector [W/m^2], ρ is density [kg/m^3], c_p is specific heat [J/kg K], T is temperature [K], t is time [s] and S a source term [W/m^3].

The Fourier law (i=x,y,z) is

$$\dot{q}_i=-\lambda\frac{\partial T}{\partial x_i} \qquad (7.4)$$

and inserting (7.4) in (7.3) (for constant λ)

$$-\lambda\left(\frac{\partial^2 T}{\partial x^2}+\frac{\partial^2 T}{\partial y^2}+\frac{\partial^2 T}{\partial z^2}\right)+\rho c_P\frac{\partial T}{\partial t}=S \qquad (7.5)$$

or

$$\frac{\partial T}{\partial t}=\frac{\lambda}{\rho c_P}\left(\frac{\partial^2 t}{\partial x^2}+\frac{\partial^2 t}{\partial y^2}+\frac{\partial^2 t}{\partial z^2}\right)+\frac{S}{c_P} \qquad (7.6).$$

The quotient $\lambda/\rho c_P$ is the thermal diffusivity α, thus

$$\frac{\partial T}{\partial t}=a\left(\frac{\partial^2 T}{\partial x^2}+\frac{\partial^2 T}{\partial y^2}+\frac{\partial^2 T}{\partial z^2}\right)+\frac{S}{\rho c_P} \qquad (7.7).$$

For steady state conduction in one dimension, with constant properties, the heat flux can be calculated with

$$\dot{q}=\frac{\lambda}{s}(T_2-T_1) \qquad [W/m^2] \qquad (7.8)$$

where s is the distance between points at the two temperatures T_1 and T_2. The conductive heat flux is driven by the temperature (T_2-T_1). The thermal conductivity λ also has a big influence, especially for polymers, where λ is low. To get an overview, examples of thermal conductivity λ, thermal diffusivity α and density ρ values are presented for some materials in Table 7.1.

Material	T [°C]	ρ [g/cm³]	λ [W/mK]	c_P [kJ/kgK]	α 10^{-6} [m²/s]
Air (1bar)	20.0	0.0012	0.0260	1.0071	21.47213
Water (1bar)	20.0	0.998	0.5996	4.1816	0.14336
PE-HD	20.0	0.95	0.43	2.2	0.19517
PC	20.0	1.2	0.1	1.15	0.14957
PVC	20.0	1.39	0.17	1.836	0.12744
Iron (Fe)	0.0	7.87	84.0	0.0435	24.53650
1.4301 (X 5 CrNi 18 10)	20.0	7.9	25.0	0.47	4.03986
Brass (Ms58)	20.0	8.45	113.0	0.41	31.17330
Aluminium (AlMg 1 Si 0.5)	20.0	2.7	125.0	1.106	68.98390

Table 7.1: Example values of density, thermal conductivity, specific heat and thermal diffusivity [138,139]

The low thermal diffusivity of polymers is significant, as this limits cooling rates during the calibration process.

7.2.2 Radiation

The heat flux by radiation from the surface at absolute temperature T can be calculated as

$$\dot{q}_{RAD} = \varepsilon \sigma T^4 \qquad [W/m^2] \qquad (7.9)$$

with Stefan-Boltzman constant σ ($5.67*10^{-8}$ W/m^2K^4), emissivity ε, which is the ratio of the radiation flux from the real body to that from a black body.

The heat flux exchange due to radiation between two surfaces can be calculated with

$$\dot{q}_{RAD} = \varepsilon_1 \varepsilon_2 C_{12} q (T_1^4 - T_2^4) \qquad (7.10)$$

where ε_1 and ε_2 are the emissivities of the two surfaces and C_{12}, the geometric factor, is dependent on the position and size of the two surfaces [138].

An emissivity of 0.95 can be used for polymers at thicknesses from a few tenths of a millimetre to a few millimetres. Below a few tenths of a millimetre, the influence of thickness must be taken into account [176].

7.2.3 Convection

The third mechanism in heat transfer is the convection. This contributes to the heat flux from the outer body surface to the environment, due to the motion of air or a coolant at a lower bulk temperature. Here, the heat flux can be expressed in terms of the temperature difference between the body surface T_2 and environment (air or coolant) T_1 and a heat transfer coefficient h

$$\dot{q}_{CONV} = h (T_2 - T_1) \qquad [W/m^2] \qquad (7.11).$$

It is clear to see that the heat transfer coefficient has an important function in this equation. The relative importance of convection and conduction can be represented with the Nusselt number Nu

$$Nu = \frac{hl}{\lambda} \qquad (7.12).$$

The characteristic length l must always be indicated for the calculations, and it must be made clear whether λ applies to the convecting fluid or the solid body. By dimensional analysis the heat transfer by convection can be expressed for the most general case by

$$Nu = f(Gr, Pr, Re) \qquad (7.13)$$

and for free convection

$$Nu = f(Gr, Pr) \tag{7.14}$$

and finally for pure forced convection

$$Nu = f(Pr, Re) \tag{7.15}.$$

The Grashof number Gr is defined as

$$Gr = \frac{\rho - \rho_0}{\rho} \frac{l^3}{\nu^2} \tag{7.16}$$

with the kinematic viscosity ν, densities ρ, ρ_0 and characteristic length l [177].

The Prantl number Pr represents the ratio of the momentum and thermal exchange due to heat diffusivities and can be expressed by

$$Pr = \frac{\nu}{\alpha} \tag{7.17}$$

with the kinematic viscosity ν and the thermal diffusivity α.

Finally the Reynolds number Re is defined as the inertia forces over the friction forces due to viscosity and can be obtained by

$$Re = \frac{\mathrm{v}\, l}{\nu} \tag{7.18}$$

with the velocity v, the characteristic length l, and viscosity ν.

A general overview of heat transfer coefficient values is given in Table 7.2.

Medium	Heat transfer coefficient [W/m^{2}K]
Static air	3 - 20
Flowing air	100 - 600
Static water	10 - 100
Flowing water	500 - 10,000
Boiling water	1,000 - 20,000
Condensing water steam	5,000 - 15,000

Table 7.2: Heat transfer coefficients in different media [138]

The heat transfer coefficients in Table 7.2 show a wide range of values. The reason is the influence of boundary conditions, e.g. laminar or turbulent flow in water or air. In a flow along a surface with a laminar layer on it, the laminar flow will be dominant in the heat transfer. At higher flow velocities, the boundary layer is changed from laminar to turbulent flow with a small remaining laminar sub-layer as shown for a flat plate in Figure 7.2.

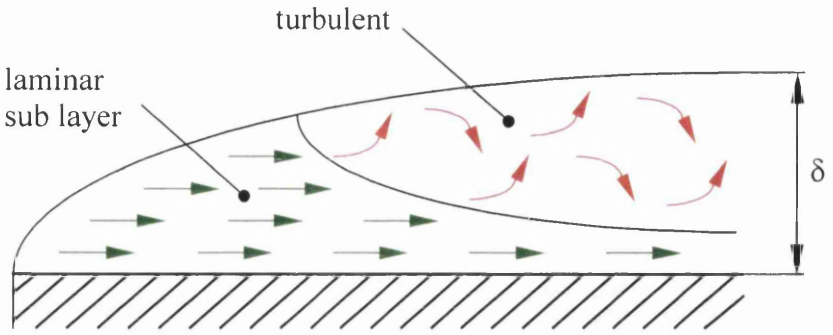

Figure 7.2: Turbulent boundary layer and laminar sub-layer for flow along a plate

The heat exchange accelerates in turbulent flow. This can be also achieved in calibration by stripping off the laminar layer in the water bath with discs or baffles that nearly touch the profile surface. This effect by stripping off was proved in [178] and is also patented in [179]. The heat transfer can also be improved by reducing the distance between the calibration discs in the water bath. A reduction from 50 mm to 20 mm in pipe calibration at 2 m/min increased the heat transfer coefficient by 67% [180].

In the calibration units, the heat from the profile is removed by the cooling agent in the cooling channels of the calibrator. An increase of heat flux can be achieved with an increase of temperature difference between the profile and the coolant and/or an increase of heat transfer coefficient, as mentioned before. The heat transfer coefficient can be increased significantly with turbulent flow in the cooling channels and to obtain this the Reynolds number Re must be higher than 2300. Turbulence may be induced for $Re < 2300$ by fittings, bends, etc. in pipes and channels (as in calibrators). Re can be calculated for circular pipes as

$$Re = \frac{v\, d}{\nu} = \frac{v\, d\, \rho}{\eta} \qquad (7.19)$$

with replacing of the characteristic length l in Eq. (7.18) with the pipe diameter d or using the density ρ and dynamic viscosity η instead of the kinematic viscosity ν.

A direct correlation of heat transfer coefficient and Re in a cooling channel is clear (as indicated in Eq. 7.15), and this is shown in Figure 7.3. A flow channel diameter of 6 mm and characteristic length of 1 m with water as the coolant medium was used for the calculations of the heat transfer coefficients at different coolant temperatures [138].

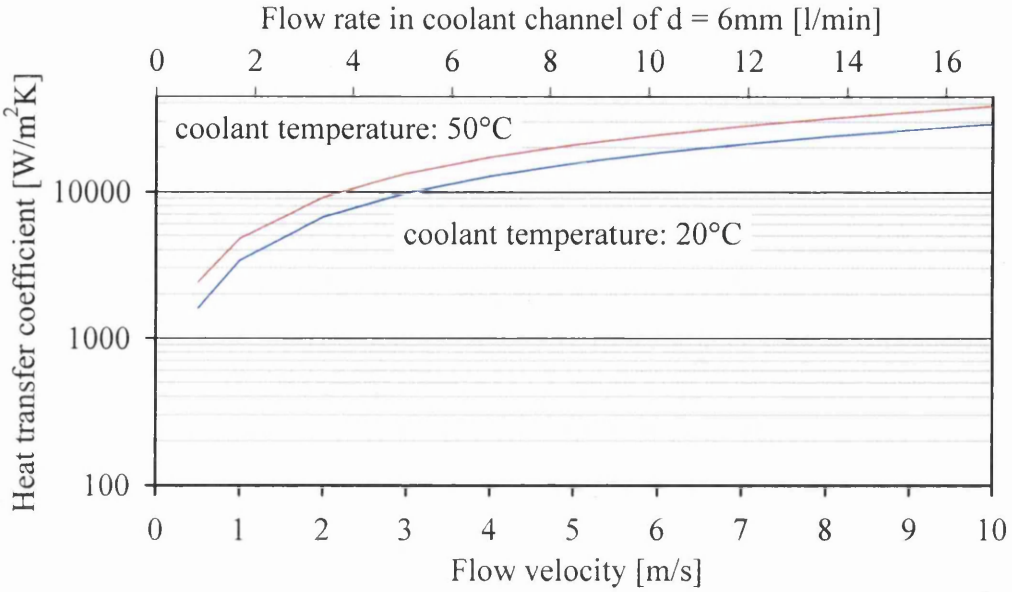

Figure 7.3: Calculated heat transfer coefficients as function of flow velocity for water at temperature of 20°C and 50°C in a pipe with inner diameter of 6 mm and length of 1 m; data in [138]

7.3 Typical heat transfer in calibration

To get an impression of the importance of the heat transfer in uPVC calibration, the thickness of the solidified layer of the profile below the glass temperature T_g of 80°C, at different line speeds, is shown in Figure 7.4. The Finite Difference Method (FDM) was used for these calculations and will be explained in a later section (Section 7.4). In the calculations, the heat transfer is present at the outer side; the inner side is set to an adiabatic boundary condition.

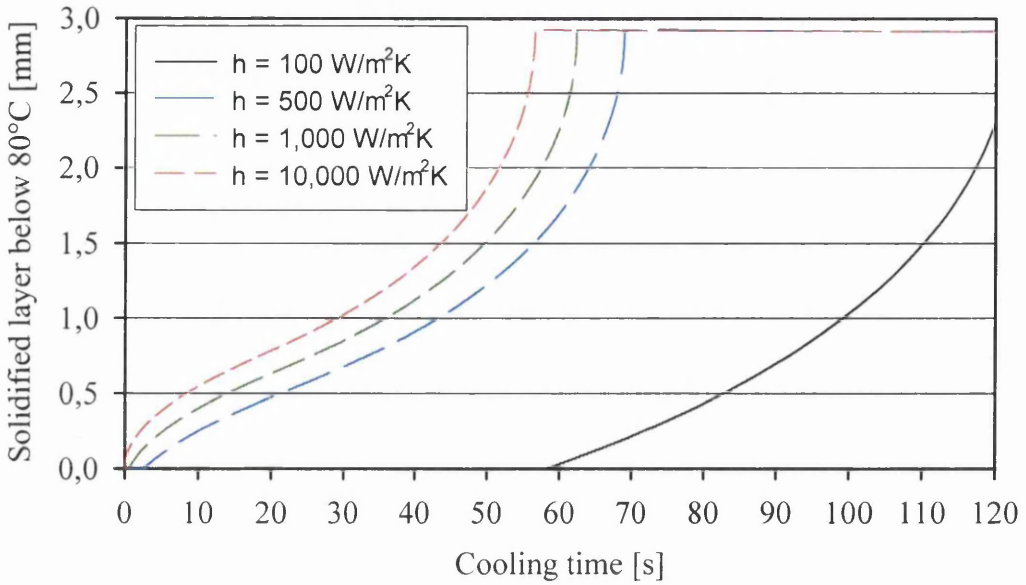

Figure 7.4: Solidified layer below 80°C of a PVC plate at different heat transfer coefficients; initial profile wall thickness 3.00 mm; adiabatic inside; coolant water temperature 20°C

The heat transfer coefficient of 10,000 W/m^2 K can be considered as corresponding to ideal contact of the calibrator and PVC. At 10,000 W/m^2 K, the solidified layer thickness at a cooling time of 10 s is approximately twice as great as for 500 W/m^2 K. This solidified layer carries tensile haul-off forces, and the thicker the solidified layer, the lower is the stress in the profile.

In addition to the heat transfer coefficient, the low thermal diffusivity of the plastic material is a limiting factor in the calibration process. An overall heat transfer coefficient H can be defined for a plate by

$$\frac{1}{H} = \frac{1}{\frac{1}{h_{OUT}} + \frac{s}{\lambda} + \frac{1}{h_{INS}}} \qquad [\mathrm{m^2\,K/W}] \qquad (7.20)$$

where h is the heat transfer coefficient at the outer or inner surface, s is the material thickness and λ its thermal conductivity. In general, (7.20) applies only for steady state heat transfer when the thermal resistance of the plastic can be expressed as s/λ. With an adiabatic boundary condition at the inner side, as shown before in Fig. 7.4, the quotient $1/h_{INS}$ can be neglected in (7.20).

In Figure 7.5, the reciprocal value of the overall heat transfer coefficient H, is presented as function of plate thickness s, calculated with (7.20) using heat transfer coefficients from 500,

1,000, 2,500 to 5,000 W/m^2 K, thermal conductivity of PVC λ_{PVC} = 0.17 W/m K and adiabatic inside.

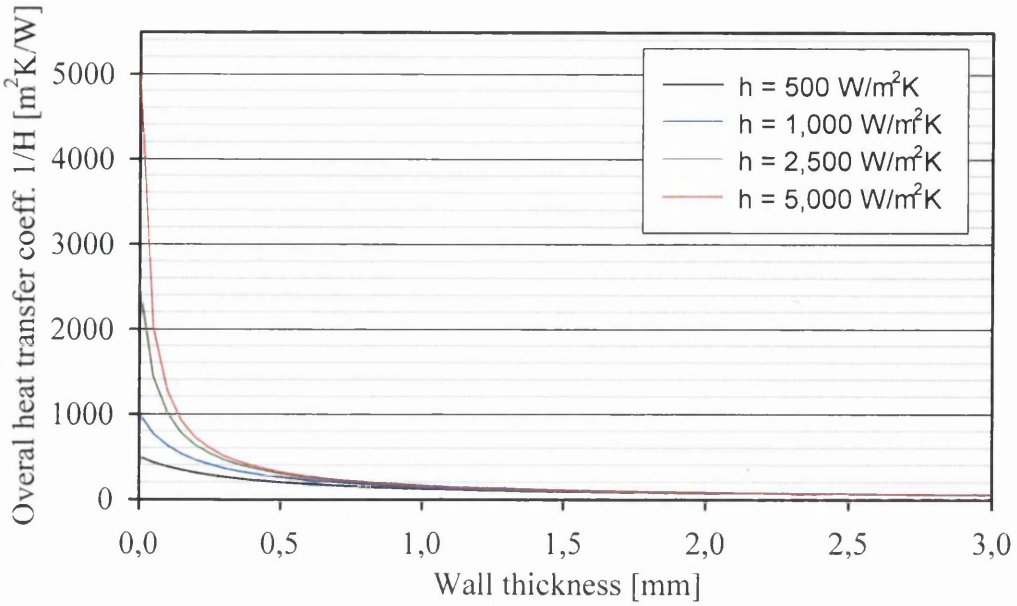

Figure 7.5: Reciprocal value of the overall heat transfer coefficient H of uPVC as function of wall thickness for different heat transfer coefficients h, λ_{PVC} = 0.17 W/m K

For wall thickness of around 0.6 mm, the reciprocal value of the overall heat transfer coefficient is similar for all heat transfer coefficients from 500 to 5000 W/m^2 K, because the thermal conductivity and so the thermal diffusion of the uPVC dominates.

This leads to the conclusion, that the heat transfer coefficient has a weaker influence with increase of cooling length in the calibration process. According to equation (7.11), the heat flux is a function of heat transfer coefficient and the temperature difference. To see their influence in downstream region, the Finite Difference Method (FDM) is used for the calculation of the cooling of a infinite plate. In these calculations, the heat transfer coefficients and coolant temperatures are varied in the water bath after the calibration units (calibration section) in an exemplary calibration line of 12 m length. The calibration section is set-up with 6 calibration units of length 450 mm, with intermediate water baths of 50 mm length. In the calculations, heat transfer coefficients are assumed of 1000 W/m^2 K in the calibrator, 500 W/m^2 K in the intermediate water baths and an overall coolant temperature of 20°C in the calibrator section. The initial melt temperature was set to 195°C. In the first set of calculations, the heat transfer coefficients in the water bath after the calibration section are varied from 100, 500, 1,000 to 10,000 W/m^2 K at constant coolant temperature of 20°C. In

second set, the coolant temperatures are varied from 20, 10, -20 to –40°C for constant heat transfer coefficient h of 500 W/m^2 K.

First, the influence of the heat transfer coefficient on the solidified layer in the downstream water bath is shown in next Figure 7.6.

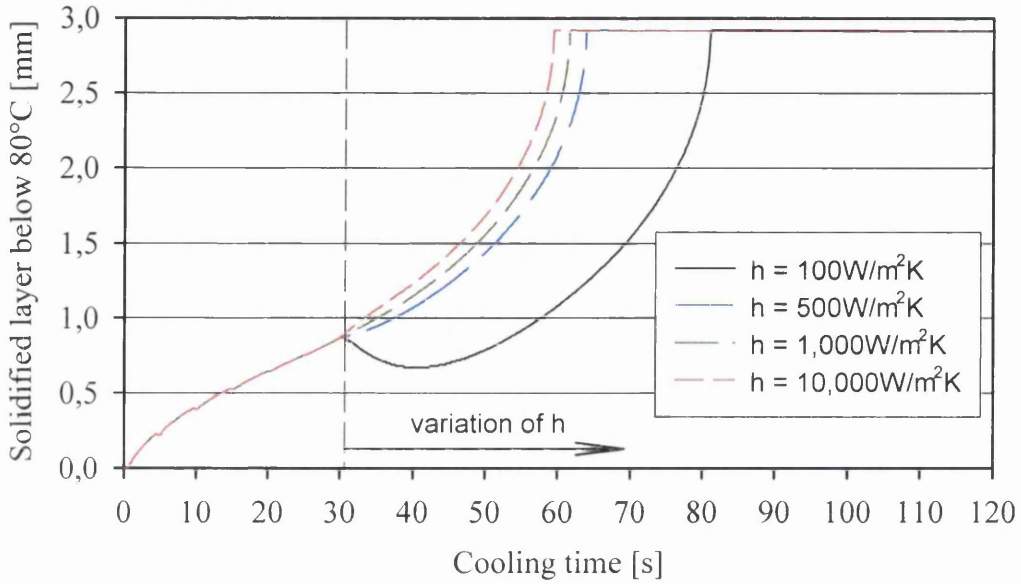

Figure 7.6: Solidified layer below 80°C of a PVC plate at different outside heat transfer coefficients in the water bath after calibration section; initial profile wall thickness 3.00 mm, adiabatic inside; outside coolant water temperature 20°C

At 100 W/m^2 K, a re-heating of the profile is visible after the calibration units, which reduces the layer below 80°C due to higher heat transfer from the inner profile to the outer surface and reduced heat transfer from the outer profile surface to the water bath.

An increase of the heat transfer coefficient from 500 W/m^2 K to 10,000 W/m^2 K reduces the cooling time by 6 %, but the highest heat transfer coefficient cannot be achieved with a normal water bath, except possibly in the presence of highly turbulent flow. The other factor in the cooling is the coolant temperature, and a reduction leads to reduced cooling time, see Figure 7.7.

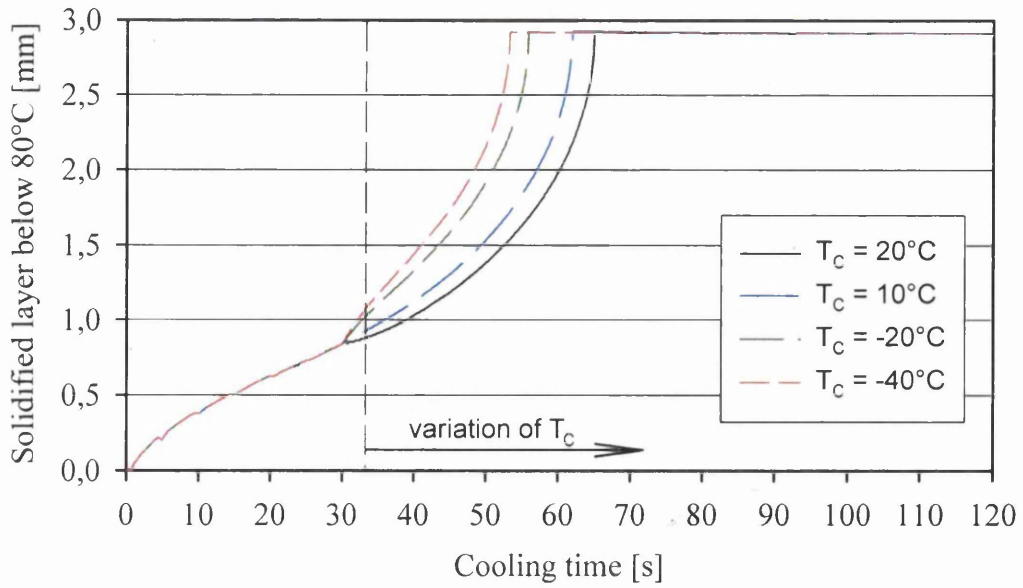

Figure 7.7: Solidified layer below 80°C of a PVC plate at different coolant temperatures in the water bath after calibration units; thickness 3.00 mm, inside adiabatic; outside heat transfer coefficient in water bath 500 $W/m^2 K$

Coolant temperatures below freezing point of course, cannot be achieved in water-cooling. So other processes, e.g. liquid nitrogen, must be used to obtain lower coolant temperatures. Using a coolant temperature of –20°C, the cooling time is reduced by 12.5% and with –40°C the cooling time could be reduced by 16%. Cooling with liquid nitrogen is used in cable production [176] and can increase the line speed in production of doorframes up to 110% [181].

7.3.1 Published heat transfer coefficients in the calibration process

Many investigations were done in the past to estimate the heat transfer coefficients in PVC calibration. An overview is given in following Tables 7.3a and 7.3b.

Ref.	System	Type	Line speed [m/min]	Heat transfer coefficient [$W/m^2 K$]	Comment
[182]	Spray tank	Pipe	0.4 – 2.2	1,500 – 250	Decrease in downstream direction
[68]	Vacuum tank	Pipe	0.5 – 1.7	500 - 600	
[68]	Water bath	Pipe	0.5 – 1.7	600 - 450	
[66]	Water bath	Pipe	2.2	850 –550	Decrease in downstream direction
[66]	Water bath	Pipe	0.95 – 3.75	600 – 960	Increase with line speed
[180]	Water bath	Pipe	2.0	410	Free convection
[180]	Water bath with calibration discs	Pipe	2.0	580 – 920	Higher values for shorter distance of calibration discs
[180]	Spray	Pipe		1,750	
[180]	Air	Pipe		10	

Table 7.3a: Heat transfer coefficients in PVC pipe calibration

Ref.	System	Type	Line speed [m/min]	Heat transfer coefficient [W/m^2 K]	Comment
[183]		Profile extrusion		500 – 2,500	General
[184]	Calibrator	Shutter	1.1 – 1.4	360 - 560	T-section
[184]	Calibrator	Shutter	1.1 – 1.4	1,700 – 2,100	Plate section between two T-sections
[184]	Calibrator	Shutter	1.1 – 1.4	600 - 900	Two side cooling
[184]	Calibrator	Picture frame	1.8 – 1.9	1,450 – 2,200	T-section
[184]	Calibrator	Picture frame	1.8 – 1.9	1,500 – 2,480	Plate section
[184]	Calibrator	Picture frame	1.8 – 1.9	820 – 1,200	Two side cooling
[184]	Calibrator	Curtain rail	1.1 – 1.4	1,230 – 2,300	T- section
[184]	Calibrator	Curtain rail	1.1 – 1.4	1,020 – 1,730	Plate section
[184]	Spray		0.48	300 - 400	Flat cone sprayer
[184]	Spray		0.48	190 - 320	Full cone sprayer
[184]	Water bath		0.48	210 - 230	
[154]		Picture frame	2.5	850 – 2000	
[154]		Hollow chamber	1.0	700 – 2,000	
[154]		Hollow chamber	1.9	600 – 2,500	
[154]		Curtain rail	1.0	400 - 1800	
[185]	Calibrator	Rectangular profile	0.5 – 1.5	10 – 10,000	Decrease with Fourier number

Table 7.3b: Heat transfer coefficients in PVC profile calibration

7.4 Experimental results for profile surface and calibrator wall temperatures

In the overview of the experiments results in Chapter 5, some examples of temperatures along the calibration line were shown, and more details are now presented here.

7.4.1 Effects of vacuum in wet and dry calibration at different line speeds

It was shown in Chapter 5 that the profile surface temperatures are close to the coolant temperature of 14°C to 16°C at downstream distance of 200 mm for the low line speed of 1m/min, and at 400 mm for the highest line speed of 8 m/min. Further, the profile surface temperatures are higher at higher line speeds, and this results from the shorter cooling time of the profile at the same downstream distance.

A re-heating of the profile surface is present between calibrators in wet and dry calibration, see following Figures. In dry calibration, the re-heating is significantly higher than in wet calibration, where only a slight re-heating was measured. This is based on a higher heat transfer coefficient in the water baths compared with coefficients in air, as mentioned before. The re-heating effect is more pronounced in the first water bath, and less pronounced in the downstream water baths. This is based on the steepness of the temperature gradient in the profile wall. The gradient in the outer layers decreases in downstream direction and in combination with the low diffusivity of the material, a longer distance is necessary to obtain the same level of re-heating.

A remarkable effect was observed in the temperatures measured at the centre and close to the edges of the profile. This was presented for dry calibration in Figures 5.13 and 5.14 and to recall these, the same Figures are inserted again here as Figures 7.8 and 7.9.

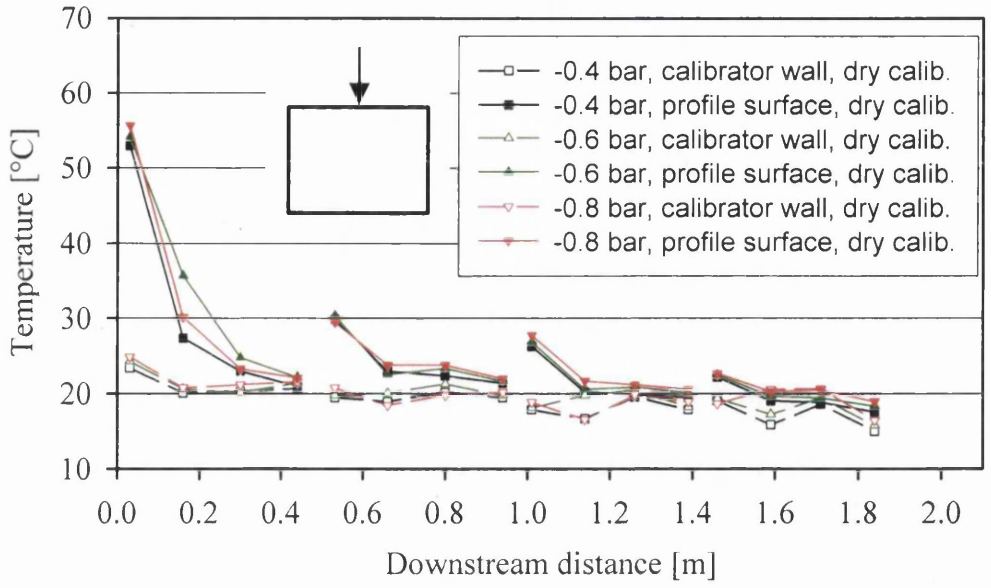

Figure 7.8: Profile surface and calibrator wall temperatures at the centre for different vacua; 3 m/min line speed; 2.50 mm die exit; 2.50 mm profile wall thickness; dry calibration

A direct comparison of temperatures in dry calibration at the centre and at the edge shows better cooling at the centre.

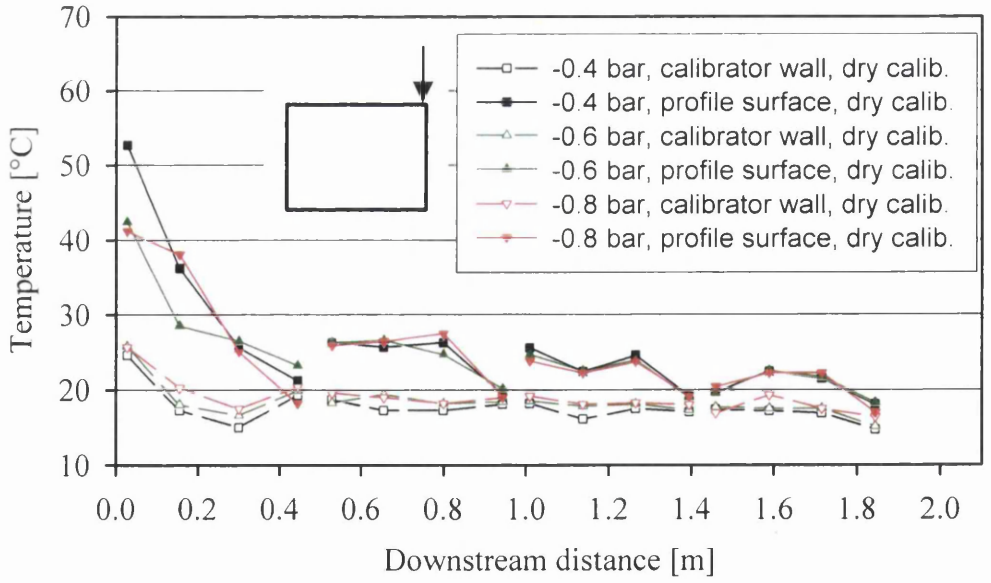

Figure 7.9: Profile surface and calibrator wall temperatures near the right edge for different vacua; 3 m/min line speed; 2.50 mm die exit; 2.50 mm profile wall thickness; dry calibration

This is based on a loss of contact of profile surface and calibrator wall at the edges of the profile. Other interesting effects are also present in wet calibration and to recall this, the Figures 5.15 and 5.16 are inserted now as Figure 7.10 and 7.11.

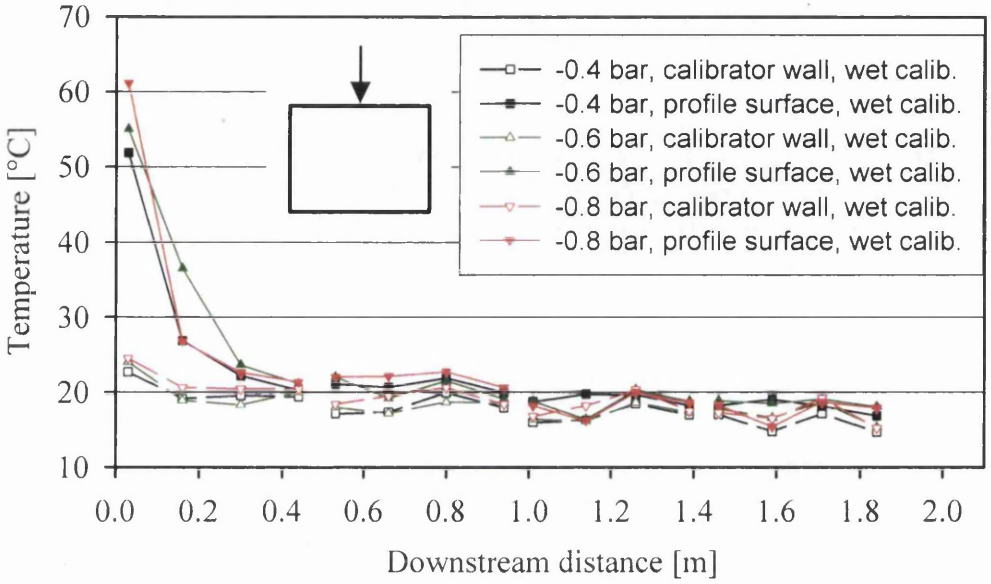

Figure 7.10: Profile surface and calibrator wall temperatures at the centre for different vacua; 3 m/min line speed; 2.50 mm die exit; 2.50 mm profile wall thickness; wet calibration

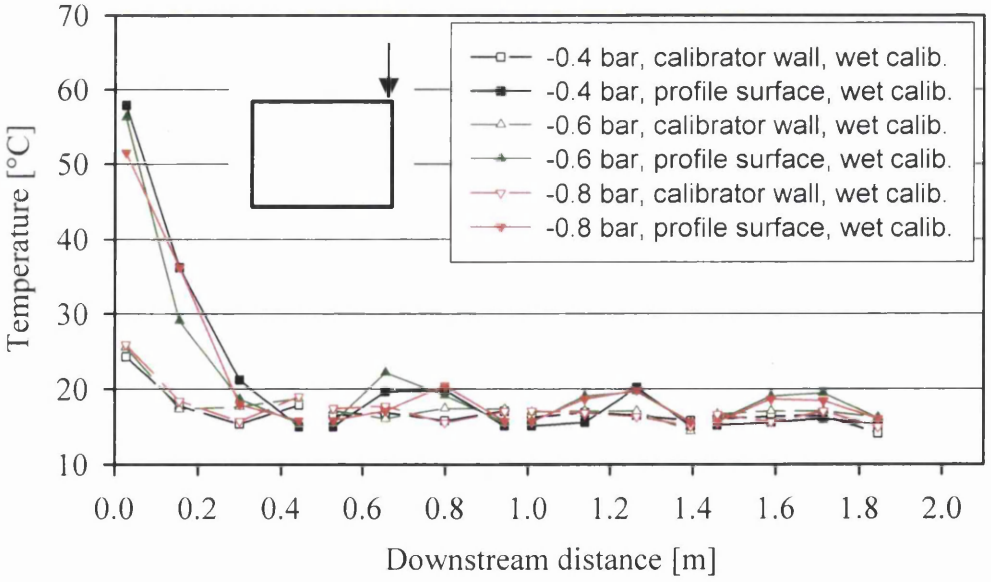

Figure 7.11: Profile surface and calibrator wall temperatures near the right edge for different vacua; 3 m/min line speed; 2.50 mm die exit; 2.50 mm profile wall thickness; wet calibration

For direct comparison, the calibrator wall and profile surface temperatures are plotted separately, first the calibrator wall temperatures in Figure 7.12.

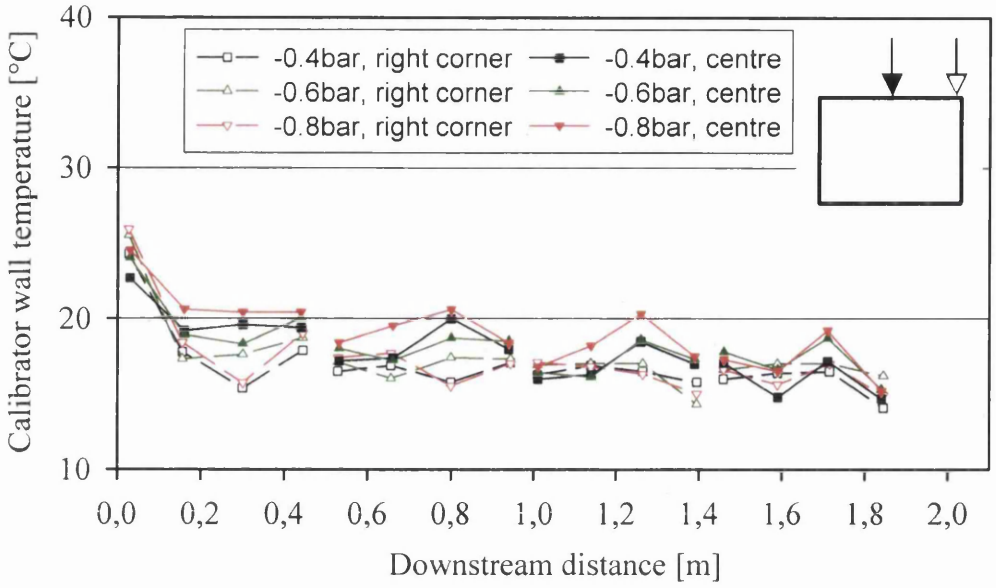

Figure 7.12: Temperatures of the calibrator wall at different vacuum at the centre and near to the right edge; 3 m/min line speed, 2.50 mm die exit; 2.50 mm profile wall thickness; wet calibration

The calibrator wall temperatures are higher for the centre than for the edge, except at a few points.

At the edge, the temperatures seem to be lower at the entrance and exit, especially in Calibrators 3 and 4. It may be that there is an effect of coolant water in the intermediate water baths, which is drawn in by the applied vacuum into the calibrator. If this is the case, the same effect should be visible for the profile temperatures as well.

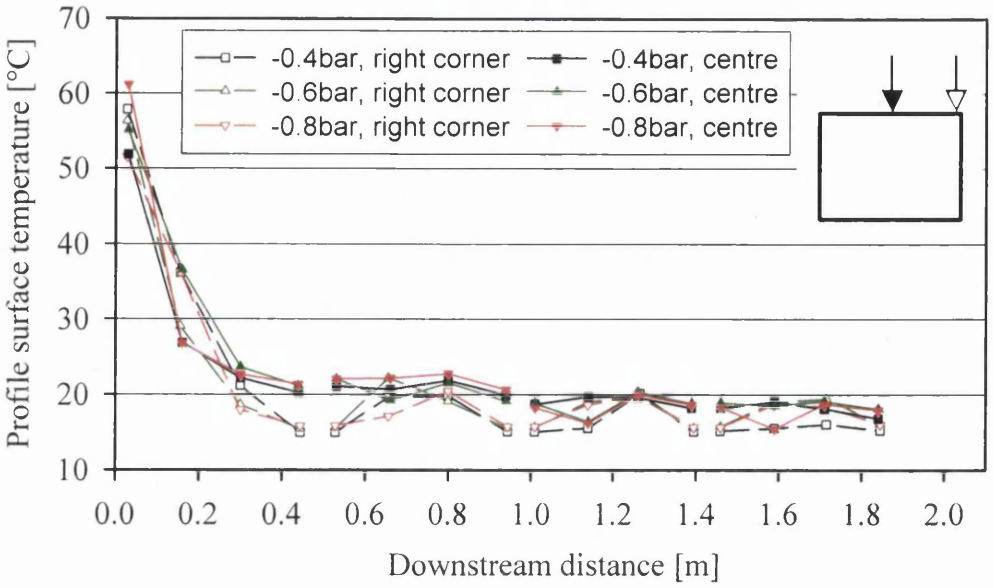

Figure 7.13: Temperatures of the profile upper surface at different vacuum at the centre and near to the right edge; 3 m/min line speed, 2.50 mm die exit; 2.50 mm profile wall thickness; wet calibration

The profile surface temperature is lower at the edges due to reduction of corner dimensions, as shown the Section 6.2 about profile geometry, and is seems that the surface temperature at the edges is the same as the coolant temperature in the water baths of 14°C to 16°C. In Figure 7.13 the corner temperature is higher than the temperature at the centre at 100 mm:

The reason for this seems to be based on a draw down in Calibrator 1. Another effect must be stated. The increase of profile surface temperatures within the downstream calibrators can be based on a reduction of cooling near the calibrator mid point. This makes sense, because the water from the water baths is drawn into the calibrator from both sides due to applied vacuum. Then the water flows directly into the vacuum system, and this leads to the well know air-water mixture in the vacuum system, and leaving the mid-region of the calibrator without water in the clearance between calibrator and profile surface.

These effects are also present in Figure 7.14 for a line speed of 5 m/min, as for a line speed of 3 m/min in the foregoing Figure 7.13.

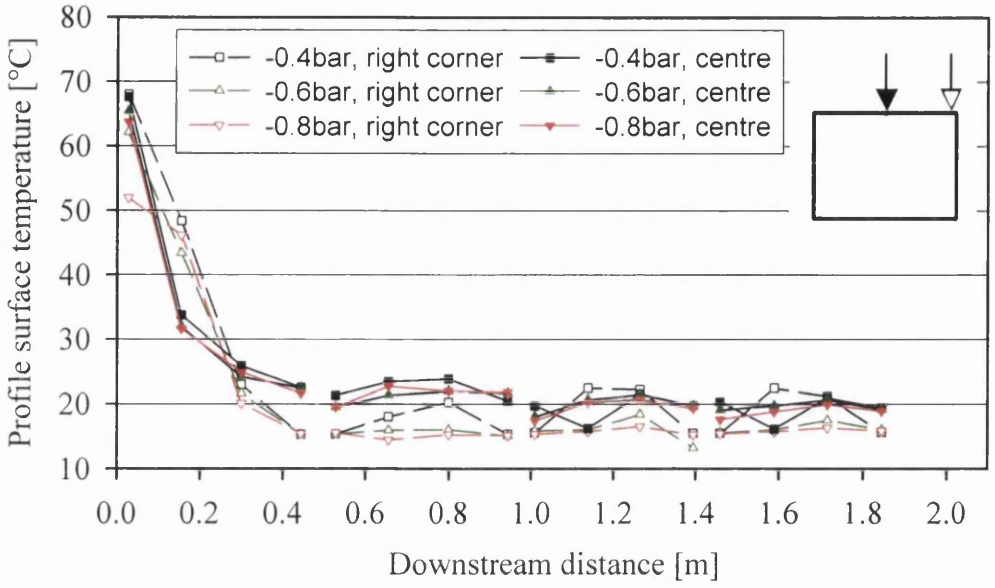

Figure 7.14: Temperatures of the profile upper surface at different vacuum at the centre and near to the right edge; 5 m/min line speed; 2.50 mm die exit; 2.50 mm profile wall thickness; wet calibration

The effect of re-heating is more developed at higher line speeds of 7 m/min and 8 m/min, as seen in Figure 7.15, due to the higher temperature gradients near the surface in the plastic.

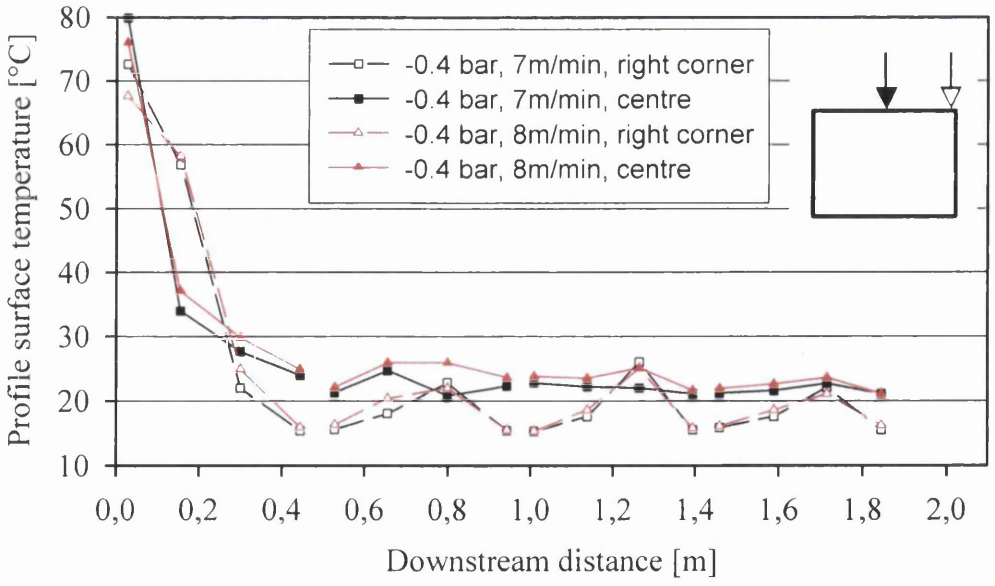

Figure 7.15: Temperatures of the profile upper surface at the centre and near to the right edge for 7 m/min and 8 m/min line speed and –0.4 bar vacuum; 2.50 mm die exit; 2.50 mm profile wall thickness; wet calibration

The loss of contact between the profile surfaces in Calibrator 1 is also visible at the highest line speeds as indicated by the higher profile surface temperatures at short downstream

distances (100-200 mm). It seems that the loss of contact if shifted towards the inlet of Calibrator 1 with increase of line speed. This increases the gaps between the profile and calibrator, and with the effect of the inflow of water from the water bath, the heat transfer coefficient is higher at the downstream end of the Calibrator 1, and at the ends of the other calibrators. The reduction of the profile dimension leads to an increase of the inflow area, which is marked in Figure 7.16.

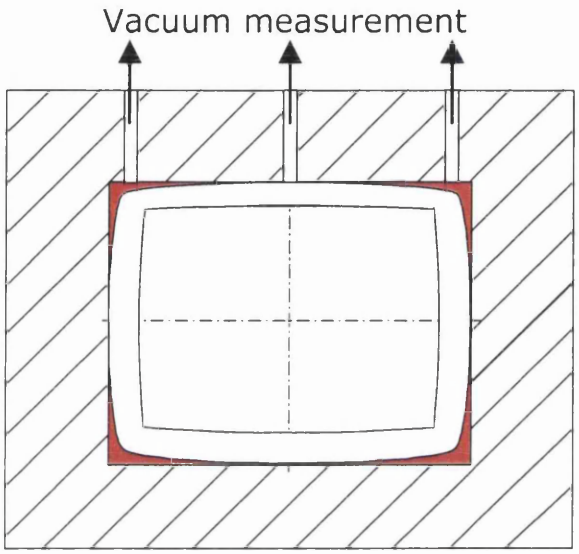

Figure 7.16: Cross section of calibrator and profile with measurement points for vacuum at the centre and edges. Distortion of the profile cross section is exaggerated. Calibrator-profile clearance space shown in red

The water in the vacuum-air mixture was measured with a simple separation process as described in Chapter 4, on the experimental set-up.

Higher vacuum leads to higher inflow rates of water from the intermediate water baths into the all four Calibrators, and this is shown in Figure 7.17.

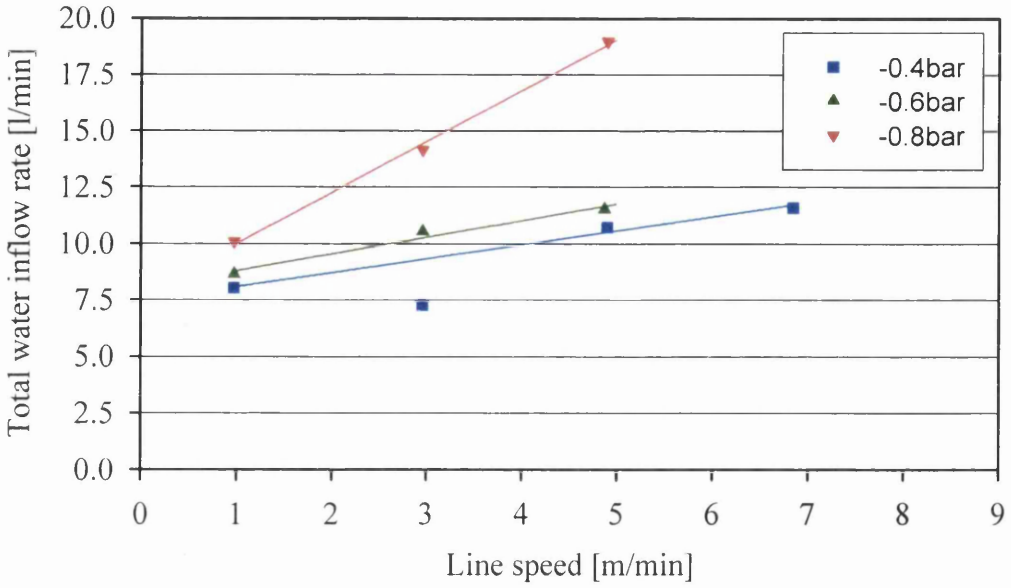

Figure 7.17: Total water inflow rates of the four Calibrators at different line speeds and applied vacuum for all calibrators; 2.50 mm die exit; 2.50 mm profile wall thickness; wet calibration

The trend lines look similar to the forces as function of line speed, which were shown before in Chapter 6. The forces reduce the profile dimensions, especially the corner dimension C, see Section 6.2. So an increase of flow rate seems to be based on a reduction of profile dimensions. This is confirmed in Figure 7.18, where the total inflow rate is shown as function of the circumference C.

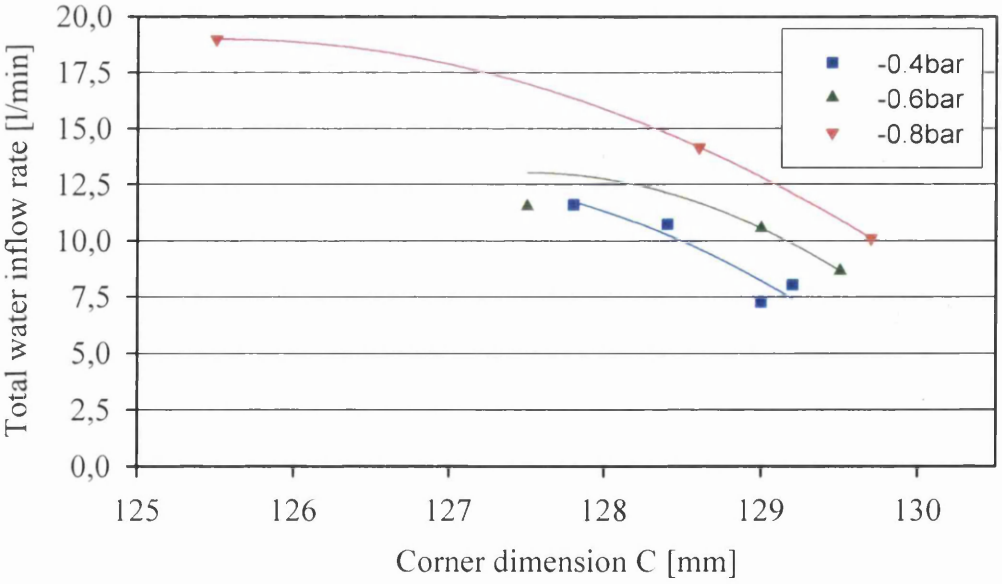

Figure 7.18: Total water inflow rates of the 4 Calibrators as function of the corner dimension C at different applied vacuum for all calibrators; 2.50 mm die exit; 2.50 mm profile wall thickness; wet calibration

A clear correlation of total inflow rate and C is visible in Figure 7.18, with higher values at higher vacua. A similar correlation is given for Calibrator 1 in Figure 7.19, because most of draw down occurs here.

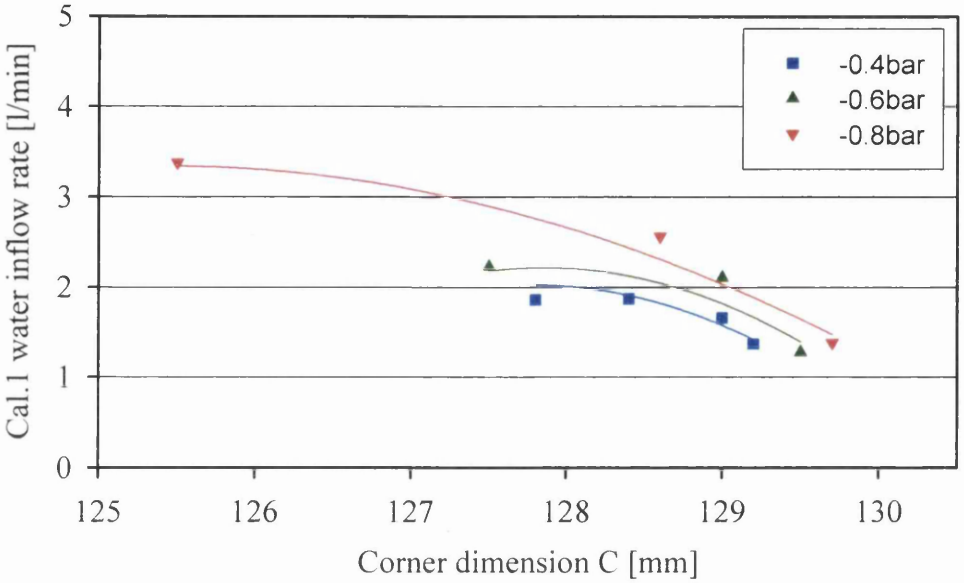

Figure 7.19: Calibrator 1 water inflow rates of the 4 Calibrators as function of the corner dimension C at different applied vacuum for all calibrators; 2.50 mm die exit; 2.50 mm profile wall thickness; wet calibration

The higher inflow rate at higher vacuum may be the explanation of the lower profile surface temperatures at the higher line speed of 5 m/min in Figure 7.14. A higher inflow rate increases the velocity in the gaps between profile and calibrator wall. A higher vacuum tends to draw in the water further into the calibrator than for lower vacuum. These two effects can explain the influence of the better cooling within the calibrator at higher line speeds.

In the following Figures, only the profile surface temperature will be shown, for variations of profile wall thickness, vacuum and melt extrusion and coolant temperatures.

7.4.2 Effects of wall thicknesses in wet calibration

The variation of the profile wall thickness has no significant influence on the profile surface temperatures; they are close for the same vacuum and line speed, see Figure 7.20.

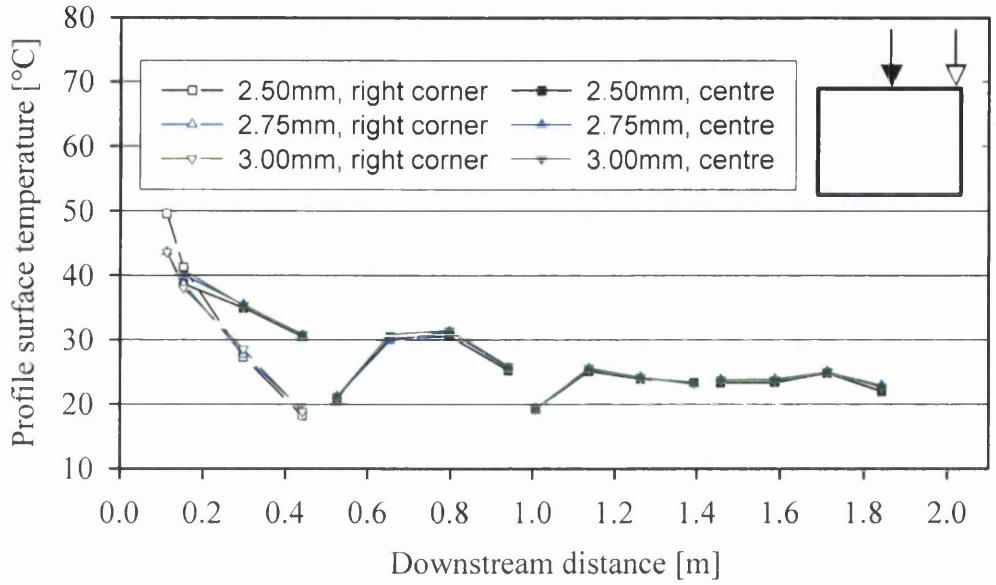

Figure 7.20: Temperatures of the profile upper surface for different profile wall thicknesses at the centre and near to the right edge; 8 m/min line speed; -0.4 bar vacuum; 2.50 mm die exit; wet calibration

The temperature near the edge is higher in the upstream direction. This leads to the conclusion that a higher line speed drags the inflowing water back into the water bath following the calibrator in the haul-off direction. Another, not to be neglected factor, is the draw down immediately downstream from the Calibrator 1 inlet, which can lead to a loss of contact of the profile surface and the calibrator wall within the first 200 mm of Calibrator 1.

7.4.3 Effects of vacuum in Calibrator 1 and wall thicknesses in wet calibration

The variation of vacuum in Calibrator 1, for constant vacuum in downstream calibrators, has no significant influence on the surface temperatures at the centre for a profile thickness of 2.50 mm. But the temperatures near the edge show an influence of vacuum, see Figure 7.21.

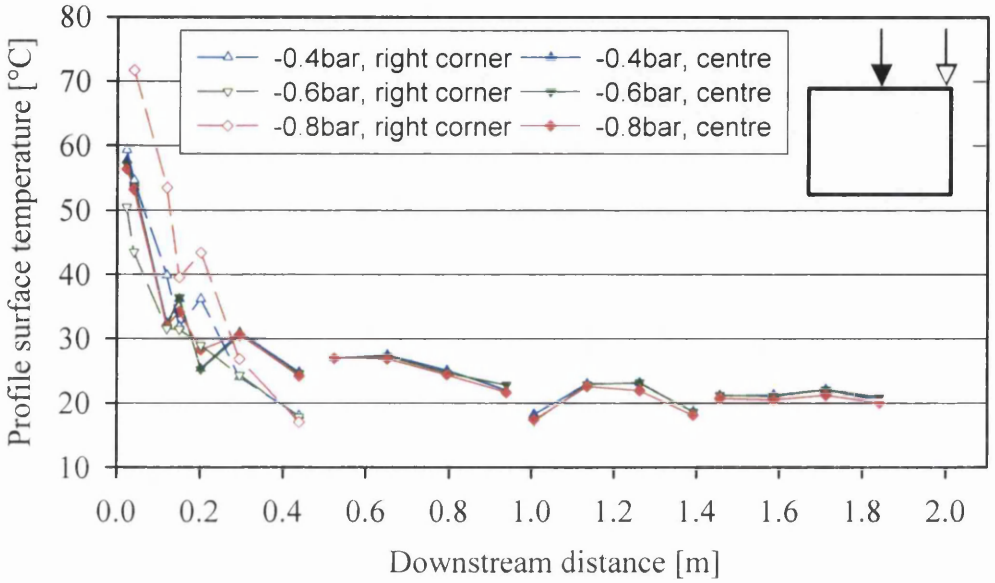

Figure 7.21: Temperatures of the profile upper surface for different vacua in Calibrator 1 at the centre and near to the right edge; 2.50 mm profile wall thickness; 4 m/min line speed; -0.4 bar vacuum in downstream calibrators; 2.50 mm die exit; wet calibration

Near the inlet to Calibrator 1, temperatures increase at the highest applied vacuum level. This is probably due to increased draw down and loss of contact at the edge due to the higher forces at higher vacuum. However, at the downstream end of Calibrator 1, the vacuum draws water into the clearance, resulting profile surface temperature close to the coolant temperature.

Another factor is the profile wall thickness. The effect of water inflow is reduced with increase of wall thickness and this in shown in following Figures 7.22 to 7.24.

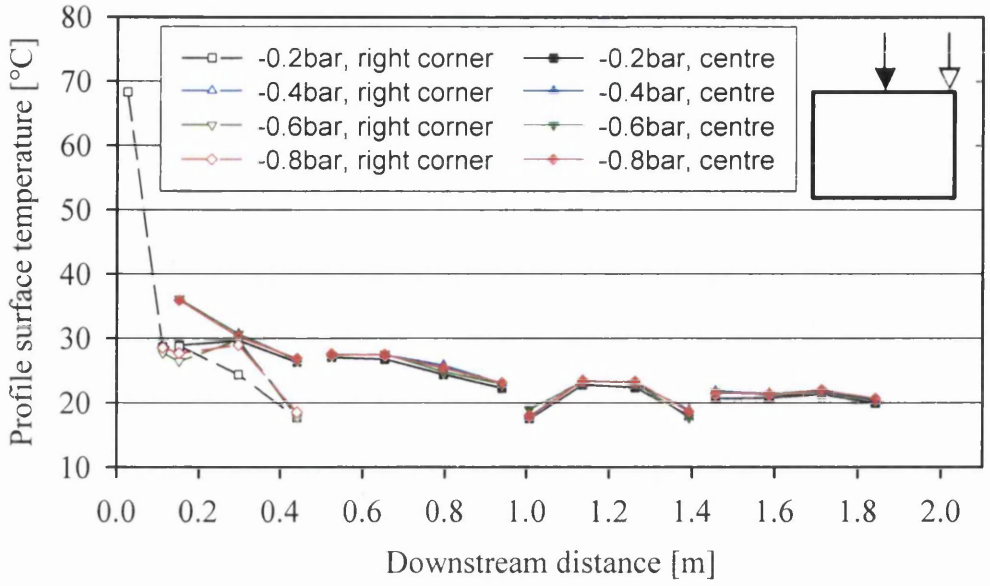

Figure 7.22: Temperatures of the profile upper surface for different vacua in Calibrator 1 at the centre and near to the right edge; 2.75 mm profile wall thickness; 4 m/min line speed; -0.4 bar vacuum in downstream calibrators; 2.50 mm die exit; wet calibration

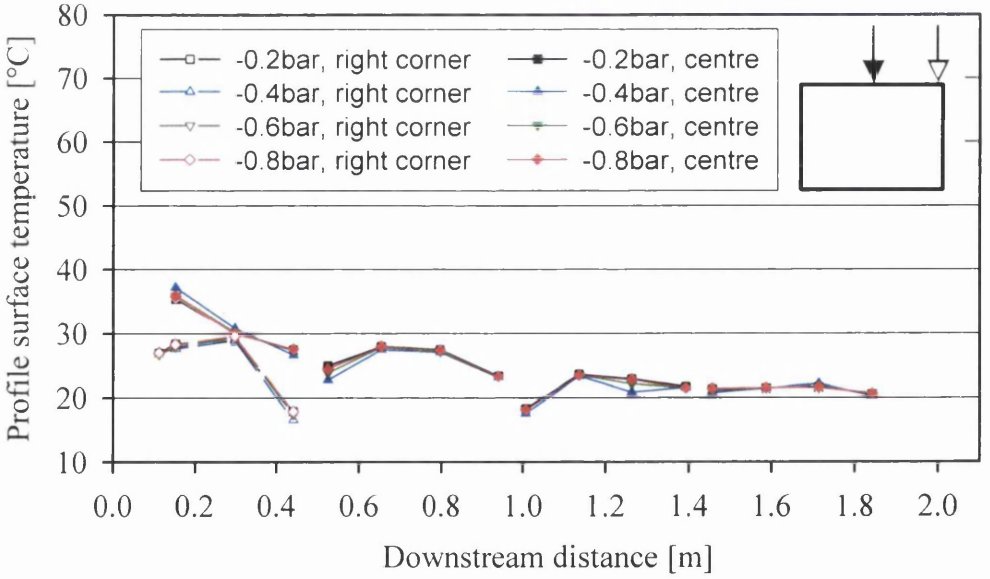

Figure 7.23: Temperatures of the profile upper surface for different vacua in Calibrator 1 at the centre and near to the right edge; 3.00 mm profile wall thickness; 4 m/min line speed; -0.4 bar vacuum in downstream calibrators; 2.50 mm die exit; wet calibration

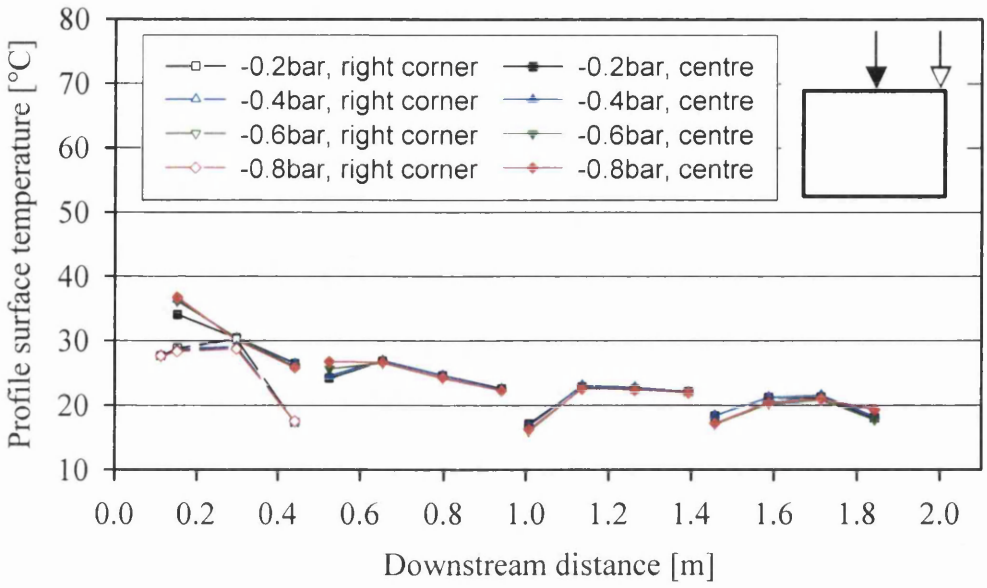

Figure 7.24: Temperatures of the profile upper surface for different vacua in Calibrator 1 at the centre and near to the right edge; 3.25 mm profile wall thickness; 4 m/min line speed; -0.4 bar vacuum in downstream calibrators; 2.50 mm die exit; wet calibration

The variation of vacuum in downstream calibrators will not be presented, because the major effects of draw down appear for the profile corners in Calibrator 1.

7.4.4 Effects of melt extrusion and coolant temperatures in wet calibration

An increase of melt extrusion temperature produces higher re-heating at the entrance of second calibrator, but the profile surface temperatures are not effected elsewhere, see Figure 7.25.

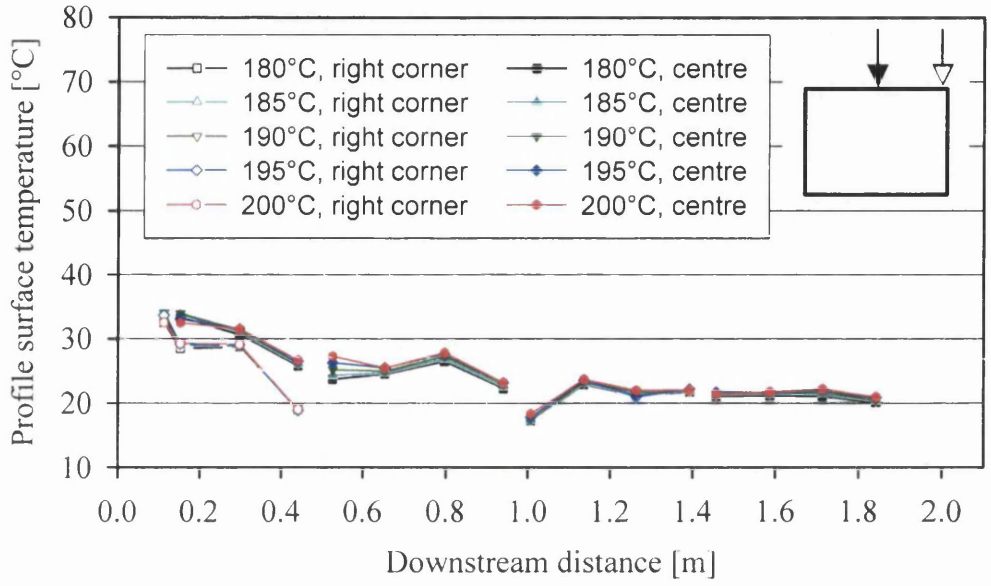

Figure 7.25: Profile surface temperatures for different melt extrusion temperatures at the centre and near to the right edge; -0.4 bar vacuum; 4m/min line speed; 2.50 mm die exit; 2.75 mm profile wall thickness; wet calibration

An increase of coolant temperatures in Calibrator 1 (whilst maintaining a coolant temperature of 14–16°C in downstream water baths and calibrators) shows an influence on surface temperatures, as visible in Figure 7.26.

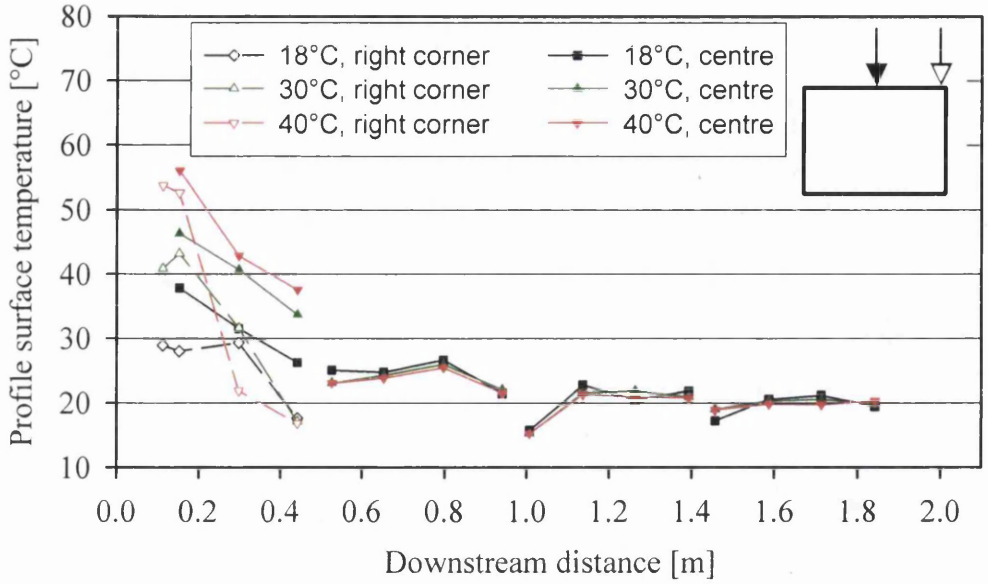

Figure 7.26: Profile surface temperatures for different coolant temperatures in Calibrator 1at the centre and near to the right edge; -0.8 bar vacuum; 4 m/min line speed; 2.50 mm die exit; 3.00 mm profile wall thickness; wet calibration

The centre temperatures increase noticeably with increase of coolant temperatures in Calibrator 1. In comparison, the edge temperatures show no influence at the exit of Calibrator 1, but increase towards the inlet with rising coolant temperatures. The reason for this is no doubt the inflow of water into the gap between the profile and calibrator at the edges from the water bath at 14-16°C.

7.5 Estimation of heat transfer coefficients with numerical methods

The heat transfer coefficient is an important parameter in the calibration process. Low coefficients lead to longer cooling times and this reduces the profitability of the line. For numerical simulations of the calibration, an idea of the magnitude of the transfer coefficients is necessary for the boundary conditions in the calibration process, together with their dependence on the process parameters.

Estimations were done in the past and the results were presented in Table 7.3a and 7.3b. They were obtained with the Finite Difference Method (FDM) and the Finite Element Method (FEM). The FEM should be used for complex profile geometries with several chambers in the profile, because the radiation and free convection in the chambers must be included in the calculation, as is proved in [186].

For the profile used in present work, the FDM is sufficient, because the geometry is simple and the calculation times are therefore shorter.

7.5.1 Finite difference method

The equation (7.7) is simplified by deleting the source of heat and assuming that conduction in the PVC in line direction (z-), and cross direction (y-) is small compared with conduction in the thickness (x-)

$$\frac{\partial T}{\partial t} = a \frac{\partial^2 T}{\partial x^2} \qquad (7.21).$$

Using initial conditions at $t = 0$ of

$$0 \le x \le l, \qquad T = T_{INITIAL} = T_{MELT(=195°C)} \qquad (7.22)$$

and boundary condition for $t > 0$:

$$x = 0, \qquad \frac{\partial T}{\partial x} = 0 \text{ (adiabatic conditions at the inner side of the profile)} \qquad (7.23)$$

$$x = l, \qquad k \frac{\partial T}{\partial x} = h (T - T_0) \qquad (7.24)$$

with the thermal conductivity k, (overall) heat transfer coeffcient h and coolant temperature T_0.

For the solving of (7.21), the explicit method is used due to its computational simplicity. Here, the calculation is stable if (7.25) is valid

$$\alpha \frac{\Delta t}{\Delta x^2} \leq 0.5 \qquad (7.25).$$

The calculation scheme uses for the first derivative the approximation

$$\frac{\partial T}{\partial t} = \frac{T_{i,j+1} - T_{i,j}}{\Delta t} \qquad (7.26)$$

and for the second derivative

$$\frac{\partial^2 T}{\partial x^2} = \frac{T_{i+1,j} - 2T_{i,j} + T_{i-1,j}}{(\Delta x)^2} \qquad (7.27)$$

which on substitution into (7.21) give

$$\frac{T_{i,j+1} - T_{i,j}}{\Delta t} = \frac{T_{i+1,j} - 2T_{i,j} + T_{i-1,j}}{(\Delta x)^2} \qquad (7.28).$$

In the calculations, the thermal conductivity is set as constant, whereas the specific volume and the specific heat are used temperature dependent. With change in density, the step size Δx changes with temperature. In the calculation routine, the step size Δx was set equal with Δx_{NEW} and this was calculated by

$$\Delta x_{NEW} = \Delta x_{START} \sqrt[3]{\left(\frac{v_{NEW}}{v_{START}} \right)} \qquad (7.29)$$

with the initial increment Δx_{START}, the specific volume v_{NEW} calculated with last temperature of increment Δt_{-1} and the initial specific volume v_{START}.

The specific heat was also calculated with temperature of last increment Δt_{-1}.

Here, as indicated in Figure 7.27, j is the time index, and i the x-position index, with grid increments Δt and Δx.

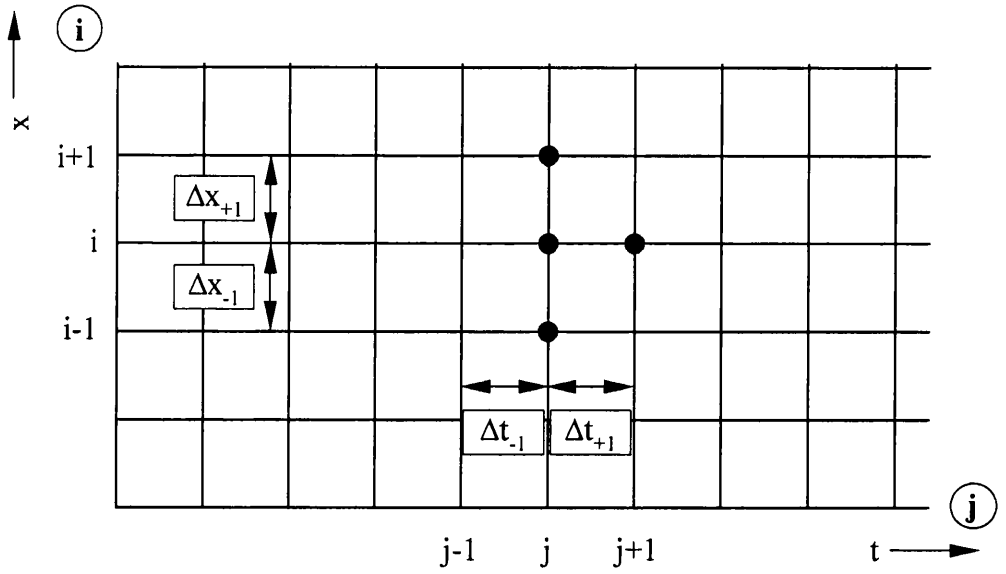

Figure 7.27: Coordinates for the Finite-Difference-Method (FDM)

At the inside of the profile, an adiabatic condition was assumed, and at the outside, the heat transfer coefficient and the coolant temperature are used to define the boundary conditions.

7.5.2 Calculation of heat transfer coefficients with FDM

In the calculation of heat transfer coefficients, the coolant temperature was used to calculate the overall heat transfer from the profile to the coolant water and the results will be shown first. Followed in a sub Chapter by the breakdown of the individual coefficients from profile surface to calibrator wall, from calibrator wall to coolant channel wall and from coolant channel wall to cooling water.

The heat transfer coefficient is calculated with an iterative method. The secant method is used for this. In the first step of calculation the heat transfer coefficients, the initial temperature is set to the melt temperature at the entrance of Calibrator 1. Thereafter, an initial estimate of heat transfer coefficient is used in the first calculation. If the difference of the calculated and measured profile surface temperatures of the next downstream position is smaller than a certain value, the calculated value is stored as result of the downstream distance, also the temperature distribution in the profile at the end of the calculated section. This temperature distribution is used now as the initial melt temperature distribution for the next section.

The flow chart presents the iterative method in Figure 7.28.

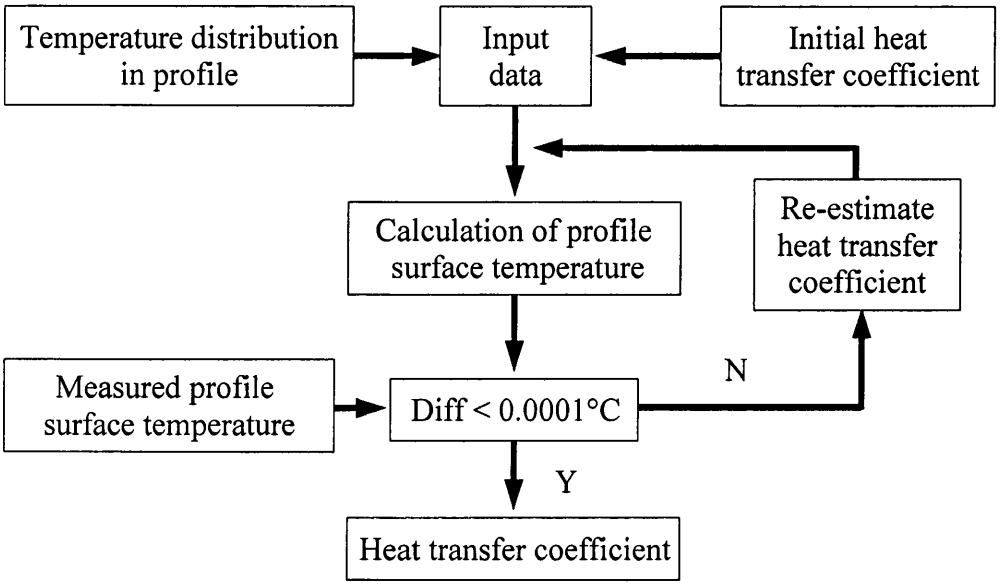

Figure 7.28: Flow chart of the calculation of the heat transfer coefficient on the outer profile surface

The input data consists of

- line speed
- final profile wall thickness (start thickness will be calculated)
- measurements of profile surface temperatures as function of position in line direction
- melt extrusion temperature

Furthermore, the physical properties of uPVC are used internal in the program

- specific heat (temperature dependent)
- thermal conductivity
- specific heat, respectively density (temperature dependent)

as well as values

- Δx_{START} = 0.01 mm
- Δt = 0.0001 s

The incremental values for Δx_{START} and Δt gives a good accuracy of the obtained results.

We have seen before that the measured profile surface temperature was in a few cases lower than the coolant water, may be as result of experimental error. It is also possible that the profile surface temperature is lower than the calibrator wall temperature due to the flow of water from the intermediate water baths into a small gap between the profile surface and calibrator wall due the present vacuum. In this condition, a calculation does not make sense, because we would get a negative heat transfer.

If the profile surface temperature is less than the coolant temperature, a corrected coolant was used in the calculations. This corrected coolant temperature was calculated with the profile surface temperature minus 0.2°C. These corrected calculations were filtered afterwards before the data processing has started.

A further simplification had to be used in the calculations. The positions of the temperature measurements points are close to the entrance and exit of the calibration units, but not exactly at the beginning or end of the calibrators. This leads to an over-estimated heat transfer coefficients of the water bath, because these are influenced by the higher heat transfer coefficients at the ends of the calibrators. An example of calculated profile surface temperatures is shown in Figure 7.29, together with the locations of the temperature measurement points.

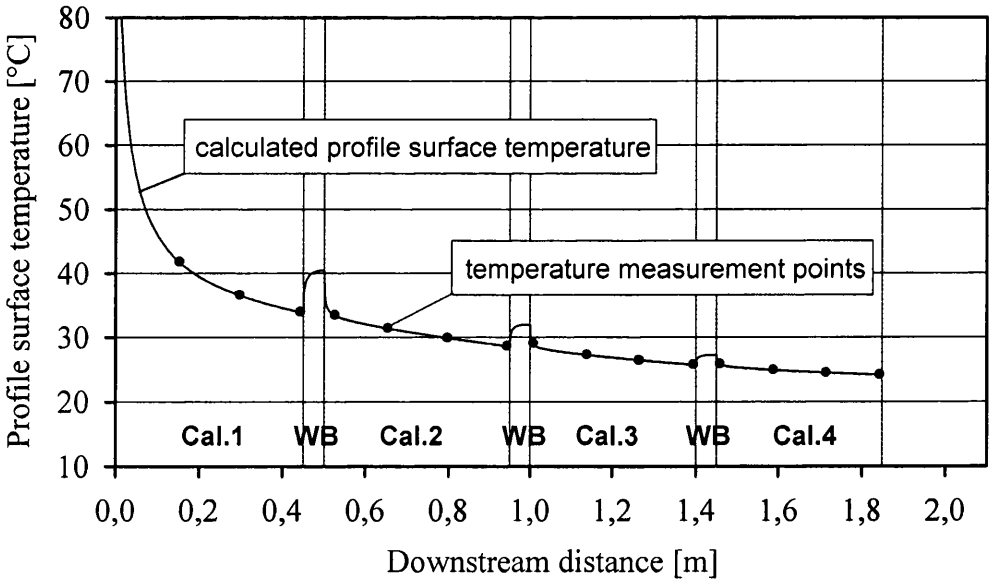

Figure 7.29: Profile surface temperatures of present calibration line; calculated with heat transfer coefficients of 500 W/m^2 K in the water baths (WB) and 1,000 W/m^2 K in the calibration units

In the following section, the dependence of heat transfer coefficients on the process parameters is shown, excluding the coefficients in the water baths for the reasons explained above. Furthermore, the calculations are based on the coolant water temperatures at the outer surface, as noted previously.

7.6 Overall heat transfer coefficients

7.6.1 Effects of line speed in wet and dry calibration on overall heat transfer coefficients

The trails were carried out in two sets, as mentioned before. In the 1st set, the profile wall thickness was constant of 2.50 mm and the vacua, line speed in dry and wet calibration were varied. The 2nd set, the profile wall thickness was varied from 2.50 to 3.25 mm wall thickness at constant die exit of 2.50 mm. Due to incorrect measured coolant water temperature in 2nd set, the coolant temperature had to be set to 16°C, similar to the coolant temperatures of 1st set to obtain useful results.

A selection of results is presented here to find dependencies on process parameters. All the calculated coefficients are presented in more detail in Appendix C to reduce the number of Figures in the main Chapter.

Now, the calculated overall heat transfer coefficients of the 1st set are presented in Figure 7.30 for a profile wall thickness for a vacuum of –0.4 bar at different line speeds.

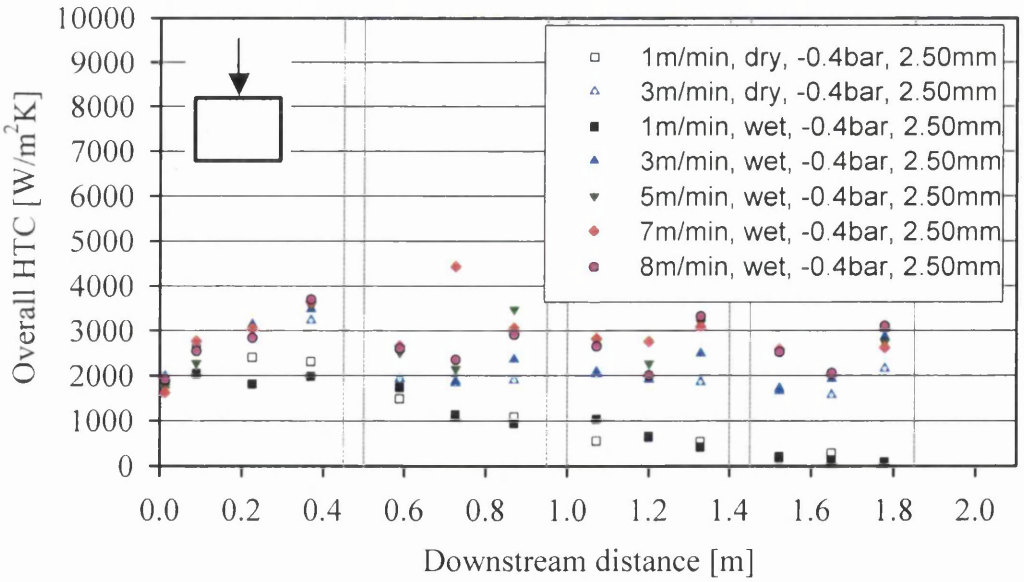

Figure 7.30: Overall heat transfer coefficients at the centre of the upper profile surface in wet and dry calibration for a vacuum of –0.4 bar at different line speeds; 2.50 mm die exit; 2.50 mm profile wall thickness

At line speed of 1m/min, the overall heat transfer coefficients on the centre line are decreasing in downstream distance for both wet and dry calibration. An increase of line speed leads to more nearly constant coefficients in downstream calibrators, except Calibrator 1.
In Calibrator 1, from 0 to 450 mm, an increase of heat transfer is recognizable at higher line speeds. The 2nd set for the 2.50 mm wall thickness shows a similar behaviour, Figures C4 to C6. The coefficients are similar in dry and wet calibration for a line sped of 1 m/min. For higher line speed of 3 m/min, the coefficients are higher in wet than in dry calibration. This behaviour is also present for a line speed of 1 m/min at higher vacua of –0.6 and –0.8 bar, which is shown in Figures C2 and C3 for the 1st set of experiments.

The dependence of heat transfer for the variation of wall thickness of 2.75 mm, 3.00 mm and 3.25 mm are shown in Figures C 7 to C15.

In the downstream calibrators, higher coefficients are present at the centre of the upper profile surface close to the inlet and outlet of each calibrator at higher line speeds. This leads to the assumption that the profile surface temperature is higher within the calibrator. In Figure 5.5, Chapter 5, the temperature course show higher profile surface temperatures in wet calibration within the downstream calibrators at same process parameters.

The trends of coefficients near to the profile edge show similar trend for a line speed of 1 m/min and vacuum of –0.4 bar in comparison with the coefficients at the centre of the upper profile surface, Figure 7.31.

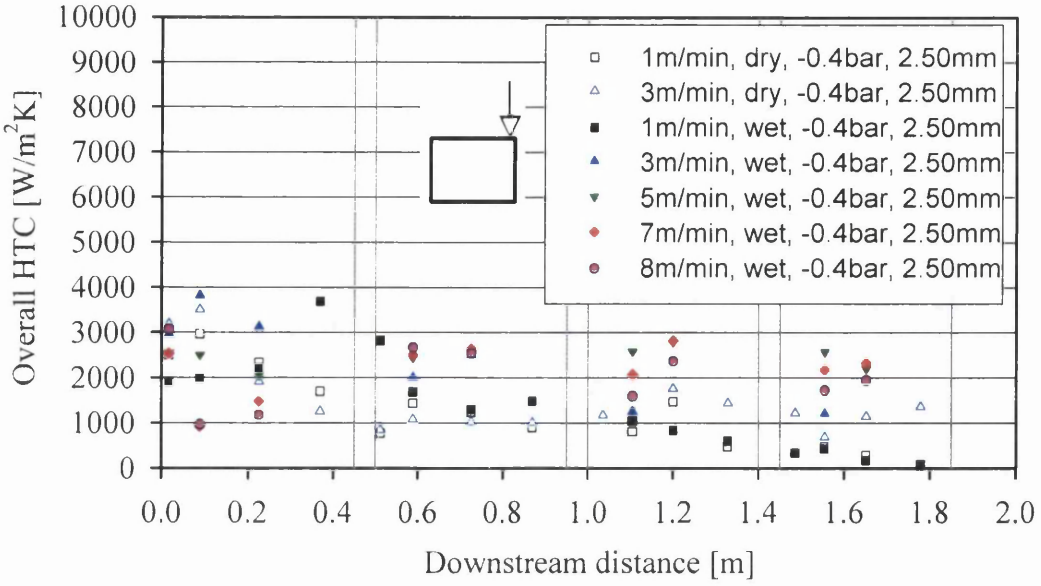

Figure 7.31: Overall heat transfer coefficients near the edge of the upper profile surface in wet and dry calibration for a vacuum of –0.4 bar at different line speeds; 2.50 mm die exit; 2.50 mm profile wall thickness

Here, the heat transfer coefficients neat the edge are approximately the same as for the centre in Figure 7.30 at low line speeds. For higher line speeds of 7 m/min and 8 m/min, lower coefficients for the edge are present compared with the centre. This is likely to be due to draw down, which increases the gap between the profile and calibrator and reduces the contact area of the profile surface and calibrator wall.

The coefficients within Calibrator 1 show an opposite trend to those at the centre; they decrease in the downstream direction, Figure 7.30, except at 1 m/min in wet calibration. For higher vacua, the trends are similar; Figures C32 and C33.

The overall heat transfer coefficients near the edge were measured only in the first set of experiments, so that the temperatures are not available for downstream calibrators of the 2nd set.

The time dependence of the overall heat transfer coefficients at different line speeds might allow a more detailed analysis. For this, the coefficients will be shown as function of time, first for the centre of the upper profile surface in Figure 7.32.

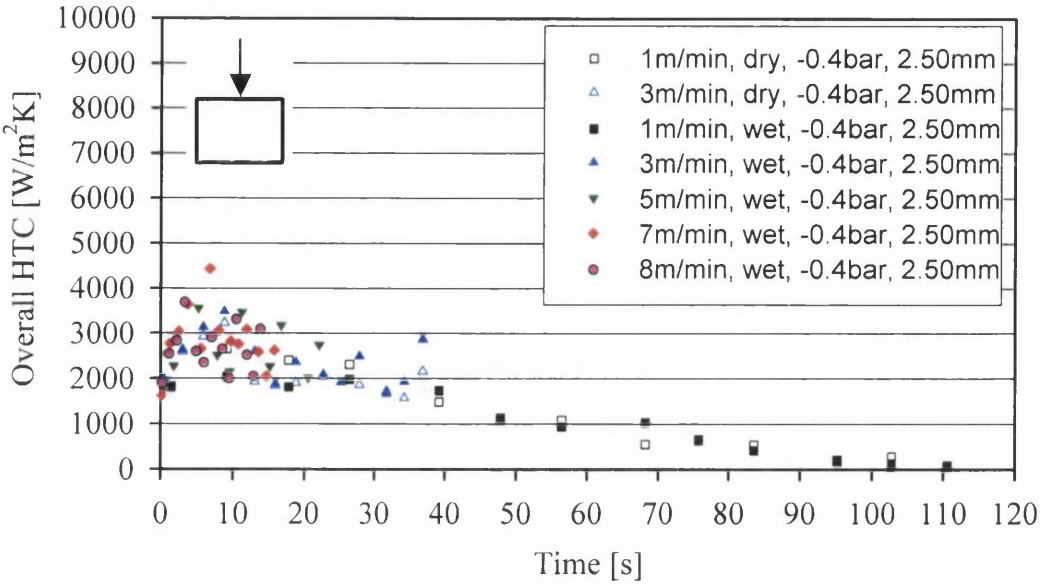

Figure 7.32: Overall heat transfer coefficients at the centre of the upper profile surface as function of the time in dry and wet calibration for –0.4 bar vacuum at different line speeds; 2.50 mm die exit; 2.50 mm profile wall thickness

The coefficients at low line speed show a reduction with increase of time, which also was visible as function of downstream direction in Figure 7.30. To see the coefficients at higher line speeds in more detail, the time scale of Figure 7.32 was reduced in Figure 7.33.

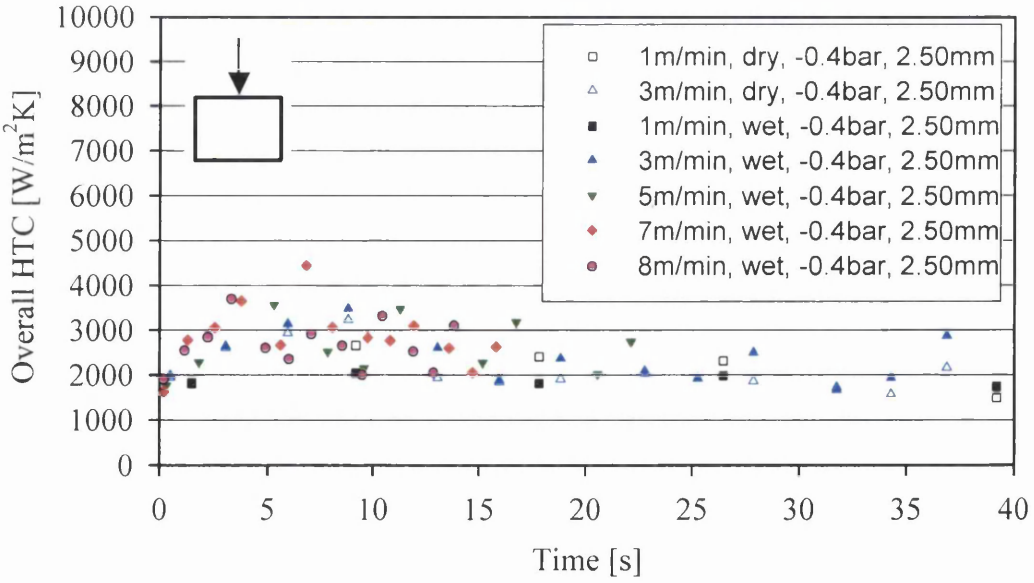

Figure 7.33: Overall heat transfer coefficients at the centre of the upper profile surface as function of the time in dry and wet calibration for –0.4 bar vacuum at different line speeds; 2.50 mm die exit; 2.50 mm profile wall thickness

The increase of heat transfer coefficients at the centre of the upper profile surface in Calibrator 1 shows the same trend as mentioned before.

The Figures 7.34 and 7.35 show the overall heat transfer coefficients near the edge as function of time. The trend of decrease with time is also visible for low line speeds.

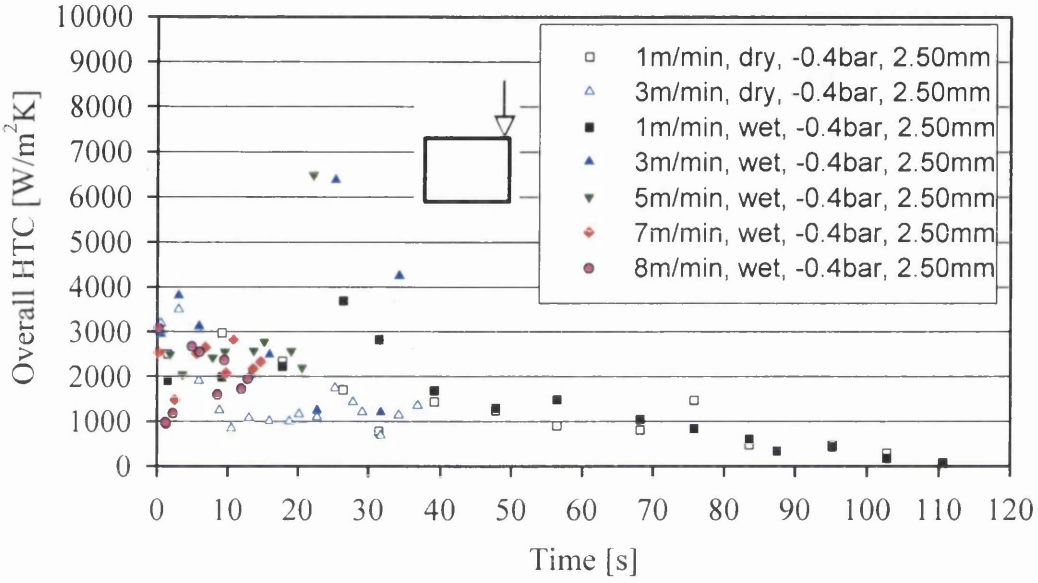

Figure 7.34: Overall heat transfer coefficients near the edge of the upper profile surface as function of the time in dry and wet calibration for –0.4 bar vacuum at different line speeds; 2.50 mm die exit; 2.50 mm profile wall thickness

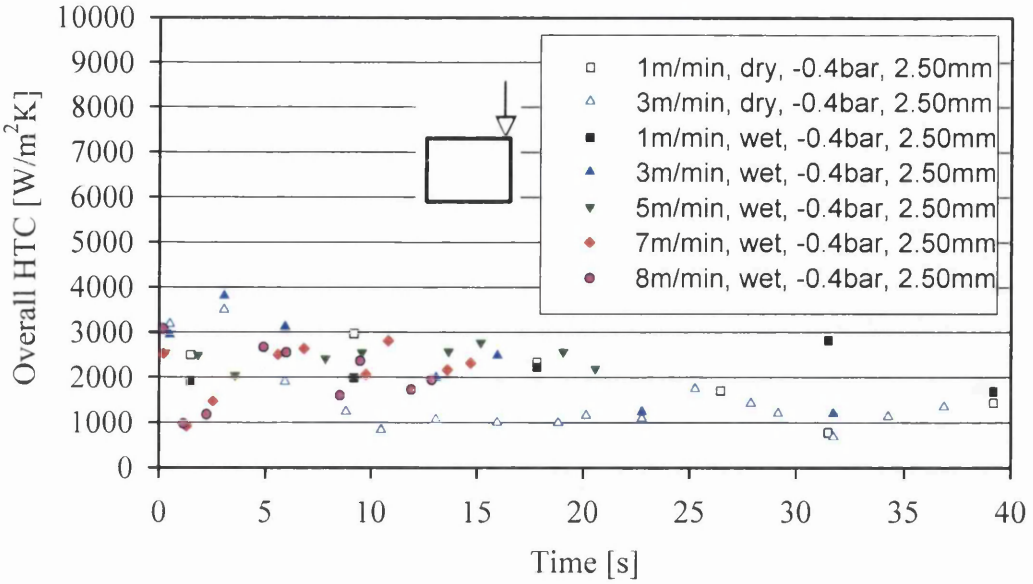

Figure 7.35: Overall heat transfer coefficients near the edge of the upper profile surface as function of the time in dry and wet calibration for –0.4 bar vacuum at different line speeds; 2.50 mm die exit; 2.50 mm profile wall thickness

In an attempt to systemize the results, it might be useful to use a dimensionless number for transient cooling. For this, the Fourier number Fo, which was introduced before, will be used in the next section.

7.6.2 Overall heat transfer coefficients as function of the Fourier number

A literature review has shown, that some investigations were done on the cooling of profiles in the past. In one reference, Fradette [185] found a correlation of heat transfer coefficients and Fourier number. The published coefficients for a hollow square profile, similar to the profile used in experiments present here, in dry calibration decrease from 10000 W/m^2 K down to 10 W/m^2 K for Fourier numbers from 0 to 5.3, for line speeds between 0.5 and 1.5 m/min. The profile surface temperatures were measured in [185] with an infrared thermometer at entry and exit of each calibrator in the calibration line, which was built out of three calibrators. Two surface temperatures were measured within the calibrators with thermocouples. In the calibrators, the have used a coolant water temperature of 13°C. Furthermore they have assumed a heat transfer coefficient of 5 W/m^2 K between the calibrators in their calculations.

The calculated coefficients obtained in the present experiments are presented now in the following Figures, for a profile wall thickness of 2.50 mm with die exit of 2.50 mm, as a function of the Fourier number; firstly, in Figure 7.34 for the centre of the upper profile surface and –0.4 bar vacuum.

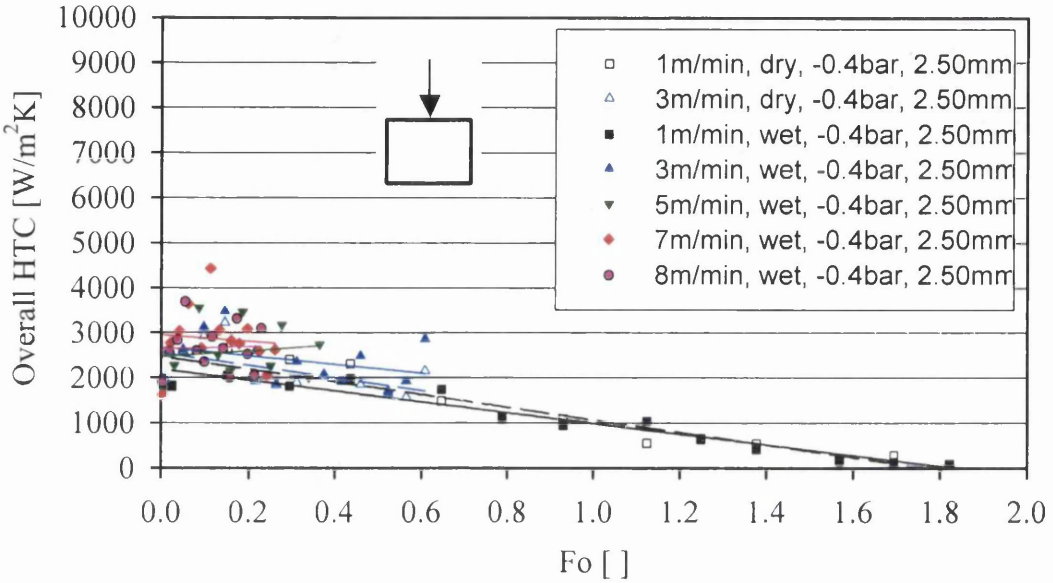

Figure 7.36: Overall heat transfer coefficients at the centre of the upper profile surface as function of the Fourier number in dry and wet calibration for –0.4 bar vacuum at different line speeds; 2.50 mm die exit; 2.50 mm profile wall thickness

The observed decrease of the overall heat transfer coefficients with Fourier number is consistent with literature data, i.e. at low line speeds of 1 m/min in wet and dry calibration, although the values are rather lower than found by Fradette, where values of approximately 10,000 Wm^2/K were presented at Fo = 0. At higher line speeds, the coefficients tend to increase slightly with increase of line speed, as also shown in the results of Fradette.

The same behaviour is also present near the edge of the upper profile surface and this is shown in Figure 7.37.

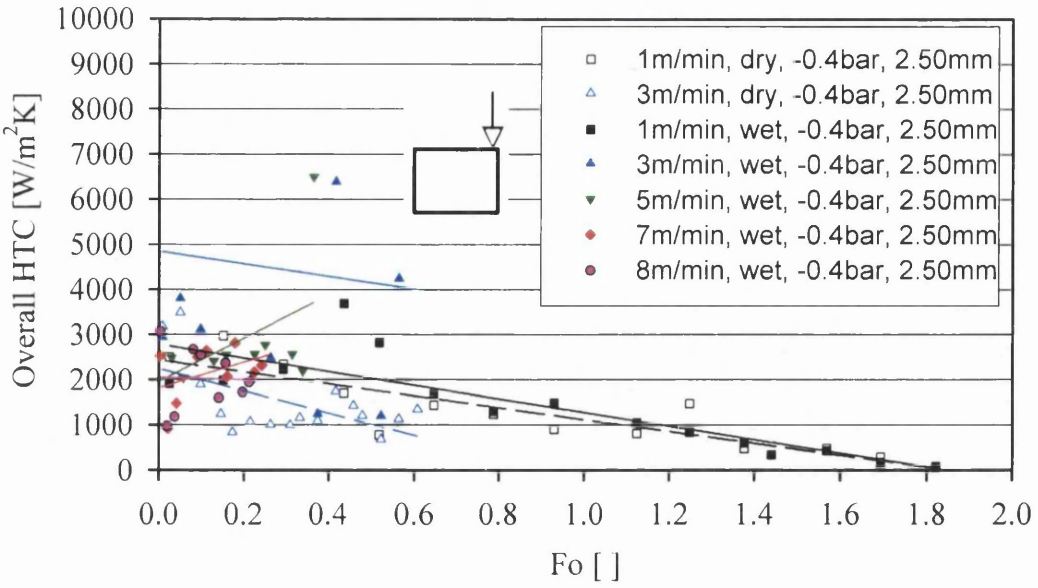

Figure 7.37: Overall heat transfer coefficients near the edge of the upper profile surface as function of the Fourier number in dry and wet calibration for –0.4 bar vacuum at different line speeds; 2.50 mm die exit; 2.50 mm profile wall thickness

7.6.3 Nusselt vs. Fourier for overall heat transfer coefficients

Using the dimensionless Nu number, the trend of decreasing Nu with an increase of an increasing Fo is expected. This is confirmed for the centre in Figure 7.38 and in Figure 7.39, where the values near to the edge are shown.

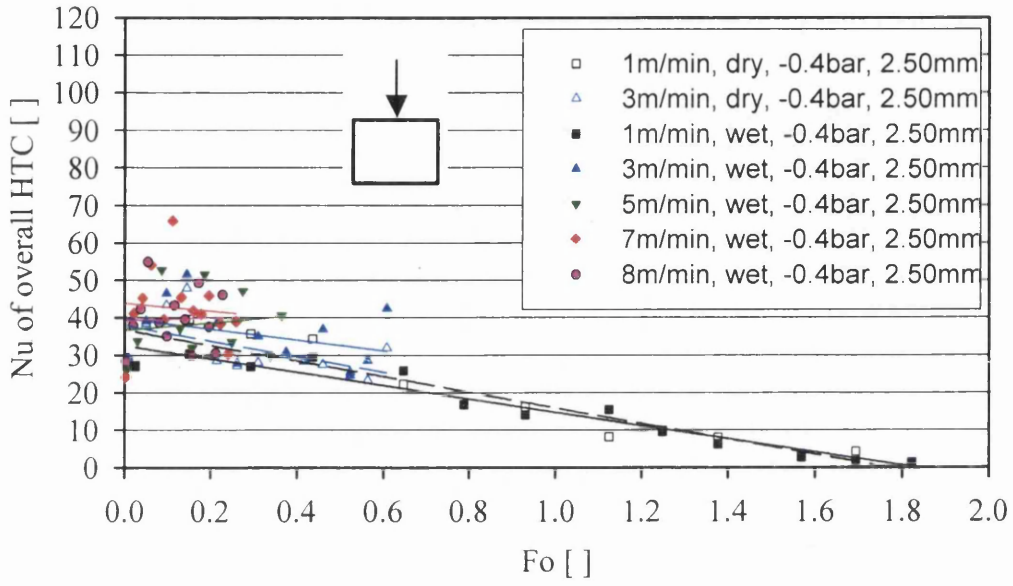

Figure 7.38 Nusselt numbers of overall heat transfer at the centre of the upper profile surface as function of the Fourier number in dry and wet calibration for a vacuum of –0.4 bar at different line speeds; 2.50 mm die exit; 2.50 mm profile wall thickness

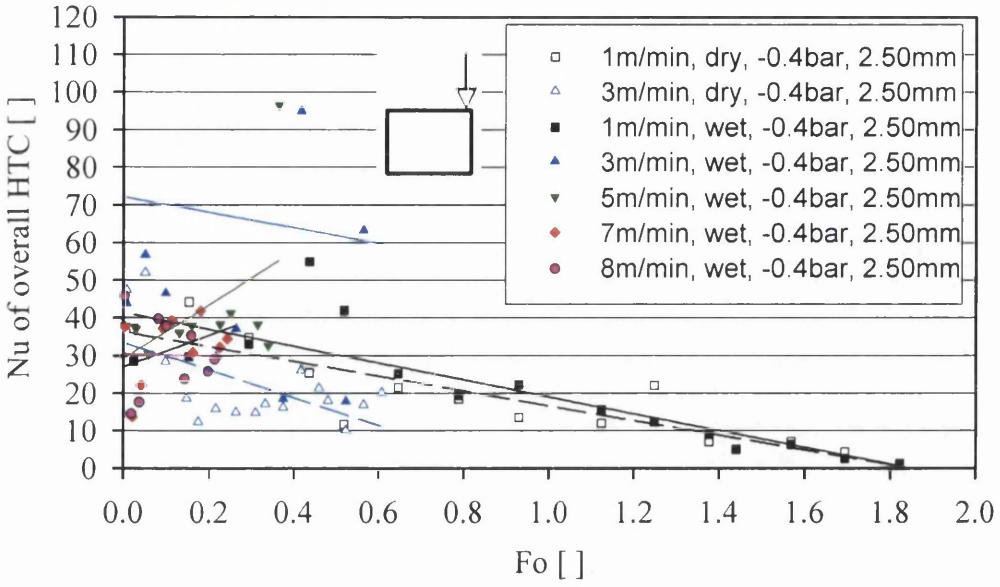

Figure 7.39 Nusselt numbers of overall heat transfer near the edge of the upper profile surface as function of the Fourier number in dry and wet calibration for a vacuum of –0.4 bar at different line speeds; 2.50 mm die exit; 2.50 mm profile wall thickness

7.7 Comparison of overall heat transfer coefficients with an analytical approach

To provide some insight into the trends observed in the experimental heat transfer coefficients, an approximate calculation based on an analytic solution is used.

The idealised problem is stated

$$t = 0, \qquad 0 \le x \le l, \qquad T = T_i \tag{7.30}$$

$$t > 0, \qquad x = 0, \qquad \frac{\partial T}{\partial x} = 0 \tag{7.31}$$

$$x = l, \qquad T = T_S. \tag{7.32}$$

Defining $$V = T_i - T_S \tag{7.33}$$

and $$v = T - T_S, \tag{7.34}$$

the solution is given [187] as

$$v = \frac{4V}{\pi} \sum_{n=0}^{\infty} \frac{(-1)^n}{2n+1} e^{-a(2n+1)^2 \frac{\pi^2 t}{4l^2}} \cos\frac{(2n+1)\,\pi\, x}{2\,l} \tag{7.35}$$

with x describing the distance from the inner side towards the maximum position l on the outer side.

The use of $$Fo = \frac{at}{l^2} \tag{7.36}$$

and $$\xi = \frac{x}{l} \tag{7.37}$$

leads to

$$\frac{v}{V} = \frac{4}{\pi} \sum_{n=0}^{\infty} \frac{(-1)^n}{2n+1} e^{-(2n+1)^2 \frac{\pi^2 Fo}{4}} \cos \frac{(2n+1)\,\pi\,\xi}{2} \tag{7.38}.$$

This solution represents an approximation of the profile cooling, since the profile surface temperature rapidly falls to an approximately constant value.

By summation of the series in (7.38), a graph can be created, see Figure 7.40, which shows the dimensionless temperature v/V against the dimensionless length ξ.

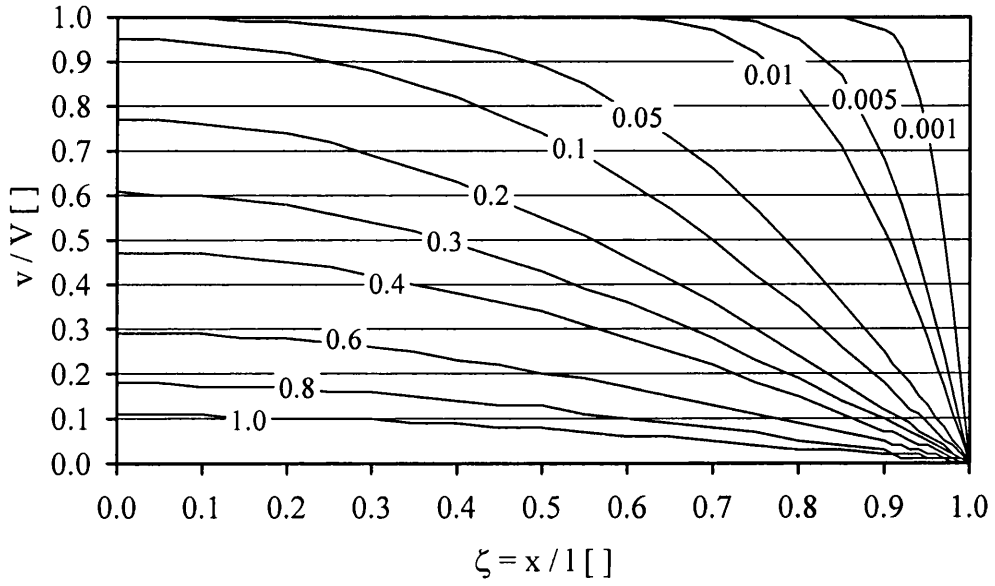

Figure 7.40: Dimensionless temperature versus position, parameter Fo

From this data, calculated values of the gradient of $\frac{dT^*}{d\xi^*}_S$ for a defined Fo number at the outer surface $\xi = 1$ can be obtained by numerical differentation.

Then, using $$T^* = \frac{v}{V} = \frac{T - T_S}{T_i - T_S}. \tag{7.39}$$

and $$\frac{dT}{dx}_S = \frac{T_i - T_S}{l} \frac{dT^*}{d\xi^*}_S \tag{7.40}.$$

The heat flux at the surface can be calculated, and equated to the term involving the overall heat transfer coefficient to the coolant

$$q = h\,(T_S - T_0) = k\left.\frac{dT}{dx}\right|_S \tag{7.41}$$

where T_S is the surface temperature and T_0 the coolant temperature. Finally, the overall heat transfer coefficient from the analytical solution is

$$h = \frac{k\left.\frac{dT}{dx}\right|_S}{(T_S - T_0)} \tag{7.42}.$$

Using values for the heat flux as function of time from the analytic solution, together with experimental values of the initial profile temperature (T_i) and the profile surface temperature (T_S), overall transfer coefficients can be estimated. In this calculation the actual surface temperature at a particular time, or position down the line is used. The results are shown in Figure 7.41.

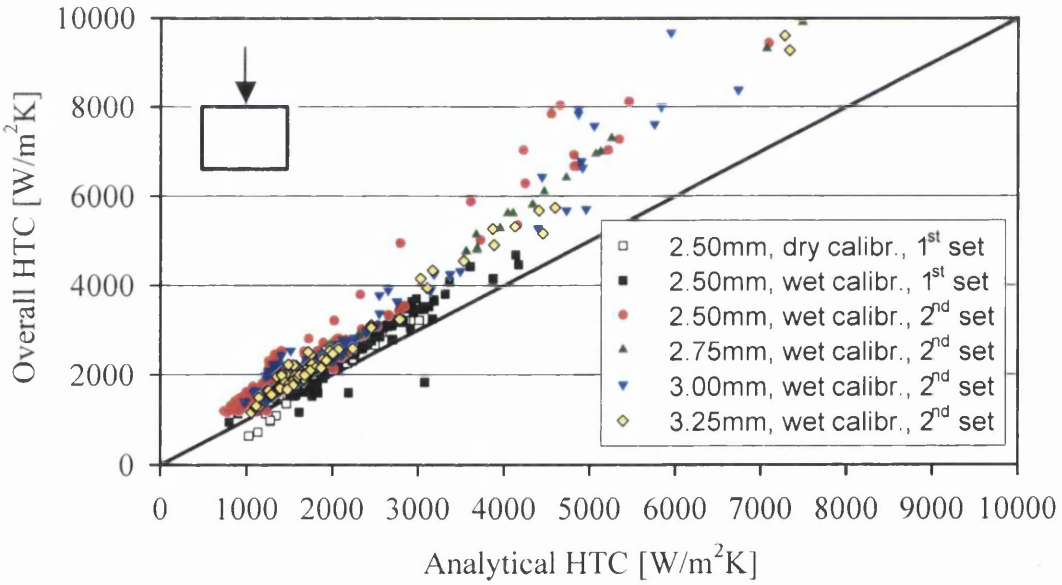

Figure 7.41 Comparison of overall heat transfer coefficients at the centre of the upper profile surface calculated with the FDM and an analytical solution

As time increases, the surface temperature gradient and hence the heat flux decreases. But so also does the experimental profile surface temperature (T_S), and the temperature difference ($T_S - T_0$) during the heat transfer (The changes in T_S are small compared with $T_i - T_S$, except in the very early stages of profile cooling, so the analytic solution is a reasonable approximation to the real case).

From (7.42) it is then clear that h will increase or decrease with time, depending on the relative rates of decrease of $\left(\frac{dT}{dx}\right)_S$ and $(T_S - T_0)$.

Figure 7.41 shows the estimated values of h are in close agreement with those obtained from experimental data at low h values. At higher values, the experimental values rise about 25% above the estimated ones. This is probably because high values occur at short time, when the analytic solution is less applicable.

The critical factor in determining trends in h appears to be the experimental values of the temperature differences $(T_S - T_0)$.

These cannot be predicted, and are a complex function of processing conditions.

Nevertheless, Figure 7.42 shows how, using the experimental values of $(T_S - T_0)$, the trends in h are well reproduced.

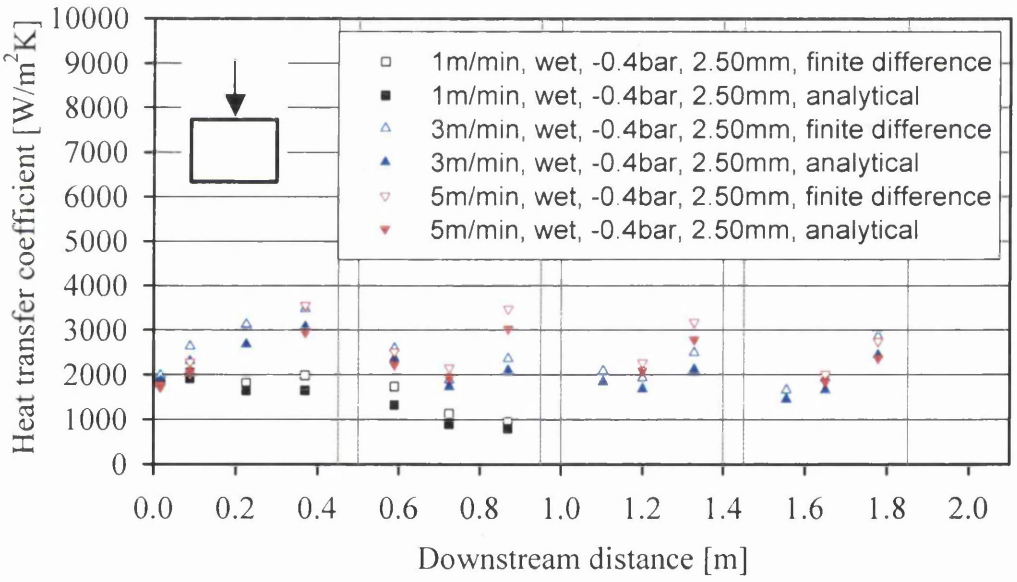

Figure 7.42 Comparison of overall heat transfer coefficients at the centre of the upper profile surface calculated with the FDM and the analytical solution as function of downstream distance in wet calibration for –0.4 bar vacuum at different line speeds; 2.50 mm die exit; 2.50 mm profile wall thickness

The results in this section confirm the validity of the h values extracted from the experiments using the finite difference solution, and provide some insights into the origins of the trends that have been observed.

7.8 Breakdown of overall heat transfer coefficients

The foregoing Sections have reported the overall heat transfer coefficients for heat transfer from the profile surface to the cooling circulating in the calibrators, to get an overview of the influence of processing conditions on the profile calibration process.

In this Section, the heat transfer from profile to the coolant medium will be investigated in more detail. The cooling process is driven by the heat transfer coefficients and temperature differences. Now the previously shown overall heat transfer is separated into its sequential parts. Firstly, the heat of the profile is transferred from the profile surface into the calibrator wall. From the calibrator wall, the heat is transported through the metal of the calibrator to the surface of the coolant channels. Finally, the heat is transferred from the coolant channel surface to the coolant medium. All details are shown in Figure 7.43.

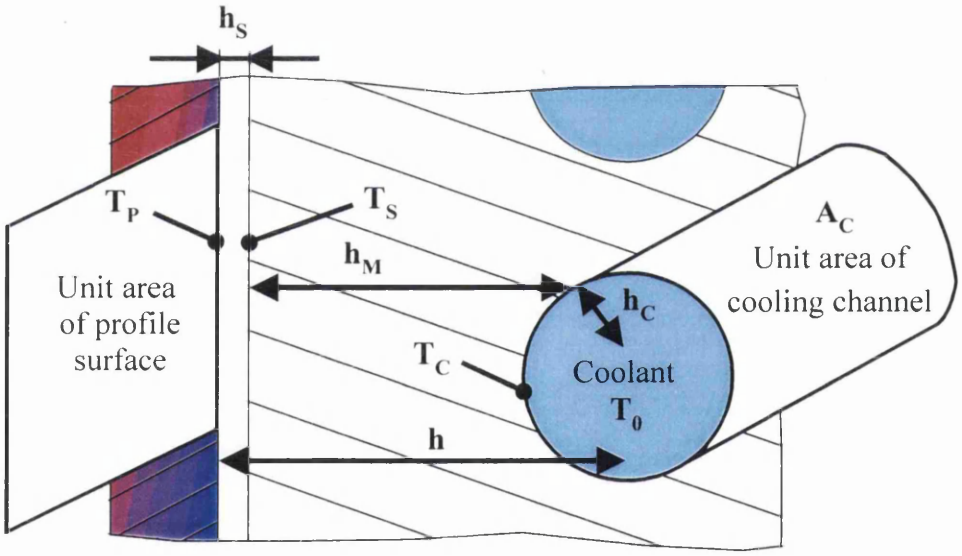

Figure 7.43: Heat transfer from profile surface to circulating coolant

The overall thermal resistance from the profile surface to circulating coolant can therefore be broken down into:

- thermal resistance between the profile surface and adjacent calibrator wall.
- thermal resistance of the calibrator metal between the surface adjacent to the profile and the surface of the coolant channels.
- thermal resistance between the surface of the coolant channel and the bulk of the circulating coolant.

The addition of the foregoing thermal resistances will lead to the overall thermal resistance from the profile surface to the coolant medium, and by subtracting out the thermal resistance of the metal and coolant film, the interfacial heat transfer from the profile to the calibrator wall can be calculated. This is the component most closely dependent on processing conditions, the other parts being constant or approximately so.

We consider a constant (for steady conditions) heat flux q and using the continuity of the heat flux from the profile surface to the coolant: $q = h\, A_P\, (T_P - T_0)$ (7.43),

the profile to calibrator surface: $q = h_S\, A_P\, (T_P - T_S)$ (7.44),

the calibrator surface to cooling channel surface: $q = h_M\, A_M\, (T_S - T_C)$ (7.45),

the cooling channel surface to coolant: $q = h_C\, A_C\, (T_C - T_0)$ (7.46),

where A_P is a specific area of the profile surface (e.g. unit area)

T_P is profile surface temperature

T_S is calibrator surface temperature

T_C is coolant channel temperature

T_0 is coolant bulk temperature.

The area of coolant channels corresponding to area A_P of profile surface is A_C, and A_M represents the mean area perpendicular to the flux direction for transfer through the metal.

To get the necessary dimensions for the calculations, the general design of calibrators used in this set of trials is shown in Figure 7.44. Because of the simplifications to the heat transfer model embedded in equations 7.43 – 7.46, several approximations to conduction path length and areas must be made. Inevitably, these involve some arbitrary results. Nevertheless, the resulting calculations provide useful insight into the relative importance of the different components of the overall thermal resistance in the calibration process.

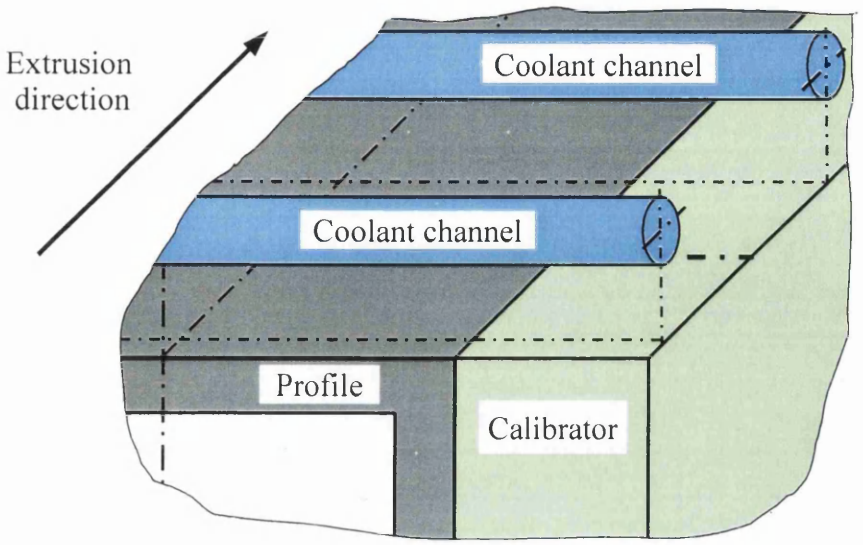

Figure 7.44: General design of the calibrators used in trials

The heat from the upper profile surface is removed mainly with the cooling channels shown in the foregoing Figure. Some convective heat transfer is also present from the outer calibrator surface to the ambient air, but this is neglected in the present calculations. More details of the dimensions used in the calculations are shown in Figure 7.45.

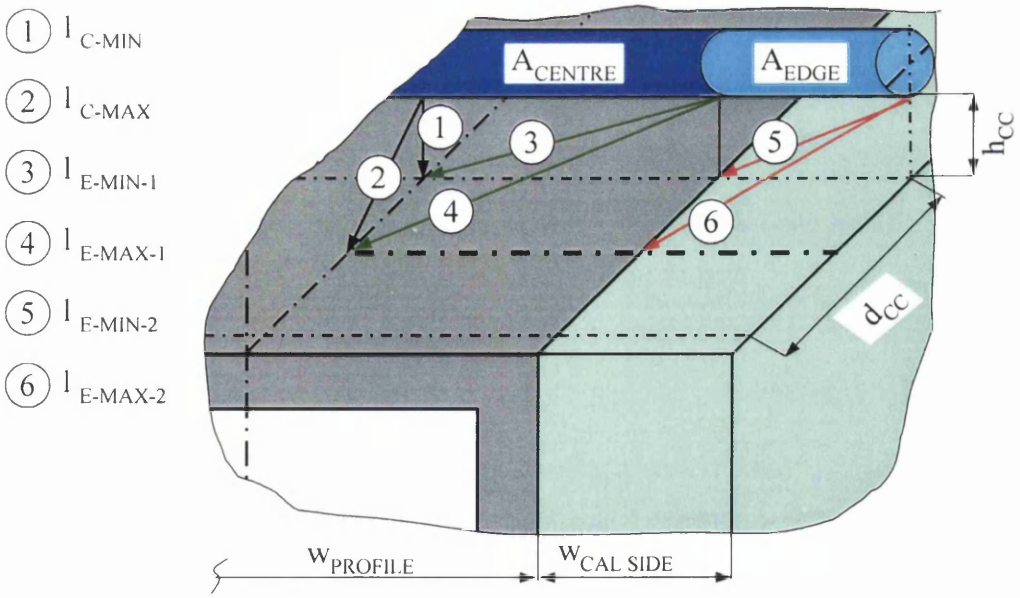

Figure 7.45: Dimensions used for the calculations

To estimate the thermal resistance of the metal, heat transfer to the central parts of the cooling channels (directly above the profile), and to the parts of the outer edge of the calibrator, are separated.

Replacing $h_M A_M$ with $\left(h_{M\_CENTRE} \frac{A_{CENTRE} + A_P}{2} + h_{M\_EDGE} \frac{A_{EDGE} + A_P}{2} \right)$ in (7.45) leads to

$$q = \left(h_{M\_CENTRE} \frac{A_{CENTRE} + A_P}{2} + h_{M\_EDGE} \frac{A_{EDGE} + A_P}{2} \right) (T_S - T_C) \qquad (7.47)$$

where the areas for conductivity through the metal are taken as the averages of the areas of the profile surface and coolant channels.

Using the dimensions in Figure 7.45, the mean conduction path lengths are estimated as

$$\frac{1}{l_{M\_CENTRE}} = \frac{1}{2} \left(\frac{1}{l_{C-MAX}} + \frac{1}{l_{C-MIN}} \right) \qquad (7.48),$$

$$\frac{1}{l_{M\_EDGE}} = \frac{1}{4} \left(\frac{1}{l_{E-MIN\,1}} + \frac{1}{l_{E-MAX\,1}} + \frac{1}{l_{E-MIN\,2}} + \frac{1}{l_{E-MAX\,2}} \right) \qquad (7.49),$$

and the heat transfer coefficients are then

$$h_{M\_EDGE} = k \frac{1}{l_{M\_EDGE}} \qquad (7.50),$$

$$h_{M\_CENTRE} = k \frac{1}{l_{M\_CENTRE}} \qquad (7.51),$$

where k is the thermal conductivity of the metal.

Solving equations 7.43 – 7.46 for $(T_P - T_0)$ and with $h_M A_M$ expanded as in Equation 7.47 leads to

$$\frac{1}{h A_P} = \frac{1}{h_S A_P} + \frac{1}{\left(h_{M\_CENTRE} * \frac{A_{CENTRE} + A_P}{2} + h_{M\_EDGE} * \frac{A_{EDGE} + A_P}{2} \right)} + \frac{1}{h_C A_C} \qquad (7.52).$$

From 7.52, together with 7.50 and 7.51, the interfacial heat transfer coefficient h_S can be calculated.

The film heat transfer coefficient h_C from the coolant channel surface the coolant to is calculated by using equations from VDI-W rmeatlas [138] for heat transfer of turbulent water, flow using the measured coolant water flow rates and channel dimensions.

The results of calculated interfacial heat transfer coefficients are shown in the next Sections.

7.8.1 Comparison of thermal resistances in the calibration process

Before the detailed values are presented in more detail, the next three Figures show the magnitudes of the coolant, calibrator and the interfacial thermal resistances for a profile wall thickness of 2.50 mm for a vacuum of –0.4 bar at varying line speeds of 1, 3 and 5 m/min.

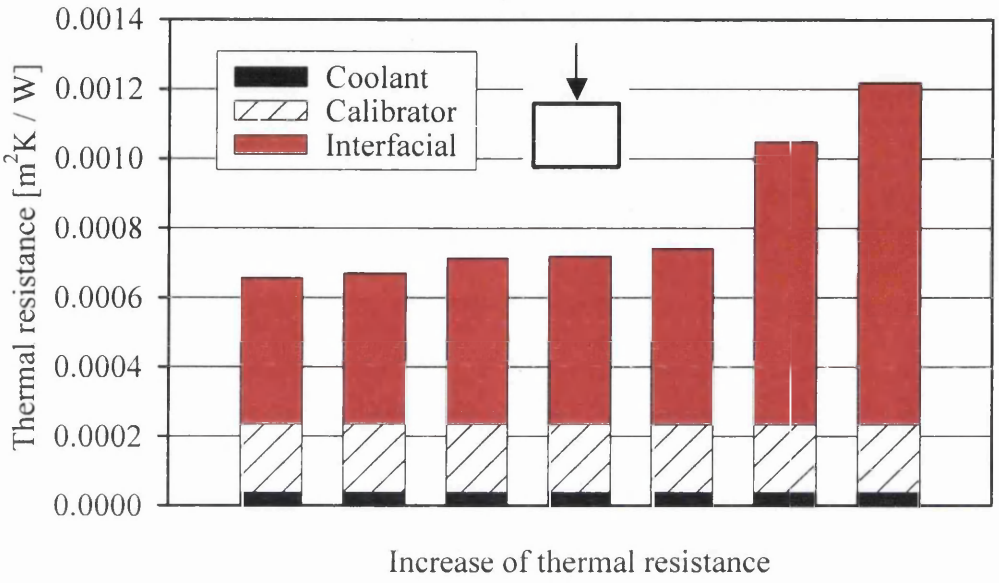

Figure 7.46: Thermal resistances at the centre of the upper profile surface in wet calibration for a line speed of 1 m/min and –0.4 bar vacuum; 2.50 mm die exit; 2.50 mm profile wall thickness

The thermal resistance of the coolant and calibrator are nearly constant with increasing of the overall thermal resistance, whilst the interfacial resistance increases with the increase of overall resistance. The relatively small contribution from the calibrator metal thermal resistance justifies the approximations made in the calculation explained above (Figure 7.41 etc.). An important conclusion from these calculations is that the interfacial thermal resistance is usually the major component of the overall resistance. Only for the higher overall heat transfer coefficients does the interfacial resistance become similar to the other components, see Figures 7.47 and 7.48.

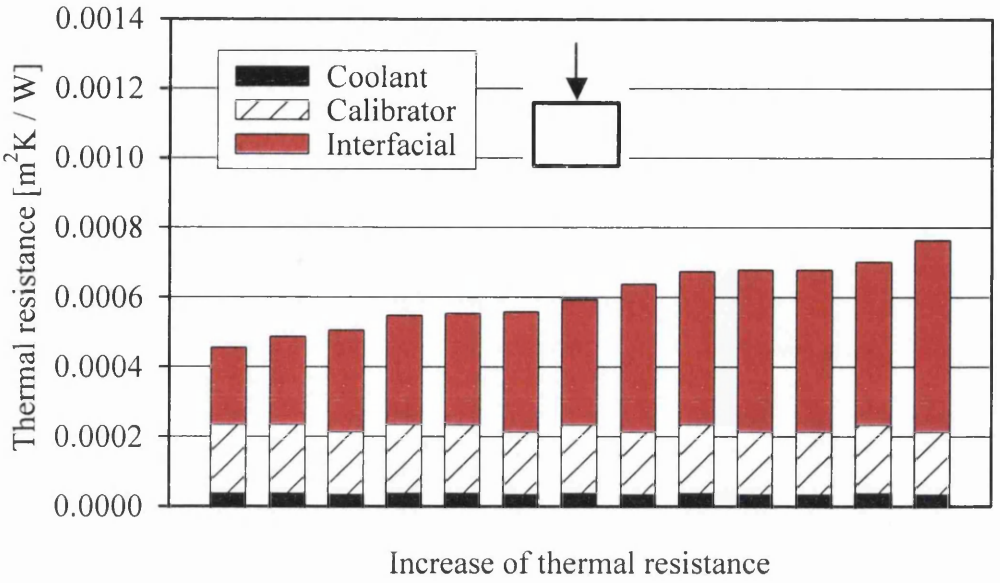

Figure 7.47: Thermal resistances at the centre of the upper profile surface in wet calibration for a line speed of 3 m/min and –0.4 bar vacuum; 2.50 mm die exit; 2.50 mm profile wall thickness

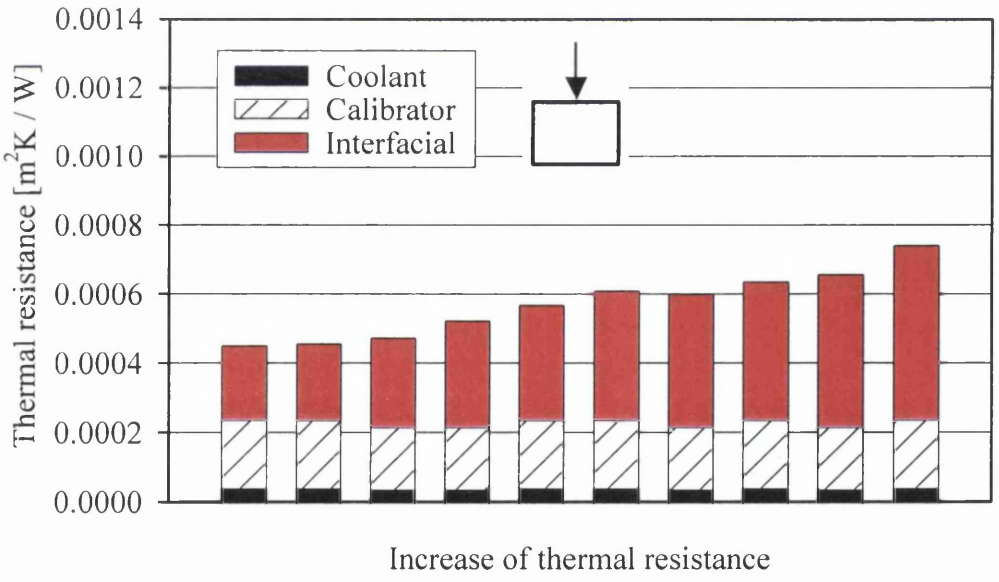

Figure 7.48: Thermal resistances at the centre of the upper profile surface in wet calibration for a line speed of 5 m/min and –0.4 bar vacuum; 2.50 mm die exit; 2.50 mm profile wall thickness

7.8.2 Effects of line speed in wet and dry calibration on interfacial heat transfer coefficients

All the data obtained by calculations of the interfacial heat transfer coefficients are presented in Appendix C2. Here, some results and the final data will be shown to reduce the number of Figures. Since the overall thermal resistance that have been subtracted out are constant (metal) or nearly so (coolant film), the trends in the interfacial coefficients shown below are the same as for the overall coefficients, but here with the trends magnified.

The interfacial heat transfer coefficients are first shown in Figure 7.49 for the centre of the upper profile surface, with same parameters as for the overall heat transfer in Figure 7.30.

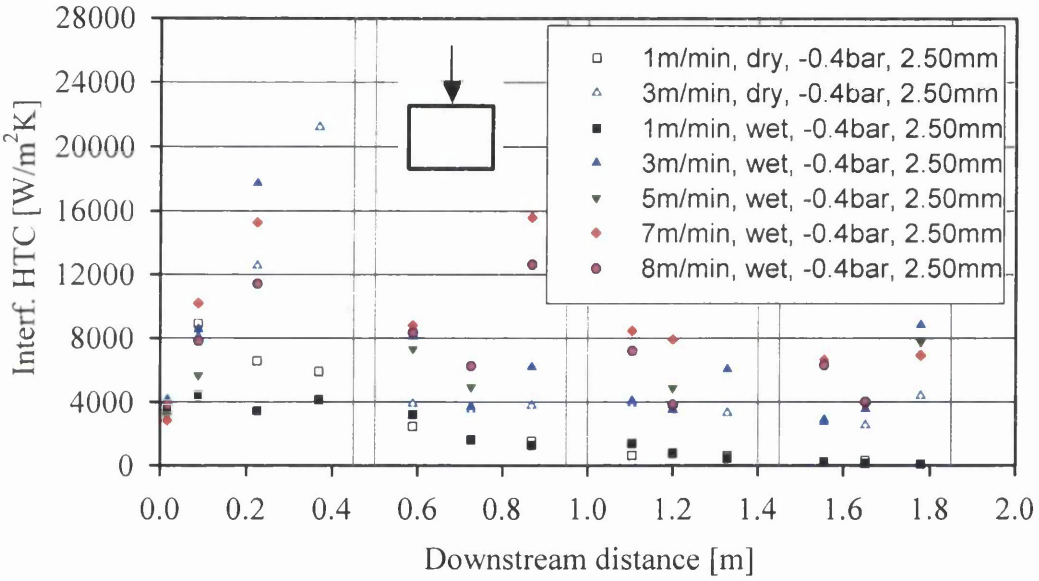

Figure 7.49: Interfacial heat transfer coefficients at the centre of the upper profile surface in wet and dry calibration for a vacuum of –0.4 bar at different line speeds; 2.50 mm die exit; 2.50 mm profile wall thickness

The interfacial coefficients are decreasing downstream at lowest line speed in wet and dry calibration, similar to overall coefficients. This decrease is also recognizable for the coefficients near the edge of the upper profile surface in Figure 7.50, where the overall coefficients were shown in Figure 7.31.

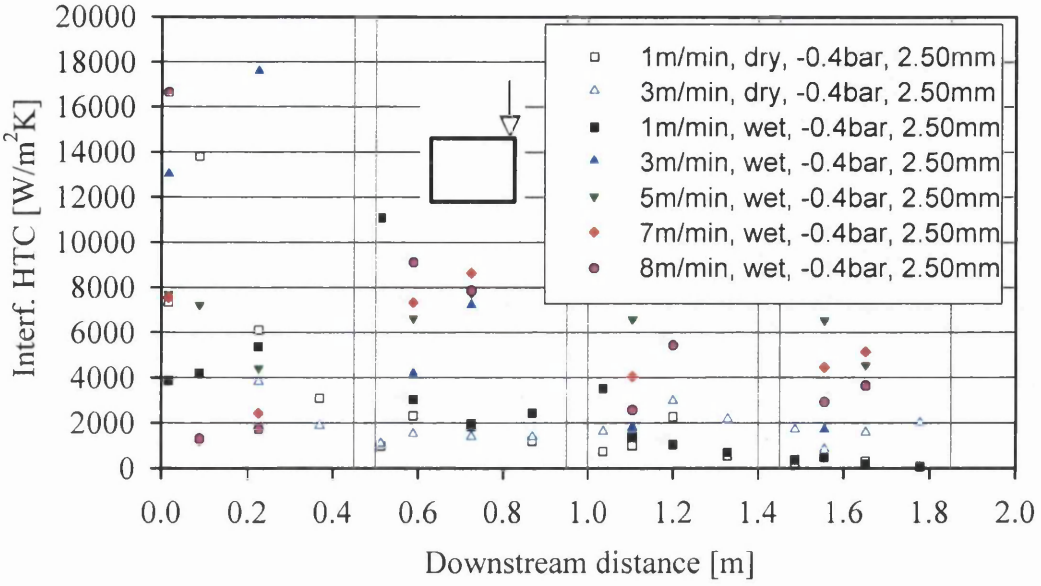

Figure 7.50: Interfacial heat transfer coefficients near the edge of the upper profile surface in wet and dry calibration for a vacuum of –0.4 bar at different line speeds; 2.50 mm die exit; 2.50 mm profile wall thickness

7.8.3 Interfacial heat transfer coefficients as function of the Fourier number

As shown previously for the overall coefficients, the interfacial values are presented as function of Fo for the centre and near to the edge of the upper profile surface in Figures 7.51 and 7.52. The corresponding Figures for the overall coefficients are 7.36 and 7.37.

The same trend is visible for both measurement positions as seen before, where the coefficients decrease with increase of Fo.

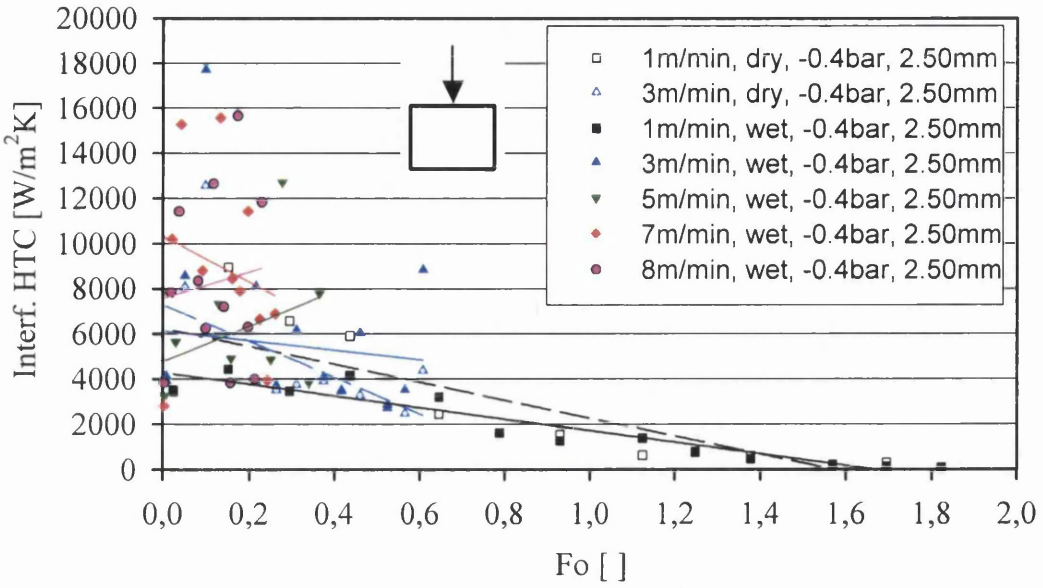

Figure 7.51: Interfacial heat transfer coefficients at the centre of the upper profile surface as function of the Fourier number in dry and wet calibration for –0.4bar vacuum at different line speeds; 2.50 mm die exit; 2.50 mm profile wall thickness

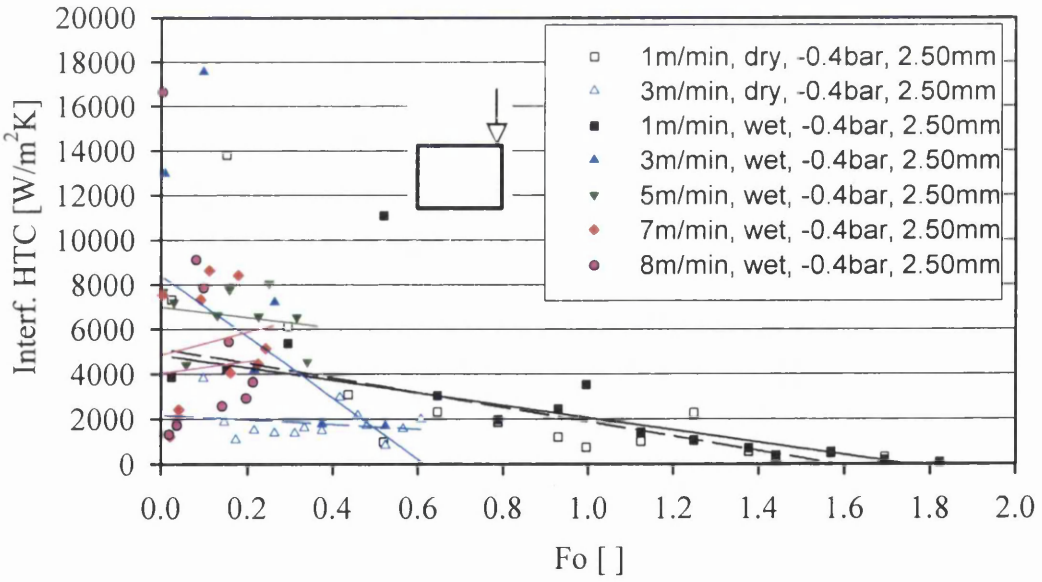

Figure 7.52: Interfacial heat transfer coefficients near to the edge of the upper profile surface as function of the Fourier number in dry and wet calibration for –0.4bar vacuum at different line speeds; 2.50 mm die exit; 2.50 mm profile wall thickness

7.8.4 Nusselt vs. Fourier for interfacial heat transfer coefficients

In this section, Nu is shown in the next Figures as function of Fo for the same measurement positions, as before in Figures 7.38 and 7.39 for the overall heat transfer coefficients.

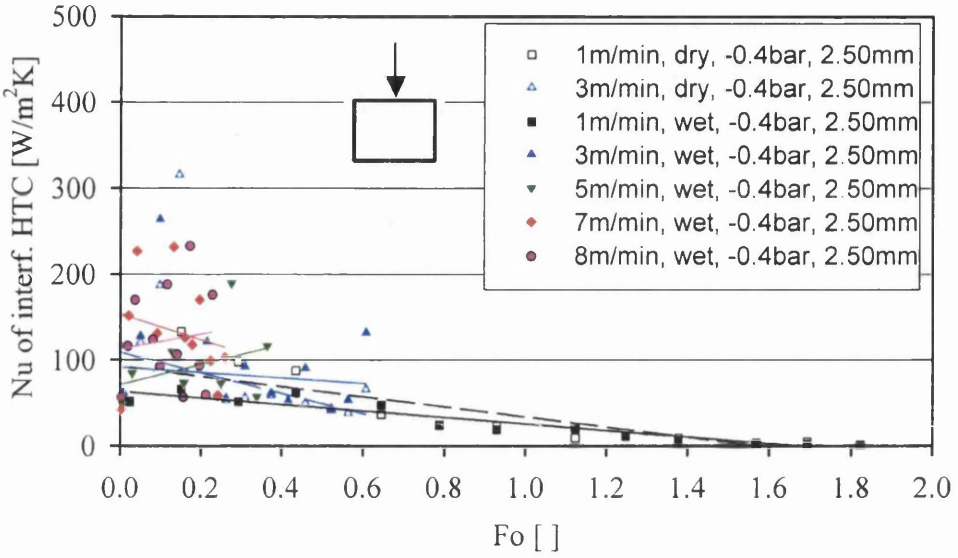

Figure 7.53 Nusselt numbers of interfacial heat transfer at the centre of the upper profile surface as function of the Fourier number in dry and wet calibration for a vacuum of –0.4 bar at different line speeds; 2.50 mm die exit; 2.50 mm profile wall thickness

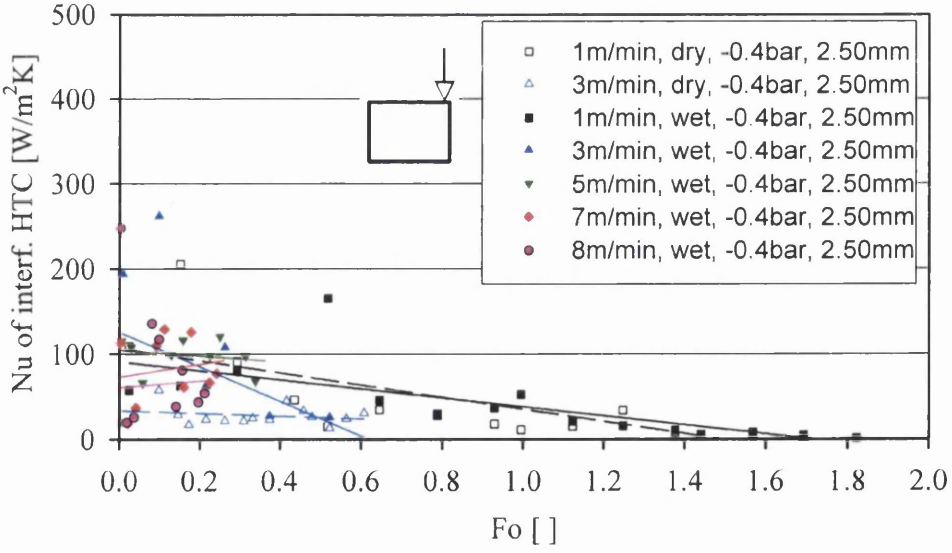

Figure 7.54 Nusselt numbers of interfacial heat transfer near to the edge of the upper profile surface as function of the Fourier number in dry and wet calibration for a vacuum of –0.4 bar at different line speeds; 2.50 mm die exit; 2.50 mm profile wall thickness

The foregoing Figures lead to the conclusion that trend lines might be used to show dependencies on process parameters.

7.8.5 Intercepts and slopes of trend lines for interfacial heat transfer coefficients

The trend line fitting was linear, and so the intercept and slopes of these lines are used now to shown possible dependencies on line speed in dry and wet calibration, first for the centre of the upper profile surface, followed by coefficients near to the edge. In the fitting procedure using SigmaPlot© [188], the standard error was obtained for each fit and these are now shown as error bars in the next Figures.

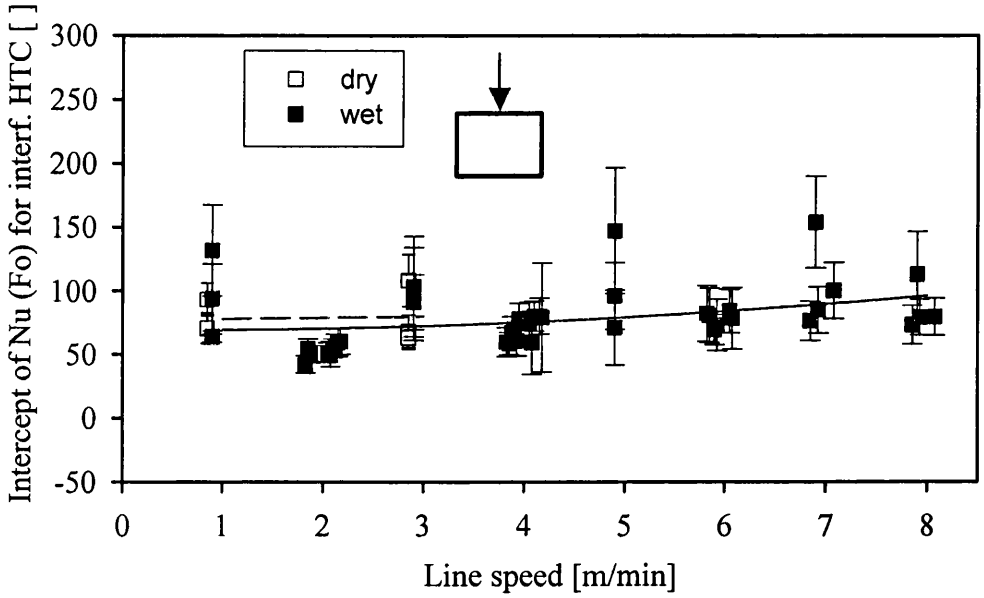

Figure 7.55: Intercept of the interfacial heat transfer coefficient (vs. Fo) at Fo = 0 at the centre of the upper profile surface in dry and wet calibration as a function of line speed; 2.50 mm die exit

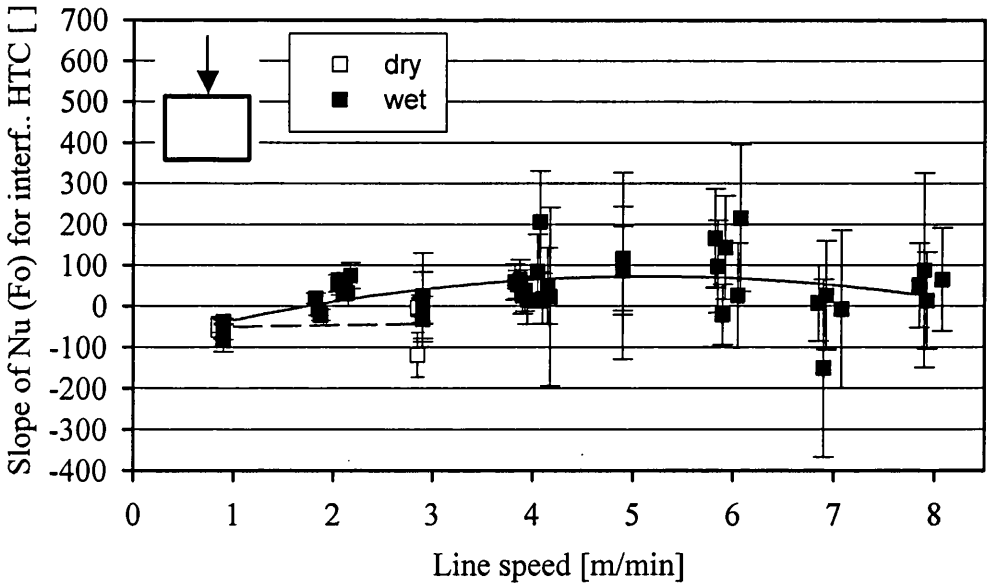

Figure 7.56: Slope of the interfacial heat transfer coefficient (vs. Fo) at the centre of the upper profile surface in dry and wet calibration as a function of line speed; 2.50 mm die exit

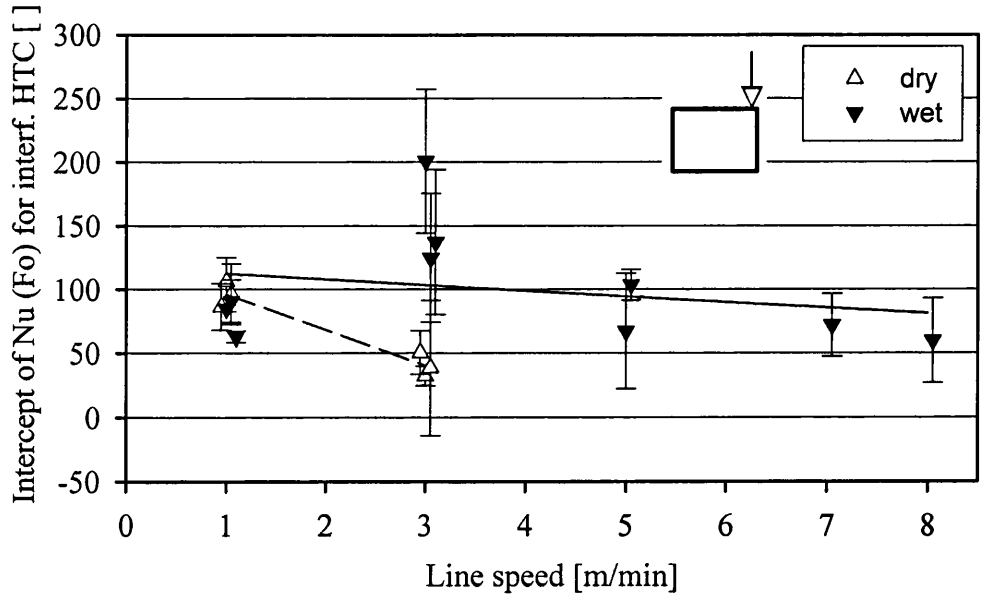

Figure 7.57: Intercept of the interfacial heat transfer coefficient (vs. Fo) at Fo = 0 near to the edge of the upper profile surface in dry and wet calibration as a function of line speed; 2.50 mm die exit

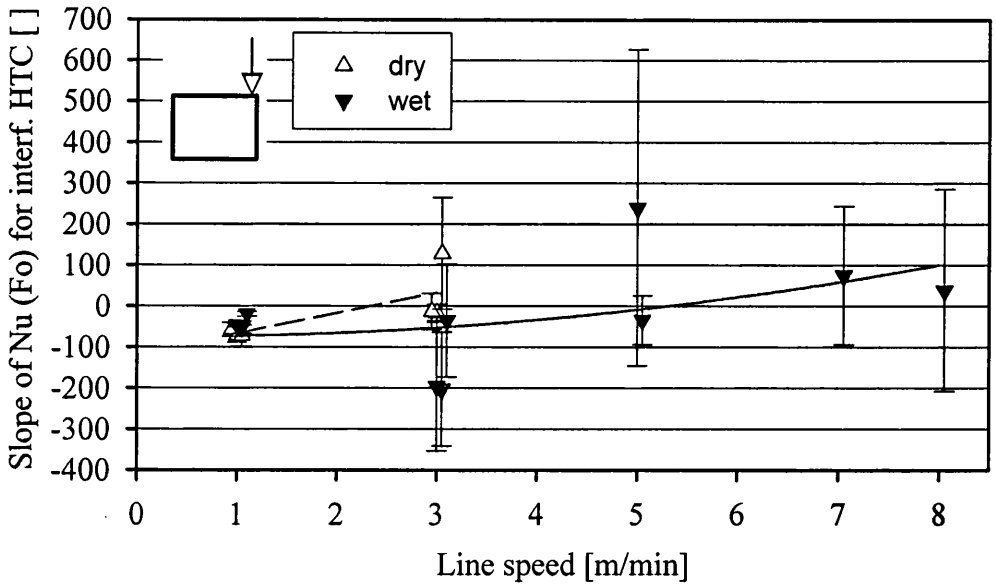

Figure 7.58: Slope of the overall heat transfer coefficient (vs. Fo) at the edge of the upper profile surface in dry and wet calibration as a function of line speed; 2.50 mm die exit

In dry calibration, the intercepts are higher at the centre of the upper profile surface and remain nearly constant up to a highest line speed of 3 m/min, whilst near to the edge, the intercepts are lower than in wet calibration with a decrease towards higher line speed. This might be based on the loss of contact of profile and calibrator, as discussed before for the heat transfer coefficients and for the profile dimensions in Chapter 6.

At low line speeds, a negative slope is present for both positions of measurements, at the centre and near the edge. Only a few results are available for the position near to the edge. So these values and the standard errors must be regarded more cautiously. More values are available for the centre of the profile. Although scatter and standard errors are present, the trend shows an increase of the slope up to a line speed of 5 m/min, and at higher line speeds, the slope is still positive, but decreases slightly.

In the last Figures considerable scatter of the intercepts and slopes of the trend lines was seen. The standard errors included the last Figures are also large. The scatter arising from experimental uncertainties (primarily the values of the small temperature differences between profile surface and coolant) is here magnified by the subtraction of the (approx.) constant parts of the overall thermal resistance. Nevertheless, some trends were obtained with recent experiments.

Summary

Detailed investigations of the heat transfer have given an overview of the complexity of cooling in the calibration process. The profile used has reduced the complexity, because no inner cavities are present. The FDM was used to calculate the heat transfer coefficients from the profile to the calibrator walls. The obtained results have confirmed the published values from Schmidt [184] in a range of 1,500 to 2,500 $W/m^2 K$ for a comparable line speed of 2 m/min. The findings of Fradette [185] can be also confirmed. He found a decrease of the heat transfer coefficients with increase of Fo number for line speeds up to 2 m/min. At higher speeds in the recent experiments, the coefficients increase with increasing Fo number.
The dependence of the heat transfer from the profile to the coolant on the process parameters has been shown. Here, the differences in dry and wet calibration were clear to see. Furthermore, the loss of contact near to the edges due to draw down has decreased the heat transfer from profile surface to the calibrator wall, especially in dry calibration. In wet calibration, water from the intermediate water baths helps to cool the profile surface near to the edge, where draw down leads to a gap between profile surface and calibrator wall.
It was also seen that the profile surface temperature falls rapidly down nearly to coolant temperature in the first section of Calibrator 1.

An insight into the trends exhibited by the heat transfer coefficients has been provided using an approximate calculation based on an analytic solution. The key factor emerges as the temperature difference between the profile surface and the coolant, and the dependence of this on processing conditions has been investigated thoroughly.
Separation of the overall thermal resistance in calibration into the component parts shows that the interfacial resistance between the profile surface and the calibrator is usually much more important than the thermal resistance in the metal and the coolant film. Only for the cases where the overall thermal resistance is lowest are the other components comparable to the interfacial resistance. Despite the scatter in the data, values and trends have been presented which will be valuable in predicting cooling rates in calibration for a wide range of processing conditions.

CHAPTER 8

Comparison of experimental results for profile geometry and forces with numerical calculations

This Chapter gives a preliminary comparison of the experimental results for forces, profile geometry and deformation with Finite Element Method (FEM) calculations carried out by others in a parallel project.

The calculations are based on a model, presented in [189-191].
For the heat transfer and cooling, it includes heat loss from the profile surface to the calibrators / air / water baths, governed by specific heat transfer coefficients and coolant temperatures, and models non-linear conduction in the plastic (temperature dependent properties) together with heat exchange between internal surfaces of the profile by free convection and radiation. Convection and radiation are not significant when temperatures around and within the profile are uniform, as is the case in the simple test profile with one inner chamber used in present work.
The mechanical model includes thermal shrinkage and deformation of the profile during calibration, using a temperature-dependent small strain linear viscoelastic model for material behaviour. Results for temperature as a function of position and time are read back from the cooling simulation and used to adjust the density and mechanical properties of the PVC, for which a generalised Maxwell model is used. A cross-sectional slice of the profile is modelled as it moves down the calibration line. This involves the assumption that the effects of downstream deformations are not transmitted back upstream. Boundary conditions include the effect of applied vacuum, and a contact algorithm is used to model the constraining effect of the calibrators. This provides the contact area and contact forces between the profile and the calibrators. Using empirically assigned friction coefficients, these data are used to compute the frictional drag on the profile. This is integrated along the line to provide the haul-off force. Deformation of the profile arises from a combination of the effects of thermal stresses, application of vacuum and haul-off forces. The use of a viscoelastic model allows for both the development and relaxation of stresses.

Data for the generalised Maxwell model of PVC was obtained from a comprehensive survey of the literature.

For the cooling of the outer profile surface, heat transfer coefficients were used, which were obtained from calculations with the Finite Difference Method (FDM), see Chapter 7 in the present work. The experimentally measured coolant temperatures, used in the FDM calculations of the heat transfer, were also used here in the FEM calculations. Due to the simple profile geometry with one inner chamber, the heat transfer between internal surfaces was neglected, as mentioned before, to save calculation time. But this must to be taken into account for profiles with more chambers, where the conduction in the material of the inner walls, free convention due to temperature differences and, finally, radiation cannot be ignored, as shown in [192]. The cooling simulation including conduction, free convection and radiation in the FEM calculations has shown good agreement with experimental results for a wide range of complex profiles [192].

The initial conditions of the simulations are assumed as constant temperature and uniform velocity of the melt at the inlet of Calibrator 1. The cooling of the outer profile surface between the die exit and the inlet of Calibrator 1 was ignored, due to the short distance between them, and the low heat transfer coefficient for free convection to air.

The friction coefficients for the contact of the outer profile surface and calibrator walls used in the calculations were empirically determined as 0.6 for Calibrator 1 and 0.3 for the downstream calibrators due to a lubrication effect of the water in wet calibration. Friction coefficients of 0.6 were presented in literature for medium hard PVC at a temperature of 160°C and 0.25 at 60°C [143]. Similar friction coefficients of 0.35-0.40 were shown in [145] at lower temperatures.
More details about friction coefficients were presented in Chapter 3.

The haul-off forces and profile dimensions calculated with the use of the FEM simulations are compared with experimental results in following sections.

8.1 Comparison of calculated and experimental haul-off forces

Details of the dependence of haul-off forces on process parameters were shown in Chapter 6. Now, in this section, comparisons of calculated and experimental forces are shown to get an idea of the performance of the simulation and indication of improvements required in the future.

In Figures 8.1 to 8.4, the differences of calculated and experimental haul-off forces are shown for different profile wall thicknesses. The differences are shown as a percentage on the basis of experimental forces.

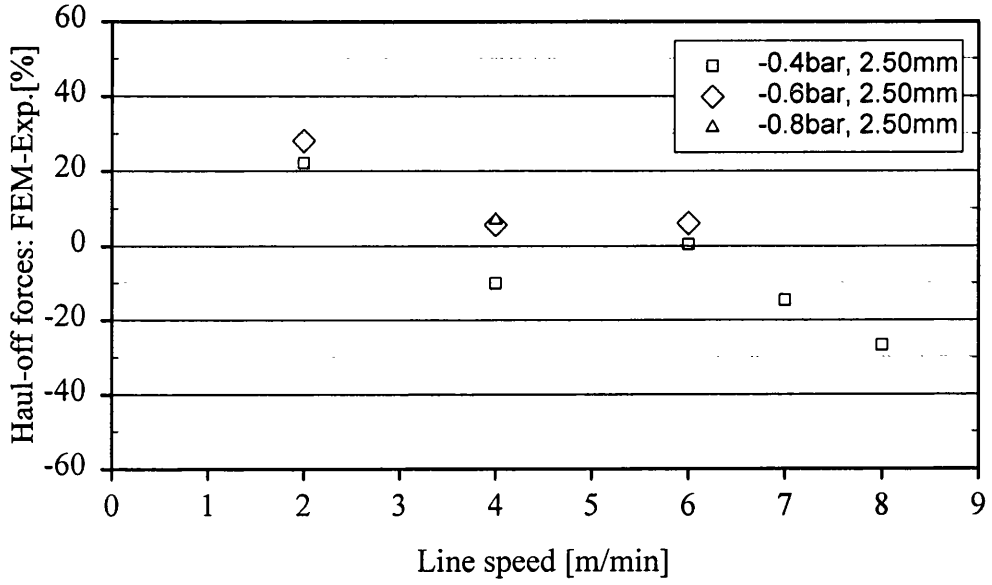

Figure 8.1: Differences between calculated and experimental haul-off forces as function of line speed for different vacuua in wet calibration for a profile wall thickness of 2.50 mm; vacuum constant in all calibration units; 2.50 mm die exit

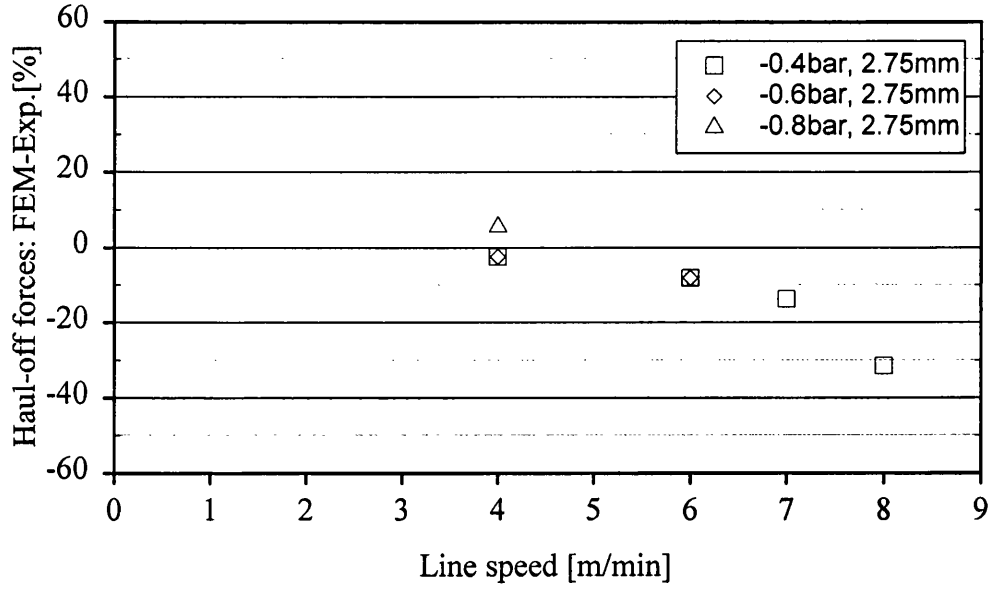

Figure 8.2: Differences between calculated and experimental haul-off forces as function of line speed for different vacuua in wet calibration for a profile wall thickness of 2.75 mm; vacuum constant in all calibration units; 2.50 mm die exit

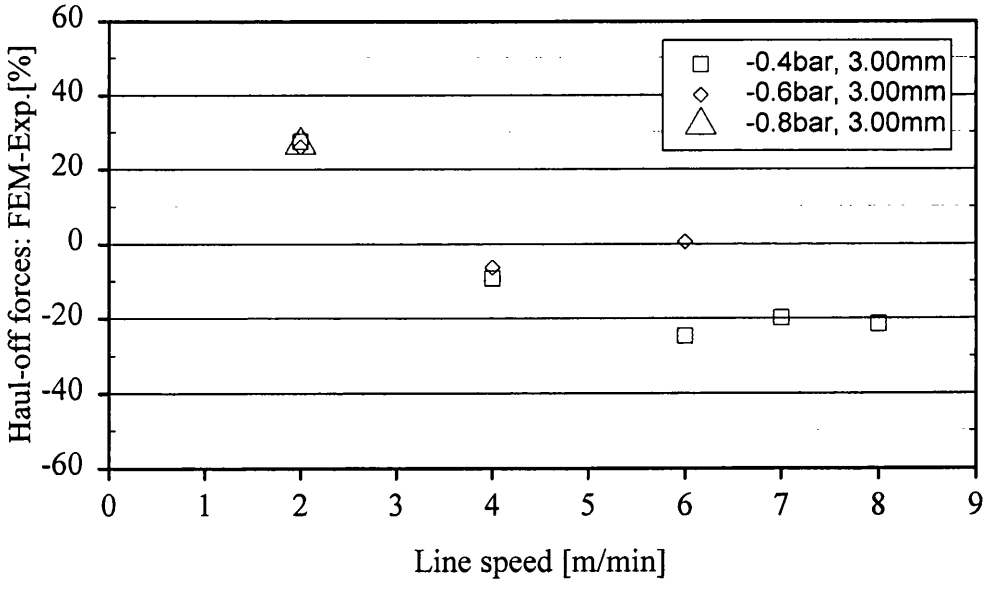

Figure 8.3: Differences between calculated and experimental haul-off forces as function of line speed for different vacuua in wet calibration for a profile wall thickness of 3.00 mm; vacuum constant in all calibration units; 2.50 mm die exit

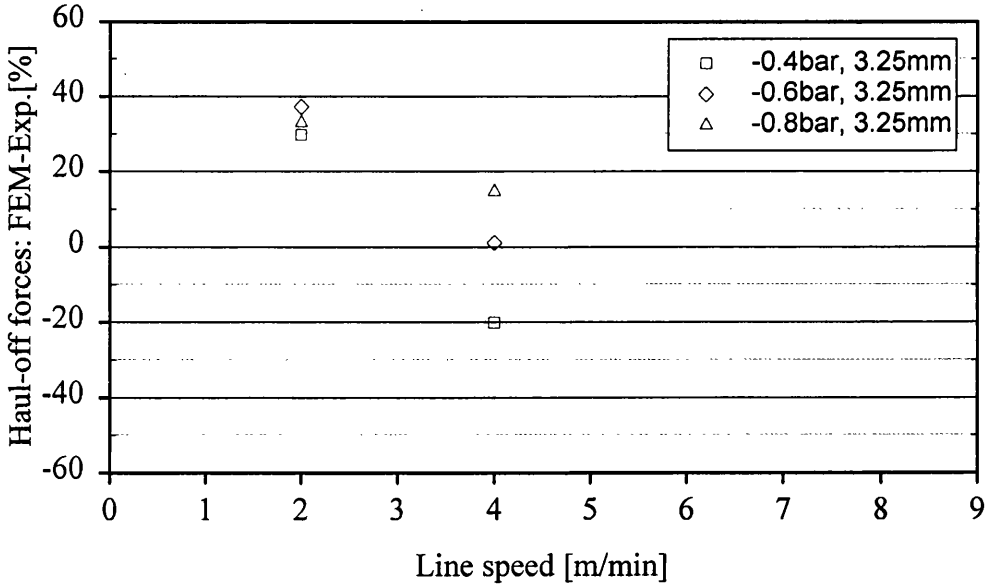

Figure 8.4: Differences between calculated and experimental haul-off forces as function of line speed for different vacuua in wet calibration for a profile wall thickness of 3.25 mm; vacuum constant in all calibration units; 2.50 mm die exit

It is seen that in the mid-range of line speeds, corresponding to typical production conditions, the predicted haul-off forces are within 20% of experimental values for all vacuum levels. For practical purposes, this result can be judged as fairly satisfactory.

As shown in Chapter 6, most of the forces in wet calibration are present within Calibrator 1. So in the next Figures, the forces in Calibrator 1 are shown instead of the total haul-off forces as given in the foregoing Figures.

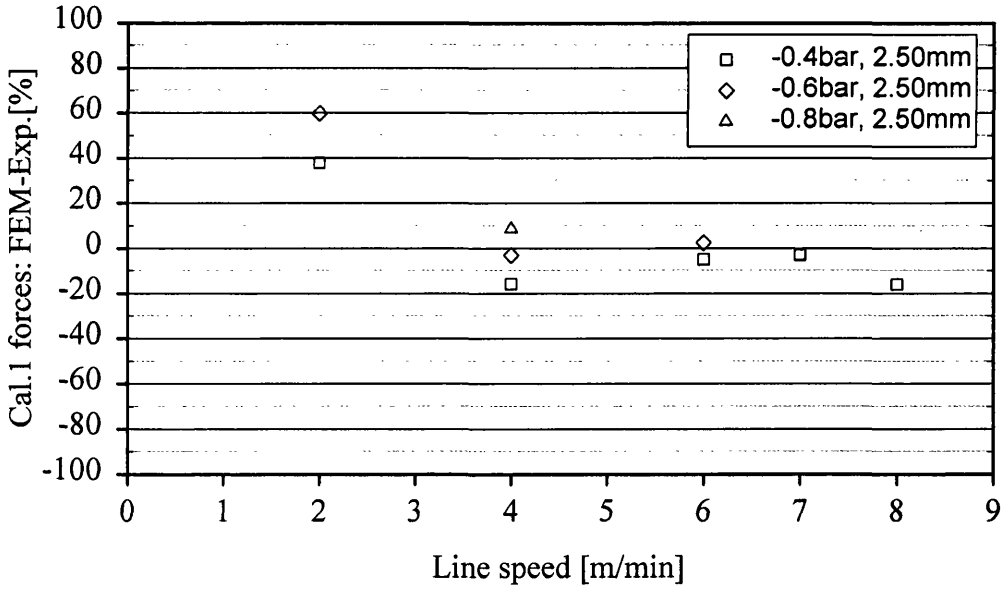

Figure 8.5: Differences between calculated and experimental forces in Calibrator 1 as function of line speed for different vacuua in wet calibration for a profile wall thickness of 2.50 mm; vacuum constant in all calibration units; 2.50 mm die exit

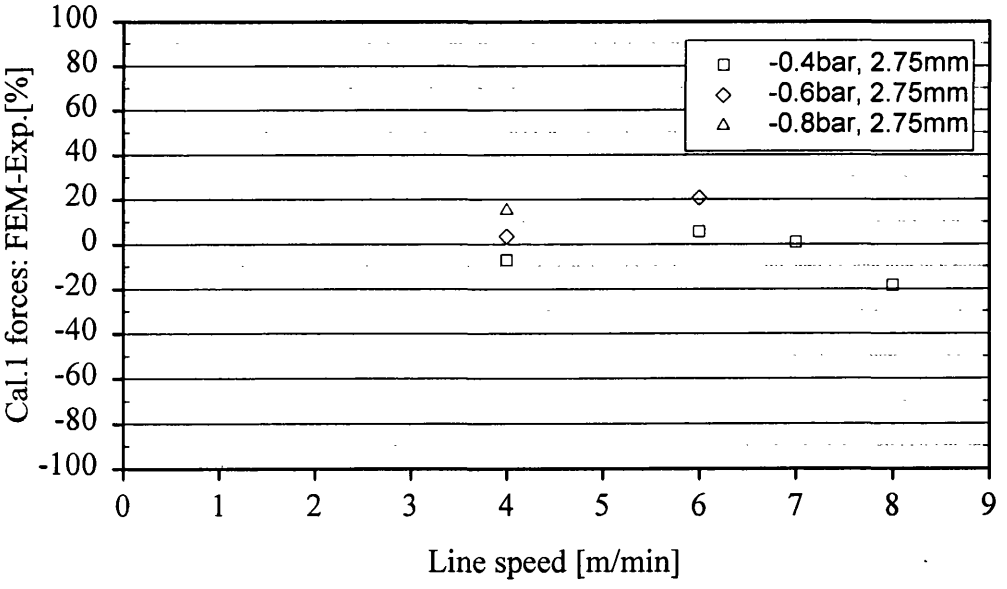

Figure 8.6: Differences between calculated and experimental forces in Calibrator 1 as function of line speed for different vacuua in wet calibration for a profile wall thickness of 2.75 mm; vacuum constant in all calibration units; 2.50 mm die exit

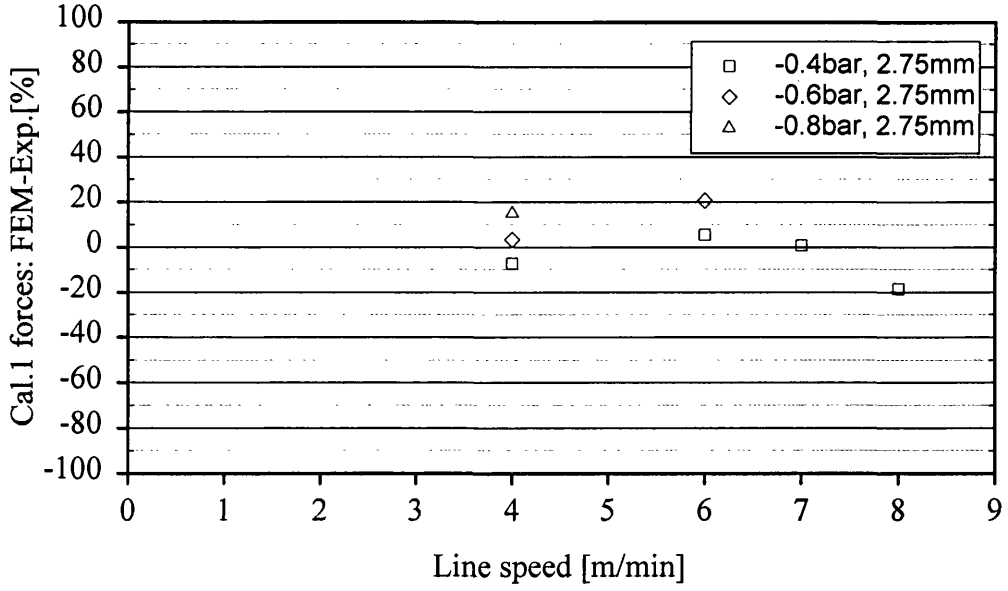

Figure 8.7: Differences between calculated and experimental forces in Calibrator 1 as function of line speed for different vacuua in wet calibration for a profile wall thickness of 3.00 mm; vacuum constant in all calibration units; 2.50 mm die exit

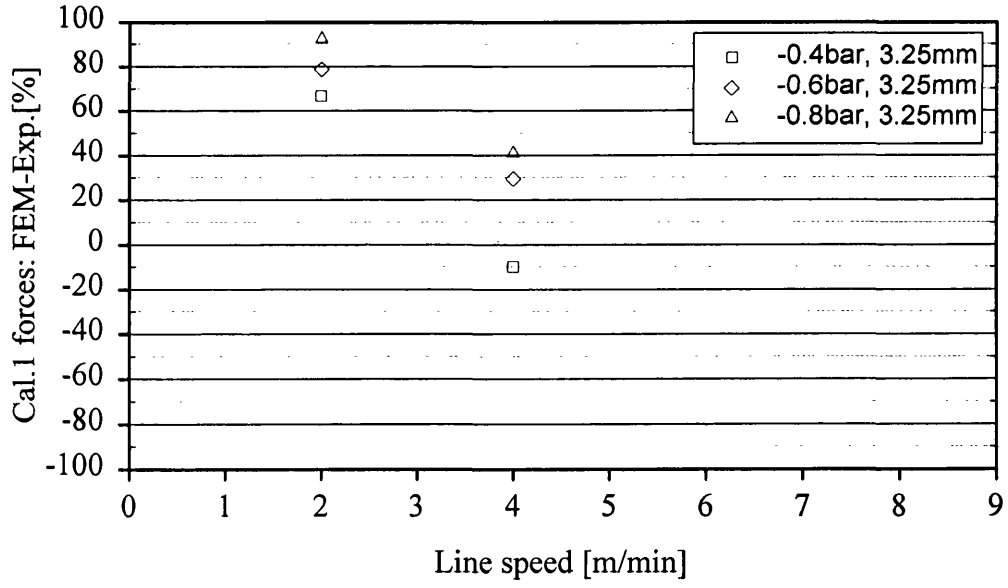

Figure 8.8: Differences between calculated and experimental forces in Calibrator 1 as function of line speed for different vacuua in wet calibration for a profile wall thickness of 3.25 mm; vacuum constant in all calibration units; 2.50 mm die exit

For Calibrator 1 forces the comparison shows trends similar to those for the total haul-off forces. The higher forces at low line speed may result from the use of the high friction coefficient of 0.6 in Calibrator 1. Furthermore, the inlet area of Calibrator 1, which is conical

to provide good pre-forming of the corner sections of the profile, could have an influence on the forces. At the end of Calibrator 1, in the downstream direction, the friction coefficient may be too high. Water coming from the intermediate water bath after Calibrator 1 can flow between the profile surface and the calibrator wall due to applied vacuum, and this will reduce the friction with a lubrication effect.

Another trend is visible in foregoing Figures, where thicker walls have shown larger differences between predicted and measured forces.

To get more insight, the vacuum in Calibrator 1 was varied from –0.2 bar to –0.8 bar whilst leaving the downstream calibrators at a constant vacuum of –0.4 bar. The comparison of calculated and measured forces in Calibrator 1 is presented now in Figure 8.9.

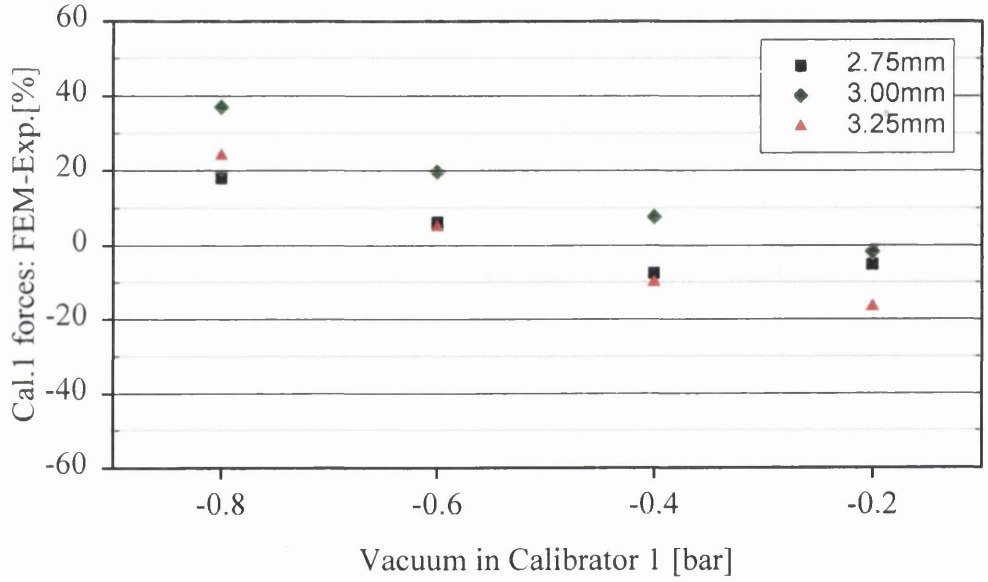

Figure 8.9: Differences between calculated and experimental forces in Calibrator 1 as function of vacuum in Calibrator 1 for different profile wall thicknesses in wet calibration; 4 m/min line speed; constant vacuum of –0.4 bar in downstream calibrators 2, 3 and 4; 2.50 mm die exit

Here, the larger discrepancies for thicker walls are not visible. But in general, the higher the forces (at higher vacuum) the higher are the percentage differences between calculated and measured forces.

Overall, it is clear that the assignment of precisely appropriate friction coefficients is very difficult, and must be based on an accumulation of data comparing simulations and experiments. The results obtained so far are, however, encouraging, and provide predictive capabilities not previously available.

8.2 Comparison of calculated and experimental profile dimensions

The dependence of profile dimensions on processing conditions was presented in Chapter 6. Here, the experimental data are now compared with the FEM calculations. The characteristic dimensions of the profile used in Chapter 6 are shown again in Figure 8.10.

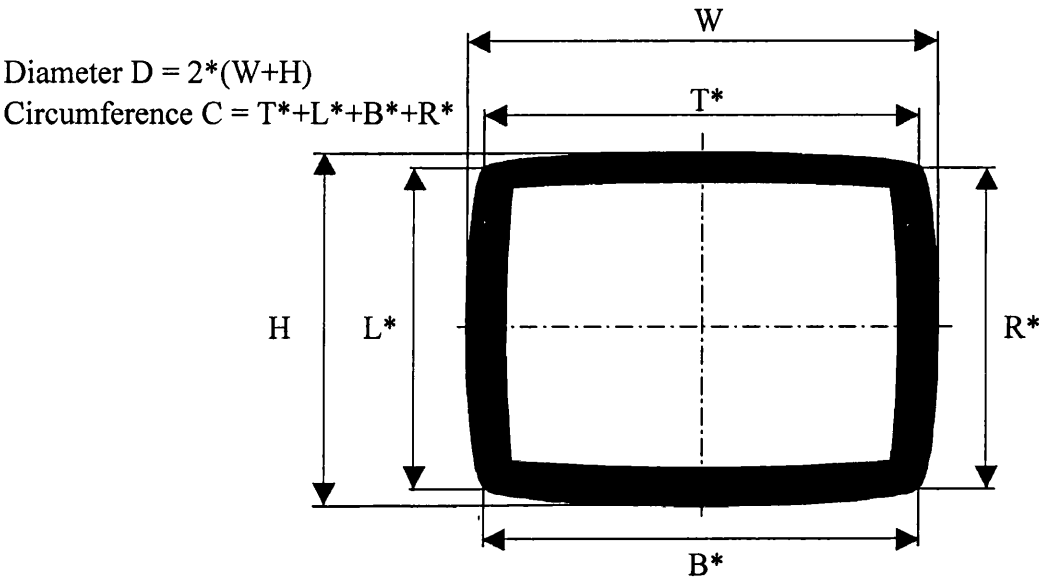

Figure 8.10: Dimensions of the profile

It was shown in Chapter 6, that D was not so strongly influenced by the haul-off forces, whilst more influence on circumference C was found. The comparison of calculated and measured profile dimension D is shown now for the same parameters of vacuum and profile wall thickness as used previously for the forces.

In the following figures, the difference is calculated as the values from FEM calculations minus the experimental values. E.g. if the computed dimension is larger than the experimental one, the difference is positive and this means that the predicted draw down is less than in the experiments. Conversely, if the difference is negative, the predicted draw down is larger than in the experiments.

First, the differences between FEM calculations and experimental results for the diameter D are presented.

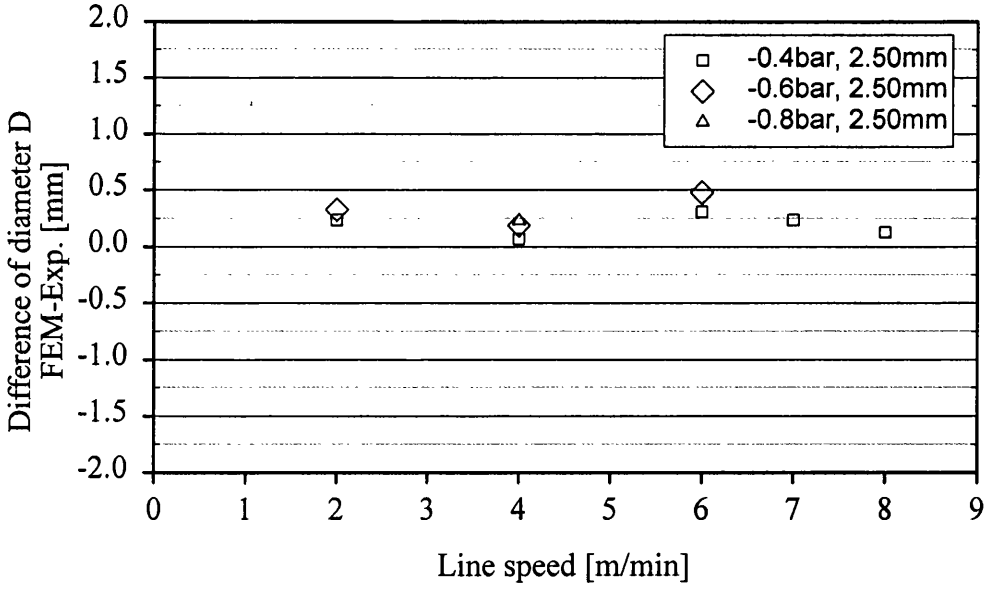

Figure 8.11: Differences between calculated and experimental profile dimension D as a function of line speed for different vacuua in wet calibration for a profile wall thickness of 2.50 mm; vacuum constant in all calibration units; 2.50 mm die exit

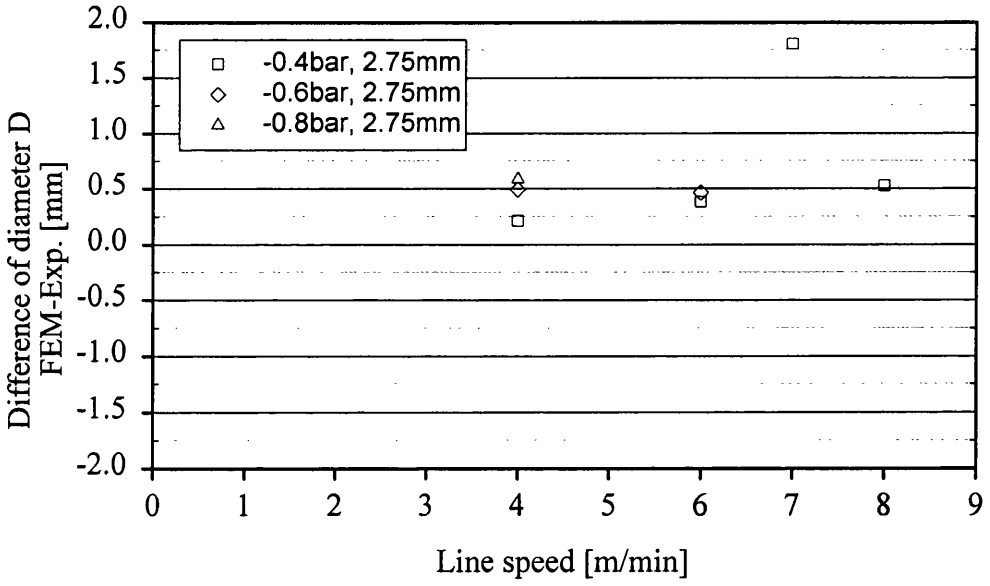

Figure 8.12: Differences between calculated and experimental profile dimension D as a function of line speed for different vacuua in wet calibration for a profile wall thickness of 2.75 mm; vacuum constant in all calibration units; 2.50 mm die exit

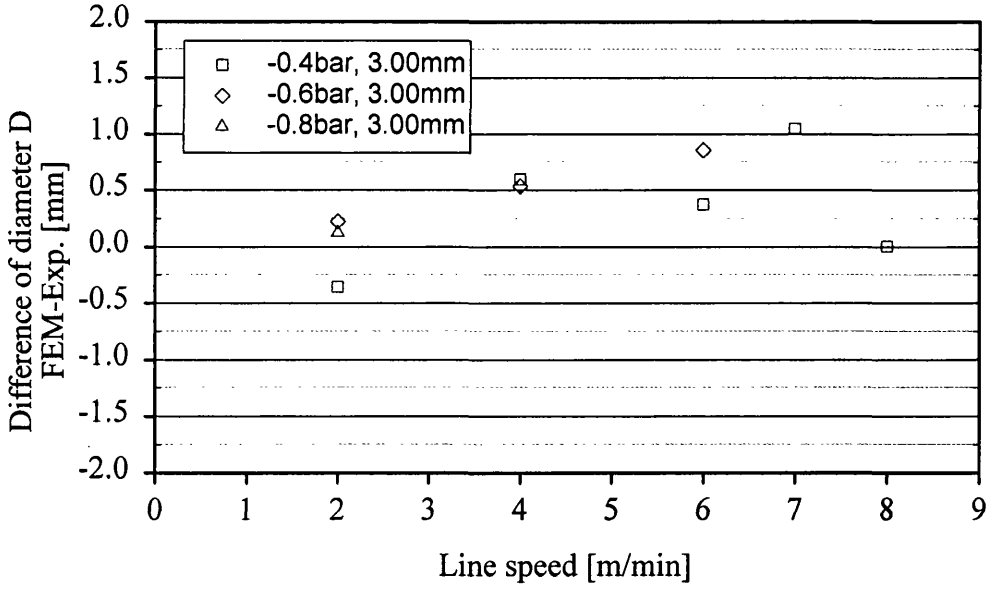

Figure 8.13: Differences between calculated and experimental profile dimension D as a function of line speed for different vacuua in wet calibration for a profile wall thickness of 3.00 mm; vacuum constant in all calibration units; 2.50 mm die exit

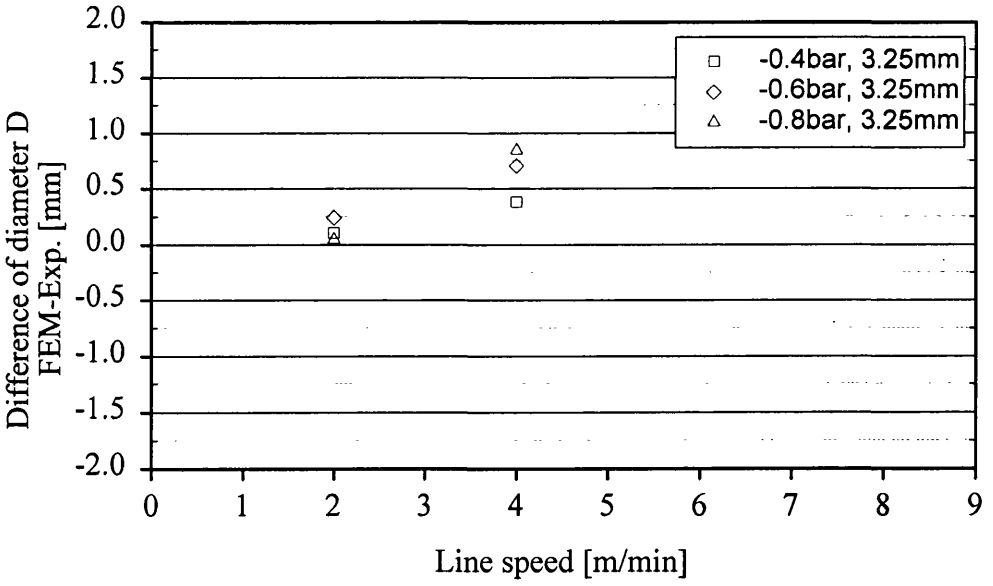

Figure 8.14: Differences between calculated and experimental profile dimension D as a function of line speed for different vacuua in wet calibration for a profile wall thickness of 3.25 mm; vacuum constant in all calibration units; 2.50 mm die exit

In general, the predicted diameter was larger than the experimental. Typically, the under prediction of D is around 0.5 mm, which amounts to 0.125 mm across each diameter of the profile. The value of 0.5 mm is to be compared with value of D at the inlet of Calibrator 1,

which is 132.86 mm. For a profile wall thickness of 2.50 mm, the line speed has shown no significant influence on differences, but for thicker profile walls, an increase in the difference is visible with an increase of line speed.

The difference in circumference C may show the same trend.
Here, typical errors in predicted values of C of 1.0 mm correspond to an error of 0.25 mm in a single corner-to-corner dimension L*, B*, R* and T*. As for the diameter D, the value of 1.0 mm has to be compared with the inlet value of C in Calibrator 1 of 132.86 mm.

The differences in circumference are shown in the next Figures.

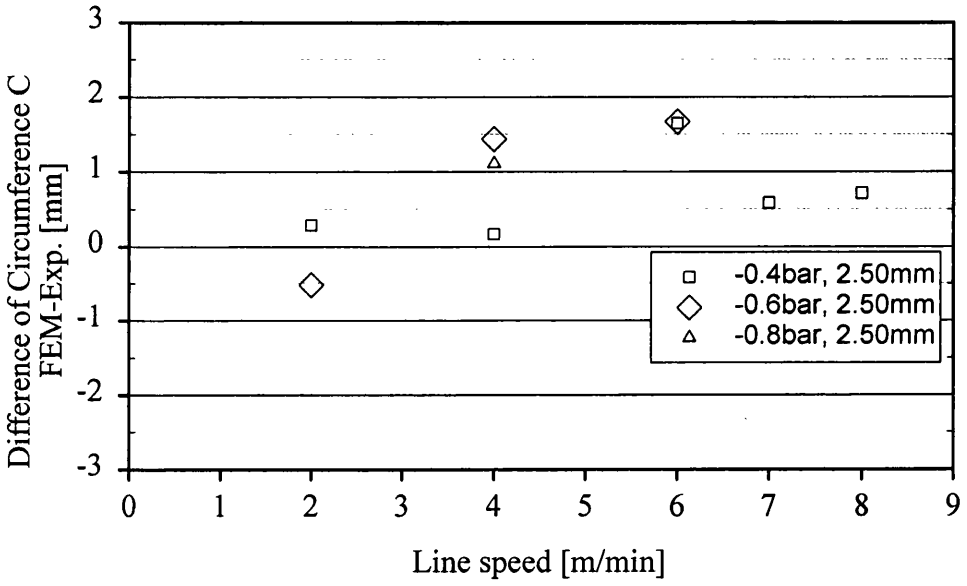

Figure 8.15: Differences between calculated and experimental profile circumference C as a function of line speed for different vacuua in wet calibration for a profile wall thickness of 2.50 mm; vacuum constant in all calibration units; 2.50 mm die exit

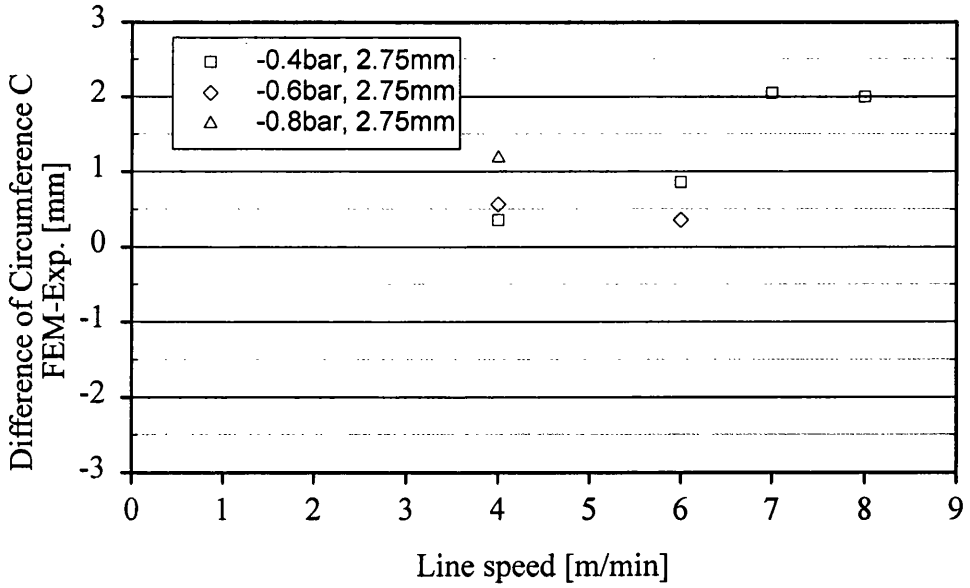

Figure 8.16: Differences between calculated and experimental profile circumference C as a function of line speed for different vacuua in wet calibration for a profile wall thickness of 2.75 mm; vacuum constant in all calibration units; 2.50 mm die exit

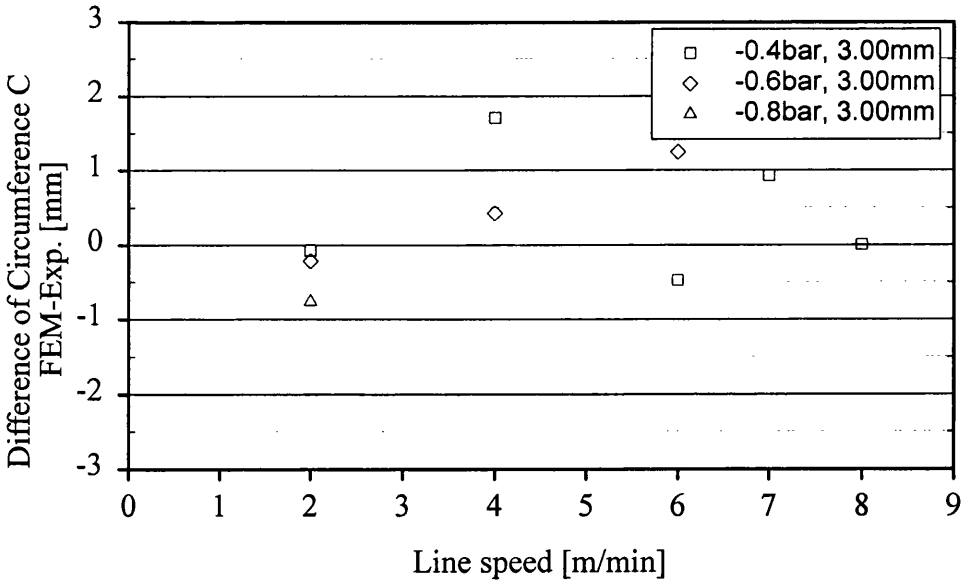

Figure 8.17: Differences between calculated and experimental profile circumference C as a function of line speed for different vacuua in wet calibration for a profile wall thickness of 3.00 mm; vacuum constant in all calibration units; 2.50 mm die exit

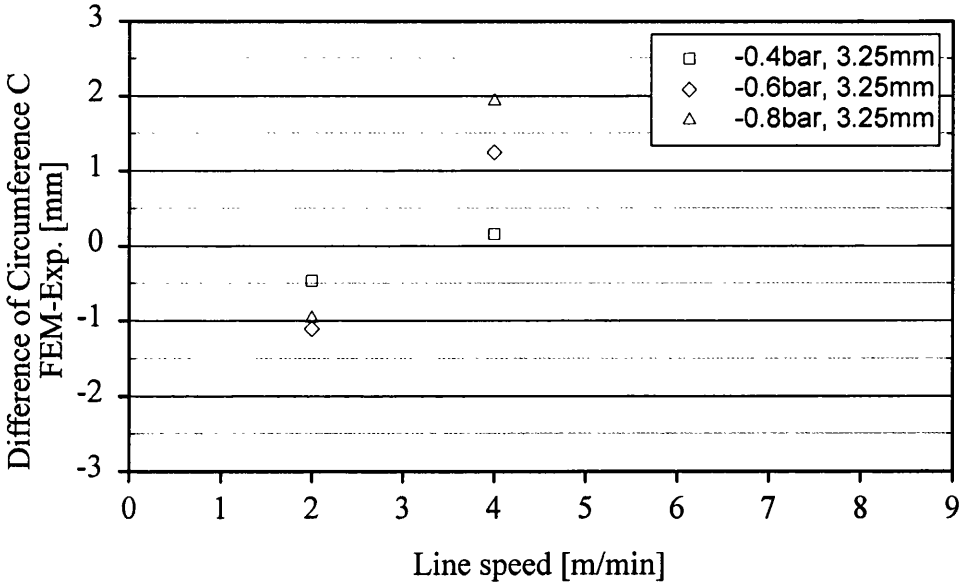

Figure 8.18: Differences between calculated and experimental profile circumference C as a function of line speed for different vacuua in wet calibration for a profile wall thickness of 3.25 mm; vacuum constant in all calibration units; 2.50 mm die exit

The results for the circumference C show the same general trends as for dimension D with an under prediction of draw down at higher line speeds.

Before conclusions are drawn, the differences in profile dimensions are shown in Figures 8.19 and 8.20 for the case where vacuum in Calibrator 1 is varied with constant vacuum of –0.4 bar in downstream calibrators, first for the diameter D.

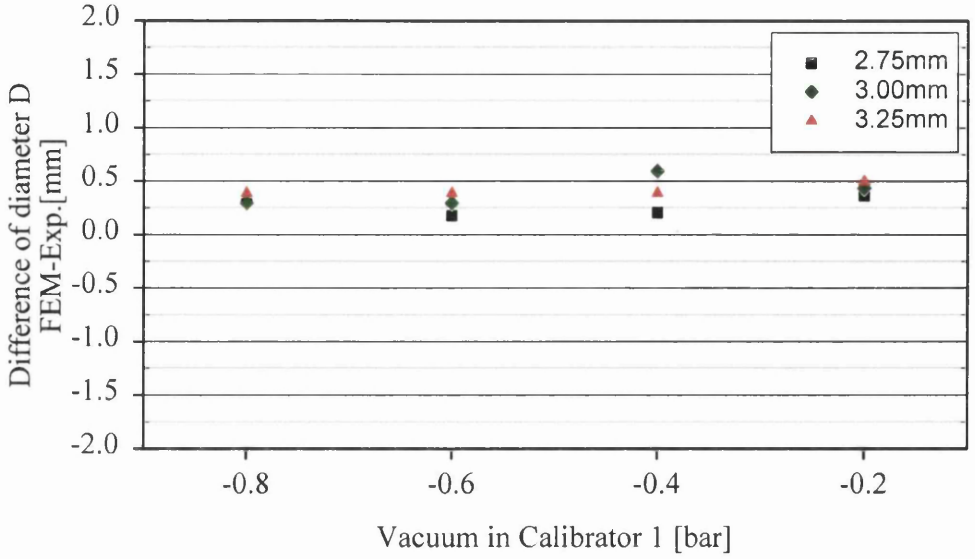

Figure 8.19: Differences between calculated and experimental profile dimension D as function of vacuum in Calibrator 1 for different profile wall thicknesses in wet calibration; 4 m/min line speed; constant vacuum of –0.4 bar in downstream calibrators 2, 3 and 4; 2.50 mm die exit

The predicated diameter D is in general larger than in the experiments, but shows no significant trend with variation of vacuum in Calibrator 1. The circumference C shows over predicted values at low vacuum of –0.2 bar. Towards higher vacuum levels, the prediction shows smaller values, scattered around zero, Figure 8.20.

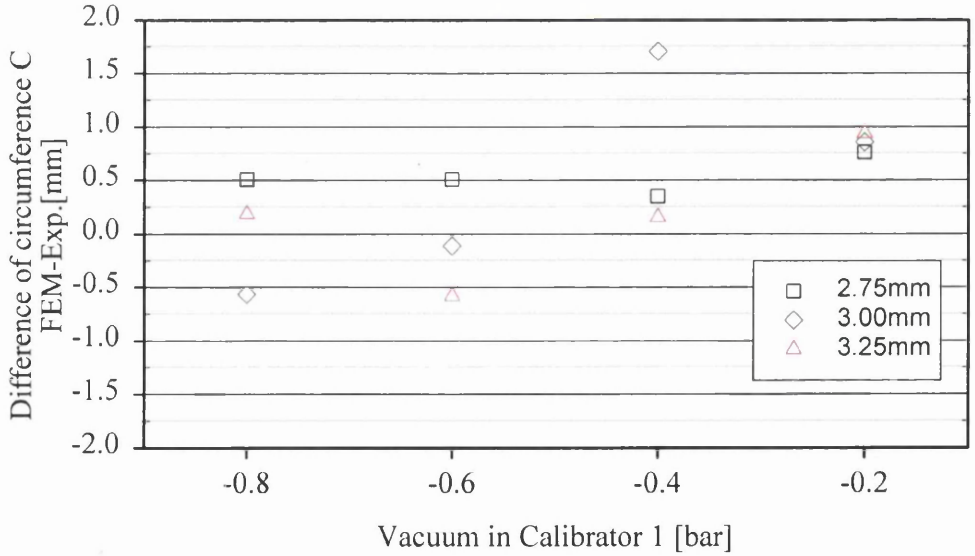

Figure 8.20: Differences between calculated and experimental profile circumference C as function of vacuum in Calibrator 1 for different profile wall thicknesses in wet calibration; 4 m/min line speed; constant vacuum of –0.4 bar in downstream calibrators 2, 3 and 4; 2.50 mm die exit

In general, however, draw down in C is under-predicted at higher line speeds. We have seen earlier in this Chapter that the haul-off forces are also generally under-predicted at higher line speed. This leads to the conclusion that over-predicted forces in the calculation produce under prediction of draw down in corner dimensions. The differences between the predicted and experimental dimensions are therefore shown now as a function of errors in the predicted haul-off forces, first for the profile diameter D in Figure 8.21.

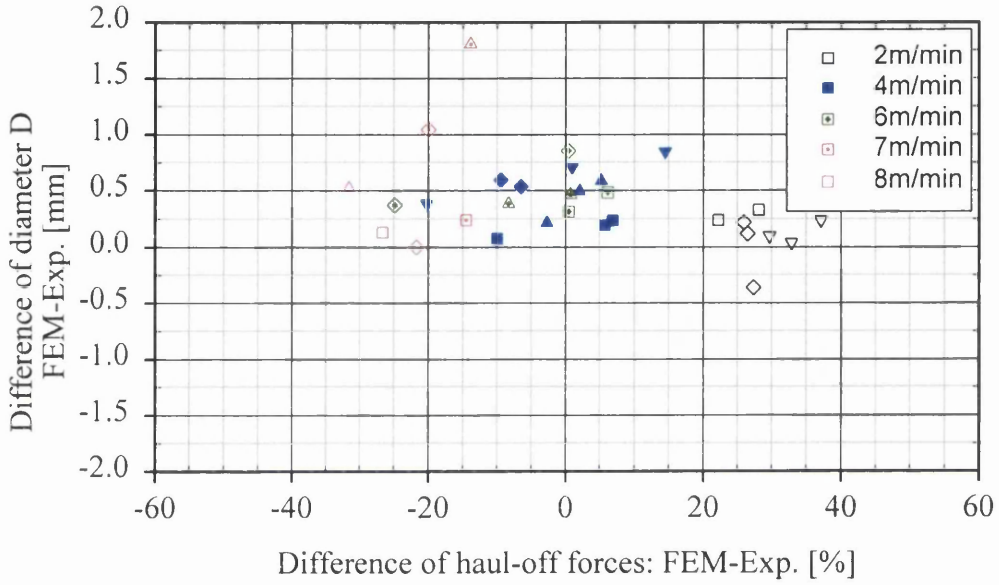

Figure 8.21: Differences in predicted diameter D as a function haul-off force errors in wet calibration for all profile wall thicknesses and vacua at different line speeds; constant vacuum in all calibration units; 2.50 mm die exit

The diameter errors do not vary very significantly with the errors in haul-off forces, although a weak correlation is visible; under-prediction of forces is associated with positive errors in predicted dimension D are under-prediction of draw down.

The circumference C has shown more sensitivity to forces, Chapter 6, and in Figure 8.22, the circumference errors are shown as function haul-off force errors.

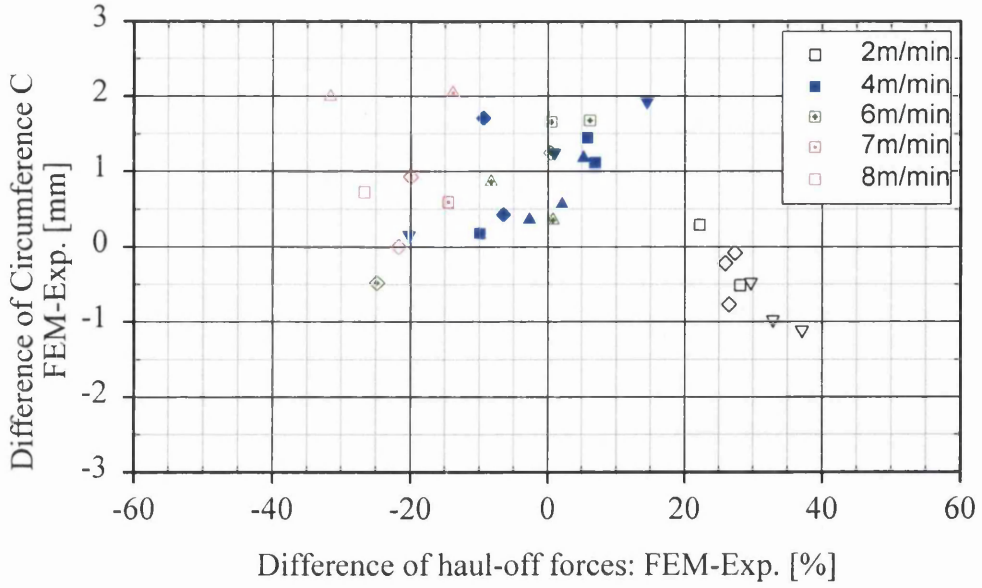

Figure 8.22: Differences in predicted circumference C as a function haul-off force errors in wet calibration for all profile wall thicknesses and vacua at different line speeds; constant vacuum in all calibration units; 2.50 mm die exit

Here a stronger correlation is visible; the forces are over predicted for a line speed of 2 m/min and the draw down of the circumference C is over predicted. At higher line speeds, the trends are opposite.

Summary

The comparisons of measured and calculated forces and profile dimensions have shown trends, which are a step forward in the simulation of the calibration process. There are several possibilities for the differences. It seems that a key parameter is the friction between profile surface and calibrator surface. Here, the friction coefficient is dominant. It was presented in Chapter 3, that the friction coefficient is dependent on several parameters, e.g. surface roughness, lubrication, temperature, line speed, etc.. The next step would be here to use more parameters in the modelling of the friction. This means that the friction must be investigated in more detail. Another problem seems to be the inlet of Calibrator 1. It is conical to promote a good pre-forming of the corner sections of the profile as mentioned before. At the moment, the cross section of the calibrator inlet is not modelled with its conical shape. A 3-D model should improve the prediction in this section. Another problem is also present here, because the profile surface temperatures are close to the melt extrusion temperature and this could

cause problems in the modelling due to non-availability of friction data at higher temperatures.

Altogether, the preliminary results have shown a good start point for the simulation of the calibration process.

CHAPTER 9

Conclusion

This work has provided a comprehensive overview of the uPVC calibration process with details and correlations showing the influence of the process parameters and resultant conditions on the calibration line on profile properties and geometry. Additionally, a preliminary comparison of experimental results with computer simulations of calibrator forces and resulting profile geometry has been made.

Summaries of conclusions have been given at the end of each main section in the proceeding Chapters, to which the reader is referred for more quantitative detail. In this final Chapter the main conclusions are highlighted qualitatively.
In the experiments, the processing parameters in wet and dry calibration included line speed, vacuum, profile wall thickness, melt extrusion and coolant temperatures. These were varied over a wide range to investigate their influence on calibrator forces, haul-off forces and heat transfer coefficients in the process, and on shrinkage, dimensions, impact and stress of the final profile. To provide a clear picture, a simple rectangular section hollow profile was chosen as the test profile.

The dry calibration system in general showed higher haul-off forces at a given applied vacuum in comparison with wet calibration, where water was used in the intermediate water baths between the calibration units. In Calibrator 1, the forces in wet and dry calibration were similar, whereas in the downstream calibrators, the forces in dry calibration are higher than in wet calibration. In dry calibration, where no coolant water contacts the outer profile surface, the forces in the calibration process are higher due to the absence of lubricating effect.
This leads finally to higher draw down (reduction of dimensions) in dry calibration, especially for the corners of the profile, whereas the width and height dimensions were not influenced so strongly, being more effectively controlled by the applied vacuum.

An increase of vacuum in general increased the calibrator forces, as is well known in practice.

The variation of vacuum in Calibrator 1, whilst maintaining constant vacuum in the downstream calibrators, gave more insights into the importance of the design of Calibrator 1.

An increase of melt extrusion temperature led to an increase of forces between the profile surface and calibrator walls. This results mainly from the increase of friction coefficients at higher melt temperatures. In contrast, an increase of coolant temperature led to a reduction of forces, and this is likely to be the result of increased stretching of the profile due to a reduced thickness of the solidified layer, which carries the tensile haul-off forces and so to a loss of contact of profile and calibrator wall.
Higher profile surface temperatures are also visible in Calibrator 1 at higher line speeds. However, the haul-off forces are decreasing and this again is due to increased draw down and loss of contact.

The use of the simple profile geometry made possible correlations for the reduction of corner dimensions with haul-off forces in the process. The variation of vacuum in Calibrator 1 has shown most influence, because here the solidified layer of the profile is too weak to resist the forces. The use of thicker profile walls has shown less reduction of corner dimensions than with a thinner wall. This leads to the conclusion that the stiffness of the thicker wall is very important.

The profile quality specification gives a limit for the shrinkage values of the final product. Measured shrinkage shows a good correlation with forces in the process, especially the forces in Calibrator 1. Likewise the maximum stress in the profile, calculated from the bending of strips cut out of the profile, correlates with haul-off forces. The observed shrinkage results from superimposed effects in the calibration process. An initial component is present at the die exit due to the orientation and stretching of the uPVC whilst passing the die. On the way to the inlet to Calibrator 1, the shrinkage potential can be reduced by allowing some strain recovery, achieved by an increase of profile wall thickness as line speed is reduced at constant extruder throughput.
During the calibration, the haul-off forces are stretching both the thin solidified layer below glass transition temperature and the molten parts of the profile. In the solidified layer, the strains are frozen in, whereas in the molten layer the strains can recover. This leads to higher shrinkage values in the initially formed solidified layers.

Impact strength has shown a dependence on melt temperature. For the impact measurement, it is necessary to keep the thickness of the specimen constant. A variation of thickness can give misleading values in the impact tests.

Heat transfer in the calibration process was also investigated in detail. This was based on measured profile surface and calibrator wall temperatures, as well as on coolant temperatures. Most interesting was the influence of line speed and wet or dry calibration. At higher lines speeds, the profile surface temperatures are higher than those at lower line speeds. Dry calibration showed significant reheating of the profile surface between the calibrators.
Notable was the loss of contact between profile and calibrator near to the corners, due to draw down, and this resulted in higher profile surface temperatures and decreased heat transfer coefficients. Separation of thermal resistances in the calibration system has shown that heat transfer between profile surface and calibrator wall is most important in the cooling process.

Finally, a preliminary comparison of experimental results with computer simulations for the forces in the calibration process, and for the final profile dimensions, has indicated areas for the improvement of the simulations. The forces were over-predicted at low line speed as was the draw down, whereas at higher line speeds, the forces and draw down were under-predicted. The key factor seems to be the assumed value of the friction coefficient between the profile and the calibrator surface. Here, more investigations and improvements must be made to reduce the error in simulations. A further area for improvement will be the use of data on heat transfer coefficients as a function of positions around the profile and along the line, in place of the constant values currently assumed in the simulations.

Altogether, the preliminary results show promising and significant progress in simulating and predicting the profile calibration process on a computer.

CHAPTER 10

References

[1] *ECVM:* European Council of Vinyl Manufacturers, http://www.ecvm.org, 2003

[2] *E.J. Krüger*: Aufbereitung von PVC. Thesis, RWTH Aachen, 1985

[3] *D. Braun, G.W. Becker, H.K. Felger*: Kunststoff-Handbuch: Polyvinylchlorid 2/1 and 2/2, Hanser-Verlag, 1986

[4] *L.I. Nass, C.A. Heiberger*: Encyclopedia of PVC, Marcel Dekker-Publisher, 1986

[5] *G. Matthews*: PVC: Production, Properties and Uses, Publisher: Institute of Materials, London, 1996

[6] *A. Stieneker*: Herstellung, Eigenschaften und Anwendungen von PVC. In: PVC, Rezeptierung, Aufbereitung, Verarbeitung und Recycling. VDI-Verlag, 2002

[7] *G. Goldbach*: Physikalische Struktur. In: Polyvinylchlorid 2/1. Kunststoff-Handbuch, Hanser-Verlag, 1986

[8] *B. Terwiesch*: Einfluß des Herstellungsverfahren auf die Eigenschaften von Roh-PVC. In: Polyvinylchlorid 2/1. Kunststoff-Handbuch, Hanser-Verlag, 1986

[9] *H. Finkmann*: Einführung in die Verarbeitung von PVC. In: Polyvinylchlorid 2/1. Kunststoff-Handbuch, Hanser-Verlag, 1986

[10] *J. Warmuth*: Rheologische und thermodynamische Grundlagen der PVC-Verarbeitung. In: Polyvinylchlorid 2/2. Kunststoff-Handbuch, Hanser-Verlag, 1986

[11] *G. Schröter*: Anwendungstechnische Eigenschaften von PVC und Normung. In: Polyvinylchlorid 2/1. Kunststoff-Handbuch, Hanser-Verlag, 1986

[12] *G.A. Crolla*: Morphologische und verfahrenstechnische Untersuchung an PVC. Thesis, RWTH Aachen, 1988

[13] *A. Polte, H.-U. Schreiter, H.-D. Herrmann*: Extrudieren von Rohren, Profilen, Schläuchen und Ummantelungen. In: Polyvinylchlorid 2/1. Kunststoff-Handbuch, Hanser-Verlag, 1985

[14] *G. Menges, N. Berndtsen*: Beeinflussungsmöglichkeiten der Überstruktur von PVC durch gezielte Änderung der Verarbeitungsparameter bei der Extrusion und Feststellung der Zusammenhänge, Institut für Kunststoffverarbeitung, RWTH Aachen, 1978

[15] *J.W. Summers, E.B. Rabinovitch*: The effects of polyvinylchloride hierarchical structure on processing and properties. In: Journal of Vinyl Technology, 13(1), 1991

[16] *K. Flatau*: Kommerzielle Vinylchlorid-Polymerisationsverfahren. In: Polyvinylchlorid 2/1. Kunststoff-Handbuch, Hanser-Verlag, 1986

[17] *J. Warmuth*: Analyse des Verarbeitungsprozesses von schlagzähem PVC. Thesis, RWTH Aachen, 1978

[18] *M. Gilbert, Z. Liu*: Effect on orientation on PVC structure and properties, PVC'87, 1987. Brighton, UK

[19] *J.W. Summers*: The Nature of poly(vinyl chloride) Crystallinity - The Microdomain Structure. In: Journal of Vinyl Technology, 3(2), 1981

[20] *D.J. Hitt, M. Gilbert*: Tensile properties of PVC at elevated temperatures. In: Materials Science and Technology, 8, 1992

[21] *M. Gilbert, Z. Liu, D.J. Hitt*: Biaxial orientation of poly(vinyl chloride) compounds: Interaction between drawing, structure and properties. In: Polymer Engineering and Science, 37, November, 1997

[22] *J.A. Covas, J.M. Maia*: Relationship between gelation and wall slip in unplasticised poly(vinyl chloride) compounds. In: Plastics, Rubber and Composites, 28, 1999

[23] *J.A. Covas, M. Gilbert, D.E. Marshall*: Twin screw extrusion of a rigid PVC compound - effect on fusion and properties. In: Plastics and Rubber Processing and Applications, 9, 1988

[24] *M.W. Allsopp*: Mechanism of gelation of rigid PVC. In: Manufacturing and processing of PVC. 1982

[25] *H. Hubbert*: Prüfmethoden für PVC. In: Polyvinylchlorid 2/1. Kunststoff-Handbuch, Hanser-Verlag, 1986

[26] *J. Parey*: Untersuchungen zum Gelierverhalten von PVC. Thesis, RWTH Aachen, 1981

[27] *D.J. Calvert, B. Haworth, R.C. Stephenson*: The use of fracture mechanics to describe the impact strength of PVC window profiles, PVC'90, 1990. Brighton, UK

[28] *B. Cora, B. Daumas, A. Zegers*: Impact strength and morphology in poly(vinyl chloride) window profiles - relationship with gelation level. In: Plastic, Rubber and Composites, 28, 1999

[29] *O.P. Obande, M. Gilbert*: Effect of formulation and processing conditions on PVC fusion. In: Plastics and Rubber Processing and Applications, 10, 1988

[30] *B. Terselius, J. Bystedt*: Gelation of rigid PVC pipes. In: Journal of Macromolecular Science and Physics, B, 20, 1981

[31] *J.A. Covas, M. Gilbert*: Single screw extrusion of PVC: Effect on fusion and properties. In: Polymer Engineering and Science, 32, 1992

[32] *T. Kuriyama, I. Narisawa, R. Shiina, M. Kotaki*: Effects of morphology on the fracture toughness of PVC-U pipe. In: ANTEC '98, 1998

[33] *D.J. Hitt, M. Gilbert*: Biaxial orientation of poly(vinyl chloride) compounds, Part2 - Structure-property relationships and their time dependency. In: Plastics, Rubber and Composites, 29, 2000

[34] *A. Selwood, A.K. Taraiya, I.M. Ward*: The preparation and properties of die-drawn polyvinlychloride tubes. In: Plastics and Rubber Processing and Applications, 10, 1988

[35] *M. Gilbert, D.J. Hitt, J.B. Harte*: The biaxial orientation of PVC compounds: I. mechanical properties. In: Plastics, Rubber and Composites Processing and Applications, 22, 1994

[36] *S. Zeidler*: Aussagefähige Messmethoden zur Beurteilung von PVC-Rezepturen. In: PVC, Rezeptierung, Aufbereitung, Verarbeitung und Recycling. VDI-Verlag, 2002

[37] *K.P. Klenk*: Beitrag zur werkstoffgerechten Verarbeitung von PVC-Hart-Pulver auf Einschneckenextrudern. Thesis, RWTH Aachen, 1969

[38] *B. Kemper, G. Menzel*: Abbau von PVC. In: Polyvinylchlorid 2/1. Kunststoff-Handbuch, Hanser-Verlag, 1986

[39] *J. Thomssen*: Additive und Zuschlagsstoffe für PVC. In: PVC, Rezeptierung, Aufbereitung, Verarbeitung und Recycling. VDI-Verlag, 2002

[40] *H. Andreas*: PVC-Stabilisatoren. In: Polyvinylchlorid 2/1. Kunststoff-Handbuch, Hanser-Verlag, 1986

[41] *H. Neumann*: Pigmente und Farbstoffe für PVC. In: Polyvinylchlorid 2/1. Kunststoff-Handbuch, Hanser-Verlag, 1986

[42] *W. Reith*: Rezeptierung von PVC. In: PVC, Rezeptierung, Aufbereitung, Verarbeitung und Recycling. VDI-Verlag, 2002

[43] *P. Kläß*: Aktuelle Aspekte der PVC-Stabilisierung. In: PVC, Rezeptierung, Aufbereitung, Verarbeitung und Recycling. Series "Kunststofftechnik", VDI-Verlag, 2002

[44] *J.W. Summers, E.B. Rabinovitch, J.G. Quisenberry*: Polyvinyl Chloride Processing Morphology: Part III - Twin Screw Extrusion. In: Journal of Vinyl Technology, 4(2), 1982

[45] *R. Kling*: Gleitmittel für die PVC-Verarbeitung. In: PVC, Rezeptierung, Aufbereitung, Verarbeitung und Recycling. VDI-Verlag, 2002

[46] *B. Terselius, J.-F. Jansson, J. Bystedt*: Gelation of PVC, Part 4: Impact strength. In: Plastics and Rubber Processing and Applications, 5, 1985

[47] *G. Menzel*: Hochpolymere Additive zur Verbesserung der Schlagzähigkeit von PVC. In: Polyvinylchlorid 2/1. Kunststoff-Handbuch, Hanser-Verlag, 1986

[48] *W.J. McGill, T. Wittstock*: The effect of processing temperature on the impact strength of PVC blended with a particulate acrylic modifier. In: Plastics and Rubber Processing and Applications, 7, 1987

[49] *L. Gervat, J.P. Disson, C. Bianchi, C. Marvalin, P. Morel*: Temperature and impact rate dependence of the ductile/brittle transition of impact modified PVC, PVC'96, 1996. Brighton

[50] *N. Berndtsen*: Einfluss der Verarbeitung auf Struktur und Eigenschaften von Polyvinylchlorid (PVC). Thesis, RWTH Aachen, 1978

[51] *J.W. Summers*: A review of Vinyl Technology. In: Journal of Vinyl & Additive Technology, 3, June 1997, 1997

[52] *D. Seiffert*: Pigmentierung und Einfärbung von Hart-PVC. In: PVC, Rezeptierung, Aufbereitung, Verarbeitung und Recycling. VDI-Verlag, 2002

[53] *E.E. Lang*: Füllstoffe für PVC. In: Polyvinylchlorid 2/1. Kunststoff-Handbuch, Hanser-Verlag, 1986

[54] *M. Grosse-Aschhoff*: Optimierung des Mischprozesses bei PVC für Fensterprofile. In: Kunststoffe, 89, 1999

[55] *T. Hülsmann, A. Bos*: Plate-out in Extrusionsprozessen. In: PVC, Rezeptierung, Aufbereitung, Verarbeitung und Recycling. VDI-Verlag, 2002

[56] *D. Braun, E. Bezdadea*: In: Die Angewandte Makromolekulare Chemie, 113, 1983

[57] *R.F. Lippoldt*: Postulated mechanism for plate-out from PVC processing systems, ANTEC'78, 1978.

[58] *G. Bussmann, H. Ruse, B. Herr*: Plate-out bei der PVC-Verarbeitung. In: Kunststoffe, 88, 1998

[59] *M. Gilbert, N. Varshney, K.v. Soom, M. Schiller*: Plate-out in PVC extrusion, PVC 2002, 2002. Brighton, UK

[60] *G. Menges, P. Thienel, W. Kemper*: Das physikalische Verhalten von Thermoplasten bei der Aufnahme von p-v-T-Diagrammen unter verschiedenen Meßbedingungen. In: Plastverarbeiter, 28, 1977

[61] *P.A. Rodgers*: Pressure-volume-temperature relationships for Poly(vinylidene fluoride) and Polyamide-11. In: Journal of Applied Polymer Science, 50, 1993

[62] *P.A. Rodgers*: Pressure-volume-temperature relationships for Polymeric liquids: A review of equations of state and their characteristics for 56 polymers. In: Journal of Applied Polymer Science, 48, 1993

[63] *J.M. Hutchinson*: Relaxation processes and physical aging. In: The physics of glassy polymers. Kluwer Academic Publishers, 1997

[64] *H.-J. Ott*: Physikalische Alterung von amorphen Thermoplasten im Glaszustand. Thesis, TH Darmstadt, 1979

[65] *VDMA*: Kenndaten für die Verarbeitung thermoplastischer Kunststoffe, Teil 1, Thermodynamik, Carl Hanser Verlag, 1979

[66] *E. Grünschloss, L. Radtschenko*: Experimentelle Bestimmung der Wärmeübergangszahlen bei der Kühlung extrudierter Kunststoffrohre aus HD-PE im Wasserbad. In: Plastverarbeiter, 30. Jahrgang, 1979

[67] *U. Kleindienst*: Einflußgrößen beim Vakuumkalibrieren von extrudierten Kunststoffrohren. In: Kunststoffe, Bd. 63, 1973

[68] *E. Haberstroh*: Analysis of cooling sections in extrusion lines. Thesis, RWTH Aachen, 1981

[69] *A.v. Harnier*: Kühlen von Flachfolien. In: Kühlen von Extrudaten. Düsseldorf, VDI-Verlag, 1978

[70] *H.G. Fritz, S. Fang*: Rechnergestützte Auslegung von Kalibrierwerkzeugen. In: Extrusionswerkzeuge, Schwerpunkt Profilwerkzeuge. VDI-Verlag, 1996

[71] *S. Fang, H.-G. Fritz*: Auslegung und Optimierung von Profilwerkzeugen komplexer Geometrien mittels FEM. In: Extrusionswerkzeuge, Schwerpunkt Profilwerkzeuge. VDI-Verlag, 1996

[72] *W. Michaeli*: Extrusionswerkzeuge für Kunststoffe und Kautschuk, VDI-Verlag, Düsseldorf, 1991

[73] *W. Sommer*: Elastisches Verhalten von Polyvinylchlorid bei statischer und dynamischer Beanspruchung. In: Kolloid-Zeitschrift, Band 167, 1959

[74] *F. Povolo, G. Schwartz, E.B. Hermida*: Temperature and Strain Rate dependence of the Tensile Yield Stress of PVC. In: Journal of Applied Polymer Science, 61, 1996

[75] *A. Crugnola, M. Pegoraro, F. Danusso*: High-temperature mechanical behaviour of unplastizied Poly(vinyl chloride). In: Journal of Polymer Science: Part A2, 6, 1968

[76] *K.L. Ngai, A.F. Yee*: Somme Connections between Viscoelastic Properties of PVC and Plastizised PVC and Molecular Kinetics. In: Journal of Polymer Science, Part B, Polymer Physics, 29, 1991

[77] *H. Bastian*: Development of a viscoelastic model for extruded u-PVC profiles. Thesis, University of Wales Swansea, 1997

[78] *M. Pahl, W. Gleissle, M. Laun*: Praktische Rheologie der Kunststoffe und Elastomere, VDI-Verlag-Gesellschaft Kunststofftechnik, Düsseldorf, 1991

[79] *V. Hayes*: Effect of formulation variables on rheology of rigid PVC, ANTEC'99, 1999.

[80] *M.A. Huneault, P.J. Carreau, P.G. Lafleur, V.P. Gupts*: Effect of selected additives on extrudate swell and rheological properties of rigid PVC. In: ANTEC'92, 1992

[81] *L.A. Ultracki*: Melt viscosity of Poly(Vinyl Chloride) formulations. In: Polymer Engineering and Science, 14, April, 1974

[82] *L.A. Ultracki*: Rheology of PVC. Part 5: Melt elasticity. In: Journal of Vinyl Technology, 8, December, 1986

[83] *P.L. Shah*: New development in melt rheology aid formulating rigid Vinyl compounds with improved extrusion processing. In: Journal of Vinyl & Additive Technology, 2, 1996

[84] *E.L. Hinrichsen, P. Thorsteinsen*: Effects of processing and degree of fusion on the rheology of PVC. In: Journal of Vinyl & Additive Technology, 2, March, 1996

[85] *W. Grässley, S. Glassock, R. Crawley*: Die swell in molten polymers. In: Transactions of the society of rheology, 14, 1970

[86] *S.B. Driscoll, C.P. Grolman*: The rheology of PVC. In: Journal of Vinyl Technology, 9, June, 1987

[87] *T. Glomsaker, E.L. Hinrichsen, A. Larsen, P. Thorsteinsen*: Rheological properties of suspension PVC formulations in extrusion dies. In: Plastic, Rubber and Composites, 1999

[88] *T. Glomsaker, E.L. Hinrichsen, F. Iregens, P. Thorsteinsen*: Numerical simulations of extrusion of S-PVC formulations in a capillary rheometer. In: Rheologica Acta, 2000

[89] *D. Riley*: The effects of lubricants on Processing - Part I. Detection by PVC melt flow. In: J. of Vinyl and Additive Technology, 1999

[90] *B. Schmid*: Betrachtung von Düsenkonzepten. In: Extrusionswerkzeuge, Schwerpunkt Profilwerkzeuge. VDI-Verlag, 1996

[91] *I. Szarvasy, J.F.T. Pittman*: Pressure drop and die surface changes in uPVC extrusion. In: Polymer Enginering & Science, August, 2003

[92] *H. Offermann*: Die Rheometrie wandgleitender Kunststoffschmelzen untersucht am Beispiel von Hart-PVC. Thesis, RWTH Aachen, 1972

[93] *G.A. Martin, W. Schuler*: Verknüpfung von Werkzeugbau und Profilproduktion durch fraktale Organisationsstrukturen - ein Weg nach vorn. In: Extrusionswerkzeuge, Schwerpunkt Profilwerkzeuge. VDI-Verlag, 1996

[94] *H.C. Wessel*: Auslegung von Profilwerkzeugen mit konventionellen Methoden. In: Extrusionswerkzeuge. VDI-Verlag, 1993

[95] *K. Kapfer, H.D. Aeppli*: Granulieren von PVC. In: PVC, Rezeptierung, Aufbereitung, Verarbeitung und Recycling. VDI-Verlag, 2002

[96] *H. Richter, N. Bruns*: Werkstoffliches Recycling von PVC - Ein Erfahrungsbericht. In: PVC, Rezeptierung, Aufbereitung, Verarbeitung und Recycling. VDI-Verlag, 2002

[97] *M.H. Pahl*: Mischen , Fördern und Dosieren. In: Kunststoffe, 88, 1998

[98] *R. Baumann*: Automatische Heiz-Kühlmischerbeschickung mit PVC, Füllstoffen und Additiven. In: PVC, Rezeptierung, Aufbereitung, Verarbeitung und Recycling. Series "Kunststofftechnik", VDI-Verlag, 2002

[99] *J. Heine*: Mischen von PVC. In: PVC, Rezeptierung, Aufbereitung, Verarbeitung und Recycling. VDI-Verlag, 2002

[100] *H. Wilms, G. Veit*: Lagern, Mischen und Fördern von PVC bei der Herstellung und Verarbeitung. In: PVC, Rezeptierung, Aufbereitung, Verarbeitung und Recycling. VDI-Verlag, 2002

[101] *G.A. Martin*: Verunreinigungen im Dryblend, Umlauf- und Recyclingmaterial. In: PVC, Rezeptierung, Aufbereitung, Verarbeitung und Recycling. VDI-Verlag, 2002

[102] *W. Schuler*: Abstimmung von Rezeptur und Schnecke bei Doppelschneckenextrudern. In: PVC, Rezeptierung, Aufbereitung, Verarbeitung und Recycling. VDI-Verlag, 2002

[103] *W. Michaeli, K. Hartwig*: Analytische und numerische Verfahren zur Auslegung von Extrusionswerkzeugen. In: Extrusionswerkzeuge, Schwerpunkt Profilwerkzeuge. VDI-Verlag, 1996

[104] *A. Sobotta*: Werkzeuge für die Profilextrusion. In: Auslegung von Extrusionswerkzeugen. Aachen, VDI-Verlag, 1996

[105] *U. Dombrowski*: Ein Beitrag zur rheologischen Auslegung von Profilwerkzeugen. Thesis, RWTH Aachen, 1989

[106] *W. Michaeli, K. Hoffman*: Grundlegendes Auslegen und anschließende Überprüfung der Ergebnisse von Extrusionswerkzeugen mittels FEM. In: Extrusionswerkzeuge, Schwerpunkt Profilwerkzeuge. VDI-Verlag, 1996

[107] *M. Kalwa*: Application of the Finite Element method for the simulation of heat transfer phenomena in plastic processing. Thesis, RWTH Aachen, 1990

[108] *B. Gesenhues*: Rechnerunterstützte Auslegung von Fließkanälen für Polymerschmelzen. Thesis, RWTH Aachen, 1984

[109] *K. Hoffmann*: Fließkanalberechnung an Profilwerkzeugen mit Finite-Element-Methoden. In: Extrusionswerkzeuge. VDI-Verlag, 1993

[110] *A. Lawal, S. Railkar, D. Kalyon*: Mathematical modelling of three-dimensional die flows of viscoplastic fluids with wall slip, ANTEC'99, 1999.

[111] *J. Pfendler, C. Caldwell*: Verification of a CAE extrusion simulation package with an actual profile extrusion die. In: Antec '96, 1996

[112] *W.A. Gifford*: The use of three-dimensional computational fluid dynamics in the design of extrusion dies, ANTEC'96, 1996.

[113] *CPPSD:* Centre for Polymer Processing Simulation and Design, University of Wales Swansea, UK, 2001

[114] *Fluent:* http://www.fluent.com, 1998

[115] *W. Limbach*: Von der Anfrage zum Profilwerkzeug: Methodische Vorgehen in der Produktionsvorphase. In: Extrusionswerkzeuge, Schwerpunkt Profilwerkzeuge. VDI-Verlag, 1996

[116] *R. Kössl, T. Mayer*: Entwicklungstendenzen bei der Profilextrusion. In: PVC, Rezeptierung, Aufbereitung, Verarbeitung und Recycling. VDI-Verlag, 2002

[117] *F. Wimmer, M. Kronegger*: Prozeßkette Werkzeugherstellung. In: Das Extrusionswerkzeug - Leitfaden zur Gestaltung und Handhabung. VDI-Verlag, 2000

[118] *H.J. Ettinger, J. Sienz, J.F.T. Pittman*: Automated optimization of extrusion die design for PVC profiles, 6th International ESAFORM Conference, 2003. Salerno, Italy

[119] *I. Szarvasy, J. Sienz, J.F.T. Pittman, E. Hinton*: Computer aided optimization of profile extrusion dies: Definition and assessement of the objective functions. In: Int. Polymer Processing, 15, 2000

[120] *J. Sienz, S.D. Bulman, J.F.T. Pittman*: Optimization strategies for extrusion die design, 4th International ESAFORM Conference, 2001. Liege, Belgium

[121] *P.B. Junk*: Betrachtungen zum Schmelzeverhalten beim kontinuierlichen Extrusionsblasformen. Thesis, RWTH Aachen, 1978

[122] *M.A. Huneault, P.J. Carreau, P.G. Lafleur*: Extrudate swell and viscoelasticity of rigid PVC compounds. In: Journal of Vinyl Technology, 14, December, 1992

[123] *M.A. Huneault, P.G. Lafleur, P.J. Carreau*: Extrudate swell and draw-down effects on extruded profile dimensions and shape. In: Polymer Engineering and Science, 30, Mid-December, 1990

[124] *F. Röthemeyer*: Elastische Effekte bei der Extrusion von Kunststoffschmelzen. Thesis, Universität Stuttgart, 1970

[125] *E.B. Rabinovitch, J.W. Sumers, P.C. Booth*: Die design for rigid PVC - The effect of die land design on extrudate swell. In: ANTEC '91, 1992

[126] *F. Ramsteiner*: Einfluß der Düsengeometrie auf Strömungswiderstand, Strangaufweitung und Schmelzebruch von Kunststoffschmelzen. In: Kunststoffe, Bd. 62, 1972

[127] *Y. Sasaki, M.R. Kamal, I. Ansari, W. Frydrychowicz, M.E. Ryan*: Numerical study of extrudate swell. In: ANTEC '94, 1994

[128] *W. Michaeli, K. Hoffmann*: Untersuchungen zum Schwellverhalten von Thermoplasten bei der Verarbeitung in der Profilextrusion, RWTH Aachen, 1995

[129] *G. Menges, B. Gesenhues, C. Schwenzer*: Bei der Auslegung von Profilwerkzeugen wird die Strangaufweitung berechenbar. In: Kunststoffe, Band 75, 1985

[130] *M. Huneault, P. Lafleur, P. Carreau*: Extrudate swell and drawdown in profile extrusion. In: Plastics Engineering, September '89, 1989

[131] *C. Han, M. Charles*: A method for the determination of polymer melt die swell. In: Transactions of the society of rheology, 14, 1970

[132] *W.A. Gifford*: The effect of surface tension on extrudate swell from square and rectangular channels. In: Polymer Engineering and Science, 38, July, 1998

[133] *V. Delvaux, M.J. Crochet*: Numerical simulation of delayed die swell. In: Rheologica Acta, 1990

[134] *H. Barth*: Kalibrieren und Kühlen von Profilen. In: Kühlen von Extrudaten. Series "Kunststofftechnik", Düsseldorf, VDI-Verlag, 1978

[135] *F. Wimmer*: Die intelligentexten Lösungen sind immer die einfachsten.... Greiner Post-Co-Extrusionsverfahren (PCE) - die patentierte Lösung. In: Extrusionswerkzeuge, Schwerpunkt Profilwerkzeuge. VDI-Verlag, 1996

[136] *P. Sheehy, P.A. Tanguy*: A Finite Element model for complex profile calibration. In: Polymer Engineering and Science, 34, April, 1994

[137] *L. Fradette, P.A. Tanguy, F. Thibault, P. Sheehy*: Optimal design in profile extrusion calibration. In: Journal of Polymer Engineering, 14, 1995

[138] *VDI-Wärmeatlas*: VDI-Verlag, Düsseldorf, 1994

[139] *H. Domininghaus*: Die Kunststoffe und ihre Eigenschaften, VDI-Verlag, 1992

[140] *H.G. Fritz*: FEM-Simulation Kalibrieren: Anordnung der Kühlkanäle für gleichmäßige Oberflachentemperaturen. In: Das Extrusionswerkzeug - Leitfaden zur Gestaltung und Handhabung. VDI-Verlag, 2000

[141] *T. Ide*: Verschleißschutz bei Extrusionswerkzeug- und Kalibriersystemen. In: Extrusionswerkzeuge. VDI-Verlag, 1993

[142] *D. Repenning*: Werkstoffe und Oberflächen für Düsen und Kalibrierung. In: Das Extrusionswerkzeug - Leitfaden zur Gestaltung und Handhabung. VDI-Verlag, 2000

[143] *L. Kreft, Z. Doboczky*: Berechnung und Konstruktion von Kalibrierdüsen. In: Kunststoff und Gummi, 1 (1962), 1962

[144] *C. Krohmer, U. Conrad, G.A. Martin*: Vorgänge beim Kalibrieren und Abkühlen. In: Das Extrusionswerkzeug - Leitfaden zur Gestaltung und Handhabung. VDI-Verlag, 2000

[145] *G.M. Bartenev, V.V. Lavrentev*: Friction and wear of polymers, 1981

[146] *E. Brunnhofer*: Extrusionswerkzeuge für Kunststoffprofile. In: Extrusionswerkzeuge - Schwerpunkt Profilwerkzeuge-. VDI-Verlag, 1993

[147] *Conatex:* Meß- und Regeltechnik, St. Wendel, Germany, http://www.conatex.de, 1997

[148] *Advantech:* http://www.advantech.com, 1997

[149] *Linseis:* Selb, Germany, http://www.linseis.com, 1997

[150] *DATALOG:* Mönchengladbach, Germany, http://www.datalog.de, 1997

[151] *J. Breil*: Produktionssicherung bei der Extrusion von PVC-Profilen. In: Plastverarbeiter, 35. Jahrgang, 1984

[152] *H. Weiler*: Untersuchung der Wandstärkenkonstanz bei der Extrusion von PVC-Fensterpofilen. Thesis, Berufsakademie Mannheim, 1997

[153] *M. Semmler*: Ermittlung der Verteilung des Schrumpfpotentials über der Wanddicke eines extrudierten PVC-Profiles in Abhängigkeit verschiedener Verfahrensparameter. Thesis, Fachhochschule Kaiserslautern, Fachbereich Maschinenbau, 1995

[154] *G. Menges, M. Kalwa*: Berechnung von Eigenspannungs- und Schwindungsverläufen in extrudierten Profilen mit Hilfe der Finiten Elemente, Institut für Kunststoffverabeitung, RWTH Aachen, 1988

[155] *W. Matek, D. Muhs, H. Wittel*: Roloff/Matek, Maschinenelemente, 1984

[156] *J. Breil*: Automatisierungsmöglichkeiten an Rohr- und Profilextursionsanlagen. Thesis, RWTH Aachen, 1986

[157] *P. Berger, A. Krämer*: Kalibrieren von Rohren bei hohen Abzugsgeschwindigkeiten. In: Kunststoffe, Bd. 65, 1975

[158] *RAL:* Gütesicherung RAL-GZ 716/1, Abschnitt 1: Kunststoff-Fensterprofile, 1998

[159] *P. Berger, G. Kress*: Beeinflussung der Halbzeugeigenschaften durch das Abkühlen. In: Kühlen von Extrudaten. Series "Kunststofftechnik", VDI-Verlag, 1978

[160] *E.B. Rabinovitch, J.G. Quisenberry*: Shrinkage in rigid PVC profile extrusions. In: Journal of vinyl technology, 10, December, 1988

[161] *E. Harrell*: Approximate model for analysing frozen-in-strains and shrinkage of extruded PVC lineal profiles. In: Journal of Vinyl Technology, 4, September, 1998

[162] *R. Tempels*: Verhalten von PVC-hart gegen Stoß. In: Kunststoffe, 80, 1990

[163] *J.G. Williams*: Fracture mechanics of polymers. In: Polymer Engineering and Science, 17, 1977

[164] *S. Hashemi, J.G. Williams*: Fracture characterization of tough polymers using the J method. In: Polymer Engineering and Science, 26, 1986

[165] *D.R. Moore, R.C. Stephenson, M. Whale*: Some factors affecting toughness in uPVC pipe materials. In: Plastics and Rubber Processing and Applications, 1983

[166] *D.R. Moore, R. Prediger, R.C. Stephenson*: Relevance and application for fracture toughness measurements for uPVC. In: Plastics and Rubber Processing and Applications, 1985

[167] *H.H. Kausch*: Polymer Fracture, Springer, 1978

[168] *A.J. Kinloch, R.J. Yopung*: Fracture behaviour of polymers, Applied Science Publishers, 1983

[169] *R. Lach*: Korrelation zwischen bruchmechanischen Werkstoffkenngrößen und molekularen Relaxationsprozessen amorpher Polymere, VDI-Verlag, 1998

[170] *G.P. Marshall, M.W. Birch*: Design for toughness in polymers. 3-Criteria for high toughness in uPVC pressure pipes. In: Plastics and Rubber Processing and Applications, 1982

[171] *G. Levita, L. Parisi, A. Marchetti, L. Bartolommei*: Effects of thickness on the specific work of fracture of rigid PVC. In: Polymer Engineering and Science, 36, October, 1996

[172] *D.J. Hitt*: The mechanical properties of simultaneously and sequentially biaxially oriented UPVC sheet, PVC'96, 1996. Brighton

[173] *J.G. Williams*: Fracture mechanics. In: The physics of glassy polymers. 1997

[174] *G. Menges, M. Kalwa*: Ermittlung mechanischer Kenngrößen viskoelastischer Werkstoffe bei nicht-isothermen Umgebungsbedingungen, Institut für Kunststoffverabeitung, 1988

[175] *W. Beitz, K.-H. Küttner*: Dubbel - Taschenbuch für den Maschinenbau, 1995

[176] *E. Haberstroh*: Abkühl und Aufheizvorgänge im Extrudat, Hanser-Verlag, 1989

[177] *H. Beer*: Grundlagen der Thermodynamik, Script TH Darmstadt, 1992

[178] *W. Schröck*: Untersuchung des Wärmeüberganges in der Vakuumtankkalibrierung bei einem Extrusionsprofil. Thesis, Fachhochschule Kaiserslautern, Fachbereich Maschinenbau, 1996

[179] *G.A. Martin*: Patent DE 196 22 419, Verfahren zum Kühlen, insbesondere Kalibrieren, von Kunststoffprofilen sowie Kalibriervorrichtung für eine Kunststoffextrusionsanlage, 1997

[180] *U. Kleindienst*: Untersuchung des Abkühlvorganges und dessen Einfluß auf das Eigenspannungsfeld in der Wand extrudierter Kunststoffe. Thesis, Universität Stuttgart, 1976

[181] *Conair:* Pittsburgh, USA, How nitrogen gas cooling can increase production and profits, http://www.conairnet.com, 2000

[182] *J.F.T. Pittman, I.A. Farah, D.H. Isaac, A. Eccott*: Spray cooling heat transfer coefficients in plastic pipe manufacture. In: Plastics, Rubber and Composites Processing and Applications, 24, 1995

[183] *E. Haberstroh*: Heat transfer. In: Encyclopedia of Polymer Science, 7, 1987

[184] *J. Schmidt*: Wärmetechnische Auslegung von Profilkühlstrecken mit Hilfe der Methode der Finiten Elemente (FEM). Thesis, RWTH Aachen, 1985

[185] *L. Fradette, P.A. Tanguy, P. Hurez, D. Blouin*: On the determination of heat transfer coefficients between PVC and steel in vacuum extrusion calibrators. In: International Journal of Numerical Methods in Heat Fluid Flow, 6, 1996

[186] *I. Szarvasy, R. Sander*: Bedarfsgerechter Aufbau von Extrusionswerkzeugen. In: Kunststoffe, 89, 1999

[187] *H.S. Carslaw, J.C. Jaeger*: Conduction of heats in Solids, Oxford University Press, 1959

[188] *SPSS:* SigmaPlot, http://www.spss.com, 1997

[189] *J.F.T. Pittman, I. Szarvasy*: A viscoelastic model for shrinkage, deformation and thermal stresses in PVC calibration, ESAFORM 2000, Stuttgart

[190] *U. Conrad, J.F.T. Pittman, I. Szarvasy*: The calibration process in PVC profile production: Experimental trials and computer simulation, Materials Congress 2000, 2000. Cirencester, UK

[191] *U. Conrad, J.F.T. Pittman, I. Szarvasy*: The calibration process in PVC profile production: Modelling and simulations supported by comprehensive experimental trials, Current trends in PVC Technology, 2000. Loughborough, UK

[192] *T. Krug, I. Szarvasy*: FEM-Simulation Kalibrieren: Wärmetransportvorgänge im Profilinneren. In: Das Extrusionswerkzeug - Leitfaden zur Gestaltung und Handhabung. VDI-Verlag, 2000

Appendix A

Details of experimental set-up

In the Appendix A are shown more details and pictures of the experimental set-up.

Figure A 1: Initial design of the top of calibrator 1 with holes for profile surface temperature and vacuum measurements

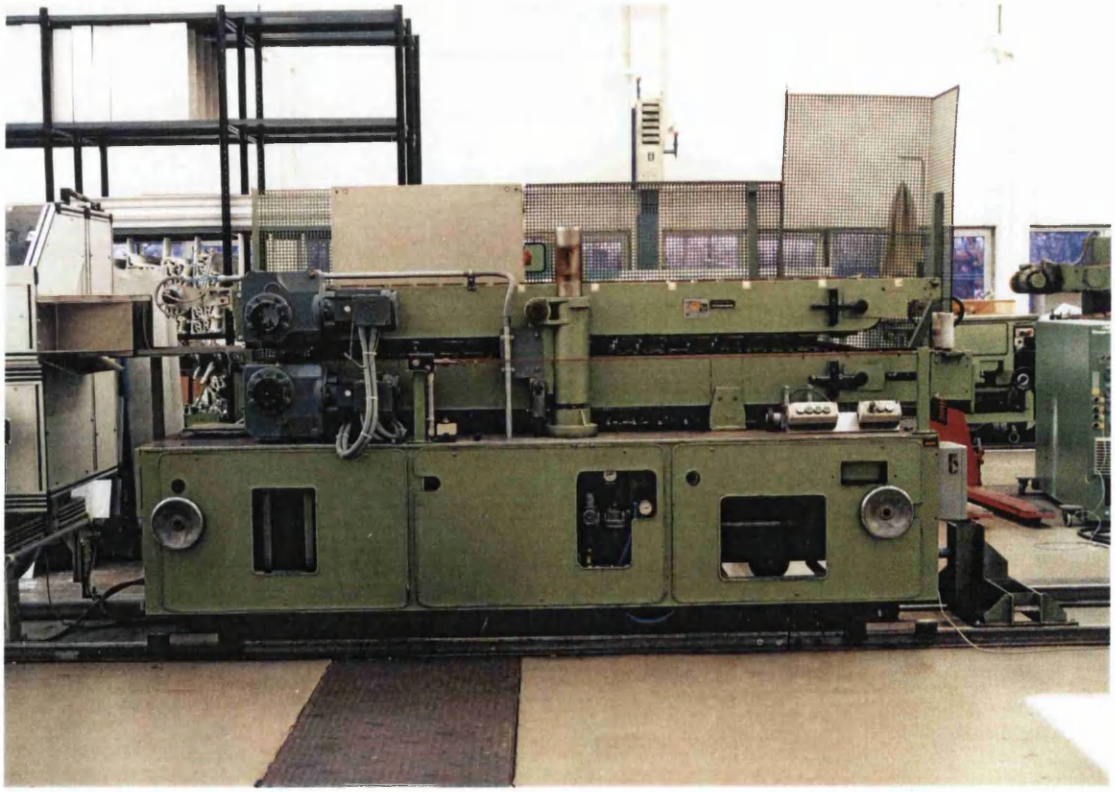

Figure A 2: Mounted Haul-off unit with force transducer

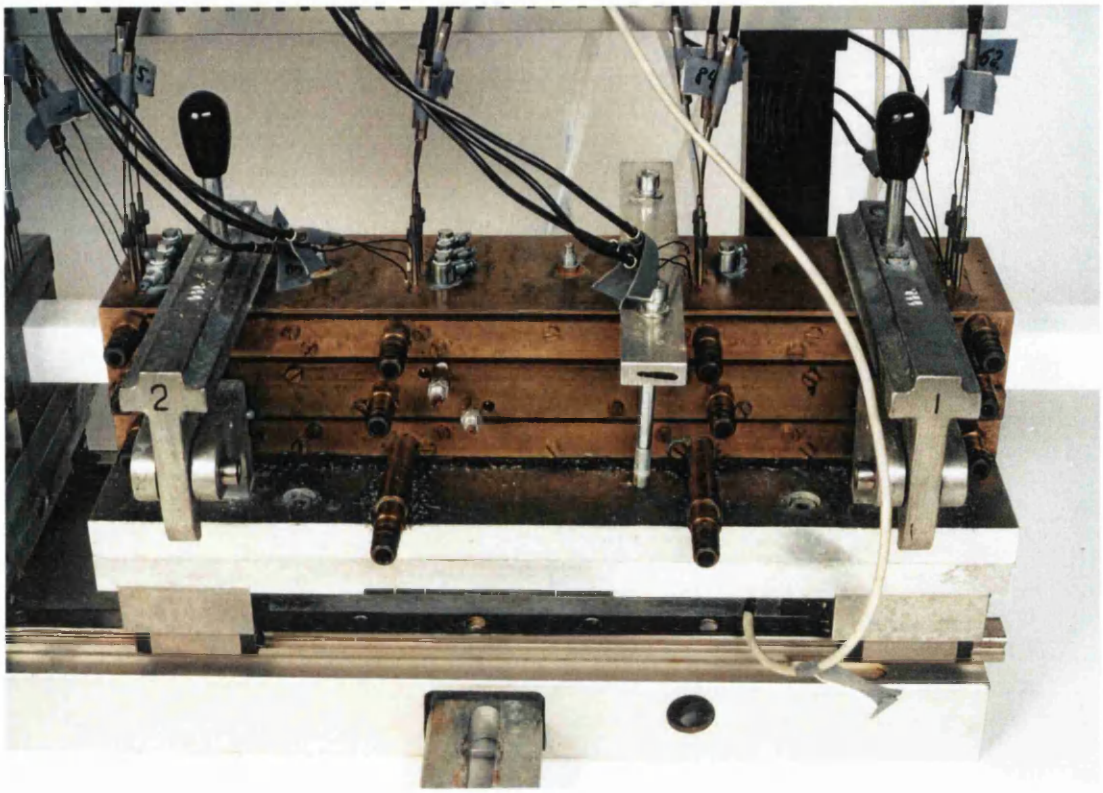

Figure A 3: Mounted calibrator 1 with fitted thermocouples

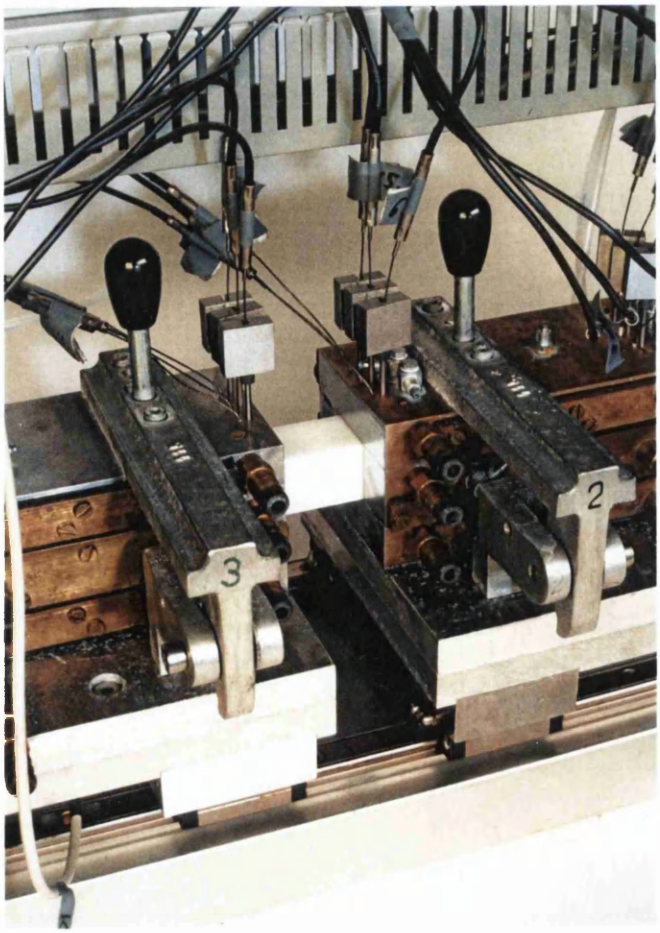

Figure A 4: Section between calibrators 1 and 2

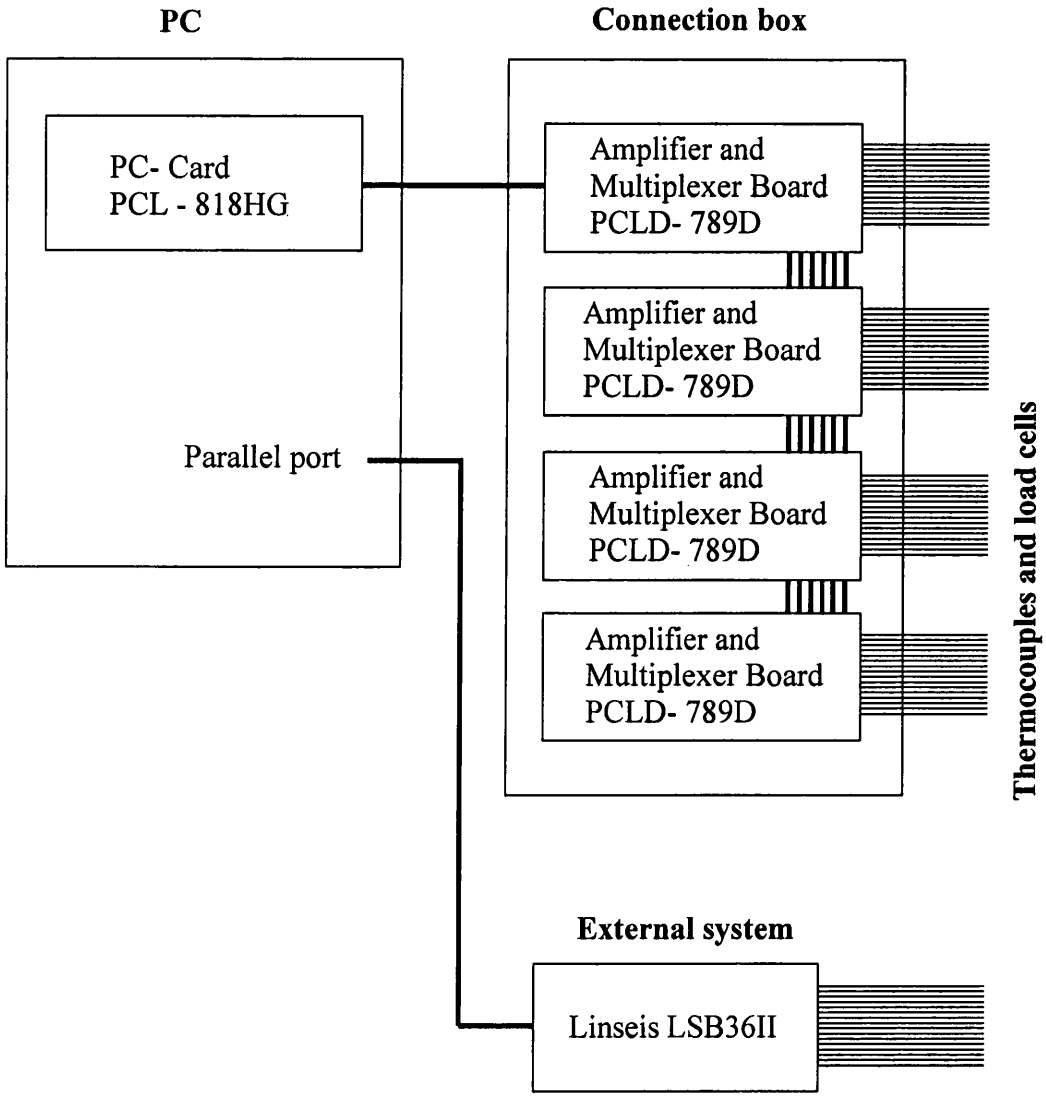

Figure A 5: Hardware of the data logging system

APPENDIX B

Detailed overview of carried out experiments

In the Appendix B are shown the varied process parameters in detail for carried out experiments.

W ⟶ wet calibration
D ⟶ dry calibration

Die exit [mm]	Line speed [m/min]	Profile wall thickness [mm]	Vacuum in calibrator 1															
			-0.2				-0.4				-0.6				-0.8			
			Vacuum in calibrator 2, 3, 4															
			-0.2	-0.4	-0.6	-0.8	-0.2	-0.4	-0.6	-0.8	-0.2	-0.4	-0.6	-0.8	-0.2	-0.4	-0.6	-0.8
1.50	1	1.50																
		1.75																
		2.00																
	2	1.50																
		1.75																
		2.00																
	3	1.50						W/D					W/D					D
		1.75																
		2.00																
	4	1.50						W					W					
		1.75						W					W					W
		2.00						W					W					W
	5	1.50						W					W					
		1.75																
		2.00																
	6	1.50																
		1.75																
		2.00																
	7	1.50						W										
		1.75																
		2.00																
	8	1.50																
		1.75																
		2.00																

Figure B1: Experimental overview for the 1.50 mm die

W ⟶ wet calibration
D ⟶ dry calibration

Die exit [mm]	Line speed [m/min]	Profile wall thickness [mm]	Vacuum in calibrator 1: -0.2 / Vacuum in calibrator 2, 3, 4: -0.2	-0.4	-0.6	-0.8	Vacuum in calibrator 1: -0.4 / Vacuum in calibrator 2, 3, 4: -0.2	-0.4	-0.6	-0.8	Vacuum in calibrator 1: -0.6 / Vacuum in calibrator 2, 3, 4: -0.2	-0.4	-0.6	-0.8	Vacuum in calibrator 1: -0.8 / Vacuum in calibrator 2, 3, 4: -0.2	-0.4	-0.6	-0.8
2.50	1	2.50						W/D					W/D					W/D
		2.75																
		3.00																
		3.25																
	2	2.50						W					W					W
		2.75																
		3.00						W					W					W
		3.25						W					W					W
	3	2.50						W/D					W/D					W/D
		2.75																
		3.00																
		3.25																
	4	2.50		W				W				W	W			W		W
		2.75		W				W	W	W		W	W			W	W	W
		3.00		W				W	W			W	W	W		W	W	W
		3.25		W				W				W	W			W		W
	5	2.50						W					W					W
		2.75																
		3.00																
		3.25																
	6	2.50						W					W					
		2.75						W					W					
		3.00						W					W					
		3.25																
	7	2.50						W										
		2.75						W										
		3.00						W										
		3.25																
	8	2.50						W										
		2.75						W										
		3.00						W										
		3.25																

Figure B2: Experimental overview for the 2.50 mm die

Die exit [mm]	Profile wall thickness [mm]	Line speed [m/min]	Coolant temperature [°C]	Melt temperature [°C]	Vacuum -0.4	Vacuum -0.6	Vacuum -0.8
2.50	2.75	4.0	40	195			W
			30				W
			16				W
			16	200	W		
				195	W		
				190	W		
				185	W		
				180	W		

Die exit [mm]	Profile wall thickness [mm]	Line speed [m/min]	Number of water injection points	Vacuum -0.4	Vacuum -0.6	Vacuum -0.8
2.50	2.75	4.0	0	W	W	W
			1	W	W	W
			2	W	W	W
			3	W	W	W
			4	W	W	W

W → wet calibration
D → dry calibration

Figure B3: Experimental overview of varied coolant and melt temperatures and water injection points

Appendix C

Detailed results of calculated heat transfer coefficients and dimensionless Nusselt numbers in the calibration units

The Figures in this Appendix are presented in more detail to learn more about the correlations of the parameters in the calibration process (here the calibration units) on the heat transfer coefficients. These Figures are used to get trend lines, which might lead to a parameterisation. Furthermore, a selection and/or results of Figures shown here are presented also in Chapter 7.

In Section C.1, the calculated overall heat transfer coefficients will be shown. This section is subdivided to get a better overview. The Figures C1 to C15 are presenting the overall heat transfer coefficients for 1st and 2nd set of experiments on the dependence of downstream distance for different line speeds, vacua and wall thicknesses, followed by Figures C16 to C30 in Section C.1.2 for the dependence of the overall heat transfer coefficients on the Fourier number Fo at same conditions.
In Section C.1.3 the results for the edge of the upper profile surface are shown in dependence on downstream distance and Fourier number; Figures C31 to C36, only for the 1st set of experiments. This is because the profile surface temperatures were measured in 2nd set only near the edge in Calibrator 1.
Section C.1.4 presents the results for calculated dimensionless Nusselt number Nu, replacing the heat transfer coefficient in Section C1.2, Figures C37 to C51.
The Figures C52 to C54 in Section C.1.5 show the results of calculated Nusselt numbers for the edge of the upper profile surface for the 1st of experiments.

The results of the calculated interfacial heat transfer coefficients, details of calculations see Chapter 7, will be shown in Section C.2 in same order.

C.1 Overall heat transfer coefficients

C.1.1 Overall heat transfer coefficients at the centre of the upper profile surface in downstream distance

First, the calculated heat transfer coefficients are shown in Figures C1 to C15 for the centre of the upper profile surface in dependence on downstream distance. The Figures C1 to C3 shows the calculated heat transfer coefficients for the 1st set of experiments and 2nd set is presented in Figures C4 to C15.

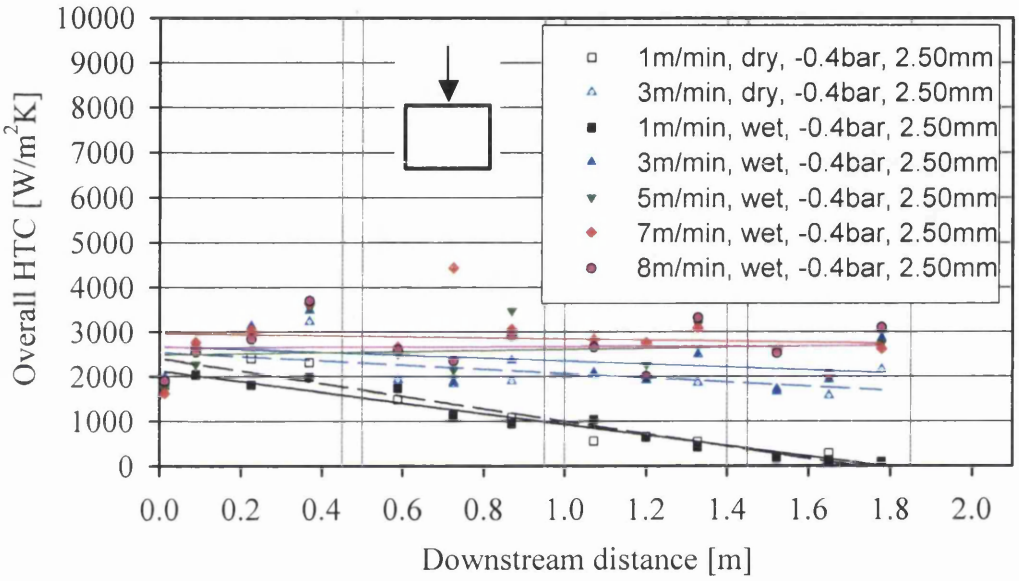

Figure C1: Overall heat transfer coefficients at the centre of the upper profile surface in dry and wet calibration for a vacuum of –0.4 bar at different line speeds; 2.50 mm die exit; 2.50 mm profile wall thickness

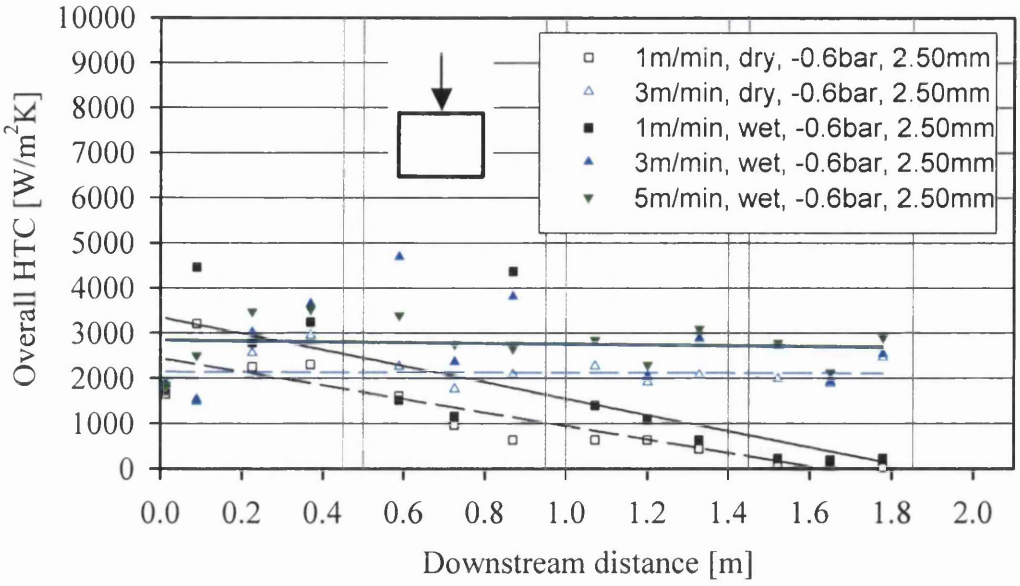

Figure C2: Overall heat transfer coefficients at the centre of the upper profile surface in dry and wet calibration for a vacuum of –0.6 bar at different line speeds; 2.50 mm die exit; 2.50 mm profile wall thickness

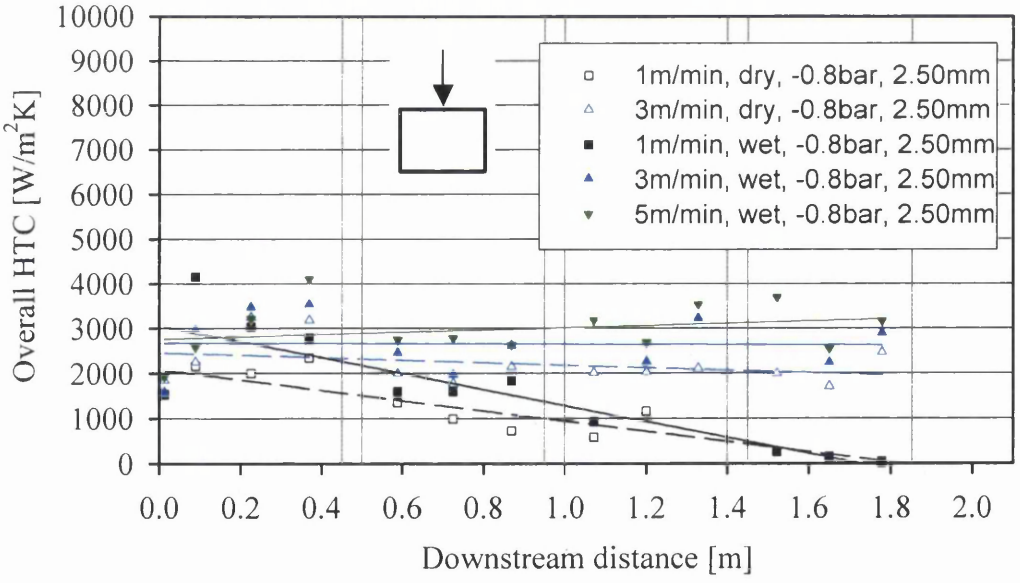

Figure C3: Overall heat transfer coefficients at the centre of the upper profile surface for a vacuum of –0.8 bar at different line speeds for a profile wall thickness of 2.50 mm in dry and wet calibration; 2.50 mm die exit

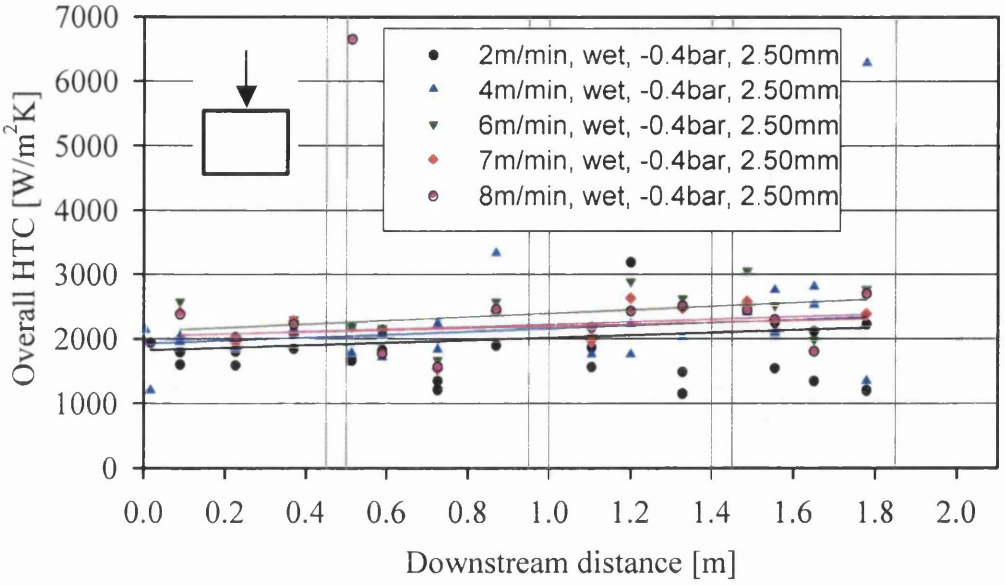

Figure C4: Overall heat transfer coefficients at the centre of the upper profile surface in wet calibration for a vacuum of –0.4 bar at different line speeds; 2.50 mm die exit; 2.50 mm profile wall thickness

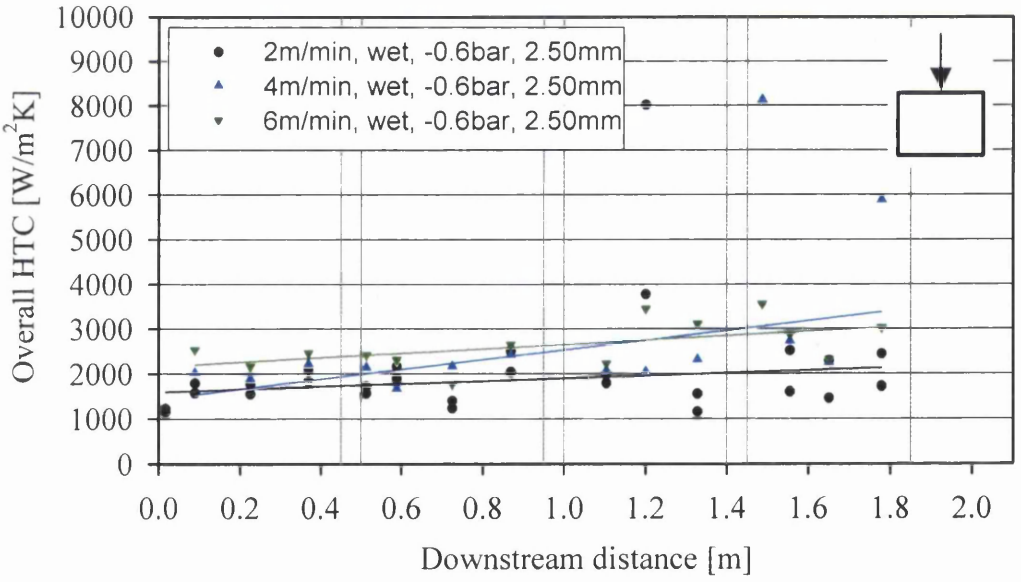

Figure C5: Overall heat transfer coefficients at the centre of the upper profile surface in wet calibration for a vacuum of –0.6 bar at different line speeds; 2.50 mm die exit; 2.50 mm profile wall thickness

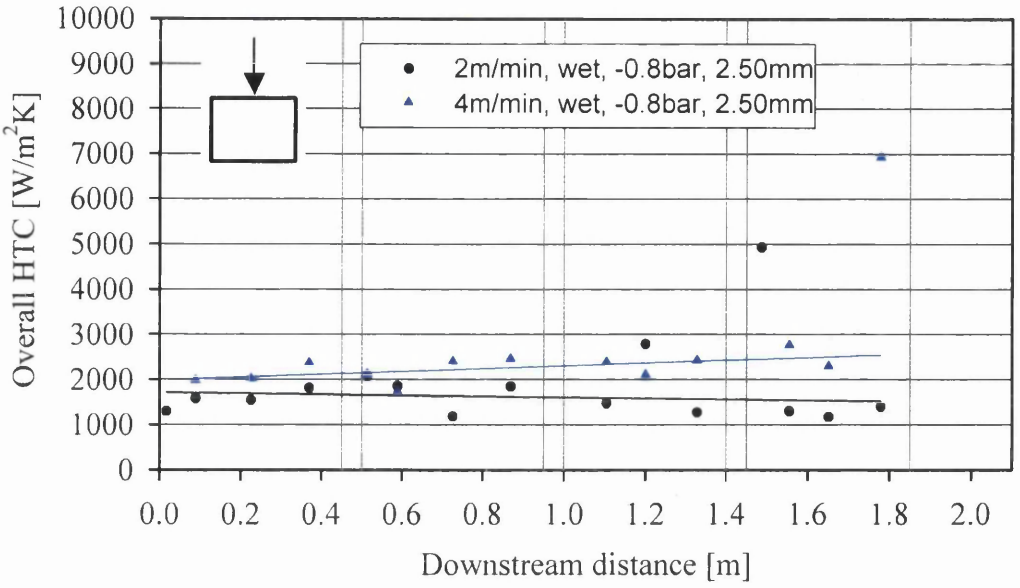

Figure C6: Overall heat transfer coefficients at the centre of the upper profile surface in wet calibration for a vacuum of –0.8 bar at different line speeds; 2.50 mm die exit; 2.50 mm profile wall thickness

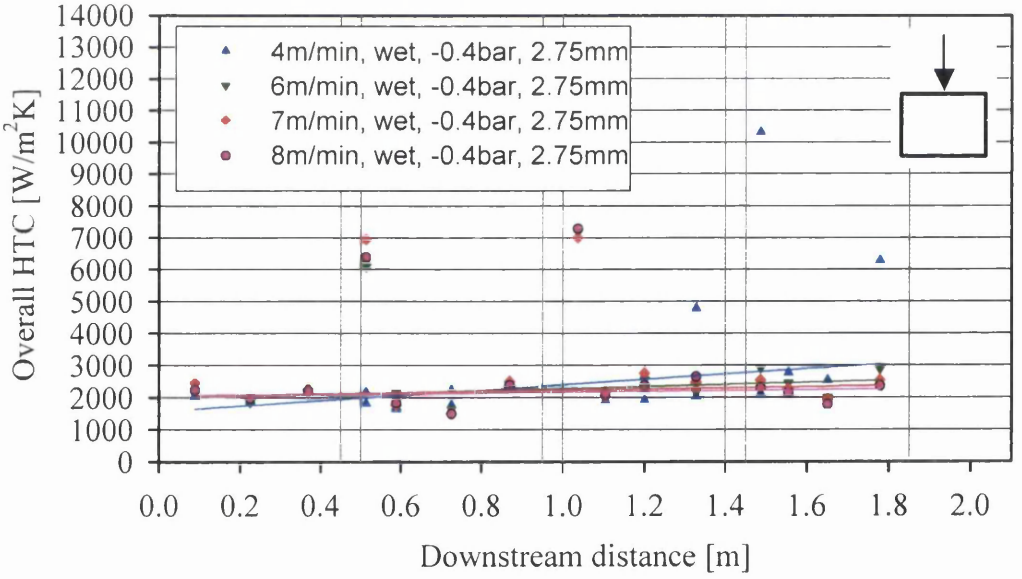

Figure C7: Overall heat transfer coefficients at the centre of the upper profile surface in wet calibration for a vacuum of –0.4 bar at different line speeds; 2.50 mm die exit; 2.75 mm profile wall thickness

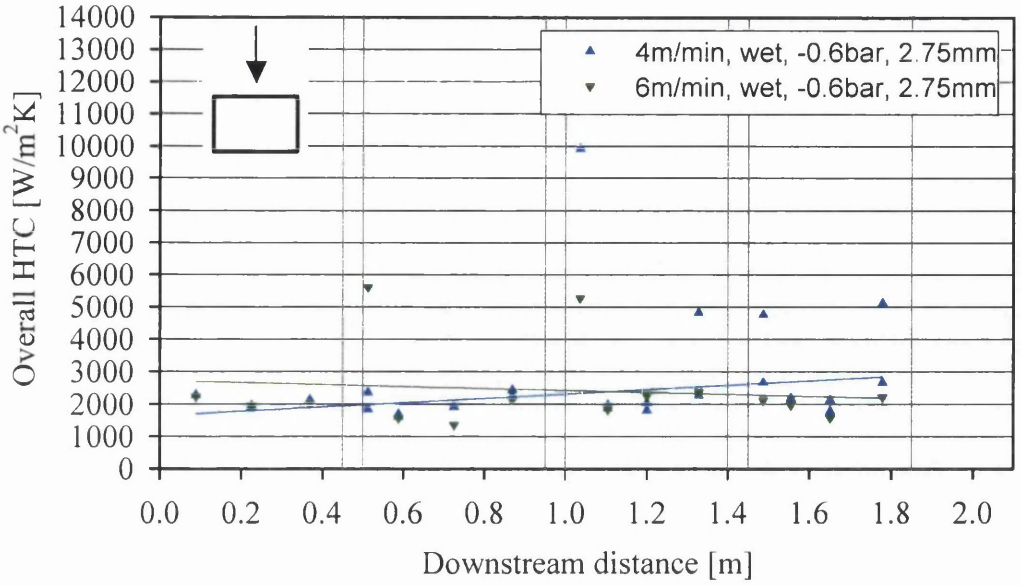

Figure C8: Overall heat transfer coefficients at the centre of the upper profile surface in wet calibration for a vacuum of –0.6 bar at different line speeds; 2.50 mm die exit; 2.75 mm profile wall thickness

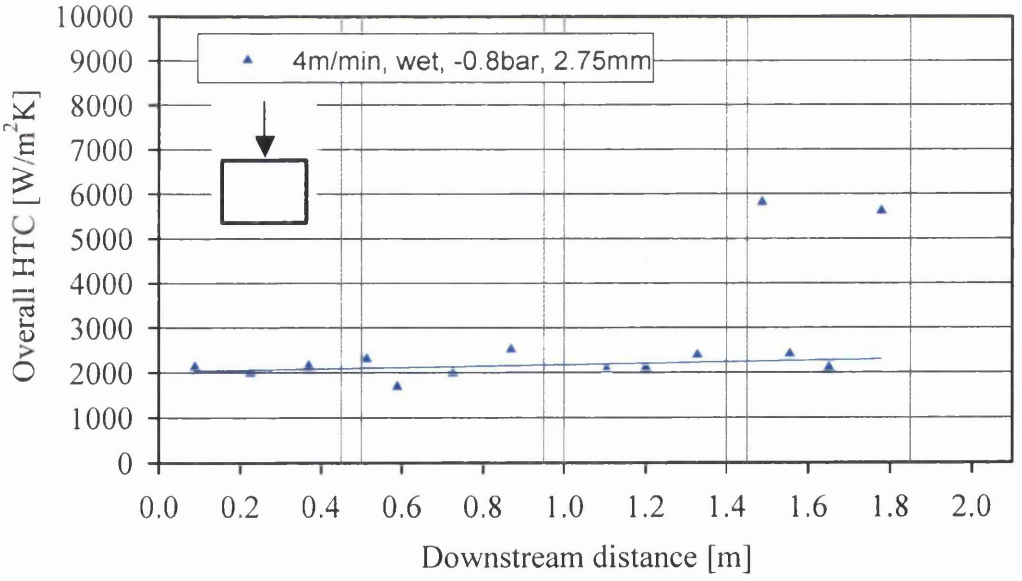

Figure C9: Overall heat transfer coefficients at the centre of the upper profile surface in wet calibration for a vacuum of –0.8 bar at different line speeds; 2.50 mm die exit; 2.75 mm profile wall thickness

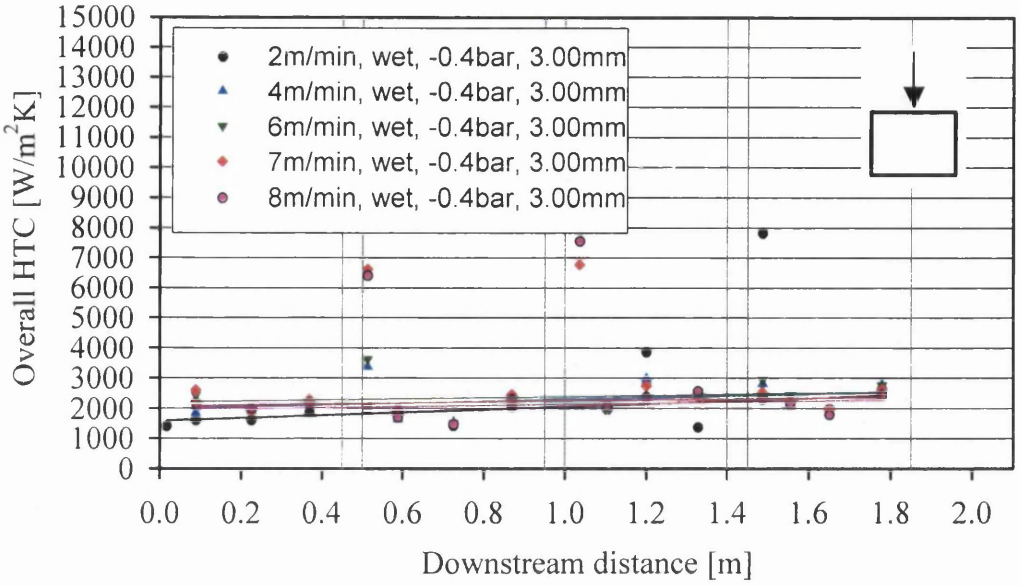

Figure C10: Overall heat transfer coefficients at the centre of the upper profile surface in wet calibration for a vacuum of –0.4 bar at different line speeds; 2.50 mm die exit; 3.00 mm profile wall thickness

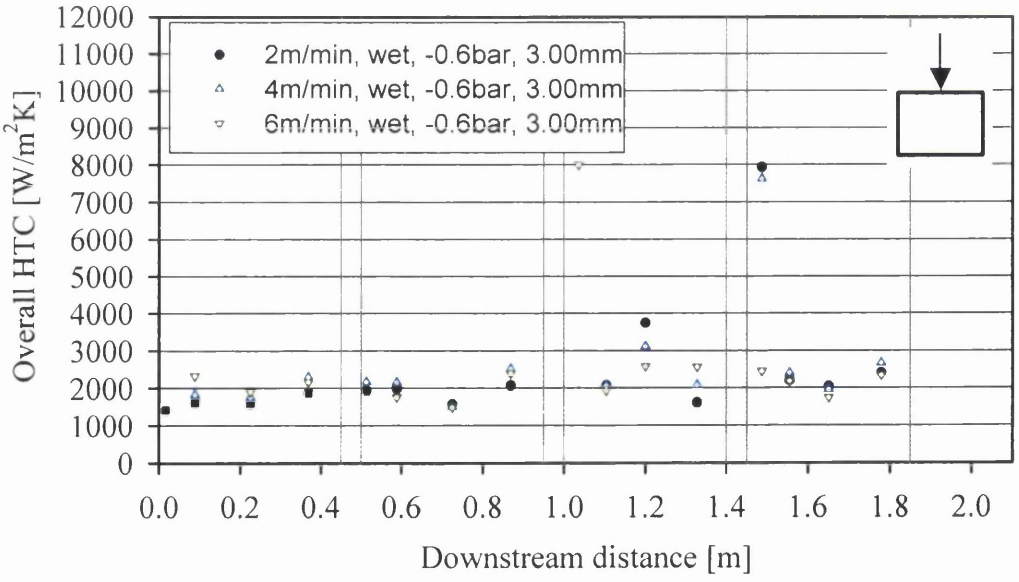

Figure C11: Overall heat transfer coefficients at the centre of the upper profile surface in wet calibration for a vacuum of –0.6 bar at different line speeds; 2.50 mm die exit; 3.00 mm profile wall thickness

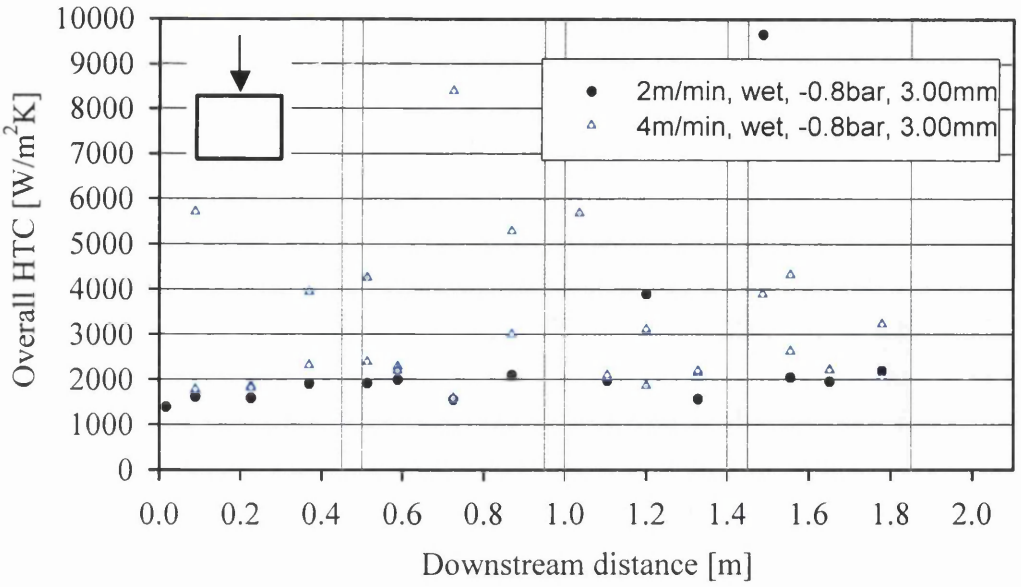

Figure C12: Overall heat transfer coefficients at the centre of the upper profile surface in wet calibration for a vacuum of –0.8 bar at different line speeds; 2.50 mm die exit; 3.00 mm profile wall thickness

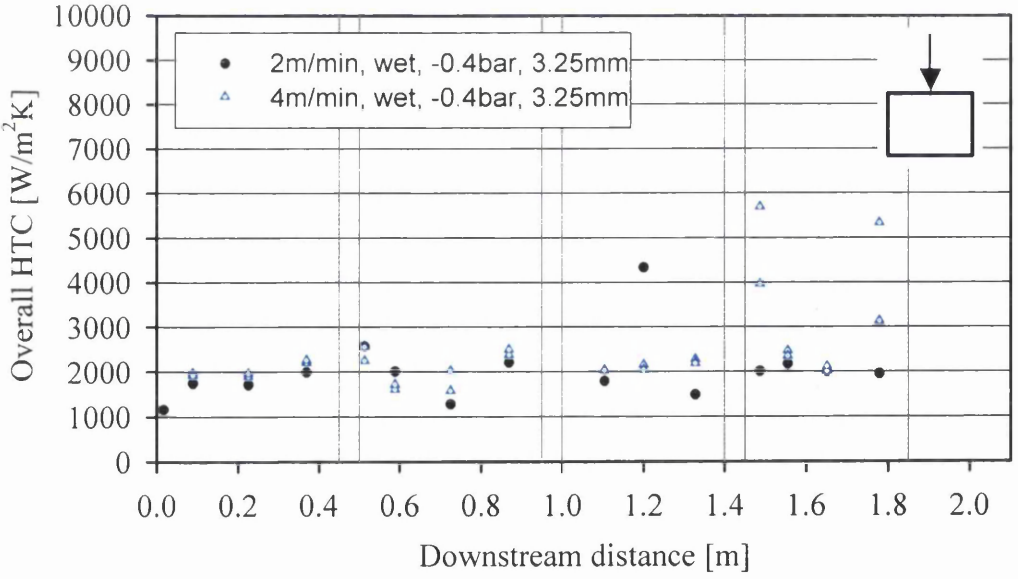

Figure C13: Overall heat transfer coefficients at the centre of the upper profile surface in wet calibration for a vacuum of –0.4 bar at different line speeds; 2.50 mm die exit; 3.25 mm profile wall thickness

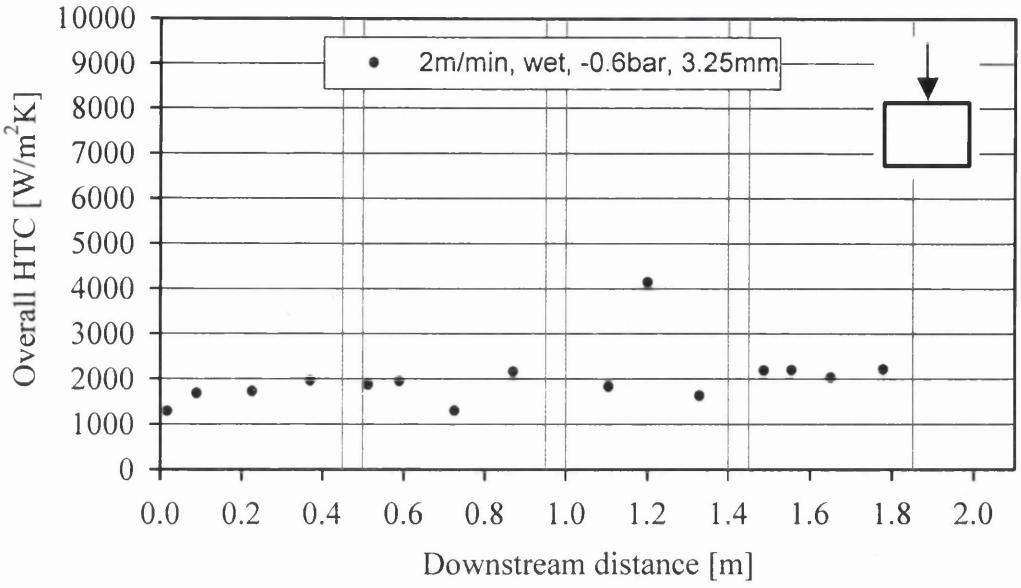

Figure C14: Overall heat transfer coefficients at the centre of the upper profile surface in wet calibration for a vacuum of –0.6 bar at different line speeds; 2.50 mm die exit; 3.25 mm profile wall thickness

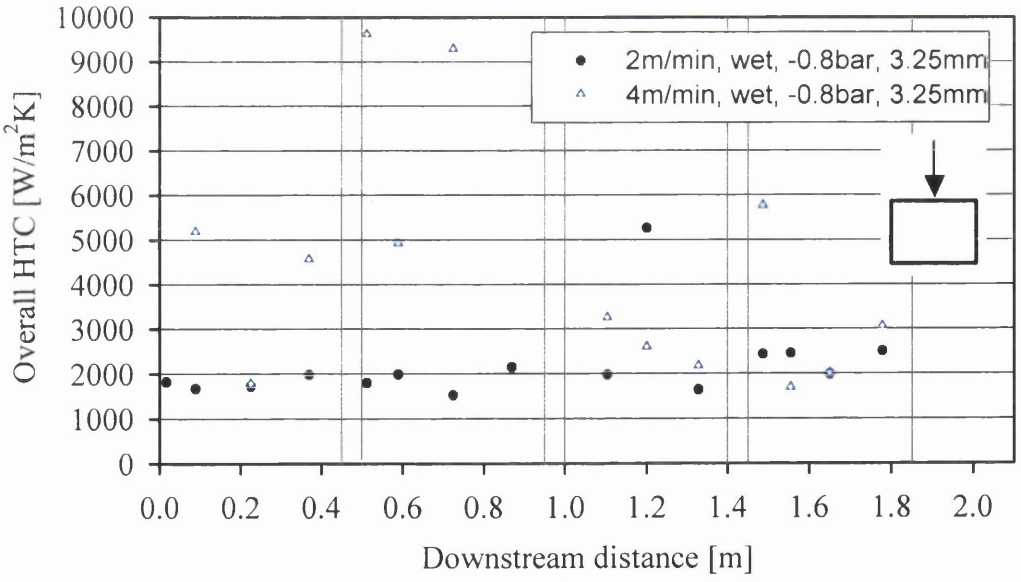

Figure C15: Overall heat transfer coefficients at the centre of the upper profile surface in wet calibration for a vacuum of –0.8 bar at different line speeds; 2.50 mm die exit; 3.25 mm profile wall thickness

C.1.2 Overall heat transfer coefficients at the centre of the upper profile surface as function of Fourier number

In the following Figures C16 to C30, the calculated overall heat transfer coefficients are shown for the centre of the upper profile surface on the dependence on the Fourier number.

As for the Figures above, here the Figures C16 to C18 presents the calculated overall heat transfer coefficients for the 1st set of experiments and in Figures C19 to C30, the 2nd set is shown.

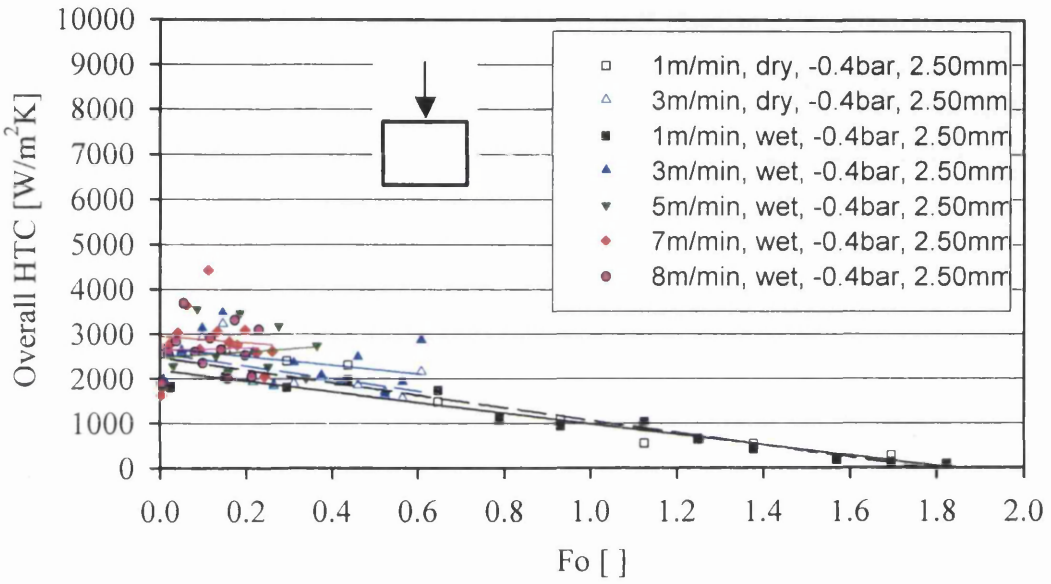

Figure C16: Overall heat transfer coefficients at the centre of the upper profile surface as function of the Fourier number in dry and wet calibration for a vacuum of –0.4 bar at different line speeds; 2.50 mm die exit; 2.50 mm profile wall thickness

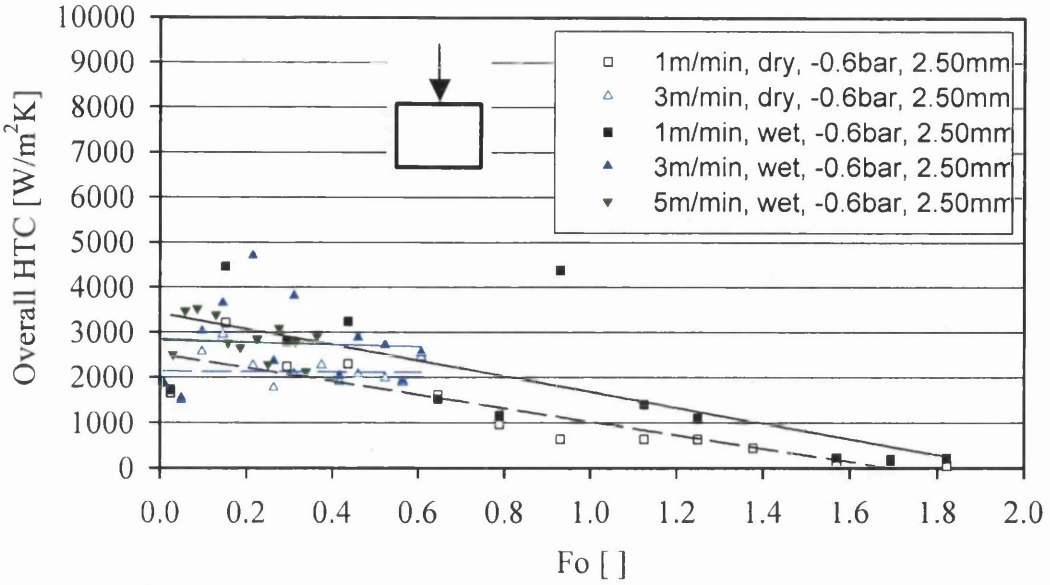

Figure C17: Overall heat transfer coefficients at the centre of the upper profile surface as function of the Fourier number in dry and wet calibration for a vacuum of –0.6 bar at different line speeds; 2.50 mm die exit; 2.50 mm profile wall thickness

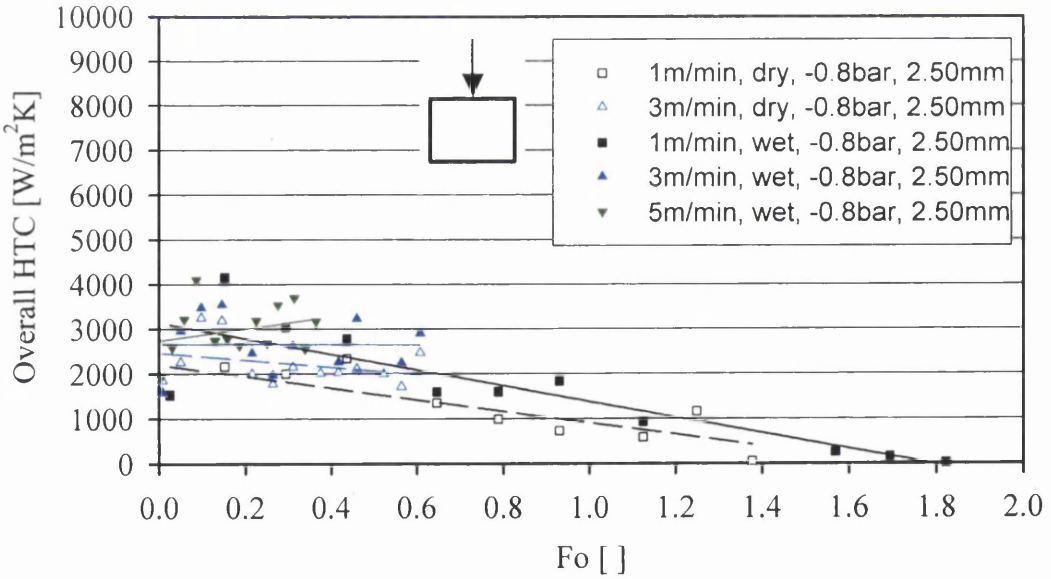

Figure C18: Overall heat transfer coefficients at the centre of the upper profile surface as function of the Fourier number in dry and wet calibration for a vacuum of –0.8 bar at different line speeds; 2.50 mm die exit; 2.50 mm profile wall thickness

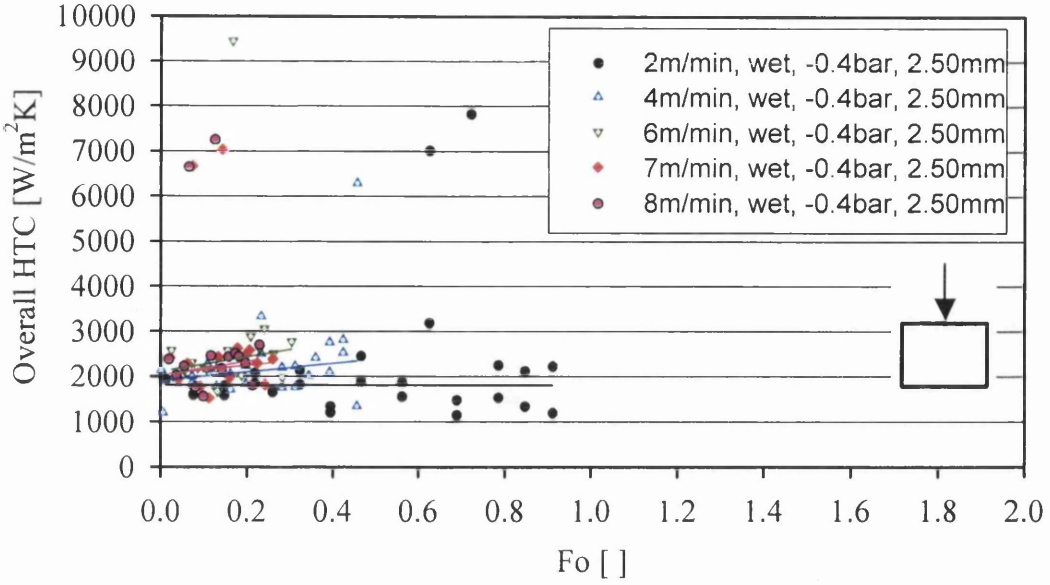

Figure C19: Overall heat transfer coefficients at the centre of the upper profile surface as function of the Fourier number in wet calibration for a vacuum of –0.4 bar at different line speeds; 2.50 mm die exit; 2.50 mm profile wall thickness

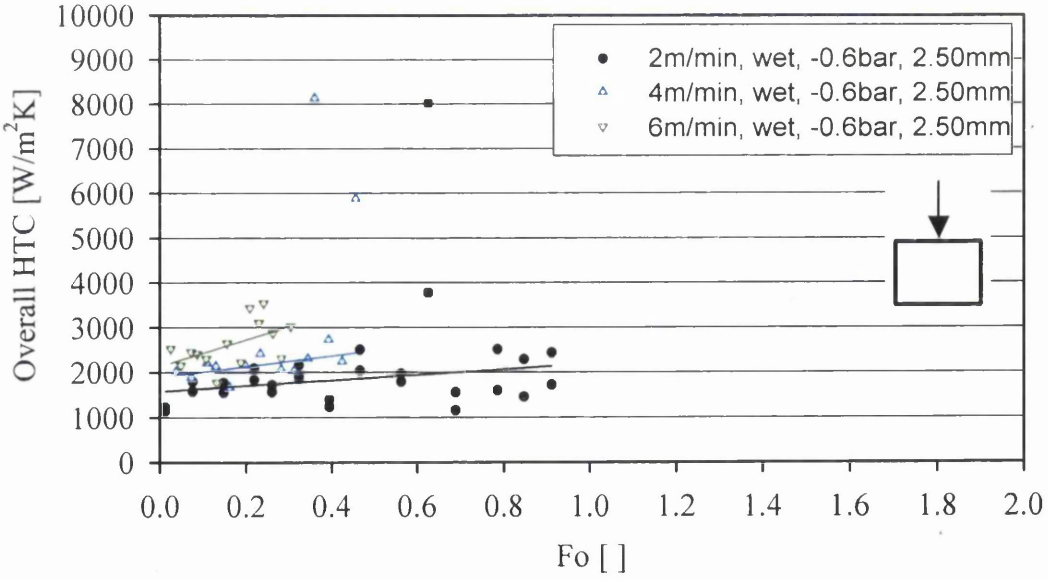

Figure C20: Overall heat transfer coefficients at the centre of the upper profile surface as function of the Fourier number in wet calibration for a vacuum of –0.6 bar at different line speeds; 2.50 mm die exit; 2.50 mm profile wall thickness

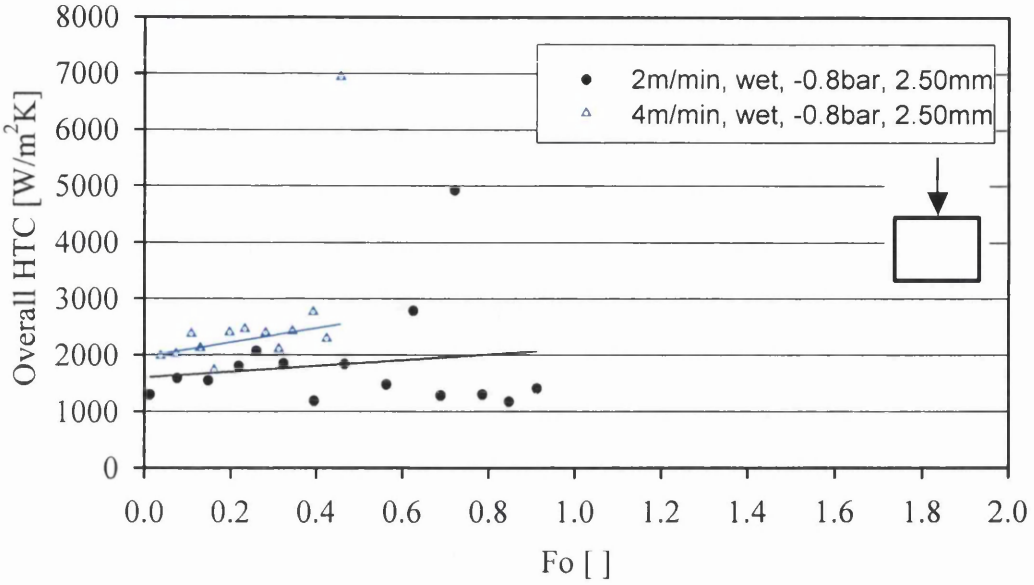

Figure C21: Overall heat transfer coefficients at the centre of the upper profile surface as function of the Fourier number in wet calibration for a vacuum of –0.8 bar at different line speeds; 2.50 mm die exit; 2.50 mm profile wall thickness

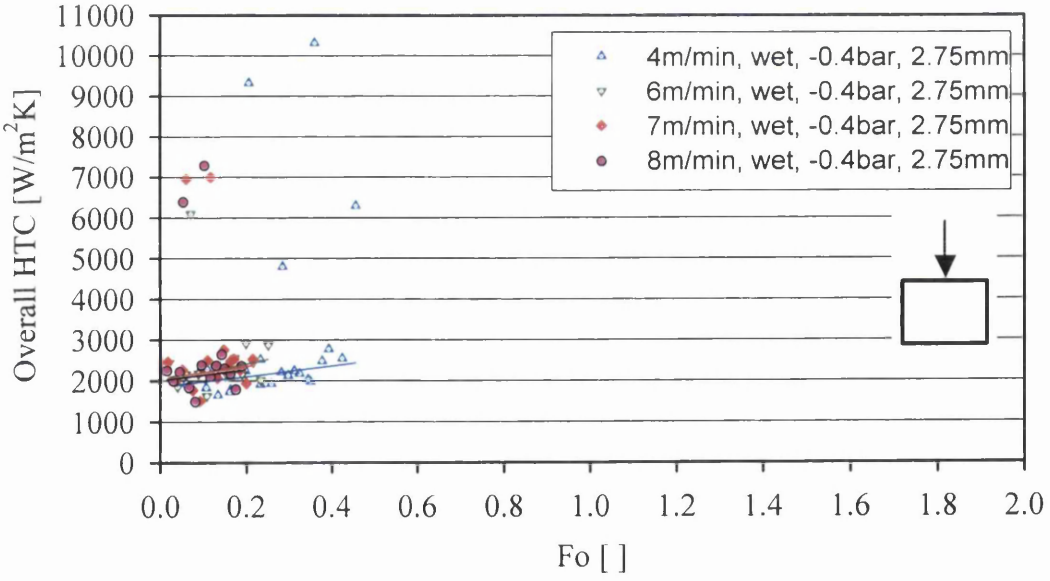

Figure C22: Overall heat transfer coefficients at the centre of the upper profile surface as function of the Fourier number in wet calibration for a vacuum of –0.4 bar at different line speeds; 2.50 mm die exit; 2.75 mm profile wall thickness

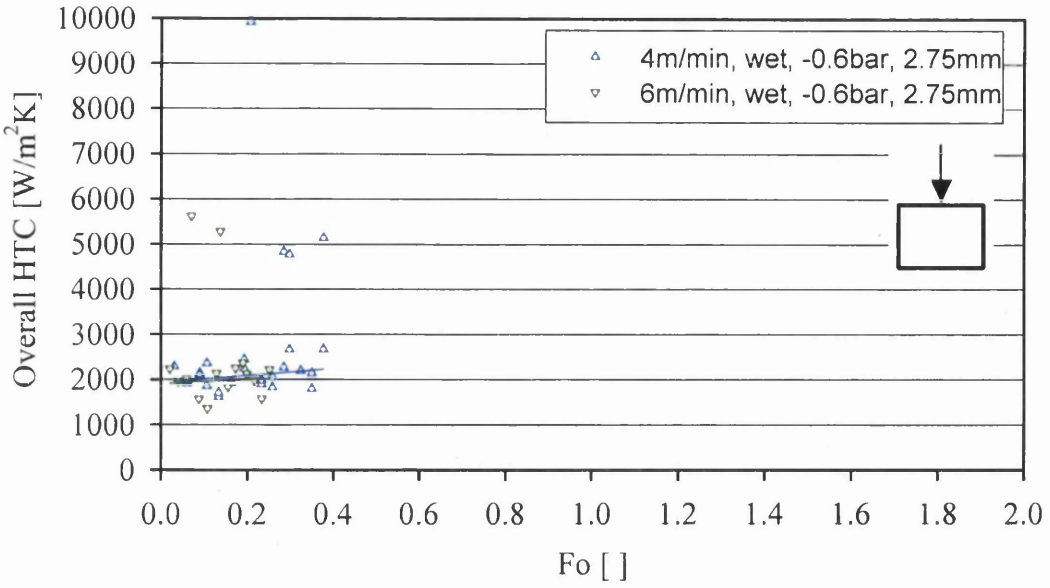

Figure C23: Overall heat transfer coefficients at the centre of the upper profile surface as function of the Fourier number in wet calibration for a vacuum of –0.6 bar at different line speeds; 2.50 mm die exit; 2.75 mm profile wall thickness

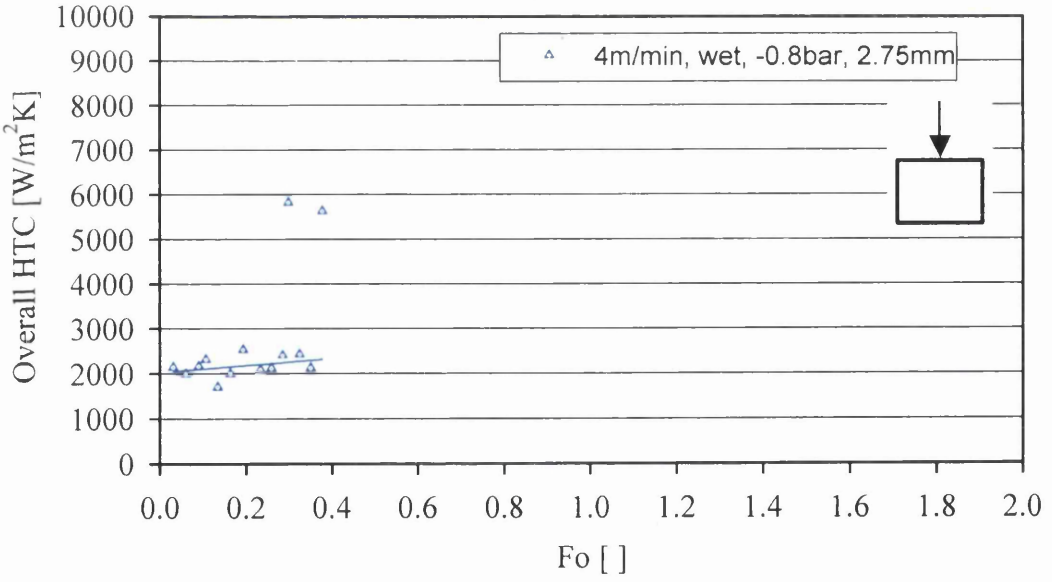

Figure C24: Overall heat transfer coefficients at the centre of the upper profile surface as function of the Fourier number in wet calibration for a vacuum of –0.8 bar at different line speeds; 2.50 mm die exit; 2.75 mm profile wall thickness

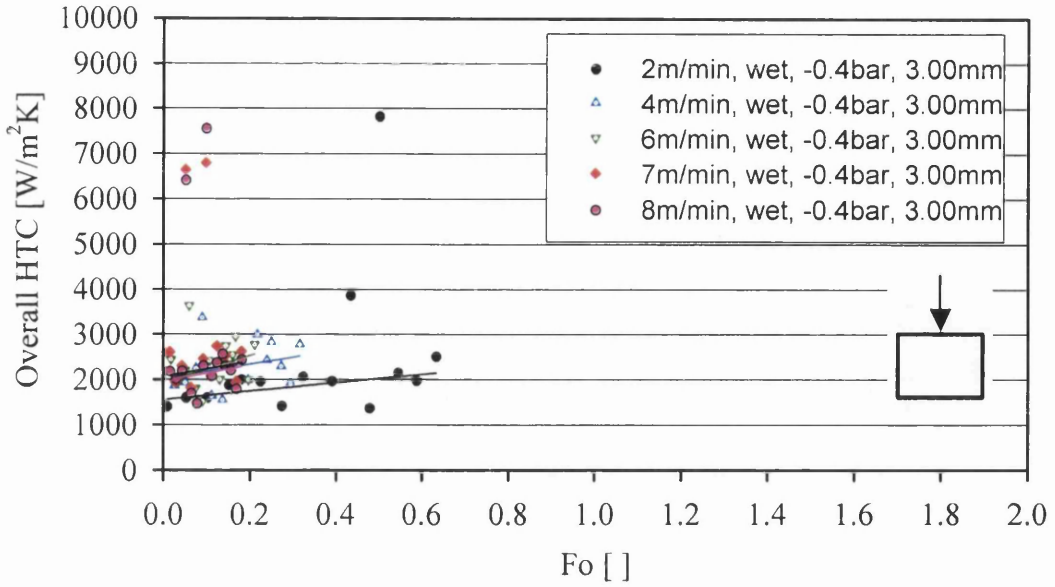

Figure C25: Overall heat transfer coefficients at the centre of the upper profile surface as function of the Fourier number in wet calibration for a vacuum of –0.4 bar at different line speeds; 2.50 mm die exit; 3.00 mm profile wall thickness

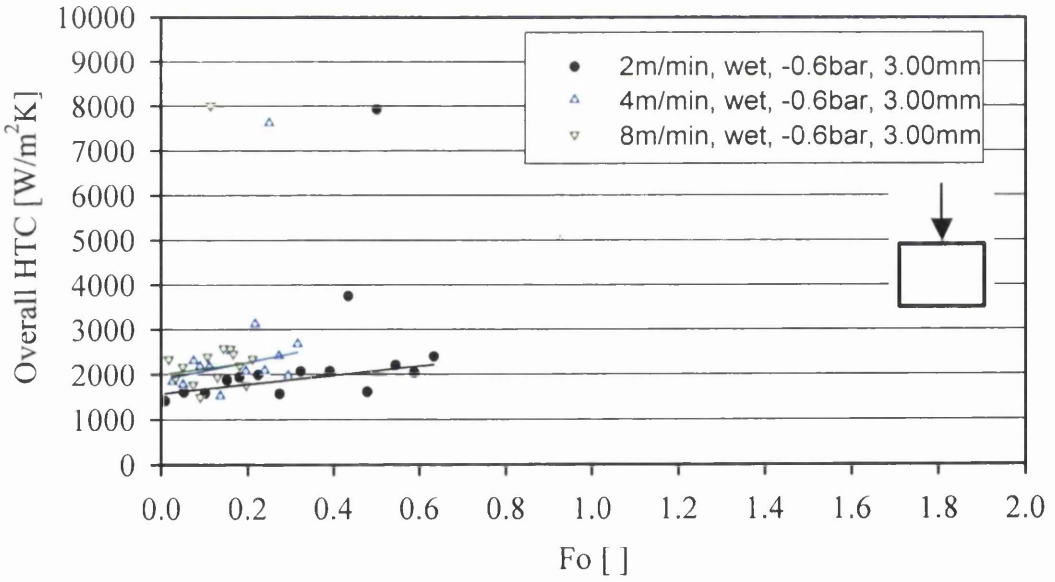

Figure C26: Overall heat transfer coefficients at the centre of the upper profile surface as function of the Fourier number in wet calibration for a vacuum of –0.6 bar at different line speeds; 2.50 mm die exit; 3.00 mm profile wall thickness

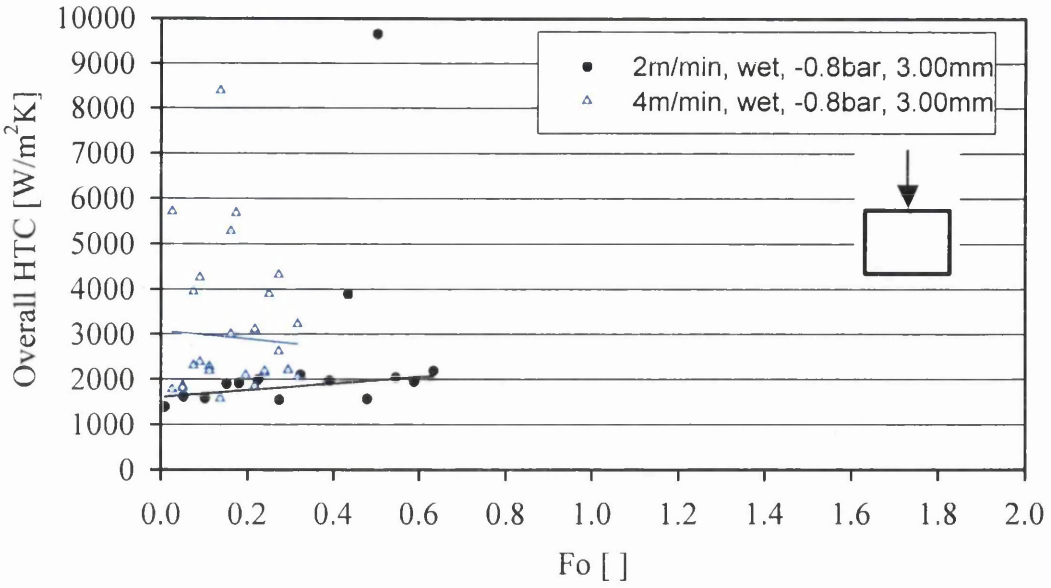

Figure C27: Overall heat transfer coefficients at the centre of the upper profile surface as function of the Fourier number in wet calibration for a vacuum of –0.8 bar at different line speeds; 2.50 mm die exit; 3.00 mm profile wall thickness

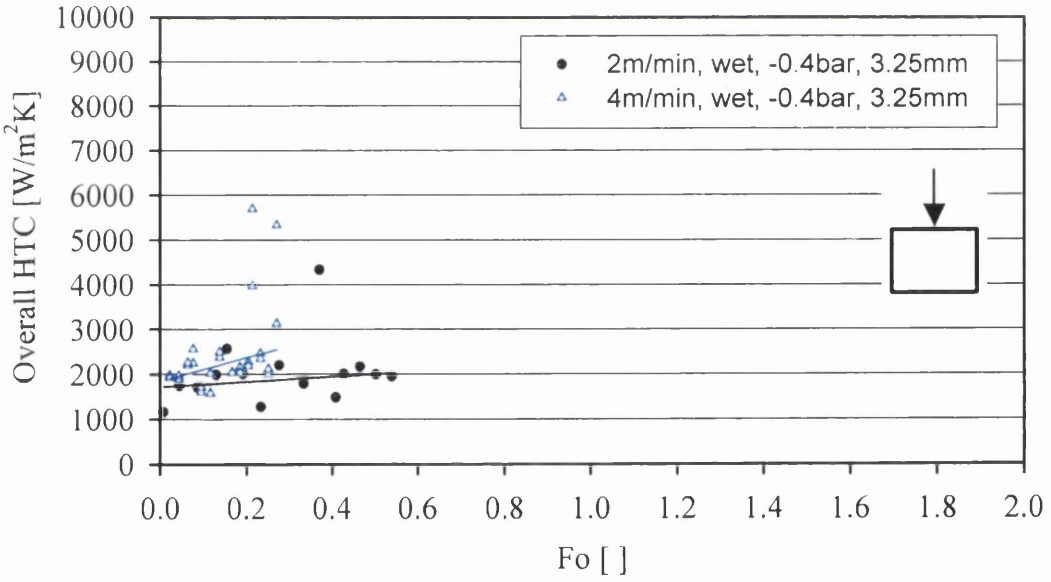

Figure C28: Overall heat transfer coefficients at the centre of the upper profile surface as function of the Fourier number in wet calibration for a vacuum of –0.4 bar at different line speeds; 2.50 mm die exit; 3.25 mm profile wall thickness

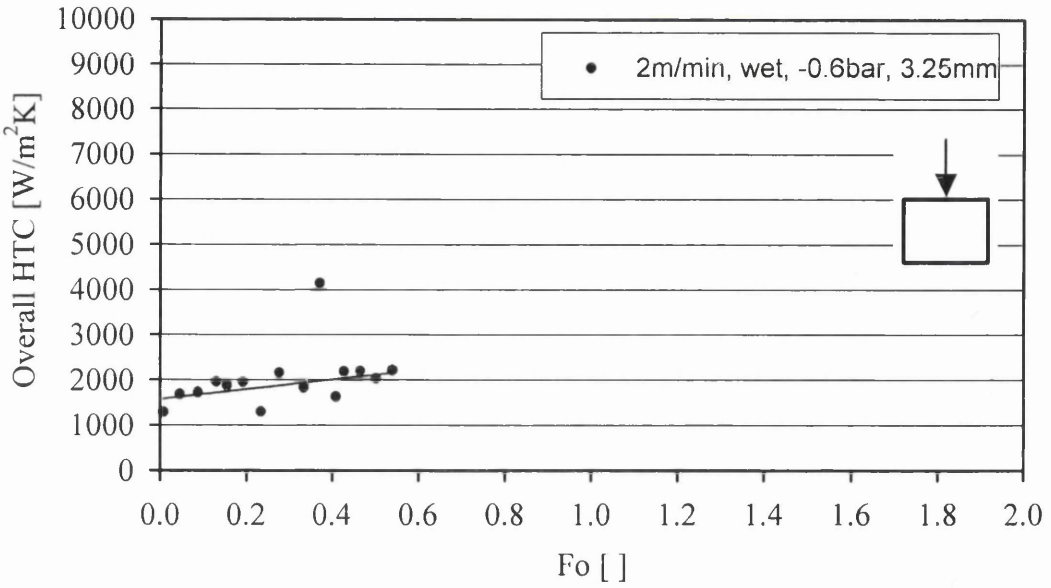

Figure C29: Overall heat transfer coefficients at the centre of the upper profile surface as function of the Fourier number in wet calibration for a vacuum of –0.6 bar at different line speeds; 2.50 mm die exit; 3.25 mm profile wall thickness

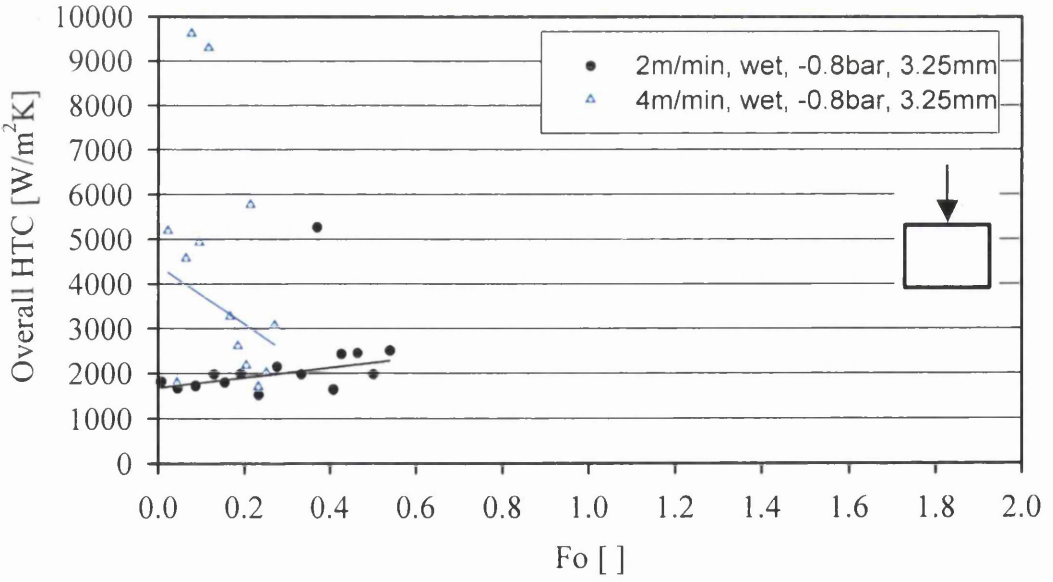

Figure C30: Overall heat transfer coefficients at the centre of the upper profile surface as function of the Fourier number in wet calibration for a vacuum of –0.8 bar at different line speeds; 2.50 mm die exit; 3.25 mm profile wall thickness

C.1.3 Overall heat transfer coefficients near the edge of the upper profile surface in downstream distance

In Figures C31 to C33, the calculated overall heat transfer coefficients are shown surface in dependence on downstream distance for the measurements near the edge of the upper profile surface.

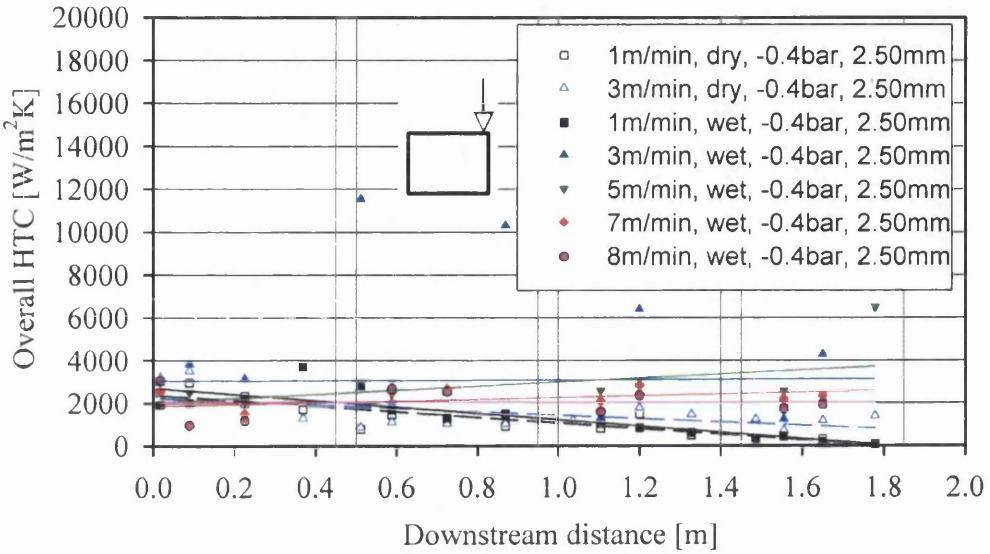

Figure C31: Overall heat transfer coefficients near the edge of the upper profile surface in dry and wet calibration for a vacuum of –0.4 bar at different line speeds; 2.50 mm die exit; 2.50 mm profile wall thickness

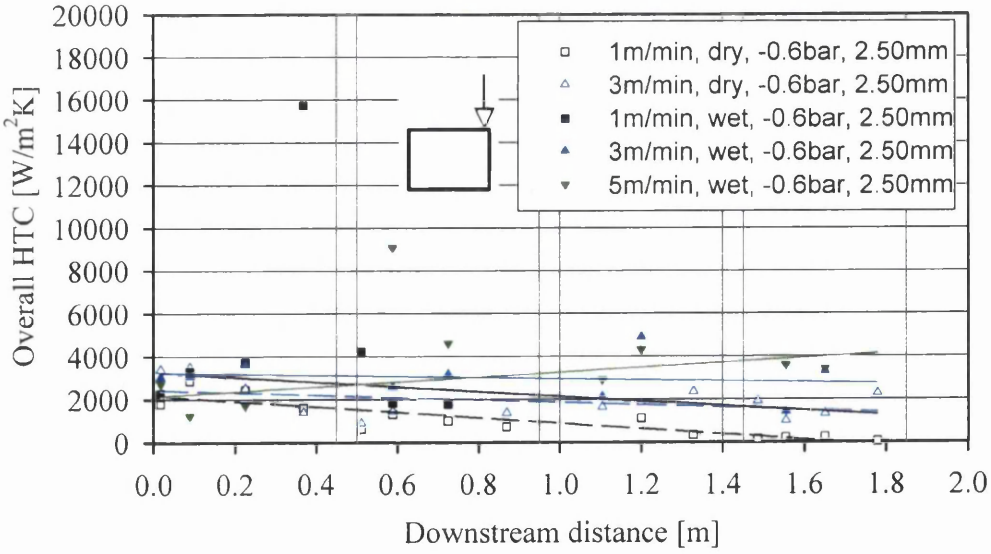

Figure C32: Overall heat transfer coefficients near the edge of the upper profile surface in dry and wet calibration for a vacuum of –0.6 bar at different line speeds; 2.50 mm die exit; 2.50 mm profile wall thickness

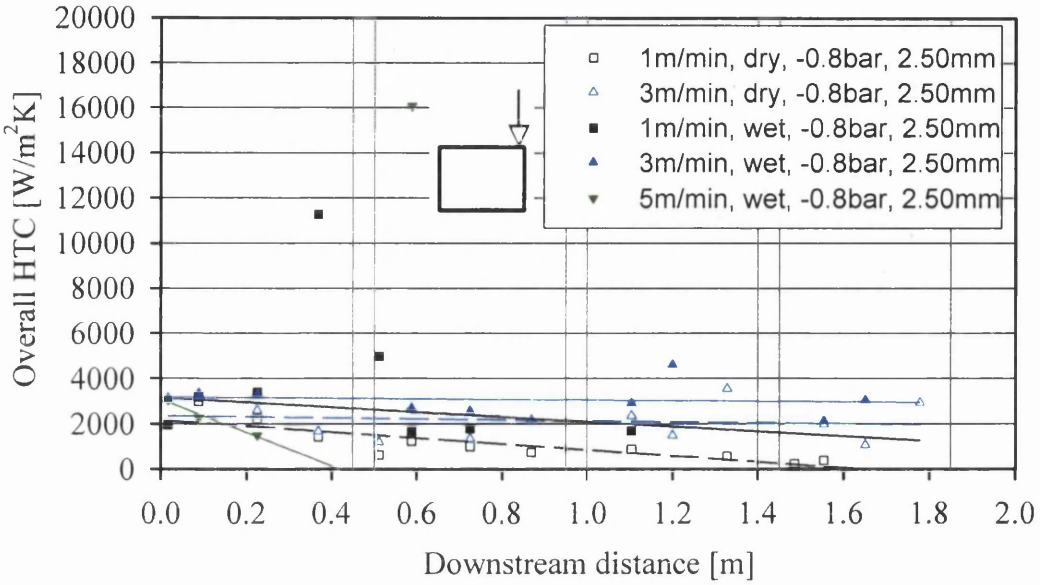

Figure C33: Overall heat transfer coefficients near the edge of the upper profile surface in dry and wet calibration for a vacuum of –0.8 bar at different line speeds; 2.50 mm die exit; 2.50 mm profile wall thickness

In Figures C34 to C36, the calculated overall heat transfer coefficients are shown surface in dependence on Fourier number for the measurements near the edge of the upper profile surface.

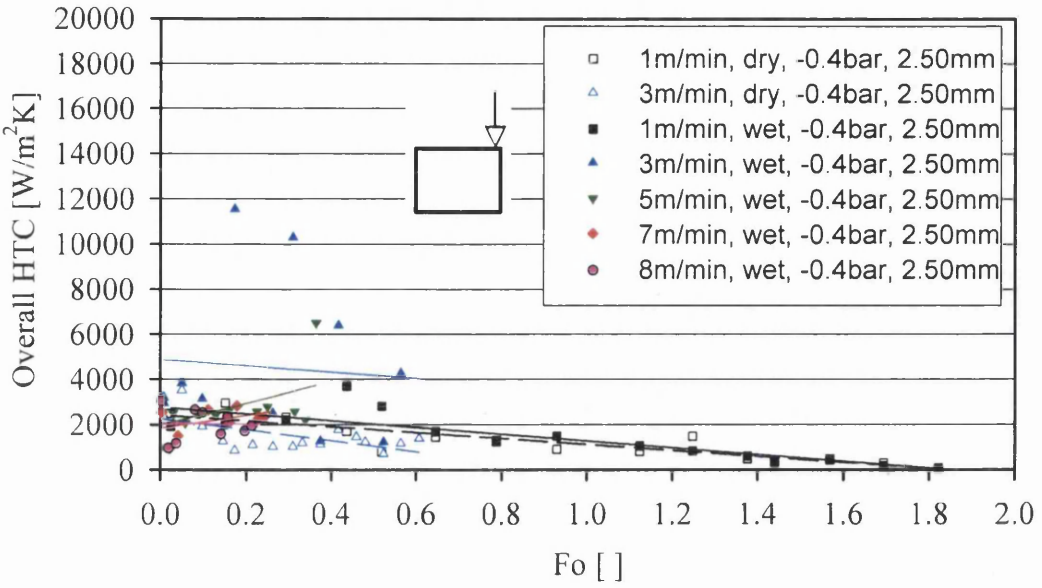

Figure C34: Overall heat transfer coefficients near the edge of the upper profile surface as function of the Fourier number in dry and wet calibration for a vacuum of –0.4 bar at different line speeds; 2.50 mm die exit; 2.50 mm profile wall thickness

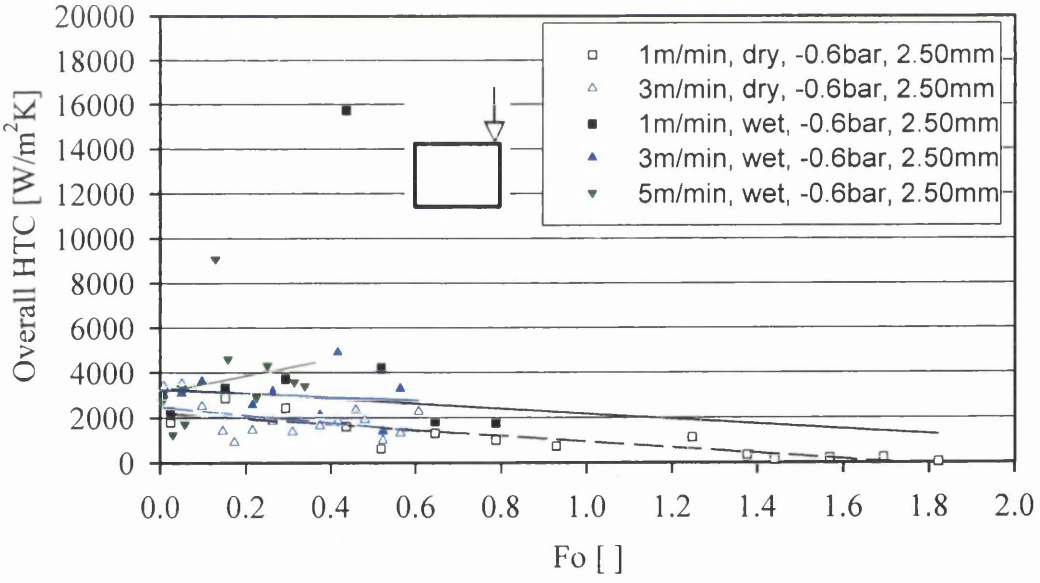

Figure C35: Overall heat transfer coefficients near the edge of the upper profile surface as function of the Fourier number in dry and wet calibration for a vacuum of –0.6 bar at different line speeds; 2.50 mm die exit; 2.50 mm profile wall thickness

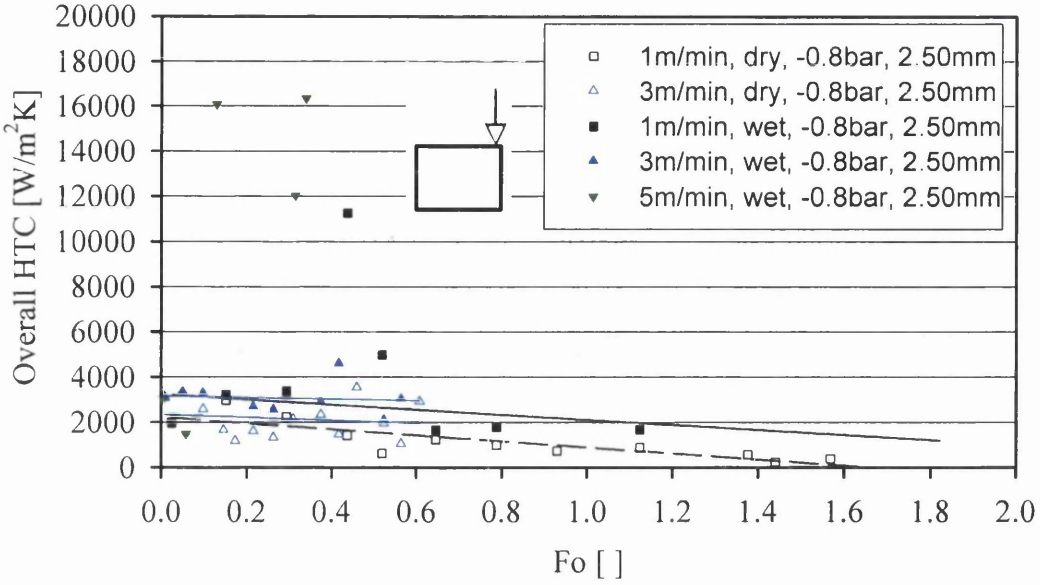

Figure C36: Overall heat transfer coefficients near the edge of the upper profile surface as function of the Fourier number in dry and wet calibration for a vacuum of –0.8 bar at different line speeds; 2.50 mm die exit; 2.50 mm profile wall thickness

C.1.4 Nusselt numbers of overall heat transfer coefficients at the centre of the upper profile surface as function of the Fourier number

In the following Figures C37 to C51, the Nusselt numbers Nu of calculated overall heat transfer are shown for the centre of the upper profile surface on the dependence on the Fourier number. Trend lines are fitted as well. The Figures C37 to C39 represents the calculated Nusselt numbers for the 1st set of experiments in wet and dry calibration for vacua of –0.4 to –0.8 bar at constant wall thickness of 2.50 mm. In Figures C40 to C51, the 2nd set is shown with variation of wall thickness from 2.50 to 3.25 mm and vacua of -0.4 to -0.8 bar.

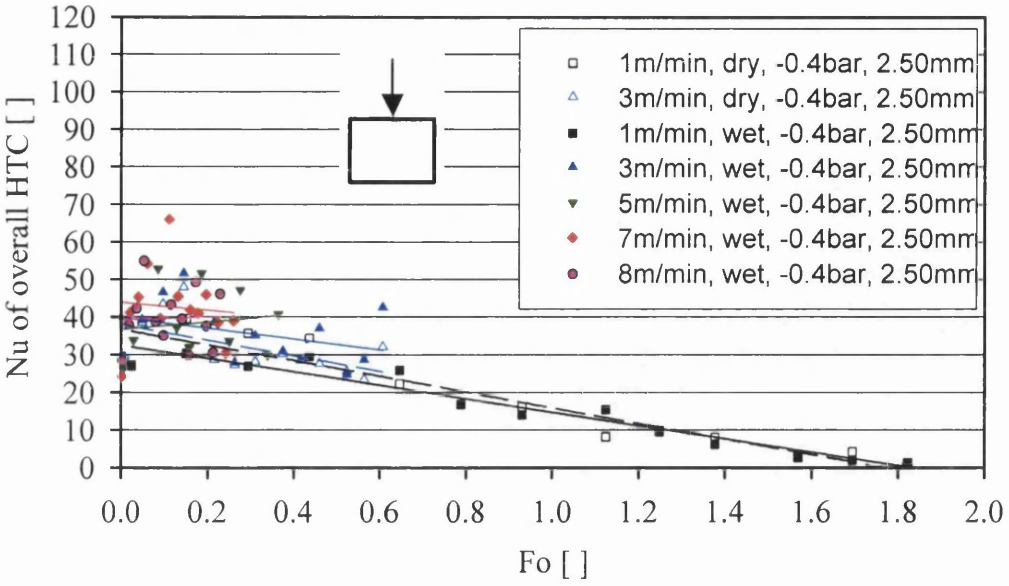

Figure C37: Nusselt numbers of overall heat transfer at the centre of the upper profile surface as function of the Fourier number in dry and wet calibration for a vacuum of –0.4 bar at different line speeds; 2.50 mm die exit; 2.50 mm wall profile thickness

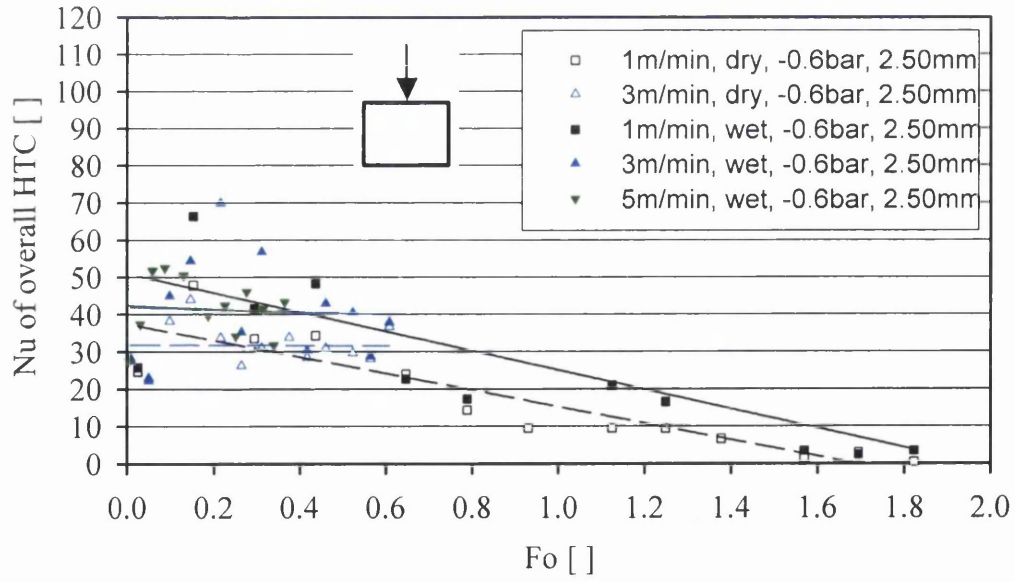

Figure C38: Nusselt numbers of overall heat transfer at the centre of the upper profile surface as function of the Fourier number in dry and wet calibration for a vacuum of –0.6 bar at different line speeds; 2.50 mm die exit; 2.50 mm profile wall thickness

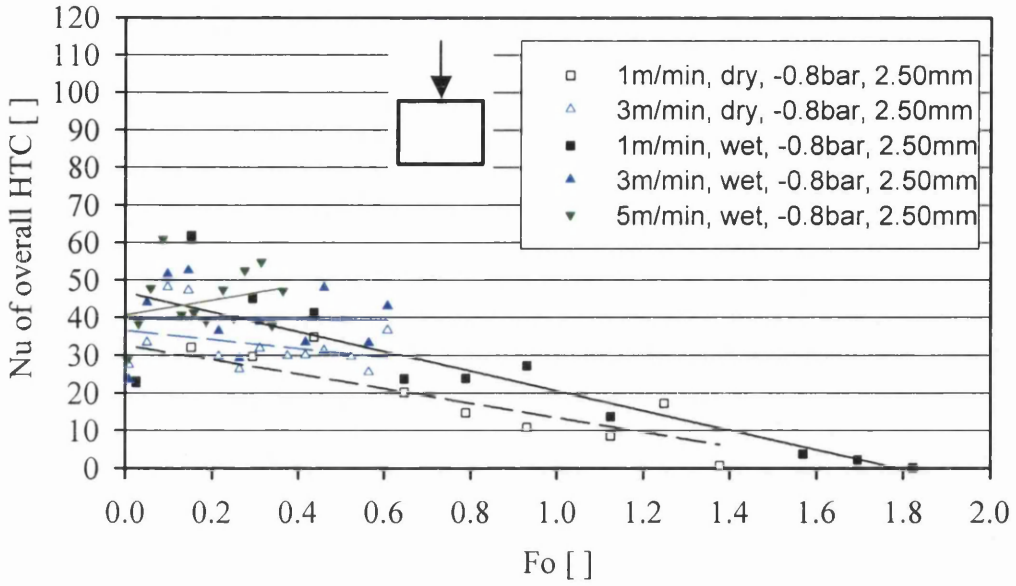

Figure C39: Nusselt numbers of overall heat transfer at the centre of the upper profile surface as function of the Fourier number in dry and wet calibration for a vacuum of –0.8 bar at different line speeds; 2.50 mm die exit; 2.50 mm profile wall thickness

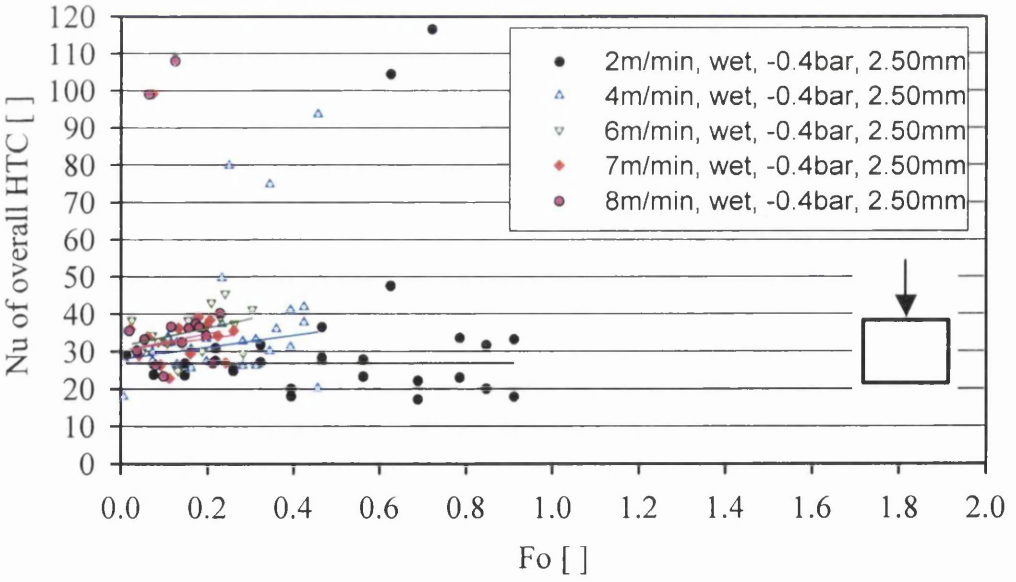

Figure C40: Nusselt numbers of overall heat transfer at the centre of the upper profile surface as function of the Fourier number in wet calibration for a vacuum of –0.4 bar at different line speeds; 2.50 mm die exit; 2.50 mm profile wall thickness

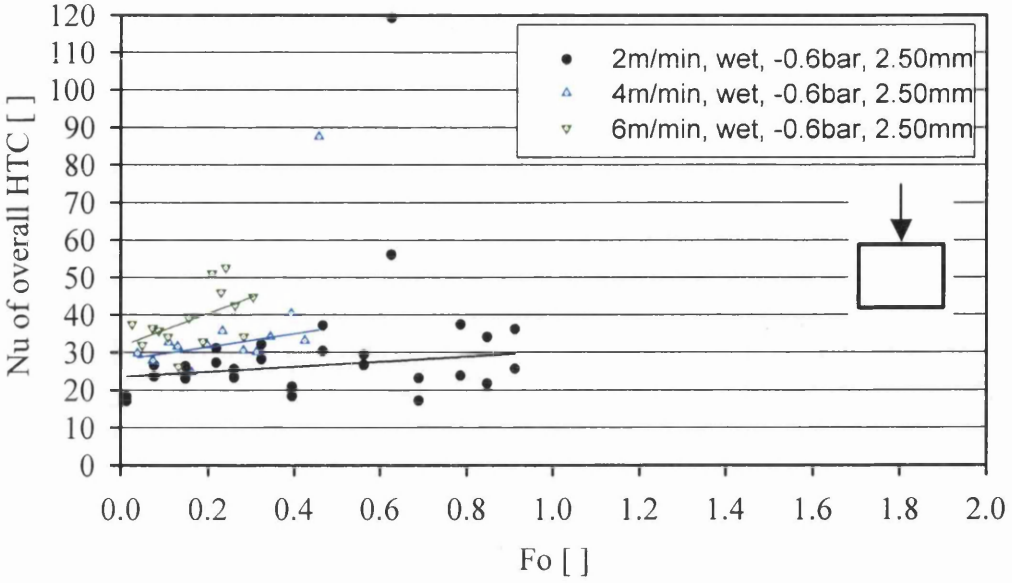

Figure C41: Nusselt numbers of overall heat transfer at the centre of the upper profile surface as function of the Fourier number in wet calibration for a vacuum of –0.6 bar at different line speeds; 2.50 mm die exit; 2.50 mm profile wall thickness

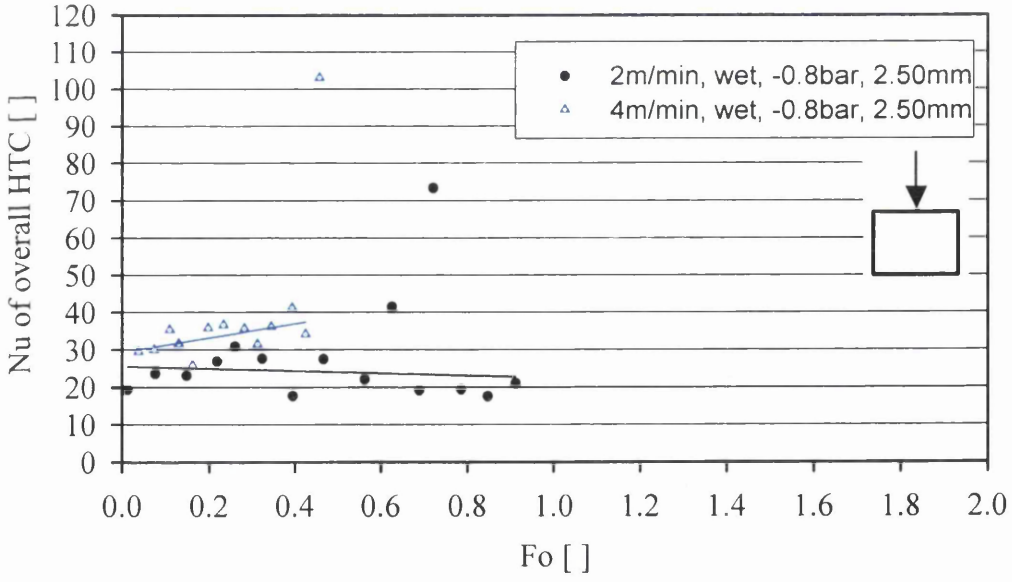

Figure C42: Nusselt numbers of overall heat transfer at the centre of the upper profile surface as function of the Fourier number in wet calibration for a vacuum of –0.8 bar at different line speeds; 2.50 mm die exit; 2.50 mm profile wall thickness

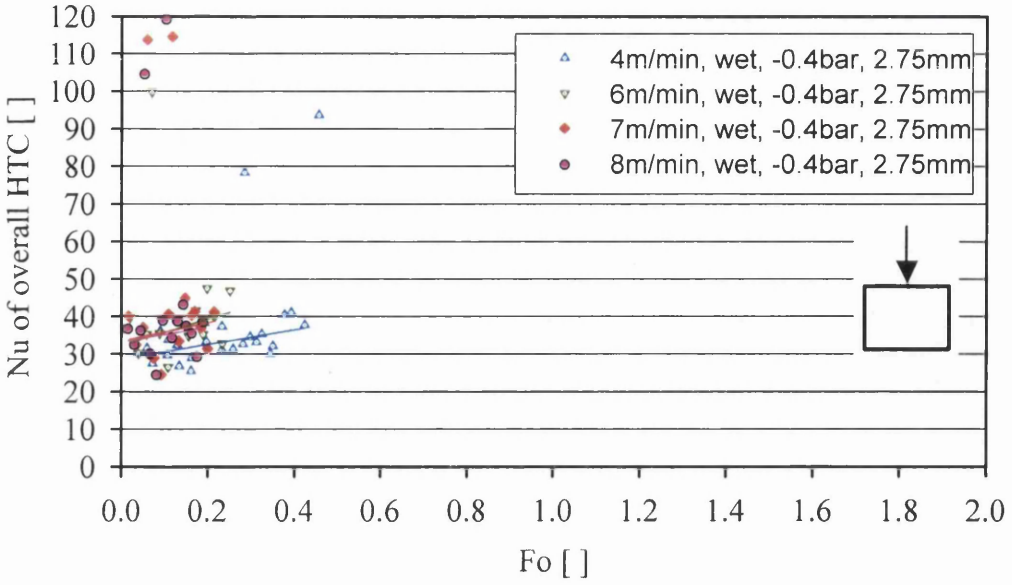

Figure C43: Nusselt numbers of overall heat transfer at the centre of the upper profile surface as function of the Fourier number in wet calibration for a vacuum of –0.4 bar at different line speeds; 2.50 mm die exit; 2.75 mm profile wall thickness

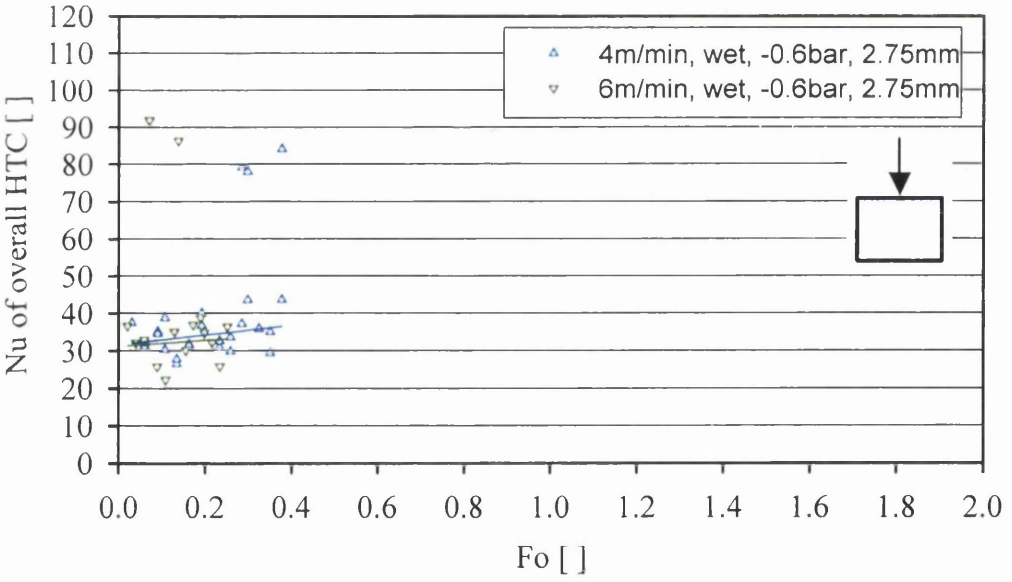

Figure C44: Nusselt numbers of overall heat transfer at the centre of the upper profile surface as function of the Fourier number in wet calibration for a vacuum of –0.6 bar at different line speeds; 2.50 mm die exit; 2.75 mm profile wall thickness

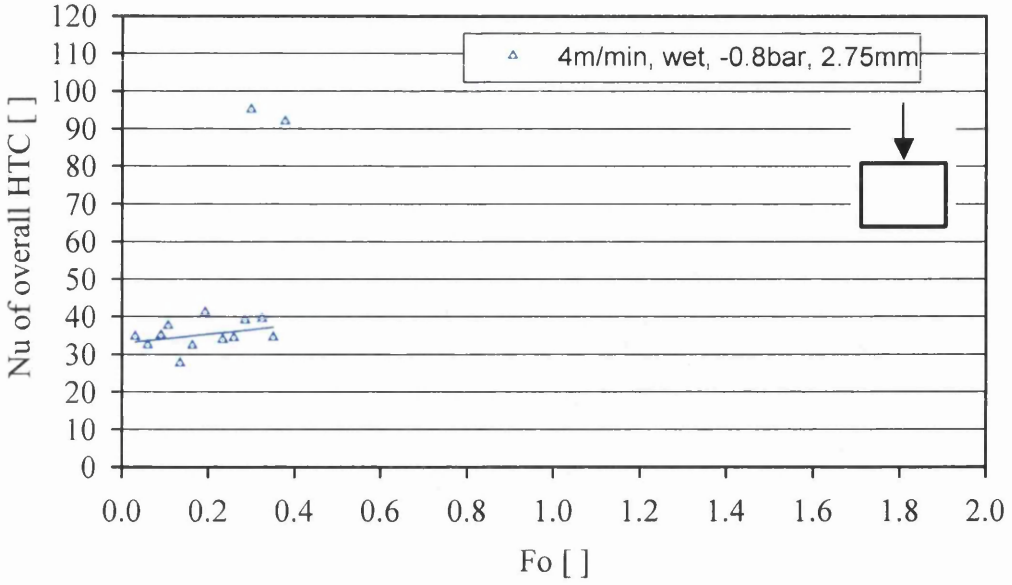

Figure C45: Nusselt numbers of overall heat transfer at the centre of the upper profile surface as function of the Fourier number in wet calibration for a vacuum of –0.8 bar at different line speeds; 2.50 mm die exit; 2.75 mm profile wall thickness

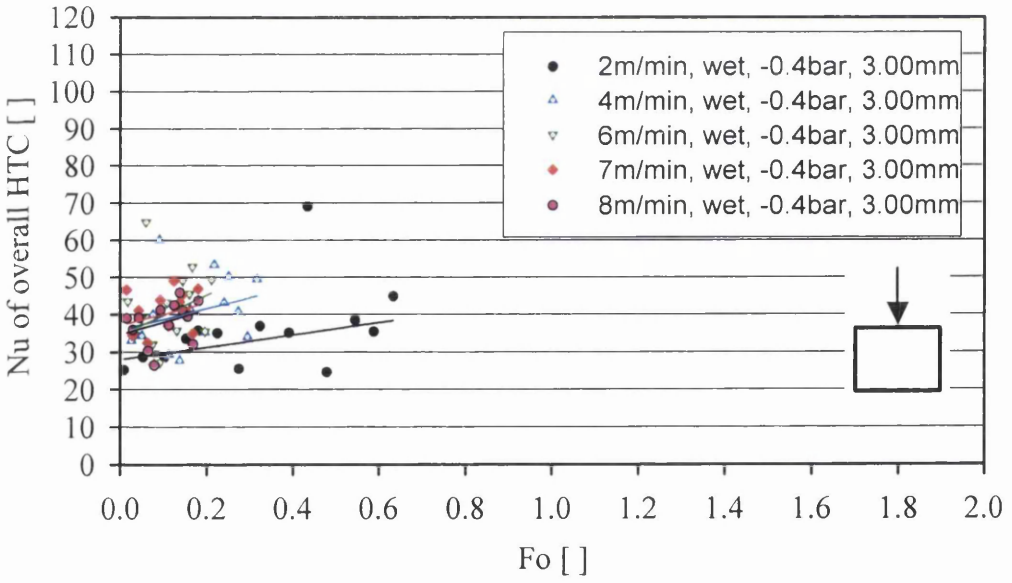

Figure C46: Nusselt numbers of overall heat transfer at the centre of the upper profile surface as function of the Fourier number in wet calibration for a vacuum of –0.4 bar at different line speeds; 2.50 mm die exit; 3.00 mm profile wall thickness

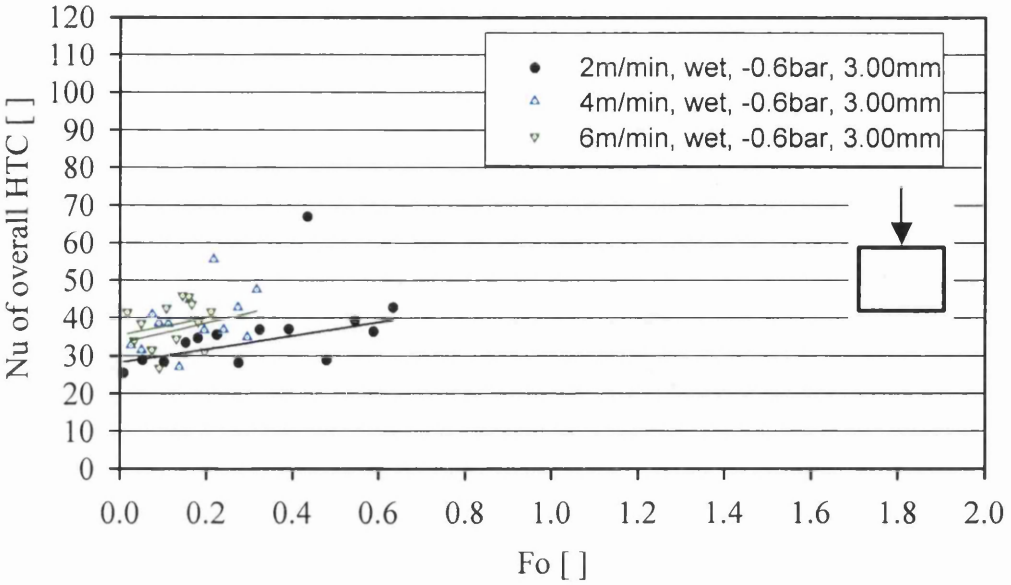

Figure C47: Nusselt numbers of overall heat transfer at the centre of the upper profile surface as function of the Fourier number in wet calibration for a vacuum of –0.6 bar at different line speeds; 2.50 mm die exit; 2.75 mm profile wall thickness

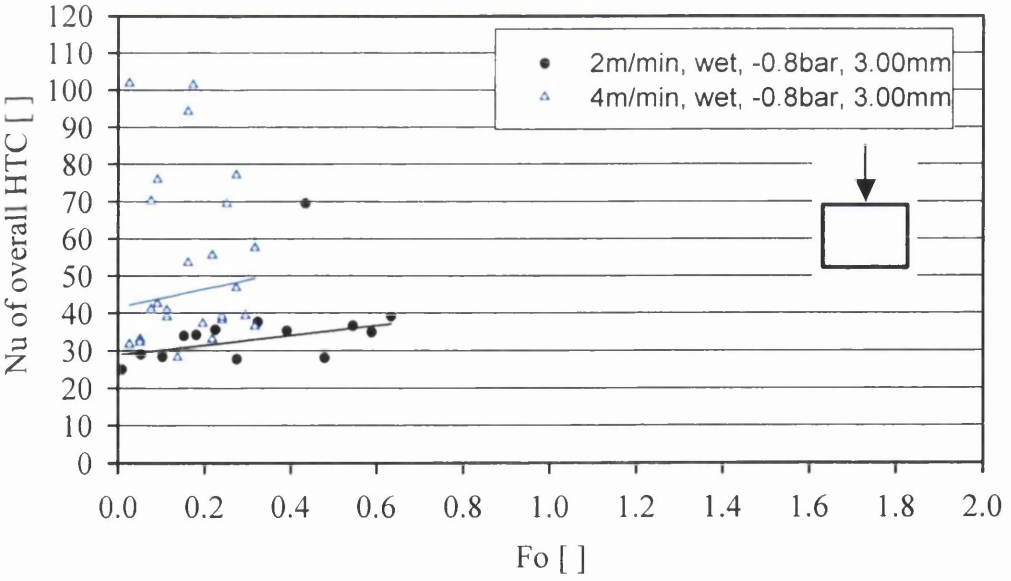

Figure C48: Nusselt numbers of overall heat transfer at the centre of the upper profile surface as function of the Fourier number in wet calibration for a vacuum of –0.8 bar at different line speeds; 2.50 mm die exit; 3.00 mm profile wall thickness

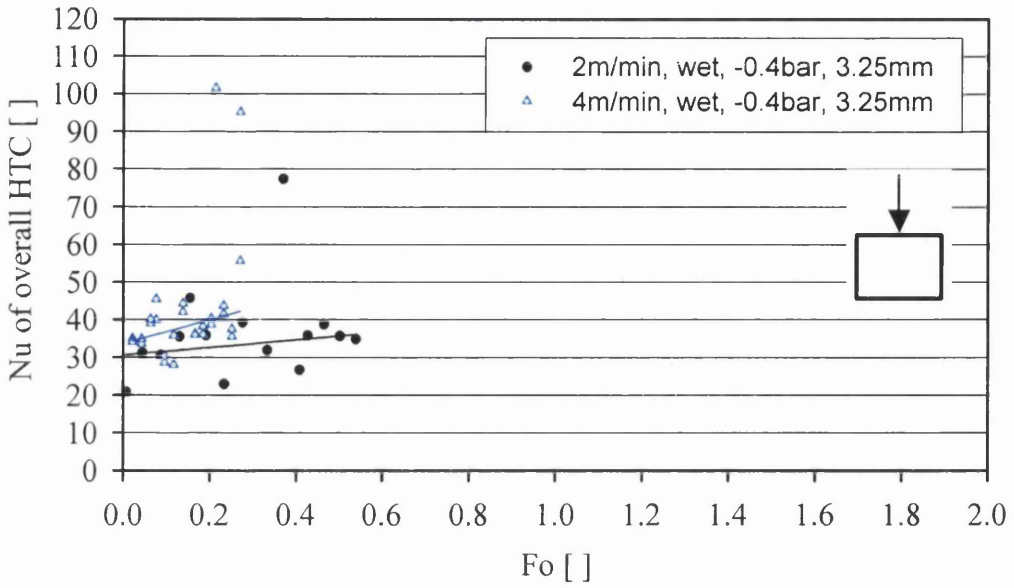

Figure C49: Nusselt numbers of overall heat transfer at the centre of the upper profile surface as function of the Fourier number in wet calibration for a vacuum of –0.4 bar at different line speeds; 2.50 mm die exit; 3.25 mm profile wall thickness

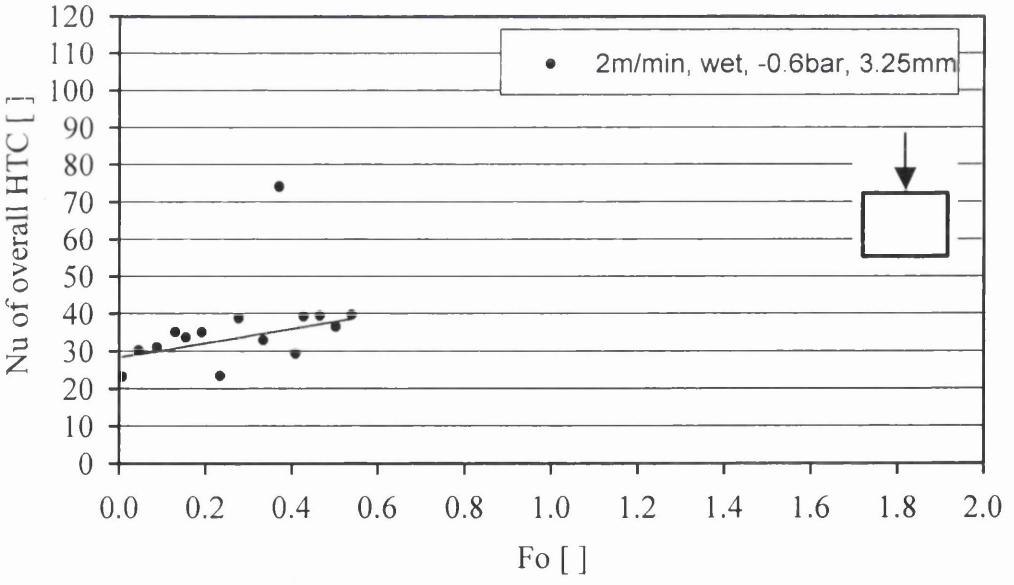

Figure C50: Nusselt numbers of overall heat transfer at the centre of the upper profile surface as function of the Fourier number in wet calibration for a vacuum of –0.6 bar at different line speeds; 2.50 mm die exit; 3.25 mm profile wall thickness

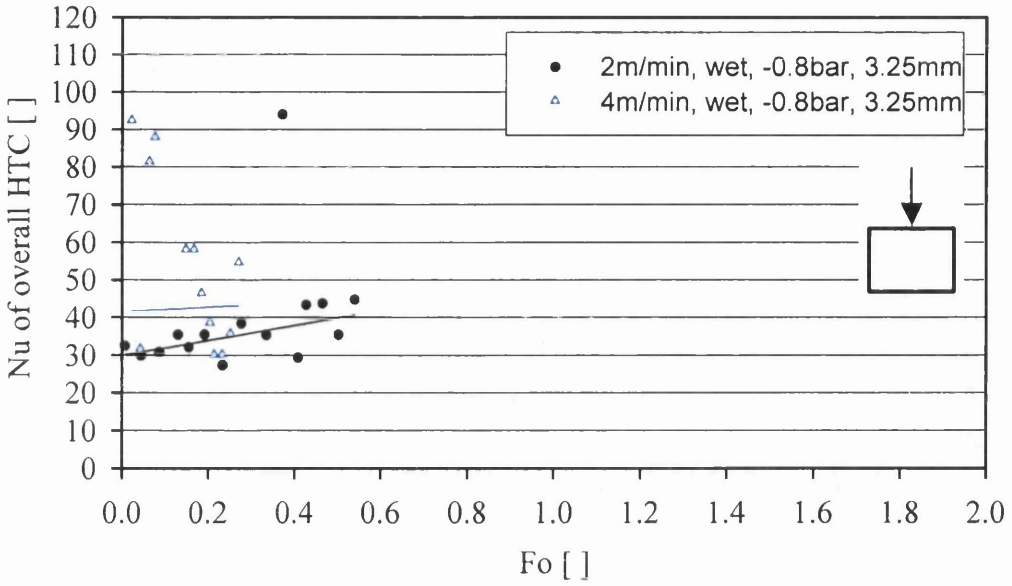

Figure C51: Nusselt numbers of overall heat transfer at the centre of the upper profile surface as function of the Fourier number in wet calibration for a vacuum of –0.8 bar at different line speeds; 2.50 mm die exit; 3.25 mm profile wall thickness

C.1.5 Nusselt numbers near the edge of the upper profile surface as function of the Fourier number

In Section C.1.5, the calculated Nu numbers of the 1st set of experiments are shown on dependence of the Fo number for vacua of –0.4 to –0.8 bar at constant wall thickness of 2.50 mm.

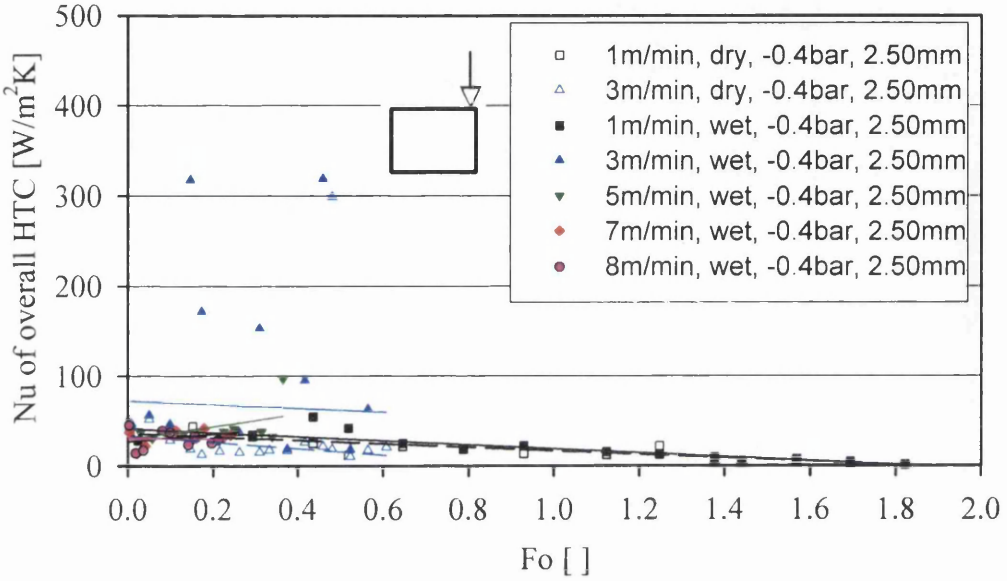

Figure C52: Nusselt numbers of overall heat transfer near the edge of the upper profile surface as function of the Fourier number in dry and wet calibration for a vacuum of –0.4 bar at different line speeds; 2.50 mm die exit; 2.50 mm profile wall thickness

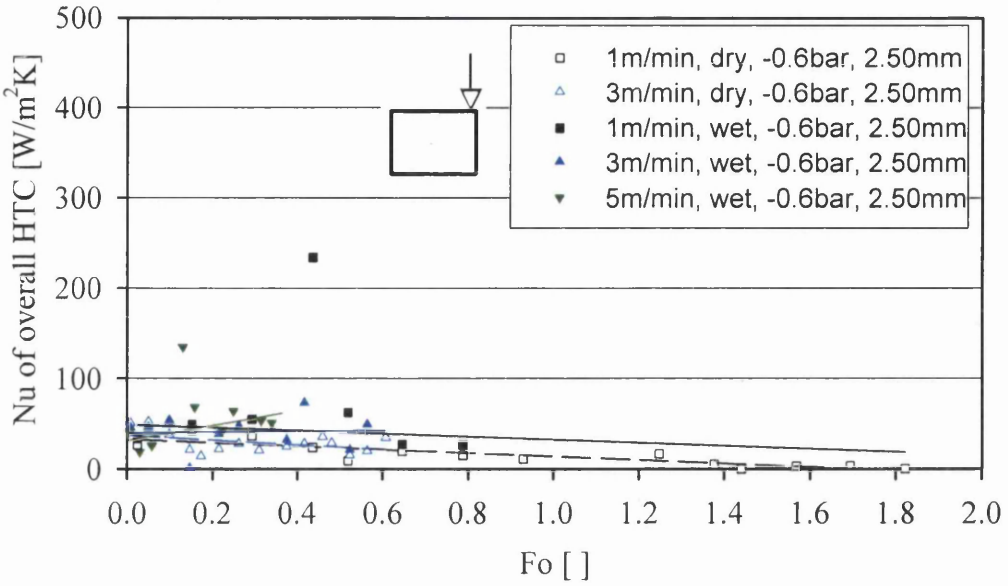

Figure C53: Nusselt numbers of overall heat transfer near the edge of the upper profile surface as function of the Fourier number in dry and wet calibration for a vacuum of –0.6 bar at different line speeds; 2.50 mm die exit; 2.50 mm profile wall thickness

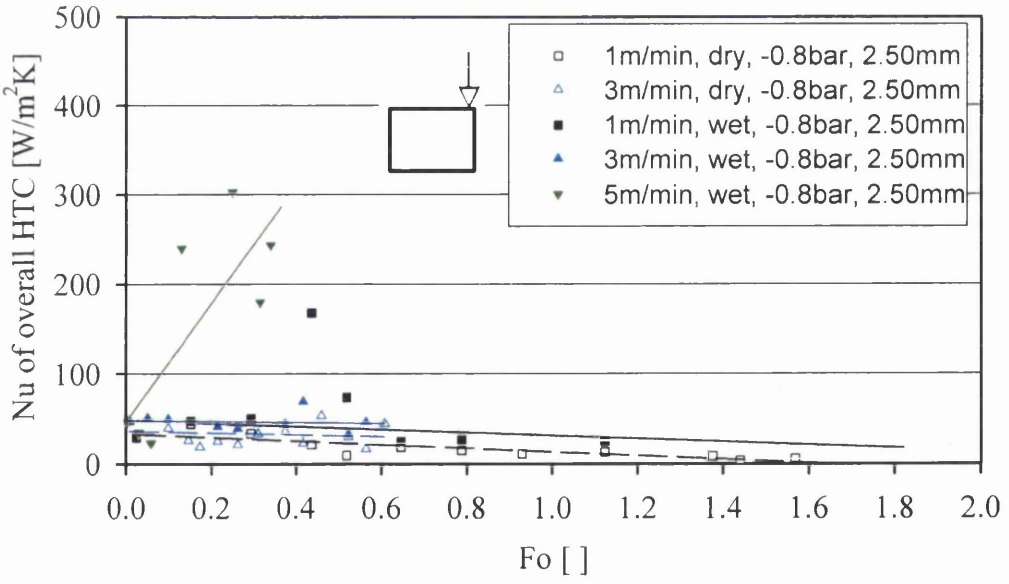

Figure C54: Nusselt numbers of overall heat transfer near the edge of the upper profile surface as function of the Fourier number in dry and wet calibration for a vacuum of –0.8 bar at different line speeds; 2.50 mm die exit; 2.50 mm profile wall thickness

C.2 Interfacial heat transfer coefficients

In this Section, the calculated interfacial heat transfer coefficients will be shown.

The Figures C55 to C69, Section C.2.1, are presenting the interfacial heat transfer coefficients for 1st and 2nd set of experiments on the dependence of downstream distance for different line speeds, vacua and wall thicknesses. This is followed by the dependence of the interfacial heat transfer coefficients on the Fourier number Fo in Figures C70 to C84 at same conditions in Section C.2.2.

In Section C.2.3 the results for the edge of the upper profile surface are shown only for the 1st set of experiments along the line in Figures C85 to C90. This is because the profile surface temperatures were measured in 2nd set only near the edge in Calibrator 1.

Section C.2.4 presents the results for calculated dimensionless Nusselt number Nu, using the calculated interfacial heat transfer coefficients, replacing the interfacial heat transfer coefficient in Section C2.2, Figures C91 to C105.

The Figures C106 to C108 in Section C.2.5 show the results for the edge of the upper profile surface for the 1st of experiments.

C.2.1 Interfacial heat transfer coefficients at the centre of the upper profile surface in downstream distance

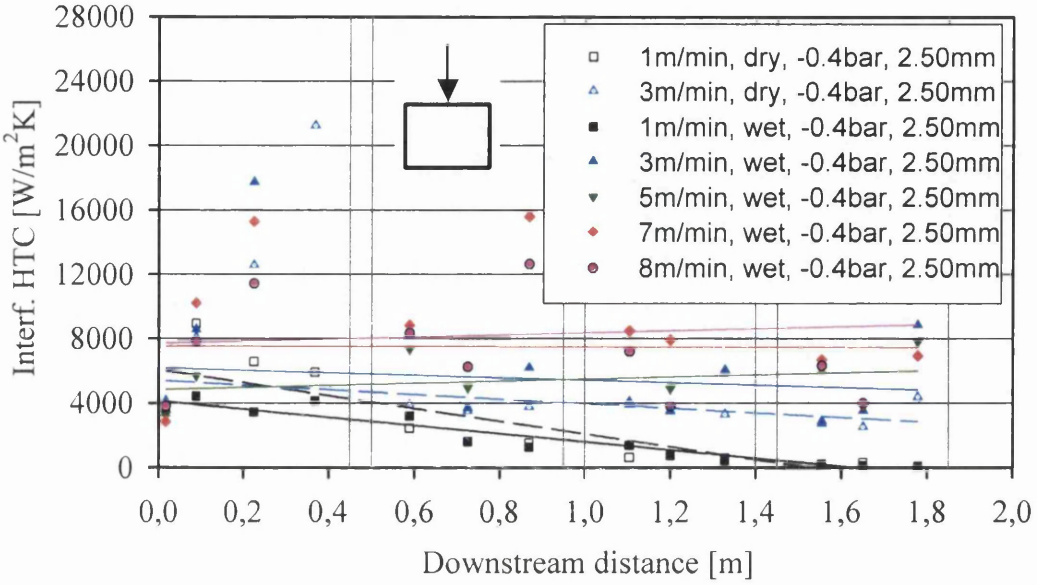

Figure C55: Interfacial heat transfer coefficients at the centre of the upper profile surface in dry and wet calibration for a vacuum of –0.4 bar at different line speeds; 2.50 mm die exit; 2.50 mm profile wall thickness

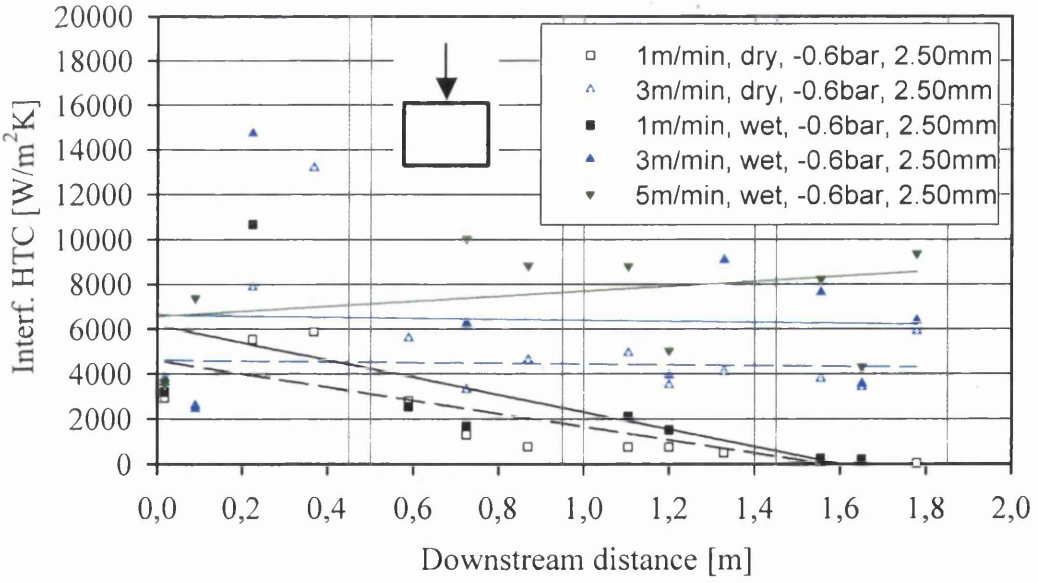

Figure C56: Interfacial heat transfer coefficients at the centre of the upper profile surface in dry and wet calibration for a vacuum of –0.6 bar at different line speeds; 2.50 mm die exit; 2.50 mm profile wall thickness

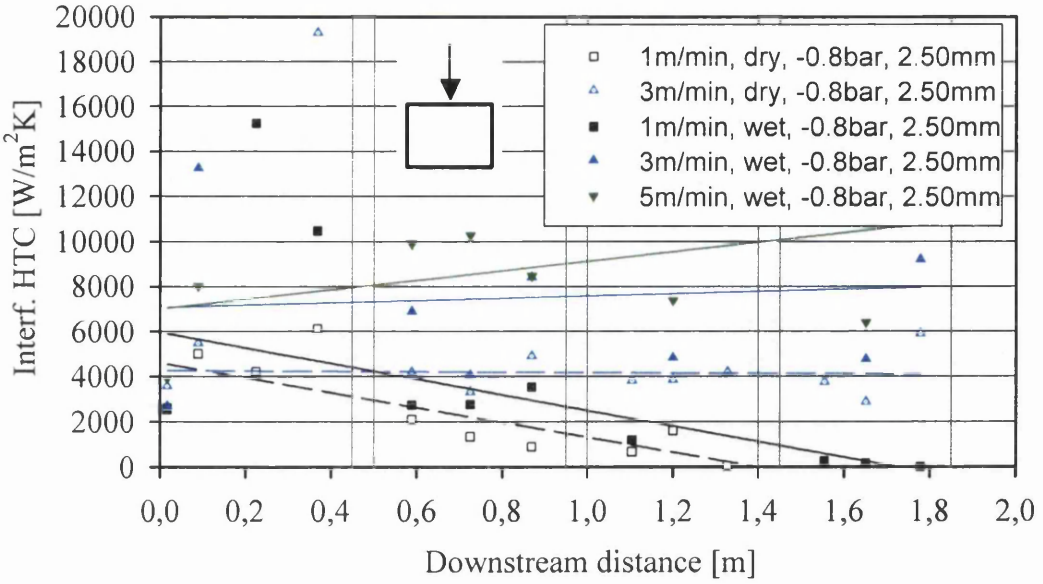

Figure C57: Interfacial heat transfer coefficients at the centre of the upper profile surface in dry and wet calibration for a vacuum of –0.8 bar at different line speeds; 2.50 mm die exit; 2.50 mm profile wall thickness

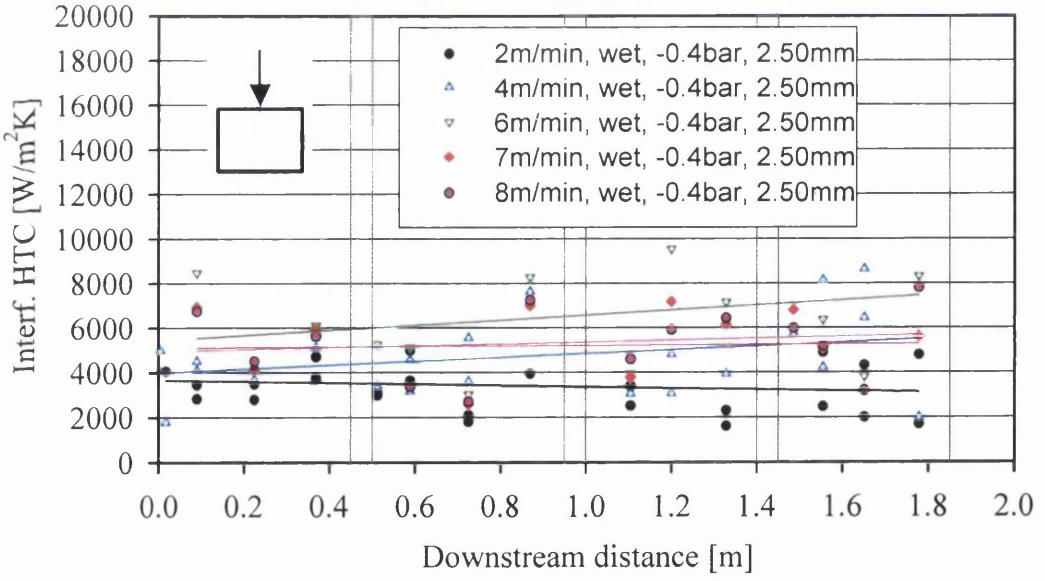

Figure C58: Interfacial heat transfer coefficients at the centre of the upper profile in wet calibration for a vacuum of –0.4 bar at different line speeds; 2.50 mm die exit; 2.50 mm profile wall thickness

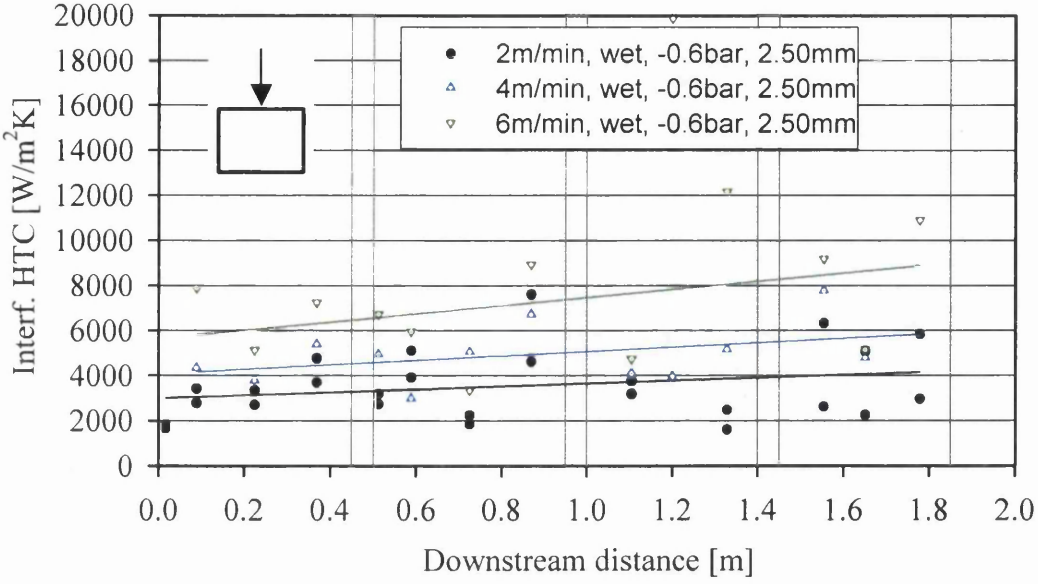

Figure C59: Interfacial heat transfer coefficients at the centre of the upper profile in wet calibration for a vacuum of –0.6 bar at different line speeds; 2.50 mm die exit; 2.50 mm profile wall thickness

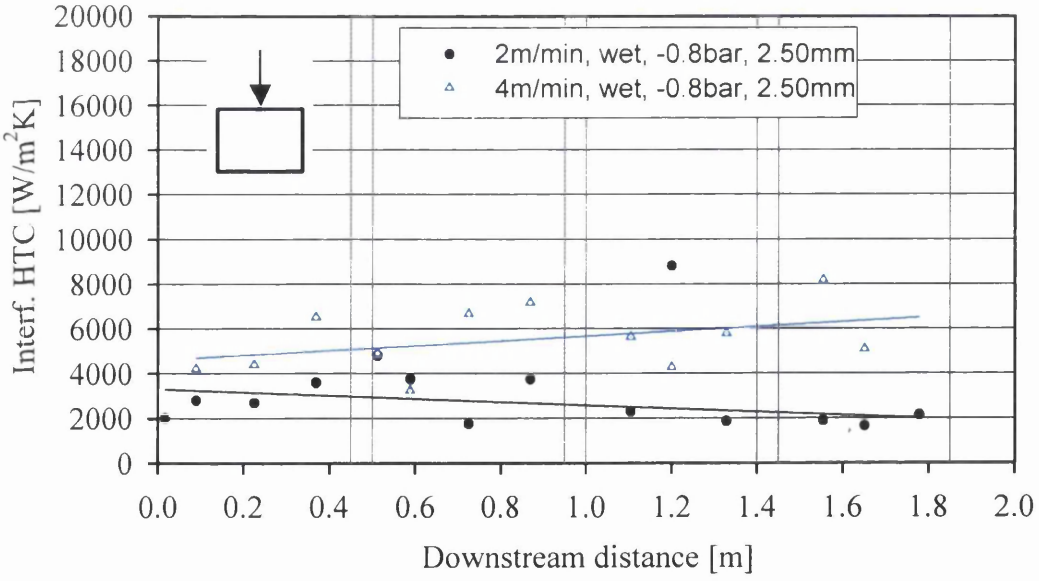

Figure C60: Interfacial heat transfer coefficients at the centre of the upper profile in wet calibration for a vacuum of –0.8 bar at different line speeds; 2.50 mm die exit; 2.50 mm profile wall thickness

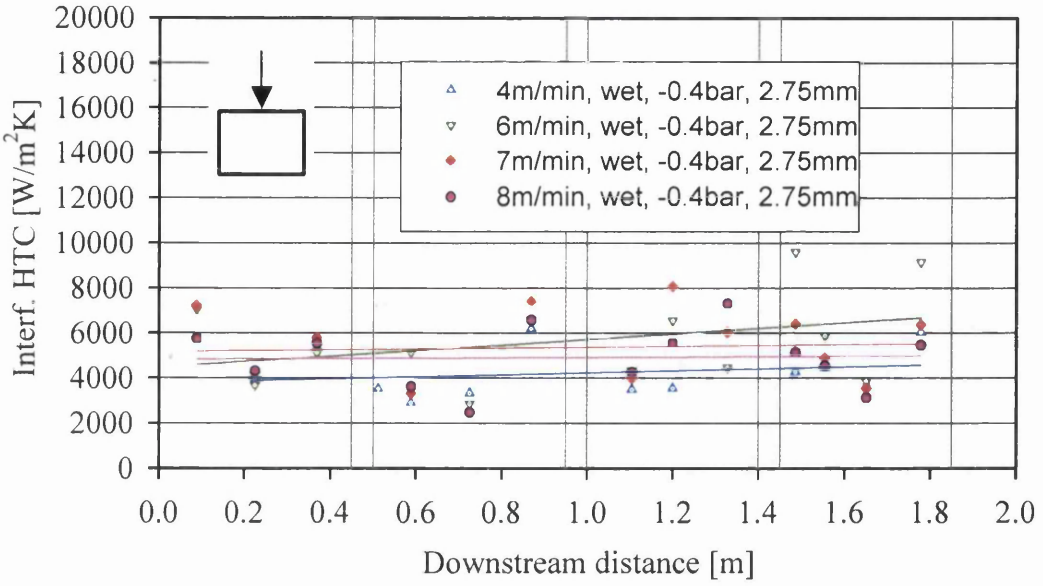

Figure C61: Interfacial heat transfer coefficients at the centre of the upper profile in wet calibration for a vacuum of –0.4 bar at different line speeds; 2.50 mm die exit; 2.75 mm profile wall thickness

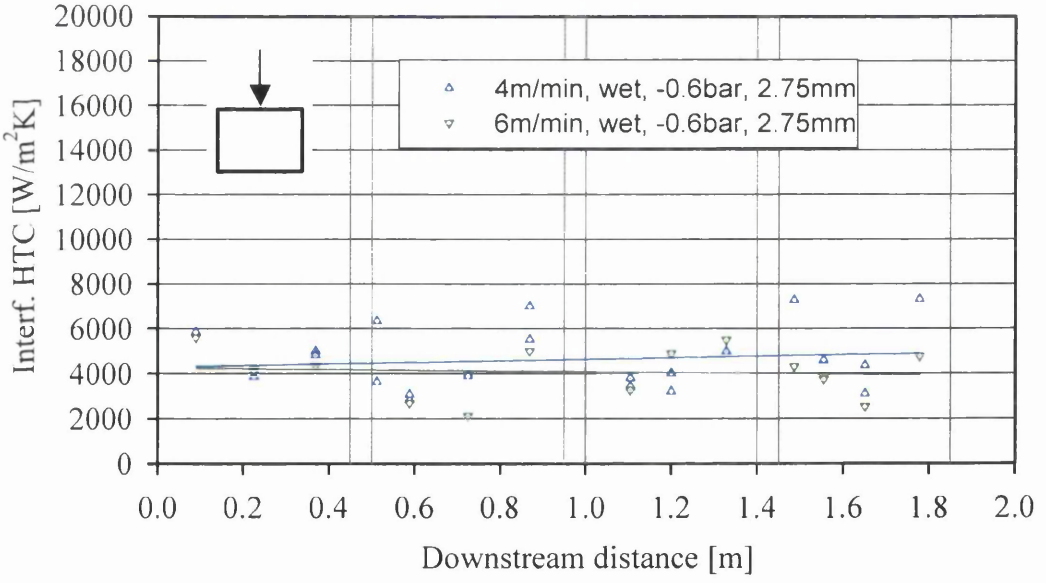

Figure C62: Interfacial heat transfer coefficients at the centre of the upper profile in wet calibration for a vacuum of –0.6 bar at different line speeds; 2.50 mm die exit; 2.75 mm profile wall thickness

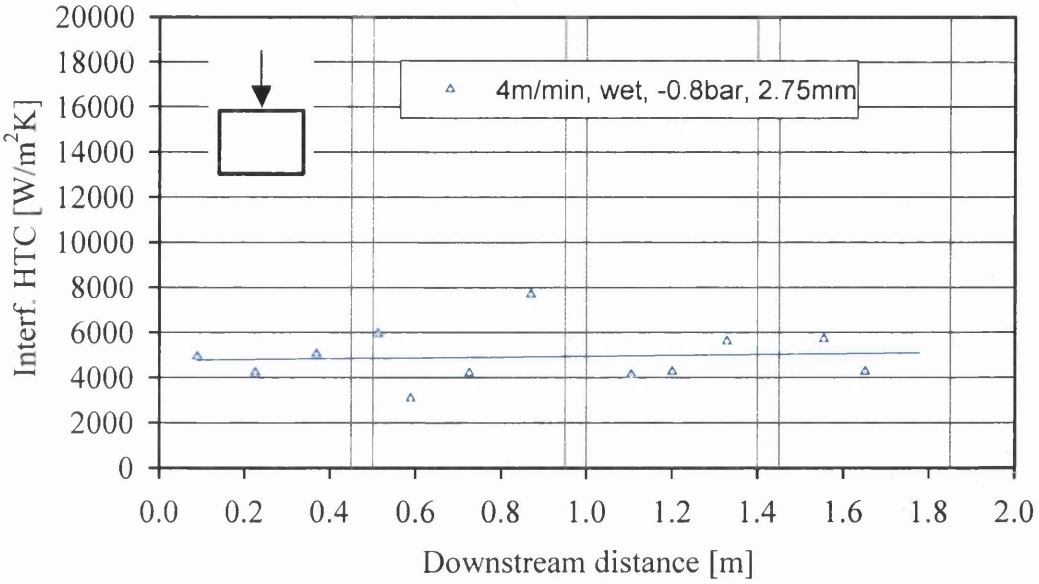

Figure C63: Interfacial heat transfer coefficients at the centre of the upper profile in wet calibration for a vacuum of –0.8 bar at different line speeds; 2.50 mm die exit; 2.75 mm profile wall thickness

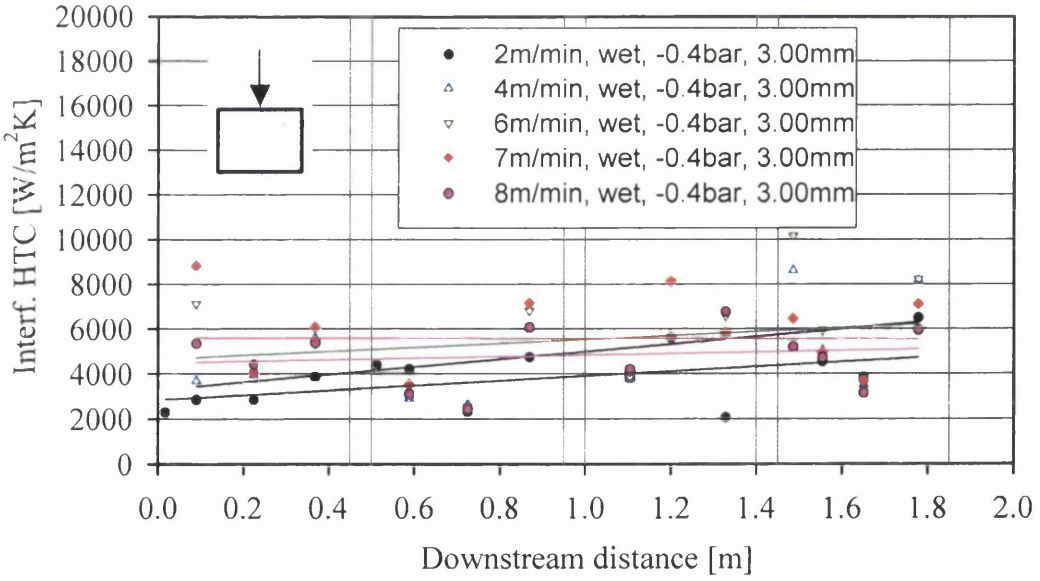

Figure C64: Interfacial heat transfer coefficients at the centre of the upper profile in wet calibration for a vacuum of –0.4 bar at different line speeds; 2.50 mm die exit; 3.00 mm profile wall thickness

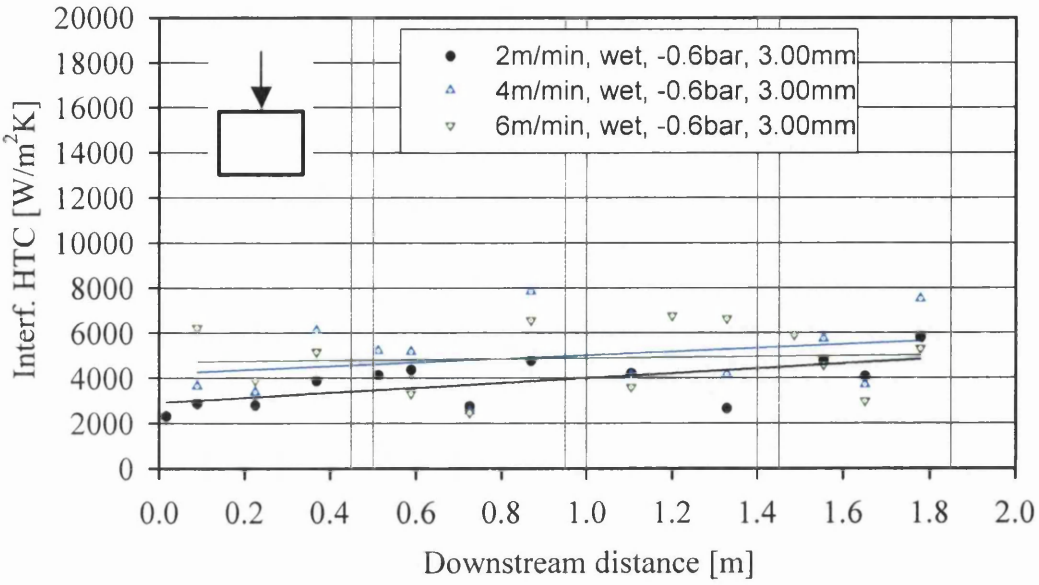

Figure C65: Interfacial heat transfer coefficients at the centre of the upper profile in wet calibration for a vacuum of –0.6 bar at different line speeds; 2.50 mm die exit; 3.00 mm profile wall thickness

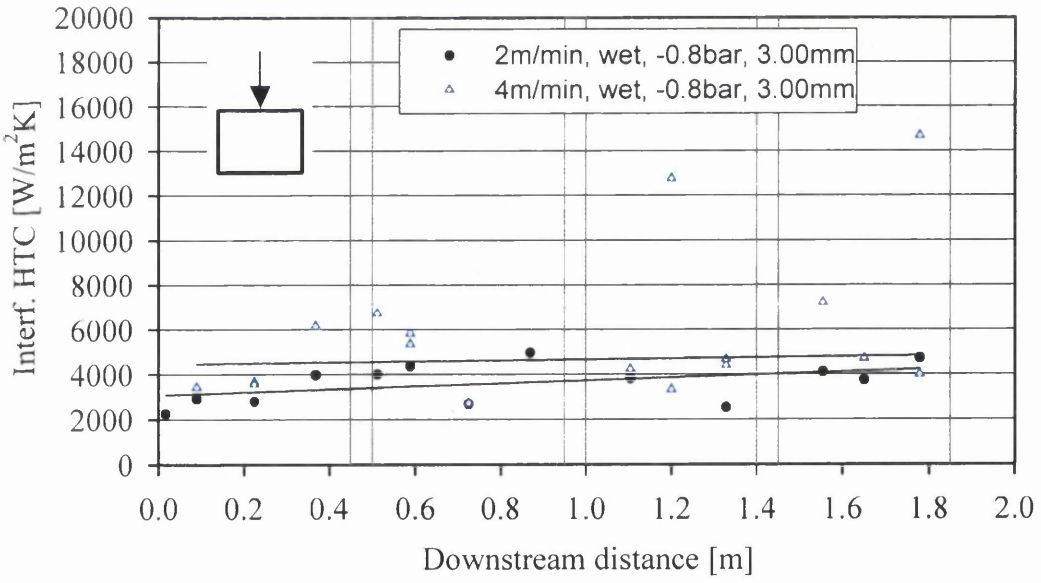

Figure C66: Interfacial heat transfer coefficients at the centre of the upper profile in wet calibration for a vacuum of –0.8 bar at different line speeds; 2.50 mm die exit; 3.00 mm profile wall thickness

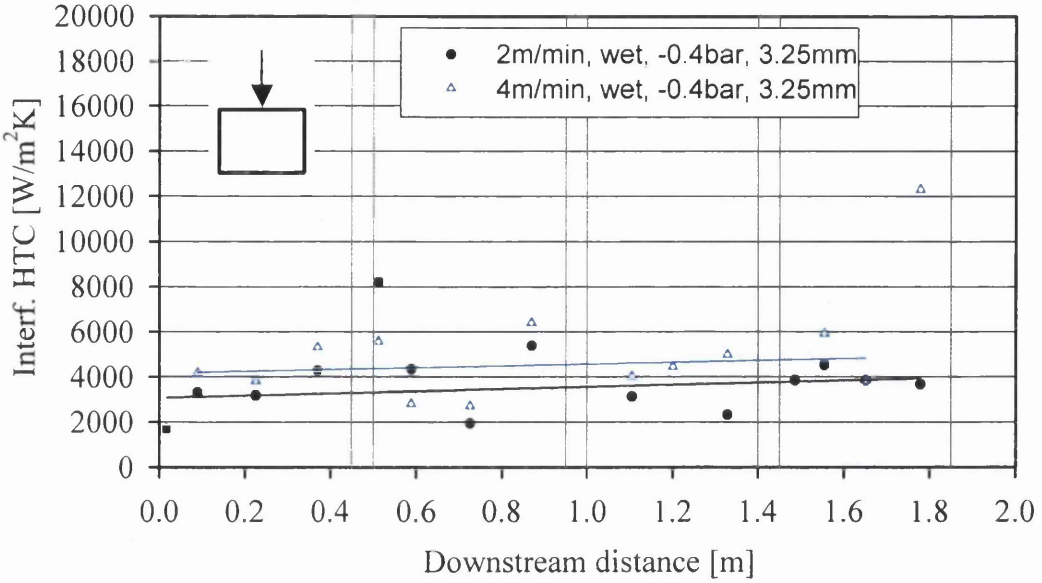

Figure C67: Interfacial heat transfer coefficients at the centre of the upper profile in wet calibration for a vacuum of –0.4 bar at different line speeds; 2.50 mm die exit; 3.25 mm profile wall thickness

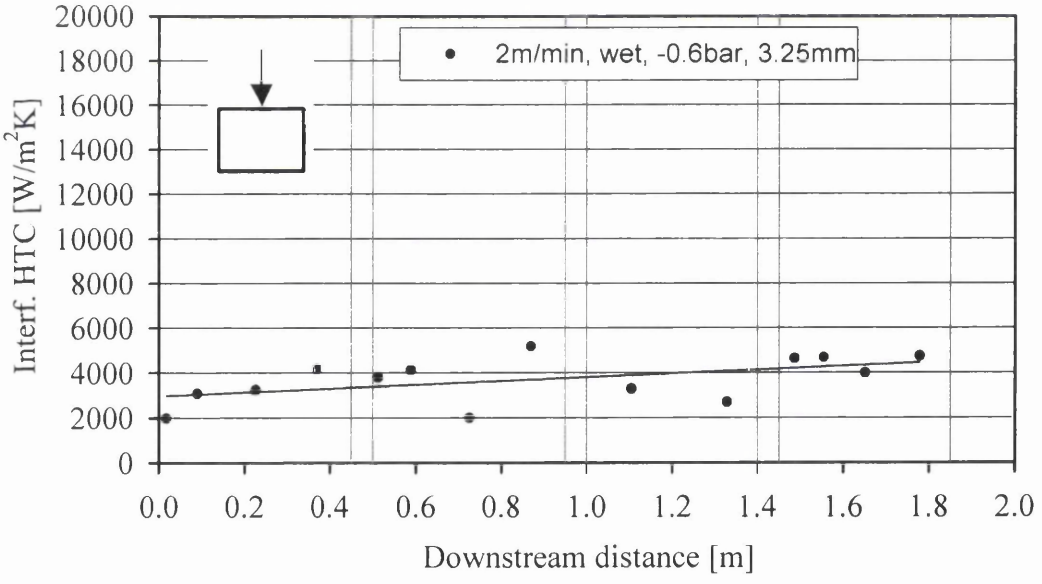

Figure C68: Interfacial heat transfer coefficients at the centre of the upper profile in wet calibration for a vacuum of –0.6 bar at different line speeds; 2.50 mm die exit; 3.25 mm profile wall thickness

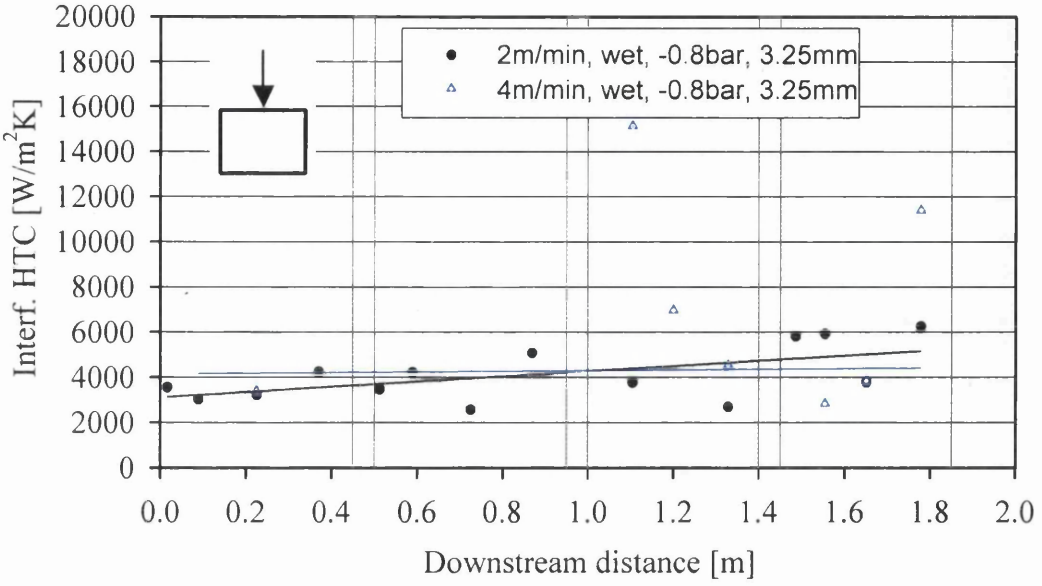

Figure C69: Interfacial heat transfer coefficients at the centre of the upper profile in wet calibration for a vacuum of –0.8 bar at different line speeds; 2.50 mm die exit; 3.25 mm profile wall thickness

C.2.2 Interfacial heat transfer coefficients at the centre of the upper profile surface as function of Fourier number

In the following Figures C70 to C84, the calculated interfacial heat transfer coefficients are shown for the centre of the upper profile surface on the dependence on the Fourier number.
As for the Figures above, the Figures C70 to C72 presents the calculated values for the 1st set of experiments and in Figures C73 to C84, the 2nd set is shown.

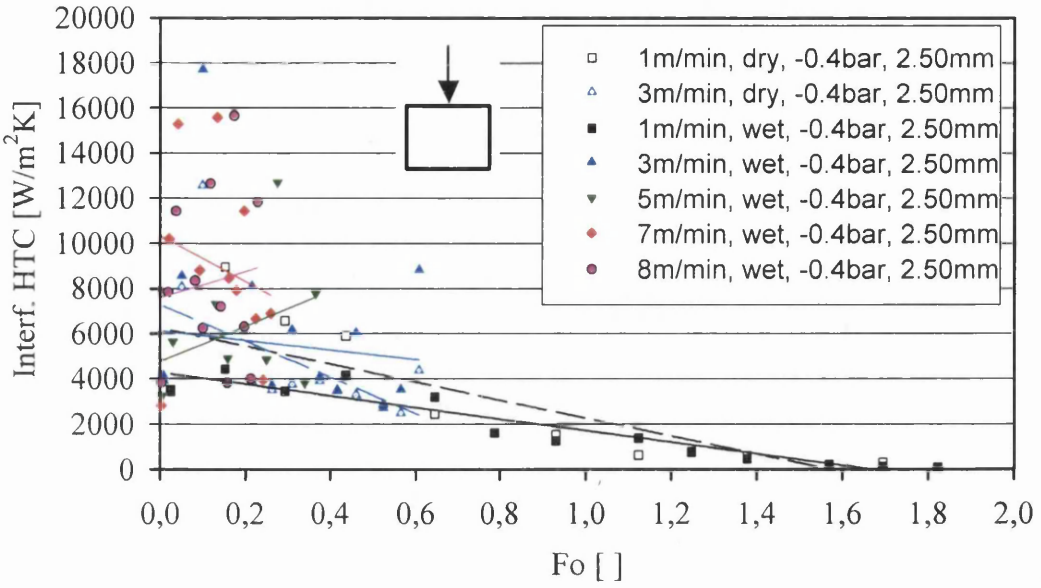

Figure C70: Interfacial heat transfer coefficients at the centre of the upper profile surface as function of the Fourier number in dry and wet calibration for a vacuum of –0.4 bar at different line speeds; 2.50 mm die exit; 2.50 mm profile wall thickness

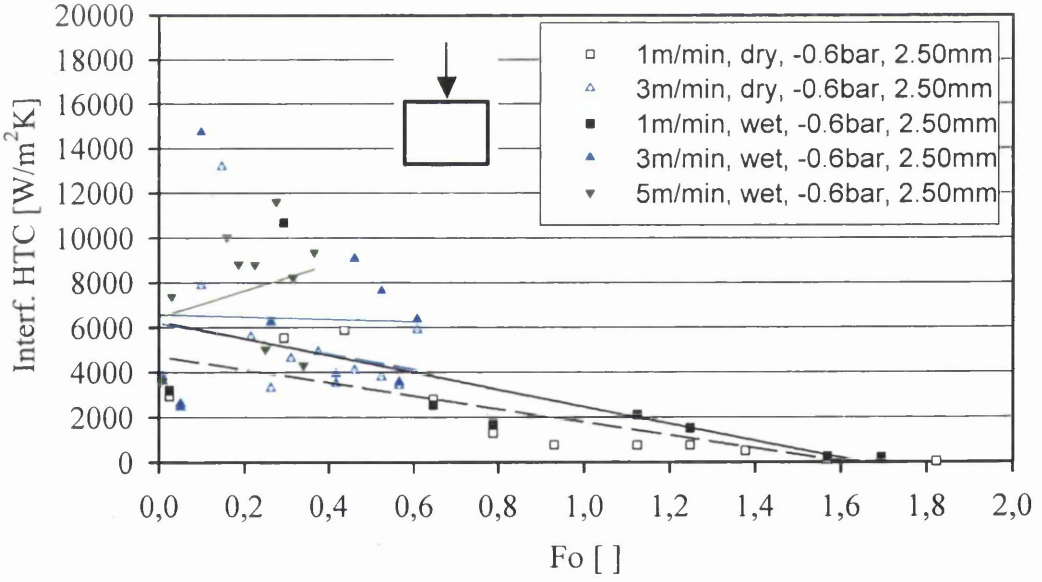

Figure C71: Interfacial heat transfer coefficients at the centre of the upper profile surface as function of the Fourier number in dry and wet calibration for a vacuum of –0.6 bar at different line speeds; 2.50 mm die exit; 2.50 mm profile wall thickness

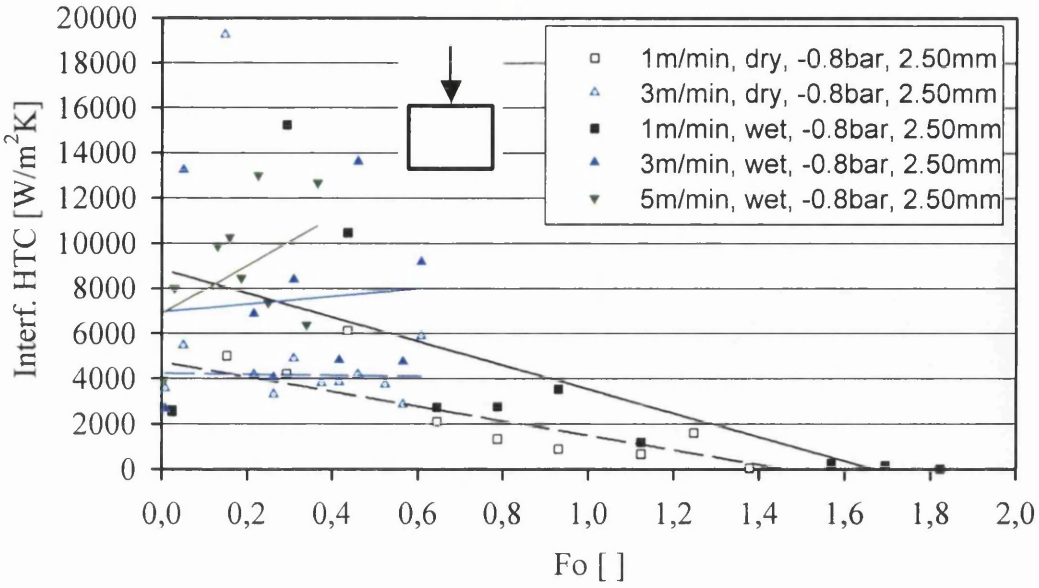

Figure C72: Interfacial heat transfer coefficients at the centre of the upper profile surface as function of the Fourier number in dry and wet calibration for a vacuum of –0.8 bar at different line speeds; 2.50 mm die exit; 2.50 mm profile wall thickness

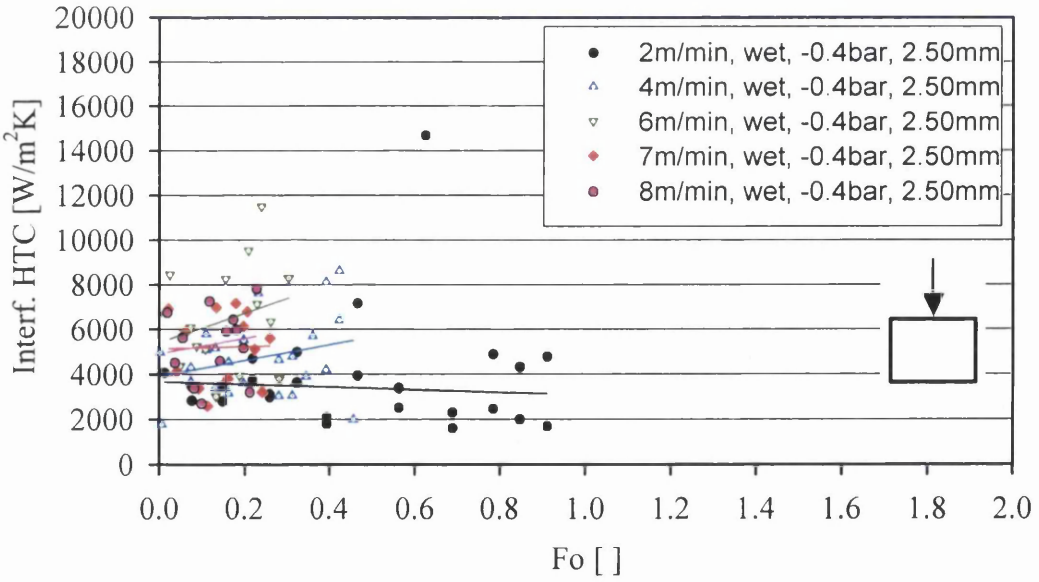

Figure C73: Interfacial heat transfer coefficients at the centre of the upper profile surface as function of the Fourier number in wet calibration for a vacuum of –0.4 bar at different line speeds; 2.50 mm die exit; 2.50 mm profile wall thickness

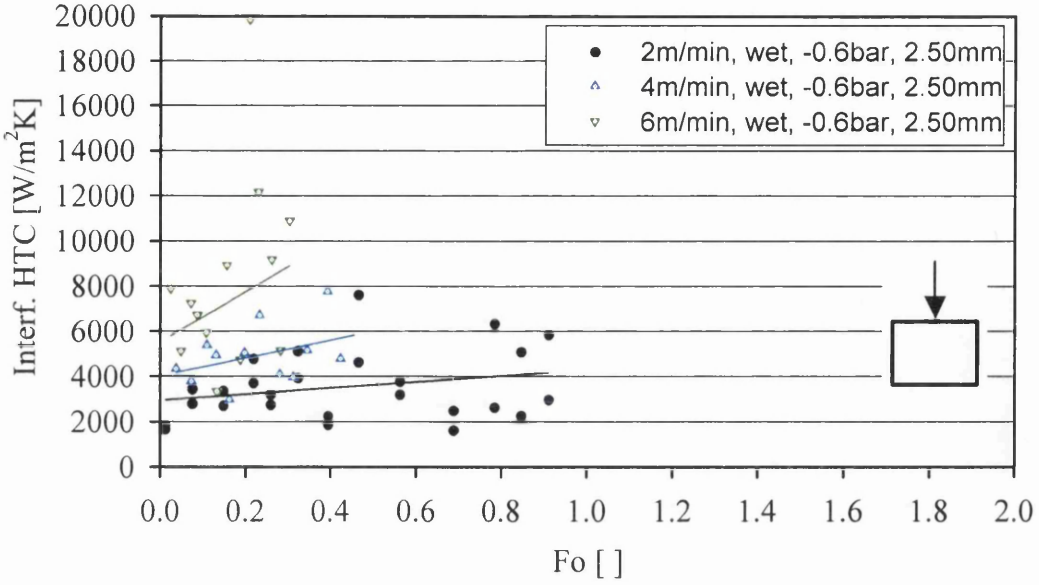

Figure C74: Interfacial heat transfer coefficients at the centre of the upper profile surface as function of the Fourier number in wet calibration; for a vacuum of –0.6 bar at different line speeds; 2.50 mm die exit; 2.50 mm profile wall thickness

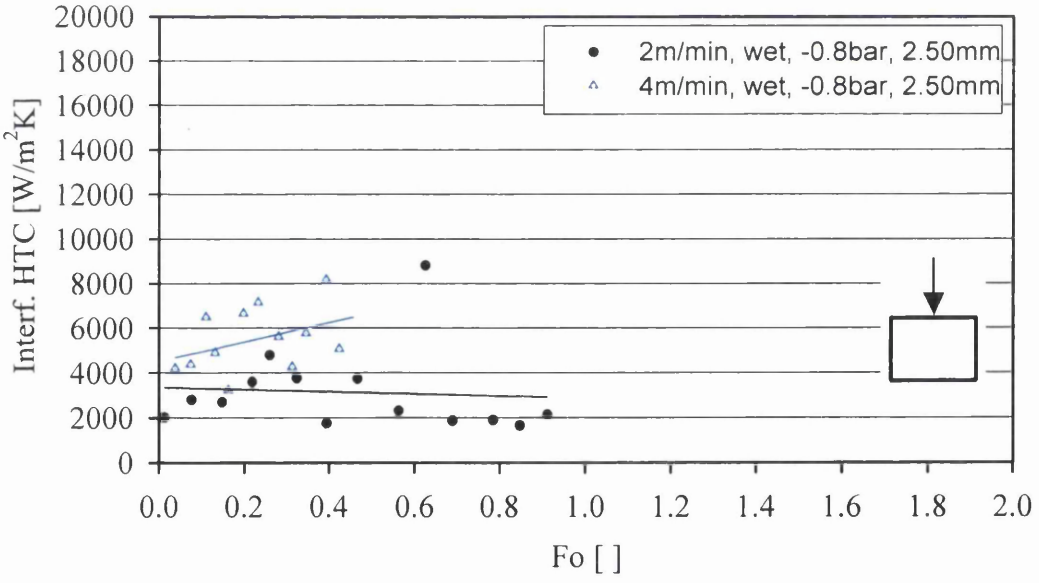

Figure C75: Interfacial heat transfer coefficients at the centre of the upper profile surface as function of the Fourier number in wet calibration for a vacuum of –0.8 bar at different line speeds; 2.50 mm die exit; 2.50 mm profile wall thickness

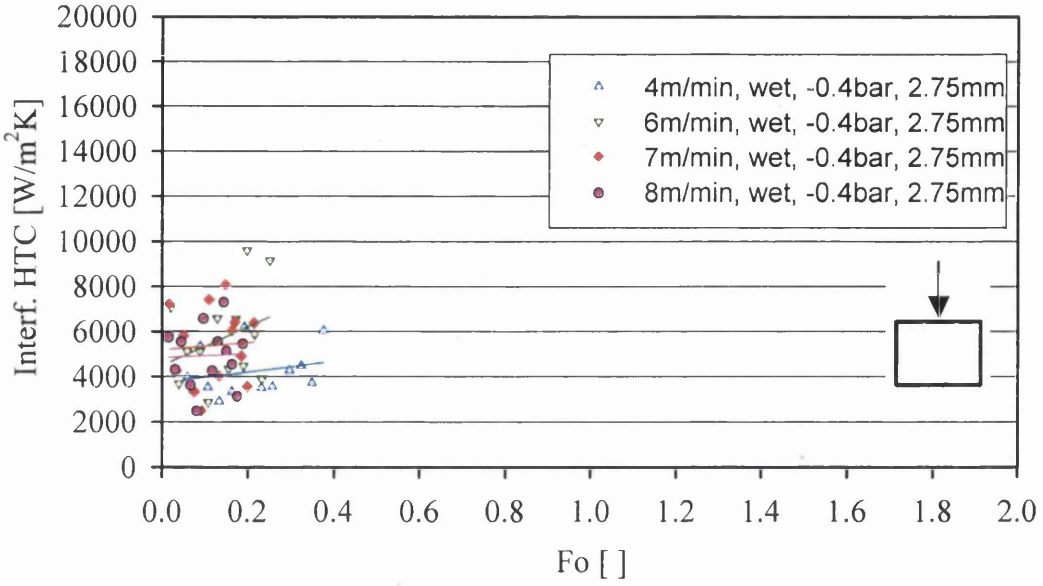

Figure C76: Interfacial heat transfer coefficients at the centre of the upper profile surface as function of the Fourier number in wet calibration for a vacuum of –0.4 bar at different line speeds; 2.50 mm die exit; 2.75 mm profile wall thickness

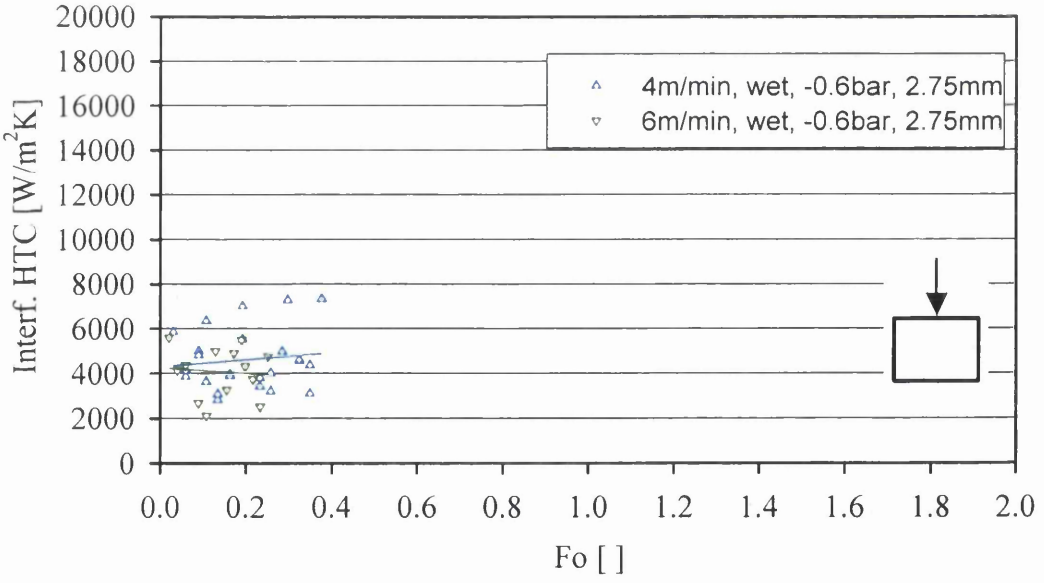

Figure C77: Interfacial heat transfer coefficients at the centre of the upper profile surface as function of the Fourier number in wet calibration for a vacuum of –0.6 bar at different line speeds; 2.50 mm die exit; 2.75 mm profile wall thickness

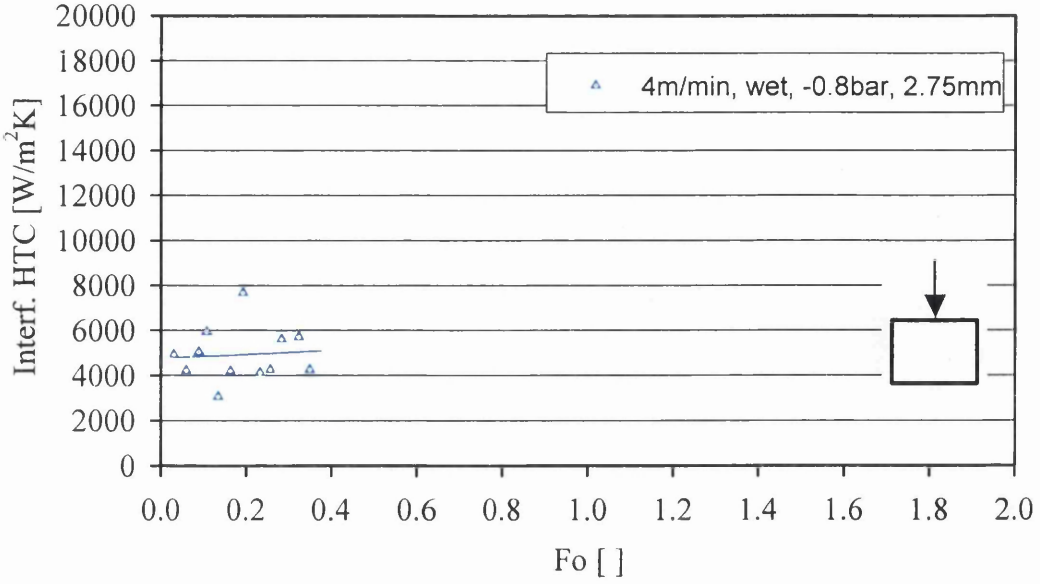

Figure C78: Interfacial heat transfer coefficients at the centre of the upper profile surface as function of the Fourier number in wet calibration for a vacuum of –0.8 bar at different line speeds; 2.50 mm die exit; 2.75 mm profile wall th

1.0 1.2
Fo [ ]

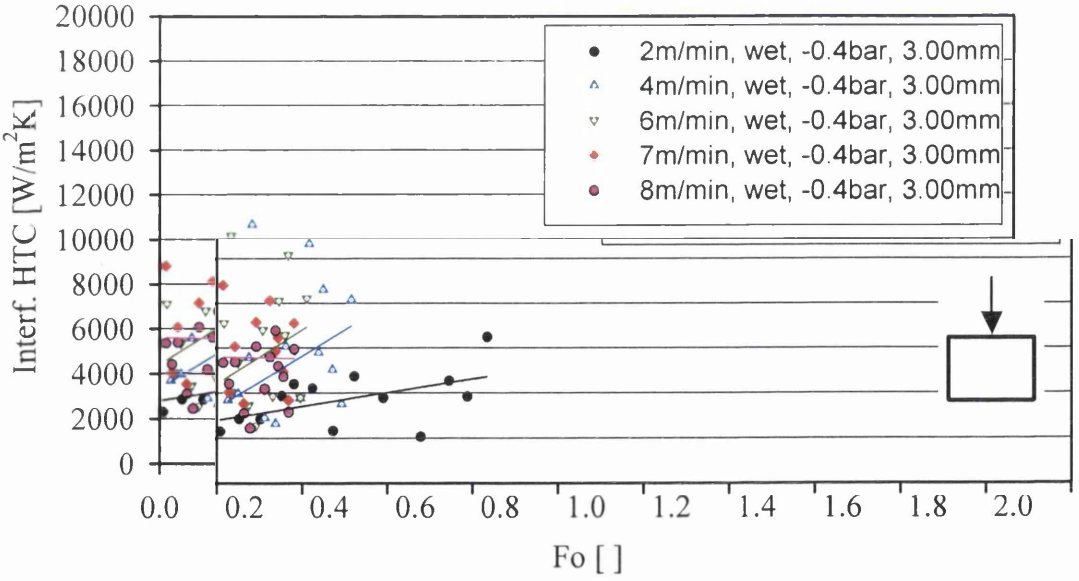

Figure C79: Interfacial heat transfer coefficients at the centre of the upper profile surface as function of the Fourier number in wet calibration for a vacuum of –0.4 bar at different line speeds; 2.50 mm die exit; 3.00 mm profile wall thickness

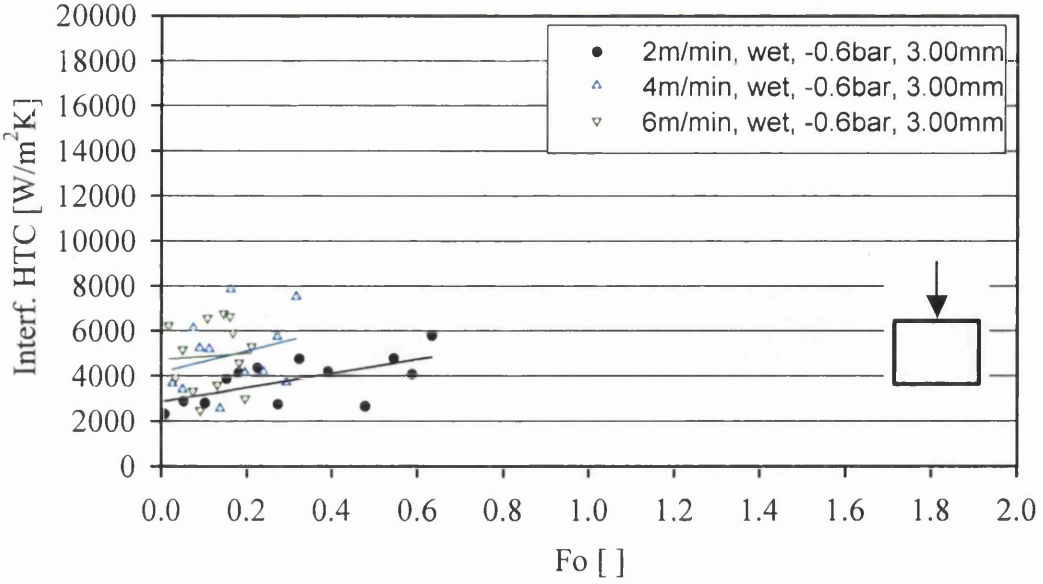

Figure C80: Interfacial heat transfer coefficients at the centre of the upper profile surface as function of the Fourier number in wet calibration for a vacuum of –0.6 bar at different line speeds; 2.50 mm die exit; 3.00 mm profile wall thickness

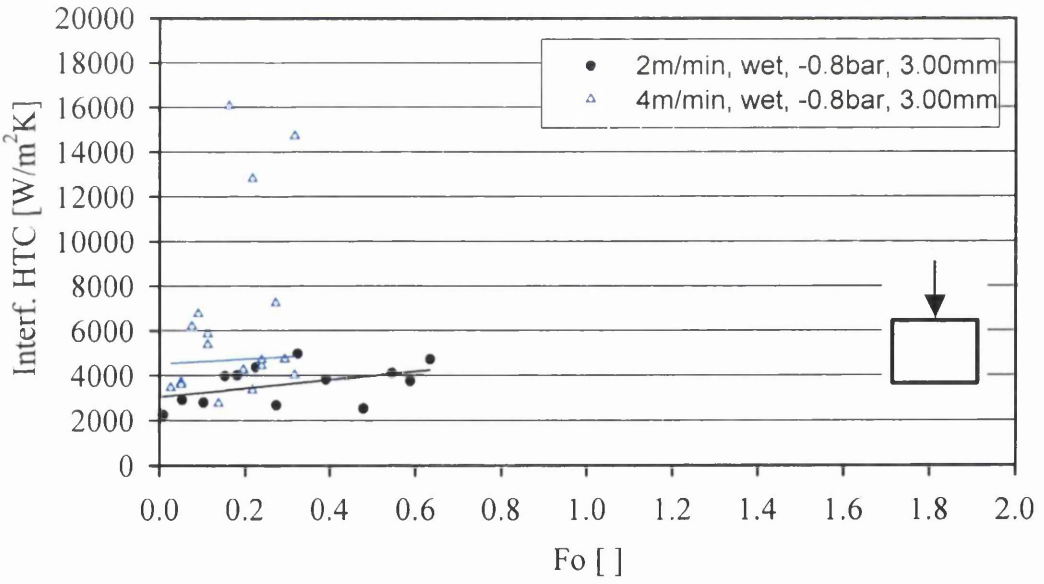

Figure C81: Interfacial heat transfer coefficients at the centre of the upper profile surface as function of the Fourier number in wet calibration for a vacuum of –0.8 bar at different line speeds; 2.50 mm die exit; 3.00 mm profile wall thickness

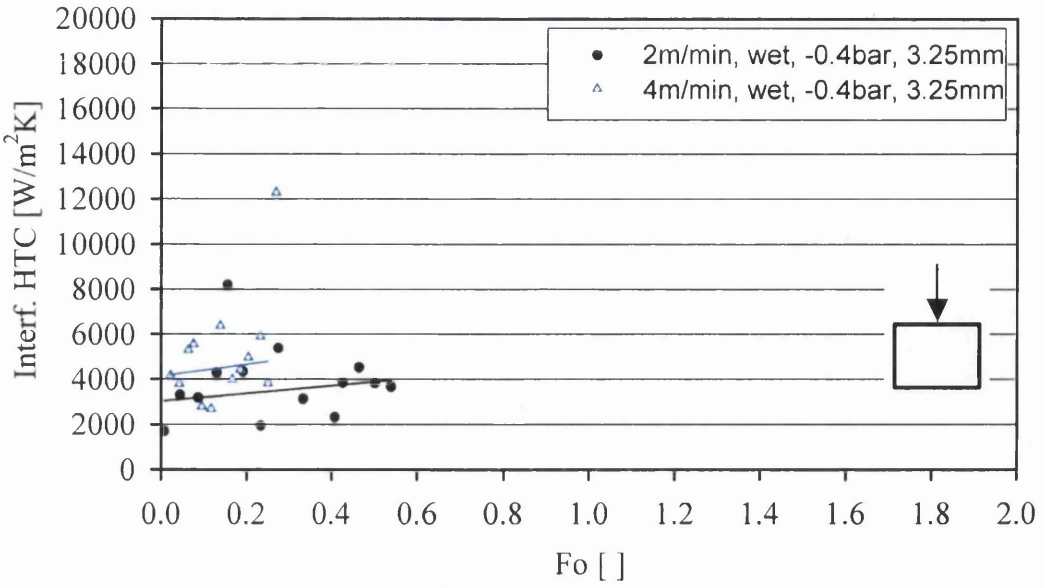

Figure C82: Interfacial heat transfer coefficients at the centre of the upper profile surface as function of the Fourier number in wet calibration for a vacuum of –0.4 bar at different line speeds; 2.50 mm die exit; 3.25 mm profile wall thickness

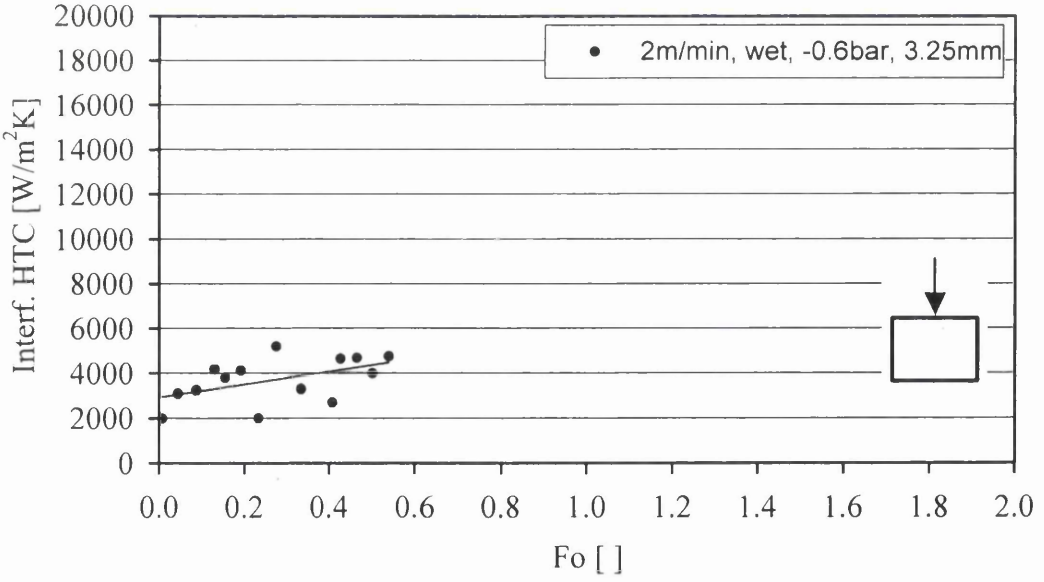

Figure C83: Interfacial heat transfer coefficients at the centre of the upper profile surface as function of the Fourier number in wet calibration for a vacuum of –0.6 bar at different line speeds; 2.50 mm die exit; 3.25 mm profile wall thickness

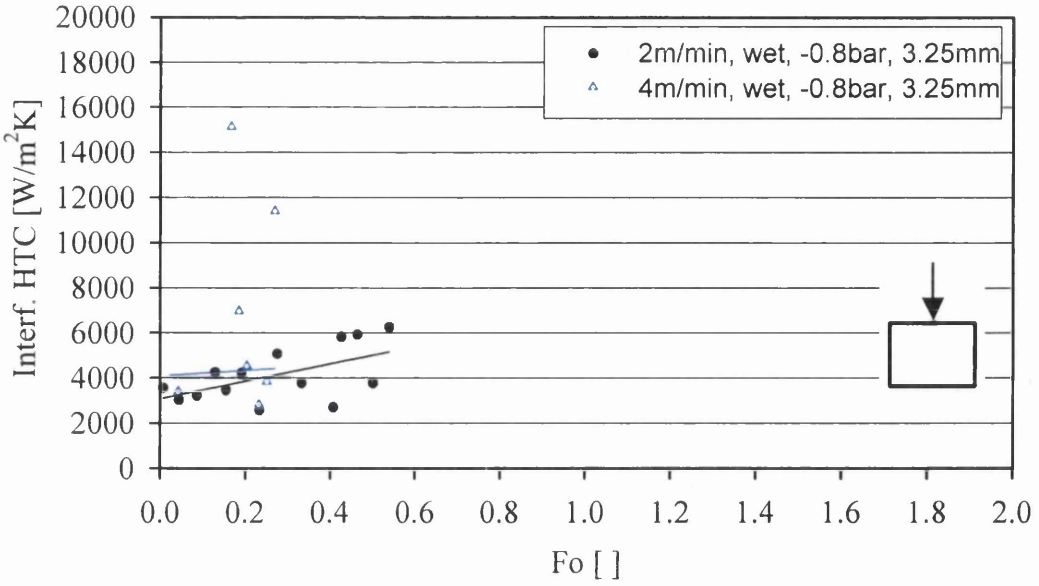

Figure C84: Interfacial heat transfer coefficients at the centre of the upper profile surface as function of the Fourier number in wet calibration for a vacuum of –0.8 bar at different line speeds; 2.50 mm die exit; 3.25 mm profile wall thickness

C.2.3 Interfacial heat transfer coefficients near the edge of the upper profile surface in downstream distance

In Figures C85 to C87, the calculated interfacial heat transfer coefficients are shown surface in dependence on downstream distance for the measurements near the edge of the upper profile surface.

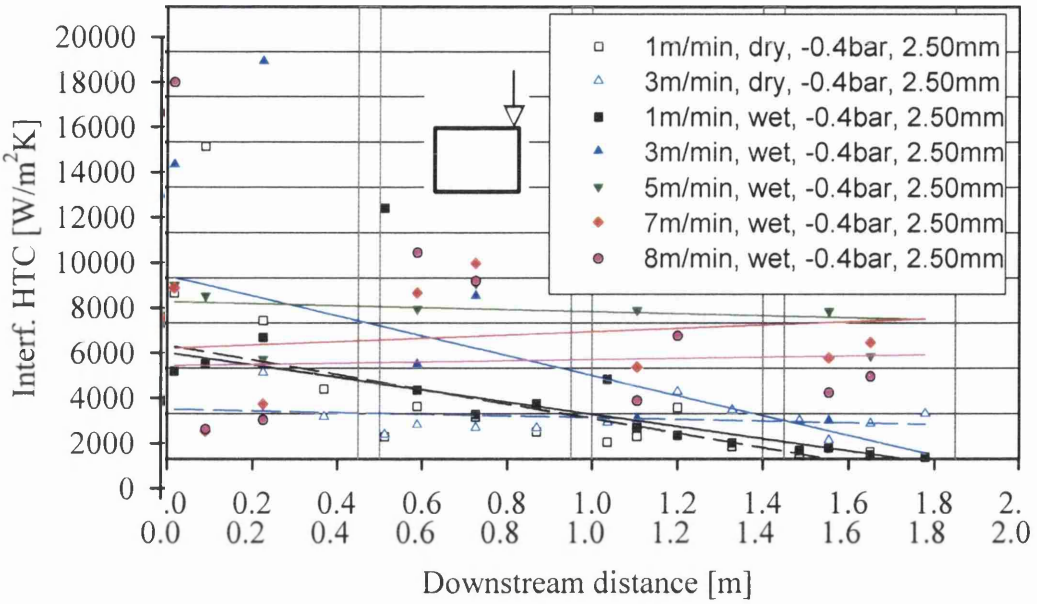

Figure C85: Interfacial heat transfer coefficients near the edge of the upper profile surface in dry and wet calibration for a vacuum of –0.4 bar at different line speeds; 2.50 mm die exit; 2.50 mm profile wall thickness

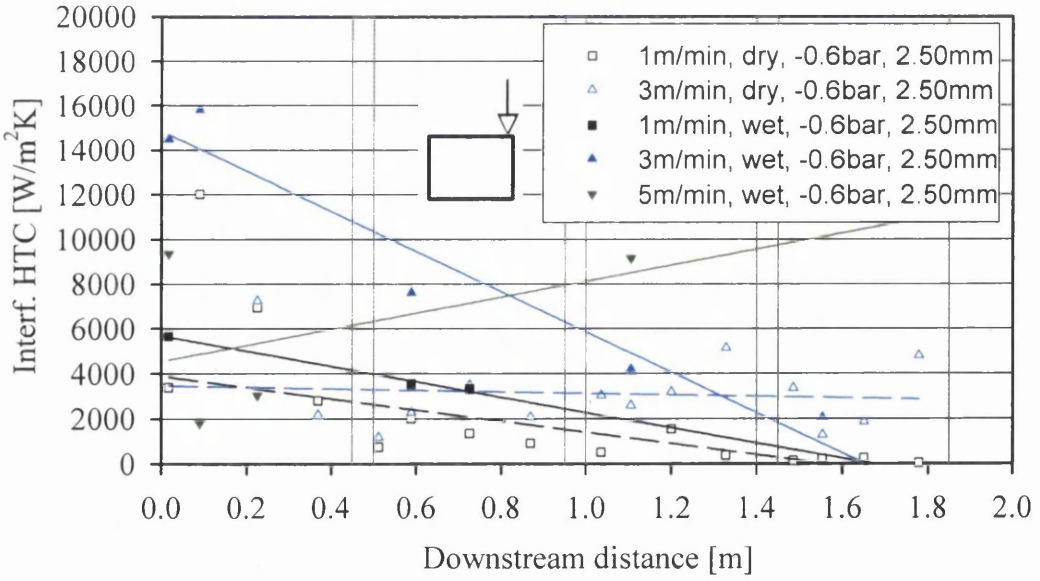

Figure C86: Interfacial heat transfer coefficients near the edge of the upper profile surface in dry and wet calibration for a vacuum of –0.6 bar at different line speeds; 2.50 mm die exit; 2.50 mm profile wall thickness

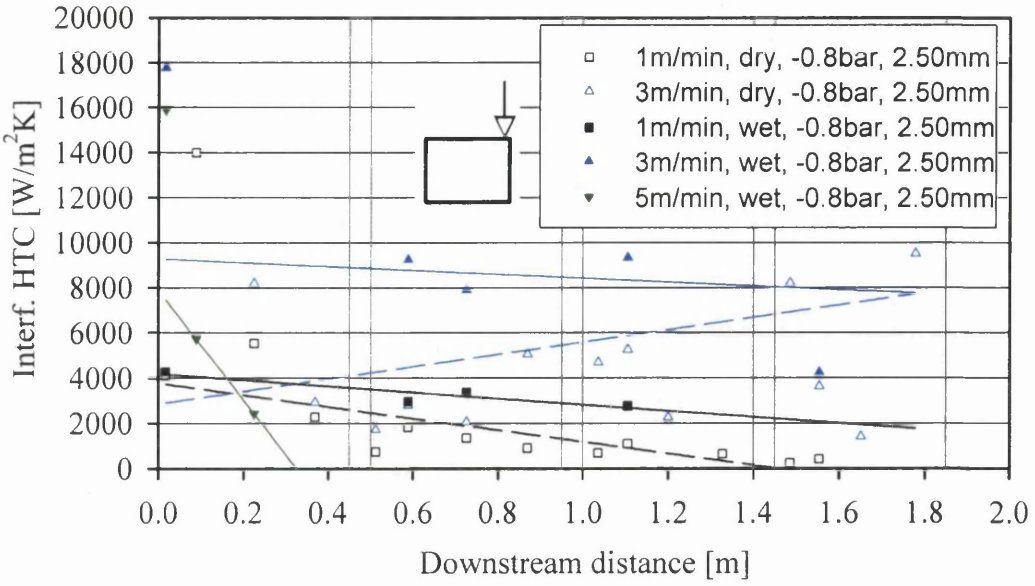

Figure C87: Interfacial heat transfer coefficients near the edge of the upper profile surface in dry and wet calibration for a vacuum of –0.8 bar at different line speeds; 2.50 mm die exit; 2.50 mm profile wall thickness

In Figures C88 to C90, the interfacial heat transfer coefficients are shown in dependence on Fourier number for the edge of the upper profile surface.

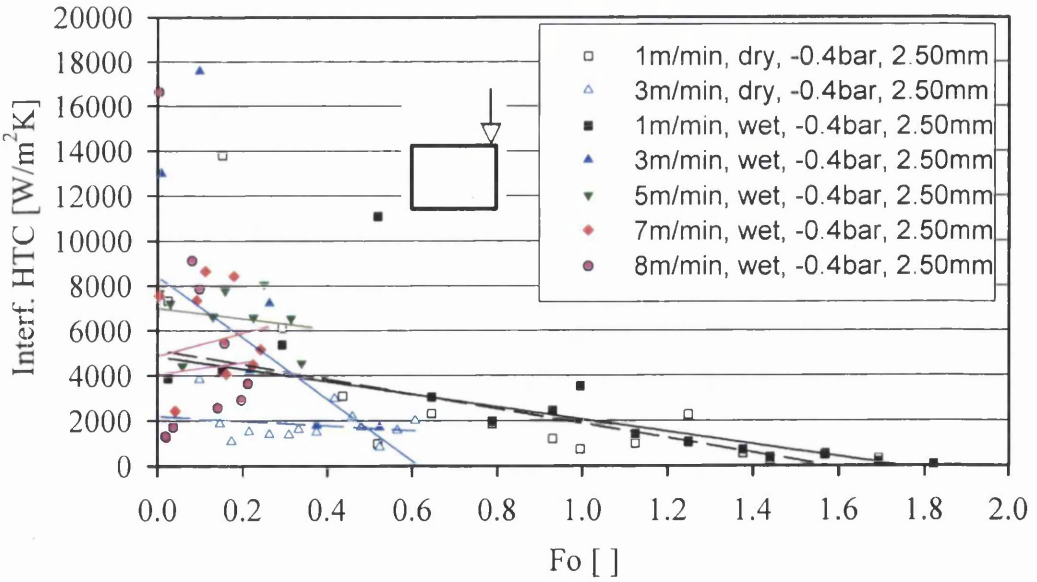

Figure C88: Interfacial heat transfer coefficients near the edge of the upper profile surface as function of the Fourier number in dry and wet calibration for a vacuum of –0.4 bar at different line speeds; 2.50 mm die exit; 2.50 mm profile wall thickness

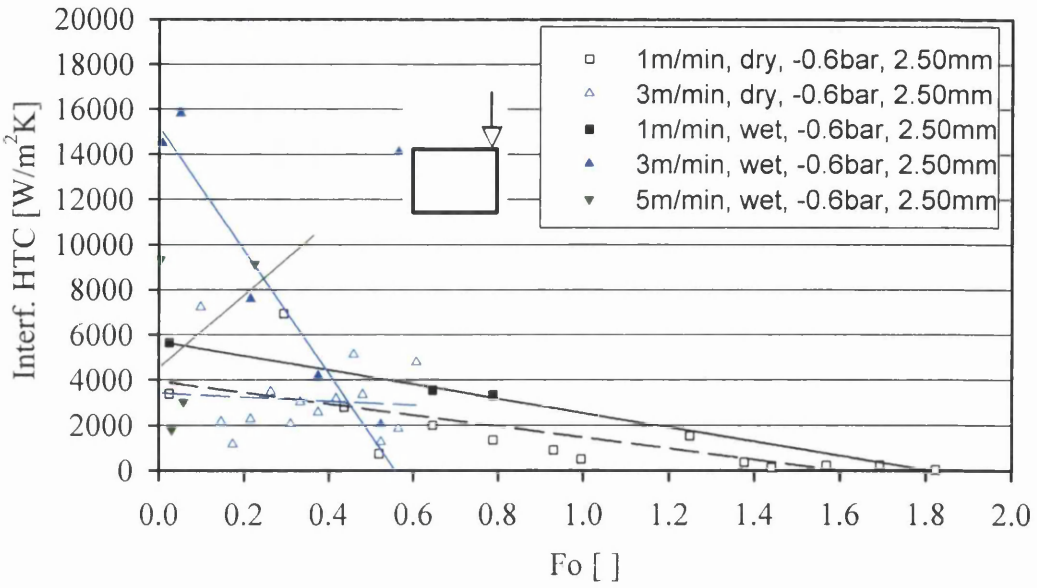

Figure C89: Interfacial heat transfer coefficients near the edge of the upper profile surface as function of the Fourier number in dry and wet calibration for a vacuum of –0.6 bar at different line speeds; 2.50 mm die exit; 2.50 mm profile wall thickness

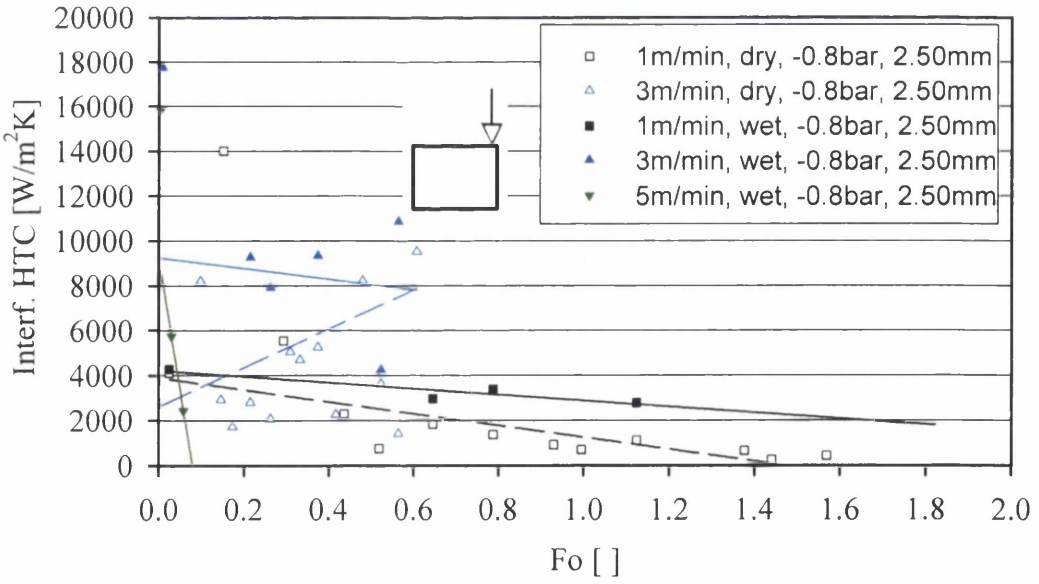

Figure C90: Interfacial heat transfer coefficients near the edge of the upper profile surface as function of the Fourier number in dry and wet calibration for a vacuum of –0.8 bar at different line speeds; 2.50 mm die exit; 2.50 mm profile wall thickness

C.2.4 Nusselt numbers of interfacial heat transfer coefficients at the centre of the upper profile surface as function of the Fourier number

In the following Figures C91 to C105, the Nusselt numbers Nu of the calculated interfacial heat transfer coefficients are shown for the centre of the upper profile. The results for the 1st set of experiments are presented in Figures C91 to C93. Figures C94 to C105 show the results of the 2nd set with variation of wall thickness from 2.50 to 3.25 mm and vacua of -0.4 to -0.8 bar.

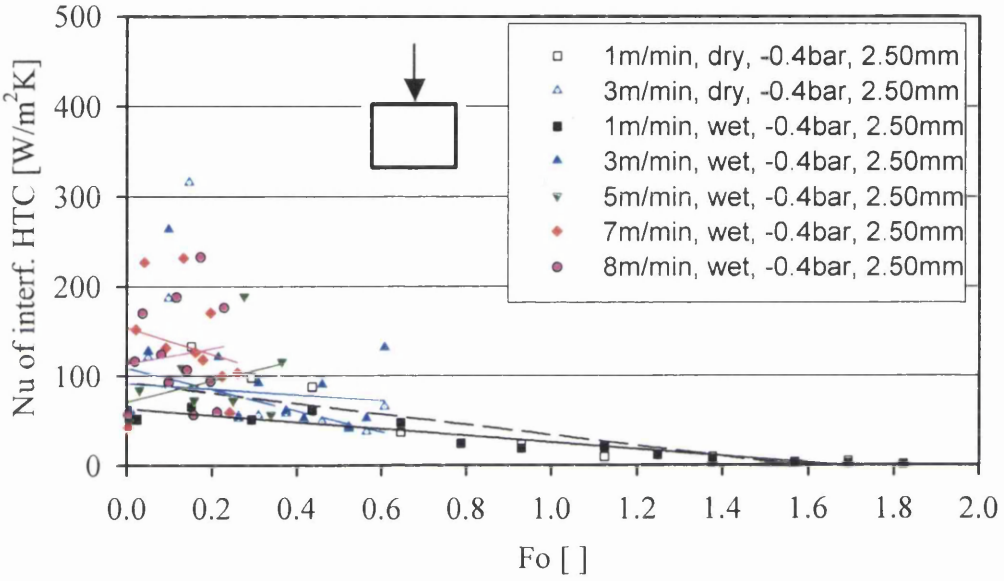

Figure C91: Nusselt numbers of interfacial heat transfer at the centre of the upper profile surface as function of the Fourier number in dry and wet calibration for a vacuum of –0.4 bar at different line speeds; 2.50 mm die exit; 2.50 mm profile wall thickness

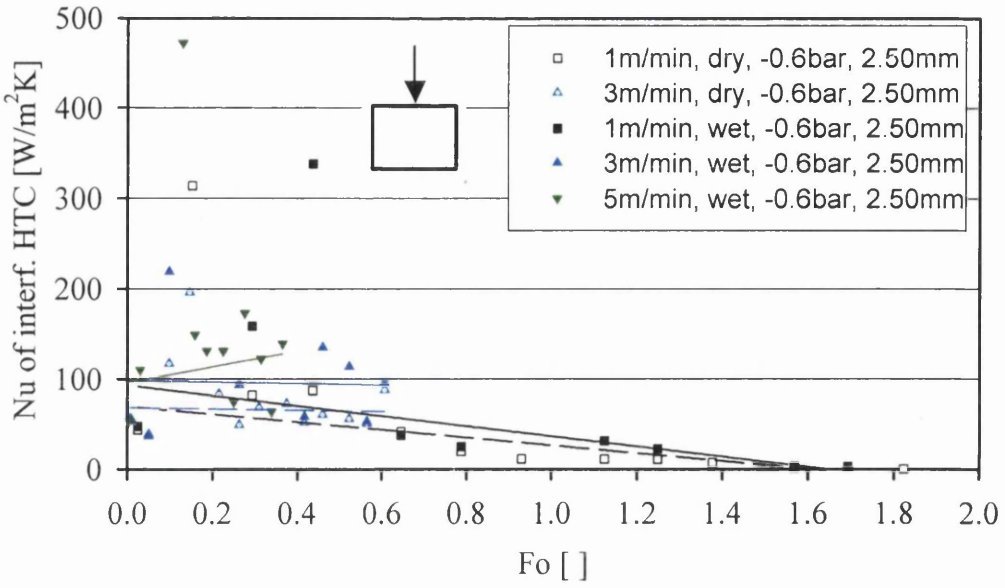

Figure C92: Nusselt numbers of interfacial heat transfer at the centre of the upper profile surface as function of the Fourier number in dry and wet calibration for a vacuum of –0.6 bar at different line speeds; 2.50 mm die exit; 2.50 mm profile wall thickness

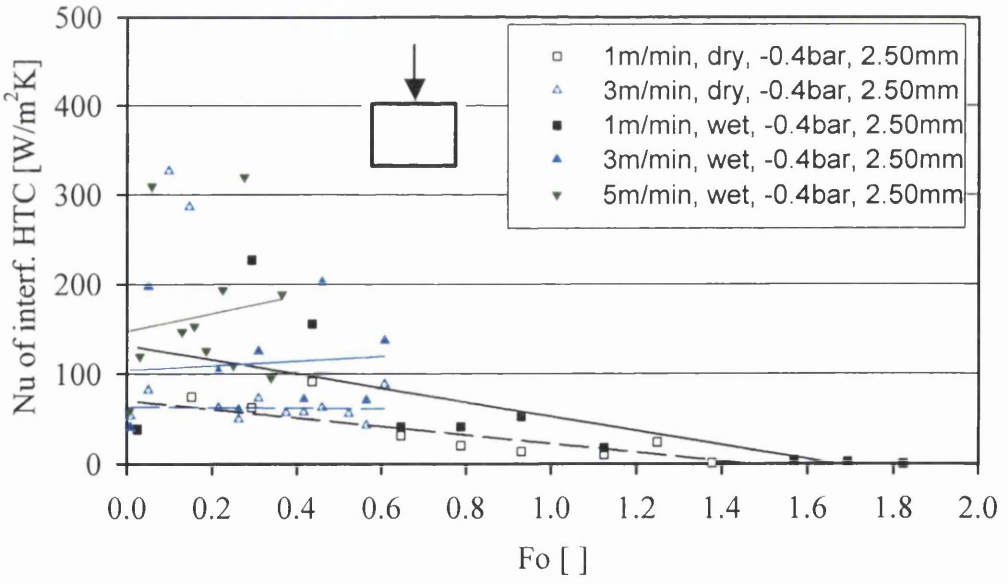

Figure C93: Nusselt numbers of interfacial heat transfer at the centre of the upper profile surface as function of the Fourier number in dry and wet calibration for a vacuum of –0.8 bar at different line speeds; 2.50 mm die exit; 2.50 mm profile wall thickness

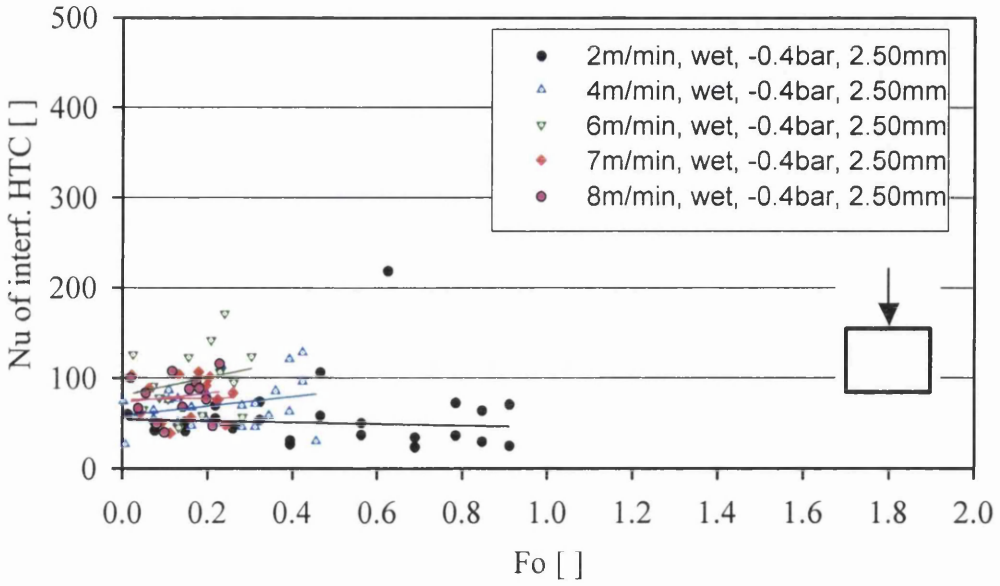

Figure C94: Nusselt numbers of interfacial heat transfer at the centre of the upper profile surface as function of the Fourier number in wet calibration for a vacuum of –0.4 bar at different line speeds; 2.50 mm die exit; 2.50 mm profile wall thickness

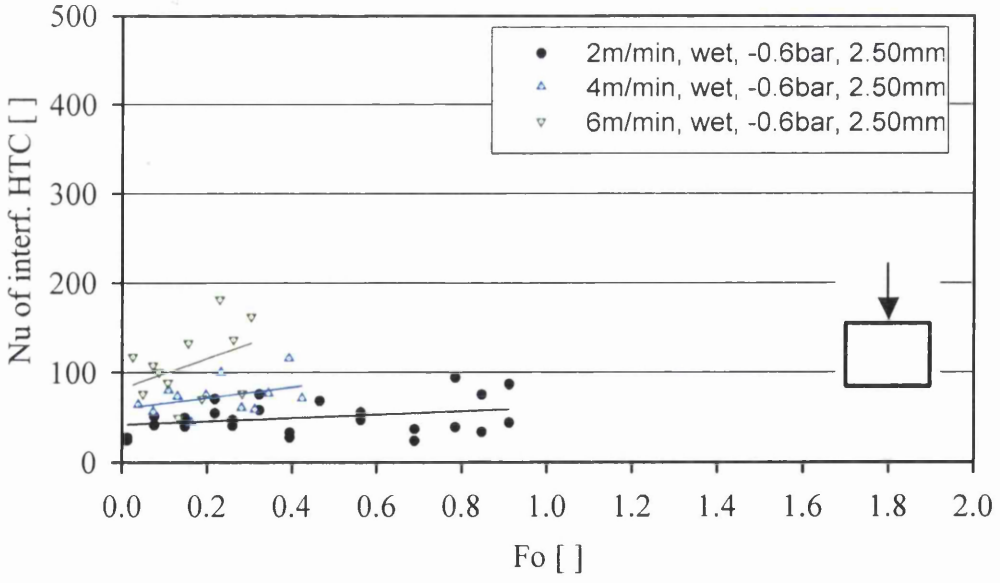

Figure C95: Nusselt numbers of interfacial heat transfer at the centre of the upper profile surface as function of the Fourier number in wet calibration for a vacuum of –0.6 bar at different line speeds; 2.50 mm die exit; 2.50 mm profile wall thickness

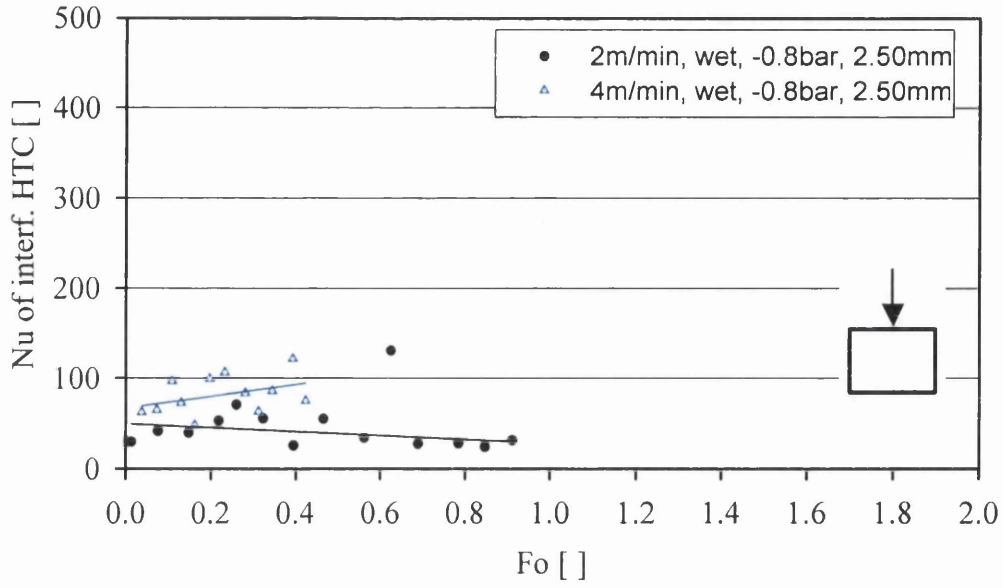

Figure C96: Nusselt numbers of interfacial heat transfer at the centre of the upper profile surface as function of the Fourier number in wet calibration for a vacuum of –0.8 bar at different line speeds; 2.50 mm die exit; 2.50 mm profile wall thickness

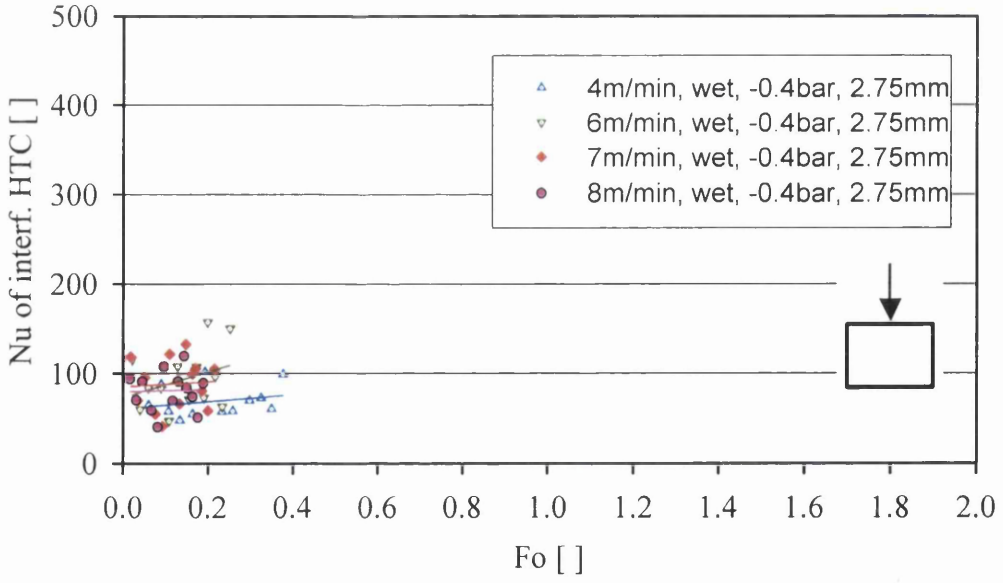

Figure C97: Nusselt numbers of interfacial heat transfer at the centre of the upper profile surface as function of the Fourier number in wet calibration for a vacuum of –0.4 bar at different line speeds; 2.50 mm die exit; 2.75 mm profile wall thickness

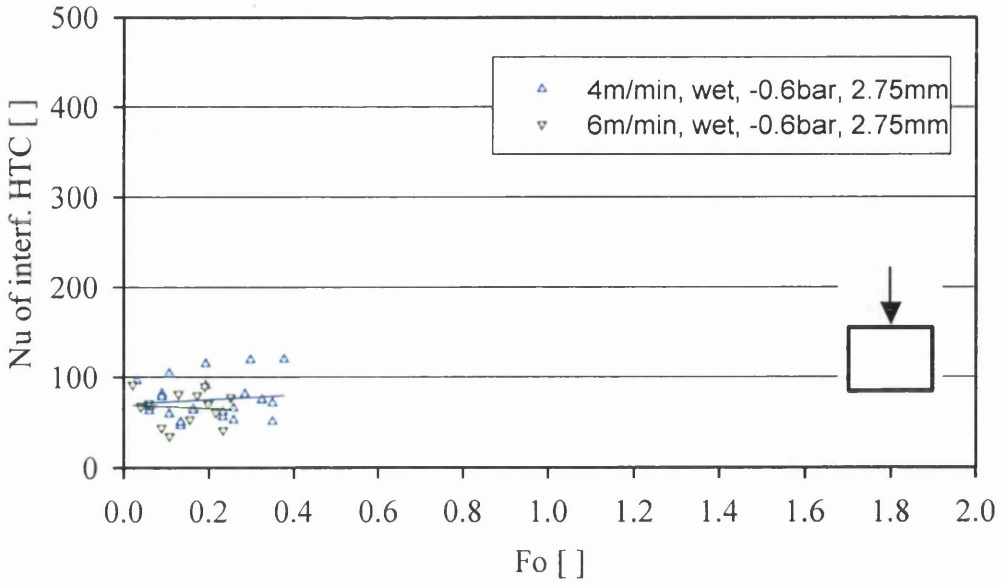

Figure C98: Nusselt numbers of interfacial heat transfer at the centre of the upper profile surface as function of the Fourier number in wet calibration for a vacuum of –0.6 bar at different line speeds; 2.50 mm die exit; 2.75 mm profile wall thickness

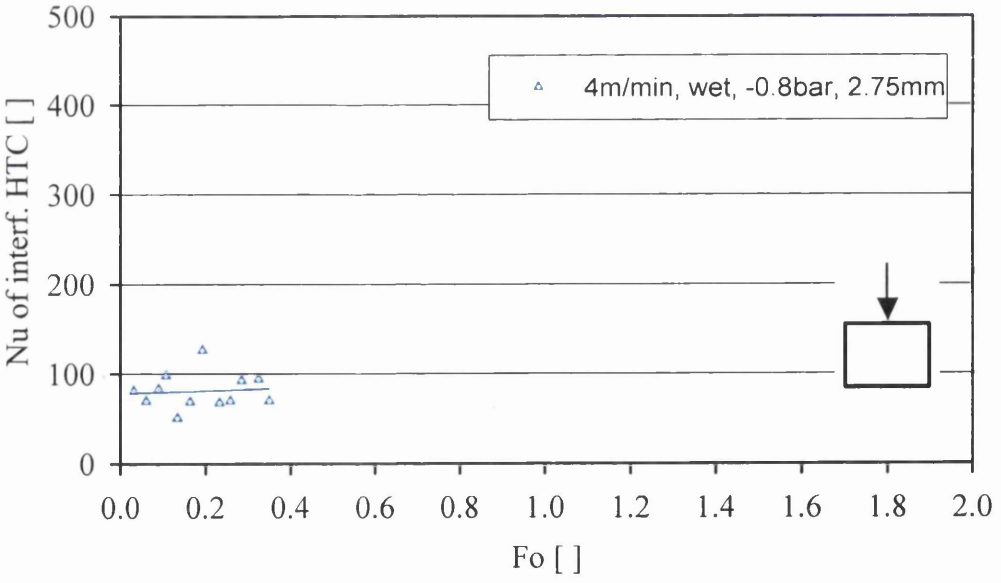

Figure C99: Nusselt numbers of interfacial heat transfer at the centre of the upper profile surface as function of the Fourier number in wet calibration for a vacuum of –0.8 bar at different line speeds; 2.50 mm die exit; 2.75 mm profile wall thickness

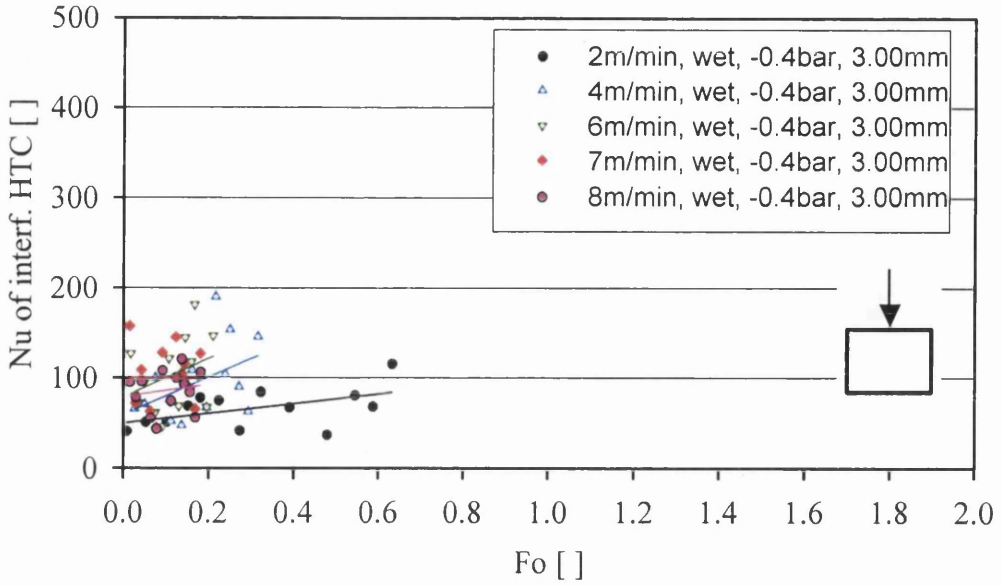

Figure C100:Nusselt numbers of interfacial heat transfer at the centre of the upper profile surface as function of the Fourier number in wet calibration for a vacuum of –0.4 bar at different line speeds; 2.50 mm die exit; 3.00 mm profile wall thickness

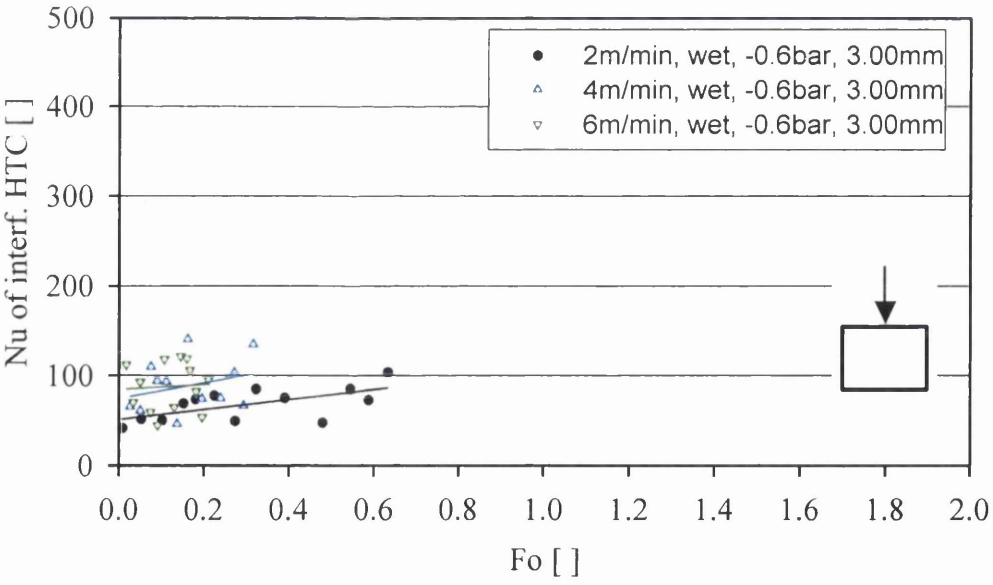

Figure C101:Nusselt numbers of interfacial heat transfer at the centre of the upper profile surface as function of the Fourier number in wet calibration for a vacuum of –0.6 bar at different line speeds; 2.50 mm die exit; 3.00 mm profile wall thickness

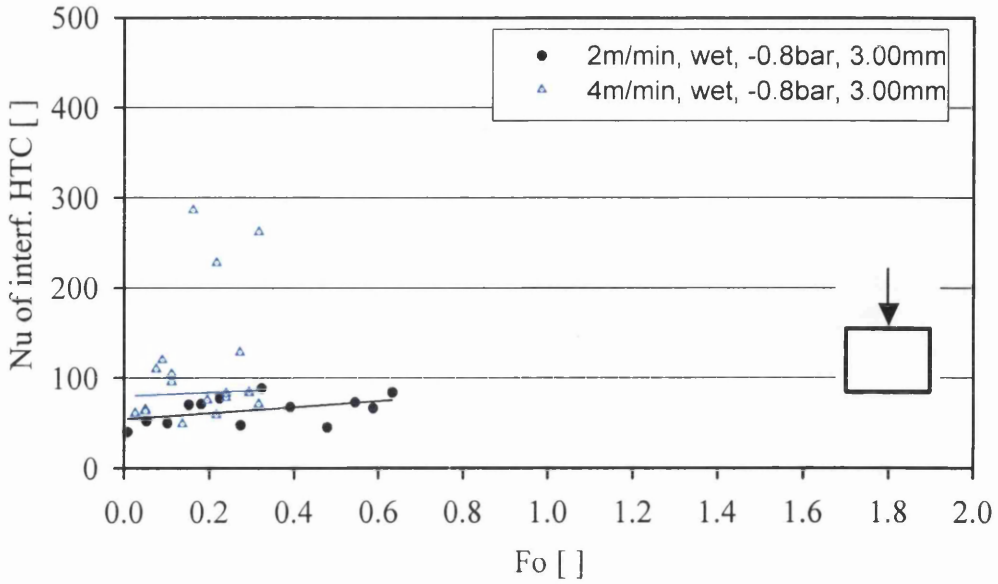

Figure C102:Nusselt numbers of interfacial heat transfer at the centre of the upper profile surface as function of the Fourier number in wet calibration for a vacuum of –0.8 bar at different line speeds; 2.50 mm die exit; 3.00 mm profile wall thickness

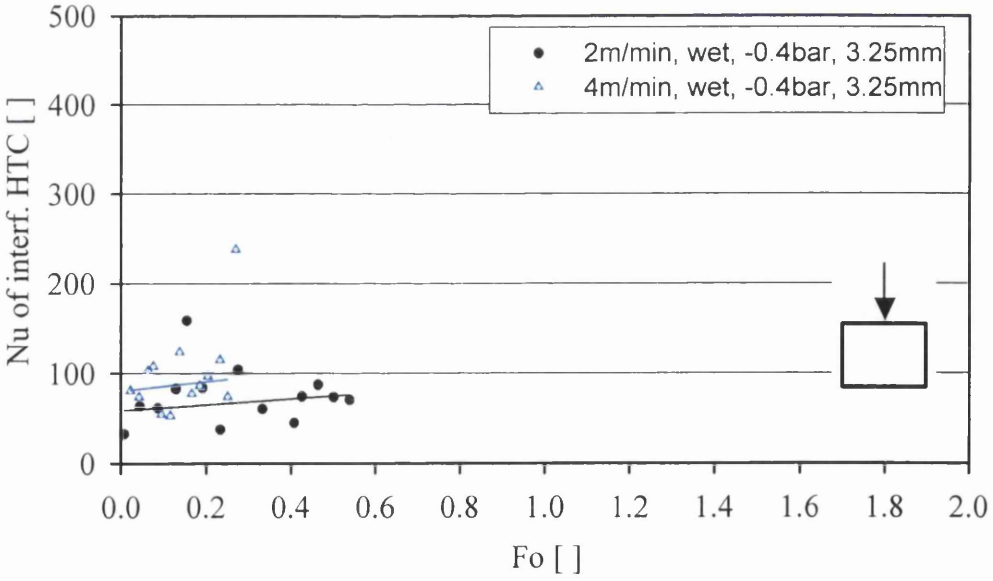

Figure C103:Nusselt numbers of interfacial heat transfer at the centre of the upper profile surface as function of the Fourier number in wet calibration for a vacuum of –0.4 bar at different line speeds; 2.50 mm die exit; 3.25 mm profile wall thickness

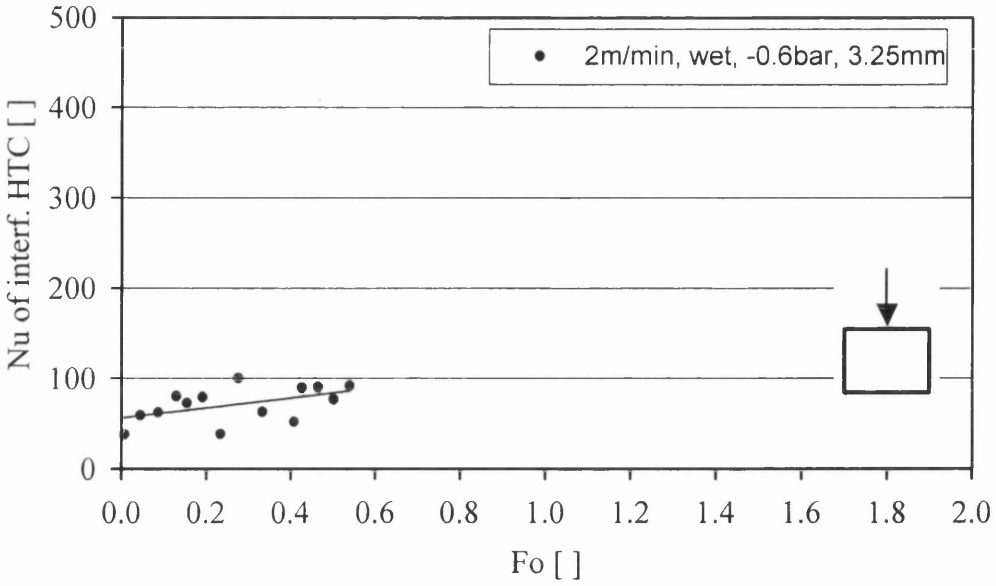

Figure C104:Nusselt numbers of interfacial heat transfer at the centre of the upper profile surface as function of the Fourier number in wet calibration for a vacuum of –0.6 bar at different line speeds; 2.50 mm die exit; 3.25 mm profile wall thickness

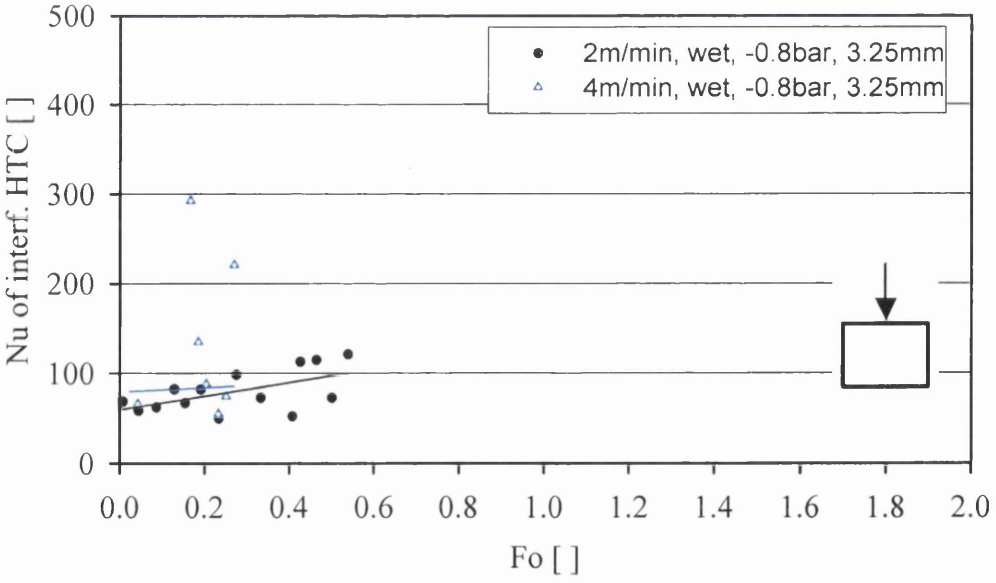

Figure C105:Nusselt numbers of interfacial heat transfer at the centre of the upper profile surface as function of the Fourier number in wet calibration for a vacuum of –0.8 bar at different line speeds; 2.50 mm die exit; 3.25 mm profile wall thickness

C.2.5 Nusselt numbers of calculated interfacial heat transfer coefficients near the edge of the upper profile surface as function of the Fourier number

In Section C.2.5, the Nu numbers for the edge of the 1st set of experiments are shown on dependence of the Fo number for vacua of –0.4 to –0.8 bar at constant wall thickness of 2.50 mm, Figures C106 to C108.

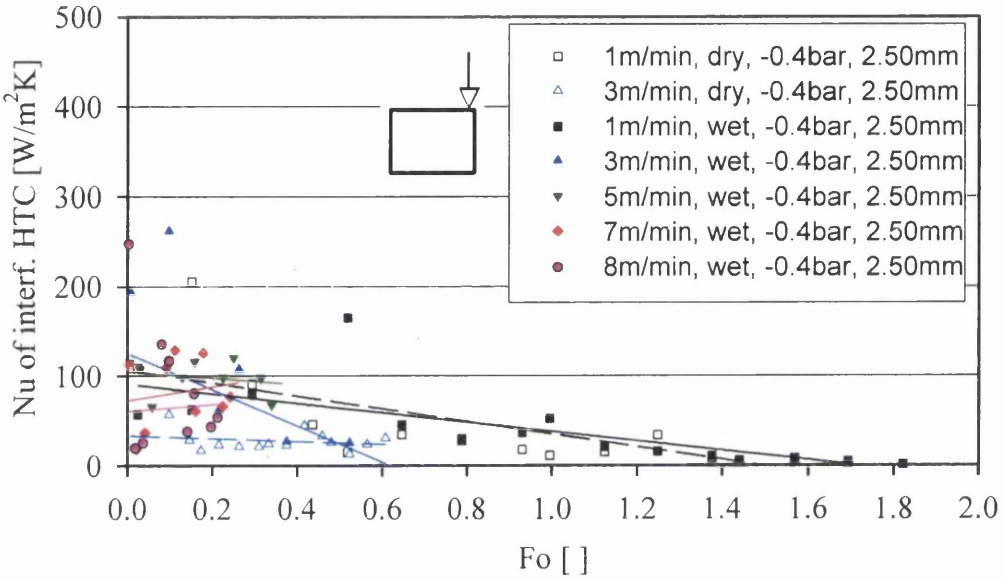

Figure C106:Nusselt numbers of interfacial heat transfer near the edge of the upper profile surface as function of the Fourier number in dry and wet calibration for a vacuum of –0.4 bar at different line speeds; 2.50 mm die exit; 2.50 mm profile wall thickness

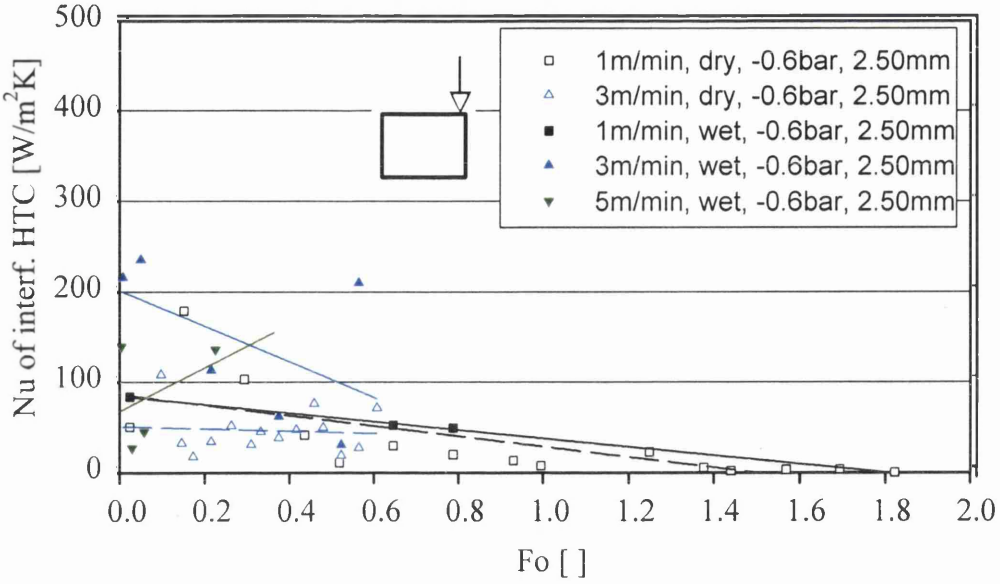

Figure C107:Nusselt numbers of interfacial heat transfer near the edge of the upper profile surface as function of the Fourier number in dry and wet calibration for a vacuum of –0.6 bar at different line speeds; 2.50 mm die exit; 2.50 mm profile wall thickness

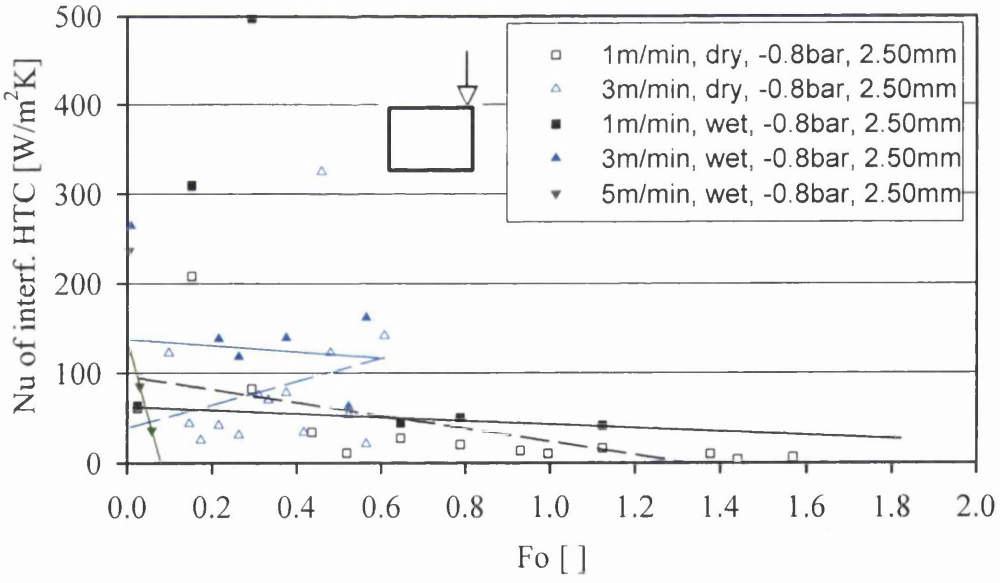

Figure C108:Nusselt numbers of interfacial heat transfer near the edge of the upper profile surface as function of the Fourier number in dry and wet calibration for a vacuum of –0.8 bar at different line speeds; 2.50 mm die exit; 2.50 mm profile wall thickness